MECHANICAL TESTING FOR DEFORMATION MODEL DEVELOPMENT

Rohde/Swearengen, *editors*

ASTM STP 765

MECHANICAL TESTING FOR DEFORMATION MODEL DEVELOPMENT

A symposium
sponsored by ASTM
Committee E-28
on Mechanical Testing
Bal Harbour, Fla., 12–13 Nov. 1980

ASTM SPECIAL TECHNICAL PUBLICATION 765
R. W. Rohde and J. C. Swearengen,
Sandia National Laboratories, editors

ASTM Publication Code Number (PCN)
04-765000-23

1916 Race Street, Philadelphia, Pa. 19103

Library of Congress Catalog Card Number: 81-69407

Printed in Baltimore, Md.
April 1982

Foreword

The Symposium on Mechanical Testing for Deformation Model Development, sponsored by ASTM Committee E-28 on Mechanical Testing, was held in Bal Harbour, Florida, on 12–13 November 1980. R. W. Rohde and J. C. Swearengen, Sandia National Laboratories, served as symposium chairmen and have edited this publication.

Related ASTM Publications

Stress Relaxation Testing, STP 676 (1979), 04-676000-23

Formability Topics—Metallic Materials, STP 647 (1978), 04-647000-23

Reproducibility and Accuracy of Mechanical Tests, STP 626 (1977), 04-626000-23

Selection and Use of Wear Tests for Metals, STP 615 (1977), 04-615000-23

Recent Developments in Mechanical Testing, STP 608 (1976), 04-608000-23

A Note of Appreciation to Reviewers

This publication is made possible by the authors and, also, the unheralded efforts of the reviewers. This body of technical experts whose dedication, sacrifice of time and effort, and collective wisdom in reviewing the papers must be acknowledged. The quality level of ASTM publications is a direct function of their respected opinions. On behalf of ASTM we acknowledge with appreciation their contribution.

ASTM Committee on Publications

Editorial Staff

Contents

MICROSTRUCTURAL EVOLUTION AND DERIVED MODELS

SUMMARY

Introduction

Lately there has been increased emphasis placed on the development of models to describe and predict the inelastic deformation of metals. This effort has been motivated by the need for structural materials to perform reliably in increasingly severe chemical, mechanical, and thermal environments. Historically, progress in modeling followed two paths. The applied mechanics discipline attempted to describe observed macroscopic behavior on the basis of analytically tractable empirical or phenomenological models. While such models could be made to describe data with considerable precision, they were not physically or microstructurally based and could not be extrapolated beyond areas of measurement with confidence, since deformation mechanisms could change and alter material behavior. Alternatively, the materials discipline sought to understand the micromechanisms of plastic deformation and to quantify unit processes. Numerous microscopic deformation mechanisms have been discovered and quantified but, unfortunately, attempts to cast deformation models by combining simple unit processes results in such complex general expressions as to render them useless.

Recent years have seen the amalgamation of the often empirical analytical mechanics approach and the more complex but physically based materials science approach with the proposal of a number of "unified creep-plasticity" or "equation-of-state" descriptions of deformation. So called equation-of-state models represent an awareness that current deformation behavior is dependent upon microstructure and its evolution, and they are often cast in terms of equations whose functional forms are found in more fundamental microstructural models. Moreover, if such models could appropriately map microstructure evolution and damage they could find applicability to describing and predicting fracture.

It was the intent of this symposium to stimulate further this interdisciplinary approach to deformation modeling by providing a vehicle for increased communication between analytical mechanics and materials science disciplines. This intent is reflected in the organization of papers published in this volume. Three categories have been chosen:

Implications of Experimental Techniques—demonstrating the need for careful experimentation and data interpretation in model development and the utility of specific experimental approaches.

Phenomenological Modeling and Applications—presenting techniques, often based on unified creep-plasticity or equation of state concepts, to describe and predict inelastic deformation. These techniques are essentially mechanics based, without explicit reference to microstructure.

Microstructural Evolution and Derived Models—stressing studies of micromechanisms of deformation and the development of deformation microstructures, with attempts to include these microscopic details in more global deformation descriptions. Basically this section presents materials science studies.

It is obvious that because there can be considerable overlap in these selected areas, some papers can be appropriately placed under more than one heading. The location of these papers was thus somewhat arbitrary, but motivated by a desire for topical balance.

Major topics in each of the three categories are covered through comprehensive invited papers. These, supported by the contributed papers, provide a state-of-the-art representation of the field, thereby making the volume useful to the advanced practitioner. It is hoped that this volume will serve as a source work to those developing advanced deformation models by combining under one cover current analytical methods and those microstructural and microdeformation observations necessary for inclusion if current deformation models are to be improved. The volume also includes several papers of a review or tutorial nature which can be of value to the worker planning entrance into the field.

This publication is sponsored by ASTM Committee E-28 on Mechanical Testing. We acknowledge the contributions made by authors, reviewers, and the session chairmen, R. D. Krieg, T. H. Alden, E. Krempl and A. K. Miller.

R. W. Rohde

Sandia National Laboratories, Albuquerque, New Mexico; symposium co-chairman and co-editor

J. C. Swearengen

Sandia National Laboratories, Livermore, California; symposium co-chairman and co-editor

Implications of Experimental Techniques

Erhard Krempl[1]

The Role of Servocontrolled Testing in the Development of the Theory of Viscoplasticity Based on Total Strain and Overstress

REFERENCE: Krempl, Erhard, "**The Role of Servocontrolled Testing in the Development of the Theory of Viscoplasticity Based on Total Strain and Overstress,**" *Mechanical Testing for Deformation Model Development, ASTM STP 765,* R. W. Rohde and J. C. Swearengen, American Society for Testing and Materials, 1982, pp. 5-28.

ABSTRACT: The rate-dependent properties of AISI Type 304 stainless steel and of the high-strength Ti-7Al-2Cb-1Ta alloy obtained with tension specimens using a servocontrolled testing machine at room temperature are discussed. Tests involve strain rates between 10^{-8} and 10^{-2} s^{-1}, strain rate changes, relaxation periods, stress rates between 10^{-1} and 10^{2} MPa s^{-1}, and creep periods.

The viscoplasticity model based on total strain and overstress is introduced and shown to qualitatively reproduce the properties observed under strain control. The theory is then examined for its qualitative prediction under stress control, and it is found that the average creep rate need not increase with an increase in stress owing to the overstress (effective stress) dependence of the creep rate. Numerical experiments illustrate this property, which is then confirmed by real experiments.

The theory has two material functions representing work hardening and rate dependence. A method of determining the function representing rate dependence from strain rate change tests is discussed. For Type 304 stainless steel this function is represented by two equivalent expressions which can be used from static (10^{-8} s^{-1}) to dynamic strain rates (10^{3} s^{-1}). A rate sensitivity factor M (akin to the m-factor used in materials science) is introduced. It is shown to vary with overstress or strain rate.

KEY WORDS: stainless steel, Ti-alloy, rate dependence, creep, relaxation, servocontrolled testing, constitutive equations, viscoelasticity, viscoplasticity

Servocontrolled mechanical testing machines using feedback principles have been frequently employed in fatigue (low and high cycle) as well as in fracture mechanics testing. They have, however, not been widely used in the

---

[1] Professor of Mechanics, Department of Mechanical Engineering, Rensselaer Polytechnic Institute, Troy, N.Y. 12181.

study of the deformation behavior of solids. Servocontrolled testing machines together with proper extensometry can give considerable insight into the phenomenological, time-dependent properties of structural metals which is vital for deformation model (constitutive equation) development. In turn, when a deformation model has been found it suggests specific tests which can be carried out reliably with servocontrolled testing machines. The purpose of the paper is to demonstrate the interplay between testing and deformation model development, and the determination of material functions using the viscoplasticity theory based on total strain and overstress as an example.

Experimental Setup and Test Material

All tests were run on tension specimens with a cylindrical uniform gage section (their diameter ranged from 6.35 to 7.62 mm) using an MTS clip-on extensometer of 25.4 mm gage length. Both load (stress) and displacement (strain) control were used to govern the rate of load application of an MTS tension-torsion servohydraulic testing machine operating in the axial mode. Only the ramp option of the function generator was used together with "hold" to introduce periods of creep (when in load control) or of relaxation (when in displacement control).

Load and displacement were recorded on Esterline Angus XY recorders. In some cases the optional time base of these recorders was used.

During a relaxation and a creep test the variation of stress and of strain with time can be recorded, respectively. From these records the instantaneous stress (strain) rate can be computed. A measure of the average stress (strain) rate is the total stress (strain) change observed on the σ-ϵ plane in a *constant* time interval. A high average rate causes more change than a low average rate.

AISI Type 304 stainless steel (from DOE Reference Heat 9T2796, donated by the Department of Energy) in the annealed condition and the Ti-7Al-2Cb-1Ta titanium alloy (donated by the Naval Research Laboratory through T. W. Crooker) after β-anneal were tested at *room temperature*. The stainless steel is a low-strength, high-ductility material with considerable work-hardening capacity. The Ti-alloy possesses a high strength and low ductility and shows very little work hardening.

Details of the experimentation, specimen size, and heat treatment are given in Krempl [*1*] and Kujawski and Krempl [*2*].[2]

Data Analysis

A macroscopically uniform state of stress (engineering stress $\sigma \equiv$ load/initial area) and a uniform state of strain (axial strain $\epsilon \equiv$ change in

---

[2] The italic numbers in brackets refer to the list of references appended to this paper.

gage length/initial gage length, and two transverse strain components) are assumed to exist. If only slow motions (acceleration terms are negligible) are employed, then the measured relation between σ and ϵ represents the material response under the applied input (command signal). The servocontrol and the displacement measurement on the gage length ensure that machine influences on the measured responses are minimized. Since stress is determined entirely by equilibrium considerations, it is not possible to measure internal stresses (stresses resulting from inhomogeneous material distributions, such as grains and grain boundaries) by this method.

Stress and strain rate are simply obtained by time differentiation of the stress and strain versus time signal. A distinction is made between load (stress) control and displacement (strain) control. A creep test occurs if $\dot{\sigma} = 0$; for relaxation, $\dot{\epsilon} = 0$ is required. While time-dependent processes normally referred to as creep act during relaxation we do not refer to them as creep in this paper. This term is reserved for time-dependent deformation under constant engineering or true stress.

Experimental Results

Dependence of Relaxation on Prior Strain Rate

Tension tests in the plastic range (where the tangent modulus is small compared with the elastic modulus and changes slowly with strain) involving constant strain rates throughout the test and periods of piecewise constant positive strain rates (between 10^{-8} and 10^{-2} s^{-1}) followed by relaxation tests showed that [*1,2*]:

1. Stress-strain curves obtained at two different strain rates differ ultimately by a constant stress and are nonlinearly spaced. A tenfold increase of the strain rate causes a flow stress increase which is much less than tenfold. Flow stress is the measured stress in the plastic range obtained at constant loading rate after transient effects have died out. ("Loading rate" is used for stress and strain control.)
2. An instantaneous large change (more than one order of magnitude) in strain rate results in an instantaneous elastic slope of the stress-strain curve at every point in the plastic range.
3. For a variable loading history involving only positive stresses the flow stress characteristic of a given strain rate is, after a transient period, always reached again. Under these loading histories the two materials forget their prior history. They do not exhibit a strain rate history effect [*3,4*].
4. At a given strain the average relaxation rate depends on the strain rate preceding the relaxation test. It increases with an increase in prior strain rate.
5. If the relaxation is started after the *flow stress characteristic of a par-*

ticular strain rate is reached, the amount of relaxation in a given period of time (and therefore the average relaxation rate) is independent of the stress and strain at the start of the relaxation test but depends only on the strain rate preceding the relaxation test.

These characteristics were observed up to 15 percent strain in AISI Type 304 stainless steel and up to about 7 percent for the Ti-alloy (at these strains cracking was experienced).

Items 1 to 5 concern relaxation behavior together with the behavior in a strain controlled tension test. They confirm other relaxation data [*5,6*] and general notions about the behavior in a tension test.

The Proposed Deformation Model

General Description

A material deformation model replaces the specimen in theoretical calculations. The controls (the boundary conditions) are, however, the same in both cases. A deformation model (constitutive equation) should be such that it can be "operated like a servocontrolled testing machine".

This requirement leads to the investigation of

$$m[\sigma,\epsilon]\dot{\epsilon} + g[\epsilon] = \sigma + k[\sigma,\epsilon]\dot{\sigma} \tag{1}$$

where σ is the engineering stress, ϵ is the engineering total strain, and a superposed dot denotes differentiation with respect to time. Square brackets designate "function of".

Equation 1 represents a nonlinear viscoelastic solid with three unknown material functions. The function $g[\epsilon]$ is the "equilibrium stress-strain curve". It is odd in ϵ and is the curve which is traced out as the loading rate approaches zero [*7*]; it is a material property. (The concept of an equilibrium stress-strain curve has also been introduced in Refs *8* to *10.*) One way to determine it is by extrapolating relaxation tests [*11*]. The functions $m[\ ]$ and $k[\ ]$ are positive. If for all values of the argument

$$\frac{m[\ ]}{k[\ ]} = E \tag{2}$$

where E is the modulus of elasticity the following behavior will be represented by Eq 1 (different choices of m/k are investigated in Ref *7*):

A. Elastic slope for $\sigma = 0$ and $\epsilon = 0$ as well as $\sigma - g[\epsilon] = 0$. A departure from the equilibrium stress-strain curve is therefore always elastic.

B. Elastic behavior for infinitely fast loading.

C. Property 2 above. This feature is demonstrated in Refs *11* and *12.* Using Eq 2 we can rewrite Eq 1 as

$$\dot{\epsilon} = \dot{\sigma}/E + \frac{1}{E}\frac{\sigma - g[\epsilon]}{k[\sigma,\epsilon]}$$

or (3)

$$\dot{\epsilon} = \dot{\epsilon}_{e\ell} + \dot{\epsilon}_{in}$$

where the last expression corresponds to familiar usage. In our case $\dot{\epsilon}_{in}$ depends, however, on *total strain.* Equation 3 represents an equation of state. At any instant in time any three of the variables (stress, stress rate, strain, and strain rate) determine the fourth uniquely.

An extensive study of the mathematical properties of Eq 1 showed that Eq 3 is an acceptable model for monotonic deformation behavior if the function k (dimension of time) is made to depend on σ,ϵ *only* through $\sigma - g[\epsilon]$ [*7*]. Following previous usage in applied mechanics $\sigma - g[\epsilon]$ was called the overstress [*7,11*]. A quantity similar to the overstress but of different conceptual origin is called the effective stress in material science, see Ref *13,* p. 13.) The proposed model for metal deformation is

$$\dot{\epsilon} = \frac{\dot{\sigma}}{E} + \frac{1}{E}\frac{\sigma - g[\epsilon]}{k[\sigma - g[\epsilon]]} \tag{4a}$$

or

$$\frac{d\sigma}{d\epsilon} = E - \frac{\sigma - g[\epsilon]}{\dot{\epsilon}k[\sigma - g[\epsilon]]} \tag{4b}$$

provided the overstress does not change sign. (This point will be discussed later.) For the derivation of Eq 4*b* the chain rule was used.

For creep Eq 4*a* reduces to

$$\dot{\epsilon} = \frac{1}{E}\frac{\sigma_0 - g[\epsilon]}{k[\sigma_0 - g[\epsilon]]} \tag{5}$$

and for relaxation

$$-\dot{\sigma} = \frac{\sigma - g[\epsilon_0]}{k[\sigma - g[\epsilon_0]]} \tag{6}$$

is the appropriate expression. In Eqs 5 and 6, σ_0 and ϵ_0 represent the quantities that are kept constant during the creep and the relaxation tests, respectively. For the solution of Eq 4*a* the stress or strain history (stress or strain control) must be specified as a function of time together with appropriate initial conditions. Initial conditions are also required for the solutions of Eqs 5 and 6.

It is shown in Ref *7* that Eqs 1 and 4*a* have the following asymptotic solutions for large time (mathematically infinite time):

$$\{\sigma - g[\epsilon]\} = \left(E - \left\{\frac{dg}{d\epsilon}\right\}\right) k[\{\sigma - g[\epsilon]\}]\dot{\epsilon} \tag{7}$$

and

$$\left\{\frac{d\sigma}{d\epsilon}\right\} = \left\{\frac{dg}{d\epsilon}\right\} \tag{8}$$

where { } has been used to indicate that Eqs 7 and 8 are limiting solutions. These limiting solutions are valid for strain control for every value of $dg/d\epsilon = g'$; they apply to stress control *only* if $g' > 0$. In this case it is necessary to substitute $\dot{\sigma}/g'$ for $\dot{\epsilon}$ in Eq 7.

Although Eqs 7 and 8 apply strictly at infinite times, numerical experiments performed in Refs *7* and *11* demonstrate that the limits of Eqs 7 and 8 are rapidly attained. Accordingly Eqs 7 and 8 are used for the interpretation of the theory in the plastic range for constant loading rate.

The theory predicts (see Eq 8) that all stress-strain curves ultimately have slopes equal to the slope of the equilibrium stress-strain curve. Integration of Eq 8 requires that the limiting overstress be constant. It is seen from Eq 7 that this is strictly true if g' = constant and if $\dot{\epsilon}$ = const. However, since $g' \ll E$ a small variation in g' has no significant influence in strain control with $\dot{\epsilon}$ = const and the limiting overstress value is obtained even when g' changes slightly with ϵ. In stress control with $\dot{\sigma}$ = constant, however, the right-hand side of Eq 7 is divided by g' so that the overstress is much more sensitive to small variations in g'. Consequently the limiting overstress may not be rapidly reached in stress control and the slopes of stress-strain curves obtained in stress and strain control may differ somewhat if g' is a function of strain. This has been observed (see Fig. 2 of Ref *2*). These properties of Eq 4*a* are demonstrated by the numerical experiments shown in Figs. 1*a* and 1*b*.

The theory therefore requires that the slopes of stress-strain curves obtained at various constant loading rates are approximately equal. There may be an influence of the type of control. The stress-strain curves are, however, nonlinearily spaced (see Eq 7); the spacing is controlled by k. To see this consider two tests with $\dot{\epsilon}_1$ and $\dot{\epsilon}_2$. Equation 7 then gives

$$\{\sigma\}_{\dot{\epsilon}_1} - \{\sigma\}_{\dot{\epsilon}_2} = (E - g')(k[\{\sigma - g[\epsilon]\}_{\dot{\epsilon}_1}]\dot{\epsilon}_1 - k[\{\sigma - g[\epsilon]\}_{\dot{\epsilon}_2}]\dot{\epsilon}_2) \tag{9}$$

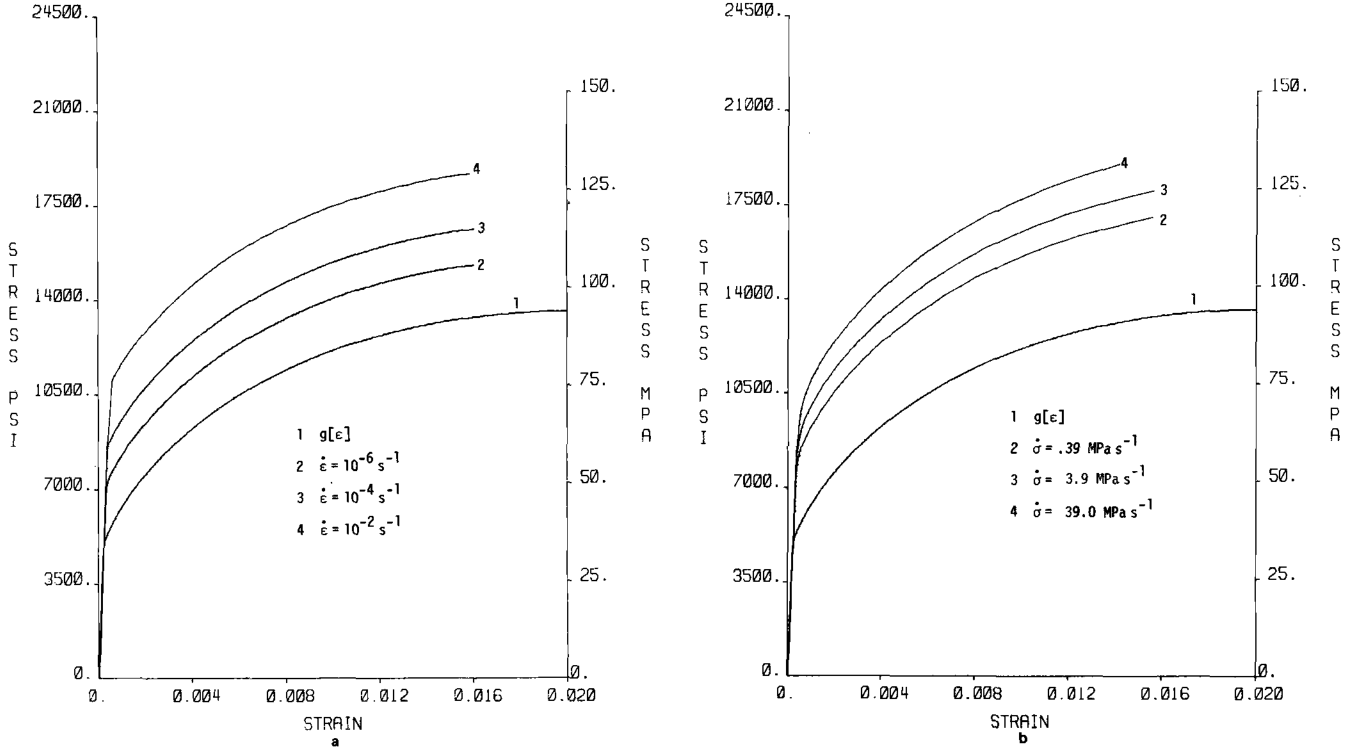

FIG. 1—*The influence of strain control* (Fig. 1a) *and of stress control* (Fig. 1b) *on the overstress limit for* g′ [ϵ]. *The figures represent results of numerical experiments obtained by numerically integrating Eq* 4a. *(See Table 1 for the material functions used.)* Figure 1a *shows an optically constant overstress for* $\epsilon > 8\ 10^{-4}$. *For stress control* (Fig. 1b) *constant overstress is not reached on the graph. (The integrations were performed using the computer program developed in Ref* 11*).*

where the subscripts $\dot{\epsilon}_1$ and $\dot{\epsilon}_2$ are used to designate the quantities associated with two tests run at $\dot{\epsilon}_1$ and $\dot{\epsilon}_2$, respectively. If k were constant, the spacing $\{\sigma\}_{\dot{\epsilon}_1} - \{\sigma\}_{\dot{\epsilon}_2}$ would linearly depend on the strain rate difference. If k is a function of the overstress, the theory predicts Observation 1.

For a constant strain rate test a constant limiting overstress is obtained, which is very nearly independent of strain even if g' changes somewhat with strain (Fig. 1*a*). When a relaxation test is started after the limiting overstress has been reached, the relaxation rate will only depend on this limiting overstress, and will be independent of the stress and strain at which the relaxation test commences (Eq 6). Therefore the theory predicts Observation 5 above. (A different demonstration of this property is given in Ref *11*)

If k is a decreasing function of its argument ($k' < 0$), then an increase in strain rate causes an increase in the limiting overstress. Therefore Observation 4 is reproduced. (It can be shown that the overstress at any strain increases monotonically with loading rate [*7*]).

To demonstrate that Eq 4*a* has Property 3 above, it is best transformed into an integral equation [*7*].

A pictorial representation of the model is given in Fig. 2. The curve *OA* is the equilibrium stress-strain curve which is postulated to be a material property. The thin curves represent curves of constant overstress $\sigma - g[\epsilon]$. At given loading rate the curve *OB* is traced out which initially cuts lines of equal overstress but ultimately coincides with one. If a relaxation test is started at any point between *C* and *B*, the relaxation rate is indistinguishable. Since the overstress is positive, Eq 6 predicts a negative stress rate which decreases as the overstress decreases. Relaxation will terminate on the equilibrium stress-strain curve, point *C'* in Fig. 2, after infinite time [*7*].

It is also possible to start a creep test at *C*. Equation 5 shows that the strain rate is then positive and strain increases. If $g' > 0$, then the strain rate decreases with increasing strain. If the stress level of the creep test is below the largest value of $g[\epsilon]$, creep terminates after infinite time at the strain ϵ which satisfies $\sigma_0 = g[\epsilon]$. If $\sigma_0 > g[\epsilon]$, creep does not terminate. (A detailed discussion of this subject is given in Ref *14*.)

If only positive loading rates (loading can be under stress or strain control), creep and relaxation tests are involved, the stress for any solution of Eq 4*a* will be in the sector between *OA* and *OD*. The area between the ϵ-axis and *OA* can only be penetrated from above *OA* by negative loading rates. Equation 4*b* predicts that for nonzero strain rate the slope is equal to E at the point where $\sigma = g[\epsilon]$. It follows that $g[\epsilon]$ can only be crossed with elastic slope. But even if σ is in the neighborhood of $g[\epsilon]$ a nearly elastic slope can be obtained since a decrease in $\sigma - g[\epsilon]$ decreases the numerator and increases the denominator on the right-hand side of Eq 4*b* simultaneously. Equation 4*b* shows that the slope depends inversely on the strain rate. For these

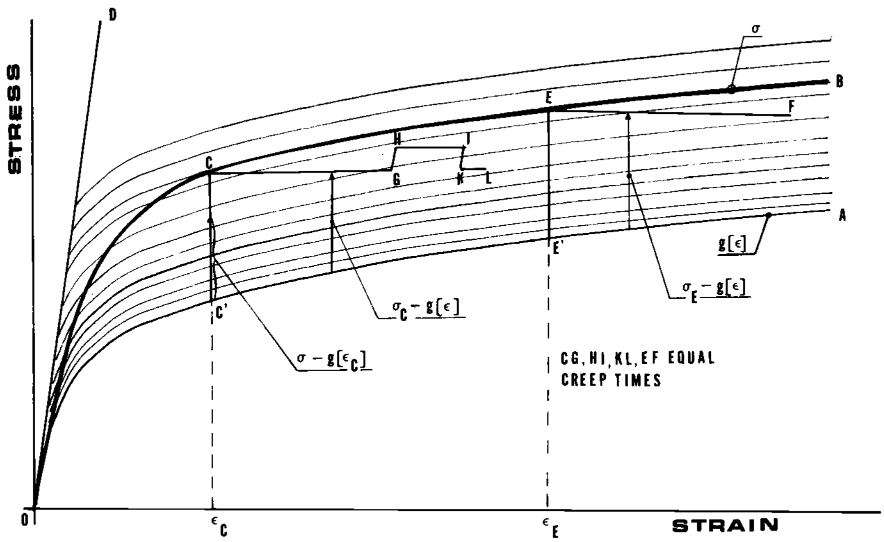

FIG. 2—*Schematic illustrating the properties of Eq 4*a.

reasons nearly elastic slopes can be obtained well above $g[\epsilon]$ (see the numerical experiments in Ref *11*).

Another way to obtain nearly elastic slopes is by instantaneous changes in loading rate [*7,11,12*]. However, these elastic slopes are not an indication of true elastic (reversible) behavior. The only true elastic region represented by Eq 4*a* is the neighborhood of the origin where $g' = E$ [*7*]. This elastic region can be small or large; it is completely controlled by the slope of g. If $g' < E$, beyond some strain the elastic region terminates and inelasticity begins.

Prediction of the Overstress Model for Creep

The overstress increases with increasing loading rate. It follows from Eq 5 that the initial creep rate increases with the loading rate which is applied to obtain the stress level of the creep test.

The creep tests started at C and E in Fig. 2 have the same initial creep rate. However, since the hypothetical g in Fig. 2 is more curved for $\epsilon > \epsilon_C$ than for $\epsilon > \epsilon_E$ creep will continue to be at a higher rate for the test started at E than that started at C. If $g' = \text{const}$ or if the slope of g changes equally for $\epsilon > \epsilon_C$ and for $\epsilon > \epsilon_E$, then both tests would creep at the same rate although $\sigma_E > \sigma_C$. The subscript denotes the constant stress.

These points are illustrated in Fig. 3 by numerical examples.

Suppose that another creep test is started at H such that $\sigma_C < \sigma_H < \sigma_E$. (Point H can be reached by $OCGH$ in Fig. 2 or by any other history.) At H the

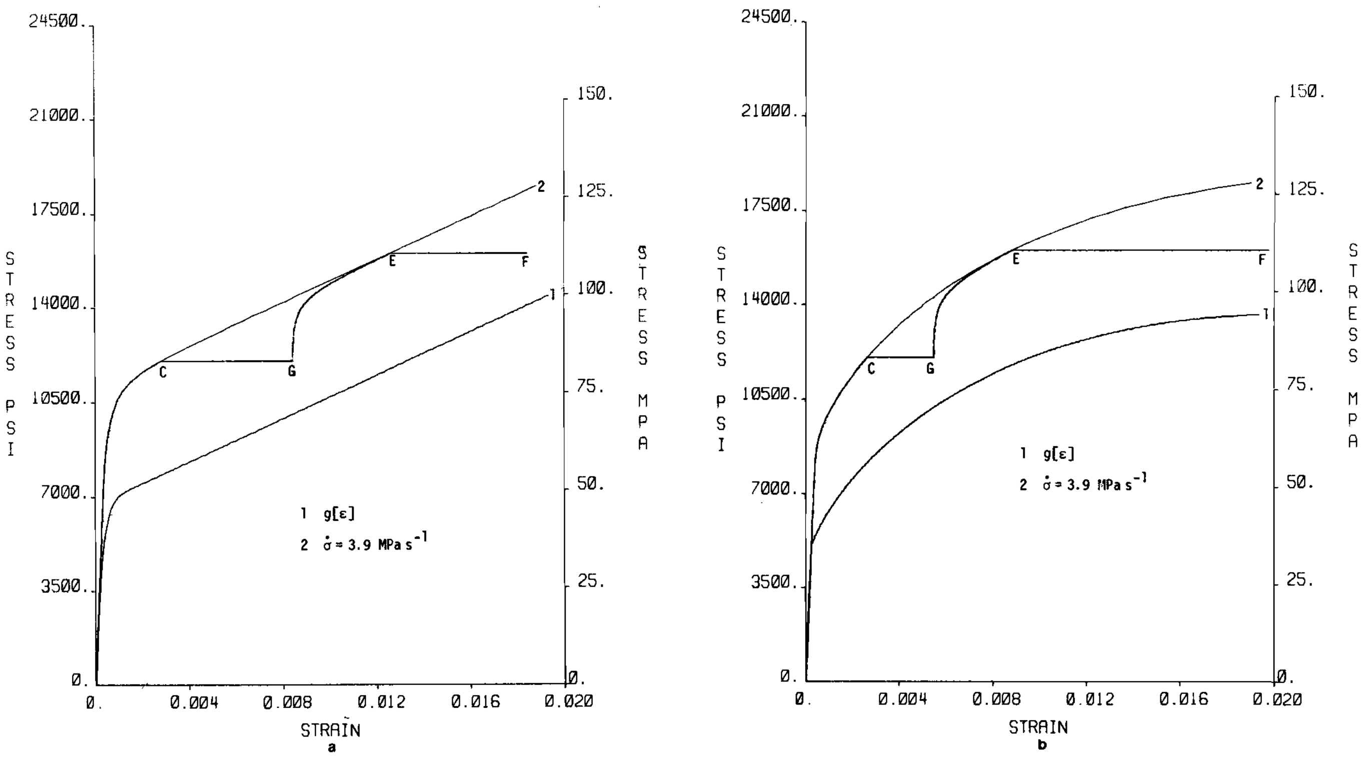

FIG. 3—*Numerical experiments demonstrating the influence of the equilibrium stress-strain curve on the creep behavior. The loading rate is 3.9 MPa* s^{-1} *(except for creep periods) and the stress levels for creep are 82.7 MPa and 110.3 MPa in each case. In* Fig. 3a, $g' = $ *const and the overstress is constant for* $\epsilon > 0.003$. *The creep strain accumulated in 10 min at the two stress levels is therefore equal. (Distance* CG = EF.*) Since* g′ *is not constant, the overstress is not constant in* Fig. 3b. *The creep strain accumulated in 10 min at the two stress levels is different (*CG ≠ EF*) on account of the different overstresses at* C *and* E *and on account of the changing slope of* g[ε]. *Note that the overstress at* E *in* Figs. 3a *and* 3b *is equal. The difference in creep strain at the high stress level in* Figs. 3a *and* 3b *is entirely owing to the different slope of the equilibrium stress-strain curve in the two cases. Material data are given in Table 1.*

Table 1—*Hypothetical material properties used in numerical experiments.*

Figures 1 to 3

$k[X] = A \exp (B \exp - (|X|/C)^{\alpha})$
with $A = 2.1$ E-4 s
$B = 21.$
$C = 26.01$ MPa
$\alpha = 1.10$

Figures 1*a*, 1*b*, 3*b*, 4*b*

$g[\epsilon] = E\epsilon - a(\epsilon - \epsilon_0)^n$
with $E = 149.6$ GPa
$a = 158.6$ GPa
$\epsilon_0 = 2.3$ E-4
$n = 1.02$

Figures 3*a*, 4*a*

$g[\epsilon]$ is Eq 10 of Ref *35*
with $E = 149.6$ GPa
$E_t = 0.018$ E
$\sigma_s = 46.1$ MPa
$\epsilon^* =$ E-4

---

flow stress characteristic of the stress rate has not been reached, and the test at H starts at smaller overstress than the test at C. Therefore $\dot{\epsilon}_H < \dot{\epsilon}_C$ although $\sigma_H > \sigma_C$. *Consequently the creep rate of a test at a high stress level can be less than that of a test at a low stress level.* This fact can only be observed if $g' > 0$ for all $\epsilon > \epsilon_C$. If $g' \leq 0$ for $\epsilon > \epsilon_C$, then an increase in stress level results in an increase in creep rate. Figure 4 gives the illustration of this prediction by numerical experiments.

If in Fig. 2 the stress is reduced at point I to the previous stress level so that $\sigma_K = \sigma_C$, then the creep rate for the test started at C will be much higher than of the one started at K, provided $g' > 0$. For a given creep time $\overline{CG} > \overline{KL}$ always. Figure 4 illustrates this point also. Note, however, that point K is indistinguishable from point L, since the creep strain rate is very low due to the small overstress at K. The creep strain accumulated in 10 min is therefore not visible on Fig. 4.

In summary the overstress model predicts the following unusual features for creep:

I. At a given stress level the initial creep rate increases with an increase in the prior loading rate.

II. It is possible that two creep tests show the same initial creep rate although their stress levels are different (points C and E in Figs. 2 and 3*a*).

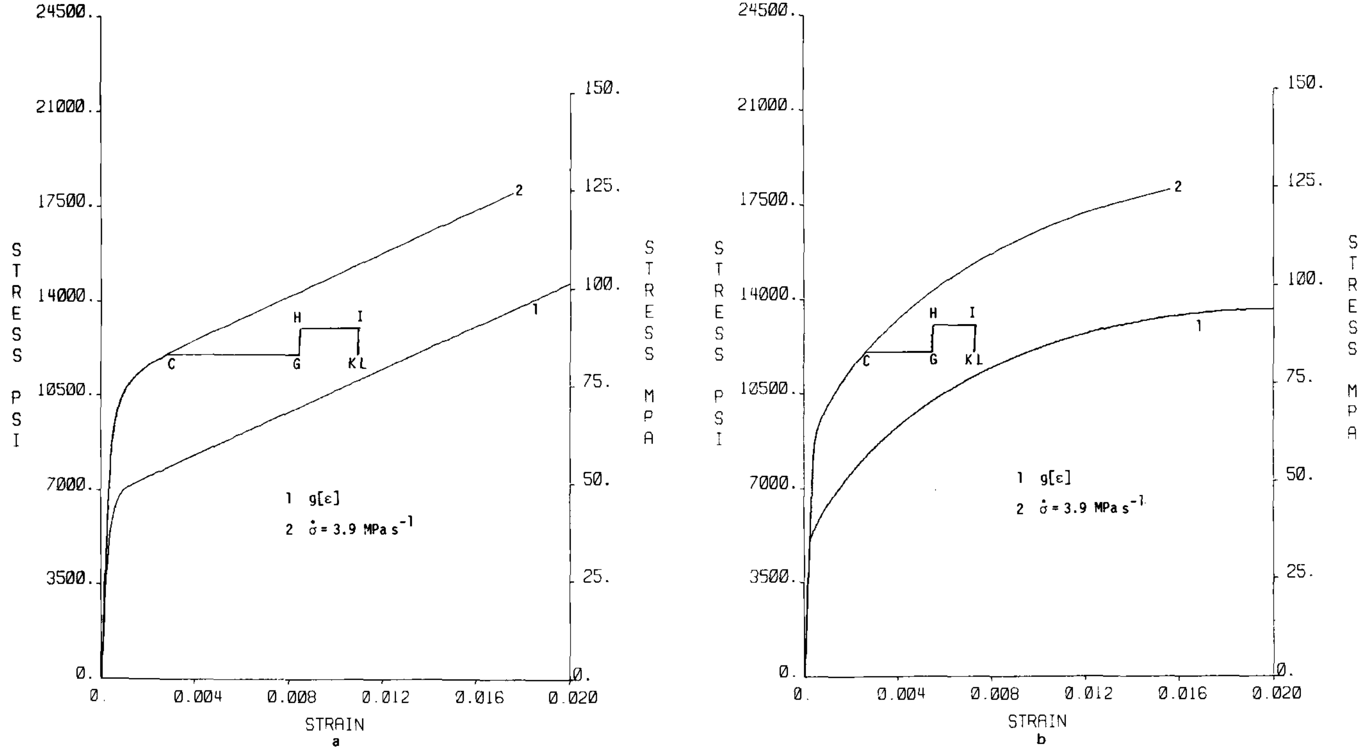

FIG. 4—*Illustration of anomalous behavior in creep by numerical experiment. During stress changes* $|\dot{\sigma}| = 3.9$ *MPa* s^{-1}*; all creep tests last 10 min. Although the stress at* H($\sigma_H = 89.62$ *MPa) is higher than at* C($\sigma_C = 82.72$ *MPa), the creep strain accumulated in 10 min is less at the high stress level* (*Distance* HI) *than at the low stress level* (*Distance* CG). *When the stress is lowered to 82.72 MPa at* K *no creep strain is noticeable* (*Distance* KL ≈ 0). *The stress-strain diagram for* $\dot{\sigma} = 3.9$ *MPa* s^{-1} *is shown to demonstrate that the characteristic flow stress was not reached at points* H *and* K. *The qualitative prediction of the model is not altered when an equilibrium stress-strain curve with* $g' = const$ (Fig. 4a) *is replaced by* $g'[\epsilon]$ (Fig. 4b). *Material data are given in Table 1.*

III. Creep rate does not necessarily increase with an increase in stress level. Even if a constant loading rate is used to change stress levels the creep rate at a high stress level may be less than the one obtained at a low stress level (points *C* and *H* in Figs. 2 and 4).

IV. At a given stress level the initial creep rate can be higher than the one obtained at the same stress level following loading and unloading (points *C* and *K* in Figs. 2 and 4).

Experimental Verification

Verification of these theoretical predictions requires an accurate control of rate in the load controlled mode ("soft" testing machine characteristics) which can easily be obtained with a servosystem. The following evidence exists to support Predictions I to IV above:

I. Figures 2,3,8, and 9 of Ref *15* verify this statement for Type 304 stainless steel.

II. Figures 2 and 5 of Ref *15* show that stress levels 2 and 3 of Specimen III have the same creep rate.

III. To verify this statement the test shown in Fig. 5 was run. Each creep period lasted for 5 min. It is seen that the creep strain accumulated in this period, and therefore the creep strain rate does not necessarily increase with stress. If the stress of the creep test is not on the stress-strain diagram appropriate for the stress rate (the "flow stress" has not been reached), the average creep rate is less than at the next lower stress level which is on the σ-ϵ diagram appropriate for the loading rate (compare points *A,B* and *C,D*). This test was repeated for the fully annealed Type 304 stainless steel and for the Ti-alloy. All the results confirm the qualitative prediction of the theory in this case.

IV. This property is demonstrated in Fig. 12 of Ref *15* and in Fig. 11 of Ref *2*. Also Fig. 5 supports this statement [compare the creep strain accumulated in 4200 s at 270 MPa upon second loading (point *m*) and upon first loading (between points *h* and *i*)].

The experiments therefore support the qualitative prediction of the theory including the anomalous results cited above. The terms unusual and anomalous creep behavior introduced above are relative to the predictions of theories of primary and secondary creep and relative to "effective stress" creep theories where the "internal or back stress" is constant. All of these theories predict an increase in creep rate with an increase in stress.

A discrepancy between theory and experiment was reported in Ref *15*, Fig. 4. Equation 5 requires that for a given stress level the creep rate be only a function of strain. Figure 4 of Ref *15*, taken from tests at the "knee" of the stress-strain curve, shows that the creep rate for a given strain is not equal for

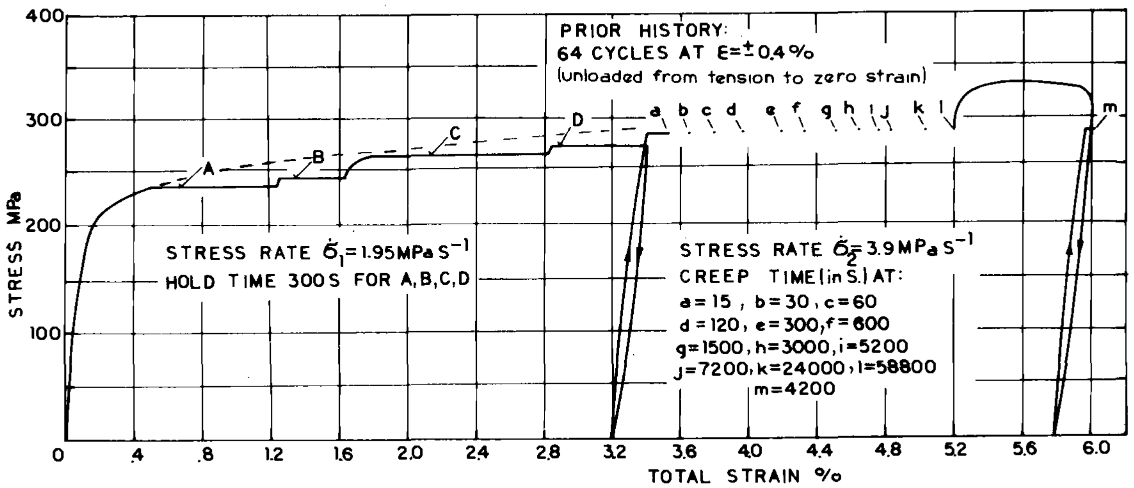

FIG. 5—*Experiments designed to demonstrate the anomalous creep behavior predicted by the theory (maximum prestress 235 MPa). The assumed stress-strain curve for* $\dot{\sigma}_1$ = *1.95 MPa* s^{-1} *is shown dashed. The stress levels of the creep tests at* B *and* D *are not on that curve, and the creep strain is reduced compared with the one at the stress level below (points* A *and* C, *respectively). Points* a-ℓ *show creep strain accumulated in 16.3 h. Note the reduced creep strain at* m, *which has the same stress level as* a. *Type 304 stainless steel, room temperature.*

the three tests. As the tests progress the three curves tend to merge. This discrepancy is considered a transient phenomenon, especially since theory and experiment agree in the fully plastic range. Presently a theory is considered that contains second derivatives of stress and strain for the modeling of these transient phenomena [*16*].

Material Functions of the Theory

The theory contains two material functions: the equilibrium stress-strain curve $g[\epsilon]$ (dimension stress) and $k[\sigma - g[\epsilon]]$ (the viscosity function with the dimension of time). It depends only on the overstress.

The function $g[\epsilon]$ is the repository for work hardening and implies the existence of a "range of stresses where the solid can be in equilibrium" [*13*]; it could correspond to the "mechanical threshold" postulated in Ref *13*, p. 6. The time (rate) dependent deformation is controlled by the deviation from equilibrium, owing to the dependence of k on the overstress. It is similar to the "effective stress concept", (Ref *13*, p. 13); we cannot identify $g[\epsilon]$ with the internal stress. Within a phenomenological theory internal stresses cannot be determined in a tension test; rather, "the total deformation resistance" is determined via "the applied stress in (or at the limit of) equilibrium" (Ref *13*, p. 14). A very slow test is required.

It was found that equilibrium is not yet reached at a strain rate of 10^{-8} s^{-1}. Theoretically $g[\epsilon]$ is obtained as $\dot{\epsilon}$ approaches zero. Further an infinite time is required before the relaxation tests terminate at $\sigma = g[\epsilon_0]$ [this is a property of the differential equation (*6*)]. It is therefore necessary to use extrapolation methods to find $g[\epsilon]$ [*11*].

For small values of the overstress the viscosity function is large (the theory requires $k > 0$ and $k' < 0$). Departures from the equilibrium stress-strain curve are elastic, since the second term on the right-hand side of Eq 4*a* is zero at the equilibrium stress-strain curve. As the overstress increases, the second term in Eq 4*a* can become significant, since k decreases with an increase in overstress. "Inelasticity" develops. The "viscosity" (as measured by k) of the model is dependent on the overstress; it is high around the "equilibrium stress-strain curve" and decreases rapidly as the overstress increases.

Determination of the k*-function*

When $g[\epsilon]$ is known, k can be obtained from relaxation tests [*11*]. The viscosity function k and the function g can also be determined from strain rate change tests (see Fig. 5 of Ref *1*; Figs. 2 and 5 of Ref *2*). To accomplish this the stress level at an arbitrarily chosen strain rate is taken as a reference, and the stress differences between the flow stresses at various strain rates are plotted versus strain rate (see Fig. 10 of Ref *1*).

A suitable k-function is chosen and Eq (7) is, for a given E and g', numerically inverted to obtain

$$\{\sigma - g[\epsilon]\} = f[\dot{\epsilon}] \tag{10}$$

Using the graph of Eq 10 the curve of flow stress differences can be plotted (using the same reference stress, as in the experimental results) and compared with the experimental results, such as shown in Fig. 10 of Ref *1*. The constants in the function are then varied through a trial-and-error procedure until the experimental and the theoretical curves match. The graphs shown in Fig. 6 contain four different k-functions together with the data of Fig. 10 of Ref *1* for illustration.

The k-functions are

$$\left.\begin{aligned} k1 &= A\left(\log_{10}\left[10 + \frac{|X|}{C1}\right]\right)^{-D1} \\ k2 &= A\left(1 + \frac{|X|}{C2}\right)^{-D2} \\ k3 &= A\left(\frac{|X|}{C3}\right)^{-D3} \\ k4 &= RO\,\exp\left(R1\,\exp - \frac{|X|}{R2}\right) \end{aligned}\right\} \tag{11}$$

where

$$X = \sigma - g[\epsilon]$$

and where

$$\begin{array}{llll} A = 314\,200\text{ s} & C1 = 10.87\text{ MPa} & D1 = 76.70 \\ & C2 = 71.38\text{ MPa} & D2 = 21.98 \\ & C3 = 9.15\text{ MPa} & D3 = 7.00 \\ RO = 0.2296\text{ E-3 s} & R1 = 21.28 & R2 = 58.27\text{ MPa} \end{array}$$

The function $k4$ is the $k1$-function used in Ref *11*. The constants of $k1$ were determined to match the data in Fig. 6 by the trial-and-error procedure. The constants for $k2$ and $k3$ were found by requiring that their value equal $k1$ at 19.61 MPa and at 55.15 MPa. Figures 6 and 7 show that the four curves coincide for an interval of the overstress and strain rate, respectively. Curves $k1$ and $k2$ drop very fast and diverge at overstress values larger than 150 MPa. It was commented in Ref *11* that $k4$ was not useful for dynamic strain rates ($\dot{\epsilon}$

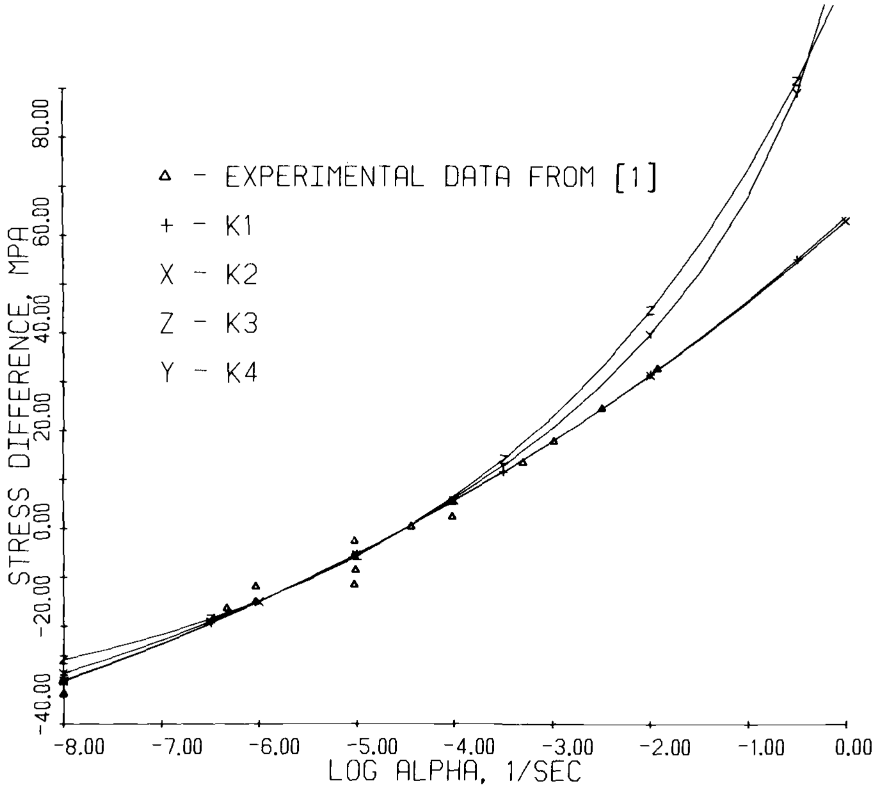

FIG. 6—*Stress difference in a tension test (the stress at* $\dot{\epsilon} = 10^{-4.5}$ s^{-1} *is taken as reference and set equal to zero) versus strain rate for theory and experiment (Type 304 stainless steel at room temperature). For the theory, Eq 7 and the* k*-functions of Fig. 7 were used.* E = *195 GPa;* $g' = 0.016$E.

$> 10^{-1}$), since its use resulted in excessive overstress values. The functions $k1$ and $k2$ do not suffer from this drawback.

Based on the match shown in Fig. 7, $k1$ and $k2$ are considered to be useful k-functions up to strain rates of 10^3 s^{-1}. The functions $k3$ and $k4$ are applicable only for a limited strain rate interval.

Rate-Dependence Index M

In material science the measure of rate sensitivity is the dimensionless number m (see Ref *13*, p. 231) given by

$$m \equiv \frac{\partial \ell n \dot{\gamma}}{\partial \ell n \sigma} \tag{12}$$

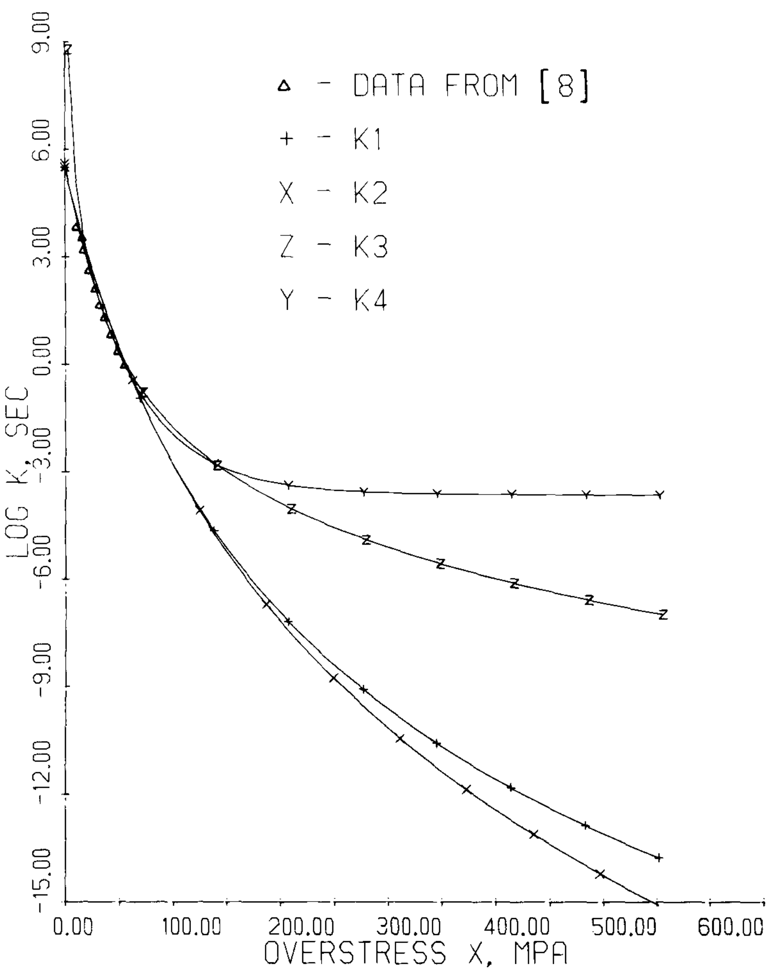

FIG. 7—*The* k*-functions for Type 304 stainless steel at room temperature obtained by matching the data of Fig. 6.*

where $\dot{\gamma}$ is the inelastic strain rate and σ is the applied stress. The procedures and difficulties of determining m are discussed in Ref *17*.

Using this theory a similar number can be derived from Eqs 5, 6, and 7. Differentiation of these equations yields

$$\frac{d\,\ell n\,Y}{d\,\ell n\,X} = 1 - \frac{X k'[|X|]}{k[|X|]}\,\text{sgn}\,X \equiv M \tag{13}$$

The quantities X and Y are defined as follows:

Test	Y	X
monotonic loading	$\dot{\epsilon}$	$\{\sigma - g[\epsilon]\}$
relaxation	$\dot{\sigma}/E$	$\sigma - g[\epsilon_0]$
creep	$\dot{\epsilon}$	$\sigma_0 - g[\epsilon]$

(subscript 0 means that this quantity is constant and $\operatorname{sgn} X = \begin{cases} 1 X > 0 \\ 0 X = 0 \\ -1 X < 0 \end{cases}$).

It is remarkable that M has the same mathematical form in each of the three tests, and this observation suggests that it might be a useful parameter. A graph of M versus overstress for the four k-functions is given in Fig. 8, which also contains a strain rate obtained from Eq 7 using $k1$. For overstress values for which the k-functions in Fig. 7 overlap the M-values are approximately equal. The $k3$-function yields a constant M-value. However, since it matches the data in Fig. 7, a variable M based on $k1$ or $k2$ appears to be realistic.

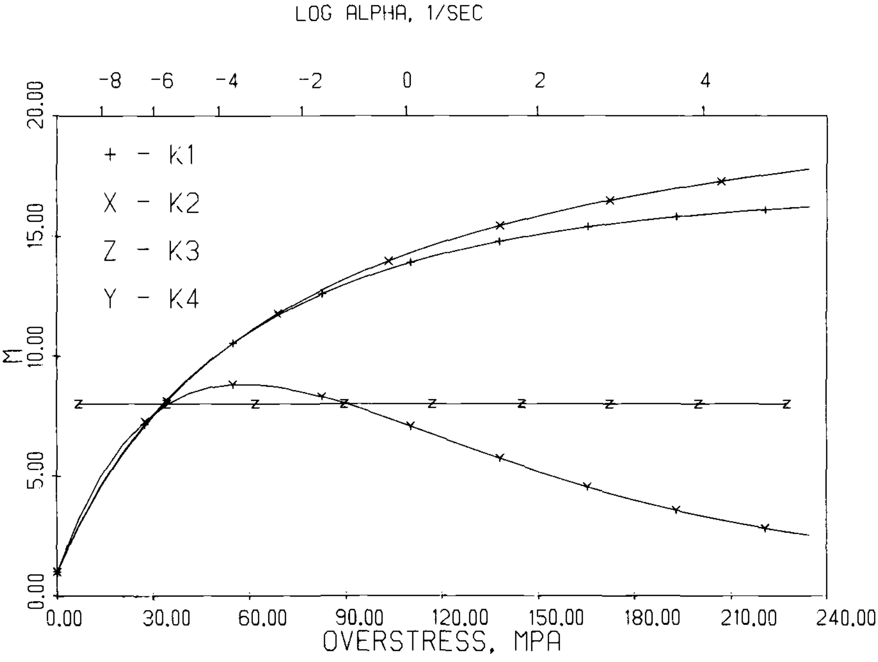

FIG. 8—*The rate dependence index* M *defined in Eq 13 versus overstress. The strain rate scale is obtained from Eq 7 for* k1. *It is also valid for* k2 *but not for* k3 *and* k4.

Although the numerical values of M are in the range found for m, it should be noted that their definitions are different. In Eq 12 stress is used, whereas overstress is the dependent variable in Eq 13. This feature is deemed advantageous since M is independent of the actual stress level and therefore of work hardening. The conventional parameter m depends on the stress level, and must therefore be different for the annealed and the cold worked material.

Our limited test data [*1,2*], however, suggest that rate dependence is independent of work hardening. (Rate dependence includes loading rate sensitivity, creep, and relaxation.) In the plastic range the relaxation drop in a fixed period of time was shown to depend only on the preceding strain rate, to cite just one example. Stress differences between curves of flow stress for various strain rates are independent of strain (see also Ref [*18*], Fig. 9). It is for this reason that M is preferred.

The definition M differs further from that of m through the use of total strain in monotonic loading. For creep and relaxation the inelastic strain rate is used in both cases. This difference is considered to be minor.

The theory given in this paper shows that M can be derived from the model, and that it is generally not constant. (A comment in Ref *13*, p. 232, implies that m varies also.) The specific example valid for Type 304 stainless steel at room temperature indicates that M changes in the range of strain rates normally employed in testing. The functions k and M have been derived from test data. The dependence of M on strain rate suggests that m may also vary with strain rate. The author is not aware of publications that report a nonconstant m for Type 304 stainless steel at room temperature.

Discussion

The discussion of the properties of the theory and of the experimental results have been entirely qualitative. Qualitative studies are essential when highly nonlinear relations are considered. Good numerical fits of theoretical responses with experimental ones over a limited range of test parameters are easily achieved with nonlinear equations. Considerable discrepancies can be experienced when these perfectly fitted equations are applied to other test parameters than the ones used for the fitting. A case in point is the $k3$-function derived to fit the data in the strain rate interval 10^{-6} to 10^{-4} s^{-1}. It gives bad results outside this range.

The development of the theory would not have been possible without the use of servocontrolled testing and strain measurement on the gage length which enable the observation of real material responses without testing machine bias. (This statement assumes that the machine is properly adjusted and used.) After the theory was shown to have the qualitative attributes found in strain controlled tests such as strain rate change and relaxation tests, its prediction in stress control and creep was examined. Subsequent tests showed that these predictions were realistic. The tests required accurate control of rate of loading and the use of stress or strain control. Only servosystems can provide these capabilities.

The servocontrolled tests and the simultaneous mathematical development suggested strongly the existence of the equilibrium stress-strain curve and the introduction of the overstress concept. They also emphasized the importance of the type of control on the material response. As an example the different behavior upon loading rate changes and upon unloading in stress and strain control depicted in Fig. 1 of Ref *15* is cited. The important role of the type of control on material response is not emphasized in materials science.

The theory presented herein differs from state variable theories [*19-26*], but also has some features in common with them.

All the theories are "unified" as they do not separate creep strains and plastic strains. They consider inelastic deformation to be rate dependent, and the inelastic strain rate depends on a function of stress minus some quantity. (The theories proposed in Refs *24* and *25* do not share this feature.) The quantities subtracted from the stress have different interpretations; they may be constants or functions of the deformation variables. It appears that the dependence of the inelastic strain rate on stress minus a quantity permits the existence of a steady-state or asymptotic solution for large times without requiring that the functions reach constant values. (The overstress dependence is necessary for a nonlinear relation between strain rate and overstress to exist [*7*].)

Whereas no specific limitations are attached to the other theories, the presently discussed form of this theory is at least limited to temperatures where no aging, no strain aging, and no annealing effects take place. It has also not been developed for finite deformation. For cyclic loading, a growth law for $g[\epsilon]$ must be specified which is discontinuous, see Refs *27* to *29*. The augmentations will not alter the basic character of the constitutive equation. It will remain one nonlinear differential equation. (The intended modifications for aging are given [*14*]; for cyclic loadings $g[\epsilon]$ has to be augmented using "if statements" and forgetting rules [*29*].) The other approaches rely on a system of at least two, sometimes three, coupled nonlinear differential equations.

A further difference lies in the fact that the two material functions of the theory are left open (only general requirements are imposed such as continuity; $g[\epsilon] > 0$ for $\epsilon > 0$; g is odd; k is even; $k > 0$ and $k' < 0$). The functional forms and their constants must then be determined for a given material and a given temperature. In the other theories the functions are to a large extent specified and only the constants are to be determined.

The four k-functions shown in Fig. 7 satisfy the theory. However, the popular power-function $k3$ shows poor correlation with the test data. Since the theory does not require any specific form of the k-function, it is perfectly acceptable to use either $k1$ or $k2$. These functions can be used from zero strain rate to fully dynamic conditions ($\dot{\epsilon} \approx 10^3$ s^{-1}). They will give stress differences between the 10^{-2} s^{-1} and the 10^3 s^{-1} stress-strain curves comparable to those measured in dynamic plasticity [*30-32*]. The use of the functions $k3$ and $k4$ in Eq 7 will result in unrealistically large stress differences (see the comment regarding $k4$ in Ref *11*).

In the present theory total strain appears explicitly and because of this feature the theory permits an equilibrium solution. For an elastic perfectly plastic $g[\epsilon]$ the equilibrium solution was shown to correspond to the stress distribution in a pressurized cylinder obtained for an elastic perfectly plastic constitutive equation [*33*].

The test data accumulated so far in Refs *1* and *2* for positive stresses suggest that work hardening proceeds without appreciably changing the rate dependence. A similar result is found in Ref *18*, Fig. 9, for high-purity aluminum. (After reaching the cyclic steady state the strain rate change-stress change behavior of Type 304 stainless steel was shown to be different from noncyclically loaded samples in Ref *1*, Figs. 9 and 10. Strong cyclic hardening apparently alters the rate dependence.) The repository for rate dependence in the theory, the viscosity function k, depends only on the overstress. It is independent of work hardening represented by the equilibrium stress-strain curve.

This separation of the repositories for work hardening and rate dependence appears to be permissible for monotonic and cyclic loading for the Ti-alloy. For Type 304 stainless steel, which hardens very strongly under cyclic loading, the separation is only possible for monotonic loading and limited cycling. This observation implies that M and therefore m should be different for monotonically and fully cyclically deformed Type 304 stainless steel. Such a difference was indeed reported in Ref *34*.

The determination of the k-function from our strain rate change tests gives good results and is an alternative possibility to using relaxation test data. In Ref *11* use was made of relaxation data from Ref *5* to determine $k4$, which coincides with $k1$ or $k2$ determined from data presented in Ref *1* where data are available from relaxation tests. This coincidence suggests that the rate dependence of different heats of Type 304 stainless steel can be very close. Strain rate change and relaxation tests are equally suited for determining k. Creep tests are not since two unknown functions are involved in this case (Eq 5).

The slope of the equilibrium stress-strain curve in the plastic range is known from the slope of the stress-strain diagram (Eq 8). The amplitude of g can be obtained by extrapolating relaxation tests [*11*] or by plotting Eq 10 once the match shown in Fig. 6 has been achieved (For a given strain rate $g[\epsilon] = (\sigma[\epsilon] - \{\sigma - g\})$. Both methods give satisfactory results. It is further known that in the elastic range $g' = E$. The initial and the "plastic" part of $g[\epsilon]$ can be determined. They must be connected so that when used in the integration of Eq 4*a* reasonable stress-strain curves are obtained. Here a trial-and-error procedure may be necessary.

Equation 4*a* represents a nonlinear viscoelastic solid or an equation of state involving σ, $\dot{\sigma}$, ϵ, and $\dot{\epsilon}$. The experimental evidence and the numerical examples [*1,2,7,11*] suggest that the deformation of Type 304 stainless steel and the Ti-alloy can be modeled by such a constitutive equation so long as the overstress does not change sign. Under these loadings three of the above variables will uniquely determine the fourth at any given time irrespective of what happened prior to that time.

For a limited range involving loading, partial unloading, creep and relaxation, metal deformation can be modeled by an equation of state. The structure changes are modeled by $g[\epsilon]$. This implies that different histories not involving a sign change of the overstress have, at a given ϵ, the same microstructure. (At point *G* in Fig. 2 the microstructure should be the same whether *G* is reached by *OCG* or by a fast tension test and then unloading to *G*.)

This simple modeling of metallic deformation ceases to be true when the overstress changes sign at some strain ϵ_1. The equation of state is then no longer a realistic representation and $g[\epsilon]$ must be discontinuously updated [*29*] to represent real metal deformation behavior. This updating changes the viscoelasticity model (Eq 1) into a viscoplasticity model which is history dependent in the sense of plasticity [*27*].

Acknowledgments

This work was supported by grants from the National Science Foundation and the Office of Naval Research. D. Lim and H. Lu prepared the computer graphs. The test shown in Fig. 5 was run by D. Kujawski.

References

[*1*] Krempl, E., *Journal of the Mechanics and Physics of Solids*, Vol. 27, 1979, pp. 363-375.

[*2*] Kujawski, D. and Krempl, E., *Journal of Applied Mechanics, Transactions of ASME*, Vol. 103, 1981, pp. 55-63.

[*3*] Klepaczko, J., *Journal of Materials Science and Engineering*, Vol. 18, 1975, pp. 121-135.

[*4*] Nicholas, T., *Experimental Mechanics*, Vol. 11, 1971, pp. 370-374.

[*5*] Yamada, A. H. and Li, Che-Yu, *Metallurgical Transactions*, Vol. 4, 1973, p. 2133.

[*6*] Thomas, J. F. and Yaggee, F. L., *Metallurgical Transactions*, Vol. 6a, 1975, p. 1835.

[*7*] Cernocky, E. P. and Krempl, E., *International Journal of Non-Linear Mechanics*, Vol. 14, 1979, pp. 183-203.

[*8*] Gurtin, M. E. and Herrera, I., *Quarterly Applied Mathematics*, Vol. 23, 1965, pp. 235-245.

[*9*] Eisenberg, M. A., Lee, C. W., and Phillips, A., *International Journal of Solids and Structures*, Vol. 13, 1977, pp. 1239-1255.

[*10*] Walker, K. P. and Krempl, E., *Mechanics Research Communications*, Vol. 14, 1978, pp. 179-190.

[*11*] Liu, M. C. M. and Krempl, E., *Journal of the Mechanics and Physics of Solids*, Vol. 27, 1979, pp. 377-391.

[*12*] Cernocky, E. P. and Krempl, E., *Journal of Thermal Stresses*, Vol. 4, 1981, pp. 69-82.

[*13*] Kocks, U. F., Argon, A. S., and Ashby, M. F., *Thermodynamics and Kinetics of Slip*, Pergamon Press, Oxford, 1975.

[*14*] Krempl, E., *Journal of Engineering Materials and Technology, Transactions of ASME*, Vol. 101, 1979, pp. 380-386.

[*15*] Kujawski, D., Kallianpur, V., and Krempl, E., *Journal of the Mechanics and Physics of Solids*, Vol. 28, 1980, pp. 129-148.

[*16*] Cernocky, E. P. and Krempl, E., "A Uniaxial, Nonlinear Second-Order Differential Overstress Model for Rate-Dependence, Creep and Relaxation," RPI Report CS 81-4, Dec. 1981.

[*17*] Arieli, A. and Rosen, A., *Scripta Metallurgica*, Vol. 10, 1976, pp. 471-475.

[*18*] Karnes, C. H. and Ripperger, E. A., *Journal of the Mechanics and Physics of Solids*, Vol. 14, 1966, pp. 75-88.

[*19*] Chaboche, J. L., *Bulletin de L 'Academie Polonaise des Sciences*, Vol. XXV, 1977, pp. 33-42.

[*20*] Hart, E. W., *Journal of Engineering Materials and Technology, Transactions of ASME*, Vol. 98, 1976, pp. 193-202.

[*21*] Miller, A. K., *Journal of Engineering Materials and Technology, Transactions of ASME*, Vol. 98, 1976, pp. 97-113.

[*22*] Rohde, R. W. and Swearengen, J. C., *Journal of Engineering Materials and Technology, Transactions of ASME*, Vol. 102, 1980, pp. 207-214.

[*23*] Walker, K. P., "Representation of Hastalloy-X Behavior at Elevated Temperature with a Functional Theory of Viscoplasticity," *Journal of Engineering Materials and Technology, Transactions of ASME*, to appear.

[*24*] Bodner, S. R. and Partom, Y., *Journal of Applied Mechanics*, Vol. 42, 1975, pp. 385-389.

[*25*] Laflen, J. H. and Stouffer, D. C., *Journal of Engineering Materials and Technology. Transactions of ASME*, Vol. 100, 1978, pp. 363-380.

[*26*] Lee, D. and Zaverl, F., Jr., *Acta Metallurgica*, Vol. 26, 1978, pp. 1771-1780.

[*27*] Krempl, E., *Acta Mechanica*, Vol. 22, 1975, pp. 53-90.

[*28*] Cernocky, E. P. and Krempl, E., *International Journal of Solids and Structures*, Vol. 16, 1980, pp. 723-741.

[*29*] Krempl, E., forthcoming.

[*30*] Albertini, C. and Montaganani, M., *Nuclear Engineering and Design*, Vol. 37, 1976, p. 115.

[*31*] Albertini, C. and Montagnani, M., "Dynamic Material Properties of Several Steels for Fast Breeder Reactor Safety Analysis," Report EUR 5875.e, Ispra, Italy, 1977.

[*32*] Isozaki, T. and Oba, T., *Nuclear Engineering and Design*, Vol. 55, 1979, pp. 375-387.

[*33*] Zirin, R. M. and Krempl, E., ASME Paper 80-C2/PVP33, 1980, *Journal of Pressure Vessel Technology, Transactions of ASME*, to appear.

[*34*] Swearengen, J. C. and Rohde, R. W., *Scripta Metallurgica*, Vol. 8, 1974, pp. 1409-1413.

[*35*] Liu, M. C. M., Krempl, E., and Nairn, D. C., *Journal of Engineering Materials and Technology, Transactions of ASME*, Vol. 98, 1976, pp. 322-329.

T. H. Alden[1]

Time-Independent and Time-Dependent Deformation of Metals

REFERENCE: Alden, T. H., "**Time-Independent and Time-Dependent Deformation of Metals,**" *Mechanical Testing for Deformation Model Development, ASTM STP 765*, R. W. Rohde and J. C. Swearengen, Eds., American Society for Testing and Materials, 1982, pp. 29–50.

ABSTRACT: In most contemporary theories the deformation of metals is treated as a time-dependent or viscous process. A quasi time-independent character is sometimes introduced by means of an athermal back "stress" from long-range obstacles, but only at $T = 0$ K or in other limited temperature ranges is the deformation predicted to show time-independent behavior. Several experimental results, mainly on pure face-centered-cubic metals, are in disagreement with this theoretical approach. The most important results are that (*1*) time-independent strain (loading strain) has been measured on sudden increase of stress during creep deformation, even for very small stress increments; and (*2*) the strain rate ratio measured in a load relaxation experiment, $R = \dot{\epsilon}_r/\dot{\epsilon}_\ell$, is consistently less than unity and increases toward unity as the stress approaches saturation. These results are reviewed and new data from load relaxation on lead and the superplastic Pb-Sn eutectic are presented. It is the author's conclusion from these data that time-independent deformation may be more important than is normally acknowledged. Thus, in future efforts at modeling plasticity, the possibility of a dual time-dependent, time-independent nature ought to be considered.

KEY WORDS: plastic flow, dislocation theory, load relaxation, recovery creep, viscous creep, thermal activation, mechanical activation

Theory of Plastic Flow

The pervasive modern view of the nature of plastic deformation was stated as early as 1940 by Orowan: "... that plastic gliding obeys a 'dynamic' law; that is to say the time rate of strain, not the strain itself, is a function of stress. The time rate of strain will depend, besides, on temperature and the 'state of strain hardening' of the crystal" [*1*].[2] This belief, more briefly

---

[1] Professor, Metallurgical Engineering Department, University of British Columbia, Vancouver, British Columbia, Canada.

[2] The italic numbers in brackets refer to the list of references appended to this paper.

stated, that the plastic strain rate depends only on the stress, the structure, and the temperature is the basis of virtually all the recent and current literature of plasticity, exemplified by the detailed study of thermally activated flow [*2-4*] and dislocation dynamics [*5*].

There have been, however, significant observations and theories which do not fit this pattern. In face-centered-cubic metals, the yield stress or isostructural flow stress ratio is said to show an athermal plateau between $T/T_m \simeq 0.3$ to 0.5 [*6*]. Similar plateaus are reported for body-centered-cubic metals near and above room temperature [*7*]. The principal models of creep, the recovery models [*8-10*], contain the assumption that the strain process is athermal while the rate-controlling recovery process is of course thermal. Direct evidence for athermal strain in creep experiments includes delay times on stress decrease and "instantaneous" (loading) strains on stress increase, either incremental [*11,12*] or at the start of the creep test [*13*]. Finally, the presence of an athermal component of the flow stress is acknowledged in the widely discussed "effective stress" theory [*6,14,15*]. In this theory the strain process is thermal, even for very small effective stress. However, the limiting case of $\sigma = \sigma_i$ is not excluded in principle and is sometimes claimed to hold experimentally (σ is the applied stress, σ_i the back stress) [*16*]. For this case, presumably, straining should occur without thermal activation.

At the microstructural level, each of these "athermal" cases seems to involve a flow stress controlled by a dislocation microstructure in either a network or pile-up array. This, in turn, is consistent with the concept of dislocations as long-range obstacles, that is, obstacles which are virtually immune to passage with the aid of thermal fluctuations.

If thermal flow is not possible, either because of the nature of the glide dislocation-obstacle interaction or because thermal activation is weak (short time, low temperature), then strain may be activated by a rising stress [*17,18*]. This case, time-independence or *mechanical-activation* of strain is described by a differential equation of stress σ and structure S of the form:

$$d\epsilon = \epsilon(\sigma,S)\, d\sigma \tag{1a}$$

The function $\epsilon\ (\sigma,S)$ may depend weakly on temperature. An example is elastic deformation:

$$d\epsilon = \frac{1}{E}\, d\sigma \tag{1b}$$

where E is Young's modulus. For the case of $\sigma = \sigma(t)$, the equation may be written as

$$\dot{\epsilon}_e = \frac{\dot{\sigma}}{E} \tag{1c}$$

The corresponding equation for plastic strain is

$$\dot{\epsilon} = \frac{\dot{\sigma}}{h} \tag{1d}$$

where h is the "plastic modulus", usually interpreted as a strain-hardening coefficient (associated with dislocation accumulation), but possibly of other physical origin [*17,18*].

If the structure is thermally unstable, recovery will enhance the strain rate. The case of thermal obstacles which are also thermally unstable was treated by Cottrell and Aytekin [*19*]. However, it seems that among the ordinary sources of metal or alloy hardening, only dislocations show significant thermal instability. If dislocations are assumed to be athermal obstacles, then for the case where a single obstacle controls the flow stress, recovery and mechanically activated strain are more naturally coupled than recovery and thermally activated flow. The usual equation is

$$\dot{\epsilon} = \frac{\dot{\sigma} + r_y}{\theta_y} \text{ for } \sigma = \tau_y \tag{2a}$$

where $r_y = -\partial\tau_y/\partial t|_\epsilon$ is the recovery rate, θ_y is the strain-hardening coefficient, and τ_y is the yield [*17*] or mechanical threshold [*4,18*] stress. A more general form [*17*] is

$$\dot{\epsilon} = \frac{\dot{\sigma} + r}{h} \tag{2b}$$

In this case $r = (r_y + r_v)$ describes the thermal change of two structure parameters: τ_y, which relates to the dislocation density, and τ_v, which relates to the distribution. h is a hardening parameter which seems to depend primarily on the free slip area; for example, $h = \theta_y/A_r$ where A_r is a free area function [*17,20*].

The effective stress theory is the principal attempt to combine the ideas of thermally activated and mechanically activated strain. It implies two obstacle sets, one of a short-range nature and one of a long-range (or a complex single set, such as forest dislocations). In Seeger's theory of strain-hardened metals [*6*] the plateau stress (in the flow stress versus temperature curve) was identified as the internal stress σ_i and was associated with dislocation pile-ups. Then

$$\dot{\epsilon} = \dot{\epsilon}_0(\sigma_e, S) \exp^{-Q(\sigma_e, S)/RT} \tag{3}$$

where $\sigma_e = (\sigma - \sigma_i)$ is the effective stress. Ahlquist and co-workers extended the theory by allowing σ_i to recover [*21*]. This theory is quite powerful in interpreting, for example, transient and steady-state creep [14,21] and low-temperature flow in body-centered-cubic metals [22]. It is, however, a theory of *time-dependent* flow (Eq 3), except in the extreme and experimentally uninteresting case of $T = 0$ K or in the athermal plateau region, which is normally only a small part of the flow stress versus temperature curve. Even in this region, loading strains on fast incremental loading should not be observed [12].

Identification of Time-Independent Response

Two methods have been employed to evaluate time-independent response. In a creep machine the strain response associated with a stress increase, usually rapid incremental, is measured. If the strain process is time-independent, an *extra strain* (loading strain) occurs during the time of the load increment; for time-dependent strain the strain rate only increases during this time [12]. In an Instron machine, comparison is made of the loading and relaxation strain rates. Because time-independent strain responds directly to stress increase, the loading strain rate exceeds the relaxation strain rate. However, for time-dependent strain alone, these rates are equal. These latter measurements are the principal topic of the experimental section of this paper. The former are not widely known and will be reviewed in some detail.

In a study of pure lead at 77 K, ($T_H = 0.128$) Clark and Alden [12] measured the strain response to stress increases using an LVDT, chart recorder, and recording oscilloscope. Intermittent slow stress increases ($\dot{\sigma} = 0.458$ MPa/s separated by periods of constant stress $\dot{\sigma} = 0$) produced nearly identical qualitative response in elastic and plastic samples;[3] namely, high stress rate was correlated with high strain rate (Fig. 1*a*). In the plastic sample only, a strain rate greater than zero (creep) was observed at $\dot{\sigma} = 0$, especially at high stresses. The results also indicated that there was a discontinuous decrease in strain rate at the instant of stress rate of ($\dot{\sigma} = 0.458 \rightarrow \dot{\sigma} = 0$). Such a discontinuity (Fig. 1*b*) is clear evidence of time-independent response.[4] The experimental uncertainty in this conclusion was significant, but was reduced by the closely corresponding behavior of elastic and plastic specimens.

The response to rapid stress increase was a rapid strain increment, similar again in the elastic and plastic samples, in fact identical qualitatively except for a non-zero strain rate in the plastic case on both sides of the stress increase. However, even for the small stress increment of 98 KPa (a fractional

---

[3] Elastic samples were pre-stressed to σ_0, then tested at about $\sigma_0/2$. Plastic samples were monotonically loaded from above the yield stress.

[4] And that $R = (\dot{\epsilon})_{\dot{\sigma}=0}/(\dot{\epsilon})_{\dot{\sigma}>0}$ is less than unity. This is the same ratio measured by the load relaxation technique and discussed below.

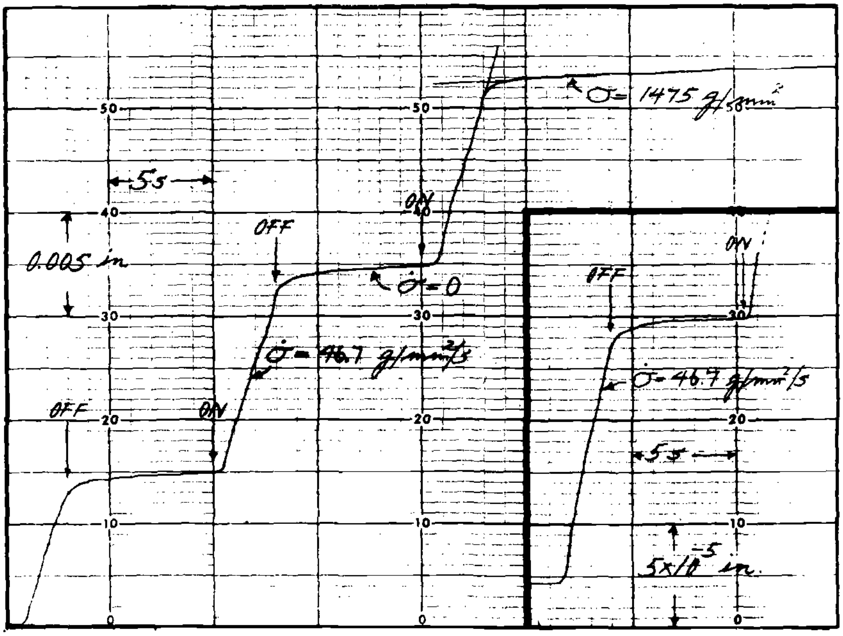

FIG. 1*a—Length versus time in lead, subjected to intermittent stress increases* ($\dot{\sigma} > 0$) *at 77 K. These are photographs of the original strip chart records* [12]. *The data in the box, lower right, are for the elastic sample. Conversion factors are 1 in. = 2.54 cm; 1 g/mm² = 9.8 × 10³ Pa.*

increase of 0.0056), the plastic specimen showed a larger strain increment than the elastic. Some time-independent plastic strain was always observed.

The measured strain increment $\Delta\epsilon$ (Fig. 2) was divided into three parts: $\Delta\epsilon = \Delta\epsilon_{pt} + \Delta\epsilon_{pi} + \Delta\epsilon_e$. $\Delta\epsilon_{pt}$ is the estimated time-dependent component, equal to product of the average creep rate before and after the stress increment and the time increment of the stress increase $\Delta t \simeq 50$ ms. $\Delta\epsilon_{pt}$ is always small. At $\Delta\sigma = 20$ g/mm² (196 KPa), $\Delta\epsilon_e$ (the elastic strain) and $\Delta\epsilon_{pi}$ are approximately equal; at higher stress increments the time-independent plastic component ($\Delta\epsilon_{pi}$) dominates (Fig. 3). Significantly, from a theoretical viewpoint, there is no evidence for a *threshold stress* for time-independent response.

A similar study was done for aluminum at a higher temperature ($T_H = 0.507$) by Oikawa and Sugawara [*23*]. The experimental method was identical to the above except that larger fractional stress increments were used. The minimum increase was about 5 percent, equal roughly to the maximum increase in the study of lead. This difference is associated with the higher T_H for aluminum, as shown in a separate study of lead by Alden [*24*]. The results were also identical qualitatively, though Oikawa and Sugawara did not

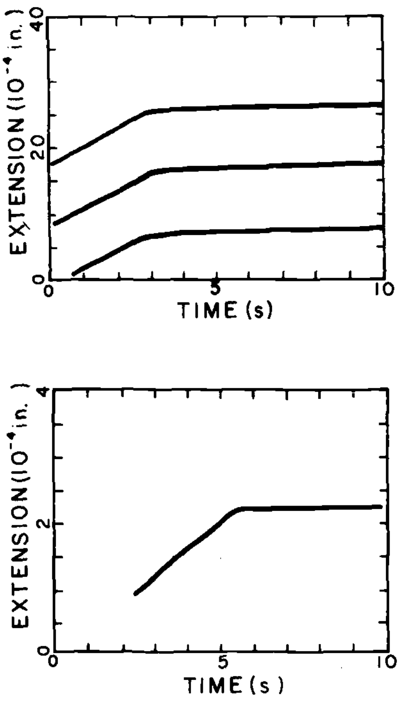

FIG. 1*b*—*Change of length versus time, recording oscilloscope traces (upper box plastic, lower box elastic).*

estimate $\Delta\epsilon_{pl}$. $\Delta\epsilon_e$ was determined by a stress decrement. Oikawa and Sugawara also studied Al-5.5Mg and discovered no time-independent response.

Stress Relaxation Studies

The second method for identification of time-independent response is stress relaxation [*20*]. Near the starting point of relaxation $t = 0$, inequality of the loading strain rate $\dot{\epsilon}_\ell$ and relaxation strain rate $\dot{\epsilon}_r$, $(\dot{\epsilon}_\ell)_{t=-dt} > (\dot{\epsilon}_r)_{t=dt}$, is evidence for such response. Equality of these strain rates (strain rate continuity) can mean either thermally activated flow or mechanically activated flow controlled totally by recovery. The present state of experimental knowledge of strain rate continuity is unsatisfactory and conflicting [*20,25,26*]. Alden found values for the strain rate ratio $R = \dot{\epsilon}_r/\dot{\epsilon}_\ell$ consistently less than unity in aluminum over a range of temperatures from $T_H = 0.08$ to $T_H = 0.64$, and rising from zero toward unity (Fig. 4) as the stress increased or the stress rate decreased [*20*]. Superficially similar results were reported by Abe et al [*26*], with $R \simeq 0.45$ near $T = 300°\text{C}$ and $R \simeq 0.3$ near $T =$

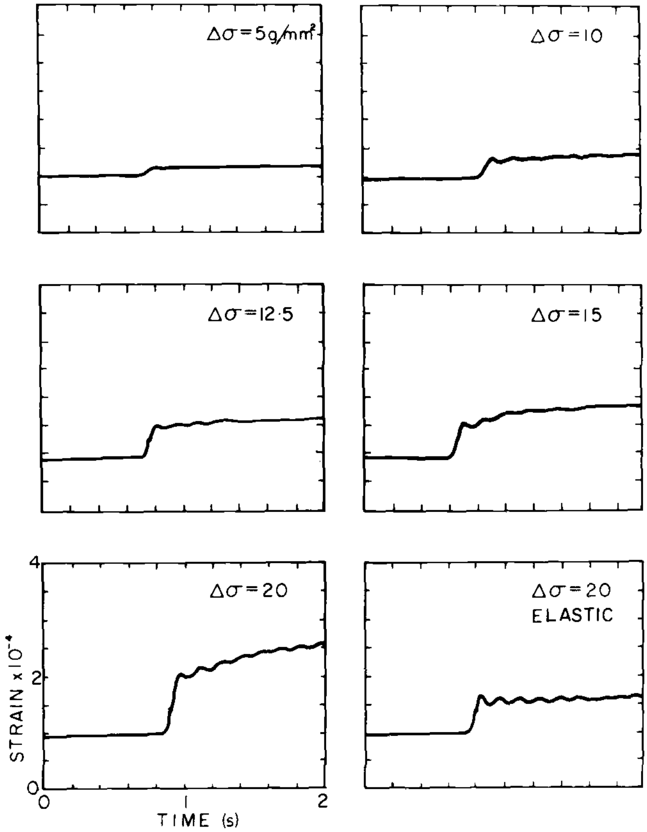

FIG. 2—*Incremental strain response in lead due to rapid small stress increases* $\Delta\sigma$, $T = 77$ *K.* $\Delta\epsilon_{pi} > 0$ *is always measured.* ($\Delta\epsilon_{pi}$ *is the time-independent incremental plastic strain.*) *It becomes dominant at the higher values of* $\Delta\sigma$. *Elastic oscillations of the system always accompany a stress increase.*

400°C in a narrow stress range. In this case, however, the specimens were apparently in steady state ($\dot{\sigma} = 0$) prior to relaxation. Since there can be no direct mechanical activation of strain in this case,[5] R must equal unity regardless of whether the fundamental law of strain is time-dependent or time-independent. It is unfortunate that the results of Abe et al must be suspect because they report additionally that $R = 1.0$ in Al-5.7Mg. This finding would tend to reinforce the distinction between aluminum and Al-Mg mentioned above in connection with response to rapid loading [*23*].

Finally, Holbrook et al found R-values near unity for aluminum, nickel,

---

[5] Any mechanical activation must be the result of recovery. The recovery rate is continuous through the relaxation point.

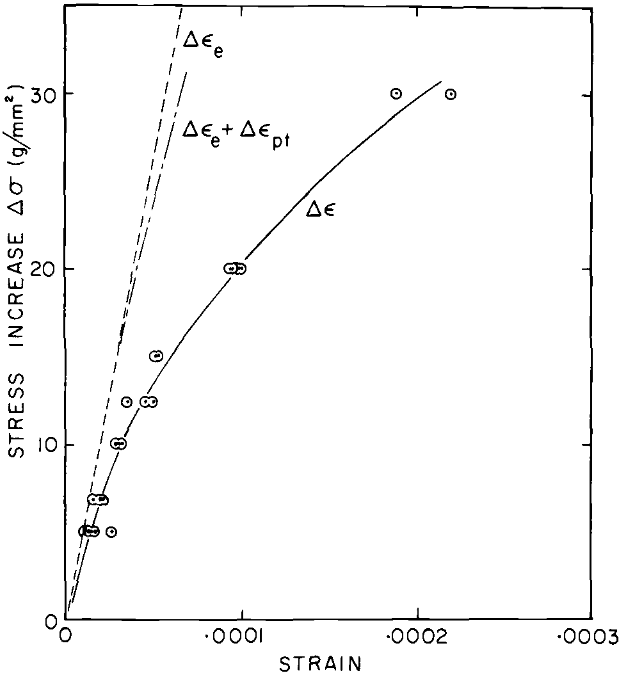

FIG. 3—*Stress variation of the three components of* $\Delta\epsilon = \Delta\epsilon_{pt} + \Delta\epsilon_{pi} + \Delta\epsilon_e$. *There is no evidence for a threshold stress increment* $\Delta\sigma_t$ *for* $\Delta\epsilon_{pi} > 0$.

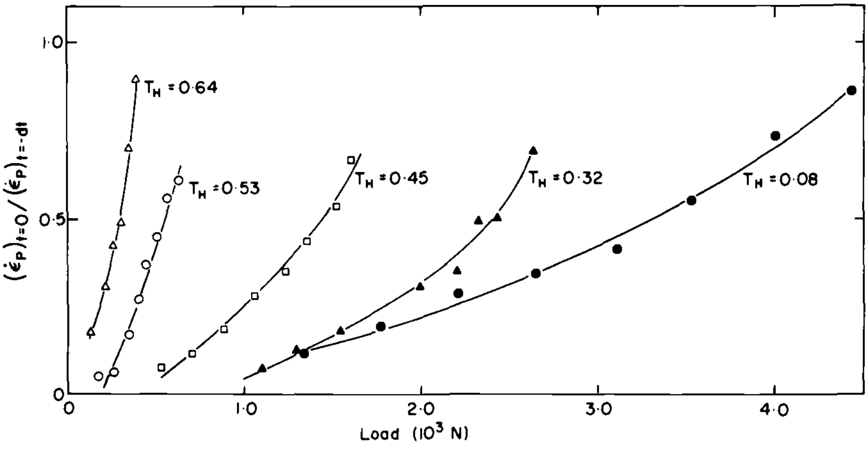

FIG. 4—*Strain rate ratio* R = $\dot{\epsilon}_r/\dot{\epsilon}_f$ *evaluated at* t = *0; aluminum (111) single crystals deformed in compression at various temperatures.* R *varies from near zero at low load to near unity at high load* [20].

steel, and stainless steel at room temperature [25]. For the cases where R was measured to be less than unity, they argue that there is inadequate time and load resolution in the measuring equipment. Such inadequate resolution was certainly possible in the study of aluminum [20]. They conclude that $R < 1$ is not a physically meaningful result, and that the strain rate is indeed a function only of the stress, structure, and temperature.

Experimental Methods

Tension tests were done on cylindrical samples of coarse-grained lead approximately 5 cm in length. Material labeled Pb-A, 99.999 percent pure, was used for most of the tests; Pb-B was doped with 0.005 percent silver which prevented recrystallization during long periods of relaxation. After extrusion of air melted and cast billets from 2.5 to 0.52 cm diameter, specimens were cut from the extruded rod with a jeweller's saw, straightened by rolling on a glass plate and annealed in oil, 160°C for 1 h. Specimens of eutectic Pb-Sn were prepared in an identical manner using 99.999 percent tin.

Extension was done in a floor-model Instron machine. The problem of load and time resolution during relaxation, discussed by Holbrook et al [25] was minimized in a two-fold manner. Firstly, the lowest cross-head speed [8.47 × 10^{-5} cm/s (0.002 in./min)] was normally used to reduce $(\dot{\epsilon}_\ell)_{t=-dt}$. $(\dot{\epsilon}_r)_{t=dt}$ was also reduced in a nearly proportional manner. Secondly, in most cases the spring constant K of the loading train was reduced to roughly a tenth of its usual value by supporting the load cell on compression springs with ground ends. Since during relaxation

$$\dot{P}_r = \dot{\ell}_r K \tag{4}$$

for a given rate of plastic extension of the specimen $\dot{\ell}_r$, $\dot{P}_r$ is reduced in proportion to K. For comparison, K-values in previous and current work by the author [20] using a conventional hard loading train were 3.5 to 5.26 × 10^4 N/cm (2 to 3 × 10^4 lb/in.); in the present work, K was about 3.15 × 10^3 N/cm (1.8 × 10^3 lb/in.). Typical maximum values for $\dot{P}_r$ (at the start of relaxation) were 0.22 N/s (0.05 lb/s), much less than the response capability of the recorder [220 N/s (50 lb/s)].

R-values versus stress were normally obtained from a single specimen by intermittent load relaxations during a test in which the load gradually rose from near zero to near its maximum value.

Measurement of loading and relaxation slopes was done graphically using a Starrett machinist's protractor with a rotating arm. In some cases, the recorded trace was measured directly at or as near as possible to the inflection point, $t = 0$. In others, the traces on either side of this point were matched and pencil lines drawn over at least 50.8 mm (2 in.) and through the inflection point using one of a large set of French curves. Angles were then measured at the intersection point of the two pencil lines. While the author believes that the second method is more accurate (particularly in the case of lead, where the relaxation slope changes quite rapidly with time), the results and conclusions of the study are basically independent of the method chosen.

Experimental Results

Measurements of R in lead (Pb-A) at $T = 23°C$ using the hard test configuration (load cell bolted to the Instron frame) show a monotonic increase of R, but with $R_{\max} \simeq 0.3$ at $\dot{\sigma}$ somewhat greater than zero [*27*]. Similar results are found at lower temperatures down to $T = -196°C$, except that R increases more slowly with stress as the temperature is lowered, as in aluminum [*20*]. The maximum value of R is near 0.4 at $\dot{\sigma} \simeq 0$. Since all theories predict $R = 1.0$ at $\dot{\sigma} = 0$, it must be that the measured values are systematically low, probably for the reasons discussed by Holbrook et al [*25*]. It should be noted, however, that the R-values are *not constant* near 0.4 as might be expected for thermally activated flow, but increase from near zero as the stress increases (and stress rate decreases) [*27*].

In order to have confidence in the measurement, it is necessary to measure $R \simeq 1.0$ for the steady state case, $\dot{\sigma} = 0$. Using the slowest available extension rate and small K-value (soft configuration), R-values at $T = 23°C$ for lead near steady state are found [*27*] to scatter around unity with an average value of 0.94.[6] Measurements of R versus stress using the same experimental parameters show the characteristic monotonic increase (Fig. 5), but with absolute values about a factor of two larger than in the previous case and a maximum value near unity at the highest stress [6.9 MPa (10^3 lb/in.^{2})].

Given the normal shapes of the stress-strain curves of lead, $\dot{\sigma}$ decreases as the stress increases. From tests run at various cross-head speeds, R-values may be plotted versus stress rate. This experiment was done with material Pb-B. R shows a scattered, monotonic decrease with increasing stress rate (Fig. 6). Additional measurements were done on several specimens loaded continuously (without intermittent relaxation) to the same stress [8.28 MPa (1.2×10^3 lb/in.^{2})], but at different cross-head speeds. At the lowest speed, this stress is achieved only after considerable strain and near $P_{\max}$, whereas at the highest speed the strain is small and the load rising rapidly. Again, R decreases with increasing stress rate. However, in this case both $\dot{\epsilon}_\ell$ and $\dot{\epsilon}_r$ were measured. Both increase with stress rate, but $\dot{\epsilon}_r$ increases more slowly (Fig. 7, lower curve).

Similar measurements were done with the superplastic Pb-Sn alloy with generally similar results. The strain rate ratio was measured at several

---

[6] Anelastic contraction would tend to reduce R to below unity, even if that is the expected value.

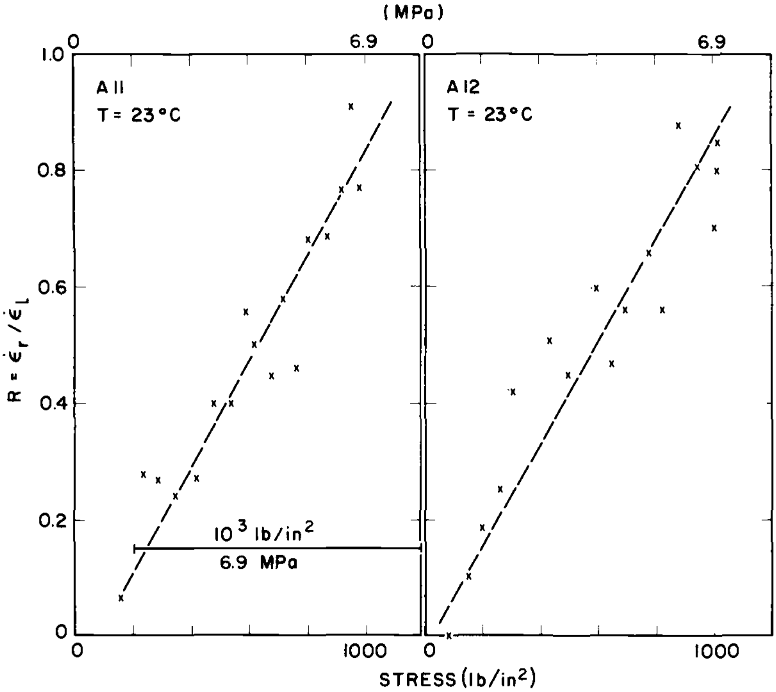

FIG. 5—R *versus stress using the elastically soft testing machine. The values are about a factor of two higher than for the hard machine and approach unity at the highest stress.*

temperatures and shows a steady increase toward unity as the stress is increased (Fig. 8). Again, the curves are shifted to higher stress as the temperature is decreased. (The average homologous temperature for this alloy [*28*] at $T = -10°C$ is $T_H = 0.497$, similar to lead at $T = 23°C$, $T_H = 0.493$.) The superimposed curve for lead shows that R rises for Pb-Sn over a much larger stress range. This distinction would, of course, depend significantly on the strain rate as well; as the strain rate is increased, the maximum stress rises much more rapidly for Pb-Sn than for coarse-grained lead.

Again, similar to lead, both $\dot{\epsilon}_r$ and $\dot{\epsilon}_\ell$ are affected by stress rate. This is shown in Fig. 7, upper curve. This figure shows that there is a quantitative difference between the superplastic and nonsuperplastic material not evident in Fig. 8; that is, the stress rate has a lesser effect on the loading strain rate in Pb-Sn so that the R versus stress rate curve lies at higher R-values. This same effect is shown in Fig. 9. The $\dot{\epsilon}_\ell$ and $\dot{\epsilon}_r$ curves versus $\dot{\sigma}$ diverge so as to yield an increasing R for both materials. The divergence is, however, weaker in Pb-Sn. Moreover, the stress rate effect on both strain rates is substantially smaller.

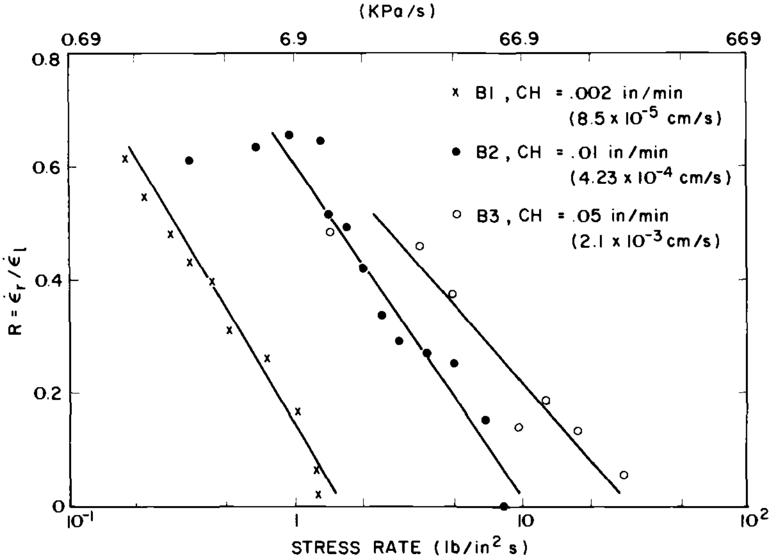

FIG. 6—R *versus log stress rate, soft machine. Stress rate was varied by selection of different cross-head speeds, CH.*

Discussion

The weight of the evidence from previous and present work favors the importance of mechanically activated strain, particularly in pure face-centered-cubic metals. The present results on the strain rate ratio, R, in polycrystalline lead measured by load relaxation tests are roughly consistent with the earlier study in aluminum single crystals. R increases monotonically from near zero at low stress to values near 0.40 or 0.95 at high stress, depending on whether the test equipment is in the hard or soft configuration. The measurement of $R \simeq 1.0$ for $\dot{\sigma} = 0$ indicates that the resolution of the measurement is adequate for determination of $\dot{\epsilon}_r$. Particularly compelling in this respect is that similar conclusions about the variation of R with stress were made from earlier experiments [*12*] in a creep machine with high-speed length recording capability, in which the *stress* rate was turned on and off periodically rather than the *strain* rate. Other evidence for athermal response is provided by the measurement of plastic strain in the rapid incremental loading tests, both in aluminum [*23*] and lead.

Holbrook et al [*25*] derived an empirical equation in order to calculate the necessary resolution time, $t(R)$, for detection of a specified R-value, typically 0.95. Three experimental factors increased the need for short resolution time: a stiff testing machine, a fast strain rate, and a high stress sensitivity of the strain rate. For their experiments, with the equipment stiffness equal to

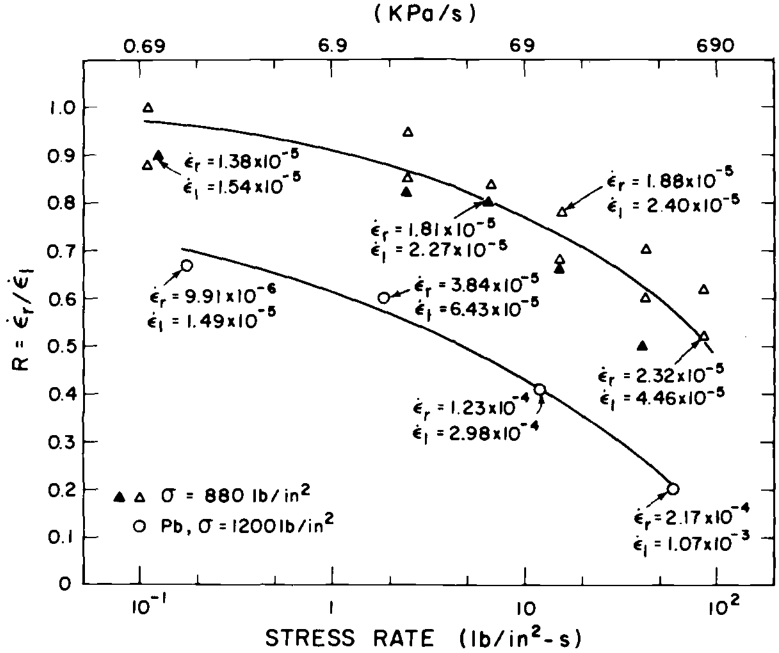

FIG. 7—R *versus stress rate at constant stress for lead, lower curve, and for Pb-Sn, upper curve. Both* $\dot{\epsilon}_r$ *and* $\dot{\epsilon}_\ell$ *increase with stress rate but* $\dot{\epsilon}_\ell$ *increases more rapidly. The stress rate is less effective in the superplastic alloy.*

the sample modulus, $t(R)$-values were typically 0.02 to 0.05 s. For Pb-Sn using the soft machine with a modulus about ×100 smaller, $t(R)$ is near 10 s, far longer than the resolution capabilities of the recording equipment [27].

It is not clear that their analysis is applicable to lead at 23°C, but the very low modulus of the soft machine and the results of Fig. 5 suggest that in this case $t(R)$ is not so short as to be a problem.

It is important to recognize that although a hard machine may be desirable for long-time relaxation tests to achieve more nearly constant structure (assuming the recovery rate is small), this feature is not at issue in the present experiments. Since only the initial relaxation rate is measured, constant structure may be assumed with some certainty even with a soft machine, in order to gain the advantage of a slow relaxation.

This being said, the conflict among the conclusions from various load relaxation measurements remains disturbing and the case will not be clear until this conflict can be resolved. Moreover, it is certainly not the author's intention to argue that all metals and alloys at various temperatures show time-independent behavior. This is a matter that needs much further exploration once the experimental problems have been resolved. At present, it seems

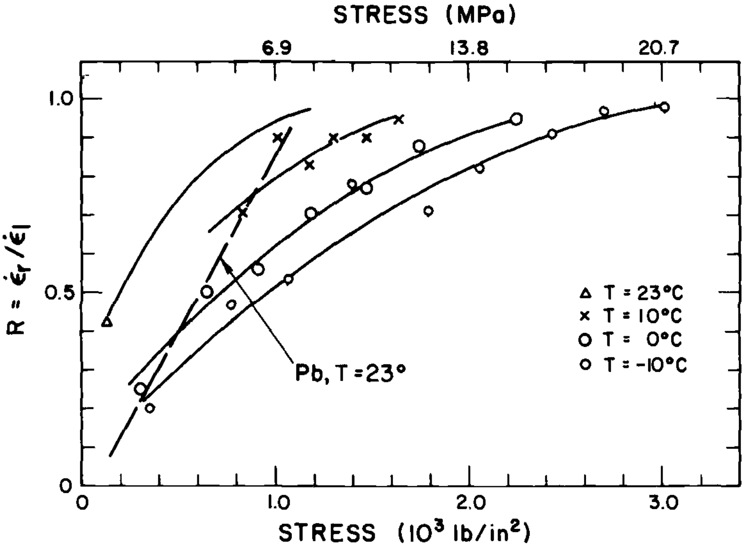

FIG. 8—R *versus stress at various temperatures for the Pb-Sn eutectic. It shows a monotonic increase, as for lead, but over a broader stress range. The testing machine is in the soft configuration, cross-head speed 0.002 in./min. Lead data are shown for comparison.*

likely that body-centered-cubic metals at low temperature, highly alloyed or irradiated materials hardened by point defects, and intermetallic compounds may be examples of nearly pure time-dependent deformation. The particular case of Al-Mg seems quite well-documented both by rapid loading and relaxation experiments [*26*], though the previously mentioned ambiguity in the load relaxation results is unfortunate. In this context, Clark [*29*] studied lead alloys of the Class I and Class II types using incremental loading and unloading.[7] A clear pattern of time-independent response in the Class II alloys and time-dependent response in the Class I alloys (as classified by the steady-state creep behavior) did not emerge from this study. Pb-In (Class I) and Pb-Bi (Class II) alloys showed loading strain increments during small rapid increases of stress, indicative of time-independent behavior. The transients following either stress increase or stress decrease were complex.

The superplastic Pb-Sn alloy shows behavior so nearly similar to pure lead in the present experiments that one must strongly suspect its deformation mechanism to be a form of recovery creep [*30,31*]. However, it must be very different in mechanistic detail from recovery creep of coarse-grained metals, because so many other properties of the superplastic alloy are distinctive

---

[7] Class II alloys are said to show recovery controlled creep, which implies a time-independent strain process; Class I alloys are glide-controlled, a time-dependent process.

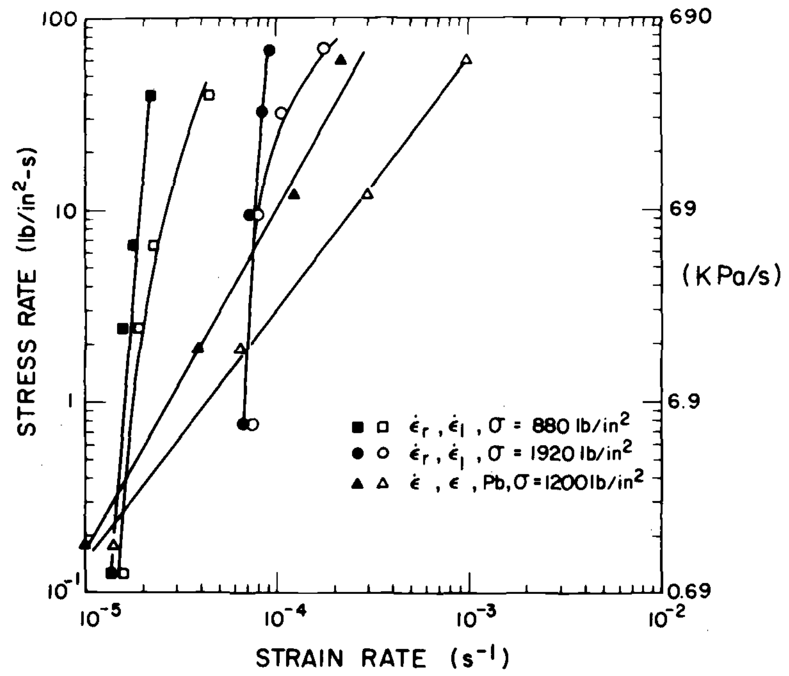

FIG. 9—*Loading and relaxation strain rates versus stress rate. The stress is constant. Both the divergence of the curves and the quantitative impact on the strain rates is less in Pb-Sn than in pure lead.*

[*28*]. One clue is that the recovery rate of fine-grained metals is very fast and has a weak temperature dependence. Alden [*32*] found recovery rates 10^4 to 10^5 times faster in 3.5-μm Pb-5Cd than in the 15-μm grain size alloy.

Since the strain rate is given by an equation such as Eq 2*b*, by comparison to coarse-grained lead at the same strain rate, h must be also very large. Contrary to most of the literature [*23,24*], h is not a strain-hardening coefficient in the usual sense (associated with dislocation accumulation), but depends mainly (and inversely) on the free area for easy, rapid slip, that is, the local area over which the stress is above the mechanical threshold. In the superplastic alloy, this area should be on the order of but perhaps substantially less than the small grain area. The weak dependence of strain rate $\dot{\epsilon}_\ell$ on stress rate (Fig. 9) may be understood in this manner as may the small strain on initial or incremental loading in a creep machine. The model also seems to imply a relatively small increase in dislocation density during straining so that the indirect stress rate effect (structure difference effect), namely, the increase of $\dot{\epsilon}_r$ with $\dot{\sigma}$, is also small.

The analysis on which the measurement of R depends has not included the possibility of anelastic strain. If an anelastic extension rate is included, then

$$\dot{\ell}_{\mathrm{CH}} = \dot{\ell}_{\mathrm{e}} + \dot{\ell}_{\mathrm{an}} + \dot{\ell}_{\mathrm{pl}} \tag{5}$$

where $\dot{\ell}_{\mathrm{CH}}$ is the cross-head speed. If the time constant for anelastic strain is small, the anelastic and elastic extensions may be combined so that for an experimental determination of the system elastic constant K:

$$K = \frac{\dot{P}}{\dot{\ell}_e + \dot{\ell}_{\mathrm{an}}} \tag{6}$$

K was in fact determined this way by occasional unloading and reloading during a test rather than by calculation from the machine constant and specimen Young's modulus. The occurrence of anelastic strain should not interfere with the measurement of R in this case, or for the other extreme case where the time constant is large, for which the anelastic "element" is effectively rigid in experimental times.

It is possible, though not entirely clear to this author, that at intermediate time constants the anelastic extension should be added to the *plastic* extension (Eq 5). Since $\dot{\ell}_{\mathrm{an}} = \dot{\ell}_{\mathrm{an}}\,(\dot{\sigma})$, it will increase the extension rate during loading and decrease it during relaxation; both effects will tend to decrease R below unity, even if that is its "true" value. However, in coarse-grained strain-hardened lead the anelastic strain should occur by a dislocation process (for example, dislocation bowing) and will be larger at high dislocation density and stress; this effect alone would cause R to *decrease* as the stress increases, contrary to the observed effect. For the case of grain-boundary anelastic response, which may be dominant in the superplastic alloy, it seems unlikely at least that the anelasticity will decrease with stress, so the effect on R may be stress independent. Since R is observed to be unity at high stress, one may conclude that anelastic effects are too small to be important in the Pb-Sn alloy. A similar conclusion may hold for lead. Evidence supportive of this conclusion was found by Gibeling and Nix [*33*], who observed small anelastic recovery in lead (less than the elastic contraction) on unloading from creep experiments.

It seems likely to the author that the ordinary case of deformation is mixed with both an athermal and a thermal character. However, the dominant theory by which this situation is described, the effective stress theory, does not admit the possibility of mechanical activation of strain except in the extreme case of $\sigma = \sigma_i$, which might apply, for example, in pure face-centered-cubic metals in the athermal plateau. However, at any lower temperature the strain is thermally activated and $R \equiv 1.0$. Even in the plateau a threshold stress might be evident for time-dependent response in a load increment test (the magnitude of this stress equals σ_e); no threshold stress was detected for lead at 77 K, well below the plateau.

It seems physically reasonable that there may be a gradual transition between deformation states that are primarily mechanically activated to those that are primarily thermally activated as the nature of the alloy, the test conditions, and the temperature change. Ordinary deformation would then have a mixed character and purely thermally activated strain would be rare, as would purely mechanically activated strain. Table 1 shows this concept. Among the factors which would probably enhance mechanically activated strain are low temperature, high stress, high stress rate, and an obstacle structure of a long-range nature. Conversely, high temperature, low stress, etc., would enhance the thermally activated nature of the deformation.

The equations that describe such behavior are still unknown. The following tentative discussion may facilitate their development. Consider the problem of dislocations expanding in nonregular obstacle fields, one of short-range obstacles (Case I) and one of long-range obstacles (Case II). At the same temperature and strain rate, it is necessary in the latter case to impose a higher stress, nearer to the mechanical threshold (Fig. 10). At this stress, each activated event will produce a fairly large strain because the newly released dislocations expand over a large area. Then qualitatively if $\dot{\epsilon} = (\dot{\sigma} + r^*)/h$, $r^*_{\text{II}} < r^*_{\text{I}}$ (fewer thermal strain events) and $h_{\text{II}} < h_{\text{I}}$ (more strain per event). r^* is a parameter descriptive of the thermal release of dislocations from obstacles either because the obstacle moves or disappears, or is bypassed. The sensitivity of the strain rate to stress rate,

$$1/\frac{d\dot{\sigma}}{d\dot{\epsilon}} = 1/h \qquad (7)$$

TABLE 1—*Hypothetical conditions under which time-independent or time-dependent flow might be favored.*

	TIME DEPENDENT →	
Long Range	Obstacle Type	Short Range
Low	Temperature	High
High	Stress Rate	Low
High	Stress	Low
←	TIME-INDEPENDENT	

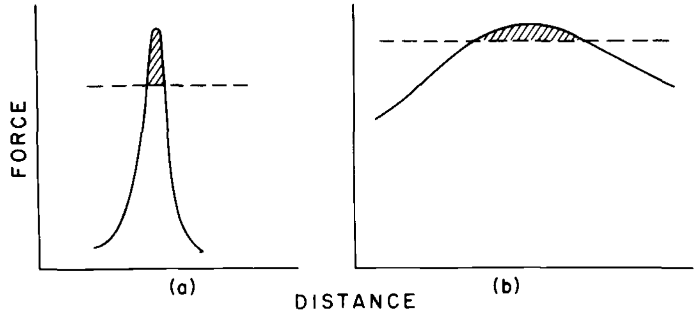

FIG. 10—*Thermal activation over* (a) *short-range obstacles and* (b) *long-range obstacles. In* (b) *the stress is nearer the mechanical threshold and the free area in a random obstacle field will be larger.*

is then smaller for the short-range obstacles; that is, the strain is primarily thermally activated rather than mechanically activated. A similar result was given in an earlier analysis of flow in strain-hardened [*17*] metals as

$$\frac{A_r}{\theta_y} = \frac{1}{h} \tag{8a}$$

$$A_r = \frac{1}{\theta_y + r_v/\dot{\epsilon}} \tag{8b}$$

A_r is dependent on the free slip area, and r_v is a measure of the thermal activation rate of slip (excluding recovery r_y). In an extension of the theory to alloys with many thermal obstacles, $r_v = r^*$ will be large and A_r small. This may be the case of almost pure thermally activated flow.

Conclusions

It is almost always claimed that plastic strain is time-dependent and that the strain rate depends only on the stress, structure, and temperature. Evidence presented in this paper indicates that this claim is incorrect for aluminum, lead, and a superplastic Pb-Sn alloy. These materials seem to exhibit a *time-independent* strain response which depends to a degree on the above variables but in addition, importantly and directly, on an *increase* of stress. The bases for this conclusion are (*1*) observation of loading strains during fast incremental loading of lead in a creep machine (the rate of this loading strain is indistinguishable from the rate of elastic strain); and (*2*) a strain rate ratio, $R \simeq \dot{\epsilon}_r/\dot{\epsilon}_\ell$, evaluated near the start of load relaxation in an Instron machine, which is generally less than unity and increases toward unity as the stress approaches its steady-state value.

Measurements by others [25] show $R = 1$ in several metals and alloys including aluminum. Further measurements of this quantity are expected to be of value in resolving this conflict and in exploring the importance of time-independent plasticity for various metals, alloys, and temperatures.

References

[1] Orowan, E., *Proceedings of the Physical Society*, Vol. 52, 1940, p. 8.

[2] Basinski, Z. S., *Philosophical Magazine*, Vol. 4, 1959, p. 393.

[3] Conrad, H., de Meester, B., Yin, C., and Donor, M. in *Rate Processes in Plastic Deformation*, Li and Mukherjee, Eds., American Society for Metals, 1975, p. 175.

[4] Kocks, U. F., Argon, A. S., and Ashby, M. F., *Progress in Materials Science*, Vol. 19, Pergamon Press, Oxford, 1975.

[5] Gilman, J. J., *Micromechanics of Flow in Solids*, McGraw-Hill, New York, 1969.

[6] Seeger, A. in *Dislocations and Mechanical Properties of Crystals*, J. C. Fisher et al, Eds., Wiley, New York, 1957, p. 243.

[7] Conrad, H. in *The Relations between Structure and Mechanical Properties of Metals*, HMSO, London, 1963, p. 476.

[8] Weertman, J., *Journal of Applied Physics*, Vol. 26, 1955, p. 1213.

[9] McLean, D., *Transactions of the Metallurgical Society*, AIME, Vol. 242, 1968, p. 1193.

[10] Alden, T. H., *Acta Metallurgica*, Vol. 17, 1969, p. 1435.

[11] Mitra, S. K. and McLean, D., *Metal Science Journal*, Vol. 1, 1967, p. 192.

[12] Alden, T. H. and Clark, M. A. in *Rate Processes in Plastic Deformation of Materials*, Li and Mukherjee, Eds., American Society for Metals, 1975, p. 656.

[13] Garofalo, F., *Fundamentals of Creep and Creep Rupture in Metals*, Macmillan, New York, 1964.

[14] Gasca-Neri, R., Ahlquist, C. N., and Nix, W. D., *Acta Metallurgica*, Vol. 18, 1970, p. 655.

[15] Cuddy, L. J., *Metallurgical Transactions*, Vol. 1, 1970, p. 395.

[16] Abe, K., Yoshinaga, H., and Morozumi, S., *Transactions of Japan Institute of Metal*, Vol. 18, 1977, p. 479.

[17] Alden, T. H., *Philosophical Magazine*, Vol. 25, 1972, p. 785.

[18] Kocks, U. F., *Philosophical Magazine*, Vol. 13, 1966, p. 541.

[19] Cottrell, A. H. and Aytekin, V., *Journal of the Institute of Metals*, Vol. 77, 1950, p. 389.

[20] Alden, T. H., *Metallurgical Transactions*, Vol. 8A, 1977, p. 1675.

[21] Ahlquist, C. N., Gasca-Neri, R., and Nix, W. D., *Acta Metallurgica*, Vol. 18, 1970, p. 663.

[22] Christian, J. W. in *Second International Conference on Strength of Metals and Alloys*, American Society of Metals, 1970, 31.

[23] Oikawa, H. and Sugawara, K., *Scripta Metallurgica*, Vol. 12, 1978, p. 85.

[24] Alden, T. H., *Metallurgical Transactions*, Vol. 6A, 1975, p. 1597.

[25] Holbrook, J. H., Rohde, R. W., and Swearengen, J. C., *Acta Metallurgica*, Vol. 29, 1981, p. 1099.

[26] Abe, K., Yoshinaga, H., and Morozumi, S., *Journal of Japan Institute of Metal*, Vol. 40, 1976, p. 393.

[27] Alden, T. H., work in progress.

[28] Alden, T. H. in *Treatise on Materials Science and Technology*, Academic Press, New York, 1975, p. 226.

[29] Clark, M. A., Ph.D. thesis, University of British Columbia, 1975.

[30] Ball, A. and Hutchinson, M. M., *Metal Science Journal*, Vol. 3, 1969, p. 3.

[31] Gifkins, R. C., *Metallurgical Transactions*, Vol. 7A, 1976, p. 1225.

[32] Alden, T. H., *American Society of Metal Transactions Quarterly*, Vol. 61, 1968, p. 559.

[33] Gibeling, J. and Nix, W. D., private communication.

DISCUSSION

Erhard Krempl[1] *(written discussion)*—The author proposes to distinguish between time-dependent and time-independent metal deformation by means of tests involving abrupt changes in loading rate. The starting point is the equation

$$\dot{\epsilon} = \dot{\sigma}\left(\frac{1}{E} + g(\sigma,\epsilon,T)\right) + f(\sigma,\epsilon,T) \qquad (9)$$

where ϵ denotes the total strain rate, and $g(\sigma,\epsilon,T)$ is the time-independent, $f(\sigma,\epsilon,T)$ the time-dependent, and $1/E$ the elastic contribution. For this discussion it is only important that the functions $f(\ )$ and $g(\ )$ do not depend on the rates.

Consider a time $t = t_o$ at which the jump in loading rate occurs and designate $\dot{\epsilon}^-$ and $\dot{\epsilon}^+$ as the strain rates immediately before and after the jump, respectively. From Eq 9:

$$\dot{\epsilon}^+ - \dot{\epsilon}^- = (\dot{\sigma}^+ - \dot{\sigma}^-)\left(\frac{1}{E} + g(\ )\right) \qquad (10)$$

where the notation used for the strain rate has been extended to the stress rate.

Equation 10 has three interpretations:

1. $\dot{\sigma}^+ = \dot{\sigma}^-$, then $\dot{\epsilon}^+ = \dot{\epsilon}^-$ irrespective of the presence or the absence of the time-independent term.

2. $\dot{\epsilon}^+ = \dot{\epsilon}^-$, then $\dot{\sigma}^+ = \dot{\sigma}^-$ irrespective of the presence or the absence of the time-independent term.

3. Neither (*1*) nor (*2*) are true. In this case

$$\dot{\epsilon}^+/\dot{\epsilon}^- = 1 + \frac{\dot{\sigma}^+ - \dot{\sigma}^-}{\dot{\epsilon}^-}\left(\frac{1}{E} + g(\ )\right) \qquad (11)$$

so that the ratio $\dot{\epsilon}^+/\dot{\epsilon}^-$ depends on the value of $g(\ )$ at the instant the jump in loading rate is taking place.

The author purports to distinguish between time-dependent and time-independent deformation on the basis of the value of $\dot{\epsilon}^+/\dot{\epsilon}^-$. This ratio

---

[1] Professor of Mechanics, Department of Mechanical Engineering, Rensselaer Polytechnic Institute, Troy, N.Y. 12181.

depends on stress, strain, and temperature at the instant at which the jump takes place. The author has not presented any evidence that $\dot{\epsilon}^+/\dot{\epsilon}^-$ depends on stress and strain. Indeed the presentations of the results inplied that it was immaterial at which point in stress-strain space the tests were performed. This practice is at variance with Eq 11.

Equation 10 can be rewritten as

$$\frac{d\sigma^+}{d\epsilon} = \frac{1}{\frac{1}{E} + g(\,)}\left(1 + \frac{\dot{\epsilon}^-}{\dot{\epsilon}^+}\frac{d\sigma^-}{d\epsilon}\left(\frac{1}{E} + g(\,)\right) - 1\right) \tag{12}$$

where we have used the chain rule. Consider now a very large strain rate jump $\dot{\epsilon}^-/\dot{\epsilon}^+ \ll 1$ in the plastic range, then ($d\sigma^-/d\epsilon \ll$ E)

$$\frac{d\sigma^+}{d\epsilon} = \frac{1}{\frac{1}{E} + g(\,)} \tag{13}$$

so that the instantaneous slope right after a large strain rate jump depends on $g(\,)$. This prediction appears to be at variance with the observation of an elastic slope immediately following large changes in strain rate.

The discusser does not understand the premise of the author and suggests that the discriminating tests between time-dependent and time-independent deformation are creep, relaxation, and tension tests performed at various loading rates.

T. H. Alden (author's closure)—The equation used by the author is somewhat specialized from that presented by Krempl; namely,

$$\dot{\epsilon}_p = \dot{\sigma}\cdot g(\sigma,S,T) + g\cdot f\,(\sigma,S,T)$$

In the author's experiments, the stress rate was always cycled between positive and zero values (effective zero for plastic flow). If we designate $\dot{\epsilon}^+$ for the case of $\dot{\sigma} > 0$ and $\dot{\epsilon}^-$ for $\dot{\sigma} = 0$, then

$$R = \frac{\dot{\epsilon}^-}{\dot{\epsilon}^+} = \frac{g\cdot f}{g\cdot(\dot{\sigma} + f\,)}$$

The function f may be near zero at low stress if it is descriptive of a recovery process, or it may be larger if dependent on thermally activated flow. In the former case, considered appropriate for pure face-centered-cubic metals, the ratio R varies from zero to unity with increasing stress as f increases and $\dot{\sigma}$ decreases. This is the result shown in Figs. 4 and 7. It is clear from these figures that R depends most definitely on stress and strain; no contrary claim has been made by the author.

Creep, relaxation, and tension tests taken as a whole are not useful in distinguishing time-independent from time-dependent strain because the separate effects of stress and stress rate are not distinguished. It is necessary to look at short-time transients associated with changes in stress rate.

Nicolas Christodoulou,[1] *J. J. Jonas,*[1] *and G. R. Canova*[1]

Determination of First and Second Order Work-Hardening and Rate-Sensitivity Coefficients for Oxygen-Free, High-Conductivity (OFHC) Copper and 99.99 Percent Aluminum

REFERENCE: Christodoulou, Nicolas, Jonas, J. J., and Canova, G. R., **"Determination of First and Second Order Work-Hardening and Rate-Sensitivity Coefficients for Oxygen-Free, High-Conductivity (OFHC) Copper and 99.99 Percent Aluminum,"** *Mechanical Testing for Deformation Model Development, ASTM STP 765,* R. W. Rohde and J. C. Swearengen, Eds., American Society for Testing and Materials, 1982, pp. 51-66.

ABSTRACT: In order to provide data for process modeling, work-hardening and rate-sensitivity coefficients of the first and second order were determined for oxygen-free, high-conductivity copper and 99.99 percent aluminum. For this purpose, tension tests were carried out at room temperature and with constant rates of deformation varying from 5×10^{-4} to 1 s^{-1}. In each test, a constant true strain rate was applied at the minimum cross-section of specially machined samples by means of a computer-interfaced, servo-controlled hydraulic testing machine. The work-hardening coefficient, $H = (\partial \ln \sigma / \partial \epsilon)_{\dot{\epsilon}}$, the rate sensitivity of the work-hardening rate, $B_\sigma = (\partial H / \partial \ln \dot{\epsilon})_\sigma$, and the curvature term, $C = -(\partial H / \partial \ln \sigma)_{\dot{\epsilon}}$, were determined from the flow curves of continuous tests. By performing strain rate changes at constant structure τ and measuring the immediate stress changes, the "instantaneous" rate sensitivity, $M = (\partial \ln \sigma / \partial \ln \dot{\epsilon})_\tau$, was also established. The dependence of the coefficients derived in this way on stress and strain rate is described. From the variation of M with σ and $\dot{\epsilon}$, the coefficients $P = -(\partial M / \partial \ln \dot{\epsilon})_\sigma$ and $Q = (\partial M / \partial \ln \sigma)_{\dot{\epsilon}}$ were evaluated. It was determined that an additional strain of 0.2 had to be imposed on the sample to take it from the UTS condition ($H = 1$) to the condition $H + B_\sigma = 1$. The latter is associated with the onset of flow localization, and the additional strain of 0.2 is a measure of the retarding effect of B_σ on the flow localization process. To assess the effect of impurities, a Haasen plot ($M\sigma$ versus σ) was constructed, which indicated that the copper was solution hardened due to the presence of $\cong$200 ppm of Ag + Mg + S, while there was no effect of solutes in the aluminum.

---

[1] Department of Mining and Metallurgical Engineering, McGill University, Montreal, Quebec, Canada H3A-2A7.

KEY WORDS: state variables, plastic deformation, flow localization, instantaneous rate sensitivity, work hardening, dynamic recovery, solute hardening, OFHC copper, 99.99 percent aluminum, constant strain rate, computerized servo-controlled testing, strain rate change testing, stress and strain rate dependence of rate sensitivity and work hardening coefficient

Since Hart [*1*][2] first suggested replacing the plastic strain with an evolutionary variable called "the hardness state," numerous papers have been published (for example, Refs *2* to *12*) in which the remembrance of the material of its past history is expressed in this way. The technique is not without its problems, however [*13-16*]. These include: (*1*) the difficulty in determining the slope, $\mu = (\partial \ln \sigma / \partial \ln \dot{\epsilon})_M$, of the scaling line under certain conditions [*16*]; and (*2*) the ambiguity that arises at very high or low stresses when the strain rate sensitivity, $M = (\partial \ln \sigma / \partial \ln \dot{\epsilon})_T$, is higher than μ.

A somewhat similar approach was adopted by Kocks in 1975, who suggested that there exists a state parameter called the "mechanical threshold" [*17*] (or, under certain restrictions, the "plane glide resistance") that also describes work hardening in a satisfactory way.

As a follow-up to this line of reasoning, Kocks et al [*18*] proposed the following evolutionary constitutive law:

$$(\partial \ln \sigma / \partial t)_x = M(\partial \ln \dot{\epsilon} / \partial t)_x + H\dot{\epsilon} \tag{1}$$

Here σ, $\dot{\epsilon}$, and t represent the true stress, true strain rate, and time, respectively, and the material coefficients, $M = (\partial \ln \sigma / \partial \ln \dot{\epsilon})_T$ and $H = (\partial \ln \sigma / \partial \epsilon)_{\dot{\epsilon}}$, depend only on the current values of true stress σ and true strain rate $\dot{\epsilon}$.

According to this view, two sets of material coefficients are needed for the complete description of the mechanical response of a plastically deforming material. These are, first of all, the rate sensitivity, $M(\sigma, \dot{\epsilon})$, already defined above and the work-hardening coefficient, $H(\sigma, \dot{\epsilon})$. A graphical description of M and H is presented in Fig. 1. These are called "first order" in the present treatment as they are first derivatives of $\ln \sigma$. A knowledge of their dependence on σ and $\dot{\epsilon}$ at constant temperature is sufficient to describe the development of σ versus t in a particular material element through Eq 1.

Although Eq 1 is of very general utility, there are applications that require a further set of material coefficients; these are the *second* derivatives of $\ln \sigma$, which are defined as:[3]

$$\begin{aligned} B_\sigma(\sigma, \dot{\epsilon}) &= (\partial H / \partial \ln \dot{\epsilon})_\sigma \\ C(\sigma, \dot{\epsilon}) &= (\partial H / \partial \ln \sigma)_{\dot{\epsilon}} \end{aligned} \tag{2}$$

---

[2] The italic numbers in brackets refer to the list of references appended to this paper.

[3] The rate sensitivity, B, of the work-hardening coefficient, H, can also be defined at constant state as $B_T = (\partial H / \partial \ln \dot{\epsilon})_T$. The relationship between B_σ and B_T is given by $B_\sigma = B_T + CM$.

$$P(\sigma, \dot{\epsilon}) = -(\partial M/\partial \ln \dot{\epsilon})_\sigma$$
$$Q(\sigma, \dot{\epsilon}) = (\partial M/\partial \ln \sigma)_{\dot{\epsilon}} \tag{3}$$

These coefficients are particularly useful when the development of strain and strain rate gradients during testing or forming is of interest. Under such conditions, the variation of H and M with position must be known, and these can in turn be specified if the dependence of σ and $\dot{\epsilon}$ on position is also known.[4]

The aim of the present investigation was to measure these parameters at room temperature for oxygen-free, high-conductivity (OFHC) copper (0.22 T_m) and for 99.99 percent aluminum (0.32 T_m). A novel feature of this work was that the tensile experiments were carried out at a constant true strain rate applied to the minimum cross section of each sample with the aid of the servo-controlled testing machine described in more detail in the next section.

Experimental Procedure

Oxygen-free, high-conductivity copper (99.95 percent) was obtained in the form of 12.7-mm-diameter hot extruded rods. The main impurities present were silver (55 ppm), magnesium (64 ppm), and sulfur (80 ppm). After ma-

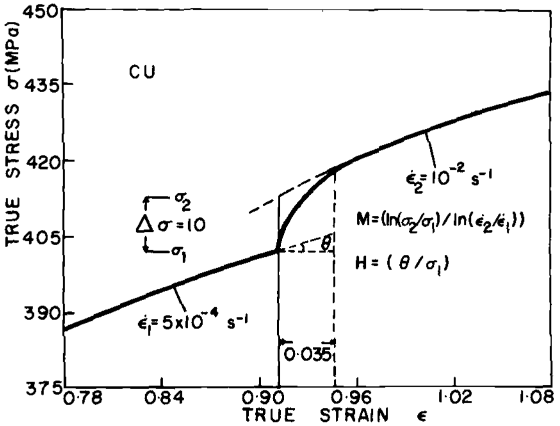

FIG. 1—*Determination of the instantaneous stress change that follows a strain rate change. The "short transient" observed during the few percent of strain that follow the strain rate change is neglected in this method by back extrapolating the high strain rate flow curve as shown.*

---

[4] A more complete description of the six material coefficients and of their use in instability calculations can be found in Ref *18*; the treatment of the above authors is the one that will be followed here.

chining, the samples were annealed for 30 min at 723 K in a dynamic vacuum of 2 × 10^{-6} torr. The resulting average grain size was approximately 0.02 mm. The 99.99 percent aluminum samples were also received in the form of 12.7-mm-diameter hot extruded bars. After machining, the samples were prestrained 12 percent and annealed at 688 K for 60 min. The average grain size produced by the treatment was approximately 0.5 mm. Due to the coarse grain size, the surface of the aluminum samples became rough during straining; this affected the accuracy of measurement of sample diameter.

The sample geometries employed for the present experiments are illustrated in Fig. 2. The geometries were chosen in order to oblige the localization to occur at the minimum cross section, and therefore at the site of the diameter transducer (Fig. 3). The latter was placed where the size of the geometric defect [*19*] was largest; for example, for the specimen of Fig. 2*a* it was 43 percent, whereas for that of Fig. 2*b* it was 5 percent.

The tensile experiments were performed in an MTS machine interfaced with a PDP 11/04 minicomputer. The computer provided the desired input signal to the servo-controller by means of real-time programming; it also ac-

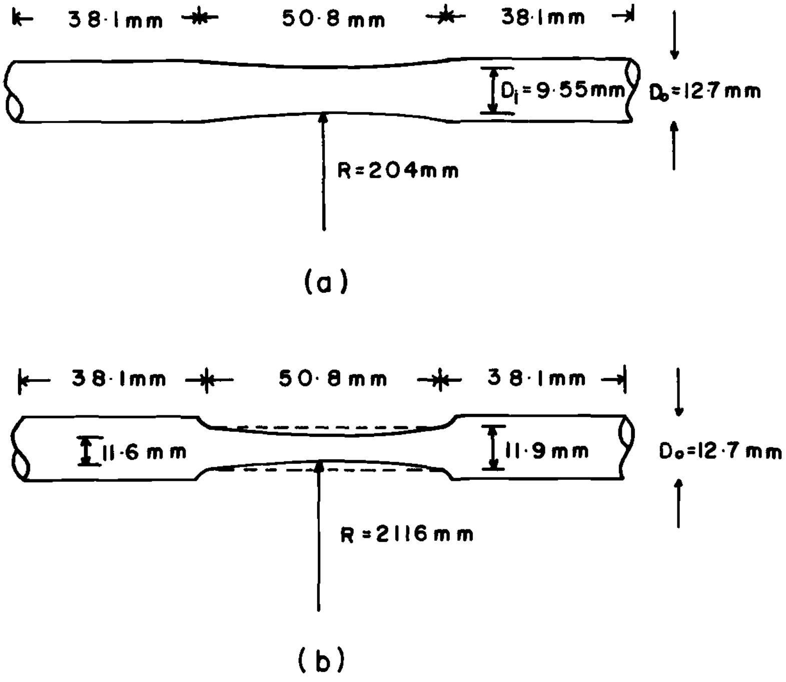

FIG. 2—*Sample geometries, showing the minimum cross sections, which correspond to defect sizes of* (a) *43 percent and* (b) *5 percent.*

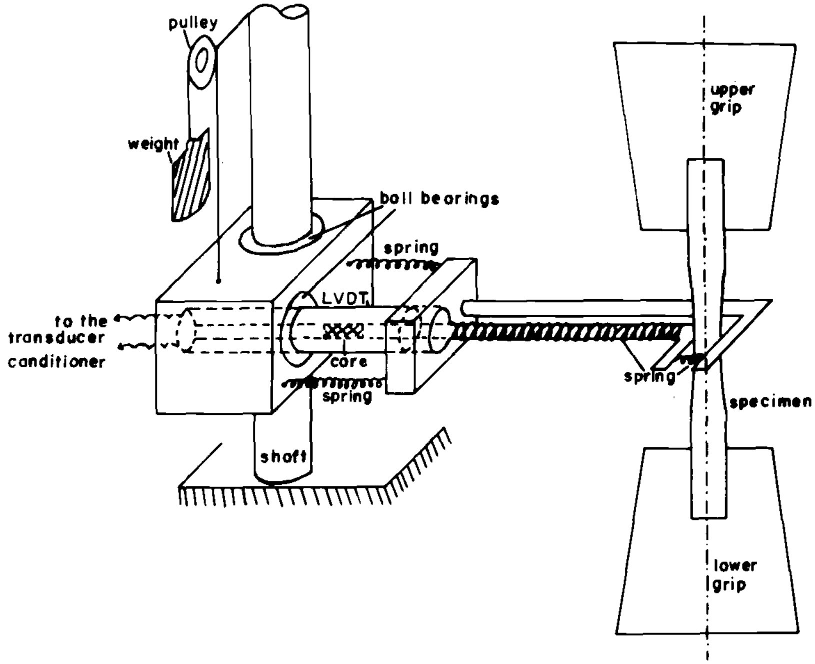

FIG. 3—*Experimental arrangement of the diameter transducer employed to apply a constant true strain rate to the minimum cross section of the tensile sample.*

quired the force and diameter data, and calculated and plotted the stress/strain curves.

The constant true strain rate was applied to the minimum sample cross section through a linear variable differential transformer (LVDT) that was modified to measure the specimen diameter, as shown in Fig. 3. In this way, friction between the specimen and the two extensometer arms was eliminated, in contrast to an earlier design in which a circumferential cable was used to measure the neck perimeter [*20*]. Although the present device worked well, the accuracy is limited when the diameter is not uniform around the circumference, as when the material contains a small number of grains in a given cross section. The LVDT was connected to the strain control mode of the testing machine to which the constant true strain rate was applied by means of the Hardware Segment Generator of the MTS interface. The strain rate range within which the experiments were performed was 5×10^{-4} to $1\ s^{-1}$. The resolution of the LVDT within its working range was around 0.02 mm; in terms of true strain, this is on the order of 0.005.

Strain rate changes were imposed on the specimen at increasing strains, and the resulting stress changes were correlated with the stress developed just before the strain rate was changed (Fig. 1). The stress change $\Delta\sigma$ was determined as follows. The flow curve at appreciable strains (for example, 0.04 to 0.12) after the change was back extrapolated until it intersected the loading line (Fig. 1). This intersection defined the stress σ_2. The back extrapolation was performed by drawing a σ/ϵ curve parallel to the *continuous* flow curve determined at $\dot{\epsilon}_2$, but displaced horizontally as required to match the discontinuous curve at the large strains.

The true stress/true strain curves that were obtained from the raw data were corrected by the method of Bridgman [*21*] to allow for the apparent increase in flow stress attributable to the development of triaxiality.

The true stress/true strain curves that were obtained with the aid of the aforementioned experimental device were in general very smooth (see, for example, Fig. 8 below). However, because taking derivatives increases the effect of even limited scatter, the flow curves were smoothed prior to differentiation by means of a modified version of IBM subroutine SSP-SG13 for three-point smoothing. This routine does not influence the trend of the data, but is designed to filter out abrupt steps due to noise. In the operation of subroutine SG13, a vector, $Z = (z_1, \ldots, z_n)$, of smoothed function values is computed, given vectors $X = (x_1, \ldots, x_n)$ of the argument values and $Y = (y_1, \ldots, y_n)$ of the corresponding function values. Except at the end points x_1 and x_n, each smoothed value z_i is obtained by evaluating, at x_i, the least-squares polynomial of degree 1 relevant to the three successive points (x_{i-1}, y_{i-1}), (x_i, y_i), and (x_{i+1}, y_{i+1}). The slope of the least-squares straight line is then the slope of the smoothed point z_i. In this way, smooth slopes were obtained and the coefficients H and B_σ were derived. For the calculation of the curvature term C, the work-hardening coefficient H was further smoothed using the same technique.

The instantaneous rate sensitivity M was calculated as follows. The strain rate was held constant at $\dot{\epsilon}_1$ and then was abruptly changed to $\dot{\epsilon}_2$ at increasing values of strain. The stress σ_2 at $\dot{\epsilon}_2$ was determined as shown in Fig. 1. Thus, when the curve σ_2 versus ϵ was computed, it was again smoothed by the same method. In this way, the scatter in the measured rate sensitivity, $M = \ln(\sigma_2/\sigma_1)/\ln(\dot{\epsilon}_2/\dot{\epsilon}_1)$, was considerably reduced.

Results and Discussion

Typical flow curves obtained from continuous tests on the two materials are presented in Figs. 4*a* and 4*b*. The large true strains obtained by employing the present experimental technique should be particularly noted. It was observed that at relatively high strain rates (above 0.05 to 0.1 s^{-1}), the temperature of the sample increased during deformation. In order to avoid any temperature effect on the measurement of the coefficients, strain rates lower than 0.1 s^{-1} were used. It is also of interest that the apparent strain

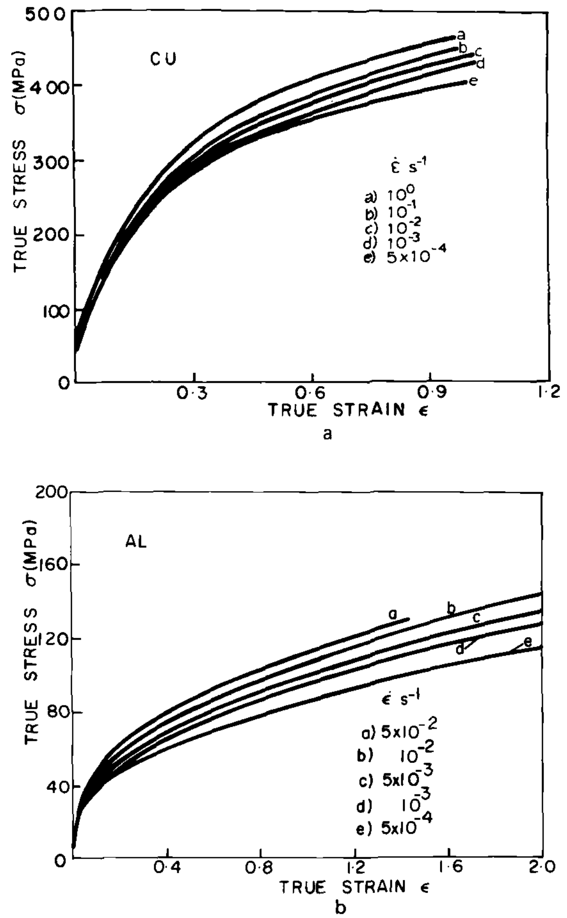

FIG. 4—*True stress/true strain curves determined at the indicated strain rates. The apparent rate sensitivities are 0.015 (copper) and 0.075 (aluminum).*

rate sensitivity, $m = d \ln \sigma / d \ln \dot{\epsilon}$, is found to be 0.015 for copper and 0.075 for aluminum. By contrast, the instantaneous rate sensitivity M was determined to be 0.006 and 0.012, respectively.

In order to assess the influence of the impurities on the two materials, a Haasen plot [22] was constructed. This is depicted in Fig. 5, where both the abscissa and the ordinate have been normalized by the respective shear moduli. The stress change $\Delta\sigma$ is the instantaneous one measured as was shown in Fig. 1. The effect of solution hardening on the rate dependence of the yield stress of copper is made evident in the diagram by the positive value of the vertical intercept. The fitted curve deviates from the straight line

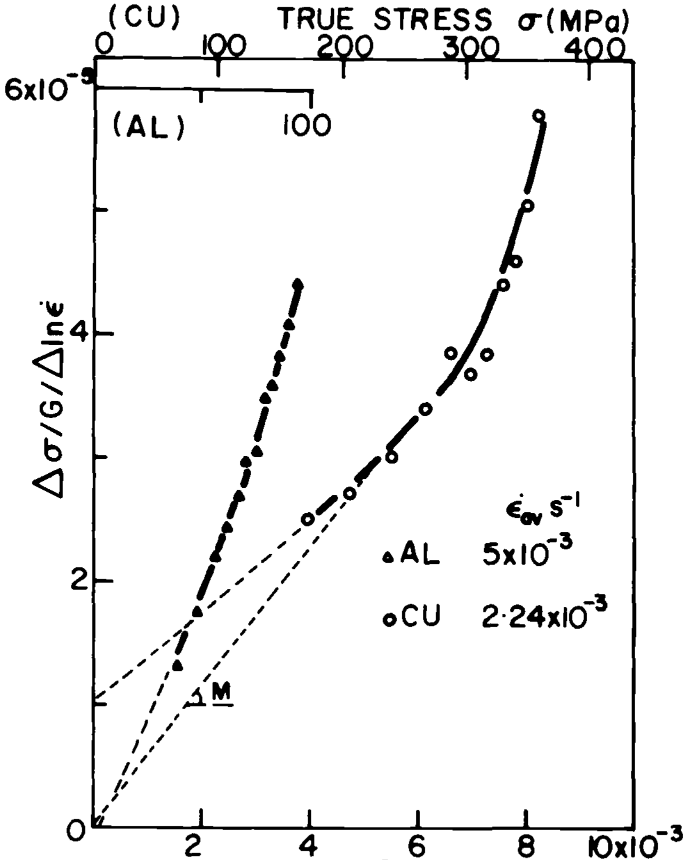

FIG. 5—*Haasen plot* (Mσ versus σ) *for copper and aluminum. The positive intercept in the case of the copper curve is attributable to the solution hardening associated with the presence of* $\cong$*200 ppm Ag + Mg + S.*

observed at lower stresses at around $\sigma/G = 6 \times 10^{-3}$ (which corresponds to $\cong$250 MPa in the case of copper). This can be attributed to the beginning of substantial dynamic recovery, as will be shown later. The aluminum curve, on the other hand, is almost straight and goes through the origin. This behavior is identical to that of the pure nickel reported by Kocks [22]; it indicates the absence of any other flow stress components but that due to dislocation interaction. It is also evident that the slope of the Haasen plot is lower for the solution-hardened metal than for the relatively pure one.

The detailed work-hardening behavior of the two materials is illustrated in Fig. 6. It can be readily seen that in the aluminum, dynamic recovery is the

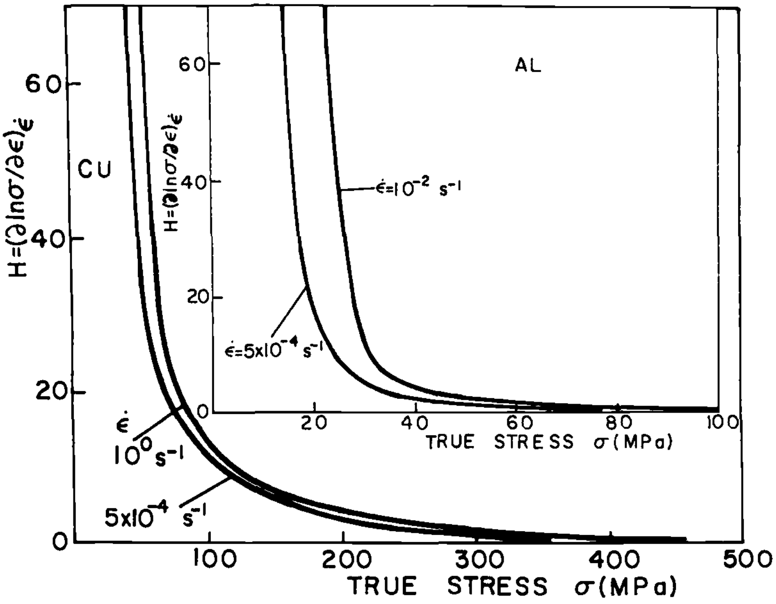

FIG. 6—*Dependence of the work-hardening coefficient* H *on stress and on strain rate for both metals.* H *for aluminum decreases faster with* σ *than for copper because dynamic recovery begins to be dominant at lower stresses for the former than for the latter metal. The stresses at maximum load are 300 and 58 MPa for the copper and aluminum respectively.*

dominant feature of flow at stress levels above 50 MPa ($\sigma/G \geqq 2 \times 10^{-3}$). In the case of the copper, H does not drop down to 2 or 3, and therefore dynamic recovery is still relatively sluggish until $\sigma \geqq 250$ MPa (that is, σ/G attains the range 6×10^{-3}). These observations, based on the H versus σ dependence, are consistent with the interpretation of the Haasen plot (Fig. 5) based on the $M\sigma$ versus σ dependence that was summarized above. It thus appears that when the *slope* of the Haasen curve for copper attains values similar to that for aluminum at stresses above 50 MPa—that is, when the curve for copper breaks upwards—then the material enters into a range of behavior where dynamic recovery is particularly important [*23*].

Second-Order Coefficients

The rate sensitivity of the work-hardening coefficient H for both metals is depicted in Fig. 7. As the stress is increased, the coefficient B_σ decreases quickly at low stress levels; the rate of decrease is diminished at higher ones. It is important to note that B_σ for copper at maximum load (indicated by the arrow) is around 0.1, whereas for aluminum it is about 0.35. The former

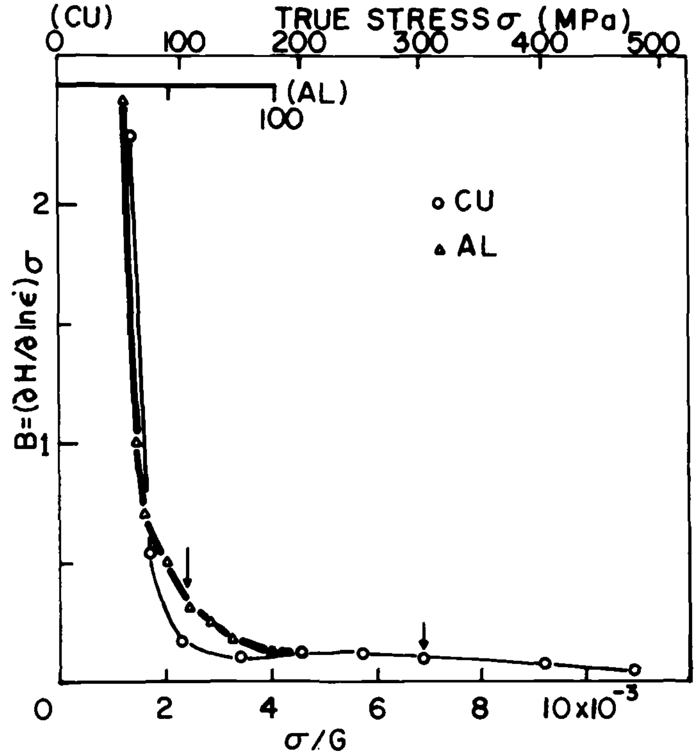

FIG. 7—*Dependence of the rate sensitivity of the work-hardening rate* B_σ *on* σ. *At the maximum load (indicated by the arrows),* B_σ *is about 0.1 and 0.35 for copper and aluminum, respectively. Note the rapid decrease of* B_σ *with* σ *at low levels of* σ.

value indicates that, at low homologous temperatures, flow localization cannot be inhibited substantially by B_σ.[5] By contrast, as the temperature is increased to 0.32 T_m, the amount of true strain that must be imposed from the point of maximum load ($H = 1$) until the condition $H + B_\sigma = 1$ is satisfied is considerable, as shown in Fig. 8. The latter criterion indicates that flow localization is unlikely to be experimentally detectable in the vicinity of the maximum load ($H = 1$), but can be expected to become visible after the specimen attains a strain of 0.2 beyond the UTS.

The C-coefficient, which is plotted as a function of σ in Fig. 9, is also a

---

[5] According to Kocks et al [*18*], the classical Considère term ($H - 1$) changes to ($H + B_\sigma - 1$) when H is rate sensitive. Furthermore, appreciable rates of flow localization cannot be established so long as $H > 1$ in a Considère material, and more generally so long as ($H + B_\sigma$) > 1. In the latter case, during the interval when H decreases below 1—for example, from 1 down to 0.70—($H + B_\sigma - 1$) can remain positive (and flow localization can therefore be prevented), so long as $B_\sigma \geq 0.30$.

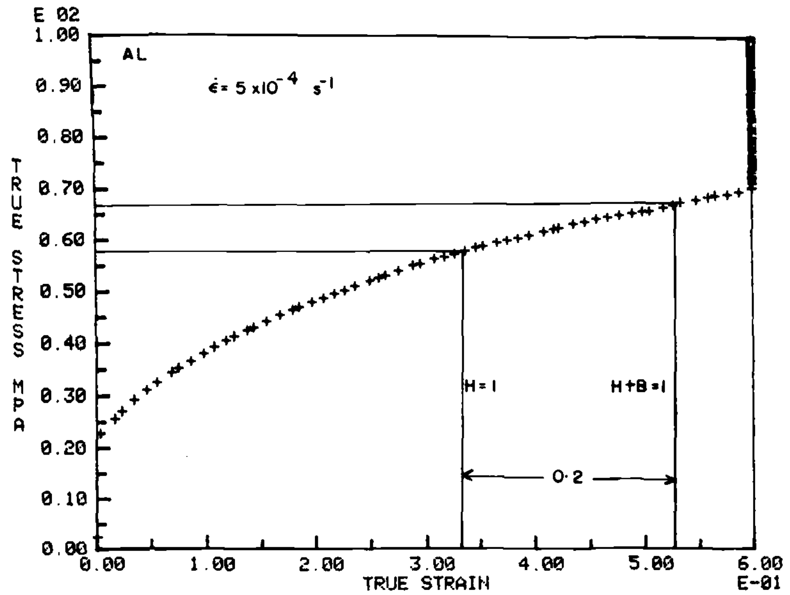

FIG. 8—*The initial part of a true stress/true strain curve for aluminum at* $\dot{\epsilon} = 5 \times 10^{-4}/s$. *Note that the condition* H = 1 *(maximum load) is separated from the condition* H + B_σ = 1 *(onset of flow localization) by a true strain of 20 percent.*

decreasing function of the flow stress. Its magnitude at maximum load is around 5 in copper and between 2.5 and 5 in aluminum, depending on the strain rate. It is evident from the figure that C becomes more rate sensitive as the temperature is increased.

From the values of B_σ and C at maximum load, the rate sensitivity, $N = (\partial \ln \sigma / \partial \ln \dot{\epsilon})_H = B_\sigma / C$ [*18*], can be evaluated for the two metals. In the case of copper, N is around 0.02, whereas for aluminum, $N \cong 0.1$. These values are somewhat lower than those of Kocks et al [*18*], but the homologous temperature in the present work is lower than theirs. It can be readily verified that N at maximum load is higher in both materials than the corresponding value of the apparent rate sensitivity m, which was mentioned earlier [m = 0.015 (copper); m = 0.075 (aluminum)]. The latter difference is important because of the strong dependence of both slow and "catastrophic" neck growth on N in the treatment of Kocks et al [*18*].

We turn now to P and Q, the rate and stress sensitivities, respectively, of M. These can be determined from the detailed dependence of M on σ and $\dot{\epsilon}$, which is illustrated in Fig. 10 for the two metals. The various curves were obtained by increasing or decreasing the strain rate by a ratio of 10, 20, or 100 from the base rate. For reference, the logarithmic *mean* strain rate associ-

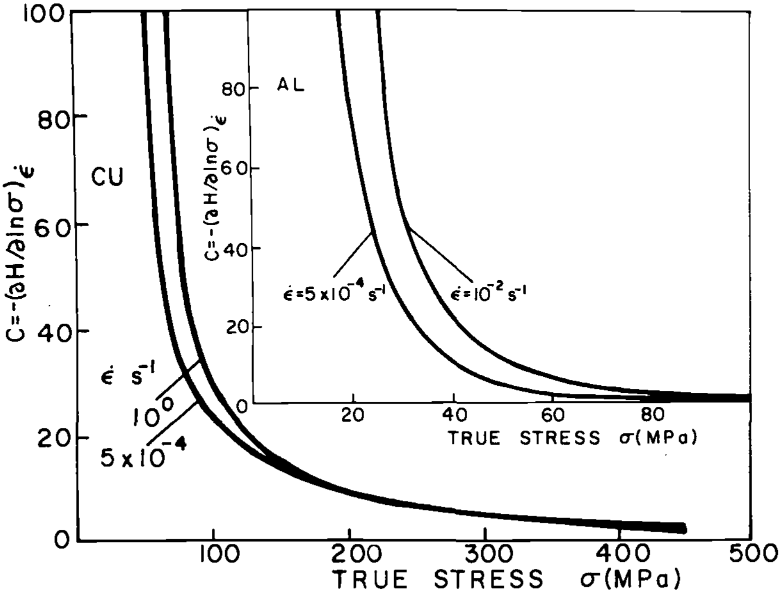

FIG. 9—*Dependence of the curvature term C on σ. The values of C at maximum load are 5 in copper and 2.5 and 5 in aluminum, depending on the strain rate.*

ated with each curve is given in the diagram. This representation is an accurate one so long as the ln σ versus ln $\dot{\epsilon}$ relaxation curve is nearly linear, a condition which is satisfied in the present case. (This is no longer valid at high or low homologous temperatures.[6])

It should be noted that the M versus σ curves for the two metals are basically different in shape. The M-curves for copper go through a minimum, and the whole curve is shifted upwards and to the right as ln $\dot{\epsilon}$ is *increased*. M for aluminum, on the other hand, increases with σ, and the whole curve is shifted upwards and to the left as ln $\dot{\epsilon}$ is *decreased*.

A possible explanation of this behavior can be based on the schematic diagram of Fig. 11. Curves a, b, and c are the stress relaxation curves corresponding to increasing states of hardness $\sigma_1{*}$, $\sigma_2{*}$, and $\sigma_3{*}$, respectively. If an experiment is performed at a constant strain rate $\dot{\epsilon}_1$, then when the state $\sigma_1{*}$ is attained, $M = M_1$. As straining progresses, the next hardness state, $\sigma_2{*}$, is attained, and M_1 decreases to M_4. Shortly afterwards, M attains its minimum value, at the moment when the point of inflection O crosses the vertical line $\dot{\epsilon} = \dot{\epsilon}_1$. Beyond this strain, M increases again, as the successive relaxation curves approach c. If the experiment is carried out at a higher strain rate—for example, $\dot{\epsilon}_2$ or $\dot{\epsilon}_3$—the minimum occurs later and at a higher

---

[6] In this case, there is no need for large strain rate changes, for the material is strongly rate sensitive and small rate changes are adequate for measuring M.

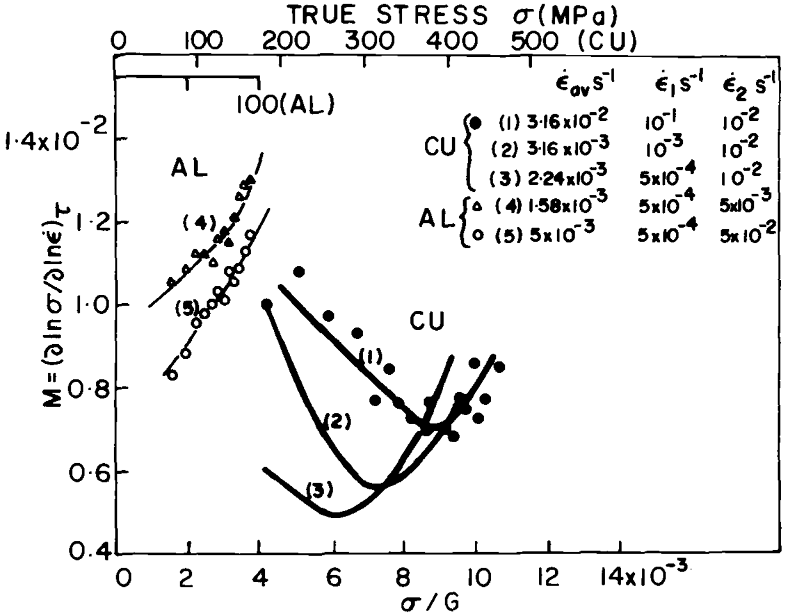

FIG. 10—*Dependence of the instantaneous rate sensitivity* M *on flow stress. The copper curves go through a minimum and* increase *with* $\dot{\epsilon}$, *whereas the aluminum curves always increase with stress and* decrease *with* $\dot{\epsilon}$.

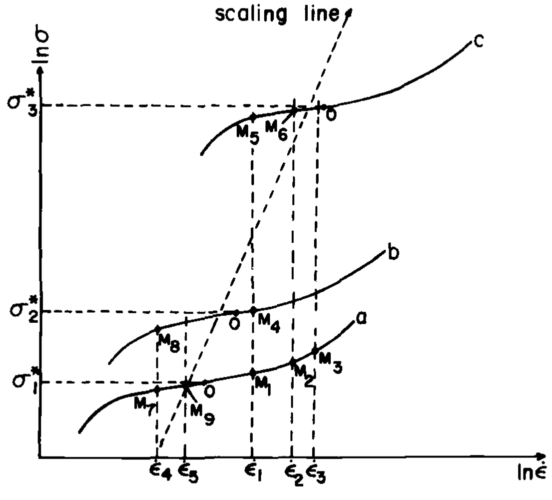

FIG. 11—*Schematic diagram of stress relaxation curves at evolving hardness states* $\sigma_1{}^*$, $\sigma_2{}^*$, $\sigma_3{}^*$, *etc. The copper and aluminum behaviors of Fig. 10 correspond to tests at* $\dot{\epsilon}_1$ *and* $\dot{\epsilon}_4$, *respectively.*

stress. Under these conditions, the M-curves intersect, as they do for copper. In the case of aluminum, the entire experiment is conducted on the left side of the point of inflection O, in keeping with the higher homologous temperature. For example, at a constant strain rate of $\dot{\epsilon}_5$, M increases continuously as we move vertically upwards. Furthermore, if a lower strain rate is selected—for example, $\dot{\epsilon}_4$—M is higher than in the previous example ($M_7 > M_9$).

This argument suggests that the difference between the dependence of M on σ in copper and in aluminum is primarily due to the difference in their homologous temperatures (rather than due to the difference in solute content). Experimental evidence supporting this interpretation can be found in the results of Mulford and Kocks [*24*] (see Figs. 8 and 10 of their work). The measured rate sensitivity of the Al-1Mg alloy they investigated decreased continuously at low temperatures (200 K), decreased and then increased with σ (strain) at intermediate temperatures (200 to 300 K), and increased monotonically with σ above 300 K. The effect of temperature on rate sensitivity can also be seen in the work of Lee and Hart on commercial purity zirconium [*25*]. It can be seen from their Fig. 5.3 that M decreases and then increases as the homologous temperature is increased from 0.22 to 0.32 T_m. There thus seems to be a definite effect of temperature on the stress dependence of M, in addition to the solute effect discussed below.

The dependence of M on σ can also be visualized with the aid of the Haasen plot (Fig. 5). The slope of the straight line which goes through the origin and an arbitrary point of the curve (dotted line) is M. It can therefore be readily shown that in the case of the copper the slope of this line decreases and then increases as points are taken along the Haasen plot. In contrast, for the case of the aluminum, the slope increases slightly because of the curvature of the $M\sigma$ versus σ plot.

We return at this point to the coefficients P and Q, which have not yet been evaluated. We can see from Fig. 10 that, in the case of copper, P is negative at first, becoming positive when the M-curves cross over. Similarly, Q is negative before the minimum and positive afterwards. For aluminum, P and Q are always positive. Although these dependences are of scientific interest, P and Q are relatively small, taking values of about 10^{-4} and 10^{-3}, respectively, under the present conditions. Given the positions they occupy in the Kocks et al [*18*] analysis of flow localization, they are unlikely to be of practical importance so long as the term $\ddot{\epsilon}/\dot{\epsilon}^2$ (Eq 20 in Ref *18*) remains relatively small. This term is expected to attain large values when M is very low and the flow is highly localized [*26*].

Conclusions

1. Constant true $\dot{\epsilon}$ tension tests to maximum strains of 1 to 2 can be performed with the aid of a diameter transducer and servo-controlled testing machine.

2. At $T_H = 0.32\ T_m$ (aluminum), *M increases* with σ (and ϵ) and decreasing $\dot{\epsilon}$. At $T_H = 0.22\ T_m$ (copper), *M decreases to a minimum* and then increases with σ (and ϵ), in keeping with the Hart model of hardness state scaling.
3. The Haasen plot ($M\sigma$ versus σ) indicates that OFHC copper is solution hardened ($\cong$200 ppm Ag + Mg + S) whereas 99.99 percent aluminum is not ($<$100 ppm impurities).
4. The rate sensitivity of the work hardening rate (B) decreases rapidly with σ (and ϵ). At the Considère strain ($H = 1$), $B_\sigma = 0.1$ and 0.35 in copper and aluminum, respectively. In aluminum, the condition $H + B_\sigma = 1$ is met at a strain of 0.2 beyond $H = 1$.
5. For $T_H = 0.22\ T_m$ (and in the presence of solutes), the second-order rate-sensitivity coefficients P and Q are first negative and then become positive as the σ and ϵ increase. For $T_H = 0.32\ T_m$ (and in the absence of solutes), both P and Q are always positive. Their values are low (on the order of 10^{-4} for P and 10^{-3} for Q), and the terms containing them can be neglected so long as $d \ln \dot{\epsilon}/d\epsilon = \ddot{\epsilon}/\dot{\epsilon}^2$ is less than about 10^3.

Acknowledgments

The authors are indebted to the Ministry of Education of Quebec (FCAC program) and to the Natural Sciences and Engineering Research Council of Canada for the financial support of the early stages of this work. They express their gratitude to the U.S. Air Force Materials Laboratory (AFSC) for supporting the later stages of the investigation through a subcontract with the Battelle Columbus Laboratories of Contract No. F 33615-78-C-5025 (Dr. Harold Gegel, program manager). The authors would also like to thank Dr. U. F. Kocks of the Argonne National Laboratories for his many stimulating comments.

References

[1] Hart, E. W., *Acta Metallurgica*, Vol. 18, 1970, p. 599.
[2] Lee, D. and Hart. E. W., *Metallurgical Transactions*, Vol. 2, 1971, p. 1245.
[3] Lee, D. and Woodford, D. A., *The Inhomogeneity of Plastic Deformation*, American Society of Metals, 1973.
[4] Hart, E. W. and Solomon, H. D., *Acta Metallurgica*, Vol. 21, 1973, p. 295.
[5] Yamada, H. and Li. C., *Metallurgical Transactions*, Vol. 4, 1973, p. 2133.
[6] Yamada, H. and Li, C., "Rate Processes in Plastic Deformation," in *J. E. Dorn Memorial Symposium*, J. C. M. Li and A. K. Mukherjee, Eds., American Society of Metals, 1975.
[7] Wire, G., Yamada, H., and Li, C., *Acta Metallurgica*, Vol. 22, 1974, p. 505.
[8] Wire, G., Yamada, H., and Li, C., *Acta Metallurgica*, Vol. 22, 1974, p. 249.
[9] Hart, E. W., Li, C., Yamada, H., and Wire, G., "Phenomenological Theory: A Guide to Constitutive Relations and Fundamental Deformation Properties," in *Constitutive Equations in Plasticity*, A. Argon, Ed., MIT Press, 1975.
[10] Woodford, D. A., *Metallurgical Transactions*, Vol. 6, 1975, p. 1693.
[11] Wire, G. L., Ellis, F. V., and Li, Che-Yu, *Acta Metallurgical*, Vol. 24, 1976, p. 677.
[12] Hart, E. W., *Journal of Engineering Materials Technology*, ASME, Vol. 98, 1976, p. 193.

[*13*] Nagy, A. T., *Scripta Metallurgica*, Vol. 9, 1975, p. 27.
[*14*] Matlock, D. K., Harrigan, W. C., and Nix, W. D., *Acta Metallurgica*, Vol. 20, 1972, p. 661.
[*15*] Evans, W. J. and Harrison, G. F., *Scripta Metallurgica*, Vol. 9, 1975, p. 239.
[*16*] Swearengen, J. C., Rohde, R. W., and Hicks, D. L., *Acta Metallurgica*, Vol. 24, 1976, p. 969.
[*17*] Kocks, U. F., "Constitutive Relation for Slip," in *Constitutive Equations in Plasticity*, A. Argon, Ed., MIT Press, 1975.
[*18*] Kocks, U. F., Jonas, J. J., and Mecking, H., *Acta Metallurgica*, Vol. 27, 1979, p. 419.
[*19*] Jonas, J. J., Christodoulou, N., and G'Sell, C., *Scripta Metallurgica*, Vol. 12, 1978, p. 565.
[*20*] G'Sell, C. and Jonas, J. J., *Journal of Materials Science*, Vol. 14, 1979, p. 583.
[*21*] Bridgman, P. W., *Studies in Large Plastic Flow and Fracture*, McGraw-Hill, New York, 1952.
[*22*] Kocks, U. F., "Strength of Metals and Alloys," in *ICSMA 5*, P. Haasen, V. Gerold, and G. Kostorz, Eds., 1979.
[*23*] Mulford, R. A., *Acta Metallurgica*, Vol. 27, 1979, p. 1115.
[*24*] Mulford, R. A. and Kocks, U. F., *Acta Metallurgica*, Vol. 27, 1979, p. 1125.
[*25*] Lee, D. and Hart, E. W., *Metallurgical Transactions*, Vol. 2, 1971, p. 1245.
[*26*] Christodoulou, N., "Computer Simulation of the Effect of Defects on Flow Localization in Tension," Master of Engineering thesis, Department of Metallurgical Engineering, McGill University, Montreal, 1978.

J. L. Gacougnolle,[1] *J. F. Peltier,*[2] *and J. de Fouquet*[1]

Creep of Aluminum under Combined Longitudinal and Shear Stresses

---

REFERENCE: Gacougnolle, J. L., Peltier, J. F., and de Fouquet, J., "**Creep of Aluminum under Combined Longitudinal and Shear Stresses,**" *Mechanical Testing for Deformation Model Development, ASTM STP 765,* R. W. Rohde and J. C. Swearengen, Eds., American Society for Testing and Materials, 1982, pp. 67–79.

ABSTRACT: The creep behavior of aluminum in primary and secondary stages has been studied under combined stresses at about 473 K. A new creep machine was designed on which the specimen is free to rotate. Thus the rotation of the specimen in addition to its elongation could be observed during creep in tension. A small constant torque is added to the tensile load for limited periods. The response of the creep of aluminum to this new stress has been analyzed. The torsional anelastic strain observed is similar to the anelastic back flow in tensile creep. The evolution of the parameters of anelastic strain and the torsional plastic strain indicates the origin of a new process of deformation before the end of primary creep.

KEY WORDS: aluminum, mechanical properties, creep

Stress change experiments during uniaxial creep tests have been widely performed in recent years [*1–5*] to obtain a better understanding of the mechanisms controlling creep.[3] Nevertheless, the controversy on the nature and effect of the internal stresses [*2,6*] still continues. The aim of the present study is to describe the behavior of aluminum when an additional small torque is applied during creep under a tensile load. For this purpose a new creep machine was designed. It was observed that the torsional strains were very sensitive to the crystalline structure.

When the torque is added to the tensile load, the torsion exhibits an anelastic component, which indicates an increase in the internal stresses, and

---

[1] Laboratoire de Mécanique et de Physique des Matériaux, 86034 Poitiers Cedex, France.

[2] Aerospatiale, Les Mureaux, France; formerly with Laboratoire de Mécanique et de Physique des Máteriaux, 86034 Poitiers Cedex, France.

[3] The italic numbers in brackets refer to the list of references appended to this paper.

a plastic component. The amplitude and kinetics of these anelastic and plastic torsional strains throughout the longitudinal creep give information on (*1*) the modification of the microstructure during primary creep, (*2*) the nature of the steady-state creep, and (*3*) the mechanical anisotropy of deformation rates.

Experimental Procedure

Equipment

The specially designed creep machine is similar to a torsion pendulum in order that the specimen can extend as well as rotate about its axis (Fig. 1). The specimen (A) is a wire of refined aluminum of length 80 mm and diameter 3 mm. The tensile stress due to the mobile part (C) is eliminated by a balancing device (E).

Thus the specimen can be annealed on the apparatus, and a torsional torque can be applied without longitudinal stress on the specimen. The creep load is applied on the scale (L) by means of dead-weights; the scale and the balance are connected to the mobile part by two thin metallic foils (H) of negligible torsional rigidity compared with that of the specimen.

The longitudinal strain of the specimen is measured by an inductive transducer (F). The applied torque is due to the attraction of two permanent magnets (M) by two symmetrical coils (D). The amplitude of the torque is calibrated from the relative positions of the magnets with respect to the coils and from the intensity of the current in the coils. The torsional strain is detected by an optical method: a light beam is reflected by the mirror (C) on a differential photoresistant cell, the current being read on a recording potentiometer.

The accuracy of the measurements is 5×10^{-5} for the extension and 5×10^{-8} for the torsion of the specimen.

Specimen Preparation

The wires of refined aluminum were thermomechanically treated before mounting on the creep apparatus. They were annealed, after mounting, for 4 at 673 K to obtain a uniform grain diameter of 200 μm.

Stress Range

The applied load corresponded to a tensile stress, σ_{zz}, close to 7.1 MPa. The shear stress, $\tau_{\theta z}$, on the surface of the wire due to the torque was deduced on the basis of linear elastic theory. Its value of 0.237 MPa corresponds to $\sigma_{zz}/30$. The elastic approach can be used because the applied torque is very

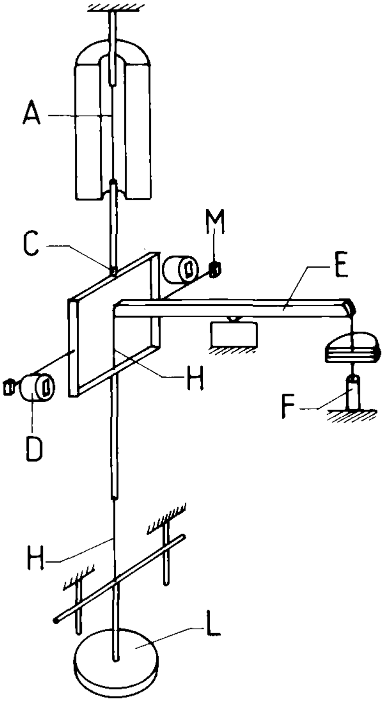

FIG. 1—*Schematic representation of the creep machine.*

small and the observed rate of torsion is proportional to the torque. The application of the torque introduces a rotation of the principal axes of the stress by 2 deg; the magnitude of the maximal shear stress can be considered as constant.

Preliminary Experiments

Contrary to the experiments performed on classical machines, a rotation of the specimen is observed during the uniaxial creep test even in the absence of external torque. Therefore, before examining the behavior of material under a combined stress state, we consider the influence of the tensile stress and of the torque separately.

Creep under Tensile Stress

The creep curves and the rotation curves of two identical specimens tested at 473 K under 8.5 MPa are shown in Figs. 2*a* and 2*b*. It appears clearly that the creep curves are very similar but the rotation curves are quite different.

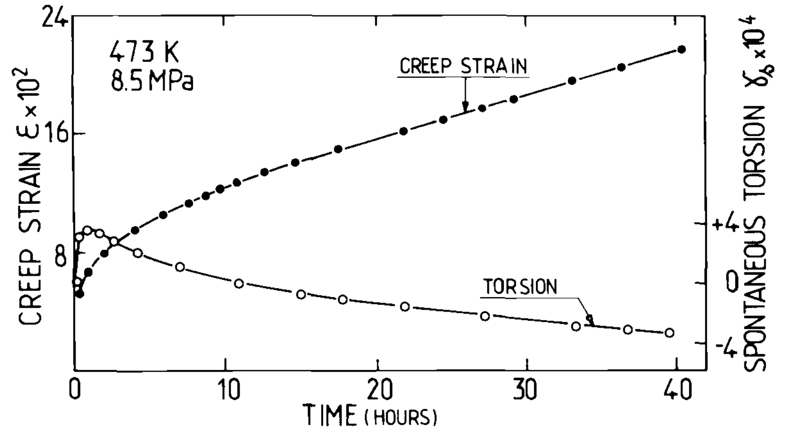

FIG. 2*a*—*Extension and spontaneous torsion of one of two identical specimens crept at the same condition.*

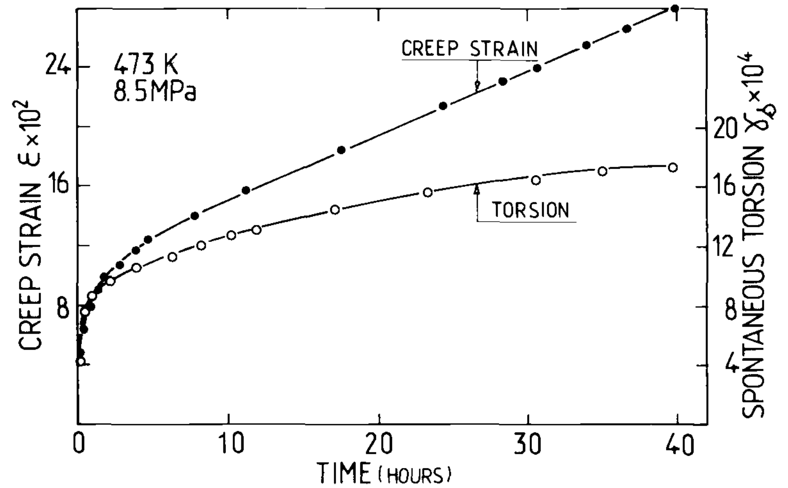

FIG. 2*b*—*Extension and spontaneous torsion of one of two identical specimens crept at the same condition.*

At the start of the creep, the rotation rate, $\dot{\gamma}_s$, is around $\dot{\epsilon}/50$ and then decreases rapidly to reach approximately $\dot{\epsilon}/400$. The direction of this torsion cannot be predicted, because in some cases it changes during creep (Fig. 2*a*). This torsional strain will be labeled as "spontaneous torsion", γ_s.

This effect is not caused by the apparatus. The whole axial symmetry was carefully checked before and after the specimen mounting; moreover, no rotation could be detected in amorphous materials like polymers. It can be assumed that this torsion is a consequence of the inhomogeneity of the deformation. It is known that the strain at the beginning of the creep is mainly located in grains having a favorable Schmidt factor. Since these grains, few in number, are not randomly distributed, this corresponds to a strong inhomogeneity which induces the rotation of the specimen. As the elongation increases, more and more grains participate in the creep so that the strain is more homogeneous and the rotation becomes very slow.

This spontaneous torsion will be taken into account when identifying the specific action of the external torque applied during longitudinal creep.

Effect of the Torque Acting Alone

In all the experiments conducted the external torque was very low, and the maximal shear stress, $\tau_{\theta z}$, on the specimen was about 0.235 MPa. The recorded torsional strain due to this torque at 445 K is shown in Fig. 3. The elastic component is $\gamma_e = 9.3 \times 10^{-6}$. It is followed by a continuous strain, $\gamma(t)$, which verifies a logarithmic law of the form $\gamma(t) = a \ln(\alpha t + 1)$. The major part of this strain is recovered, following the same law, after the removal of the torque. The coefficients a and α are respectively 0.35 and 2.9 at 496 K and 0.46 and 0.0144 at 445 K; the values of α correspond to an activation energy of 158 kJ/mol. This effect is typical for the microcreep of aluminum governed by self-diffusion.

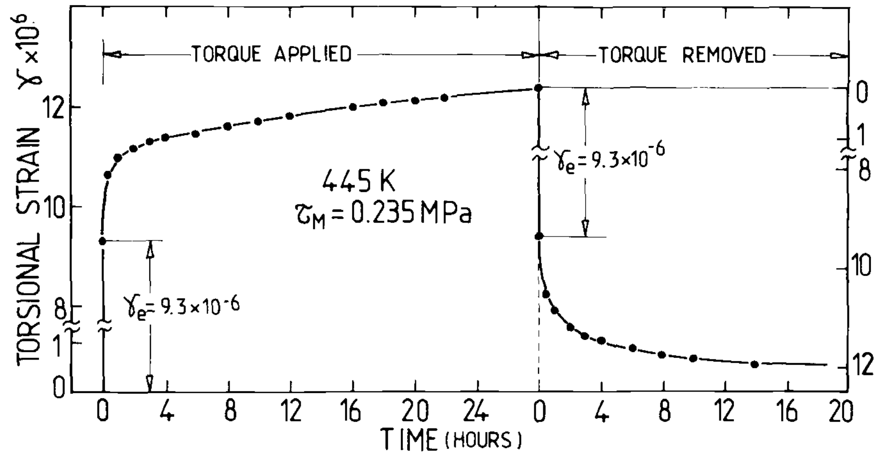

FIG. 3—*Torsion for external torque acting alone.*

Effect of an External Torque on the Creeping Specimen

The creep curve of a specimen straining under a longitudinal stress of 7.1 MPa at 473 K is shown in Fig. 4. The points $C_1, C_2, \ldots, C_8$ correspond to the application of the torque. An example of the variation of torsional strains due to this applied torque and its withdrawal is represented in Fig. 5. The initial rotation corresponds to the spontaneous torsion, γ_s. The instantaneous torsion, γ_i, due to the external torque is followed by a transient till the torsion rate becomes constant. In the same way, after the removal of the torque one observes an instantaneous torsion in the opposite direction followed by a transient, after which we observe the spontaneous torsion continuing as before.

No variation of the longitudinal creep rate could be detected during this period, and the evolution of the spontaneous torsion is not influenced by the torque. Therefore it can be assumed that the recorded torsional strain is the sum of two independant strains: the spontaneous strain and the effect of the external torque.

After subtracting the spontaneous torsion it appears that the strain due to the torque is composed of three main parts: the instantaneous strain, γ_i; an anelastic strain, $\gamma_a(t)$; and a plastic strain, $\gamma_p(t)$ (Fig. 6).

Instantaneous Strain γ_i

This strain, γ_i, is reversible but it is greater than the elastic strain, γ_e, observed for torque acting alone. For instance, $\gamma_i = 1.2\gamma_e$ at 473 K, and $\gamma_i = 1.15\gamma_e$ at 445 K (Fig. 7). The scatter of this measurement is due to the dif-

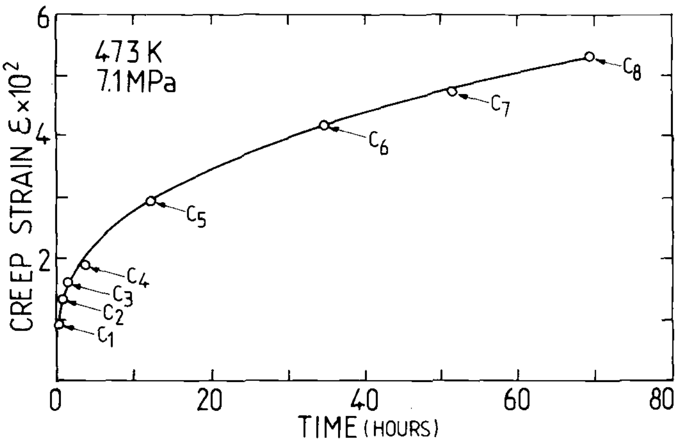

FIG. 4—*Creep curve; points* C_1, C_2 ..., C_8 *which correspond to the application of torque.*

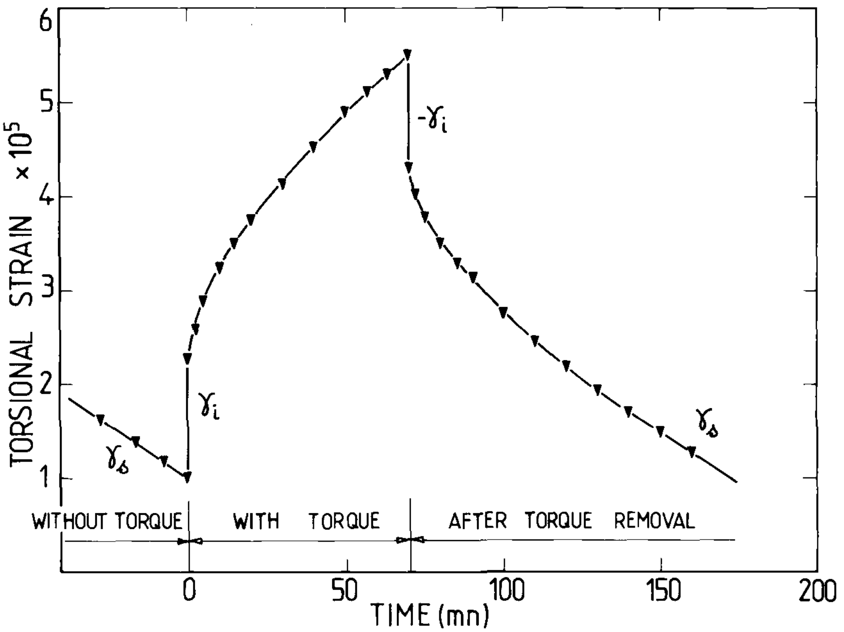

FIG. 5—*Torsional effect before, during, and after the application of the torque on the creeping specimen.*

ficulty in separating exactly the instantaneous strain from the anelastic strain. The same difficulty was met by Oikawa and Sugawara [*4*] when they measured "instantaneous" straining following stress increments in pure aluminum.

Anelastic Strain γ_a(t)

The anelastic strain, for 85 percent of its amount, appears as a pure anelastic reversible phenomenon with a single relaxation time (Fig. 8):

$$\gamma_a(t) = \gamma_R \{1 - \exp(-t/t_R)\} \quad (1)$$

where γ_R is the relaxation strain and t_R is the relaxation time. During the longitudinal creep, Eq 1 is verified each time the torque is applied. γ_R and t_R are functions of the strain and the strain rate, respectively. In Fig. 8 it appears that the straight lines meet at the same point different from the origin. This means that a small strain is added at the beginning of the anelastic strain following Eq 1. This small strain can be attributed to a microcreep component similar to that observed under torque acting alone.

The anelastic strain, γ_R, is proportional to the intensity of the torque and,

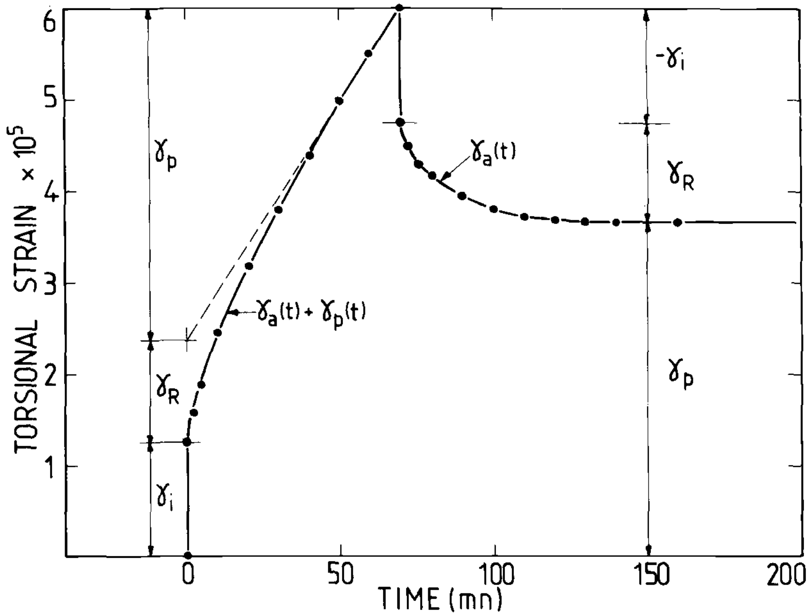

FIG. 6—*Effective torsional strain due to the addition of the torque.*

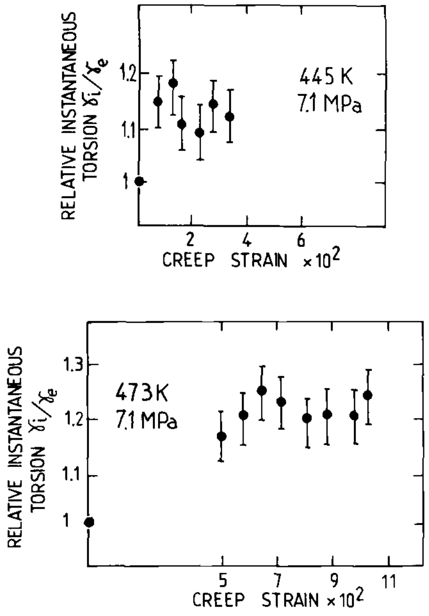

FIG. 7—*Comparison of instantaneous and elastic torsional strains at different stages of creep in tension.*

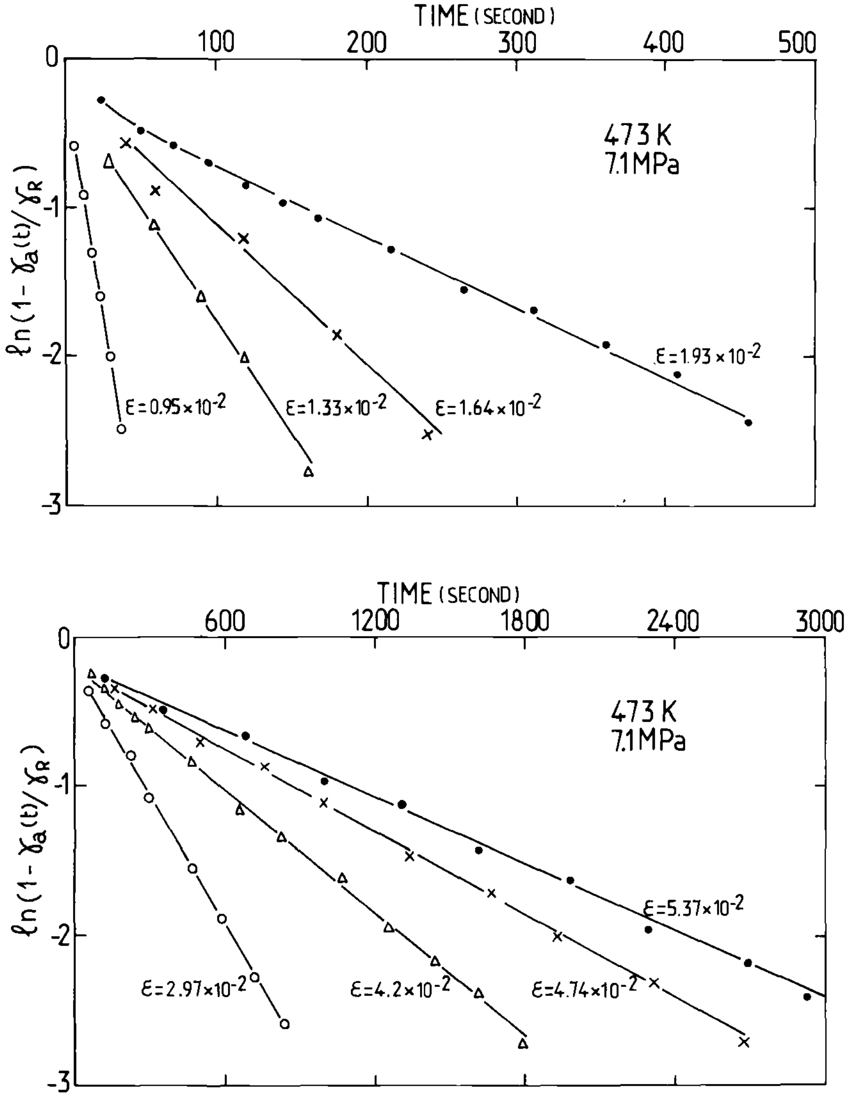

FIG. 8—*Relation between time and* $\ln (1 - \gamma_a^{(t)}/\gamma_R)$ *showing a single relaxation time. The values of* ϵ *correspond to* C_1 *to* C_8 *in Fig. 4.*

for a constant torque, its amplitude increases during the primary creep from zero to γ_i, as shown in Fig. 9 for a specimen crept at 445 K.

During the primary creep, the relaxation time, t_R, varies with the creep rate, $\dot{\epsilon}$, following the relationship $t_R^{-1} = B\, \dot{\epsilon}^{-b}$ up to an elongation of ϵ^*. To illustrate this variation for the same specimen the creep rate $\dot{\epsilon}$ is plotted ver-

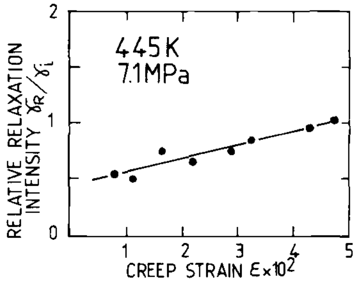

FIG. 9—*Variation of* γ_R *with elongation.*

sus strain ϵ on the right-hand side of Fig. 10 and the inverse of the relaxation time is plotted versus $\dot{\epsilon}$ on the left-hand side; in this case, ϵ^*, $= 3.4 \times 10^{-2}$, $B \simeq 10^4$, and $b \simeq 1$. For elongation beyond ϵ^*, $t_R{}^{-1}$ continues to decrease while $\dot{\epsilon}$ tends to become constant. The activation energy, Q, of the relaxation time, determined by raising the temperature from 445 to 460 K, is 125 kJ, which is similar to the activation energy of the creep rate.

Plastic Component γ_p (t)

When the effect of the anelastic component comes to an end, the torsional rate ceases to decrease and the strain observed is the plastic component $\gamma_p(t)$. For the limited period during which the torque is applied, the rate of this creep can be considered as constant; that is, $\gamma_p(t) = \dot{\gamma}_p t$. Therefore the total strain due to application of the torque follows the relationship

$$\gamma(t) = \gamma_i + \gamma_R \{1-\exp(-t/t_R)\} + \dot{\gamma}_p t \qquad (2)$$

The torsional creep rate $\dot{\gamma}_p$ is proportional to the intensity of the torque. For a given torque, $\dot{\gamma}_p$ varies as the longitudinal creep rate $\dot{\epsilon}$; that is, it decreases from 10^{-6} s^{-1} to less than 10^{-8} s^{-1} during the primary creep. In order to compare more precisely the evolutions of $\dot{\epsilon}$ and $\dot{\gamma}_p$ we shall consider the ratio $\lambda = 30\,\dot{\gamma}_p/\dot{\epsilon}$, where 30 is the constant ratio $\sigma_{zz}/\tau_{\theta z}$. λ can be calculated from the Levy-Mises relationships; its value is 3 for perfectly plastic solid [7].

The variation of λ is plotted against ϵ in Fig. 11. Immediately after loading, λ decreases with extension and reaches minimal value of 3.1 for $\epsilon \simeq$ 1 percent. On further extension till $\epsilon^* = 3.4$ percent, λ increases steadily to 5. Beyond ϵ^*, λ decreases constantly. For all tested specimens these three steps have been observed. The last decrease in λ is due to the relative increase of $\dot{\epsilon}$ as compared with $\dot{\gamma}_p$.

It must be noted that the maximum value of λ and the limit of the linear

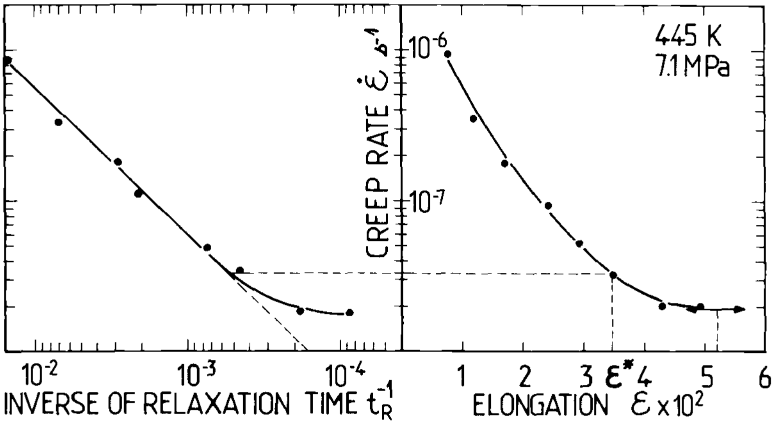

FIG. 10—*Interrelationships between* $\dot{\epsilon}$, ϵ, *and* t_R.

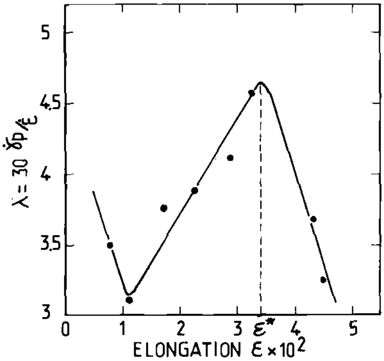

FIG. 11—*Variation of* $\lambda = 30\ \dot{\gamma}_p/\dot{\epsilon}$ *with elongation.*

relationship between $t^{-1}{}_R$ and $\dot{\epsilon}$ correspond to the same elongation ϵ^*. The two parameters, t_R and λ, specific of this torsional test, reveal that a change in the decreasing creep rate occurs before the end of the primary creep.

Discussion

The reversibility of the instantaneous torsion γ_i is similar to the reversibility of the instantaneous elongation $\Delta\ell^+$ or contraction $\Delta\ell^-$ produced by a stress increment or decrement, $\Delta\sigma$ less than $\sigma/20$, in a tensile creep test [*4*]. This reversibility indicates clearly that there is no instantaneous plastic deformation due to the torque. The structure of the metal is not permanently modified by the application of the torque, and the parameters γ_R, t_R, and λ can be considered to be specific of the structure developed during longitudinal creep.

The microcreep can be associated with the bowing of dislocations governed by the mobility of jogs, as proposed by Woirgard [*8*].

The torsional anelastic strain, γ_R, behaves as the longitudinal anelastic strain, ϵ_R, following a stress decrement. Gibeling [5] has shown that ϵ_R increases during primary creep from zero up to six times the elastic strain ϵ_e for a specimen crept at 673 K.

The ratio of anelastic to instantaneous strain in torsion γ_R/γ_e is 1.2, five times lower than that in tension. This difference is explained by the higher temperature condition in Gibeling's experiment. Caillard [*9*], working up to stationary creep at 473 K, observed an anelastic strain of about 0.4 ϵ_e, which is nearer our results.

In the case of pure longitudinal creep, as suggested by Nix and Ilschner [*10*], this anelastic strain must be associated with long-range internal back stresses. To generate these internal stresses, high localized obstacles are required, and in pure aluminum these obstacles can only be due to the presence of almost perfect subboundaries built up during primary creep. Hence the development of anelastic torsional strain observed during primary creep appears as the result of the formation of perfect subboundaries.

The single relaxation time, t_R, of the anelastic strain obtained in torsion tests reveals clearly that this strain is the consequence of a modification of the substructure involving a single type of crystal defect. The linear relationship between t_R^{-1} and $\dot{\epsilon}$ suggests that the mobile dislocations are taking part in this structural modification.

The evolution of the parameter λ (Fig. 11) associated with the plastic component $\gamma_p(t)$ shows clearly that strain is anisotropic ($\lambda \neq 3$) and that this anisotropy changes continually with creep strain. The three steps in the variation of λ indicate that the strain during primary creep takes place in three stages characteristic of the structural state. In particular, at the strain ϵ^* an important change takes place in the process of deformation. For strains smaller than ϵ^* the creep rate $\dot{\epsilon}$, the inverse of the relaxation time t_R^{-1}, and the torsional plastic strain rate $\dot{\gamma}_p$ are identical decreasing functions of the strain ϵ; they are governed by the same mechanism. The strain rate due to this mechanism is called $\dot{\epsilon}_1$ (Fig. 12). Beyond ϵ^* the observed strain rate $\dot{\epsilon}$ is higher than the extrapolated value of $\dot{\epsilon}_1$, but the constant evolution of t_R^{-1} and $\dot{\gamma}_p$ indicates that the mechanism inducing $\dot{\epsilon}_1$ is still acting. Hence an additional strain rate, $\dot{\epsilon}_2$, must be introduced such that

$$\dot{\epsilon}_2 = \dot{\epsilon} - \dot{\epsilon}_1$$

This strain rate is due to another mechanism which comes into play at strain ϵ^*. Thus the experimental strain rate is the sum of the decreasing strain rate, $\dot{\epsilon}_1$, and the slowly accelerating strain rate, $\dot{\epsilon}_2$.

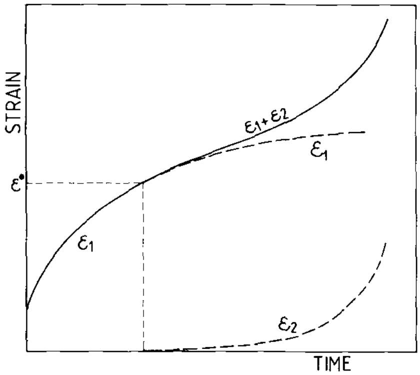

FIG. 12—*Analysis of creep mechanism.*

References

[*1*] Mitra, S. K. and McLean, D. *Proceedings of the Royal Society*, London, Vol. A295, 1966, pp. 288-299.

[*2*] Ahlquist, C. N. and Nix, W. D., *Acta Metallurgica*, Vol. 19, 1971, pp. 373-385.

[*3*] Hausselt, J. and Blum, W., *Acta Metallurgica*, Vol. 24, 1976, pp. 1027-1039.

[*4*] Oikawa, H. and Sugawara, K., *Scripta Metallurgica*, Vol. 12, 1978, pp. 85-90.

[*5*] Gibeling, J. C., Ph. D. dissertation, Stanford University, Calif., 1979.

[*6*] Gibeling, J. C. and Nix, W. D., *Acta Metallurgica*, Vol. 28, 1980, pp. 1743-1752.

[*7*] Hill, R., *The Mathematical Theory of Plasticity*, Oxford, 1967.

[*8*] Woirgard, J., *Philosophical Magazine*, Vol. 133, 1976, p. 623.

[*9*] Caillard, D., "Etude de la Microstructure de Fluage, dans l'Aluminium aux Temperatures Moyennes," Thèse de Doctorat d'Etat, Toulouse, 1980, p. 61.

[*10*] Nix, W. D. and Ilschner, B. in *Proceedings*, Fifth International Conference on the Strength of Metals and Alloys, Aachen, Pergamon Press, 1979, pp. 1503-1530.

J. H. Holbrook,[1] *J. C. Swearengen,*[2] *and R. W. Rohde*[3]

Specimen-Test Machine Coupling and Its Implications for Plastic Deformation Models

---

REFERENCE: Holbrook, J. H., Swearengen, J. C., and Rohde, R. W., **"Specimen-Test Machine Coupling and Its Implications for Plastic Deformation Models,"** *Mechanical Testing for Deformation Model Development, ASTM STP 765,* R. W. Rohde and J. C. Swearengen, Eds., American Society for Testing and Materials, 1982, pp. 80–101.

ABSTRACT: A unified and detailed evaluation of the coupling between specimen and test machine is presented. It is demonstrated that an accurate formulation of the specimen/machine coupling relation requires exact additivity of elastic and plastic strain contributions, and that additivity is only possible with a specific set of definitions for these strains. When these definitions are implemented to ensure additivity, two strain-dependent terms in the coupling relation are identified that have been treated as constants in previous studies. One term is shown to account for the decreasing true total strain rate with increasing plastic strain at a fixed crosshead speed. The second term accounts for strain dependence of the combined specimen/machine modulus due to change in length and area of the specimen.

Several applications of the coupling relation are given that illustrate the importance of treating the specimen and test machine as a well-defined system when inferring information about plastic-deformation models from raw data. Topics covered include (*1*) effect of machine stiffness on work-hardening behavior, (*2*) variation of total and plastic-strain rate during tensile deformation, (*3*) effect of machine stiffness on stress relaxation behavior, (*4*) relationship between stress rates before and after a change in crosshead speed, and (*5*) deductions about mobile dislocation density from observed stress-time behavior.

KEY WORDS: tension test, stress relaxation, strain, strain rate, machine stiffness, crosshead speed

There is no test more widely used to study the mechanical behavior of solids than the uniaxial tension test. In engineering applications, standard-

---

[1] Principal Research Scientist, Battelle-Columbus Laboratories, Columbus, Ohio 43201.
[2] Supervisor, Division 8316, Sandia National Laboratories, Livermore, Calif. 94550.
[3] Supervisor, Division 5832, Sandia National Laboratoires, Albuquerque, N.M. 87185.

ized tension-test results provide a convenient means of comparing different materials for selection or qualification purposes. It is also used extensively by workers studying fundamental deformation mechanisms of solids, because the simple specimen stress state eases interpretation of experimental data.

The term "tension test," of course, refers to the nature of the specimen loading, that is, uniaxial extension. A number of different tests fall into this category. These can be classified according to the parameter that is controlled during the test. The parameters most often selected include constant-crosshead-speed, constant-strain-rate, constant-stress (creep), constant-strain (stress relaxation), and constant-cyclic-stress (or -strain) amplitude. Investigators seeking to formulate time-dependent elevated temperature deformation models generally use data from constant-stress (creep) tests where the measured parameter is time-dependent uniaxial strain. At temperatures less than about one half of the melting temperature of the specimen, the most common methods for deformation studies include the constant-crosshead-speed extension test and the stress-relaxation test.

Several examples from the literature can be cited to indicate that the deformation response of solids depends on the nature of the test machine used. Krausz and Craig [*1*], Rohde and Nordstrom [*2*], and Smith and White [*3*] have reported that results of stress-relaxation tests depend on the stiffness of the test machine.[4] Wielke [*4*] has demonstrated that activation volumes determined using crosshead-speed cycling depend on machine stiffness. Rohde and Nordstrom [*5*] have indicated that the flow stress at a given strain and crosshead-speed and the subsequent stress-relaxation behavior from this flow stress are machine stiffness-dependent. Finally, Holbrook et al [*6*] have shown that the stress-time response following crosshead-speed changes and also its measurability are partly governed by load-train stiffness.

The need to include machine characteristics in the interpretation of tension test behavior was set forth clearly in the pioneering work of Johnston and Gilman [*7*]. That work and subsequent studies by Hahn [*8*] and Gillis [*9*] explored the influence of machine stiffness on yield-point behavior and clearly demonstrated that the specimen-test machine interaction has an important effect on observed mechanical behavior. An accurate treatment of specimen-test machine coupling has been presented previously by Hart [*10*] in a paper that is cited most frequently, however, for its treatment of tension instability. Unfortunately, the attention to detail exercised in Hart's development is seldom found in other published works. More frequently than not, specimen-machine interactions are treated in an approximate fashion in the literature without critical assessment of the significance of the approximations.

The purpose of the present paper is to provide a thorough, unified treatment of the topic of mechanical coupling between specimen and test machine. Toward this end we compile relationships that otherwise are scattered

[4] The italic numbers in brackets refer to the list of references appended to this paper.

throughout the literature, write them in a unified notation, and reformulate them to account for the geometric effects of deformation. Explicit formulations are developed for particular applications in order to facilitate interpretation of experiments and to illustrate the importance of viewing the specimen and test machine as a well-defined system whose properties should be known when drawing conclusions about deformation mechanisms from experimental data. By this means we hope to clarify how the behavior in a tension test depends on the machine used, and, given that fact, supply formulae that facilitate the analysis of experimental data.

Certain related topics necessarily must be excluded from the scope of this overview. For example, test-machine dynamics such as overshoot, drift, damping, etc. [*11–13*] are not characteristic of all machines. Real-time computation of specimen responses such as true strain and true strain rate or transformation of diametral to equivalent axial strain are specific topics worthy of separate reviews. However, the relationships developed herein, such as partitioning of total strain into elastic and plastic parts, will be important to incorporate into computer-aided testing. In the following section we give an exact development of the specimen/test machine coupling relation for a machine of arbitrary stiffness. We include outlines of several techniques for the determination of machine stiffness. Our primary concern is the accurate treatment of stiffness and the resultant effects on mechanical behavior. In the subsequent section we give a number of examples illustrating use of the coupling relation.

Specimen-Test Machine Coupling

Consider a tension specimen of initial gage length, L_0, and initial cross-sectional area, A_0, that is being elongated by the crosshead of a test machine. At any time the instantaneous specimen length is L_T and its time rate of change is denoted by $\dot{L}_T$. The total extension of the gage length is ΔL_T ($= L_T - L_0$), which, in general, includes elongation due to all sources—elasticity, plasticity, anelasticity, thermal strain, etc.—though in this paper we limit the discussion to elastic and plastic contributions to ΔL_T. If the crosshead speed is given by $\dot{X}$, we can write

$$\dot{X} = \dot{L}_T + \dot{L}_M \tag{1}$$

where $\dot{L}_M$ is the composite machine deflection rate due to deflections of the crosshead, grips, linkages, load cell, specimen shoulders, etc. If all elements of L_M are *linearly* elastic, Eq 1 can be written as

$$\dot{X} = \dot{L}_T + \frac{\dot{P}}{K} \tag{2}$$

where K is the composite spring constant and $\dot{P}$ is the time rate of change of load. Dividing through Eq 1 by L_0, we have

$$V_0 = \dot{e}_T + \frac{\dot{S}}{M_0} \tag{3}$$

where $\dot{e}_T$ is the total *engineering* strain rate, $\dot{S}$ is the *engineering* stress rate, $\dot{P}/A_0$, and we have substituted V_0 for $\dot{X}/L_0$ and M_0 for $K\,L_0/A_0$. Equation 3 is exact for a load-independent K. This is normally a good approximation in the load range where most deformation studies are conducted. For situations, however, where the nonlinearity in the load dependence of L_M cannot be neglected, K^{-1} in Eq 2 should be replaced by

$$K^{-1} = K_i^{-1} + \left(\frac{dK^{-1}}{dP}\right)_{P_i}(P - P_i) + 1/2\left(\frac{d^2K^{-1}}{dP^2}\right)_{P_i}(P - P_i)^2 + \cdots$$

where K_i is the composite spring constant evaluated at some reference load P_i, and the derivatives in the expansion are evaluated at P_i. In the remainder of the paper we focus on machine behavior that can be represented by a constant spring constant, K, and therefore a constant machine modulus, M_0.

Three additional points should be made concerning Eq 3. Firstly, it is not necessary for $\dot{X}$ to be constant for Eq 3 to hold. Secondly, implicit in the division by L_0 is the requirement that all points in the gage length are identical in area, microstructural homogeneity, temperature, etc. Clearly then, Eq 3 is not valid after the onset of any local phenomena such as necking. Finally, it should be emphasized that correct implementation of Eq 3 depends on a specific definition of the gage length L_0. Equation 2 indicates that total crosshead displacement is a sum of specimens and "machine" components. For a valid tension test and valid interpretation of that test, all inelastic displacement must necessarily be confined to an appropriate initial specimen gage length, L_0. Since inelastic deformation invariably occurs outside the application points of a clip gage extensometer, use of the extensometer gage length for L_0 is definitely incorrect. Ordinarily, L_0 is correctly specified as the length of the reduced section of a tension specimen. In some instances, however, especially for specimens that employ large radius fillets for the parallel section to shoulder transition, inelastic deformation occurs in the fillets during a tension test. This necessitates that L_0 be treated as an effective or operational gage length, slightly larger than the parallel section, over which the specimen shoulder-to-shoulder displacement (incorporating all inelastic deformation) is distributed to yield a strain equal to the uniform strain measured within the parallel section. Determination of the operational value of L_0 in these instances is readily accomplished for a given specimen design by performing a calibration with separate extensometers: one to measure shoulder-to-shoulder displacement, ΔL_T, the other mounted within the reduced section to measure the uniform strain, e_T. The operational value of L_0 is then given by

$$L_0 = \frac{\Delta L_T}{e_T}$$

To convert Eq 3 into a form useful for deformation studies, the engineering strain rate and stress rate must be converted to true strain rate and true stress rate. With the aid of the strain and strain rate definitions given in the Appendix and the definition of true stress, $\sigma = S\ (1 + e_p)$,[5] where e_p is the engineering plastic strain, we find

$$\frac{V_0}{g} = \dot{\epsilon}_T \left[1 - \frac{\sigma}{M}\right] + \frac{\dot{\sigma}}{M}\left[1 + \frac{\sigma}{E}\right] \tag{4}$$

where

$$M = gq\,M_0$$

$$g = 1 + e_T$$

$$q = 1 + e_P$$

and $\dot{\epsilon}_T$ is the true total strain rate.[6] Equation 4 is exact provided that M_0 is load-independent, that straining is uniform within the gage length, and that plastic deformation alters only the shape of the material in the gage length, not its volume. Since *true* strain rates are additive (but not engineering strain rates; see the Appendix), Eq 4 can be expressed in terms of true plastic strain rate, $\dot{\epsilon}_p$, by making the substitution

$$\dot{\epsilon}_T = \dot{\epsilon}_P + \frac{\dot{\sigma}}{E}$$

Then

$$\frac{V_0}{g} = \dot{\epsilon}_P \left[1 - \frac{\sigma}{M}\right] + \frac{\dot{\sigma}}{C} \tag{5}$$

---

[5] We have chosen to define true stress in this paper as load divided by the cross-sectional area consistent with the current *plastic* strain (unloaded area); that is, $\sigma = P/A_P = S\ (1 + e_P)$, where A_P is the area associated with the plastic strain e_P. An alternative choice would have been $\sigma = P/A_T$, where A_T is the loaded area including Poisson contraction. It is easy to show that for this definition $\sigma \exp(-2\nu\sigma/E) = S\ (1 + e_P)$, which leads to unnecessary complications in other equations in the paper.

[6] In practice, negligible error is introduced by substituting q for g, since, as shown in the Appendix, $g = (1 + e_E)q$, and $e_E \ll 1$.

where C is the combined specimen-machine modulus given by

$$\frac{1}{C} = \frac{1}{E} + \frac{1}{M} \tag{6}$$

Equation 5 contains two strain-dependent terms, g and C, that are commonly treated as constants in publications involving the use of a specimen/machine coupling equation to interpret deformation behavior. The term g accounts for decreasing true strain rate due to specimen lengthening at a fixed crosshead speed for straining in tension and an increasing true strain rate for straining in compression. The combined modulus C is strain-dependent due to the influence of strain on the effective machine modulus M. Plastic straining in tension causes an increase in length and a decrease in area of the specimen and results in an increase in the effective machine modulus M ($= gq\ M_0$). The reverse is true for plastic straining in compression.

The other term in Eq 5 that is routinely neglected is the quantity ($1 - \sigma/M$), which forms a product with the true plastic strain rate. It is customarily assumed [*10*] that σ/M is negligible compared with unity, but this is a questionable assumption for "soft" test machines. It is easy to show that

$$\frac{\sigma}{M} = \frac{P}{KL_T}$$

which indicates that for short gage lengths or large loads the quantity σ/M could be appreciable, depending on the value of K. In a survey of machine stiffnesses reported in the literature, Hamstad and Gillis [*14*] reported values of K ranging from 4.56 to 29.2 MN/m (26 000 to 166 500 lbf/in.). As an example, for a 6.25 mm diameter, 25 mm gage length steel specimen ($E = 2.07 \times 10^5$ MPa) these values of K translate to M_0-values of $E/57$ to $E/9$. Stresses routinely experienced in tension testing of steel can be on the order of $E/200$, a sizeable fraction of these M_0-values. Clearly then, neglect of the σ/M term in the coupling relation, Eq 5, can result in an error in the determination of $\dot{\epsilon}_p$ if a "soft" test machine is used.

Determination of Machine Stiffness

From the prior discussion, it is obvious that the machine stiffness must be well-known to accurately assess deformation behavior during tension tests. Through use of the coupling relation, several techniques can be identified for determining the machine stiffness.

The most straightforward method is the *total deformation* technique. With this method, a tension specimen is strained for a predetermined time τ in a machine operating at a constant crosshead speed. Provided that the strain is distributed uniformly within the gage length and the machine stiffness is constant, Eq 3 can be integrated to give

$$V_0 \tau = e_T + \frac{P_\tau}{KL_0} \tag{7}$$

where P_τ is the load at time τ. If an independent determination of the total engineering strain e_T is made with an extensometer, this equation can be solved for K. It should be emphasized that if this method is used for determining K, several values of τ should be employed to examine any variation of K with load. If significant variations are noted, Eq 7 itself is inaccurate, since the integration performed on Eq 3 assumed a constant K. For a nonconstant K, we have from Eq 3:

$$V_0 \tau = e_T + \frac{1}{L_0} \int_0^{P_\tau} \frac{dP}{K} \tag{8}$$

If K^{-1} is expressed in a power series as before, the integral in Eq 8 can be evaluated and the load dependence of K to any desired order can be determined by using a system of linear equations and measurements of e_T at various P_τ-values. For this technique a specimen material with a low yield strength and high work-hardening rate is recommended, since this combination will provide measurable strains over a wide range of loads.

A second technique for determining machine stiffness is by the *elastic loading* method. With this method, $\dot{P}$ is measured for loading situations where yielding of the specimen does not occur. Substituting into Eq 3 the identity

$$\dot{\sigma} = (1 + e_P)\dot{S} + \sigma \dot{\epsilon}_P \tag{9}$$

we have

$$\frac{V_0}{g} = \dot{\epsilon}_P \left[1 + \frac{\sigma}{E} \right] + \frac{q}{C} \dot{S} \tag{10}$$

where again, $q = (1 + e_P)$. For elastic loading, $\dot{\epsilon}_P = 0$, and Eq 10 can be solved for C to give

$$C = gq \frac{L_0}{A_0} \frac{\dot{P}}{\dot{X}} \tag{11}$$

Then M and finally K are determined by using Eq 6. For this technique a specimen material with a high yield strength is recommended to provide a large load range for an accurate determination of $\dot{P}$. Unlike the total deformation method, this method for determination of K requires knowledge of the elastic modulus of the specimen. Also, an independent measurement of strain is required to determine g and q. For a comparison of stiffness determinations using these first two techniques, the reader is referred to the paper by Hockett and Gillis [*15*].

A third technique that has been used for K-determination could be called the *crosshead speed change* method. With this method, the load rates $\dot{P}$ are measured immediately before and after a change in crosshead speed. The standard assumption when using this method is that the true plastic strain rate remains continuous at the instant of the crosshead speed change. Gillis and Medrano [*16*] and Fortes and Proença [*17*] have made machine stiffness determinations using this method. To use the method, Eq 10 can be solved for the quantity $\dot{\epsilon}_P[1 + \sigma/E]$, which is continuous during a crosshead speed change. This results in the relation

$$\frac{\dot{X}_1}{gL_0} - \frac{q}{C}\frac{\dot{P}_1}{A_0} = \frac{\dot{X}_2}{gL_0} - \frac{q}{C}\frac{\dot{P}_2}{A_0}$$

where $\dot{P}_1$ and $\dot{P}_2$ are the load rates immediately before and after a change in crosshead speed from $\dot{X}_1$ to $\dot{X}_2$. Solving for C gives

$$C = gq\frac{L_0}{A_0}\frac{\dot{P}_2 - \dot{P}_1}{\dot{X}_2 - \dot{X}_1} \tag{12}$$

from which K is found by using Eq 6. As with the elastic loading method, the crosshead speed change method requires an independent measurement of strain to determine g and q, and the elastic modulus of the specimen must be known to use Eq 6.

Gillis and Medrano [*16*] reported finding large scatter in stiffness determinations with the crosshead speed change method by using speed changes corresponding to the start of a stress relaxation test ($\dot{X}_2 = 0$). This is consistent with the work of Holbrook et al [*6*] who have demonstrated that the initial load rate during stress relaxation is a difficult quantity to measure accurately. Fortes and Proença [*17*] used crosshead speed changes corresponding to the reloading after a stress relaxation test ($\dot{X}_1 = 0$) and reported significantly less scatter in stiffness determinations. In view of the findings of Fortes and Proença [*17*] and Holbrook et al [*6*], use of the *crosshead speed change* technique can be expected to yield more reliable results for machine stiffness if determinations are limited to speed changes of the type $\dot{X}_2 > \dot{X}_1$.

A final suggested technique for measuring machine stiffness can be called the *stress relaxation* method. If the machine stiffness is constant over the range of load reduction in a stress relaxation test ($V_0 = 0$), Eq 3 yields

$$K = \frac{-\Delta P}{L_0 \Delta e_T} \tag{13}$$

where ΔP is the difference between the load at any time during relaxation and the load at the start of relaxation (a negative quantity for relaxation in tension), and Δe_T is the increase (for tension) in total engineering strain at that time from the value at the start of relaxation. This technique requires a sensitive, independent measure of strain, but does not require knowledge of the specimen modulus. A highly strain-rate-sensitive specimen material is recommended, however, as well as a reasonably large value of initial crosshead speed in order to maximize load reduction and, hence, strain increase. This technique differs from the first three methods in that the crosshead is immobile for this determination of stiffness. Depending on the machine, it is possible that the static machine stiffness is different than the effective stiffness when the crosshead is moving [*18*].

As can be seen from Eqs 3 to 6, significant simplifications in the coupling relation result if the machine modulus is very large. In particular, for $M_0 \rightarrow \infty$ we have from Eq 3:

$$V_0 = \dot{e}_T = g\dot{\epsilon}_T = g\,(\dot{\epsilon}_P + \dot{\sigma}/E) \tag{14}$$

From the definition of M_0, it can be seen that the machine modulus can be made arbitrarily large by selecting the appropriate value of L_0/A_0. Extremely large values of L_0/A_0 are not practical, however. Decreasing A_0 decreases load values in a test and results in load measurement difficulties. Increasing L_0 increases the possibility of nonuniform deformation in the gage length. The effect of an infinite machine modulus is obtainable, however, by using a servo-controlled test machine in strain-control mode. The controlled parameter in this situation is L_T (hence e_T), not crosshead position. The feedback signal for the closed-loop strain control is obtained from an extensometer measurement of L_T made directly on the specimen.

In the case of closed-loop strain control, V_0 actually varies according to Eq 3 to maintain a prescribed $\dot{e}_T$, and all that is required to determine true strains and strain rates are the definitions given in the Appendix relating these quantities to e_T and $\dot{e}_T$. It can be seen that these are the same as those in Eq 14 using the coupling relations with $M_0 \rightarrow \infty$; hence, the concept of infinite machine modulus for servo-controlled machines in strain-control follows. Before proceeding to the next section, it should be mentioned that servo-controlled machines in either load- or stroke-control do *not* simulate infinite stiffness. The characteristic stiffness of the machine must be known in these cases to use the coupling relation.

Applications

Several examples will now be given that illustrate the use of the exact form of the coupling relation in analysis of tension test data.

Interpretation of Work-Hardening Behavior

A realistic treatment of the work-hardening capacity of a material is essential for a successful deformation model. In this section we outline the technique for accurate determination of work-hardening behavior from tension tests. We distinguish between two types of work hardening behavior, *observed* and *actual.* Briefly, *observed* work hardening is the measured increase in the flow stress of the material for a measured increase in strain. As shown below, this measured behavior is influenced by machine stiffness and loading conditions, and these effects must be accounted for to deduce the *actual* work-hardening behavior.

Consider a tension specimen that is being loaded by a tensile machine and experiences an increment in total true strain $d\epsilon_T$. We may divide the differential expression

$$d\epsilon_T = d\epsilon_E + d\epsilon_P$$

by $d\sigma$ to arrive at

$$\frac{1}{H_T} = \frac{1}{H_E} + \frac{1}{H_P} \tag{15}$$

where H_T is the *observed* total work-hardening coefficient, $d\sigma/d\epsilon_T$, and H_E and H_P are similarly defined. H_T is the slope of a true stress-true strain curve at any point. By definition, $\epsilon_E = \sigma/E$; thus H_E is equal to the elastic modulus E. Since H_T is a measured quantity and E is known, Eq 15 provides us with a method for calculating H_p, the increase in flow stress for an increase in *plastic* strain. We note in passing that for loading of a tension specimen near the proportional limit (where $H_T \approx E$), Eq 15 indicates that $H_P \gg E$. We feel this behavior simply suggests that the quantity $d\sigma/d\epsilon_P$ is not well-defined for near-elastic loading. The reciprocal, $d\epsilon_P/d\sigma$, is well-defined, however. Representation of stress-strain test results by plotting H_P versus σ has become popular of late.[7] It would appear, in light of the near-yield peculiarity with H_P, that an alternative graphical representation of stress-strain behavior using $1/H_P$ versus σ is advisable.

---

[7] See, for example, U. F. Kocks, this publication, pp. 121-138.

Next, consider substituting the identity

$$\dot{\epsilon}_p = \frac{\dot{\sigma}}{H_P}$$

into the coupling relation, Eq 5, and solving for $1/H_P$:

$$\frac{1}{H_P} = \frac{\dfrac{V_0}{g\dot{\sigma}} - \dfrac{1}{C}}{\left(1 - \dfrac{\sigma}{M}\right)} \tag{16}$$

This equation demonstrates that the quantity H_P can be determined from measurement of $\dot{\sigma}$ and g $(= 1 + e_T)$, and also that H_P is dependent on a prescribed parameter, V_0, and on machine stiffness (through M and C). Equation 16 also clearly indicates that H_P is not a fundamental material parameter, but is dependent on the experimental loading conditions. For example, letting $V_0 = 0$ in Eq 16, which corresponds to a stress relaxation test, we find that

$$H_P = -\left(1 - \frac{\sigma}{M}\right)C$$

which is a *negative* quantity. This is not an indication of work softening during stress relaxation, but a demonstration that H_p is an *observed* work-hardening coefficient and should not be equated with the *actual* work-hardening behavior.

The correspondence between H_p and the *actual* work-hardening coefficient, θ_p, is easy to develop, however. If the specimen flow stress depends only on plastic strain and plastic strain rate, we may write

$$d\sigma = \left(\frac{\partial\sigma}{\partial\epsilon_P}\right)_{\dot{\epsilon}_P} d\epsilon_P + \left(\frac{\partial\sigma}{\partial \ln \dot{\epsilon}_P}\right)_{\epsilon_P} \frac{d\dot{\epsilon}_P}{\dot{\epsilon}_P} \tag{17}$$

The partials in this expression correspond to the work-hardening rate at constant true plastic strain rate and the strain rate sensitivity of the flow stress, respectively. Renaming these partials θ_P and γ, Eq 17 can be rewritten:

$$H_P = \theta_P + \gamma \frac{\ddot{\epsilon}_P}{\dot{\epsilon}_P{}^2} \tag{18}$$

Provided the strain rate sensitivity of the material, γ, is known, Eq 18 enables us to calculate θ_P from a measured value of H_P and a knowledge of the plastic strain rate and the plastic strain acceleration $\ddot{\epsilon}_P$. It is obvious from this equation that for a constant true plastic strain rate test [*13*], where $\ddot{\epsilon}_P = 0$, θ_P is determined directly, since it is equal to H_P. In other loading situations (for example, constant V_0), θ_P must be found from Eq 18 using experimental determinations for H_P, $\dot{\epsilon}_P$, and $\ddot{\epsilon}_P$. If the experimental data are available in the form of true stress versus time, and an independent measurement of strain is available, H_P, $\dot{\epsilon}_P$, and $\ddot{\epsilon}_P$ can be determined from Eq 16, Eq 5, and the time derivative of Eq 5, respectively.

In practice, however, the experimental record from a tension test is ordinarily in the form of engineering stress versus time or engineering stress versus total engineering strain. In this case, Eq 5 is inconvenient for calculation of $\dot{\epsilon}_p$ and $\ddot{\epsilon}_p$ to use in Eq 18. It is easy to verify that the coupling relations for $\dot{\epsilon}_p$ and $\ddot{\epsilon}_p$ in terms of engineering quantities are:

$$\dot{\epsilon}_P = \left(\frac{V_0}{g} - \frac{\dot{S}q}{C}\right)\Big/\left(1 + \frac{qS}{E}\right) \tag{19}$$

and

$$\ddot{\epsilon}_P = \left[\frac{\dot{V}_0}{g} - \frac{\ddot{S}q}{C} - \left(\frac{\dot{e}_T}{g}\right)^2 - \frac{q}{E}\left(2\dot{S}\dot{\epsilon}_P + S\dot{\epsilon}_P{}^2\right)\right]\Big/\left(1 + \frac{qS}{E}\right) \tag{20}$$

The values for $\dot{e}_T$ and $\dot{\epsilon}_P$ in Eq 20 are found from Eqs 3 and 19, respectively. Also, to a very good approximation in Eqs 19 and 20, the denominators can be equated to one since $qS \ll E$.

For tension test data in the form S versus e_T, stress rate, $\dot{S}$, is not available but is easily found from the slope of the stress-strain trace, h_T ($\equiv dS/de_T$). Using Eq 3:

$$V_0 = \dot{S}\left(\frac{1}{h_T} + \frac{1}{M_0}\right) \tag{21}$$

The expression relating engineering work-hardening rates analogous to Eq 15 for true work-hardening rates is easily shown to be

$$\frac{1}{h_T} = \frac{1 + e_P}{h_E} + \frac{1 + e_E}{h_P} \tag{22}$$

where $h_E = dS/de_E$ and $h_p = dS/de_p$. Equation 22 is not particularly useful, since h_E does not, in general, equal E ($h_E = E$ only for $\epsilon_p = 0$). Determination of h_T from Eq 21 or directly from the slope of the engineering stress-strain curve is useful, however, since h_T can be related to H_T. The correspondence is easily shown to be

$$H_T = \frac{q(gh_T + S)}{1 + \dfrac{qS}{E}} \approx q(gh_T + S) \tag{23}$$

where, as before,

$$g = 1 + e_T \approx 1 + e_P$$

$$q = 1 + e_P$$

For completeness, we include the relation between H_P and h_P:

$$H_P = q(qh_P + S) \tag{24}$$

Finally, a simple expression relating h_E to $H_E(= E)$ does not exist, since the value of h_E is dependent on the amount of prior plastic deformation. However, it can be shown that

$$\frac{h_E}{h_T} = \frac{E\left(1 + \dfrac{qS}{E}\right)}{gh_T + S} = \frac{qE}{H_T} \tag{25}$$

Variation of Strain Rate in a Tension Test

A plastically deforming specimen appears to the moving crosshead as a nonlinear element in series with the spring representing the machine response. Equation 3 can be used to solve for the partitioning of crosshead displacement between specimen and machine:

$$\dot{L}_T = \frac{\dot{X}}{1 + \dfrac{h_T}{M_0}} \tag{26}$$

where h_T is the slope of the engineering stress-strain curve. This equation illustrates that the total engineering strain rate $\dot{L}_T/L_0$ is, in general, variable for a constant crosshead speed test, depending on the instantaneous work-hardening coefficient and the machine stiffness. This behavior has been noted in a number of studies [*14,19,20*]. It can be seen from Eq 26 that only for an infinitely stiff machine (servo-controlled in strain mode) is the total engineering strain rate identically constant during a tension test.

Identification of the true strain rate behavior can be accomplished by dividing Eq 26 by $L_T = L_0\,(1 + e_T)$, giving

$$\dot{\epsilon}_T = V_0 \Big/ \left[\left(1 + e_T\right)\left(1 + \frac{h_T}{M_0}\right)\right] \tag{27}$$

If the experimental record is in terms of engineering stress versus time, Eq 21 is useful for relating h_T to $\dot{S}$. True elastic strain rate can be easily determined by using Eq 23 to solve for H_T. Then

$$\dot{\epsilon}_E = \dot{\epsilon}_T\left(\frac{H_T}{E}\right) \tag{28}$$

True plastic strain rate is then determined from

$$\dot{\epsilon}_P = \dot{\epsilon}_T - \dot{\epsilon}_E$$

Figure 1 shows an example of strain rate variation during a tension test. Chosen for illustration is the strain-rate-insensitive constitutive behavior

$$\epsilon_P = \epsilon_0\left(\frac{\sigma}{\sigma_0}\right)^N \tag{29}$$

where ϵ_0, σ_0, and N are constants. It follows, then, for this constitutive behavior that

$$\epsilon_T = \frac{\sigma}{E} + \epsilon_0\left(\frac{\sigma}{\sigma_0}\right)^N \tag{30}$$

and

$$\frac{1}{H_T} = \frac{1}{E} + N\frac{\epsilon_0}{\sigma_0}\left(\frac{\sigma}{\sigma_0}\right)^{N-1} \tag{31}$$

For purposes of this illustration, Eq 4 has been solved for $\dot{\epsilon}_T$ (instead of using Eq 27, since H_T can be inserted directly in the result:

$$\dot{\epsilon}_T = V_0 \Big/ \left[(1 + e_T)\left[1 - \frac{\sigma}{M} + \frac{H_T}{M}\left(1 + \frac{\sigma}{E}\right)\right]\right] \tag{32}$$

The curves in Fig. 1 have been calculated for a condition where both ϵ_E and ϵ_P equal 0.002 where $\sigma = \sigma_0$. Thus σ_0 represents the 0.2 percent offset yield strength occurring at $\sigma_0 = 0.002E$ [for example, 414 MPa (60 ksi) for steel]. A value of $N = 5$ has been chosen which corresponds to a work-hardening exponent of 0.2. Curves are given in Fig. 1 for two values of machine stiffness: $E/10$ and infinitely stiff. It can be seen from this figure that for the "soft" machine ($E/10$), all strain rates are variable during a constant V_0 tension test of this model material. However, for an infinite stiffness ($M_0 = \infty$), $\dot{e}_T$ is constant throughout the test, and as can be seen from either Eq 27 or 32, true total strain rate is simply $V_0/(1 + e_T)$. Clearly, true plastic strain rate is zero at the beginning of the test for either stiffness and is virtually equal to $\dot{\epsilon}_T$ after yielding. There is a rapid variation of $\dot{\epsilon}_P$ near the yield stress, the details of which are dependent on machine stiffness. It should be obvious that a true-plastic-strain-rate tension test is, in principle, not possi-

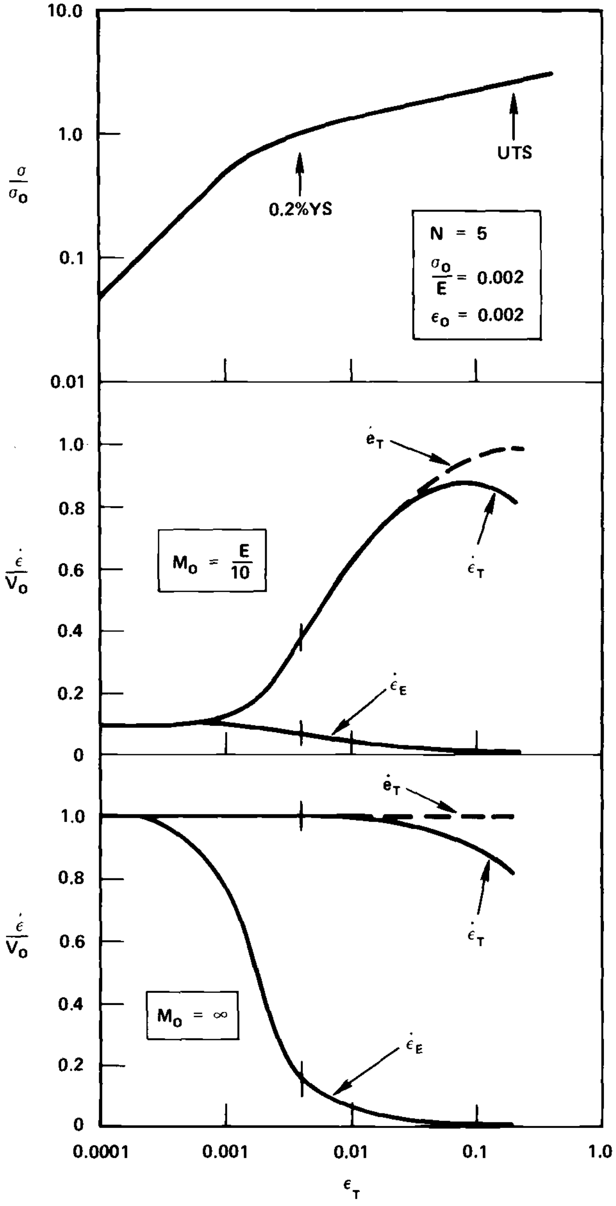

FIG. 1—*Stress-strain and strain rate-strain behavior for the strain-rate-insensitive model material described by Eq 30. Note that stress-strain is represented on a log-log plot. True plastic strain rate is the difference between the* $\dot{\epsilon}_T$ *and* $\dot{\epsilon}_E$ *curves. The vertical lines through the curves represents the strain at 0.2 percent offset yield strength.*

ble over the entire strain range. With a computer-controlled infinite-stiffness machine, however, the test can be closely approximated after yielding has occurred [*13*].

Stress Relaxation Tests

The stress relaxation test is commonly used to examine the strain rate dependence of the flow stress for a given material. The tests consists of stopping the crosshead after a predetermined amount of strain and measuring the decrease in stress with time. Using the coupling relation, the measured stress rate can be converted to a plastic strain rate, and this strain rate can be plotted against stress to ascertain the strain rate sensitivity of the flow stress.

From Eq 5, it follows immediately that during a stress relaxation test ($V_0 = 0$), the stress rate and strain rate are related by

$$\dot{\epsilon}_P = -\dot{\sigma}/C\left(1 - \frac{\sigma}{M}\right) \tag{33}$$

An unusual feature of Eq 33 is the presence of the term $1 - \sigma/M$. To the authors' knowledge, this term has never been included in published studies on stress relaxation behavior. The significance of the term depends on the stiffness of the machine used for testing. For servo-hydraulic machines in strain control, M is effectively infinite, and Eq 33 reduces to

$$\dot{\epsilon}_P = -\dot{\sigma}/E$$

For "soft" machines, the effect of the term depends on the stress level. Neglect of this term results in an underestimate of the magnitude of the plastic strain rate during relaxation.

Since raw data for a stress relaxation test are normally in the form of load versus time, it is useful to express the right-hand side of Eq 33 in engineering terms. Substituting the identity

$$\dot{\sigma} = q(\dot{S} + S\dot{\epsilon}_P)$$

into Eq 33 we arrive at

$$\dot{\epsilon}_P = q\dot{S}\Big/C\left(1 + \frac{qS}{E}\right) \approx \frac{q\dot{S}}{C} \tag{34}$$

Often an empirical constitutive law for plastic strain rate as a function of stress is substituted for $\dot{\epsilon}_p$ in Eq 33 and integrated with the assumption of constant microstructure to yield the stress-time behavior [*21*]. This is then fitted to the experimental stress-time data to identify the parameters in the empirical law. The assumption of constant microstructure is questionable, however, for a stress relaxation test [*2,22-25*]. Clearly, from Eq 33, plastic strain accrues during relaxation, the magnitude of which is dependent on machine stiffness for a given stress drop.

If the flow stress at a constant temperature depends only on microstructure (denoted by Γ) and plastic strain rate, we may write as a differential constitutive law

$$\dot{\sigma} = \left(\frac{\partial\sigma}{\partial\Gamma}\right)_{\dot{\epsilon}_p} \dot{\Gamma} + \left(\frac{\partial\sigma}{\partial \ell n \dot{\epsilon}_p}\right)_{\Gamma} \frac{\ddot{\epsilon}_p}{\dot{\epsilon}_p} \tag{35}$$

which incorporates the influence of microstructural changes on the flow stress. The coupling relation for stress relaxation, Eq 33, can then be substituted into Eq 35 to give

$$-C\left(1 - \frac{\sigma}{M}\right)\dot{\epsilon}_p = \left(\frac{\partial\sigma}{\partial\Gamma}\right)_{\dot{\epsilon}_p} \dot{\Gamma} + \left(\frac{\partial\sigma}{\partial \ell n \dot{\epsilon}_p}\right)_{\Gamma} \frac{\ddot{\epsilon}_p}{\dot{\epsilon}_p} \tag{36}$$

as a differential equation governing stress relaxation. As an example, consider the case where microstructure is dependent only on plastic strain (but not recovery or loss of mobile dislocations). Equation 36 can then be written

$$-C\left(1 - \frac{\sigma}{M}\right)\dot{\epsilon}_p = \theta_p \dot{\epsilon}_p + \gamma \frac{\ddot{\epsilon}_p}{\dot{\epsilon}_p} \tag{37}$$

which is readily integrated if the functional forms of the work-hardening coefficient θ_p and strain rate sensitivity γ are known.

Stress Rates Following a Crosshead Speed Change

Abrupt crosshead speed changes are frequently used in various types of tension tests. Examples of these are strain-rate-cycling tests, fatigue tests, and stress relaxation tests. Often the stress rate immediately following a crosshead speed change is required as a test of a deformation model [*6*] or for characterization of the test machine [*16,17*].

In using the coupling relation to solve for the stress rate following a crosshead speed change, one must make the usual assumption that true *plastic* strain rate is continuous during a speed change. Then we have from Eq 5 for a crosshead speed change from V_{01} to V_{02}:

$$\dot{\sigma}_2 = \dot{\sigma}_1 + \frac{C}{g}(V_{02} - V_{01}) \tag{38}$$

which relates the stress rate after the speed change, $\dot{\sigma}_2$, to the prior stress rate. Again, using Eq 4 to substitute for $\dot{\sigma}_1$ in Eq 38, we also have

$$\dot{\sigma}_2 = \frac{C}{g}\left(V_{02} - \frac{V_{01}}{1 + \dfrac{H_{P1}}{C\left(1 - \dfrac{\sigma}{M}\right)}}\right) \tag{39}$$

where σ is the stress at the crosshead speed change, and H_{P1} is the measured plastic work-hardening rate immediately before the change.

For a stress relaxation test, V_{02} is zero in Eq 39. We see then that the initial stress rate in a stress relaxation test is strongly dependent on machine stiffness and, through H_{P1}, on the location of the stress strain curve where relaxation is started.

Thermally Activated Dislocation Motion

For a crystalline materials deforming by dislocation motion, the plastic strain rate is related to the mobile dislocation density, ρ, and their average velocity, v, by Orowan's equation [*26*]:

$$\dot{\epsilon}_P = \alpha b \rho v \tag{40}$$

where α is a constant and b is the Burgers vector magnitude of the mobile dislocations. It is possible to substitute for $\dot{\epsilon}_P$ in this equation from the coupling relation, Eq 5. This would relate the variation of the product ρv to the crosshead speed, stress rate, and machine stiffness. An alternative representation that separates the variables ρ and v is found by forming the ratio $\ddot{\epsilon}_P/\dot{\epsilon}_P$:

$$\frac{\ddot{\epsilon}_P}{\dot{\epsilon}_P} = \frac{\dot{\rho}}{\rho} + \frac{\dot{v}}{v} \tag{41}$$

For substitution into the left-hand side of this expression, Eq 5 and its time derivative (we note that g, σ, M, and C in Eq 5 are variables and should not be treated as constants in the differentiation) or Eqs 19 and 20 may be used.

Use of Eq 41 to study the variation of ρ in a tension test requires knowledge of the behavior of v and vice versa. The dislocation velocity is commonly treated as a function of an effective stress, σ^*, which is the difference between the applied stress, σ, and an internal stress, σ_i. Equation 41 can be written

$$\frac{\ddot{\epsilon}_P}{\dot{\epsilon}_P} = \frac{\dot{\rho}}{\rho} + \frac{d\ln v}{d\sigma^*}\,\dot{\sigma}^* \tag{42}$$

The internal stress is due to the long-range stress fields characteristic of the microstructure. It can be assumed then that the internal stress varies with plastic strain according to

$$\dot{\sigma}_i = \theta_P \dot{\epsilon}_P$$

where θ_P is the true work-hardening coefficient discussed in an earlier section. Substituting this relation into Eq 42, we have

$$\frac{\ddot{\epsilon}_P}{\dot{\epsilon}_P} = \frac{\dot{\rho}}{\rho} + \frac{d\ell n v}{d\sigma^*} (\dot{\sigma} - \theta_P \dot{\epsilon}_P) \tag{43}$$

Provided the velocity dependence on σ^* and the work-hardening behavior are known, Eq 43 enables us to study $\dot{\rho}$ from observations of the stress-time or stress-strain behavior during tensile deformation.

Figure 2 illustrates this treatment for a particular load-time history, the load-transient behavior often seen in strain-rate cycling tests. Some special cases are labeled with letters in Fig. 2. At positions A, C, and D the engineering stress rate is zero. The terms $\dot{\sigma}$, $\dot{\epsilon}_P$, and $\ddot{\epsilon}_P$ in Eq 43 are defined for this situation by Eqs 9, 19, and 20, respectively. Thus $\dot{\rho}/\rho$ can be quantitatively evaluated if θ_P and $(d\ell n v)/d\sigma^*$ are known.

Summary and Conclusions

We have developed the specimen-machine coupling relation in its exact form for engineering total strain rate, true total strain rate, and true plastic strain rate in Eqs 3 to 5. With a number of applications we have shown how the coupling relation can be used to accurately interpret observed deformation behavior. We have also attempted to illustrate several cases where a

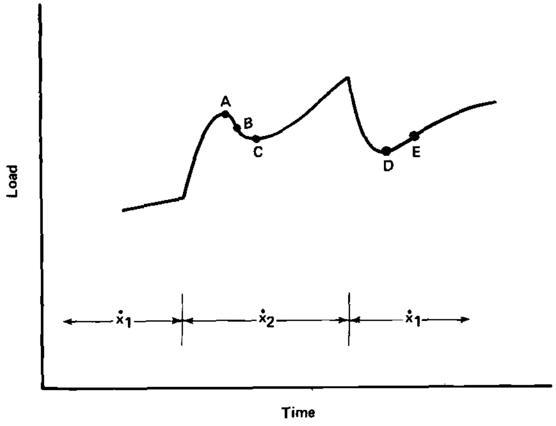

FIG. 2—*Schematic load-time behavior in a strain-rate-cycling (or crosshead-speed-cycling) experiment with* $\dot{X}_2 > \dot{X}_1$. *At locations A, C, and D,* $\dot{P}$ *is zero. Locations B and E are inflection points; thus* $\ddot{P} = 0$.

machine's stiffness characteristics actually influence the deformation response of a material during tension testing.

Several methods have been described for determining machine stiffness. In a number of cases we have indicated the benefits of performing tension tests in a servo-controlled machine in strain mode for which the machine stiffness is effectively infinite. The benefits include a strain rate behavior that is not dependent on the current work-hardening behavior of the specimen, minimal plastic strain occurring during stress relaxation tests, and a much simpler coupling relation for use in interpreting data.

APPENDIX

Development of the specimen-machine coupling relation in terms of true plastic strain rate, Eq 5, required the exact additivity of true elastic and plastic strain components. Referring to the specimen gage length at selected points on a true stress-strain curve shown in Fig. 3, it can be seen that if

$$\epsilon_E = \ln \frac{L_T}{L_P} = \frac{\sigma}{E} \tag{44}$$

and

$$\epsilon_P = \ln \frac{L_P}{L_0} \tag{45}$$

additivity is satisfied because

$$\epsilon_T = \epsilon_E + \epsilon_P = \ln \frac{L_T}{L_0} \tag{46}$$

STRAIN DEFINITIONS

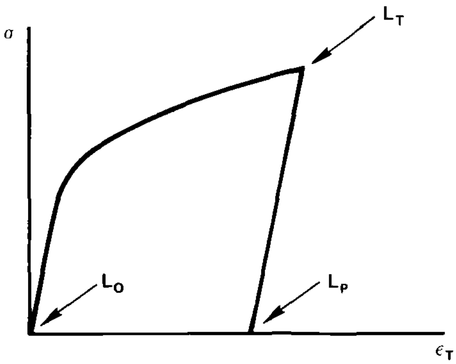

FIG. 3—*Schematic true stress-strain curve indicating specimen gage length definitions for use in strain formulae.*

True strain rates are found by differentiating Eqs 44 to 46 with respect to time:

$$\dot{\epsilon}_T = \frac{\dot{L}_T}{L_T} \tag{47}$$

$$\dot{\epsilon}_P = \frac{\dot{L}_P}{L_P} \tag{48}$$

and

$$\dot{\epsilon}_E = \frac{\dot{L}_T}{L_T} - \frac{\dot{L}_P}{L_P} = \frac{\dot{\sigma}}{E} \tag{49}$$

Engineering strain components are given by the formulae

$$e_E = \frac{L_T}{L_P} - 1 \equiv j - 1 \tag{50}$$

$$e_P = \frac{L_P}{L_0} - 1 \equiv q - 1 \tag{51}$$

and

$$e_T = \frac{L_T}{L_0} - 1 \equiv g - 1 \tag{52}$$

From comparison of Eqs 44 to 46 with Eqs 50 to 52, it can be seen that the conventional rules for connecting true to engineering strains are satisfied:

$$\epsilon_E = \ell n(1 + e_E)$$

$$\epsilon_P = \ell n(1 + e_P)$$

$$\epsilon_T = \ell n(1 + e_T)$$

Using Eq 46 it is evident that

$$1 + e_T = (1 + e_E)(1 + e_p) \tag{53}$$

or

$$g = jq$$

where the quantities $1 + e_T$ etc. are often called stretch ratios [*15*]. Equation 53 indicates that engineering strains are not additive, but in fact

$$e_T = e_E + e_P + e_E e_P \tag{54}$$

Further,

$$\dot{e}_T = (1 + e_P)\dot{e}_E + (1 + e_E)\dot{e}_P \tag{55}$$

that is, engineering strain rates are not additive. True strain rates are related to engineering strain rates by

$$\dot{\epsilon}_E = \frac{\dot{e}_E}{j} = \frac{\dot{\sigma}}{E}$$

$$\dot{\epsilon}_P = \frac{\dot{e}_P}{q}$$

$$\dot{\epsilon}_T = \frac{\dot{e}_T}{g}$$

True stress as used in the text has the conventional definition

$$\sigma = Sq = P/A_P \tag{56}$$

where $S = P/A_0$, and A_p is the unloaded area consistent with L_p. Frequently there is need in the text to convert from time stress rate to engineering stress rate. From Eq 56 we find

$$\dot{\sigma} = q\dot{S} + S\dot{e}_P = q\dot{S} + qS\dot{\epsilon}_P \tag{57}$$

References

[1] Krausz, A. A. and Craig, G. B., *Acta Metallurgica*, Vol. 14, 1966, p. 1807.
[2] Rohde, R. W. and Nordstrom, T. V., *Scripta Metallurgica*, Vol. 7, 1973, p. 317.
[3] Smith, I. O. and White, M. G., *Materials Science and Engineering*, Vol. 21, 1975, p. 185.
[4] Wielke, B., *Scripta Metallurgica*, Vol. 11, 1977, p. 87.
[5] Rohde, R. W. and Nordstrom, T. V., *Scripta Metallurgica*, Vol. 7, 1973, p. 1227.
[6] Holbrook, J. H., Rohde, R. W., and Swearengen, J. C., *Acta Metallurgica*, Vol. 29, 1981, p. 1099.
[7] Johnston, W. G. and Gilman, J. J., *Journal of Applied Physics*, Vol. 30, 1959, p. 129.
[8] Hahn, G. T., *Acta Metallurgica*, Vol. 10, 1962, p. 727.
[9] Gillis, P. P., *Journal of Applied Polymer Science*, Vol. 1, 1965, p. 1.
[10] Hart, E. W., *Acta Metallurgica*, Vol. 15, 1967, p. 351.
[11] Guiu, F. and Pratt, P. C., *Physics Status Solidi*, Vol. 6, 1964, p. 111.
[12] Guiu, F., *Scripta Metallurgica*, Vol. 3, 1969, p. 489.
[13] Hartley, C. S. and Jenkins, D. A., *Journal of Metals*, Vol. 32, 1980, p. 23.
[14] Hamstad, M. A. and Gillis, P. P., *Materials Research Standards*, Vol. 6, 1966, p. 569.
[15] Hockett, J. E. and Gillis, P. P., *International Journal of Mechanical Science*, Vol. 13, 1971, p. 251.
[16] Gillis, P. P. and Medrano, R. E., *Journal of Materials*, Vol. 6, 1971, p. 514.
[17] Fortes, M. A. and Proença, J. G., *Journal of Testing and Evaluation*, Vol. 4, 1976, p. 248.
[18] Preston, J., Instron Corporation, private communication, 1980.
[19] Bernstein, I. M., *Acta Metallurgica*, Vol. 17, 1969, p. 249.
[20] Voorhees, H. R., "A Survey of Effects of Lower-Than-Usual Rates of Strain on the Yield and Tensile Strengths of Metals," ASTM Data Series DS 44, American Society for Testing and Materials, 1969.
[21] Gupta, I. and Li, J. C. M., *Metallurgical Transactions*, Vol. 1, 1970, p. 2323.
[22] Sargent, G. A., *Acta Metallurgica*, Vol. 13, 1965, p. 663.
[23] Sargent, G., Jones, G., and Conrad, H., *Scripta Metallurgica*, Vol. 3, 1969, p. 481.
[24] Okazaki, K., Aono, Y., and Kagawa, M., *Acta Metallurgica*, Vol. 24, 1976, p. 1121.
[25] Meyers, M. A., Guimaraie, J. R. C., and Avillez, R. R., *Metallurgical Transactions*, Vol. 10A, 1979, p. 33.
[26] Orowan, E., *Proceedings of the Physical Society*, Vol. 52, 1940, p. 8.

W. B. Jones,[1] *R. W. Rohde,*[1] *and J. C. Swearengen*[1]

Deformation Modeling and the Strain Transient Dip Test

REFERENCE: Jones, W. B., Rohde, R. W., and Swearengen, J. C., "**Deformation Modeling and the Strain Transient Dip Test,**" *Mechanical Testing for Deformation Model Development, ASTM STP 765,* R. W. Rohde and J. C. Swearengen, Eds., American Society for Testing and Materials, 1982, pp. 102–118.

ABSTRACT: Recent efforts in material deformation modeling reveal a trend toward unifying creep and plasticity with a single rate-dependent formulation. While such models can often describe actual material deformation with some precision, most require a number of different experiments to generate model parameter information. These experiments can be complex, time-consuming, and expensive to perform. Recently, however, a new model has been proposed which is unique in that most of the requisite constants may be found by examining creep transients brought about through abrupt changes in creep stress, namely, the so-called strain transient dip test. While the strain transient dip test is simple in concept, it is extremely difficult to perform in actuality. The critical measurement in this test is the *absence* of a resolvable creep rate after a stress drop. As a consequence, the result is extraordinarily sensitive to strain resolution as well as machine mechanical response. This paper presents the design of a machine in which these spurious effects have been minimized and discusses the nature of the strain transient dip test using the example of aluminum. It is concluded that the strain transient dip test is not useful as the primary test for verifying any micromechanical model of deformation. Nevertheless, if a model can be developed which is verifiable by other experiments, data from a dip test machine may be used to generate model parameters.

KEY WORDS: aluminum, deformation modeling, strain transient dip test, creep

Advanced energy conversion systems such as gas turbines, nuclear fission and fusion plants, and concentrating solar thermal receivers establish the need to describe and predict the inelastic behavior of alloys. This capability is required for purposes of design to meet stringent requirements on conversion efficiency, safety, capital cost, life cycle cost, and reliability. Most of these issues demand that long-term performance be predicted from short-term tests.

---

[1] Sandia National Laboratories, Albuquerque, N.M. 87185.

The traditional approach to inelastic design, based upon phenomenological models of applied mechanics, has demonstrated reasonable success in describing steady, monotonic deformation over limited ranges of stress, temperature, and strain rate. When loading is nonsteady or involves reversals, however, considerable difficulties ensue [*1*].[2] Furthermore, phenomenological models incorporate considerable risk when they are used to predict behavior beyond the range of measured data because the relationships are not based upon the underlying physical processes, and the controlling micromechanisms may change with time, temperature, strain, stress, or strain rate.

Alternatively, the materials science approach to the issue of inelastic deformation is based upon micromechanical calculations of the motion and interaction of dislocations. This approach also has enjoyed success in describing and predicting a limited class of phenomena (for example, stress relaxation and steady-state creep) [*2,3*]. Knowledge of micromechanisms can allow extrapolation with confidence to domains beyond the measured range of the independent variables. Perhaps the clearest means to guide such extrapolations is incorporated in the concept of deformation mechanism maps [*4*]. Presently, most micromechanical models are not utilized in computer-based computations of structural response because (*1*) they are cast only in one-dimensional form and do not account for the tensorial nature of plastic deformation; or (*2*) they are not suitable for numerical integration; or (*3*) they are designed only for steady-state flow.

A new approach to inelastic deformation has emerged in the last few years; this approach eliminates the physically unrealistic partitioning of creep and plasticity common in many phenomenological models and for this reason is often referred to as "unified creep-plasticity" (UCP). Since the UCP method requires no unreasonable assumptions concerning separability of deformation processes, it is possible to include in such formulations results from micromechanical mechanism studies. Thus, potentially, the UCP approach can combine the best features of phenomenological and micromechanical modeling.

We feel, however, that there are still serious limitations to most of the recent UCP models [*5–7*]. Firstly, only a few of the models can realistically be called physically based, and whenever empiricism is involved, great care must be exercised to verify that extrapolations (or predictions instead of descriptions) are valid. Secondly, most of the models require many tedious and costly experiments to define material constants and variables. Thirdly, keeping track of history through the use of hereditary integrals on the external variables strain, strain rate, or time can be prohibitively complex.

We believe that the development of improved UÇP models must be pursued in light of these limitations. Accordingly, we have been pursuing the develop-

---

[2] The italic numbers in brackets refer to the list of references appended to this paper.

ment of a physically based unified creep plasticity model for structural metal response [*8–10*] which uses internal state variables, has some physical basis and, important to the theme of this paper, requires only one test machine to determine the model variables. All required information can be generated from creep data and calculations based on transient response of a creeping specimen to partial unloading (the strain transient dip test). The history dependence issue is addressed by incorporating operationally measurable, evolutionary internal state variables to describe microstructural state and casting the model so that deformation response depends on this internal state.

The stress and strain transient dip tests were devised to measure the average dislocation back stress or the "internal" stress (σ_i) postulated to be present in a material after steady-state creep had been established at an applied stress (σ_a) [*11,12*]. The concept of an internal stress was introduced to reconcile theoretical steady-state creep exponents with experimental measurements [*13,14*], and the existence of back stress has become an essential feature of many micromechanical models. Likewise, internal stress is essential in the UCP model under development to account for Bauschinger effects and kinematic hardening response which are evidenced upon reversed loading. For a material which responds to inelastic deformation in a purely kinematic manner, the back stress becomes the only internal state variable [*8,9*].

In concept, the strain transient dip test is simple; the load on a specimen undergoing steady-state creep is "instantaneously" reduced and the subsequent strain transient recorded. Figure 1 shows the response expected from a material that creeps by the process of jerky dislocation glide. Note that a new creep rate (it may be zero or negative) is established "immediately" after the stress drop. Some stress dip tests in the literature have been interpreted according to this model [*13*]. However, different models of creep deformation predict different transient responses. (An excellent discussion is given by Poirier [*15*].) For example, the recovery creep model requires an "incubation period" (zero strain rate) following any stress reduction in a strain transient dip test [*16,17*]. Stress dip tests that have been interpreted according to recovery creep are also reported in the literature [*16*]. Unfortunately, both the immediate creep and the incubation period responses apparently have been observed in similar materials (aluminum) at similar temperatures and after similar initial steady state creep rates. Moreover, these results have been independently used to verify different creep models. The difficulties encountered from such contradictory verifications based on results of the same experiment cannot be understated, and more work with closer examination of the data will be required to identify the creep-controlling mechanism in pure metals. In spite of this controversy over the use of strain transient dip test data to verify or deny creep mechanism, Poirier [*15*] and Gibeling and Nix [*14*] have reviewed the available data and have concluded that none of it

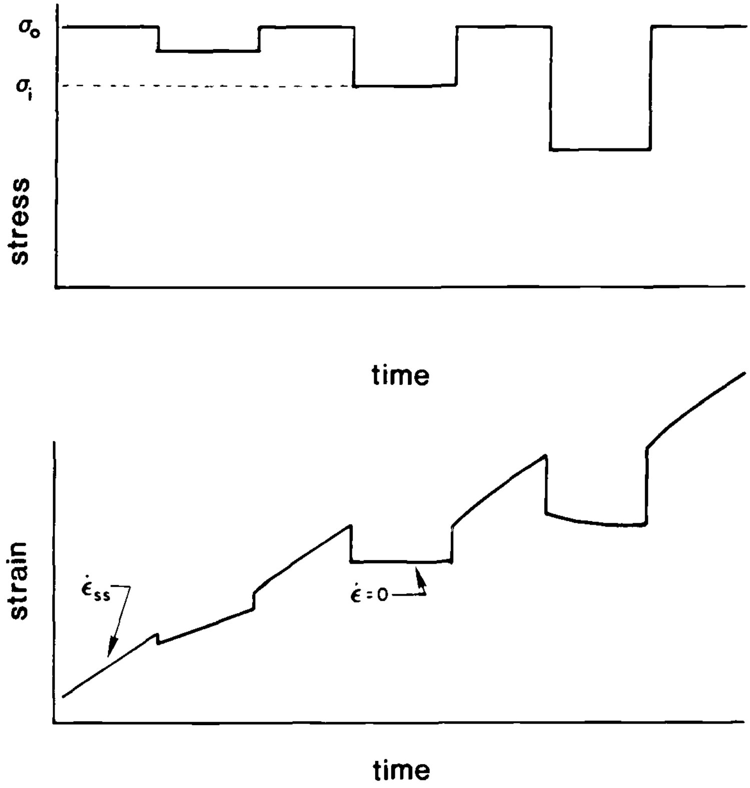

FIG. 1—*Schematic of strain transient dip test results.*

provides any basis on which to reject the concept of internal stress. On this basis, we conclude that an experimental program which attempts to measure an operationally defined back stress with strain transient dip testing is justified.

This paper discusses the design and qualification of an instrument for conducting strain transient dip tests on structural alloys over a wide range of temperatures and loads. Central to the design issue was the ability to input rapid load changes and to measure subsequent strain response with good length and time resolution. In order to verify the design adequacy of the dip test apparatus and associated electronic measuring instrumentation, the transient responses of three purities of aluminum (commercial 1100, 99.99 percent, and 99.999 percent) were measured. The results of these measurements are discussed in terms of defining an internal stress and of verifying micromechanical deformation models.

Experimental Procedure

Dip Test Machine Design

To conclude that the concept of the strain transient dip test is valid is only the first step; designing and building a test machine that adequately performs the test is a difficult task. As in any test designed to measure transient behavior, machine capabilities are critical, but an additional constraint in the strain transient dip test is that the crucial experimental output is the *absence* of a resolvable strain rate. The accuracy of the internal stress measurements are then extremely sensitive to strain-measuring resolution and strain signal stability.

The test machine which has been designed and built to conduct these exacting tests is shown in Fig. 2. The design philosophy was based on our desire to be able to test a wide range of alloys over an extended temperature range. A system was needed that would hold a steady load over a period of days or weeks and yet would have very fast response capabilities for conducting transient stress changes. The long-time load stability requirements dictates gravity loading, yet the fast load change requirements must also be in-

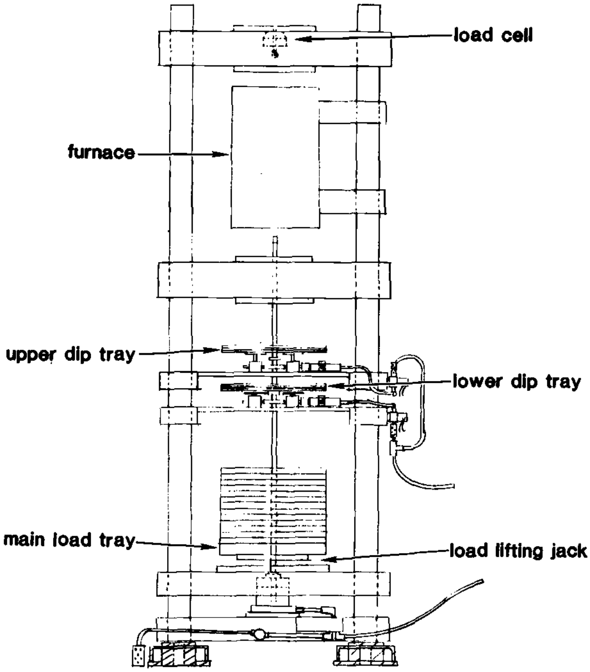

FIG. 2—*Drawing of dip test frame.*

corporated. A number of different potential loading techniques were analyzed in considerable detail. All used gravity loading but some employed levers, pulleys, or hydraulics for load amplification in contrast with the direct load application incorporated in the final design. Several different load change methods were also examined, including severed cords to drop weights and various hydraulic, pneumatic, and geared mechanisms. The predicted performance of each of these concepts was evaluated by computer analysis of the assembled system. The analysis, which determined system response to step load changes, was accomplished by treating the system as a lumped spring mass assembly. The design goal was to change loads rapidly with minimal resulting "ringing", a result which would be achieved in principle by unloading in one quarter cycle of the natural period of oscillation.

Some of the candidate designs were determined to have inherent flaws such as sliding friction or backlash. The most promising alternatives were carried to the point of performing a detailed dynamic analysis. The final design, as seen in Fig. 2, incorporated direct dead-weight loading with the stiffest possible structure. The load changes are effected by using a pneumatically operated jack to lift a circular mass off a support collar. The dynamic model for this concept is very nearly approximated by a single degree-of-freedom system with the test specimen acting as a spring and the load train-weight combination as the mass.

In determining the internal stress by stress-change tests, it is important that stress overshoot does not occur, especially on reloading. Accordingly, this machine has been designed to incorporate a variable damping mechanism to eliminate any overshoot. Since the amount of damping required is dependent on both the elastic stiffness of the specimen and the load applied, it was decided that the behavior of the actual test system should be characterized before any damping mechanism is chosen or installed.

The load train is a 19.1-mm-diameter steel rod. While this rod is made of several shorter segments, threaded couplings are used and tightened to preclude backlash. The load train is constrained against lateral motion by a bearing assembly at the point the train passes through the first crosshead below the specimen. The base load tray is also stabilized with three guide rods evenly spaced around the circumference which pass downward through the frame base plate. Vertical motion is kept free by bearings in the base plate holes; these bearings also restrain lateral or rotational motion of the load train. The base load tray is lifted and lowered by a pneumatic jack mounted on the frame base plate. Weight is added to these trays with semicircular lead plates.

Load changes are performed by lifting either one of the two dip trays shown in Fig. 2. The lifting mechanism is shown in more detail in Fig. 3. A pneumatic motor is used to drive two small jacks, one on either side of the dip tray. In the lifted position, the tray and weights are supported by 100-mm-diameter, 6.4-mm-thick steel pads which are rigidly attached to the

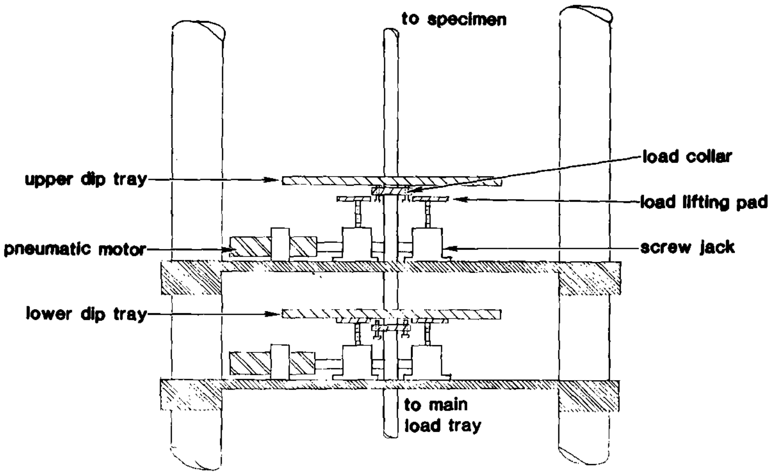

FIG. 3—*Details of load-lifting mechanism.*

jack shafts. These pads are adjusted on the jack shafts to make flat contact with the dip tray. When lowered, the dip trays rest on three contact screws attached to the load train. These contact screws are also adjusted so that the load transfer between the load train and the frame-mounted jacks occurs simultaneously around the circumference. Correct contact is confirmed through the use of a digital storage oscilloscope displaying the load cell output. The loading and unloading by this technique, without any augmented damping, occurs at a rate of about 2.22 kN/s (70 MPa/s for a 6.35-mm-diameter specimen).

Specimen and Grips

Specimens are button ended with a 38.1 mm gage length and a 6.35 mm diameter. These specimens have a lower surface-to-volume ratio than thin strip specimens, thus minimizing any surface oxide constraint effects on specimen behavior. The cylindrical design also allows specimens to be machined directly from bar stock with no need for deforming the material as part of specimen fabrication, such as rolling thin strips.

These specimens are secured to the load train by threaded grips with split collet inserts shown in Fig. 4. The primary advantage of this gripping arrangement is that all the parts can be tightened to eliminate backlash.

Strain Measurement

Two strain-measuring systems are used during testing. For one system a micrometer adjustable linear variable differential transformer (LVDT) is at-

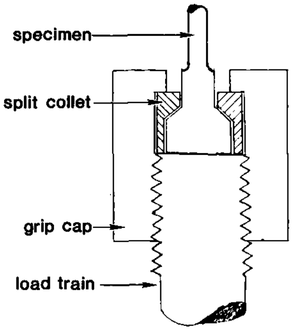

FIG. 4—*Specimen grip assembly.*

tached between the specimen and a crosshead. This LVDT has a linear displacement range of 12.7 mm and is used primarily to monitor the total specimen elongation. In this way, true strain and true stress can be calculated for each individual dip test sequence on a single specimen. The second, more precise strain measurement for characterizing the strain transient response is made with a modified axial rod extensometer. The specimen ends of the extensometer are mounted rigidly to the horizontal faces of the specimen grips in such a manner that the rods and brackets attached to the top grip do not contact the rods and brackets attached to the lower grip and neither assembly touches the load train or furnace. As a final adjustment, the LVDT is positioned with set screws so that the core moves freely in the LVDT body. This LVDT has a linear displacement of 0.635 mm and a sensitivity of 63.5 μm/V. In principle, displacements less than 30 nm can be determined with this arrangement. However, it has been found that the actual strain resolution is limited by building vibrations transmitted through the frame and extensometer. The data presented in this paper generally reflect testing conducted during quieter hours of the day. Typical displacement resolution has been 250 nm or about 7 $\mu\epsilon$.

Strains are recorded in two ways. A Leeds and Northrup thermal pen strip chart recorder is used at a recording speed of 12 s/mm and an extensometer gain of about 12 $\mu\epsilon$/mm. A Nicolet digital storage oscilloscope is used to record the load drop and the first 80 s of the strain transient. These digital data are taken at 5 ms intervals. This interval was chosen since it is the longest interval which could be used without producing an interference "beat" frequency lower than 1 Hz in the digital data between sampling frequency and any 60 Hz noise in the strain signal.

Temperature Control

The furnace for heating the specimen is a three-zone split tube furnace with an independent proportional controller for each zone. This system is capable of maintaining a constant temperature within ±0.1 K over the several hours of transient behavior following each load change, and within ±0.2 K over several days of testing. For aluminum at temperatures of interest, the linear coefficient of thermal expansion is about 24×10^{-6} m/m/K, corresponding to an apparent strain signal of 5 $\mu\epsilon$ over ±0.1 K; this error is less than the uncertainty caused by building vibrations.

Results and Discussion

Aluminum was chosen for system performance evaluations because of the comparatively large number of strain transient dip test results in the literature which were available for comparison [*13,14,16,18*] and because of our previous experience in measuring the stress relaxation behavior of the material [*10*]. Unfortunately, the weight of the load train and dip trays limits the testing flexibility for such an easily deforming material as pure aluminum. For this reason, the test results reported here were developed at temperatures of about 420 K, producing strain rates in the range of 10^{-6} to 10^{-10} s^{-1} for the minimum load constraints of the system.

Three different purities of aluminum were tested: commercial purity 1100-O, 99.99 percent, and 99.999 percent. Table 1 lists the typical impurity levels for 1100-O and the actual impurity levels measured by emission spectrographic analysis for the two higher purity heats. The commercial purity aluminum was tested in the annealed (1100-O) condition. The higher purity aluminum samples were annealed at 573 K after machining.

The influence of annealing time is readily observed in the measured steady-state creep rates listed in Table 2. The higher creep "resistance" of the commercial purity was anticipated; however, the significant difference in creep rate behavior between 30 min and 4 h annealing at 573 K of the 99.99 percent material is somewhat surprising. The measured creep rates for the 99.999 percent purity material and for the 99.99 percent material annealed for 4 h are in agreement with published high-purity aluminum creep results [*2*]. As the values of $\dot{\epsilon}/D$ in Table 2 indicate, these tests were conducted, for the most part, in the power-law breakdown region (that is, $\dot{\epsilon}/D > 10^7$ mm^{-2}). In spite of the difference in strain rate magnitudes between the high-purity materials annealed at different times, both conditions show a stress

TABLE 1—*Composition of test specimens (in ppm).*

Material	Al	Cu	Fe	Mg	Ga	Si	Mn
1100-O	>99.00 %	1200					
99.99 % Al		4	10	2	20	20	6
99.999 % Al		2	3	ND[a]	ND	2	ND

[a] ND = Not determined.

TABLE 2—*Steady-state creep behavior.*

Material	Annealing Treatment	Test Temperature, K	Stress, MPa	$\dot{\epsilon}_{ss}$, s^{-1}	$\dot{\epsilon}/D$, mm^{-2a}
1100-O	...	420	48.0	4.0×10^{-10}	...
99.99 % Al	0.5 h/573 K	417	30.6	2.0×10^{-8}	2.5×10^{7}
	0.5 h/573 K	417	36.9	2.2×10^{-7}	2.8×10^{8}
	4 h/573 K	417	17.7	5.8×10^{-8}	7.3×10^{7}
	4 h/573 K	417	23.9	2.1×10^{-6}	2.7×10^{9}
99.999 % Al	4 h/573 K	420	18.4	8.9×10^{-8}	1.1×10^{8}
	4 h/573 K	420	23.9	2.6×10^{-6}	3.3×10^{9}

[a] $D = 127 \exp(-1.43\ eV/kT)\text{mm}^2/\text{s}$ [*20*].

sensitivity exponent of 12 to 14 in this range. All the specimens tested showed typical decreasing strain rate primary creep behavior.

The load changes examined were conducted after the steady-state creep rate was reached. Because the steady-state creep rates were all low, a series of load changes could be conducted on a single specimen without significant strain accumulation or concurrent reduction in cross section. As discussed earlier, no additional damping was incorporated in this test; therefore each strain transient contained some system oscillation indicative of the undamped maximum unloading rate available on the machine. Figure 5 shows the strain oscillations for a 40 percent stress drop in a 99.99 percent purity specimen. These data were taken from the digital storage oscilloscope. The result shown here is a typical response. Occasionally, more severe oscillations were observed, in which case the data were rejected.

The first feature of the strain transients worth examination is the so-called "instantaneous" contraction upon unloading [*16*]. Examination of Fig. 5 shows that defining an instantaneous contraction is impossible; even the abrupt decrease in strain associated with the load removal is nonlinear. Time-dependent processes seem to be operating on a scale observable at the time resolution of these measurements, ~5 ms. Thus measurement of true elastic contraction upon unloading would require correlation of time-resolved measurements of both the transient stress and strain during a dip. Measurements of other values of "instantaneous" contraction are combinations of both elastic and inelastic effects and will be misleading unless the time dependence of the inelastic portion is known. For example, if "instantaneous" in our experiments is defined as 1 s, a time well beyond ring down of the system, "effective" unloading moduli can be determined. Using the Young's modulus data of Fine [*19*] as the comparison value for the 99.999 and 99.99 percent purity materials annealed for 4h, contractions fell in a band around $E_{\text{eff}} = 0.5\ E$; while for 99.99 percent purity annealed for 30 min, contractions corresponded to about $E_{\text{eff}} = 0.7\ E$ and the commercial purity material results showed $E_{\text{eff}} = 1.0\ E$. The differences between effec-

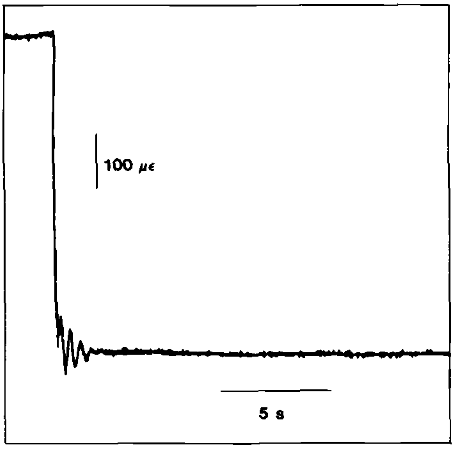

FIG. 5—*Oscilloscope trace of strain transient after a load drop.*

tive unloading moduli of these materials are mainly believed to result from anelastic effects apparently associated with the initial microstructural state of the material. As with the steady-state creep rates, these results indicate that for creep and transient testing, annealing time is critical.

It will be seen that such anelasticity on unloading can have an important effect on the apparent internal stress, measured by zero creep rate. Thus it is essential to know the relationship between any anelastic strain and unloading increment, material purity microstructural condition, and initial creep stress. These studies are currently underway.

Figures 6 to 8 show the time-dependent transient strain response of the different purity aluminum materials. Samples of 99.99 percent aluminum annealed for 4 h at 573 K showed the same transient responses as the 99.999 percent aluminum given in Fig. 8. In these figures, the horizontal lines represent the elastic-anelastic unloading increments at 1 s whose magnitudes are defined by the effective moduli reported earlier. Since the important measurement from this experiment is the absence of creep (that is, $\dot{\epsilon} = 0$), it is essential to define the resolution limits on that quantity. The strain rate resolution for this form of presentation is marked on each figure and lies between 10^{-8} and 10^{-9} s^{-1}. Over the shorter time interval of 80 s recorded on the digital oscilloscope, the minimum strain rate resolution increases to about 10^{-7} s^{-1}. Thus in these figures any strain rate less than $| 10^{-9} |$ would be seen as zero. Review of the data in Table 2 shows the steady-state creep rate of 1100-O aluminum at the initial load is 4×10^{-10} s^{-1}. This strain rate would not be resolved on the transient data presentations of Fig. 6 and would erroneously be reported as zero. This example indicates the importance of placing slopes that show the resolvable strain rate on figures presenting dip

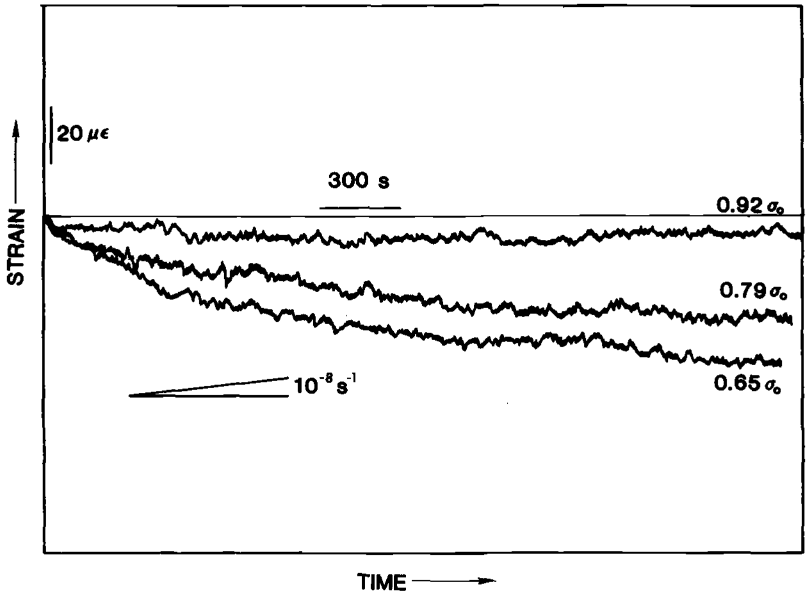

FIG. 6—*Postdip strain response of 1100-O aluminum for* σ_0 *= 48.0 MPa and* T *= 421 K.*

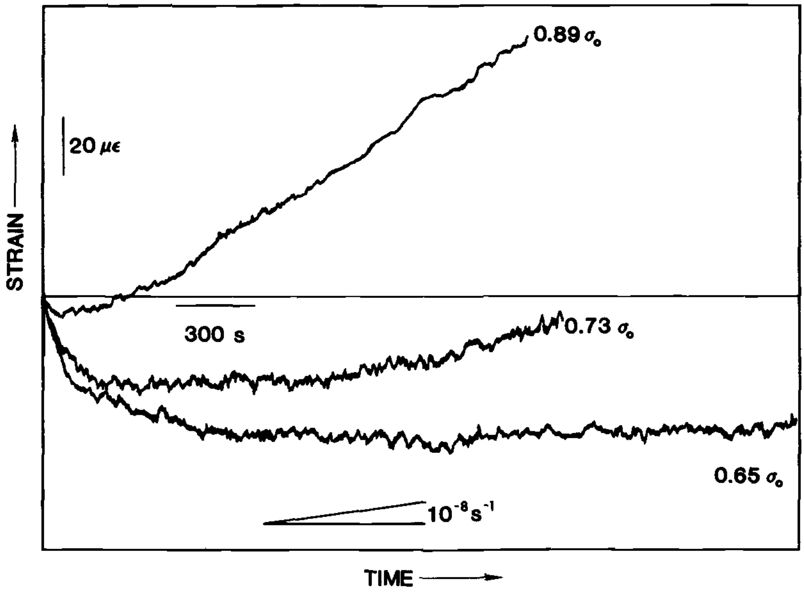

FIG. 7a—*Postdip strain responses of 99.99 percent aluminum annealed for 0.5 h at 573 K.*

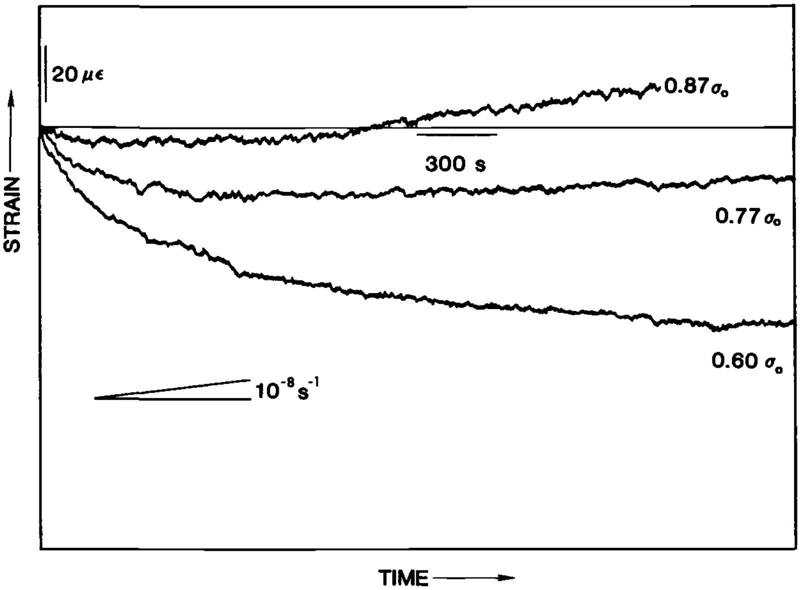

FIG. 7b—*Postdip strain responses of 99.99 percent aluminum annealed for 0.5 at 573 K* (σ_0 = *30.3 Mpa;* T = *421 K).*

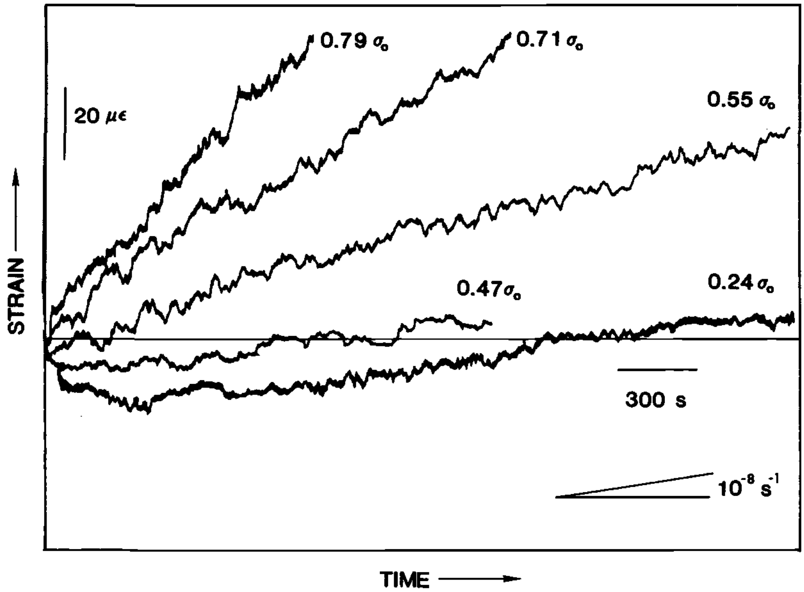

FIG. 8a—*Postdip strain responses of 99.999 percent aluminum annealed for 4 h at 573 K* (σ_0 = *23.9 MPa;* T = *419 K).*

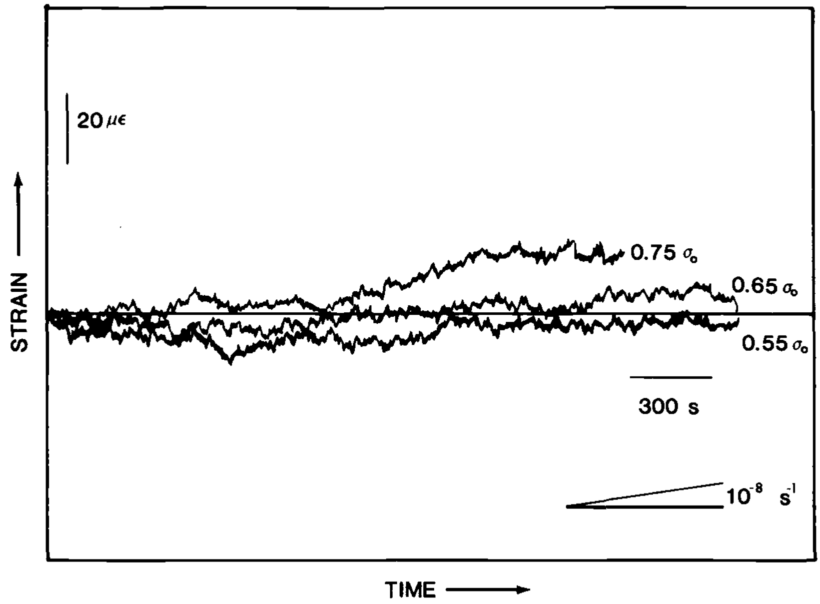

FIG. 8b—*Postdip strain responses of 99.999 percent aluminum annealed for 4 h at 573 K (σ_0 = 18.4 MPa;* T = *419 K).*

test data. Note that what is measured in a creep or dip test is strain versus time. For a given strain resolution, the strain rate resolution increases with time. (This relationship is quantitatively discussed in the Appendix.) In a dip test, the events and strain rates of interest are at short times, exactly where the strain rate, which is the quantity of interest, is most poorly resolved. This is a substantial defect in the apparently simple dip test experiment, and we feel it is one cause of much of the conflict in apparent results reported in the literature.

Examination of the actual dip test data indicates other problems. If internal stress is identified as the stress level for zero strain rate, the results for 1100-O aluminum (Fig. 6) indicate an internal stress of $\sigma_i > 0.79\ \sigma_0$; no better resolution can be claimed. Although it is tempting to set 0.92 σ_0 as the internal stress, it must be remembered that creep could be occurring, but not resolved. This is an excellent example of the inadvisability of attempting to determine a material property based on the inability to measure the critical event; that is, the actual value of that parameter can be a strong function of experimental resolution.

Measuring an actual internal stress is further complicated by the time-dependent processes occurring at very short times during unloading, which were discussed in terms of calculating the instantaneous strain drop. Consider data for higher purity aluminum in Figs. 7 and 8. If the internal stress is defined as that level where "zero" strain rate is seen for even brief times, one would place $\sigma_i > 0.89\ \sigma_o$ in Fig. 7*a*, $\sigma_i > 0.87\ \sigma_o$ in Fig. 7*b*, and $\sigma_i > 0.55\ \sigma_o$ in Fig. 8*a*. If experiments had poorer time resolution than those reported here, or if the "short time" zero strain rate behavior were discounted as a result of a spurious process, one would select $\sigma_i \cong 0.65\ \sigma_o$ in Fig. 7*a*, $\sigma_i \cong 0.77\ \sigma_o$ in Fig. 7*b*, and $\sigma_i \cong 0.47\ \sigma_o$ in Fig. 8*a*. Figure 8*b* shows that even a modest change in strain resolution would change the estimated value of internal stress through a range of $0.5\ \sigma_o < \sigma_i < 0.8\ \sigma_o$. These two different selections of apparent resolution times yield vastly different values of σ_i, and they also change the trend in the ratio σ_i/σ_o with σ_o. For the 99.99 percent aluminum data (Fig. 7) we see in the short-time case a slight increase of σ_i/σ_o with increasing initial stress, whereas in the longer time case we see a decrease. The times in which σ_i must be measured and the relationships between the ratio σ_i/σ_o and σ_o are, of course, important to modeling inelastic material behavior. That a single experiment can yield such different results, dependent upon time and strain rate resolution, renders it inappropriate for use as a verification technique.

Conclusions

While it may be justifiable to operationally define an internal stress and to utilize that variable in models, the present results show that the strain transient dip test does not produce an unambiguous value of σ_i. What is, conceptually, a simple and elegant experiment is complicated by a fundamental flaw which makes the value of the parameter measured extremely sensitive to experimental strain rate resolution. Other complications arise because of time-dependent processes that occur in the material under study during the rapid dip unloading. Thus dip testing may produce valuable information concerning the micromechanical processes of material deformation, but interpretation of dip test results must be undertaken with great care and a sound understanding of machine-specimen interactions, and on the basis of an already verified model. By its very nature, the dip test produces ambiguous data; it may be interpreted on the basis of a specific deformation model but it can never be used to verify models. This basic inability for verification is demonstrated by differing conclusions based on apparently similar data. Nevertheless, if a model can be developed which is verified by other critical experiments, data from a dip test may appropriately be used to generate model parameters.

Acknowledgments

This work was sponsored by the U.S. Department of Energy under Contract DE-AC04-DP00789. Sandia National Laboratories are a U.S. Department of Energy Facility.

APPENDIX

Since strain rate is a quantity derived from strain and time measurements, the cumulative error in the strain rate must also be derived from the errors in the experimental measurements. Now:

$$\dot{\epsilon} = \frac{\epsilon_2 - \epsilon_1}{t_2 - t_1} = \frac{\Delta\epsilon}{\Delta t} \tag{1}$$

where $\dot{\epsilon}$ is the average calculated strain rate determined from measurements (t_1, ϵ_1) and (t_2, ϵ_2). The error in $\Delta\epsilon$ is given by [*21*]:

$$\delta(\Delta\epsilon) = \delta\epsilon_1 + \delta\epsilon_2 = 2\delta\epsilon \tag{2}$$

where $\delta\epsilon$ is the absolute error in each strain measurement. The relative error in the strain rate is [*21*]:

$$\left[\frac{\delta\dot{\epsilon}}{\dot{\epsilon}}\right] = \frac{\delta(\Delta\epsilon)}{\Delta\epsilon} + \left[\frac{\delta(\Delta t)}{\Delta t}\right] \tag{3}$$

where $\delta(\Delta t)/\Delta t$ is the relative error in measuring the time interval. At the lower limits of strain rate estimation the error in time measurement is much smaller than the relative error in $\Delta\epsilon$. Thus

$$\left[\frac{\delta\dot{\epsilon}}{\dot{\epsilon}}\right] \sim \frac{\delta(\Delta\epsilon)}{\Delta\epsilon} = \frac{2\delta\epsilon}{\Delta\epsilon} \tag{4}$$

This result shows that the larger the strain increment measured, the lower the relative error in strain rate estimation.

Equation (4) can be used to estimate the minimum resolvable strain rate as a function of the time interval of interest. The minimum resolvable strain rate, $\dot{\epsilon}_{\text{min}}$, and the time interval, Δt, can be combined according to Eq 1 and substituted into Eq 4 to yield

$$\left[\frac{\delta\dot{\epsilon}}{\dot{\epsilon}}\right] = \frac{2\delta\epsilon}{\dot{\epsilon}_{\text{min}}\Delta t} \tag{5}$$

where $[\delta\dot{\epsilon}/\dot{\epsilon}]$ is the maximum acceptable relative error in the strain rate estimation. We rearrange as

$$\dot{\epsilon}_{\text{min}} = \frac{2\delta\epsilon}{[\delta\dot{\epsilon}/\dot{\epsilon}]}\,\frac{1}{\Delta t} \tag{6}$$

This result indicates that the minimum resolvable strain rate is inversely proportional to the time interval of observation.

For the experimental system described here, $\delta\epsilon = 7 \times 10^{-6}$ m/m, and if the acceptable relative error in strain rate is taken to be $[\delta\dot{\epsilon}/\dot{\epsilon}] = 0.9$ (about one order of magnitude), the minimum resolvable strain rate can be calculated. Several results are shown in Table 3.

TABLE 3—*Minimum resolvable strain rates assuming an acceptable relative error of 0.9.*

Δt	$\dot{\epsilon}_{\text{min}}$
10 s	$1.6 \times 10^{-6}\ \text{s}^{-1}$
1 min (60 s)	$2.6 \times 10^{-7}\ \text{s}^{-1}$
1 h (3.6×10^3 s)	$4.3 \times 10^{-9}\ \text{s}^{-1}$
1 day (6.6×10^4 s)	$1.8 \times 10^{-10}\ \text{s}^{-1}$

References

[1] "Office of Naval Research Plasticity Workshop," K. J. Sacralski and J. A. Stricklin, Eds., Report 75-51, Texas A&M University, College Station, Tex., June 1975.

[2] Bird, J. E., Mukherjee, A. K., and Dorn, J. E., *Quantitative Relations Between Properties and Structure,* D. G. Brandon and A. Rosen, Eds., Israel University Press, Jerusalem, 1969, pp. 255-342.

[3] *Rate Processes in Plastic Deformation of Materials,* J. C. M. Li and A. K. Mukherjee, Eds., American Society for Metals, 1975.

[4] Ashby, M. F., *Acta Metallurgica,* Vol. 20, 1972, p. 887.

[5] Jackson, M. S., Cho, C. W., Alexopoulous, P., and Li, Che-Yu, to be published.

[6] Miller, A. K., *Journal of Engineering Materials and Technology,* Vol. 98, 1976, p. 97.

[7] Liu, M. C. M. and Krempl, E., *Journal of Mechanical and Physical Solids,* Vol. 27, 1979, p. 377.

[8] Swearengen, J. C., Rohde, R. W. and Hicks, D. L., *Acta Metallurgica,* Vol. 24, 1976, p. 909.

[9] Krieg, R. D., Swearengen, J. C., and Rohde, R. W., *Inelastic Behavior of Pressure Vessel and Piping Components,* ASME, 1978, pp. 15-28.

[10] Jones, W. B., Rohde, R. W., and Swearengen, J. C., *Acta Metallurgica,* in press.

[11] Solomon, A. A., *Review of Scientific Instruments,* Vol. 40, 1969, p. 1025.

[12] Ahlquist, C. N. and Nix, W. D., *Scripta Metallurgica,* Vol. 3, 1969, p. 679.

[13] Ahlquist, C. N. and Nix, W. D., *Acta Metallurgica,* Vol. 19, 1971, p. 373.

[14] Gibeling, J. C. and Nix, W. D., *Materials Science and Engineering,* Sept. 1980.

[15] Poirier, J. P., *Acta Metallurgica,* Vol. 25, 1977, p. 913.

[16] Parker, J. D. and Wilshire, B., *Philosophical Magazine A,* Vol. 41, 1980, p. 665.

[17] Parker, J. D. and Wilshire, B., *Metallurgical Science,* Vol. 12, 1978, p. 453.

[18] Gibeling, J. C. and Nix, W. D., *Metallurgical Science,* Vol. 11, 1977, p. 453.

[19] Fine, M. E., *Review of Scientific Instruments,* Vol. 28, 1957, p. 643.

[20] Lundy, T. S. and Murdock, J. F., *Journal of Applied Physics,* Vol. 33, 1962, p. 1671.

[21] Bevington, P. R., *Data Reduction and Error Analysis for the Physical Sciences,* McGraw-Hill, New York, 1969, p. 56.

Phenomenological Modeling and Applications

U. F. Kocks[1]

Strain Hardening and 'Strain-Rate Hardening'

REFERENCE: Kocks, U. F., "**Strain Hardening and 'Strain-Rate Hardening',**" *Mechanical Testing for Deformation Model Development, ASTM STP 765,* R. W. Rohde and J. C. Swearengen, Eds., American Society for Testing and Materials, 1982, pp.121-138.

ABSTRACT: The limitations of power-law strain hardening and 'strain-rate hardening' descriptions are reviewed. It is found that significant advantages can be gained by using, instead, the Voce relation, especially in the proposed modification that accounts for the rate sensitivities of flow stress and of strain hardening. Considerable further predictive value can be derived from differential constitutive relations, which can be integrated over arbitrary paths. The material parameters to be measured are the (linear) strain-hardening rate and the rate sensitivity of the flow stress, both as a function of (pre)stress and (current) strain rate. These are history independent over substantial regimes of unidirectional deformation, where a mechanical equation of state exists.

KEY WORDS: strain hardening, strain-rate hardening, rate sensitivity, constitutive relations, state parameters, evolution

Strain hardening describes the evolution of the flow stress from the beginning of plastic deformation at yield to the beginning of fracture (or of some instability that will lead to fracture). The principal experimental facts can be abstracted as follows, with the help of a plot of true stress versus true plastic strain, as shown in Fig. 1. In the yield region, the curve exhibits either a sharp knee (*a*) or a yield drop (*b*). Neither of these phenomena is considered to be an aspect of strain hardening, even though they are described by slopes on a stress-strain diagram. From then on, the stress-strain curve proceeds with a convex upward curvature, which may be described by a "tendency toward saturation", even though plasticity usually ends when the slope on this true stress versus true strain diagram is still positive.

The physical processes underlying strain hardening are distinct from both

---

[1] Materials Science Division, Argonne National Laboratory, Argonne, Ill. 60439.

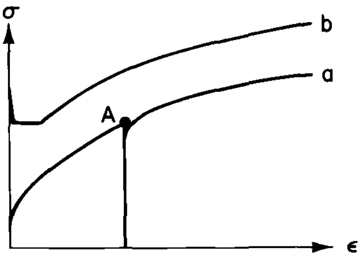

FIG. 1—*Two typical stress strain curves exhibiting qualitatively similar strain-hardening behavior, but widely different yield stresses and yield transients. Interruption of curve* a *at* A *is equivalent to testing a cold-worked material with the same yield stress as* b, *but the same strain-hardening behavior as* a *past* A.

those of yield and of fracture. As an example of the first distinction, Fig. 1 displays two curves that show, at least in a qualitative way, similar strain-hardening behavior, but widely different yield stresses. If curve *a* represents, say, pure iron at room temperature, curve *b* may correspond to pure iron at a low temperature (where the lattice friction stress is considerably higher); alternatively, curve *b* could describe, at room temperature, a test on iron with some alloying element that affects the friction stress but not the dislocation accumulation mechanism. Any empirical description that attempts to cover a wide range of conditions or materials should not attempt to describe yield and strain-hardening as if they were part of the same process. We shall see subsequently that the most common strain-hardening relation, a simple power law [*1*], suffers from this drawback; the three-parameter relations of Ludwik [*2*] and Swift [*3*], as well as the "Voce law" [*4*], do not.[2]

When a stress strain test is interrupted by mere unloading and reloading (such as at point *A* on curve *a*), the new "yield stress" equals the previously reached flow stress. In practical applications, most materials are predeformed in some way; thus their (apparent) yield stresses may differ even when the materials are identical in a metallurgical (macrostructural) sense, and the test conditions (temperature, strain rate, etc.) are the same. The number of different "material parameters" to be tabulated is unnecessarily large if identical materials are described by different strain-hardening laws when only their mechanical histories are different. Of the aforementioned relations, only the Swift and Voce laws permit introduction of a "mechanical state" parameter in the form of the initial flow stress.

"Strain-rate hardening" is a rather loose term describing the dependence of stress-strain behavior on strain rate. Figure 2 summarizes the salient features. The effect tends to be small in the yield region, and larger at large

---

[2] The italic numbers in brackets refer to the list of references appended to this paper.

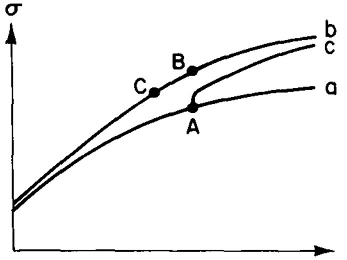

FIG. 2—*Two typical stress strain curves at widely different strain rates. The flow stress difference is often negligible at small strains, but always greater when the strain-hardening rate is low. A change at point* A *from the* a *strain rate to the* b *strain rate typically gives curve* c: *it does not continue from point* B, *but more nearly corresponds to a horizontal shift of curve* b *from point* C *on; thus the stress difference between points* A *and* C *is taken as the "instantaneous" stress change.*

strains [*5,6*]. Thus, at a given strain, not only the flow stress but also the strain-hardening rate may be strain-rate sensitive; this is generally the more true the smaller the strain-hardening rate (that is, at large strains or high temperatures) [*7*]. For this reason, it is important when plastic instabilities are considered [*8,9*]. This effect can be easily incorporated into the Voce law, but not the others [*6*].

Figure 2 also demonstrates another important aspect of material behavior: when the strain rate is abruptly changed during a test (point *A*), the flow stress does not follow the same curve as if the same amount of prestrain had been imposed at the new strain rate (namely from point *B* on). Therefore any description of mechanical behavior in terms of stress, strain rate, and *strain* is generally path dependent: a "mechanical equation of state" in this sense—that is, in terms of these parameters—does not exist [*10*]. All the conventional strain-hardening laws can therefore be applicable only to a restricted set of conditions, such as constant strain rate, or true rate independence. (A similar path dependence exists with respect to changes in direction or tensor character of the strain increment.)

Considerable effort has recently been devoted to answering the question whether a mechanical equation of state does exist in some other space; in other words, whether a suitable parameter can be found in place of the strain, which describes the state of the material. The search is sometimes successful and sometimes not. When it is, this means that corresponding states can be found on the stress-strain curves for specimens that have undergone different histories; for example, a point *C somewhere* on curve *b* in Fig. 2 that corresponds to point *A* on curve *a*. When this is not true, more than one parameter is necessary to characterize the state.

In any case, this approach requires that the *strain* dependence be described *differentially*, as a rate of evolution of the state parameter(s) with strain. It is for this reason that we proffer the use of *differential* constitutive relations in the second half of this paper.

Conventional Treatments

As pointed out in the introduction, any empirical laws that employ the strain as a state parameter can, in principle, be useful only under a restricted set of conditions. (The same is true, in creep tests, with respect to using time in any way other than differentially [*11*].) Nevertheless, such relations have proven sufficiently useful in practice to be actually used almost exclusively. It is the purpose of this section to emphasize the various inadequacies of the most common conventional treatments. In the next section, we will show that *differential* constitutive relations are in fact no harder to handle and significantly more general.

Strain Hardening

The most common empirical description of strain hardening is a simple power law [*1*]:

$$\sigma = K\epsilon^n \tag{1}$$

where the "strain-hardening exponent" n varies between about 1 and 0.1, and is typically about 1/4. Equation 1 is frequently used because it provides a simple measure of "uniform elongation"; that is, the strain to the ultimate tensile strength (UTS) according to the Considère criterion [*1*]:

$$\epsilon_{\mathrm{UTS}} = n \tag{2}$$

for n and K constant. For n between about 1/2 and 1/6, this also means

$$\sigma_{\mathrm{UTS}} = Kn^n \simeq 0.7K \tag{3}$$

Thus the "strength coefficient" K is actually a good measure of the UTS.

Figure 3 shows, on a linear plot, some hypothetical stress-strain curves that actually obey Eq 1. They are plotted only to the values of true stress and true strain that correspond to the UTS. At the lower limit, strains below 1 percent are omitted. It is evident that the value of n primarily describes the ratio of yield stress to UTS. Taking, as an example, the stress at 1 percent strain as a measure of yield, we find from Eqs 1 and 3:

$$\frac{\sigma_{1\%}}{\sigma_{\mathrm{UTS}}} \simeq \frac{10^{-2n}}{0.7} \tag{4}$$

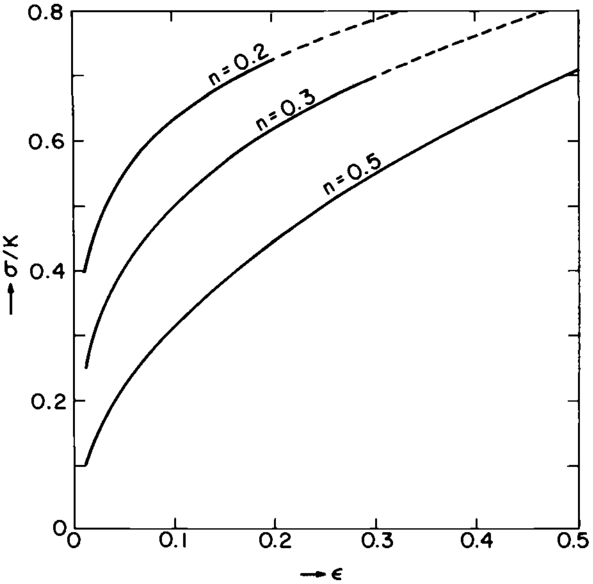

FIG. 3—*Power-law strain hardening plotted on a linear diagram of true stress versus true strain. The curves are dotted past the UTS. In the range of typical values of the exponent* n, *the strength coefficient* K *is a measure of the UTS, and 1/*n *is a measure of the yield stress.*

While this ratio may be a good qualitative indication of the overall severity of strain hardening, *n* primarily reflects the influence of the *yield stress*, once *K* has been set according to Eq 3 [*1*]; thus the identification of *n* as a "strain-hardening" parameter is misleading.

Figure 4 displays a stress-strain diagram on a double-log plot. Two limits are indicated that should be obeyed by realistic materials: at strain zero (negative infinity on the logarithmic plot), the stress should be finite: the yield stress is not zero; and again at infinite strain, the stress should be finite: infinite strengthening cannot be achieved. Clearly, a curve that proceeds from the lower to the upper limit has a sigmoidal character, and therefore a fairly extended range, near the inflection point, where a linear relation is a good approximation. This is the prime reason for the success of Eq 1 [*12*]. It also demonstrates that in any attempt to describe strain hardening over a wider range of strains, the values of *n* and *K* would have to vary; they tend to be smaller than the best fit at both small and large strains [*13*].

If test *a* were interrupted at point *A* and then restarted, the second test would be equivalent to testing a cold-worked material. Since it has a higher yield stress, curve *b* would now be followed; it will have a lower value of *n* (and possibly of *K*). This is confusing since obviously the strain-hardening behavior has not changed.

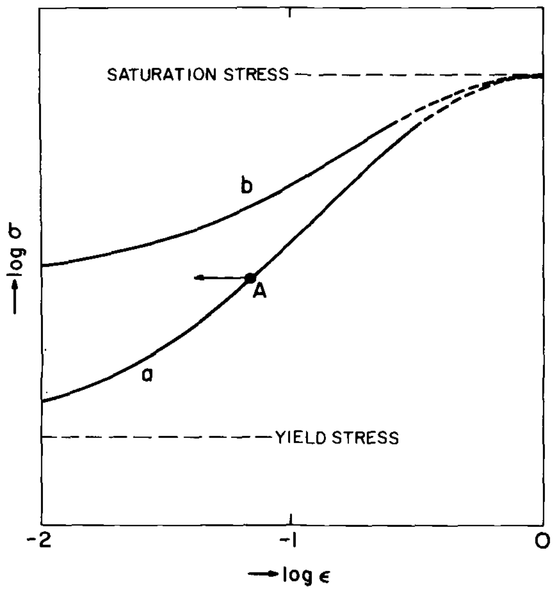

FIG. 4—*Stress-strain behavior of a typical material (actually that shown in Fig. 7), plotted double-logarithmically. The simple power law would plot as a straight line and could not explain the behavior near yield or saturation (curve* a*). Interruption at point* A *and redefinition of the strain as starting from zero in the new test gives a considerably different curve* (b).

A modification of the power law (Eq 1) that was actually introduced first [*2*], adds a yield stress:

$$\sigma = \sigma_Y + K\,\epsilon^n \qquad (5)$$

While this relation has one parameter more than Eq 1, this parameter does describe a physically distinct process, namely yielding. Figure 5 shows the appropriate plot for this relation. The advantage gained is seen at the low-strain end; n no longer depends on strain here. [Note, however, that the simple equality (Eq 2) has been lost.]

A test interruption (point A on curve a) is still not well described: if σ_Y (the yield stress of the *annealed* material) is still being subtracted from the applied stress, the new test follows curve b (with changed n and K); if, on the other hand, the previously attained flow stress σ_1 is used as the new yield stress, it follows curve c.

Another modification of the power law was proposed by Swift [*3*]; instead of an additive stress constant, an additive strain constant was used:

$$\sigma = K\cdot(\epsilon + \epsilon_0)^n \qquad (6)$$

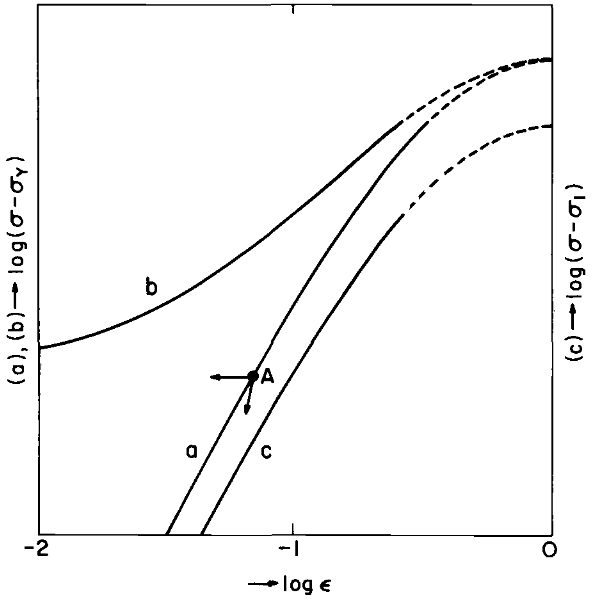

FIG. 5—*A power law with an additive yield stress (Ludwik) gives a better description at low strains (though not at high). An interruption at point* A *still gives a different curve:* b *if the yield stress is not reset,* c *if it is.*

For an annealed material, the function of ϵ_0 is precisely equivalent to a yield stress; it is only expressed in a somewhat clumsy form. For a prestrained material, however, ϵ_0 allows one to measure the strain ϵ in the new test from zero at its beginning. The effect of the prehistory is contained in ϵ_0, by way of the measurable initial flow stress $K\epsilon_0{}^n$. The parameters K and n do not depend on the mechanical history; this is the advantage of Eq 6 over Eq 5. Figure 6 demonstrates that there is a single curve for a single material, and there is no *a priori* reason for it to be curved at small strains; on the other hand, it still does not describe saturation.

When the yield stress of the annealed material is a substantial fraction of the total flow stress and depends on temperature and strain rate in a different way, its specification in terms of $K\epsilon_0{}^n$ is confusing; it would be better to add an independent yield stress to Eq 6 as a fourth parameter [*14*]:

$$\sigma = \sigma_Y + K \cdot (\epsilon + \epsilon_0)^n \tag{7}$$

This is the only power law that can describe all the important effects. Its disadvantage is that both K and n generally depend on stress, strain rate (and temperature); this is because it is not a physically based law.

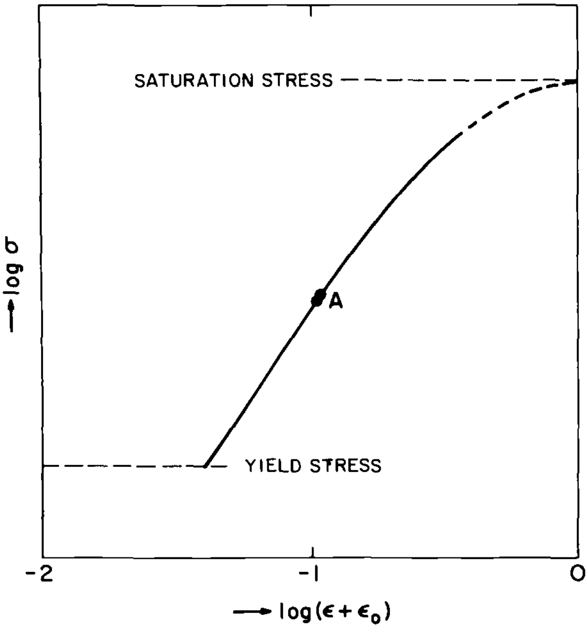

FIG. 6—*The Swift law* $\sigma = K \cdot (\epsilon + \epsilon_0)^n$ *allows* K *and* n *to be independent of mechanical history. The initial flow stress (at yield or after an interruption at* A*) is described by* $K\epsilon_0{}^n$. *A description of large-strain behavior requires decreasing values of the parameters.*

Finally, there is one empirical strain-hardening law that was especially designed to describe large strains, in the form of an exponential approach to a saturation stress σ_s, with a strain constant ϵ_c [*4*]:

$$\sigma = \sigma_1 + (\sigma_s - \sigma_1) \cdot \left[1 - \exp\left(-\frac{\epsilon - \epsilon_1}{\epsilon_c}\right)\right] \tag{8}$$

Here, σ_1 and ϵ_1 are the stress and strain at the beginning of the current test (Fig. 7). Since the latter is arbitrary and generally set to zero (as it was in all the previous relations above), the law still contains only three parameters, of which only one depends on mechanical history. In this sense it is equivalent to Eq 6. Equation 8 is a slightly more cumbersome expression, which may account for the fact that it is not frequently used. We will find subsequently that in the differential form, which is preferable on general grounds, the Voce law is in fact the simplest. Its principal merits derive, however, from a better fit over a greater stress range, and a more realistic possibility to incorporate rate effects.

For completeness, we note that there is a simple relation between the UTS and the saturation stress:

$$\frac{\sigma_{\mathrm{UTS}}}{\sigma_s} = \frac{1}{1 + \epsilon_c} \tag{9}$$

There is no simple relation for the uniform elongation, as indeed there should not be when arbitrary starting stresses σ_1 are considered.

'Strain-Rate Hardening'

The dependence of the stress-strain curve on strain rate was shown in a qualitative way in Fig. 2. A particular feature of the curves shown there, which is a realistic representation of the behavior of many materials, is that the strain-hardening rate Θ (the slope in a linear stress strain plot) is independent of strain rate for small strains [7]. In fact, it is quite insensitive to material and temperature also. In pure and solution-strengthened metals, it is even independent of stress and approximately

$$\Theta_0 \simeq E/50 \tag{10}$$

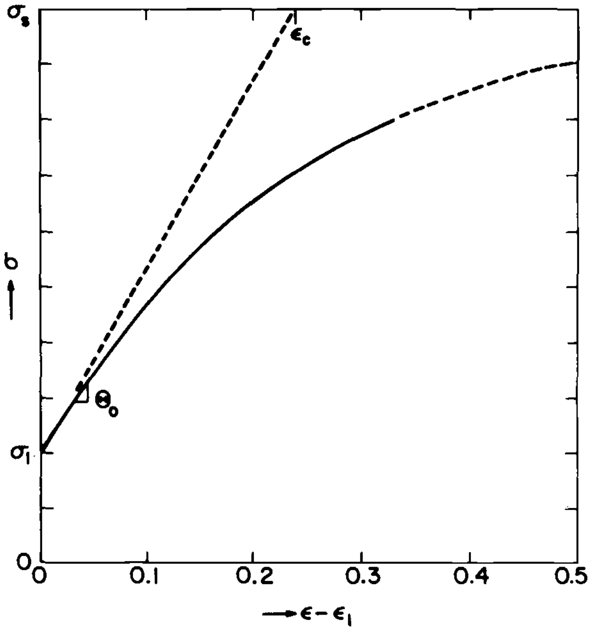

FIG. 7—*The Voce law, using a finite yield or pre-stress σ_1. The strain ϵ_1 at the beginning of the test is normally called zero. The flow stress would saturate at σ_s if other mechanisms did not intervene. The initial strain-hardening rate Θ_0 is generally independent of strain rate (and temperature).*

where E is Young's modulus. This particular value follows, for polycrystals of face-centered-cubic (fcc) lattice structure [*15*] (and typical values of Poisson's ratio) from the well-known value $\mu/200$ (μ = shear modulus) for Stage II strain hardening in single crystals, which can be explained on a physical basis in a number of ways [*16*]. (In dispersion-hardened metals, the initial strain-hardening rate is still athermal, but more nearly proportional to $1/\sigma$ [*17*].

A constant value of Θ_0 can be easily incorporated into the Voce law (Eq 8). Differentiation at $\epsilon = \epsilon_1$ and $\sigma_1 = \sigma_Y$ shows that

$$\epsilon_c = \frac{\sigma_s - \sigma_Y}{\Theta_0} \tag{11}$$

Thus, replacing ϵ_c according to Eq 11 brings in physically meaningful parameters, and does not introduce new variable parameters.

With these definitions, the Voce law can now be written in the final form:

$$\epsilon - \epsilon_1 = \frac{\sigma_s - \sigma_Y}{\Theta_0} \cdot \ln \frac{\sigma_s - \sigma_1}{\sigma_s - \sigma} \tag{12}$$

where we have treated the strain increment as the dependent variable. The three parameters other than Θ_0 all refer to single, not compound, mechanistic effects: the yield stress, σ_Y; the state parameter σ_1 that characterizes predeformation; and only one parameter, σ_s, that truly characterizes strain hardening, including its dependence on strain rate (and temperature). For these reasons, Eq 12 would be preferable over the extended power law (Eq 7), even if it did not actually fit the stress strain data better.

Inasmuch as σ_s characterizes the saturation limit, it is equivalent to steady-state creep [*6*]. This is often well described by a power-law stress versus strain-rate relation [*17a*]:

$$\sigma_s = \sigma_{s0} \left(\frac{\dot{\epsilon}}{\dot{\epsilon}_{0_s}} \right)^N \tag{13}$$

where two constants σ_{s0} and $\dot{\epsilon}_{0_s}$ have been introduced for dimensional reasons. The exponent N depends on temperature (being roughly proportional to it [*6*]). At elevated temperatures, its magnitude is usually of order 0.2; at lower temperatures, it becomes less than 0.1.

In addition to this rate sensitivity, there is one that refers to the dependence of the flow stress on strain-rate *at constant state*. It describes both the rate sensitivity of the yield stress and the stress jump upon an abrupt rate change after some strain (Fig. 2). Since it is a consequence of thermal activation, it is best described by an Arrhenius equation [*18*]. For phenomenological applications, it is, however, often convenient and adequate to express it, too, by a power relation:

$$\sigma = \sigma_0 \left(\frac{\dot{\epsilon}}{\dot{\epsilon}_0} \right)^M \tag{14}$$

This equation holds also for σ_Y and σ_1. The parameters σ_0 and $\dot{\epsilon}_0$ are any pair of values, for example, at a standard strain rate [*18,19*].

The exponent M is usually much smaller than N: less than 0.01 for two-phase alloys and pure fcc materials; less than about 0.03 for solution hardened and body-centered-cubic (bcc) materials. It is seen that this difference between the magnitudes of M and N describes the common divergence of stress-strain curves taken at different strain rates (or temperatures), as well as (in a qualitative way at least) the transient behavior in curve *c* of Fig. 2 [*20*].

Equation 12, with Eqs 10, 13, and 14, represent, in our opinion, the best empirical expressions for strain hardening and the rate effects on both flow stress and strain hardening—so long as one wishes to use relations involving the strain in integrated rather than differential form. Changes in path can be described by assuming the flow stress (rather than the strain) to be a state parameter. Then, a strain-rate change leads to an instantaneous flow stress change (such as at point A in Fig. 2), and the continuation curve is identical to that starting from the same *flow stress* at the new strain rate (point C). In other words, the zero of strain is reset. This procedure still assumes the existence of a mechanical equation of state, though the state is no longer described by the strain [*9*].

The more common descriptions of "strain-rate hardening" by a modification of any of the various power laws for strain hardening add further disadvantages to these power laws that have already been found seriously wanting. The simple power law (Eq 1) becomes [*21*]:

$$\sigma = K_0\, \epsilon^n\, \dot{\epsilon}^m \tag{15}$$

where the "strain-rate hardening exponent" m specifies the rate sensitivity of the flow stress at $\epsilon = 1$ (or at *any* fixed strain if n is *strictly* rate independent). No distinction is made between this and the other rate sensitivities discussed above.

Incorporating prestrain effects by means of the Swift law (Eq 6) gives [*22*]:

$$\sigma = K_0\, (\epsilon + \epsilon_0)^n\, \dot{\epsilon}^m \tag{16}$$

In both laws an instantaneous stress jump would be as from A to B in Fig. 2, not as actually shown and realistic.

In some materials, especially at low temperatures, the yield stress is considerably *more* rate dependent than the strain-hardening contribution to the flow stress. In such cases, one might want to use a law of the form of Eq 5 with a rate-dependent yield stress (or "overstress") σ_Y [*23*]—but one is then bound to the disadvantage of this relation concerning prestrained materials. Alternatively [*14*], one would have to add an extra term to the Swift law, as in Eq 7; then, one again has four parameters—but none of them is constant, and one has yet to describe any rate sensitivity of strain hardening.

In conclusion, the Voce law as modified for describing strain-rate dependence (Eqs 12 through 14) is the most realistic integral relation, with physically well separable parameters. It also allows for an easy incorporation of temperature effects, namely coupled with the rate effects [*6,18*].

Current Material Properties

Any material description that is to be applied to a variety of strain paths must be written in differential form and can then be integrated over any specific path. It can contain only parameters that are functions of the current mechanical state of the system (which the strain is not). Such a differential description may have been too impractical in the past. At this time, however, computer analysis of test data and computer predictions of specimen behavior would appear to be the rule rather than the exception. Thus there is no longer any reason for "simplifications" that are not physically realistic or phenomenologically sound. The advantage to be gained is twofold: fewer data need be tabulated, and extrapolations beyond the measured range can be undertaken with greater confidence.

We shall first define the relevant material properties in derivative form: namely the strain-hardening rate and the two strain-rate sensitivities, and discuss their dependence on stress and strain rate. Then we shall combine them into a single, differential constitutive relation and illustrate applications to path changes.

Strain-Hardening Rate

The most direct, as well as the physically most meaningful way of describing strain hardening is by the slope in a linear stress strain diagram, for a test run at constant strain rate:[3]

$$\Theta \equiv \left.\frac{\partial \sigma}{\partial \epsilon}\right|_{\dot{\epsilon}} = \Theta(\sigma,\dot{\epsilon}) \qquad (17)$$

---

[3] The consequences of a difference between prescribed extension rate and true strain rate have been amply discussed [*24*].

The stress and the strain rate, on which Θ is assumed to depend, are not to be understood as variables that can be independently prescribed. In the above test, $\dot{\epsilon}$ was prescribed. The parameter σ is initially the *flow* stress at which plasticity begins (suitably back-extrapolated [*19,20*]), and is thus a response of the specimen; it is a measure of the mechanical state of the material. During the subsequent continuous test, the flow stress and the measured stress remain the same, and the dependence of Θ on σ essentially describes the variation with prestrain.

Figure 8 shows a plot of the strain-hardening rate Θ versus the flow stress σ, for two strain rates. The following features are meant to be typical. First, Θ frequently has a constant initial value (Eq 10) and decreases from there; thus one may write instead of Eq 17:

$$\Theta = \Theta_0 - \Theta_r(\sigma,\dot{\epsilon}) \tag{18}$$

where Θ_r is called the dynamic-recovery rate, a fertile subject for physical theories [*25*]. Second, the simplest assumption that can possibly be made about the decrease of Θ with stress, namely that it is linear, is often a good first approximation [*6*]:

$$\Theta \propto \left(1 - \frac{\sigma}{\sigma_s(\dot{\epsilon})}\right) \tag{19}$$

If the constant Θ_0 is to characterize the initial hardening rate, at the yield stress as in Eq 12, we have

$$\Theta = \Theta_0 \cdot \left(1 - \frac{\sigma - \sigma_Y}{\sigma_s - \sigma_Y}\right) \tag{20}$$

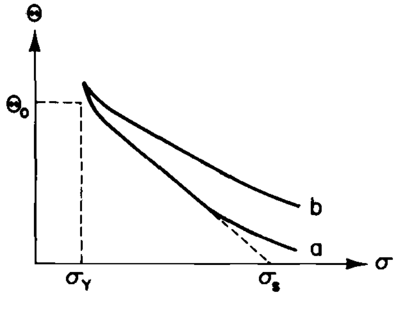

FIG. 8—*The strain-hardening rate Θ as a function of the (pre)stress σ, for different constant strain rates (curves* a *and* b*). The parameters Θ_0 and σ_s are defined as extrapolations to $\sigma = \sigma_Y$ and $\Theta = 0$, respectively.*

The meaning of the "saturation stress" σ_s, especially when the dependence is not exactly linear, as shown in Fig. 8, is only that of an extrapolation from an extended range of interest into a range that is usually not reached, or in which other mechanisms have begun to operate [*26*]. Alternatively, one may just look at $\Theta_0/(\sigma_s - \sigma_Y)$ (that is, the reciprocal of the strain constant ϵ_c in Eq 11) as the slope in diagrams of the kind shown in Fig. 8.

The two curves plotted in Fig. 8 were meant to represent two separate tests on annealed specimens, each taken at a constant but different strain rate. If Eq 17 is to be a unique (that is, history independent) function of stress and strain rate, then any changes in strain rate during a test must move the current locus from one curve to another (the ratio of flow stresses being given by an equation like Eq 14). This test of the existence of a mechanical equation of state should, in a complete investigation, be undertaken. It is known [*7*] to fail under conditions when the strain-hardening rate is low; in this case, a transient appears and the value of the test is to identify the length and effect of the transient [*20*].

The measurement of the material property Θ was undertaken in a test in which the strain is also measured. Once $\Theta(\dot{\epsilon},\sigma)$ has been tabulated for a particular material, one can *predict* the strain that will be accumulated in a subsequent test at a strain rate $\dot{\epsilon}_1$ by integrating Eq 17:

$$\epsilon - \epsilon_1 = \int_{\sigma_1}^{\sigma} \frac{d\sigma}{\Theta(\dot{\epsilon}_1,\sigma)} \tag{21}$$

It is easily seen that the (modified) Voce law (Eq 12) follows from this integration when Eq 20 is inserted for the strain-hardening rate.

Rate Sensitivities

One rate sensitivity, as has been pointed out repeatedly above, is that of the strain-hardening rate. In our specific description, this enters through the rate sensitivity of the saturation stress (Eq 13). Indeed, it must do so in a very general sense, since saturation and steady-state creep are *defined* by a property of *strain hardening*, namely its vanishing. Differentially one may define a general parameter [*8,9*]:

$$N \equiv \left.\frac{\partial \ln \sigma}{\partial \ln \dot{\epsilon}}\right|_{\Theta} \tag{22}$$

so that the N used in Eq 13 was in fact a special value of this rate sensitivity, namely for $\Theta = 0$. Another particular value of interest is that at the UTS which, as we saw above, is approximately the actual meaning of the "strain-rate hardening exponent" m (Eq 15), as it is usually used:

$$N_{\mathrm{UTS}} \equiv \left.\frac{\partial \ln \sigma}{\partial \ln \dot{\epsilon}}\right|_{\Theta = \sigma} \simeq m \tag{23}$$

Besides these measures of the rate sensitivity of *strain hardening*, there is the rate sensitivity of the *flow stress at constant state*. It can be defined either on a relative or an absolute stress change basis:

$$M \equiv \left.\frac{\partial \ln \sigma}{\partial \ln \dot{\epsilon}}\right|_{\text{state}} \tag{24}$$

which is a differential definition of the exponent in Eq 14; or

$$\beta \equiv \left.\frac{\partial \sigma}{\partial \ln \dot{\epsilon}}\right|_{\text{state}} \tag{25}$$

The latter definition has a significant advantage: under many conditions, β is a linear function of stress (in the sense of the flow stress attained during prestraining):

$$\beta = \beta_Y + M_D \cdot (\sigma - \sigma_Y) \tag{26}$$

with approximately constant coefficients [*18*]: β_Y, (the rate sensitivity of the yield stress) and M_D (the relative rate sensitivity of the flow stress contribution owing to strain hardening).

Figure 9 shows typical behavior for solution-hardened alloys at two strain rates [*27*]. At very low strain rates, especially when the temperature is high, there are significant deviations from linearity, which have been associated with dynamic-recovery processes [*7*]. The strain-rate dependence of β (or equivalently the stress dependence *at constant structure*) is what is measured, under certain circumstances, in a stress-relaxation test.

Differential Constitutive Relations

We have seen that, knowing the functional dependence of the strain-hardening rate on stress and strain rate, we can derive the strain to be accumulated in a subsequent constant-strain-rate test by integration (Eq 21). Having now also defined the strain-rate sensitivity as a function of stress and strain rate, we can obtain the strain to be accumulated along an *arbitrary* future strain-rate path, by integrating an equation of the form:

$$d\epsilon = \frac{1}{\Theta}(d\sigma - \beta\, d \ln \dot{\epsilon}) \tag{27}$$

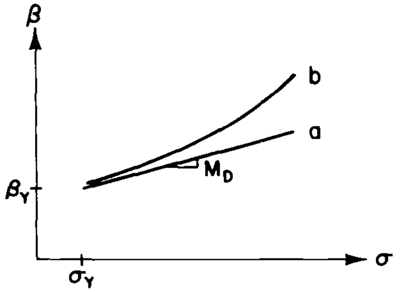

FIG. 9—*The rate sensitivity* $\beta \equiv (\partial\sigma/\partial \ln \dot{\epsilon})_{state}$, *as a function of the (pre)stress* σ, *for two widely different base strain rates. For high strain rates (and/or low temperatures), the relation is linear: both* β_Y *and* M_D *are constant (curve* a*).*

This is a general differential constitutive relation for strain-hardening and strain-rate effects, as it was first proposed by Hart [*28, 9*].[4]

Equation 27 degenerates into the definition (Eq 17) of the strain-hardening rate for $d \ln \dot{\epsilon} = 0$, and to that of the instantaneous rate sensitivity for $d\epsilon = 0$. Note that the latter implies "constant state", and is not to be used in a comparison between two specimens (or two volume elements of the same specimen, as in necking [*8, 9*]) in which the total strain has been the same, regardless of the path along which it was accumulated.

The use of Eq 27 is, however, different; the material properties $\Theta(\dot{\epsilon}, \sigma)$ and $\beta(\dot{\epsilon}, \sigma)$ are assumed known, and the strain accumulation in a future test is to be predicted. As an example, we will give the result for two successive tests: the first at a strain rate $\dot{\epsilon}_1$ to a flow stress $\sigma_1{}^A$, the second at a strain rate $\dot{\epsilon}_2$, which produces an initial flow stress $\sigma_2{}^A$ given by

$$\sigma_2{}^A - \sigma_1{}^A = \beta \cdot \ln(\dot{\epsilon}_2/\dot{\epsilon}_1) \tag{28}$$

(where the strain-rate change was assumed to be small). The total strain to a final flow stress $\sigma_2{}^B$ is

$$\epsilon^B = \int_{\sigma_Y}^{\sigma_1{}^A} \frac{d\sigma}{\Theta(\dot{\epsilon}_1, \sigma)} + \int_{\sigma_2{}^A}^{\sigma_2{}^B} \frac{d\sigma}{\Theta(\dot{\epsilon}_2, \sigma)} \tag{29}$$

When Eq 20 is valid, it can be easily derived that two terms of the modified Voce form (Eq 12) follow:

$$\epsilon^B = \frac{\sigma_s - \sigma_Y}{\Theta_0} \cdot \left[\ln \frac{\sigma_s - \sigma_Y}{\sigma_s - \sigma_1{}^A} + \ln \frac{\sigma_s - \sigma_2{}^A}{\sigma_s - \sigma_2{}^B} \right] \tag{30}$$

---

[4] An equivalent form, using a *logarithmic* derivative of the stress, has the disadvantage that there are no simple superposition laws for the coefficients $(\partial \ln \sigma/\partial\epsilon)_{\dot{\epsilon}}$ and M, as there were for Θ and β (Eqs 18 and 26). Relations that employ a logarithmic differential of the *strain* are not allowed, since they again correspond to using the integrated strain.

Finally, Eq 27 allows application to paths other than at constant strain rate; for example, at constant stress. This describes the deceleration in primary creep:

$$-\left.\frac{\partial \ln \dot{\epsilon}}{\partial \epsilon}\right|_{\sigma} = \frac{\Theta}{\beta} \tag{31}$$

Obviously, mixed paths in stress/strain-rate space can be integrated over in this way. (Equation 31 also provides a way of measuring β without abrupt changes.) It is a significant advantage of the state evolution description used here that creep tests and stress-strain tests are treated with the same formalism.

Summary

Both integrated and differential forms of constitutive relations for strain hardening and "strain-rate hardening" were reviewed. The considerable advantage to be gained from differential forms is that they use *current* material properties and can be integrated over arbitrary paths. This will allow a much broader range of predictions to be made on a relatively small data base.

The data needed, apart from the yield stress of the annealed material, are the strain-hardening rate and the strain-rate sensitivity, both as a function of (pre)stress and strain rate (as well as temperature).

The simplest form of a differential strain-hardening law, namely a linear stress dependence, is often a sufficiently close approximation to reality. Its integration leads to the Voce relation, which has been known to fit strain-hardening data over a wider range than power laws. Its chief advantages, however, become evident when its dependence on predeformation and on strain rate are considered: they enter as single, separate parameters.

Finally, when a power law is used despite all the quoted drawbacks, the Swift law, using an additive strain constant, is the only one that allows application to prestrained materials without a change in the "strain-hardening exponent".

In this discussion the existence of a mechanical equation of state, albeit not using strain as a state parameter, has been assumed. Only then are the strain-hardening rate and the strain-rate sensitivity unique (that is, history independent) functions of stress and strain rate. This is an acceptable assumption for unidirectional deformation, if certain transients are ignored. Otherwise, the differential description is still valid (in fact, even more necessary), but additional state parameters must be introduced, and their evolution described [*29*].

Acknowledgments

This work was supported by the U.S. Department of Energy.

References

[1] Hollomon, J. H., *Transactions of the American Institute of Mining, Metallurgical, and Petroleum Engineers,* Vol. 162, 1945, pp. 268-290.

[2] Ludwik, P., *Elemente der Technologischen Mechanik,* Springer, 1909.

[3] Swift, H. W., *Journal of the Mechanics and Physics of Solids,* Vol. 1, 1952, pp. 1-18.

[4] Voce, E., *Journal of the Institute of Metals,* Vol. 74, 1947/8, pp. 537-562.

[5] Kocks, U. F., Chen, H. S., Rigney, D. A., and Schaefer, R. J. in *Work Hardening,* J. P. Hirth and J. Weertman, Eds., Gordon and Breach, 1968, pp. 151-175.

[6] Kocks, U. F., *Journal of Engineering Materials and Technology,* ASME, Series H, Vol. 98, 1976, pp. 76-85.

[7] Mecking, H. and Kocks, U. F., *Acta Metallurgica,* Vol. 29, 1981, pp. 1865-1875.

[8] Kocks, U. F., Jonas, J. J., and Mecking, H., *Acta Metallurgica,* Vol. 27, 1979, pp. 1705-1716.

[9] Kocks, U. F., *Progress in Materials Science, Chalmers Anniversary Volume,* 1981, pp. 185-241.

[10] Tietz, T. E. and Dorn, J. E. in *Cold Working of Metals,* American Society of Metals, Cleveland, 1949, pp. 163-179.

[11] McCartney, L. N., *Philosophical Magazine,* Vol. 33, 1976, pp. 689-695.

[12] Mecking, H. in *Strength of Metals and Alloys,* P. Haasen, V. Gerold, and G. Kostorz, Eds., Pergamon Press, Oxford, 1980, pp. 1573-1594.

[13] Crussard, C. and Jaoul, B. *Revue de Métallurgie,* Vol. 47, 1950, pp. 589-600.

[14] Ghosh, A. K. in *Mechanics of Sheet Metal Forming,* D. P. Koistinen and N-M. Wang, Eds., Plenum Press, New York, 1978, pp. 287-312.

[15] Kocks, U. F., *Metallurgical Transactions,* Vol. 1, 1970, pp. 1121-1143.

[16] Kocks, U. F., *Philosophical Magazine,* Vol. 13, 1966, pp. 541-566.

[17] Ashby, M. F. in *Physics of Strength and Plasticity,* A. S. Argon, Ed., MIT Press, Cambridge, Mass., 1969, pp. 113-131.

[17a] Bird, J. E., Mukherjee, A. K., and Dorn, J. E. in *Quantitative Relation Between Properties and Microstructure,* D. G. Brandon and A. Rosen, Eds., Israel University Press, 1969, pp. 255-342.

[18] Kocks, U. F., Argon, A. S., and Ashby, M. F., *Progress in Materials Science,* Vol. 19, 1975.

[19] Kocks, U. F. in *Constitutive Equations in Plasticity,* A. S. Argon, Ed., MIT Press, Cambridge, Mass., 1975, pp. 81-115.

[20] Kocks, U. F. and Mecking, H. in *Dislocation Modelling of Physical Processes,* M. F. Ashby, R. Bullough, C. S. Hartley, and J. P. Hirth, Eds., Pergamon Press, Oxford, 1980, pp. 173-192.

[21] Hollomon, J. H., *Metals Technology,* American Institute of Mining, Metallurgical, and Petroleum Engineers, Vol. 13, No. 6, Sept. 1946, T. P. 2034.

[22] Marciniak, Z., Kuczynski, K., and Pokora, T., *International Journal of Mechanical Science,* Vol. 15, 1973, pp. 789-805.

[23] Ghosh, A. K., *Metallurgical Transactions,* Vol. 8A, 1977, pp. 1221-1232.

[24] Hart, E. W., *Acta Metallurgica,* Vol. 15, 1967, pp. 351-355.

[25] Kocks, U. F. and Mecking, H. in *Strength of Metals and Alloys,* P. Haasen, V. Gerold, and G. Kostorz, Eds., Pergamon Press, Oxford, 1979, pp. 345-350.

[26] Mecking, H. and Grinberg, A. in *Strength of Metals and Alloys,* P. Haasen, V. Gerold, and G. Kostorz, Eds., Pergamon Press, Oxford, 1979, pp. 289-294.

[27] Mulford, R. A., *Acta Metallurgica,* Vol. 27, 1979, pp. 1115-1124.

[28] Hart, E. W., *Acta Metallurgica,* Vol. 18, 1970, pp. 599-610.

[29] Turner, A. P. L. and Hasegawa, T., in *Mechanical Testing for Deformation Model Development, ASTM STP 765,* R. W. Rohde and J. C. Swearengen, Eds., American Society for Testing and Materials, 1982, pp. 322-341.

R. D. Krieg[1]

A Unified Creep-Plasticity Model for Halite

REFERENCE: Krieg, R. D., "**A Unified Creep-Plasticity Model for Halite,**" *Mechanical Testing for Deformation Model Development, ASTM STP 765,* R. W. Rohde, and J. C. Swearengen, Eds., American Society for Testing and Materials, 1982, pp. 139–147.

ABSTRACT: Two national energy programs are considering caverns in geological salt (NaCl) as a storage repository. One is for the disposal of nuclear wastes and the other is for the storage of oil. Both short-time and long-time structural deformations and stresses must be predictable for these applications. At 300 K, the nominal initial temperature for both applications, the salt is at 0.28 of the melting temperature and exhibits a significant time-dependent behavior. A constitutive model has been developed that describes the behavior observed in an extensive set of triaxial creep tests. Analysis of these tests showed that a single deformation mechanism seems to be operative over the stress and temperature range of interest so that the secondary creep data can be represented by a power of the stress over the entire test range. This simple behavior allowed a new unified creep-plasticity model to be applied with some confidence. The resulting model recognizes no inherent difference between plastic and creep strains yet models the total inelastic strain reasonably well including primary and secondary creep and reverse loadings. A multiaxial formulation is applied with a back stress. A Bauschinger effect is exhibited as a consequence and is present regardless of the time scale over which the loading is applied. The model would be interpreted as kinematic hardening in the sense of classical plasticity. Comparisons are made between test data and model behavior.

KEY WORDS: creep, unified, constitutive, model, primary, secondary

Halite, the naturally occurring mineral form of sodium chloride (NaCl), is commonly found around the world. Halite is easily mined and has a moderate creep rate at stresses commonly found in conventional underground room and pillar mining operations. Although salt is mined for its own sake, it is also found in proximity to potash and is removed for ease in mining the potash. Halite has, in the past few years, received attention as a candidate material in which to store oil and to dispose of radioactive wastes. In

---

[1] Member, Technical Staff, Sandia National Laboratories, Albuquerque, N.M. 87185.

spite of the vast experience in mining salt, it has not been carefully characterized as a structural material until recently.

Various people have performed tests on pure sodium chloride, but tests on naturally occurring forms are fewer in number. Of particular interest here is rock salt from southeastern New Mexico. The rock salt has impurities that result in lower creep rates than for pure halite. Hansen and Mellegard [*1*] and Wawersik and Hannum [*2,3*] are the sources of data for this particular material.[2]

Herrmann, Lauson, and Wawersik [*4,5*] studied the creep behavior of the rock salt near room temperature and up to 200°C using the data from the aforementioned investigators. The present model is based on that work.

Presentation of Equations

It is a very noble thing to attempt to derive nonlinear constitutive models based on micromechanical mechanisms. This has met with some success in time independent plasticity [*6*] and metal creep formulations. A review of the theories of Hart, Lagneborg, A. Miller, Ponter and Leckie, Pasley and Wells, and others with advanced creep models was made by Krieg [*7*]. These models were all shown to have a common basic mathematical structure, differing only in the functional forms used. Lagneborg [*8*] reviewed more recent work on advanced creep models from the micromechanical point of view. The attempt here is not nearly so lofty; the objective is simply to describe externally measurable stress in terms of externally measurable strain. This has not been entirely successful in the past and, in fact, is accomplished here only by introducing an additional state variable, the back stress.

The formulation here is a special case of the skeletal model into which most of the hardening/recovery models fall. In terms of the categories of Krieg [*7*], the present model is a kinematic hardening model. The need for a kinematic model with a back stress is consistent with observations from stress drop tests on metals [*8*]. For brevity and ease of understanding, the model is simplified here to scalar form. The volumetric behavior in the model is approximated as linear elastic, although that approximation is not obvious in the form presented here. The model is motivated principally by the experimentally observed mechanical response and partly by micromechanical considerations.

The strain rate (actually the stretching tensor, *d*) is decomposed into elastic and inelastic parts and rearranged into the form

$$\overset{\nabla}{\sigma} = E(d - d^p) \tag{1}$$

---

[2] The italic numbers in brackets refer to the list of references appended to this paper.

where $\overset{\nabla}{\sigma}$ is the stress rate and E is the elastic Young's modulus. Expressions for the "strain rate" and the evolutionary equation for the back stress are given by

$$d^p = A \exp(q|\xi|)\xi \tag{2}$$

$$\overset{\nabla}{\alpha} = Bd^p \exp(-\zeta\alpha sgn\xi) - C|\alpha|\alpha \tag{3}$$

where

$$A = A_0 \exp(-Q_A/R\theta)$$

$$B = B_0 \exp(Q_A/R\theta)$$

$$C = C_0 \exp(-Q_C/R\theta)$$

$$\xi = \sigma - \alpha$$

$$sgn\xi = \begin{cases} +1, \xi \geq 0 \\ -1, \xi < 0 \end{cases}$$

and where q, ζ, A_0, B_0, and C_0 are simple material constants; Q_A, Q_B, and Q_C are activation energies, R is the universal gas constant, and θ is absolute temperature.

The variable α is the back stress. To a metallurgist it is related to a microstructural directionality as discussed below. It might also be blindly regarded as a tensor valued state variable. In the context of plasticity, if creep surfaces were defined as surfaces of constant creep rate magnitude analogous to yield surfaces, then α would be the location of the center of that concentric set of surfaces.[3] It is in this sense of moving surfaces that the model is identified as a kinematic model. The details of the hardening and recovery terms used in Eq 3 deserve some comment.

The model incorporates a fairly realistic strain-hardening behavior used in an earlier unified creep-plasticity model by Krieg [7]. The hardening term of Eq 3 is notable in that the rate of hardening depends not only on the inelastic strain rate, but also on the component of the back stress which is in the direction of the effective stress. The strain-hardening rate decreases as the back stress saturates. The back stress can be micromechanically related [9] to the mobile dislocation density ρ as

$$\alpha = aGb\rho^{0.5}$$

where b is Burgers's vector. The saturation of the back stress in the hardening term can be interpreted then as a saturation of the mobile dislocation

[3] The experimental determination of these creep surfaces would be difficult to establish with great precision for a fixed state, α, according to the model. If the stress state were located at some general point on what is thought to be a surface, then the state changes according to Eq 3 while the creep strain rate is measured.

density in the forward direction; "forward" meaning the same direction as the effective stress. The hardening rate is enhanced if the back stress is in the direction opposite to that of the effective stress. This behavior was modeled in Gittus's early work [*10*] by definition of a forward dislocation density and a reverse dislocation density, with "forward" and "reverse" directions being defined with respect to the effective stress. Separate evolutionary equations were then defined for the foreward and reverse mobile dislocation densities. The present model incorporates this directionality in the hardening term in a continuous manner. Without the recovery term in the evolutionary equation, and with a more Heaviside-like strain rate equation replacing Eq 2, the model mimics time-independent plasticity. It is instructive to note that the behavior of this model is very much like the two-surface plasticity model [*11*]. Each of these models has good plastic behavior at small strains and a realistic Bauschinger effect.

The final point worth noting is the recovery term in Eq 3. The $(\alpha_{rs})^2$ dependence in the model is a source of some embarrassment in light of the accepted cubic dependence of Lagneborg [*9*]. For the halite it was found that a cubic recovery term could not mimic the behavior noted in the creep tests. It is felt that since a deformation mechanism change seems evident in the primary creep results [*5*], and since the simplest mathematical form was needed which would cover the entire range, then the quadratic dependence is probably only an approximation. True recovery may be the sum of a cubic term and a term of low stress dependence, with the combined behavior having roughly a quadratic behavior over the range modeled here.

Data Fitting Process

Triaxial compressive creep tests were run on 0.05 and 0.10 m diameter jacketed rock salt samples at various lateral pressure levels and axial stress levels at two different facilities [*1-3*]. Careful statistical analysis of the data [*4*] showed that the observed effective creep strains were independent of sample size, pressure, and facility where the tests were conducted. The effective creep strain rate was found to depend only upon the stress difference ($\sigma_z - \sigma_r$), where σ_z is the axial stress and σ_r is the lateral stress. These stress and strain measures are used in all the figures.

Some two and three stage tests were run by imposing two or three stress levels sequentially, and waiting for steady creep before changing stress levels. The transient part of the first stage of these tests was used, but only the secondary creep part of the later stages.

Each of the creep tests was independently fit with an expression of the form

$$e = e_o + \dot{e}_s t + e_a\,[1 - \exp(-\lambda t)] \tag{4}$$

in order to remove irregularities in the data. Three variables derived from Eq 4 and the specific values of the parameters from each test were used to fit the unified creep-plasticity model. The secondary creep rate, $\dot{e}_s$, is one of them. The second variable is the time t_3 at which the creep rate is three times $\dot{e}_s$. The third variable is the ratio $\dot{e}/\dot{e}_s$ at the time 0.5 t_3. The time and strain rate ratio were found to give a good characterization of the primary creep behavior.

Values for A_{23}, B_{23}, C_{23}, q, and ζ in Eqs 1, 2, and 3 were chosen in a regular manner for the temperature 23°C and the parameters $\dot{e}_s$, t_3, and $(\dot{e}/\dot{e}_s)^*$ calculated from the model for creep stress levels corresponding to each test. The results of all the creep tests at that fixed temperature were compared with the model predictions. Errors in the logarithms of $\dot{e}_s$ and t_3 were used with errors in the strain ratios to find a root mean square error. The steady-state creep error was given four times the weight of the other two parameters to reflect the relative confidence in the experimental data. The constants in the model were varied until a set was found which minimized the least-square error. The values found for the room temperature data were:

$\zeta = 0.310\ \text{MPa}^1$
$q = 0.203\ \text{MPa}^{-1}$
$A = 2.20\ \text{E-9}\ (\text{MPa}\cdot\text{s})^{-1}$
$B = 3.38\ \text{E4 MPa}$
$C = 7.12\ \text{E-9}\ (\text{MPa}\cdot\text{s})^{-1}$

The data and model response for secondary creep are compared in Fig. 1. The curvature of the secondary creep rate versus stress on the log-log plot of Fig. 1 shows that the model does not strictly follow a straight line characteristic of a power-law behavior. The data show roughly an order of magnitude scatter so that based on these data alone neither the model behavior nor a straight-line behavior could be said to have a better secondary creep representation.

The data at 100°C were also fitted with the same creep model, but the exponential factors were fixed at the values found from reduction of the 23°C data. This is in accordance with the assumed temperature variation given in Eqs 1 to 3. The least-square error was again used to define A_{100}, B_{100}, and C_{100} for these data. These two sets of (A, B, C) were used to find $Q_A = 8320$ cal/mol, $Q_B = 7600$ cal/mol, and $Q_C = 5110$ cal/mK for the activation energies. Note in particular that the signs of the exponentials for A, B, and C are chosen so as to increase inelastic strainrate (through A), decrease the rate of hardening (through B), and increase the recovery (through C) as the temperature is raised.

Behavior of the Model

At this point it can be said that the model mimics the primary and secondary creep behavior of southeastern New Mexico halite over the stress and temperature range observed in the tests. This is all that is ordinarily expected

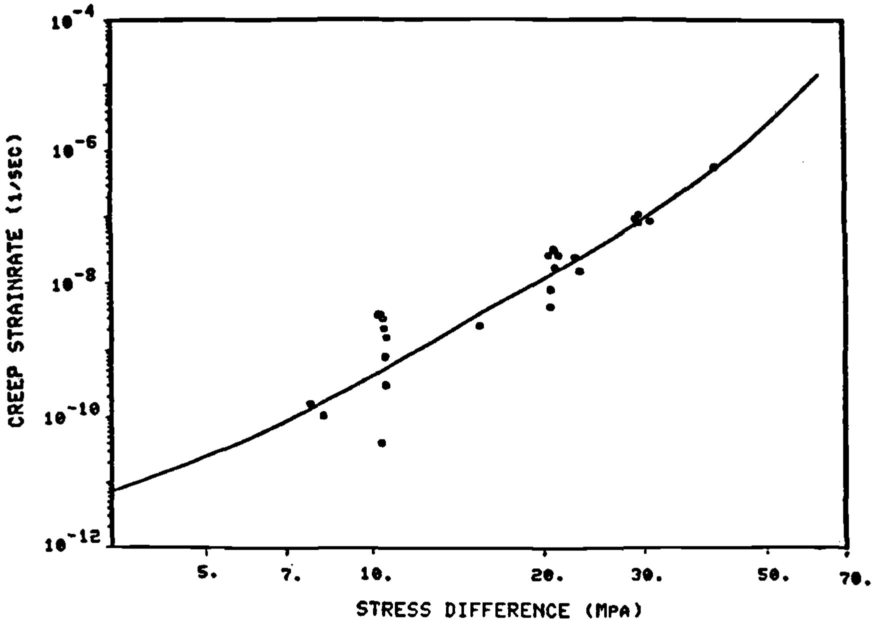

FIG. 1—*Secondary creep rate at room temperature fitted by the model and compared with experimental data.*

of a creep model for stress analyses. But if the formulation is correct, the behavior of the equations should be reasonable for any stress or strain history so long as new micromechanisms do not become dominant. Unfortunately, proof tests are difficult to interpret due to the statistical spread in data from creep-like tests, particularly on a naturally obtained mineral. At this point we will examine the qualitative behavior of the model to see that it follows the general behavior observed in tests.

The most definitive tests are the multistage creep tests which, as stated earlier, were discarded for use in data fitting for the unified creep-plasticity model. But for proof tests, the transient behavior of the second and third stages are very useful. Figure 2 is a typical strain versus time plot for one of these multistage tests as compared with the unified creep-plasticity model. The agreement is generally good, particularly in light of the scatter in the data of a factor of four above and below the modeled mean of the data, as seen in Fig. 1. Since the verified creep-plasticity model can account for prior work hardening, it appears that multistage testing is a very useful proof test procedure for this constitutive model.

Another test performed was a stress drop test. Figure 3 shows a stress drop test result. Unfortunately, it is on salt from a different depth than that for

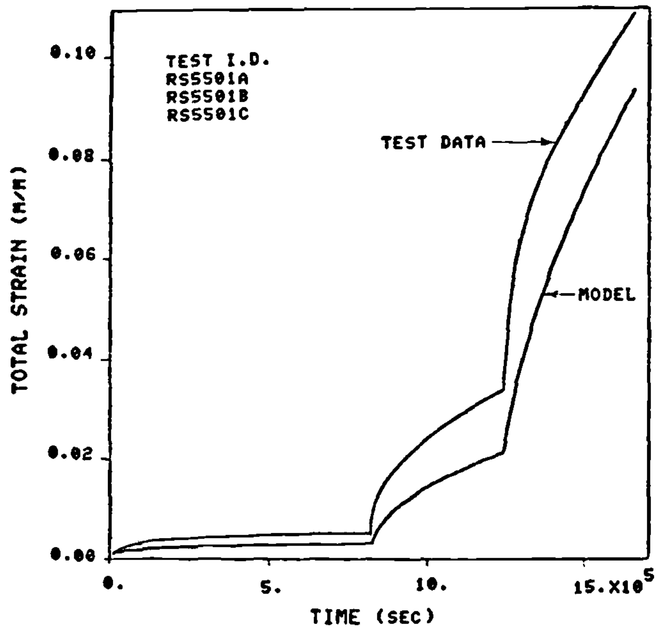

FIG. 2—*Multistage creep strain data at 10.5, 20.8, and 29.7 MPa compared with the predictions of the model.*

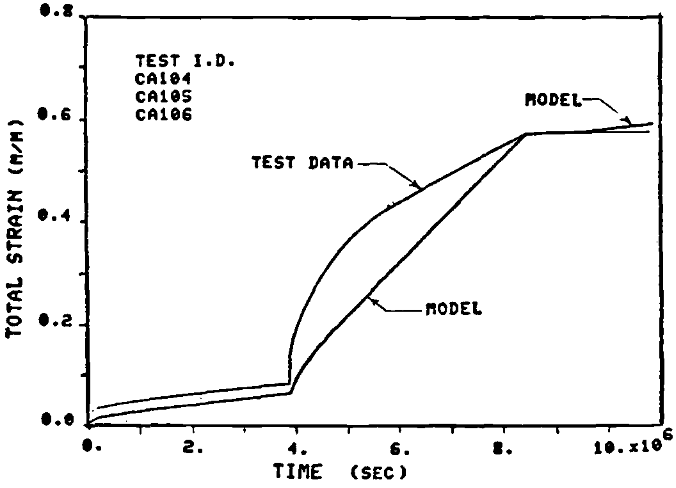

FIG. 3—*Model predictions for multistage creep test at 20.1, 30.6, and 20.3 MPa compared with data on a different salt where the strain has been scaled to coincide before the drop.*

which the data were reduced. It has generally the same behavior except that the creep rates are lower. For this reason, the entire curve of Fig. 3 has been scaled up to coincide with the model prediction before the stress drop. The drop follows a multistage test of 20.14 MPa (2920 psi) for 3.92E6 s and 30.60 MPa (4437 psi) for 4.52E6 s. The drop is to 20.33 MPa (2948 psi). Note that the time immediately following the drop is characterized by a period of almost zero stress rate.

Another series of tests, which were run by Wawersik and Hannum [2], is set at the moderately fast loading rate of 1.5 kPa/s. In terms of creep tests, this type of test is a severe case where the entire behavior is in the transient creep range. Figure 4 plots experimental and modeled strain. The results show a model behavior which is slightly too stiff. One point worth mentioning, however, is that these tests, in contrast to the creep tests, did show pressure dependent behavior and dilation.

Conclusions

A unified creep-plasticity model is presented for southeastern New Mexico halite. The model is not claimed to be micromechanically based; however, some ties can be made to other micromechanically based models. The behavior is postulated to be only kinematically hardening with postulated functional forms in the inelastic strain rate equation and the evolutionary

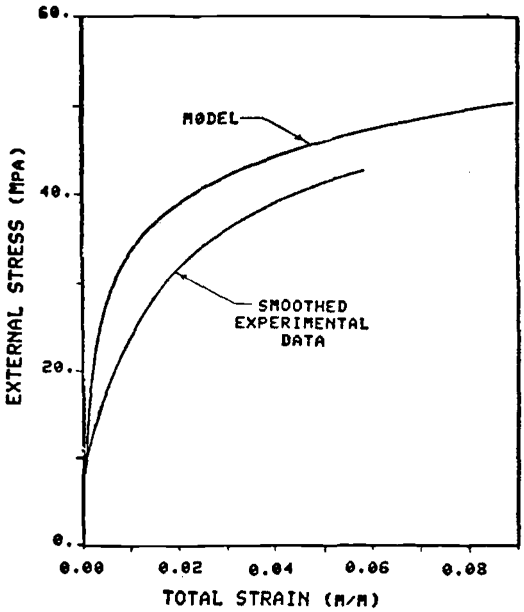

FIG. 4—*Constant stress rate test results for 1.5 kPa/s compared with model predictions.*

equation for the back stress. Arbitrary constants in the model are evaluated only based on a set of single-stage creep tests at two temperatures. Experimental verification for the model is based on comparison with four multistage creep tests, two stress drop tests, and a set of constant stress rate tests. The behavior of the model was generally satisfactory. With the variability inherent in creep behavior generally, and particularly so with the variability in rock salt, it is difficult to ascribe causes to the observed differences between the model and the test data. It is felt at this time that no serious deficiency in the model has been found unless very short time behavior is more important.

This model was implemented in a one-dimensional form in order to calculate the results presented herein. Implementation in a multidimensional finite-element structural computer program is the next step that must be taken. Only then will a model such as this be useful to the community outside materials science and applied mechanics.

Acknowledgments

This work was supported by U.S. Department of Energy (DOE) Contract DE-AC094-76DP00789. Sandia National Laboratories are a U.S. DOE facility.

References

[*1*] Hansen, F. D. and Mellegard, K. D., "Creep Behavior of Bedded Salt from Southeastern New Mexico at Elevated Temperature," SAND79-7030, Sandia National Laboratories, Nov. 1979.

[*2*] Wawersik, W. R. and Hannum, D. W., "Mechanical Behavior of New Mexico Rock Salt in Triaxial Compression up to 200C," SAND77-1192, Sandia National Laboratories, July 1979.

[*3*] Wawersik, W. R. and Hannum, D. W., "Interim Summary of Sandia Creep Experiments on Rock Salt from the WIPP Study Area, southeastern New Mexico," SAND-0115, Sandia National Laboratories, Feb. 1979.

[*4*] Herrmann, W., Wawersik, W. R., and Lawson, H. S., "Analysis of Steady State Creep of Southeastern New Mexico Bedded Salt," SAND80-0558, Sandia National Laboratories, March 1980.

[*5*] Herrmann, W., Wawersik, W. R., and Lawson, H. S., "A Model for Transient Creep of Southeastern New Mexico Rock Salt," SAND80-2172, Sandia National Laboratories, Oct. 1980.

[*6*] Havner, K. S. and Shalaby, A. H., "Further Investigations of a New Hardening Law in Crystal Plasticity," *Journal of Applied Mechanics*, Vol. 45, Sept. 1978, pp. 500–506.

[*7*] Krieg, R. D., "Numerical Implementation of Some New Unified Plasticity-Creep-Formulations," Paper M6/4, in *Proceedings*, 4th SMIRT Conference, 1977 San Francisco.

[*8*] Lagneborg, R., "Creep Deformation Mechanisms," in *Creep of Engineering Materials and Structures*, G. Bernasconi and G. Pialti, Eds., Applied Science, London, 1978, pp.7–34.

[*9*] Lagneborg, R., "Development and Refinement of the Recovery-Creep Theory," *Materials Science Research*, 1969, pp. 161–168.

[*10*] Gittus, J. H., "The Mechanical Equation of State for Dislocation-Creep Due to Stresses Varying in Magnitude and Direction," *Philosophical Magazine*, Vol. 24, Dec. 1971, pp. 1423–1430.

[*11*] Krieg, R. D., "A Practical Two Surface Plasticity Theory," *Journal of Applied Mechanics*, Vol. 42, Sept. 1975, pp. 641–646.

P. Alexopoulos,[1] *R. L. Keusseyan,*[2] *G. L. Wire,*[3] *and Che-Yu Li*[4]

Experimental Investigation of Nonelastic Deformation Emphasizing Transient Phenomena by Using a State Variable Approach

---

REFERENCE: Alexopoulos, P., Keusseyan, R. L., Wire, G. L., and Li, Che-Yu, "**Experimental Investigation of Nonelastic Deformation Emphasizing Transient Phenomena by Using a State Variable Approach,**" *Mechanical Testing for Deformation Model Development, ASTM STP 765,* R. W. Rohde and J. C. Swearengen, Eds., American Society for Testing and Materials, 1982, pp. 148–184.

ABSTRACT: This paper reviews the development of a deformation model based on a state variable approach for nonelastic deformation. The material parameters required can be determined by a combination of load relaxation and constant displacement rate tests. The experimental procedures, methods of data analysis, and the physical significance of the material parameters are discussed. The deformation model has been used to simulate a variety of deformation phenomena and has been compared with experimental data.

KEY WORDS: mechanical properties, plastic deformation, flow equation, low temperature, high temperature, grain boundary, dislocation, electron microscopy, simulation

This paper reviews the development of a particular state variable approach for the description of nonelastic deformation in polycrystalline solids. An attempt will be made to provide a detailed discussion of experimental techniques and methods of data analysis required for the determination of the material parameters of the deformation model.

---

[1] Formerly graduate student at Cornell University; presently Research Staff Member, IBM, San Jose, Calif.

[2] Formerly graduate student at Cornell University; presently Research Staff Member, IBM, Endicott, N.Y.

[3] Manager of Applied Systems and Technology, Hanford Engineering Development Laboratory, Richland, Wash.

[4] Professor, Materials Science and Engineering Department, Cornell University, Ithaca, N.Y.

The approach adopted in the present work was originally proposed by Hart [*1*].[5] It is primarily a phenomenological approach and therefore requires extensive experimental input. During the past decade this need was fulfilled by the utilization of the load relaxation test, which has permitted the examination of the flow properties of a large number of materials and the revelation of the systematic behavior shared by them covering a wide range of experimental conditions [*2,3*]. The development of deformation models in the present work has been evolutionary as more experimental data have become available, especially those resulting from transient deformation [*3*].

During the course of this work, attention was given to ensure that the deformation models proposed satisfied the following requirements: (*1*) the proposed models are based on accepted dislocation concepts and are of the simplest type with general applicability; (*2*) the material parameters of the model are uniquely measurable by experiments, and (*3*) the structural parameters of the model have corresponding microstructural features that are observable by metallographic techniques.

The constitutive equations for nonelastic deformation, resulting from the present work, have been shown to be computable in numerical analysis. They have been used successfully in applications utilizing a variety of computational techniques [*4*].

The deformation models proposed, based on the present approach, will be summarized first. A discussion of experimental techniques and methods of data analysis required for the determination of the material parameters will follow. Some examples of computer simulation will be given to demonstrate the applicability of the deformation models. Finally, the microstructural basis of the structural parameters as well as their physical significance will be discussed.

Deformation Models

State variable deformation models of increasing complexity have been developed in order to describe a wide range of deformation phenomena. Three sequential models will be discussed in this section. The simplest one, which contains three elements, was proposed originally by Hart [*1*]. It has been shown to describe grain matrix plastic properties of polycrystalline solids under monotonic loading. A second-generation model, consisting of Hart's model and two additional elements, has been proposed to describe additional phenomena such as grain matrix anelasticity, microplasticity, and the Bauschinger effect [*3*]. A third model, which was developed for grain boundary anelasticity and grain boundary sliding, is constructed by combining a grain boundary element in parallel with the grain matrix model [*5,6*].

---

[5] The italic numbers in brackets refer to the list of references appended to this paper.

Hart's Model

The physical picture on which Hart's model [*1*] is based is schematically represented in Fig. 1. It assumes the existence of a distribution of equal strength and uniformly spaced barriers to dislocation motion. A schematic representation of the combination of the three elements employed by Hart's model is also shown in Fig. 1. At low stresses, the motion of dislocations between barriers will produce anelastic deformation which is time dependent but recoverable. According to the model, the magnitude of anelastic deformation is governed by the a-element (stored anelastic strain), and the rate of its accumulation is controlled by the $\dot{\epsilon}$-element (glide friction). At low homologous temperatures, plastic deformation, which is not recoverable, is generated by high stresses that overcome barriers to dislocation motion. In this case the rate of plastic deformation is controlled by the $\dot{\epsilon}$-element (glide friction). At high homologous temperatures and low stresses, plastic deformation can be generated also by dislocation climb at a rate governed by the $\dot{\alpha}$-element (plastic element).

The flow equations for the $\dot{\epsilon}$ and $\dot{\alpha}$ elements have been found, based on experimentally observed scaling behaviors, to be state variable equations [*1*]. The form of these equations has been shown to be essentially independent of the materials tested as well as the thermal-mechanical history [*1,2,4*]. This latter result offers advantages in materials characterization that will be demonstrated in a separate section.

The constraint equations of the model are

$$\dot{\epsilon} = \dot{a} + \dot{\alpha} \tag{1}$$

and

$$\sigma = \sigma_a + \sigma_f \tag{2}$$

where σ, σ_a, and σ_f are the applied stress, back stress due to stored anelastic strain, and glide friction (effective) stress, respectively, and $\dot{\epsilon}$, $\dot{a}$, and $\dot{\alpha}$ are the nonelastic strain rate, anelastic strain rate, and plastic strain rate, respectively.

For the a-element, the stress σ_a and the stored anelastic strain a are related in a linear fashion through a modulus $\mathfrak{M}$:

$$\sigma_a = \mathfrak{M} a \tag{3}$$

The friction stress is found to be related to the nonelastic strain rate by

$$\dot{\epsilon} = \dot{a}^* (\sigma_f / G)^M \tag{4}$$

where G is the shear modulus, $\dot{a}^*$ is a rate parameter, and $M \cong 7.8$.

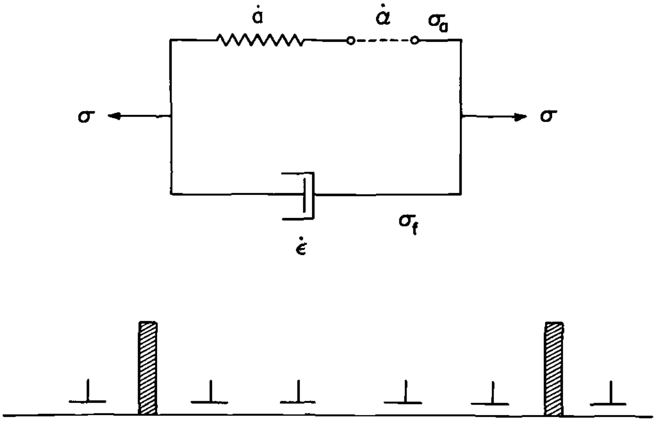

FIG. 1—*Schematic representation of Hart's model and its physical interpretation.*

Flow in the plastic element is represented by

$$\ell n(\sigma^*/\sigma_a) = (\dot{\epsilon}^*/\dot{\alpha})^{\lambda} \tag{5}$$

with scaling relation:

$$\dot{\epsilon}^* = (\sigma^*/G)^m f e^{-Q/RT} \tag{6}$$

Work hardening and recovery are incorporated by

$$d(\ell n \sigma^*)/dt = \Gamma(\sigma^*, \sigma_a)\dot{\alpha} - \mathcal{R}(\sigma^*, T) \tag{7}$$

where σ^* is the hardness parameter (similar to a yield stress at moderate strain rates), $\dot{\epsilon}^*$ is a rate parameter, $\lambda = 0.15$, $m \simeq 4.5$, f is some characteristic frequency, Q is self-diffusion activation energy, and RT has the usual meaning.

The work-hardening function Γ has been found to be [*2,4*]:

$$\Gamma = (\sigma_a/\sigma^*)^{\beta/\sigma^*}(\beta/\sigma^*)^{\delta} \tag{8}$$

where β and δ are material constants; the recovery function $\mathcal{R}$ is generally negligible at moderate homologous temperatures.

This model has been shown to describe adequately the tensile, load relaxation, and creep behavior of a number of polycrystalline solids under unidirectional loading when grain matrix plastic flow predominates. An attitude taken in the present work has been that materials under these conditions exhibit a basic matrix behavior, which is represented by the state variable model. Explicit inclusion of recovery and strain aging will be possible by time-dependent changes in the relevant state variables. Figure 2 shows the results of a creep simulation using Hart's model with material parameters determined by load relaxation and tension tests. It is seen that the simulation agrees well with experimental data [*4*].

The deficiency of Hart's model in describing grain matrix transient deformation phenomena, such as microplasticity and the Bauschinger effect, has been discussed in detail in Ref *3*. A second-generation model has been developed for the latter needs. The second-generation model reduces to Hart's model when grain matrix plastic flow predominates.

A Second-Generation Model for Transient Deformation

Figure 3 shows schematically the physical picture on which the second-generation model is based together with a rheological analogue of the model. The barrier structure in Hart's model is replaced by one which includes the co-existence of strong barriers (Hart's barriers) and a distribution of weak barriers between them. During loading, dislocations will first pile up against the weak barriers (anelastic deformation). At a sufficiently high stress, leakage through the weak barriers will occur; this contributes to the long-range pileup against the strong barriers, resulting in microplastic deformation. Upon unloading to zero stress, dislocation pileup can be trapped by the

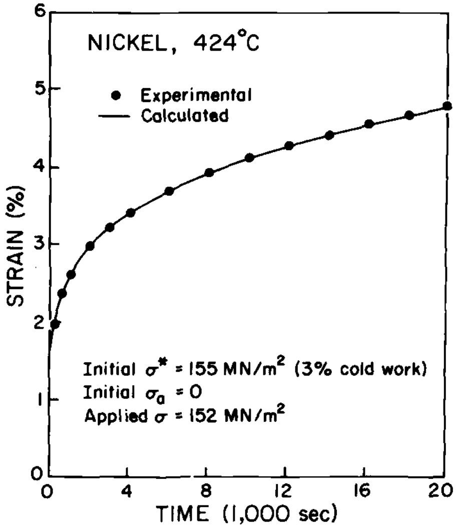

FIG. 2—*Experimental and calculated constant load creep curve for 3 percent cold-worked nickel at 424°C.*

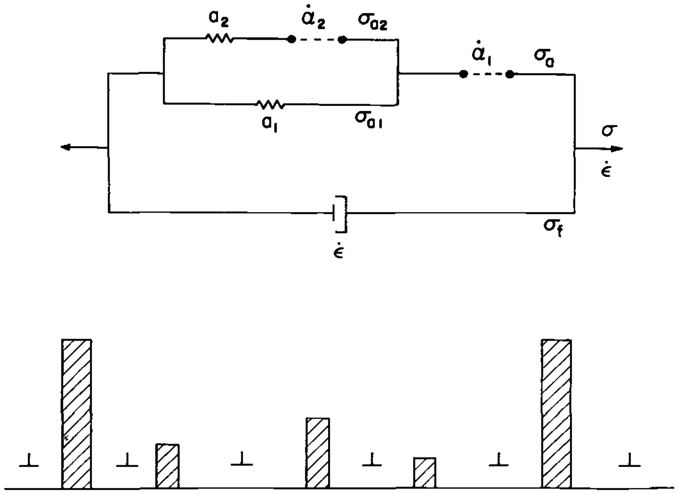

FIG. 3—*Schematic representation of the second-generation model and its physical interpretation.*

weak barriers. This stored strain will contribute to the Bauschinger effect upon reverse loading. The plastic behavior represented by Hart's model is not modified. At high stresses, the pileups in front of the weak barriers are fully developed and plastic deformation is impeded only by the strong barriers.

The deformation model shown in Fig. 3 represents the simplest possible model that incorporates the aforementioned considerations. It requires two state variables for the stored strain and thus two anelastic elements of different moduli. A flow element (microplastic element) for passage over weak barriers is also needed.

The arrangement of these three elements, the a_1, a_2, and $\dot{\alpha}_2$ elements, is shown in Fig. 3. These three elements replace the anelastic element (the a-element) in Hart's model. The long-range dislocation pileup between strong barriers is represented by the a_1-element. The short-range pileups are represented by the a_1 and a_2 elements acting together. The net force (σ_{a_2}) for dislocation passage through the weak barriers is the stress in the a_2-element.

The constraint equations of the second-generation model are

$$\sigma = \sigma_f + \sigma_a = \sigma_f + \sigma_{a_1} + \sigma_{a_2} \tag{9}$$

and

$$\dot{\epsilon} = \dot{\alpha}_1 + \dot{a}_1 = \dot{\alpha}_1 + \dot{\alpha}_2 + \dot{a}_2 \tag{10}$$

The constitutive relations for the new anelastic elements are

$$\sigma_{a_1} = \mathfrak{M}_1 a_1 \tag{11}$$

and

$$\sigma_{a_2} = \mathfrak{M}_2 a_2 \tag{12}$$

where $\mathfrak{M}_1$ depends on the strong barrier spacing, and $\mathfrak{M}_1 + \mathfrak{M}_2$ is a function of the weak barrier spacing.

For the plastic element ($\dot{\alpha}_1$) and the glide friction element ($\dot{\epsilon}$) no modification is necessary and Eqs 4 to 8 can be taken as governing relations (with appropriate subscripts).

For the $\dot{\alpha}_2$-element (microplastic), the governing relation has been found experimentally to be represented by

$$\ell n(\sigma_2^*/\sigma_{a_2}) = (\dot{\epsilon}_2^*/\dot{\alpha}_2)^{\lambda_2} \tag{13}$$

with scaling represented by

$$\dot{\epsilon}_2^* = (\sigma_2^*/G)^{m_2} f_2 e^{-Q/RT} \tag{14}$$

which are of the same form of equivalent relations for the $\dot{\alpha}_1$-element.

In the second-generation model the weak barriers are assumed to have a distribution of strengths characterized by the state variable σ_2^*. Thus as the weakest barriers are overcome, the microplastic flow will be controlled by successively stronger barriers. For a given microstructural state of a material, the evolution of σ_2^* in a tensile test is therefore a sampling effect rather than the result of work hardening. A further discussion of σ_2^* will be given in a later section.

The second-generation model has been shown to describe successfully microplasticity and the Bauschinger effect with experimentally determined parameters [*3, 7*]. However, both Hart's model and the second-generation model are concerned with deformation processes that occur in the grain matrix. At high homologous temperatures, grain boundary sliding will occur and produce grain boundary anelastic deformation and additional plastic deformation.

Grain Boundary Sliding Model

The grain boundary sliding model shown in Fig. 4 is developed to describe grain boundary anelasticity as well as plastic deformation produced by grain boundary sliding in a unified way. For grain boundary anelasticity the concept introduced by Zener and his co-workers is adopted [*8*]. Grain boundary shear is thought to be always accompanied by grain matrix deformation at

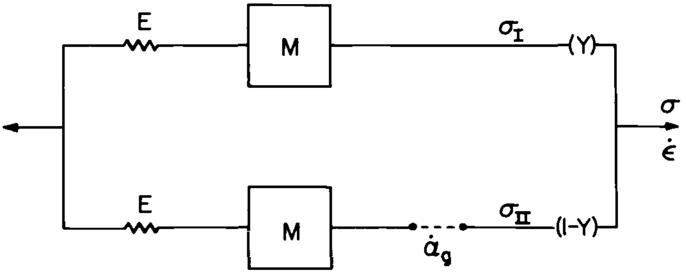

FIG. 4—*Schematic representation of the grain boundary sliding model.*

grain boundary steps and corners required for accommodation. When the extent of grain boundary shear is limited and the time scale is short, the grain matrix deformation required for accommodation will essentially be elastic and anelastic. Once the applied stress is removed, the stored elastic and anelastic strain will provide a driving force for reversed grain boundary shear. When the extent of grain boundary shear is large and the time scale is long, the grain matrix deformation required for accommodation will include plastic deformation. Thus upon the removal of the applied stress the portion of grain boundary shear that is accommodated by grain matrix plastic deformation will not recover.

Both stress and strain concentration [5] can occur at grain boundary steps and corners during grain boundary shear. The phenomenological model of interest should incorporate as many as possible of the important physical features of the phenomenon and yet remain in a simple form. Progress in this area has been hindered mainly by the limited experimental information available to determine uniquely the material parameters of the models proposed. The parallel and series models introduced by Hart [5] for describing plastic deformation produced by grain boundary sliding are examples of phenomenological models of interest.

The grain boundary sliding model shown in Fig. 4 represents an extension of Hart's parallel model to include grain boundary anelasticity [*6, 9*]. It represents a level of complexity for which experimental capabilities are available to determine the required material parameters. This model consists of two branches in parallel; the total stress is related to the stresses in the upper and lower branches (σ_I and σ_{II}) by

$$\sigma = Y\sigma_I + (1 - Y)\sigma_{II} \qquad (15)$$

where the parameter Y explicitly represents stress concentration during grain boundary sliding.

The E-elements represent elastic behavior and the M-elements represent the entire model (Figs. 1 or 3) for nonelastic deformation in the grain matrix. When no grain boundary deformation occurs ($\dot{\alpha}_g = 0$), the behavior reduces to that of the grain matrix.

Since grain boundary sliding is grain matrix deformation accommodated, the grain boundary element $\dot{\alpha}_g$ has been found experimentally for plastic deformation to be represented by

$$\ell n(\sigma_g{}^*/\sigma_{II}) = (\dot{\epsilon}_g{}^*/\dot{\alpha}_g)^{\lambda_g} \tag{16}$$

where the value of $\sigma_g{}^*$ and $\dot{\epsilon}_g{}^*$ will be related to the corresponding parameters for the grain matrix plastic element (Eq 5).

According to this model, the closed stress-strain loops obtained in a constant extension rate cycling test at high homologous temperatures will have a slope given by $Y/(1/E + 1/\mathfrak{M})$ in the range where grain boundary anelasticity is important [*6*]. This model has been used to describe successfully load relaxation data and anelastic deformation data where the grain boundary effects are significant [*9*].

Experimental Approach

The development of the present state variable approach has utilized extensively the load relaxation and the constant displacement rate tension-compression tests to determine the material parameters and flow equations of the deformation models. The principle of these experiments is described in detail in Ref *10*. In general, the load relaxation test will allow the determination of the stress-nonelastic strain rate relation of a material at an essentially constant structural state, covering a wide range of strain rates in a short experimental time. The constant displacement rate test will allow the measurement of the evolution behavior of the hardness parameters ($\sigma_1{}^*$ and $\sigma_2{}^*$) as well as the two anelastic moduli ($\mathfrak{M}_1$ and $\mathfrak{M}_2$) and the stress concentration factor Y for grain boundary sliding.

It has been the experience of the present work that a combination of load relaxation and constant displacement rate tests is more powerful than a combination of creep and constant displacement rate tests, based on the ability and efficiency of the former tests to produce a large amount of experimental information and their capabilities to detect physical effects such as thermal recovery [*11*] and grain boundary sliding [*2*]. The required experimental capabilities and methods of data analysis will be described in the next two sections.

Experimental Requirements

Constant Extension Rate Test

When the constant extension rate test is used to measure anelastic moduli in the stress range where the maximum stress is a small fraction of the plastic yield stress, the need for precision strain measurement is most demanding. Since anelastic moduli have been found to be about two orders of magnitude larger than the elastic modulus, anelastic strain is therefore usually on the order of 10^{-5}. Hence a strain-measuring capability with stability and resolution in the 10^{-6} range is required. The coefficient of thermal expansion of metals is on the order of 10^{-5}/°C. With the above requirement in strain measurement, it is apparent that a temperature stability better than 0.1°C must be maintained during an experiment. Another important requirement is the alignment of the load train. Since the shear modulus is a fraction of the elastic modulus, strain produced by shear, due to any misalignment, can be larger than the expected anelastic strain. It is important also to have a multichannel data acquisition system with high precision and speed that will record stress and strain data simultaneously.

Load Relaxation Test

All the requirements discussed for the constant extension rate test are also required for the load relaxation test in a stricter way, because it is important to be able to measure strain rates down to 10^{-9} s^{-1} range. An additional requirement of the load relaxation test is the high stiffness of the system, which is necessary for minimizing the extent of nonelastic deformation in the specimen in order to maintain a constant structural state during the experiment. A screw-driven machine of the Instron type is preferred for its stability compared to an electro-hydraulic machine even though the stiffness is less.

The experimental techniques used to meet these requirements are now described.

Temperature Stability—The entire Instron testing machine, excluding the motor, is housed in an insulated box. The temperature of the room is controlled to within ±0.5°C. Other details in temperature control are given in Ref *12*.

Load Measurement—Hermetically sealed tension-compression load cells with resolution better than 10 g (0.02 lb) are used. Resolution of the load cell has to be balanced by its stiffness, because the load cell is the most compliant part of the load train (excluding the specimen).

Strain Measurement—At room temperature, displacement is measured by a pair of linear voltage displacement transducers (LVDTs) (for example, HP 24DCDT-100) [*13*], which are mounted directly on the specimen. Particular attention is paid to the alignment of the cores so that they do not touch the inner walls of the LVDTs during the test. At high temperatures, displacement is measured by a pair of HTCP-100 capacitance probes [*12,14*] attached directly to the specimen. These probes eliminate the need for the extension rods usually used in high-temperature measurements.

Alignment—For room temperature experiments in tension and compression, alignment is achieved by the use of a three-pole die-set [*15*] with the load cell located between the die-sets. For experiments in tension at high temperatures, alignment is achieved by careful adjustment of the whole load train and the use of high-temperature, high-strength ball joints.

Data Acquisition—A multichannel digital data acquisition system with magnetic disk or cassette data storing capability is used. Variable data acquisition rates of up to 20 readings per second are available. The rate of data acquisition is independent of the number of channels and the ranges of data scanned.

Methods of Data Analysis

This section discusses the methods of data analysis required to obtain the flow equations and the material parameters of the deformation models.

The Glide Friction Element ($\dot{\epsilon}$-Element) and the Plastic Element ($\dot{\alpha}$- or $\dot{\alpha}_I$-Element)

Typical load relaxation data of the same hardness σ^* (or σ_1^*) of Type 316 stainless steel in a log σ versus log $\dot{\epsilon}$ plot as a function of temperature are shown in Fig. 5 [*14*]. This type of datum is required to determine the flow equations, Eqs 4 and 5, and related material parameters, as described in Ref *14*, to characterize these two elements.

The low-temperature data in Fig. 5, for example, are governed essentially by Eq 4 when the $\dot{\epsilon}$-element predominates. By combining Eqs 2 and 4 and setting $\sigma_a = \sigma^*$, then

$$\sigma = \sigma^* + (G^M/\dot{a}^*)^{1/M}(\dot{\epsilon})^{1/M} \tag{17}$$

Thus by using the σ and $\dot{\epsilon}$ data obtained from a load relaxation test at low homologous temperatures and the linear least-square method, Eq 17 will yield the value of the hardness parameter σ^* (or σ_1^*), the rate parameter $\dot{a}^*$, and the exponent M.

The log σ versus log $\dot{\epsilon}$ data in Fig. 5 obtained at high temperatures, for example, are governed essentially by Eq 5. Equation 5 can be rewritten, with $\sigma_f \simeq 0$ and $\dot{a}_1 \simeq 0$, as

$$\ell n\sigma = \ell n\sigma^* - (\dot{\epsilon}^*)^{\lambda}(1/\dot{\epsilon})^{\lambda} \tag{18}$$

Again, by using the σ and $\dot{\epsilon}$ data obtained from a load relaxation test at high homologous temperatures and the linear least-square method, Eq 18 will yield the value of the hardness parameter σ^* (or σ_1^*), the rate parameter $\dot{\epsilon}^*$, and the exponent λ.

The data obtained at intermediate temperatures shown in Fig. 5 can be

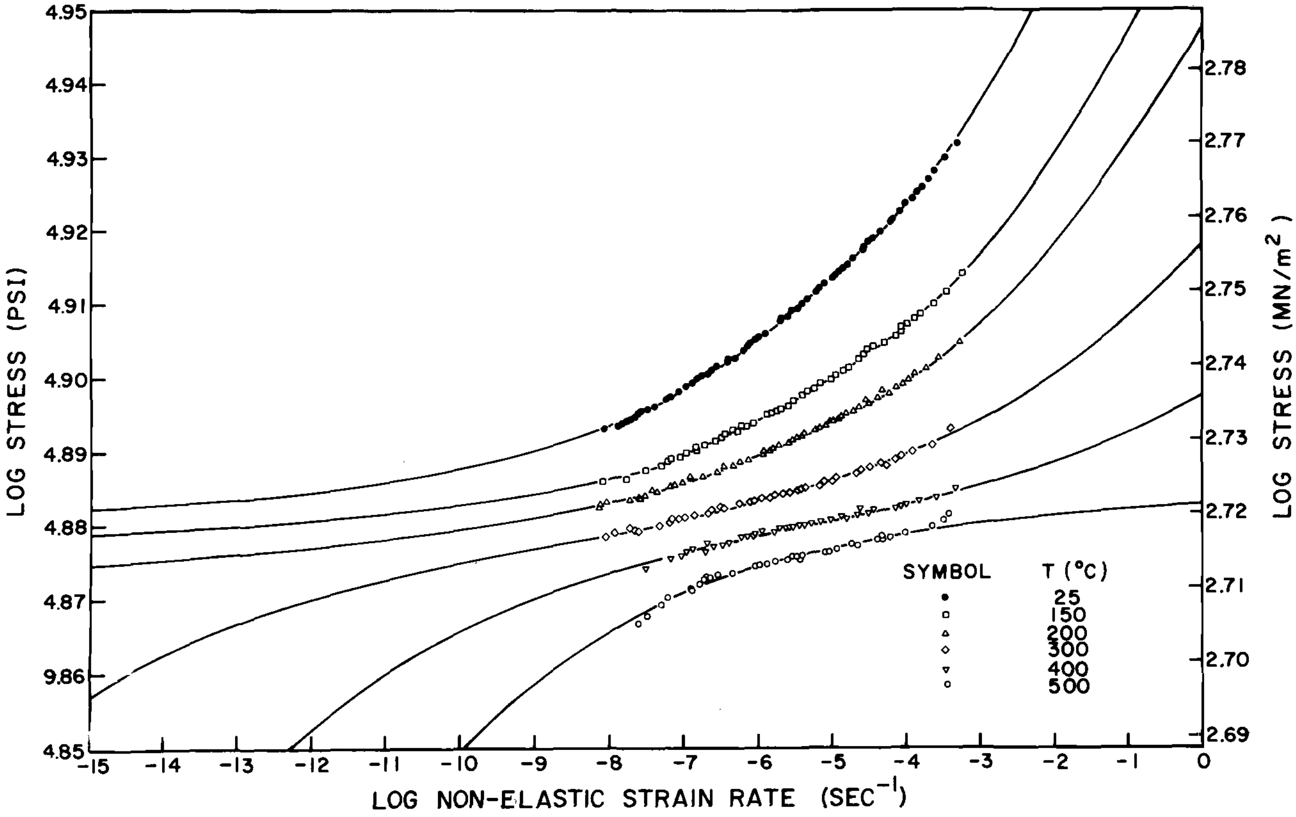

FIG. 5—*Constant hardness log σ-log ε̇ data for stabilized Type 316 stainless steel at several temperatures.*

described by a combination of Eqs 4 and 5 through Eq 2. In this case a nonlinear least-square analysis will have to be used to determine the material parameters of interest [*14*].

The scaling relation (Eq 6) can be determined also by using load relaxation data. For scaling with σ^*, data obtained at different values of hardness σ^* but at the same temperature T are needed. For scaling with temperature, data obtained at different temperatures but with the same hardness are required [*11,14*]. This scaling relation has been used as an important basis to justify the validity of the state variable approach adopted in the present work [*11*].

The determination of the work-hardening function Γ (Eq 8) will require constant displacement rate tensile data [*4,13*]. The method of data analysis is given in Ref *4*. The form of Eq 8 is determined primarily by experimental data. It suggests that the rate of work hardening Γ $(= d\ell n\sigma^*/d\alpha)$ depends only on the current state variables σ^* and σ_a, and provides a strain rate dependence through the ratio of σ_a/σ^* in the absence of thermal recovery.

The Anelastic Elements (a$_1$- and a$_2$-Elements)

The two anelastic moduli ($\mathcal{M}_1$ and $\mathcal{M}_2$) are required to characterize the anelastic elements. According to the second-generation model (Fig. 3), the magnitude of grain matrix anelastic deformation is governed by the value of $\mathcal{M}_1 + \mathcal{M}_2$, whereas the magnitude of the microplastic deformation is governed by the value of $\mathcal{M}_1$. In the anelastic region the stress-strain loop, obtained by loading and unloading in a constant displacement rate tension test, will be closed. As one enters the microplastic region at higher stresses but below plastic yielding, the stress-strain loop will no longer close upon unloading to zero stress [*16*].

The method for the determination of the combined modulus ($\mathcal{M}_1 + \mathcal{M}_2$) is given in detail in Refs *15* and *16*. It utilizes the type of stress-nonelastic strain data obtained in a constant displacement rate test shown in Figs. 6 and 7. The data in Fig. 6 were obtained in a tension loading-unloading cycle, whereas the data in Fig. 7 were obtained in a tension-compression cycle. The nonelastic strain rate of the portion of the data between σ_E and σ_A (elastic and anelastic limits respectively) is seen to remain essentially constant. The slope of the stress-total strain (ϵ_{total}) data in this range can be used to evaluate $\mathcal{M}_1 + \mathcal{M}_2$ as shown below.

In the anelastic region ($\dot{\alpha}_1 = 0$; $\dot{\alpha}_2 = 0$) and at temperatures where grain boundary anelasticity is negligible,

$$\epsilon_{\text{total}} = e + a_1 \tag{19}$$

where e is the elastic strain. By differentiating with respect to stress and utilizing Eqs 4 and 9,

$$d\epsilon_{\text{total}}/d\sigma = de/d\sigma + da_1/(d\sigma_{a_1} + d\sigma_{a_2}) \tag{20}$$

where $d\sigma_f$ can be taken to be zero if $\dot{\epsilon}$ is found to be constant in the anelastic region.

Equation 20 can be rewritten by using Eqs 11 and 12 as

$$1/(d\sigma/d\epsilon_{\text{total}}) = 1/E + 1/(\mathfrak{M}_1 + \mathfrak{M}_2) \tag{21}$$

Thus if the condition of constant $\dot{\epsilon}$ in the anelastic region is met, the slope of stress-total strain data in the region of interest will yield the value of the

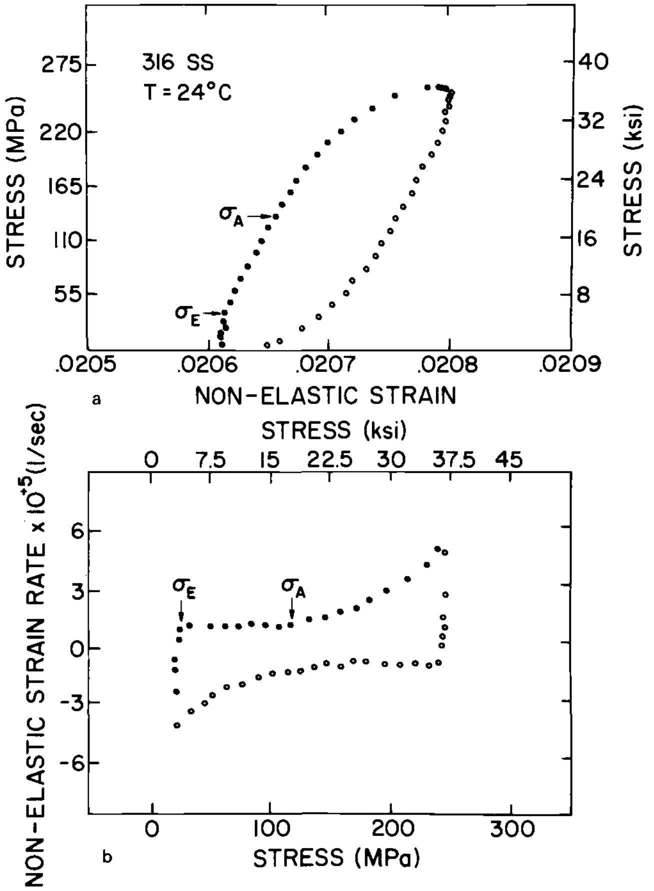

FIG. 6—(a) *Stress-nonelastic strain data for Type 316 stainless steel obtained in a constant extension rate test at room temperature in a loading-unloading cycle;* (b) *nonelastic strain rate–stress data for the same cycle. Crosshead speed = 0.05 cm/min.*

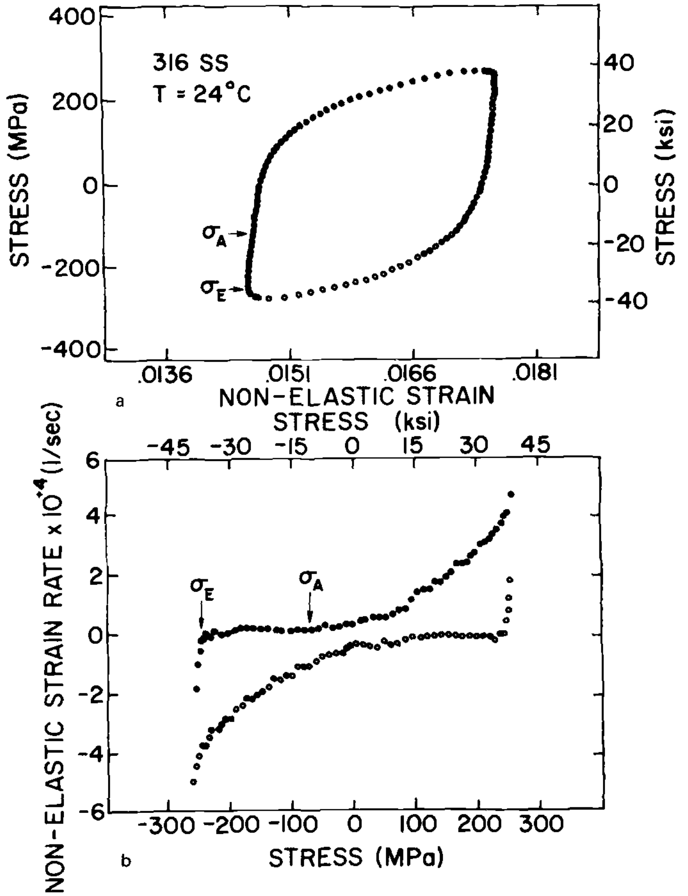

FIG. 7—(a) *Stress-nonelastic strain data for Type 316 stainless steel obtained in a constant displacement rate test at room temperature in a tension-compression cycle;* (b) *nonelastic strain rate-stress data for the same cycle. Crosshead speed = 0.05 cm/min.*

combined modulus ($\mathcal{M}_1 + \mathcal{M}_2$). Experiments have been performed utilizing both types of data of the same material as shown in Figs. 6 and 7, and the same value of $\mathcal{M}_1 + \mathcal{M}_2$ was obtained [*7,15*]. The data shown in Figs. 6 and 7 are for Type 316 stainless steel and show a value of $\mathcal{M}_1 + \mathcal{M}_2 = 1.48 \times 10^6$ MPa.

As stress continues to increase in a constant displacement rate test beyond the value of σ_A (Figs. 6 and 7), microplastic deformation will occur. The nonelastic strain rate data in the microplastic region usually do not exhibit a second plateau before plastic yielding to allow the determination of $\mathcal{M}_1$ directly from the slope of the stress-strain data.

The method for the determination of the long-range anelastic modulus $\mathcal{M}_1$ is shown in Fig. 8 [*7,15*]. A reversible and symmetrical stress-nonelastic strain loop in the microplastic region is shown. The loop is obtained after repeated cycles in a tension-compression constant displacement rate test. The σ_E and σ_A in Fig. 8 have the same meaning as those in Figs. 6 and 7. It can be argued physically that, because of symmetry, at point α_0 the specimen contains neither anelastic strain nor microplastic strain [*15*]. It can be also argued physically that at point σ_A, $\sigma \simeq \sigma_{a_1}$. This is because, during prior loading, dislocations are piled up against the strong barriers in one direction (Fig. 3); during unloading, at point σ_A all the dislocations will move in the opposite direction. At this point, σ_{a_2} will be approximately equal to a value of $\sigma_2{}^*$ representing the strength of the weakest barrier, which is a small value. The applied stress therefore can be set equal to σ_{a_1} at the point σ_A.

Experimentally the position of point σ_A can be found from the nonelastic strain rate data where the nonelastic strain rate begins to rise (Figs. 6 and 7). From Eq 11, the slope of a straight line passing through σ_A and α_0 in Fig. 8 will produce a good estimate of $\mathcal{M}_1$.

It should be recognized that in order to perform the experiments required for anelastic moduli, the type of experimental capabilities described previously are necessary. The data shown in Fig. 8 are for Type 316 stainless steel and have a value of $\mathcal{M}_1 = 34.5 \times 10^3$ MPa.

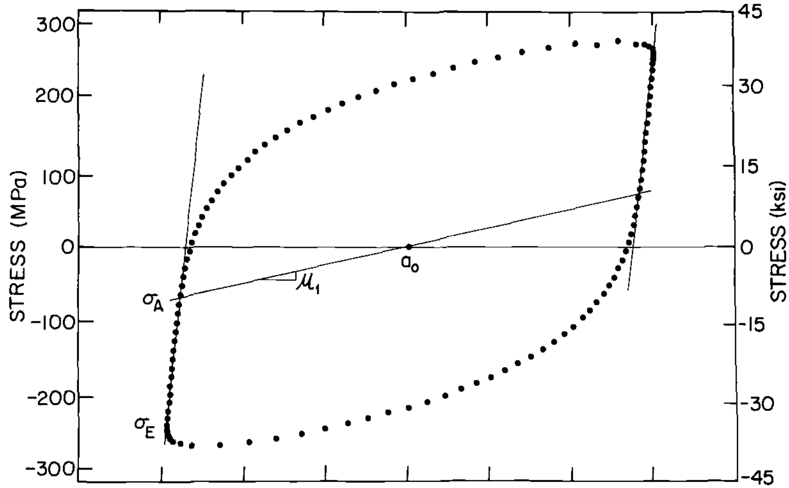

FIG. 8—*Tension-compression stress-nonelastic strain data for Type 316 stainless steel; the slope of line through* α_0 *and* σ_A *is used to calculate* $\mathcal{M}_l$. *Crosshead speed* = *0.05 cm/min.*

The Microplastic Element ($\dot{\alpha}_2$-Element)

A flow equation for the microplastic strain rate ($\dot{\alpha}_2$) and the strength distribution of the weak barriers ($\sigma_2{}^*$) are required to characterize the microplastic element.

Load relaxation experiments performed in the microplastic region where the $\dot{\alpha}_2$-element predominates can be used to obtain $\dot{\alpha}_2$ and σ_{a_2} data. The flow equation (Eq 13) is determined based on these data [*7,15*]. Constant displacement rate tension or tension-compression tests in the microplastic region can be used to sample the distribution of the weak barrier strengths.

Typical load relaxation data in the microplastic region where the $\dot{\alpha}_2$-element predominates are shown in Fig. 9. These data were obtained by interrupting a constant displacement tension-compression test at various stress levels to perform the required load relaxation tests.

To evaluate σ_{a_2}, Eq 9 is rewritten as

$$\sigma_{a_2} = \sigma - \sigma_{a_1} - \sigma_f \tag{22}$$

where σ_f is calculated from Eq 4 and the measured nonelastic strain rate $\dot{\epsilon}$.

The value of σ_{a_1} in Eq 22 can be calculated from Eq 11 if the value of a_1 is known. For any point along the stress-nonelastic strain loop, and during the load relaxation, a_1 can be calculated from

$$a_1 = \epsilon - \alpha_o - \Delta\alpha_1 \tag{23}$$

where α_o is the nonelastic strain value at the center of the loop (Fig. 9) where a_1 is practically zero as discussed previously, and $\Delta\alpha_1$ is calculated from $\dot{\alpha}_1$ (Eq 5) and the time elapsed during the experiment between $\sigma = 0$ and a point of interest.

The required material parameters for Eqs 4 and 5 can be evaluated, of course, from load relaxation tests under appropriate conditions.

To evaluate $\dot{\alpha}_2$, Eq 10 can be rewritten as

$$\dot{\alpha}_2 = \dot{\epsilon} - \dot{a}_2 - \dot{\alpha}_1 \tag{24}$$

by using Eq 12:

$$\dot{\alpha}_2 = \dot{\epsilon} - \dot{\sigma}_{a_2}/\mathcal{M}_2 - \dot{\alpha}_1$$

where $\dot{\alpha}_1$ can be calculated from Eq 5 as described previously.

The value of $\dot{\sigma}_{a_2}$ can be calculated from Eqs 9 and 11:

$$\begin{aligned}\dot{\sigma}_{a_2} &= \dot{\sigma} - \dot{\sigma}_f - \dot{\sigma}_{a_1} \\ &= \dot{\sigma} - \dot{\sigma}_f - (\dot{\epsilon} - \dot{\alpha}_1)/\mathcal{M}_1\end{aligned} \tag{25}$$

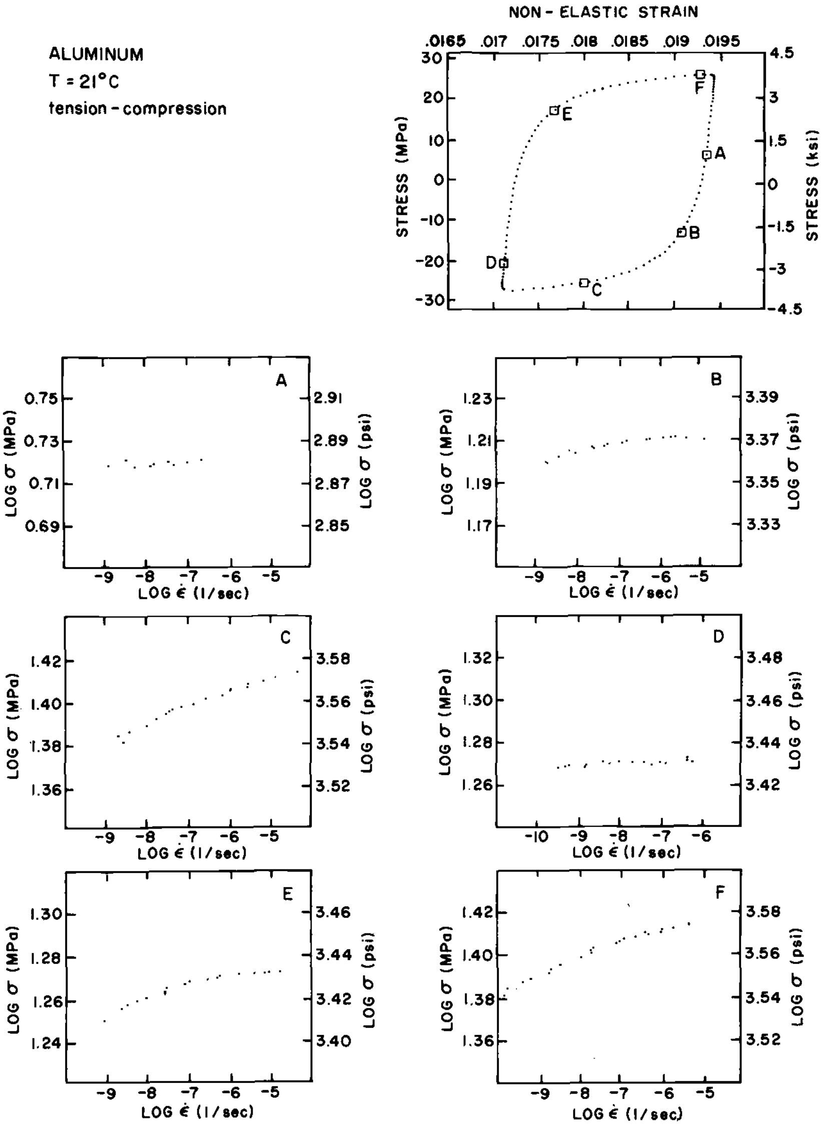

FIG. 9—*Stress-nonelastic strain data for aluminum obtained in a constant displacement rate tension-compression cycle. Also shown are log* σ*-log* $\dot{\epsilon}$ *data for load relaxation at different stress levels of the cycle. Crosshead speed* $= 0.025$ *cm/min.*

With the values of σ_{a_2} and $\dot{\alpha}_2$ obtained, the flow equation (Eq 13) and the associated scaling relation (Eq 14) can be determined by using the same method as that for the equivalent relations for the plastic element discussed previously. From the aluminum data shown in Fig. 9 the following results were obtained: $\lambda_2 = 0.15$ and $m_2 = 5.0$ for the microplastic element.

It is important to recognize that at low homologous temperatures microplastic deformation will be controlled by the glide friction element ($\dot{\epsilon}$-element). The load relaxation data of Type 316 stainless steel shown in Fig. 10 exhibit this type of behavior. These data were obtained by using the same experimental procedure as that for the data in Fig. 9. It is seen that the log σ–log $\dot{\epsilon}$ curves are concave upward; these are similar in shape to the low temperature data in the plastic region shown in Fig. 5 for the same material.

For the data in Fig. 10, $\sigma_{a_2} \simeq \sigma_2^*$, and the σ-$\dot{\epsilon}$ data can be analyzed to yield the value of the exponent M and the rate parameter $\dot{a}^*$ for Eq 4 in the microplastic region ($\sigma \ll \sigma_{\text{yield}}$). The value of $\dot{a}^*$ for these data (Fig. 10) was found to be stress dependent; for example, $\dot{a}^* = 2.2 \times 10^{25}$ l/s at $\sigma = 1.12 \times 10^2$ MPa. In contrast, in the plastic region (Fig. 5) the value of $\dot{a}^*$ is 2.1×10^{21} l/s. A further discussion of this difference will be given in a later section of the paper.

The strength distribution of the weak barriers (σ_2^*) can be considered qualitatively from the viewpoint of a sampling effect discussed previously. For a given microstructural state of the material, during a constant displacement rate tensile test, as the stress is increased in the microplastic region, the dislocation will overcome weak barriers of increasing strength. Under conditions where the load relaxation curve (Fig. 10) in this region is concave upward (low homologous temperatures and/or high microplastic strain rates), σ_{a_2} will be very close to σ_2^* according to Eqs 4, 9, and 13. On the other hand, under conditions where the load relaxation curve (Fig. 9) is concave downwards (high homologous temperatures and/or low microplastic strain rates), the ratio of σ_2^*/σ_{a_2} will be greater than one and will vary with temperature and microplastic strain rate. A state variable representation of this sampling effect in terms of stress and nonelastic rate or other appropriate state variables will be required. An attempt in this direction has been made [*3,13,15*].

In principle, for a given pair of σ and $\dot{\epsilon}$ in the microplastic region, the corresponding σ_{a_2} and $\dot{\alpha}_2$ can be calculated as described previously. If the material parameters in Eqs 13 and 14 are fully characterized, for a pair of σ_{a_2} and $\dot{\alpha}_2$ of interest, the ratio of σ_2^*/σ_{a_2} can be evaluated from these equations.

The Grain Boundary Sliding Model

The stress concentration parameter Y (Eq 15) and a flow equation (Eq 16) for the grain boundary element ($\dot{\alpha}_g$-element) are required to characterize the effects of grain boundary sliding in the plastic region.

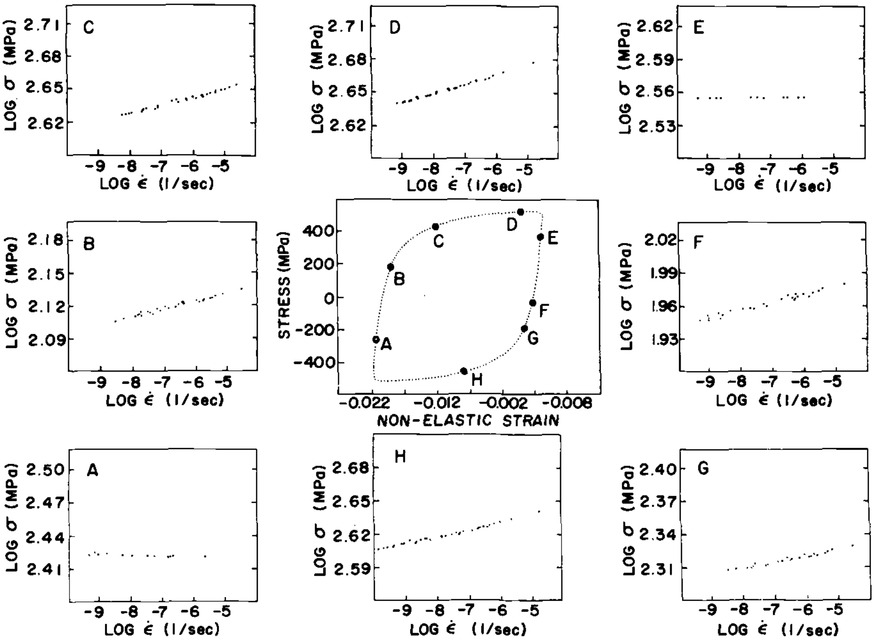

FIG. 10—*Stress-nonelastic strain data for Type 316 stainless steel obtained in a constant displacement rate tension-compression cycle. Also shown are log σ-log ε̇ data for load relaxation at different stress levels of the cycle. Crosshead speed = 0.05 cm/min.*

The parameter Y can be determined by using the load relaxation data in the plastic region where grain boundary sliding is significant if the log σ-log $\dot{\epsilon}$ data exhibit an S-shaped curve [*2,9*]. Typical load relaxation data of nickel showing this type of characteristics are shown in Fig. 11 [*9*]. Physically the S-shaped curve results from the difference in the stress dependence of grain matrix strain rate $\dot{\alpha}_I$ (Eq 5) and that of $\dot{\alpha}_g$ (Eq 16). At high stresses, $\dot{\alpha}_g \ll \dot{\alpha}_I$ and according to the grain boundary sliding model (Fig. 4), the grain boundary is unrelaxed and grain matrix deformation will be controlling. At intermediate stresses both $\dot{\alpha}_g$ and $\dot{\alpha}_I$ are important. But at low stresses $\dot{\alpha}_g \gg \dot{\alpha}_I$ such that the grain boundary is relaxed and grain matrix deformation will be controlling again, resulting in the observed S-shaped curve [*5*]. The stress shift between the position of the grain matrix curve at the high stress limit and that at the low stress limit will, according to Eq 15, yield the value of the Y-parameter; for the data in Fig. 11, $Y = 0.84$ [*9*].

The value of the Y-parameter can also be determined from closed stress-strain loops obtained by loading and unloading in a constant displacement rate tension test at high homologous temperatures. Typical loop data of nickel obtained at 600°C are shown in Fig. 12 [*6,9*]. This particular loop is

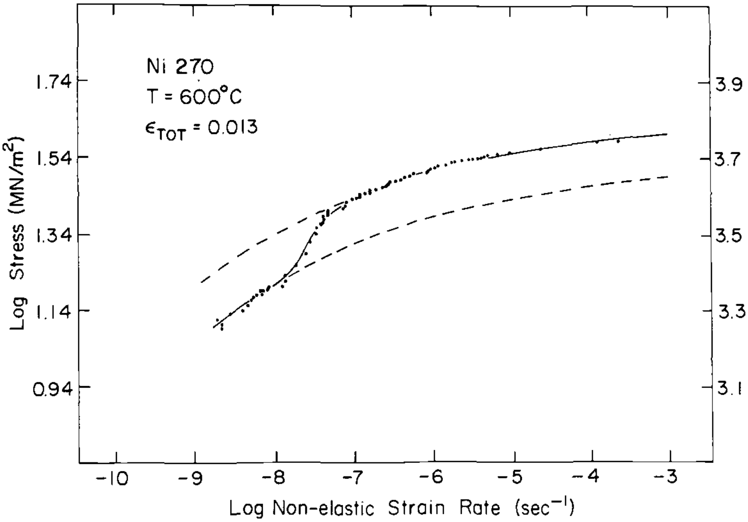

FIG. 11—*Load relaxation data for pure nickel at 600°C showing the effect of grain boundary sliding (S-shaped curve). The two dashed curves represent the limiting grain matrix controlled relaxation behavior. The solid line represents simulation results by using the model shown in Fig. 4.*

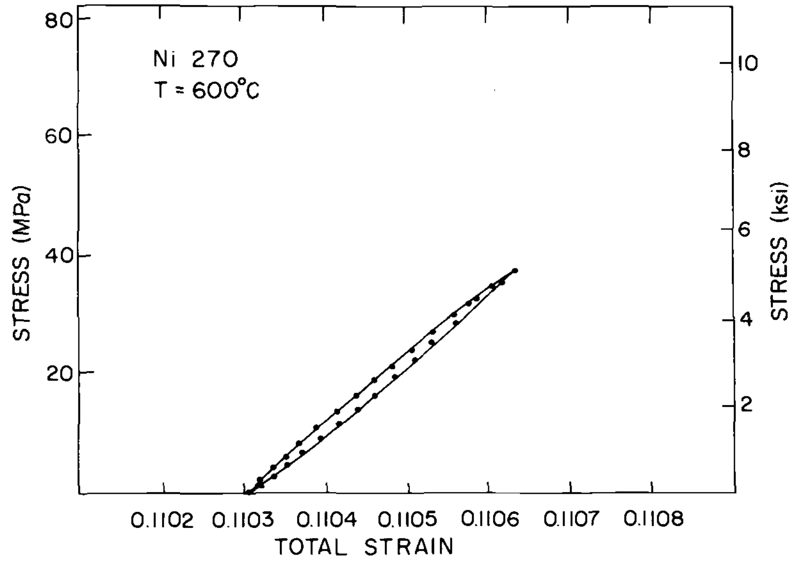

FIG. 12—*Stress-total strain data for pure nickel at 600°C in a constant extension rate tension test upon loading and unloading in the anelastic region. The solid line represents simulation results by using the model shown in Fig. 4. Crosshead speed = 0.05 cm/min.*

one of a series of loops measured at several temperatures beginning at room temperature. For nickel at room temperature the loading portion of the data reflect elastic deformation at low stresses below σ_E and elastic and grain matrix anelastic deformation at higher stresses (between σ_E and σ_A) similar to that represented by the data in Fig. 6. As the temperature is increased, the portion of the loading data controlled entirely by elastic deformation is progressively suppressed and grain boundary anelasticity will become important at high stresses. A series of measurements at several temperatures are important in order to demonstrate that the loading portion of the loop in Fig. 12 reflects elastic and grain matrix anelastic deformation at low stresses and the contribution of grain boundary anelasticity at high stresses. The slope of the high stress portion of the loading data in Fig. 12 yields a value of $Y = 0.89$ [slope $= Y/(1/E + 1/\mathfrak{M})$] [*6*].

The agreement between the values of the Y-parameter obtained by these two methods is necessary in order to justify the validity of the grain boundary sliding model of interest (Fig. 4). The data in Figs. 11 and 12 were obtained from two different specimens. The agreement between their values of the Y-parameter is considered satisfactory. It should be noted that for low melting temperature metals, such as lead and aluminum, their load relaxation data in the temperature range where grain boundary sliding is important do not exhibit S-shaped curves [*11,17*]. For these metals the parameter Y can be determined directly only from stress-strain loop data in the anelastic region.

The flow equation for the grain boundary element and associated parameters can be determined from load relaxation data (Fig. 11) obtained in the temperature range where grain boundary sliding is important. In the plastic region at high homologous temperatures, the grain matrix element (M) in Fig. 4 can be represented by Eq 5. With the value of the Y-parameter known and the appropriate constraint equations in accordance with the model in Fig. 4, the values of $\dot{\alpha}_g$ and σ_{II} for the grain boundary element can be calculated from the σ-$\dot{\epsilon}$ data, and thus the form and the material parameters of Eq 16 for grain boundary sliding.

Many of the current grain boundary sliding models (for example, that by Crossman and Ashby [*18*]) also require the parameter Y or its equivalent. It is difficult, however, to determine this parameter from creep or internal friction data. As discussed previously, the load relaxation data of low melting temperature metals cannot be used conveniently either. The high-temperature strain measurement capabilities described previously are therefore essential to obtain the anelastic stress-strain loop data at high temperatures in order to determine the value of the Y-parameter directly.

Simulation Results

General purpose computer programs have been developed based on the constitutive equations described in this paper to simulate the deformation behavior of polycrystalline solids under a variety of testing conditions [*4,9,13,15*]. These computer programs have been shown to be able to simulate deformation phenomena such as creep, load relaxation, cyclic deformation under an arbitrarily imposed temperature, and stress history by using experimentally determined parameters.

For numerical computation, Eqs 5, 13, and 16 will become very stiff when the ratio of σ^*/σ_a, σ_2^*/σ_{a_2}, or σ_g^*/σ_{11} approaches one. The form of these equations are determined experimentally and is believed to have fundamental significance [*11*]. Numerical methods have been developed to integrate these equations for a variety of applications, including finite element and boundary integral calculations [*4,19,20*]. The form of these equations have not been changed for the convenience of numerical analysis.

Examples of simulation results are described next.

Grain Matrix Plastic Deformation

The capabilities of the present state variable approach to simulate plastic properties governed by grain matrix processes can be demonstrated by the simulation results in Fig. 2 [*4*]. In this example, essentially steady-state creep behavior was obtained directly from the model calculation without the need of thermal recovery. The variation of various internal variables during creep deformation as well as their physical significance are discussed in Ref *4*. In the same reference, other examples of computer simulation and their comparison with experimental data are described, including calculations involving nonuniform stress distributions.

Grain Matrix Transient Deformation

Examples of computer simulation of microplastic deformation and the Bauschinger effect are shown in Figs. 13 and 14 [*7,15*]. The values of the experimentally determined parameters used in the calculation are given in Tables 1 and 2. It is seen from Figs. 13 and 14 that the simulation results show both qualitative and quantitative agreement with experimental data. These results can be used to justify the validity of the proposed second-generation state variable model. An important physical basis of the model is that microplasticity and the Bauschinger effect are governed by the same mechanisms with the same set of physical parameters. Some of the significance of the simulation results can be found also in Refs *7* and *15*. It is hoped that the same model can be applied with further development to phenomena such as cyclic hardening and softening [*21*] and accelerated deformation due to cyclic creep [*22*].

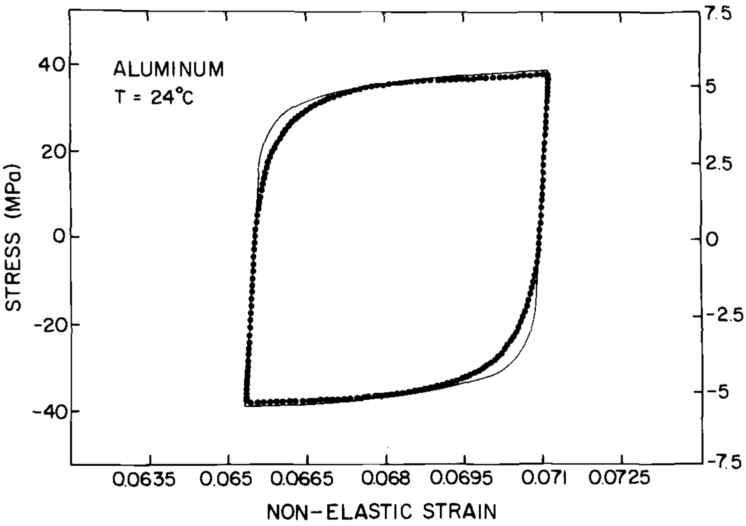

FIG. 13—*Stress-nonelastic strain data for aluminum obtained in a constant displacement rate tension-compression cycle. The solid line represents simulation results by using the model shown in Fig. 3. Crosshead speed = 0.025 cm/min.*

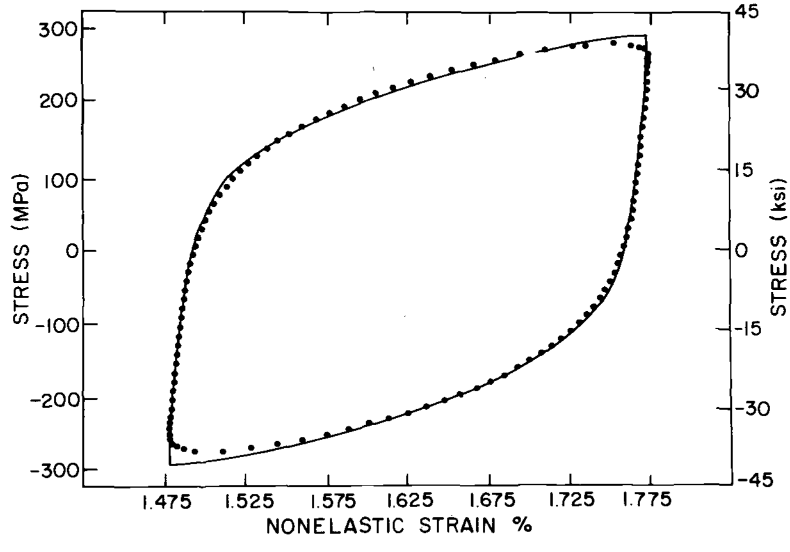

FIG. 14—*Stress-nonelastic strain data for Type 316 stainless steel obtained in a constant displacement rate tension-compression cycle. The solid line represents simulation results by using the model shown in Fig. 3. Crosshead speed = 0.05 cm/min.*

TABLE 1—*Parameters for simulation results in Fig. 13 for aluminum.*

Young's modulus = 4.82×10^4 MPa (7×10^6 psi)
Machine compliance = 8×10^{-4} MPa^{-1} (5.56×10^{-6} psi^{-1})
Initial length = 1.27 cm (0.5 in.)
Initial area = 0.223 cm^2 (3.464×10^{-2} in.^2)

Parameters for the Microplastic and Anelastic Elements

Sigma star 2 (σ_2^*) (minimum) = 0.41 MPa (60 psi)
Epsilon dot star 2 ($\dot{\epsilon}_2^*$) (minimum) = 3.678×10^{-26} (1/s)
Script M 2 ($\mathcal{M}_2$) = 2.97×10^5 MPa (43.1×10^6 psi)
Script M 1 ($\mathcal{M}_1$) = 1.37×10^3 MPa (2.0×10^5 psi)
Lambda 2 (λ_2) = 0.15
Small m 2 (m_2) = 5.0
Initial sigma a 2 ($\sigma_{a_{20}}$) = 34.0 MPa (4.948×10^3 psi)

Parameters for the Plastic Element

Initial sigma star 1 (σ_{10}^*) = 41.4 MPa (6.0×10^3 psi)
Initial epsilon dot star ($\dot{\epsilon}_{10}^*$) = 5.05×10^{-15} (1/s)
Lambda 1 (λ_1) = 0.15
Small m 1 (m_1) = 4.8
Initial sigma a 1 ($\sigma_{a_{10}}$) = 2.98 MPa (4.32×10^2 psi)
Beta (β) = 103 MPa (1.5×10^4 psi)
Delta (δ) = 2.8
Glide friction rate parameter ($\dot{a}^*$) = 5.53×10^{39} (1/s)

TABLE 2—*Parameters for simulation results in Fig. 14 for Type 316 stainless steel.*

Young's modulus = 1.46×10^5 MPa (21.2×10^6 psi)
Machine compliance = 8×10^{-4} MPa^{-1} (5.56×10^{-6} psi^{-1})
Initial length = 1 cm (0.4 in.)
Initial area = 7.06×10^{-2} cm^2 (1.09×10^{-2} in.^2)

Parameters for the Microplastic and Anelastic Elements

Sigma star 2 (σ_2^*) (minimum) = 125 MPa (1.82×10^4 psi)
Epsilon dot star 2 ($\dot{\epsilon}_2^*$) (minimum) = 7.9×10^{-18} (1/s)
Script M 2 ($\mathcal{M}_2$) = 1.45×10^6 MPa (2.1×10^8 psi)
Script M 1 ($\mathcal{M}_1$) = 3.45×10^4 MPa (5.0×10^6 psi)
Lambda 2 (λ_2) = 0.15
Small m 2 (m_2) = 5.0
Initial sigma a 2 ($\sigma_{a_{20}}$) = −140 MPa (-2.03×10^4 psi)

Parameters for the Plastic Element

Initial sigma star 1 (σ_{10}^*) = 220 MPa (3.2×10^4 psi)
Initial epsilon dot star ($\dot{\epsilon}_{10}^*$) = 5.5×10^{-49} (1/s)
Lambda 1 (λ_1) = 0.15
Small m 1 (m_1) = 4.8
Initial sigma a 1 ($\sigma_{a_{10}}$) = −49.6 MPa (-7.2×10^3 psi)
Beta (β) = 1.03×10^3 MPa (1.5×10^5 psi)
Delta (δ) = 1.33
Glide friction rate parameter ($\dot{a}^*$) = 2.1×10^{21} (1/s)

Effects of Grain Boundary Sliding

Examples of computer simulation of grain boundary anelasticity and contribution to plastic deformation by grain boundary sliding are shown in Figs. 11 and 12. The computer program used was constructed based on the grain boundary sliding model in Fig. 4 with Hart's model employed for the grain matrix. The governing equations and the value of the material parameters used are given in Tables 3 and 4. It is seen from Figs. 11 and 12 that the use of an appropriate grain boundary element through different grain matrix mechanisms of accommodation seems to be capable of describing the effects of grain boundary sliding at significantly different stress levels (anelastic versus plastic region). The stress dependence of $\dot{\alpha}_g$ can be estimated through $d(\ell n\sigma_{\mathrm{II}})/d(\ell n\dot{\alpha}_g) = \lambda_g \ell n(\sigma_g{}^*/\sigma_{\mathrm{II}})$ (from Eq 16). By using the values given in Tables 3 and 4, we see that $\dot{\alpha}_g$ shows a nearly linear behavior at low σ_{II} and a highly nonlinear behavior at high σ_{II}. In contrast, previous investigators have used a linear stress dependence for $\dot{\alpha}_g$ in both regions [*5,8,18*]. The examination of the significance of the simulation results and further experimental work in this area are currently in progress.

Engineering Applications

For engineering applications it will be difficult numerically to use the full model such as is in Fig. 4. In complicated numerical computations, the approach taken in this work has been to use only Hart's model because of its

TABLE 3—*Constitutive equations for grain boundary anelasticity and sliding.*

Constraint Equations[a]	Constitutive Relations[a]
$\sigma = Y\sigma_{\mathrm{I}} + (1 + Y)\sigma_{\mathrm{II}}$	$\sigma_{\mathrm{I}} = Ee_{\mathrm{I}}$
$\sigma_{\mathrm{I}} = \sigma_{a\mathrm{I}} + \sigma_{f\mathrm{I}}$	$\sigma_{\mathrm{II}} = Ee_{\mathrm{II}}$
$\sigma_{\mathrm{II}} = \sigma_{a\mathrm{II}} + \sigma_{f\mathrm{II}}$	$\sigma_{a\mathrm{I}} = \mathfrak{M}a_{\mathrm{I}}$
$\dot{\epsilon} = \dot{e}_{\mathrm{I}} + \dot{\epsilon}_{\mathrm{I}}$	$\sigma_{a\mathrm{II}} = \mathfrak{M}a_{\mathrm{II}}$
$\dot{\epsilon} = \dot{e}_{\mathrm{II}} + \dot{\epsilon}_{\mathrm{II}} + \dot{\alpha}_g$	$\sigma_{f\mathrm{I}} = (G^M/\dot{a}^*)^{1/M}(\dot{\epsilon}_{\mathrm{I}})^{1/M}$
$\dot{\epsilon}_{\mathrm{I}} = \dot{a}_{\mathrm{I}} + \dot{\alpha}_{\mathrm{I}}$	$\sigma_{f\mathrm{II}} = (G^M/\dot{a}^*)^{1/M}(\dot{\epsilon}_{\mathrm{II}})^{1/M}$
$\dot{\epsilon}_{\mathrm{II}} = \dot{a}_{\mathrm{II}} + \dot{\alpha}_{\mathrm{II}}$	$\ell n(\sigma^*/\sigma_{a\mathrm{I}}) = (\dot{\epsilon}^*/\dot{\alpha}_{\mathrm{I}})^{\lambda}$
	$\ell n(\sigma^*/\sigma_{a\mathrm{II}}) = (\dot{\epsilon}^*/\dot{\alpha}_{\mathrm{II}})^{\lambda}$
	$\ell n(\sigma_g{}^*/\sigma_{\mathrm{II}}) = (\dot{\epsilon}_g{}^*/\dot{\alpha}_g)^{\lambda_g}$
	$\dot{\sigma}^* = \sigma^*\Gamma\dot{\alpha}_{\mathrm{I}}$
	$\dot{\epsilon}^* = (\sigma^*/G)^m f e^{-Q/RT}$

[a] The subscripts I and II refer to grain matrix elements in the upper and lower branches of the grain boundary sliding model (Fig. 4), respectively.

TABLE 4—*Parameters used to simulate grain boundary anelasticity and sliding.*

Young's modulus = 16.88×10^4 MPa (24.48×10^6 psi)
Machine compliance = 4.64×10^{-3} MPa^{-1} (0.32×10^{-4} psi)
Initial length = 2.54 cm (1 in.)
Initial area = 0.112 cm^2 (0.0174 in.^{2})
Lambda (λ) = 0.15
Capital M = 7.6
Small m = 4.5
Glide friction rate parameter ($\dot{a}^*$) = 7×10^{29} (1/s)
Stress concentration factor (Y) = 0.84
Grain boundary lambda (λ_g) = 0.38
Sigma star GB ($\sigma_g{}^*$) = 68.95 MPa (1×10^4 psi)
Epsilon dot star GB ($\dot{\epsilon}_g{}^*$) = 0.5×10^{-6} (1/s)

Initial σ^* = 43 MPa (6225 psi) for Fig. 11
= 49.8 MPa (7220 psi) for Fig. 12

Initial $\dot{\epsilon}^*$ = 0.15×10^{-8} (1/s) for Fig. 11
= 0.99×10^{-7} (1/s) for Fig. 12

simplicity. The more detailed models can provide subroutines based on which an effective value of the various material parameters of Hart's model can be evaluated for limited ranges of applications. For example, an effective value of the exponent λ in Eq 5 can be used to represent grain matrix plastic deformation as well as the contribution of grain boundary sliding to plastic deformation for a limited temperature range. Similarly an effective value of the modulus in Eq 3 can include the effects of grain boundary anelasticity at high temperatures if the kinetics involved are sufficiently fast [*23*].

In applications where grain matrix deformation predominates, the present approach offers an advantage also in materials characterization. This is because material parameters such as λ, M, m, Q, β, and δ in Eqs 4 to 8 have been shown to be insensitive to the thermal mechanical history of a material and often do not vary significantly from one material to another. Thus only a limited number of material dependent parameters such as $\mathcal{M}$, $\dot{a}^*$, σ^*, and $\dot{\epsilon}^*$ in the same equations need to be determined for a new heat of material. These latter parameters can be measured also by a combination of creep and tensile tests [*23*] for which many laboratories are equipped.

An example of engineering application will be reviewed next in order to demonstrate some of the aforementioned possibilities.

Reference *23* reports an analysis and simulation of inelastic deformation in thin-walled tubes (20 percent cold-worked Type 316 stainless steel) under a variety of loading modes. In the analysis, the nonuniform distribution of stress and strain rate through the thickness of the tube wall was accounted for. Of particular interest is the data shown in Fig. 15, which were obtained in a rapid temperature transient experiment. During the experiment the diametral strain of the tube was measured as a function of time or

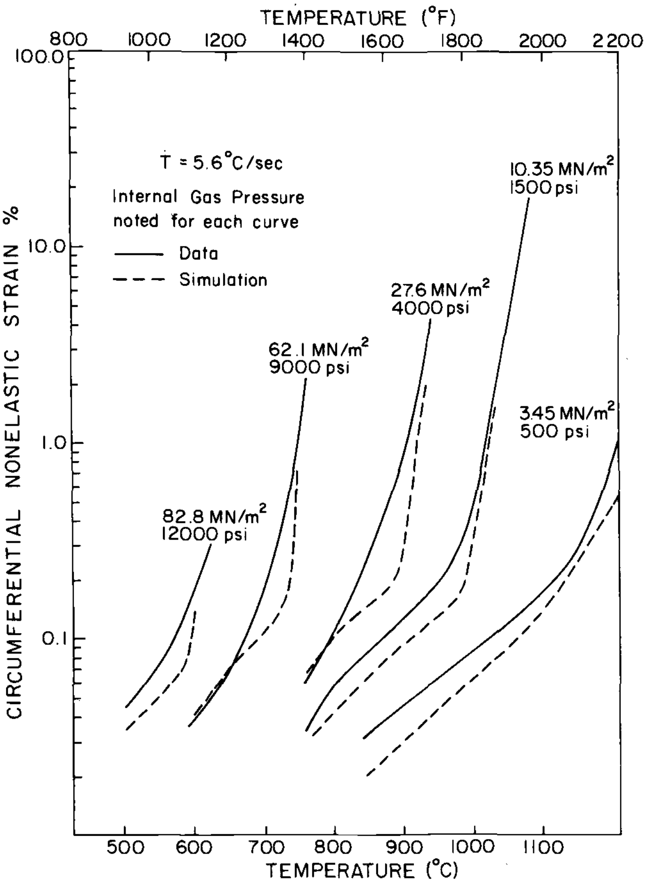

FIG. 15—*Experimental data and simulation results for thin-walled tubes at several internal gas pressures.*

temperature with the temperature rising at a rate of 5.6°C/s, while keeping the internal pressure of the tube essentially constant.

The low-strain portion of the data shown in Fig. 15 represents anelastic deformation and the high-strain portion of the data reflects plastic deformation. The temperature range of the data was such that thermal recovery and recrystallization occurred during the experiment. The ℛ-term in Eq 7 was therefore used in the simulation.

The yield stress of the tube material has been determined as a function of time at different temperatures (Fig. 16) [*23*]. It is seen from this figure that at 649°C thermal recovery of the microstructure occurred as a function of time, while at higher temperatures recrystallization was important. Since the yield

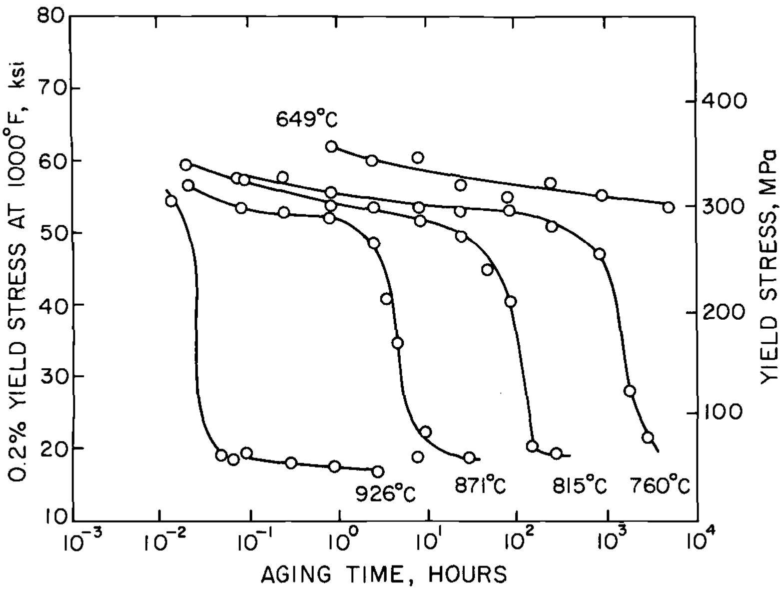

FIG. 16—*Yield stress versus time at several temperatures for 20 percent cold-worked Type 316 stainless steel.*

stress determined at moderate strain rates is a good approximation of the value of the hardness parameter σ^*, the data in Fig. 16 were used to construct an empirical $\mathcal{R}(\sigma^*, T)$ for simulation calculations [*23*].

By assuming fast kinetics the low-strain portion of the data in Fig. 15 was analyzed to yield an effective anelastic modulus as a function of temperature (Fig. 17). The other parameters required for the simulation calculation were found from Refs *2* and *14*, obtained by a combination of load relaxation and tensile tests on a different batch of materials (Table 5). It is seen from Fig. 15 that the simulation results agree reasonably well with experimental data covering a wide range of experimental conditions.

Microstructural Basis

Attempts have been made to identify the microstructural features of a material with the structural parameters of the second-generation model as a basis for the development of dislocation-based theories for the present state variable approach [*15,24*]. The structural parameters of interest include the two hardness parameters σ_1^* and σ_2^* for the strong and weak barriers and the two anelastic moduli $\mathfrak{M}_1$ (long range) and $\mathfrak{M}_2$ (short range).

During the past decade the present work has emphasized the phenomenological aspect of the state variable approach. It is believed that once the phe-

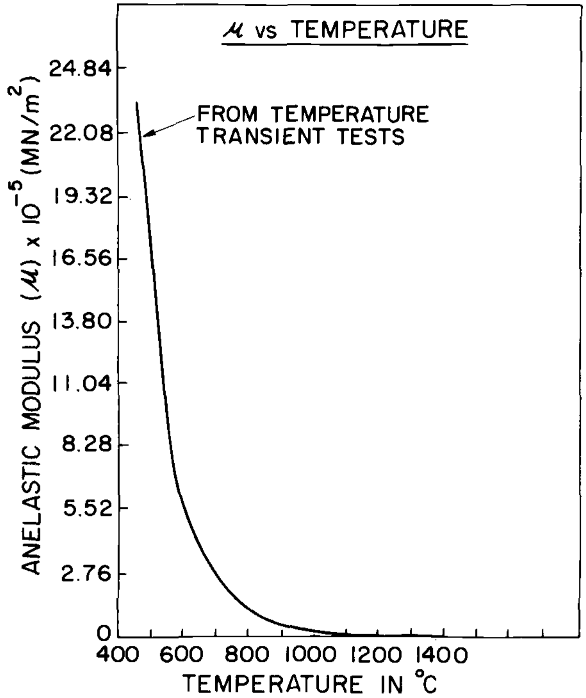

FIG. 17—*Effective anelastic modulus versus temperature for Type 316 stainless steel.*

TABLE 5—*Parameters for simulation results in Fig. 15.*

Symbol	Value
$\mathcal{M}$	see Eq 19 in Ref *23*
σ^*	see Eq 18 in Ref *23*
$\dot{\epsilon}^*$	1.33×10^{-51} (l/s)
λ	0.15
β	1.355×10^3 MPa (1.965×10^5 psi)
δ	1.33
M	8.0
$\dot{\epsilon}_0$	1.0 (l/s) see Ref *23*
σ_0	see Ref *23*
E	see Ref *23*
ν (Poisson's ratio)	0.48
$\mathcal{R}(\sigma^*, T)$	see Eq 18 in Ref *23*
Q	65 000 cal/mol
R	2 cal/mol°K

nomenology of the deformation behavior is well defined, attention can then be turned to the development of the microstructural basis and the related dislocation-based theories.

Preliminary results in the microstructural area are presented. The micrograph and the data shown in Figs. 18 and 19 are for Type 316 stainless steel [*15,24*].

Figure 18 shows a transmission electron micrograph of the microstructure of a deformed Type 316 stainless steel specimen (4 percent plastic strain at an extension rate of 0.05 cm/min at room temperature). This picture was obtained with the electron beam oriented parallel to the activated slip planes [*15*]. It is seen that well-developed low-angle grain boundaries were formed on activated slip planes with less developed low-angle grain boundaries distributed between them. The well-developed low-angle grain boundaries have been identified with the strong barriers in Fig. 3 and the less developed ones with the weak barriers in the same figure [*15*].

Some quantitative information has been obtained [*15,24*]. For example, the ratio of the square of the spacing between the well-developed low-angle grain boundaries and that between the less developed ones is found to be inversely proportional to the ratio of $\mathfrak{M}_1$ and $\mathfrak{M}_2$, the two anelastic moduli, as expected from dislocation theories [*3*]. The hardness parameter representing

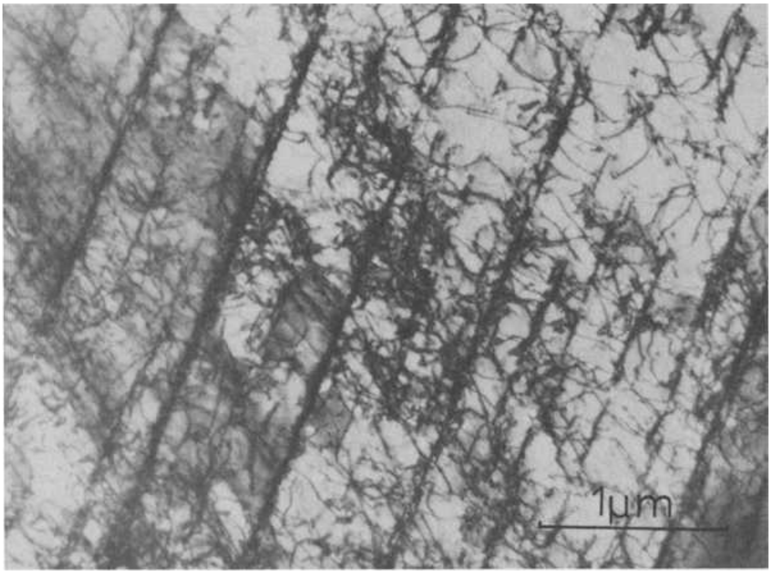

FIG. 18—*Microstructure of Type 316 stainless steel after 4 percent deformation, showing the existence of less developed low-angle grain boundaries in between fully developed low-angle grain boundaries on activated slip planes (×25000).*

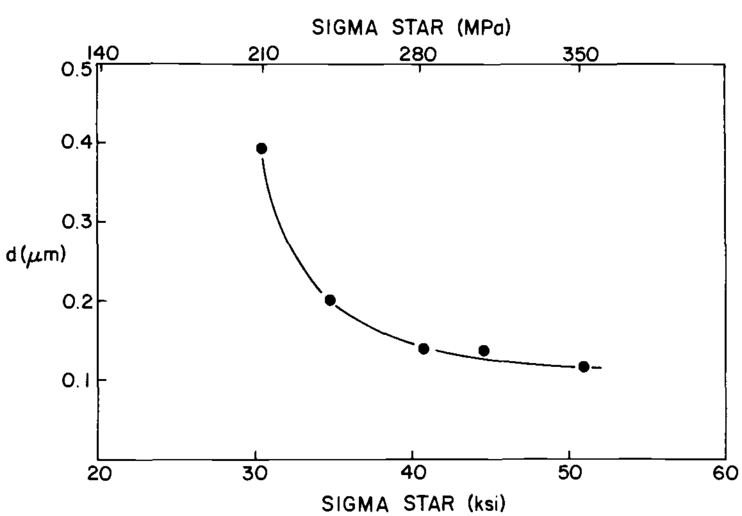

FIG. 19—*A plot of the spacing* (d) *between the activated slip planes versus the hardness parameter* σ_l*.

the strong barriers, σ_1*, is found to be correlated with the spacing of the activated slip planes (Fig. 19). The various σ_1* in Fig. 19 were obtained by deforming a specimen in a tension test at room temperature to different plastic strain levels and were measured by performing a load relaxation test.

Experimental work in this area is directed mainly to developing quantitative correlations between the microstructural data and the structural parameters of the state variable models.

Discussion

An important requirement of the present state variable approach is the compositional and microstructural stability of a material. Reasonable stability is needed in order that the material parameters of the state variable models, especially the material dependent ones (σ_1*, σ_2*, $\dot{\epsilon}_1$*, $\dot{\epsilon}_2$*, $\dot{a}$*, $\mathfrak{M}_1$, $\mathfrak{M}_2$, σ_g*, and $\dot{\epsilon}_g$*), do not change at an undesirable rate during an experiment.

The microstructural stability can be investigated by using electron microscopy. Figure 20 shows electron micrographs taken prior to (a) and after *in situ* annealing (b) of a deformed Type 316 stainless steel (4 percent plastic strain, 0.05 cm/min in tension, at room temperature). The *in situ* annealing was performed at 500°C for 2 h. These micrographs were taken from a region where dislocation tangles predominate. The tangles are less stable than well-developed low-angle grain boundaries (Fig. 18). It is seen from Fig.

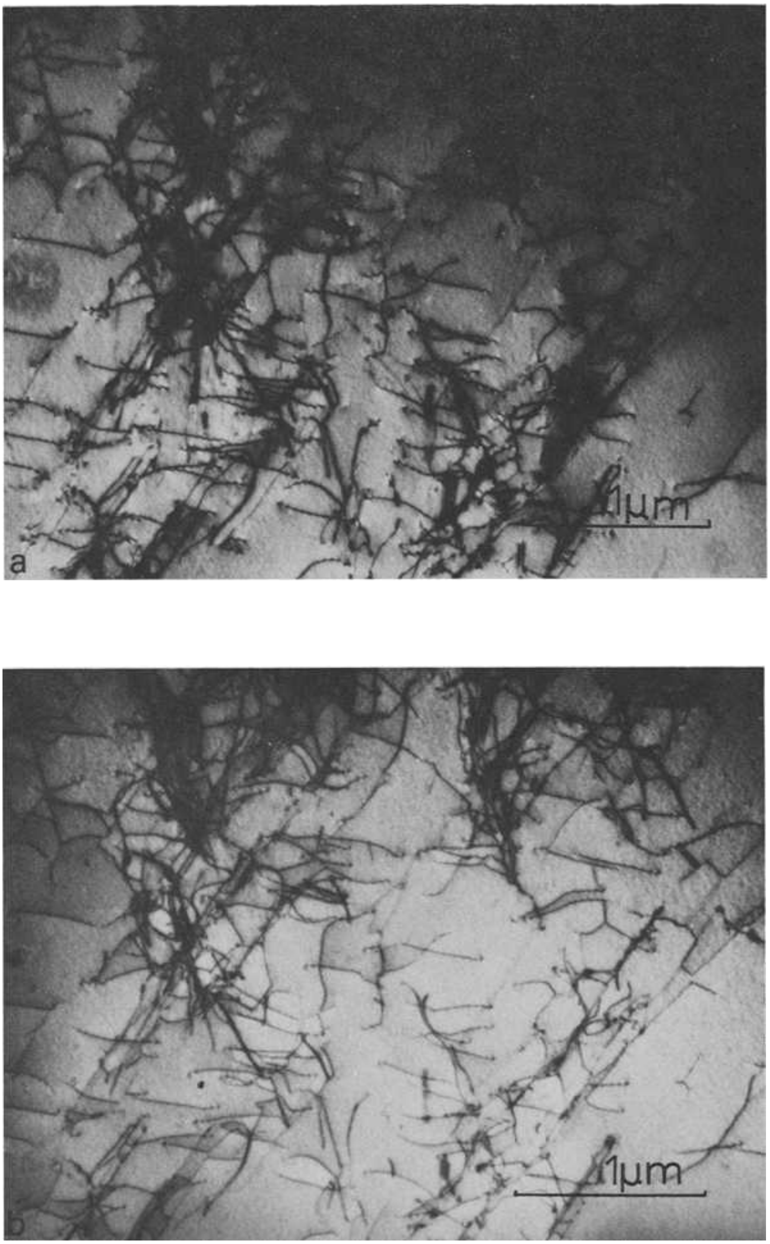

FIG. 20—(a) *The microstructure of a selected area showing dislocation structure in Type 316 stainless steel after 4 percent deformation (×25000).* (b) *The same region as* (a) *after annealing* in situ *for 2 h at 500°C, showing that the main features of the dislocation microstructure remain unchanged.*

20 that the major features of the dislocation structure remained unchanged after annealing.

This and other evidence (for example, the data in Fig. 16) suggest that the hardness parameter σ_1^* which characterizes the strong barriers is quite stable at moderate temperatures. If thermal recovery of the microstructure and recrystallization do occur (Fig. 16), the variation in σ_1^* can be represented by the function $\mathcal{R}(\sigma_1^*, T)$ (Eq 7), provided sufficient experimental information is available, as discussed in the section on Engineering Applications.

On the other hand, parameters such as σ_2^*, $\mathfrak{M}_1$, and $\mathfrak{M}_2$, which are related to the weak barrier structures, are less stable compared with the hardness parameter σ_1^* [*13,15,16*]. Their variations as a result of thermally induced microstructural changes may be responsible for some of the thermal recovery related phenomena reported in the literature. It should be noted that thermally induced recovery of dislocation pileups alone can also produce a reduction in the flow stress in the microplastic region, according to the second-generation state variable model, without any change in the barrier structure. Attention should be given to distinguish the effects caused by thermal recovery of barrier structures from those caused by thermally induced recovery of dislocation pileups, which is part of the deformation processes. The latter effects are related to phenomena such as creep recovery [*25*].

Variations in the material parameters of the state variable models can also be produced by other causes. For example, based on the data in Figs. 5 and 10, the change in the magnitude of the rate parameter $\dot{a}^*$ (Eq 4), which governs the glide friction of dislocations, is believed to be related to drag effects resulting from jog formation or solute-dislocation interactions. The value calculated from the low-temperature data in Fig. 5 (obtained above plastic yieldings) reflects a different degree of drag effect from that involved in the data in Fig. 10 (obtained below plastic yielding in the microplastic region). This type of variation can only be determined experimentally and can cause uncertainties in materials characterization, especially for transient deformation.

As mentioned previously, an attitude of the present work has been that the state variable models described are believed to represent the basic deformation behavior of polycrystalline solids. Phenomena such as thermal recovery of barrier structures and strain aging can be included by time-dependent changes in the appropriate state variables and material parameters of the model.

The work on the development of the present state variable approach is still in progress. Future efforts will be directed towards the construction of dislocation and microstructure based theories for the deformation models and areas such as irradiation effects [*26*] and the effects of thermal-mechanical service history.

Acknowledgments

The authors wish to acknowledge the contribution of their colleagues E. W. Hart, H. Mughrabi, H. Yamada, F. V. Ellis, S. Chao, F. H. Huang, C. W. Cho, C. P. Hu, M. S. Jackson, T. Hakkarainen, and M. Korhonen in the development of the present state variable approach.

The U.S. Department of Energy through the Division of Materials Sciences has provided the major portion of the support for the work reviewed and also the support for the present paper.

References

[*1*] Hart, E. W., *Journal of Engineering Materials and Technology*, Vol. 93, No. 3, 1976, pp. 193-202.

[*2*] Huang, F. H., Yamada, H., and Li, Che-Yu in *Characterization of Materials for Service at Elevated Temperatures*, G. V. Smith, Ed., Series MPC-7, American Society of Mechanical Engineers, 1978, p. 83.

[*3*] Jackson, M. S., Cho, C. W., Alexopoulos, P., and Li, Che-Yu, "A Phenomenological Model for Transient Deformation Based on State Variables," *Journal of Engineering Materials and Technology*, to be published.

[*4*] Kumar, V., Mukherjee, S., Huang, F. H., and Li, Che-Yu, "Deformation in Type 304 Austenitic Stainless Steel," Electric Power Research Institute, Report Number EPRI NP-1276, Dec. 1979.

[*5*] Hart, E. W., *Acta Metallurgica*, Vol. 15, 1967, p. 1545.

[*6*] Li, Che-Yu and Hart, E. W., "Mechanical Properties of Crystalline Solids," DOE Report COO-2172-29, Cornell University, Ithaca, N.Y., 1979.

[*7*] Alexopoulos, P. and Li, Che-Yu, "An Investigation of Cyclic Deformation and Bauschinger Effect in Aluminum and Type 316 Stainless Steel," Materials Science Center Report 4326, Cornell University, Ithaca, N.Y., 1980.

[*8*] Zener, C., *Elasticity and Anelasticity in Metals*, University of Chicago Press, 1948.

[*9*] Keusseyan, R. L. and Li, Che-Yu, "Grain Boundary Anelasticity and Sliding in Nickel," DOE Report DOE/ER/02172-37, Cornell University, Ithaca, N.Y., 1980.

[*10*] Lee, D. and Hart, E. W., *Metallurgical Transactions*, Vol. 2, 1971, pp. 1245-1248.

[*11*] Hart, E. W., Li, Che-Yu, Yamada, H., and Wire, G. L. in *Constitutive Equations in Plasticity*, A. S. Argon, Ed., MIT Press, Cambridge, Mass., 1976, pp. 149-197.

[*12*] Keusseyan, R. L. and Li, Che-Yu, *Journal of Testing and Evaluation*, Vol. 9, No. 3, 1981, pp. 214-217.

[*13*] Cho, C. W., "Inelastic Deformation and Phenomenological Modelling of Aluminum Including Transient Effect," Ph.D. thesis, Cornell University, Ithaca, N.Y., 1980.

[*14*] Huang, F. H., Ellis, F. V., and Li, Che-Yu, *Metallurgical Transactions A*, Vol. 8A, 1977, pp. 609-794.

[*15*] Alexopoulos, P. S., "An Experimental Investigation of Transient Deformation Based on a State Variable Approach," Ph.D. thesis, Cornell University, Ithaca, N.Y., 1980.

[*16*] Alexopoulos, P. S., Cho, C. W., Hu, C. P., and Li, Che-Yu, "Determination of Anelastic Modulus for Several Metals," *Acta Metallurgica*, in press.

[*17*] Wire, G. L., Yamada, H., and Li, Che-Yu, *Acta Metallurgica*, Vol. 22, 1974, p. 505.

[*18*] Crossman, F. W. and Ashby, M. F., *Acta Metallurgica*, Vol. 23, 1975, pp. 425-440.

[*19*] Mukherjee, S. in *Proceedings*, Second International Symposium on Innovative Numerical Analysis in Applied Engineering Science, R. Shaw, Ed., Montreal, 1980, pp. 361-372.

[*20*] Morjaria, M. and Mukherjee, S., "Finite Element Analysis of Time-Dependent Inelastic Deformation in the Presence of Transient Thermal Stresses," in *International Journal for Numerical Methods in Engineering*, accepted for publication.

[*21*] Feltner, C. E. and Laird, C., *Acta Metallurgica*, Vol. 15, 1967, pp. 1621-1632.

[*22*] Shetty, D. K. and Meshii, M., *Metallurgical Transactions A*, Vol. 6A, 1975, pp. 349-358.

[23] Wire, G. L., Duncan, D. R., Cannon, N. S., Johnson, G. D., Alexopoulos, P. S., Mukherjee, S., and Li, Che-Yu, "A State Variable Analysis of Inelastic Deformation of Thin Walled Tubes," *Journal of Engineering Materials and Technology*, to be published.
[24] Alexopoulos, P., Hakkarainen, T., and Li, Che-Yu, "An Investigation of the Relationship Between Microstructure and Deformation Based on State Variable Approach," Department of Energy Report DOE/ER/02172-36, Cornell University, Ithaca, N.Y., 1980.
[25] Henderson, J. and Snedden, J. D., *Journal of Mechanical Engineering Science*, Vol. 10, No. 1, 1968, pp. 24-35.
[26] Hart, E. W. and Li, Che-Yu in *Zirconium in the Nuclear Industry, ASTM STP 633*, American Society for Testing and Materials, 1976, pp. 315-325.

DISCUSSION

R. J. DiMelfi[1] *(written discussion)*—The integrated form of the Hart Equation of State that is often seen in the open literature gives, for the flow stress, σ, at constant strain-rate and temperature,

$$\sigma = \sigma^* \exp(-A\sigma^{*M\lambda})$$

where A, M, and λ are constants at constant strain rate and temperature. Examination of this equation reveals that the flow stress increases with increasing hardness, σ^*, up to some value of the hardness. Then, the flow stress decreases rapidly to a very small value upon further increase of the hardness even at low temperature. This is purely an artifact of the algebraic form of the equation, unrelated to a particular deformation mechanism. This result appears to contradict the observation of a saturation flow stress achieved in Type 316 stainless steel irradiated to high neutron fluence at low temperature. This contradiction is significant, since the foregoing equation is used by the authors of this paper to model the mechanical behavior of Type 316 stainless steel cladding tubes subjected to thermal-mechanical loading situations that are beyond standard data bases.

P. Alexopoulos, R. L. Keusseyan, G. L. Wire, and Che-Yu Li (authors' closure)—The equation presented by DiMelfi is obtained by combining the flow equation for dislocation climb controlled macroplastic deformation;

$$\ell n(\sigma^*/\sigma) = (\dot{\epsilon}^*/\dot{\epsilon})^\lambda$$

and its scaling relation:

$$\dot{\epsilon}^* = B(\sigma^*)^m$$

---

[1] Reactor Analysis and Safety Division, Argonne National Laboratory, Argonne, Ill. 60439.

For strain rates usually experienced, $\dot{\epsilon} \gg \dot{\epsilon}^*$ such that at a given strain rate and temperature σ increases with σ^*.

But at extremely low strain rates and usually experienced σ^*, the situation of σ decreasing with increasing σ^* is predicted by the above equations. There is, however, no experimental evidence to support this type of prediction. A discussion of the latter type of behavior is given in Ref *11*.

D. B. Duncan[1] *and W. H. Giedt*[2]

Prediction of Deformations During Gas-Tungsten-Arc Stationary Welds

REFERENCE: Duncan, D. B. and Giedt, W. H., "**Prediction of Deformations During Gas-Tungsten-Arc Stationary Welds,**" *Mechanical Testing for Deformation Model Development, ASTM STP 765,* R. W. Rohde and J. C. Swearengen, Eds., American Society for Testing and Materials, 1982, pp. 185–201.

ABSTRACT: Local temperature measurements on the heated and unheated surfaces and strain measurements on the unheated surfaces of unrestrained circular weld specimens of annealed and cold-rolled Nitronic 40 stainless steel during stationary welding are compared with values predicted from finite-element programs for temperature and strain variations. Experimental and predicted temperature histories agree within 10 percent. Predicted and measured hoop strain profiles (using a moiré fringe technique) for the unheated surface are compared, showing significant deviations near the central region. Transient deflection measurements of the unheated specimen surfaces show good agreement with theory during the period the arc is operating. Close agreement in deflection behavior was observed during the cooling portion of the weld cycle for the annealed specimen, whereas substantial deviations occurred for the cold-rolled specimens.

KEY WORDS: gas-tungsten-arc welding, moiré effects, numerical analysis, stainless steels, thermoplasticity, finite element analysis

The familiar process of arc welding is a combination of rather complex and rapidly interacting phenomena. A concentrated source of energy (the high-temperature plasma of the arc) supplies heat to melt a limited amount of material on either side of a joint. Joining is achieved as this material fuses together and solidifies. Although this process is simple in concept, the heating must be very intense in order to limit the amount of material melted, the thermal damage to surrounding material, and the energy required. It is apparent that very high spatial and temporal gradients will occur during both melting and solidification.

The complex thermal and metallurgical phenomena in a weld zone are ac-

---

[1] Lawrence Livermore National Laboratory, Livermore, Calif. 94550.

[2] Department of Mechanical Engineering, University of California, Davis, Calif. 95616.

companied by equally complex stress and strain variations. After initial straining due to thermal expansion, the melted region goes through a stress-free state followed by contraction during solidification and cooling of the fusion zone. Temperatures in the region surrounding the molten zone, the heat-affected zone (HAZ), are sufficient to cause some recrystallization in cold-rolled materials. This means that properties in this region will change significantly. Only in the region surrounding the HAZ can the commonly used physical properties be expected to apply during the entire process.

The interactions during melting and solidification cause complex stress and strain fields, which are very important characteristics of a welded joint. Hence considerable effort has been devoted to understanding the basic process, with the objective of being able to predict temperature variations and stress and distortions for specified welding conditions.

The application of heat-source solutions to calculate weld-zone temperatures [*1,2*] provided very helpful qualitative information.[3] The use of these results to calculate stresses and strains was very limited because of the complexity of the problem and the question of accuracy for the temperatures in the fused and heat-affected zone. The recent availability of large computers has made possible a more precise and integrated study of the problem. Both finite-element and finite-difference techniques are being used to analyze the thermal-mechanical processes occurring during welding [*3-6*]. Recent attention has been devoted to the finite-element (FE) method. This approach appears to be more adaptable to systems in which there is concurrent interest in both thermal and mechanical behavior.

A recent review [*7*] of reported analyses of gas-tungsten-arc (GTA) welding showed that the applicability of current theoretical models has not been established. This is in part due to the lack of definitive experimental measurements and required thermal and mechanical property values. The present investigation was therefore undertaken to study the behavior of a simple system so that a minimum number of factors would be involved and measurements could be clearly interpreted and compared with predictions. Experiments consisted of stationary GTA welds on circular unrestrained plates. Temperature and deformation measurements were made in a controlled-atmosphere chamber, and are compared with predictions from thermal [*8*] and mechanical [*9*] finite-element computer codes.

Procedure

The general arrangement of the test apparatus is shown in Fig. 1. The welding electrode and round plate specimens were mounted in a cylindrical chamber. The chamber was evacuated to a pressure of 300 μm, back-filled with argon, re-evacuated, and then again filled with argon to atmospheric

[3] The italic numbers in brackets refer to the list of references appended to this paper.

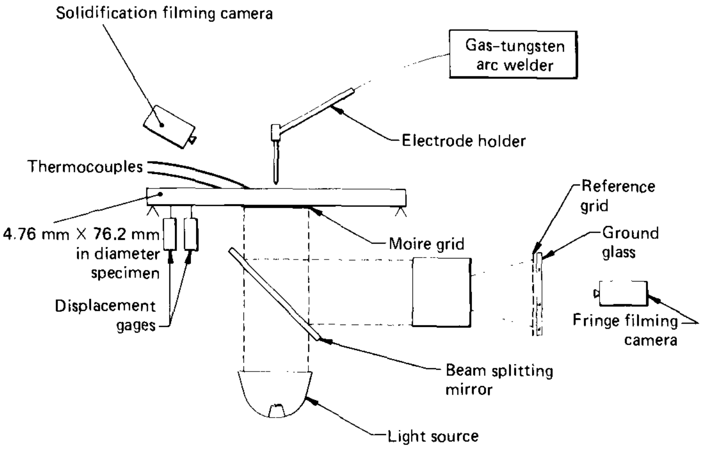

FIG. 1—*Schematic of experimental system.*

pressure. A screen-covered, toroidal orifice surrounded the electrode to direct a flow of argon gas along the axis of the electrode, causing the necessary purging of metal vapor from the arc plasma region. It was possible to form and operate an arc with the conventional shroud around the lower end of the electrode. Thus there was an unobstructed view of the arc region. A precision XYZ mechanism was used to position the electrode tip. Power was supplied by a programmable power supply.

During solidification, color motion pictures were taken with a 16-mm camera at 64 frames per second, clearly revealing the location and movement of the liquid-solid interface. Temperatures on the upper and lower surfaces were measured with Chromel-Alumel thermocouples 0.125 mm in diameter, spot welded to the specimens. The fusion zone size and shape were determined from postweld sectioning of specimens.

All specimens were made from Nitronic 40 stainless steel and were from the same heat to assure nearly identical chemical composition, which was approximately 21 percent chromium, 6 percent nickel, and 9 percent manganese. The nickel content is large enough to maintain a stable austenitic structure throughout the weld temperature cycle. Cold-rolled specimens were cross rolled to minimize in-plane anisotropic effects. All specimens were 76.2 mm in diameter and 4.75 mm thick.

The strain field on the unheated sides of the specimens were measured using a moiré fringe technique. A rectangular grid was made on a lapped and polished surface of the specimen. The grid pattern was contact-printed on a specimen that was coated with photosynthetic etch resist, from a glass slide that had a rectangular grid image. The photosynthesized areas were then etched off leaving a grid pattern such as shown in Fig. 2. Each dot was approx-

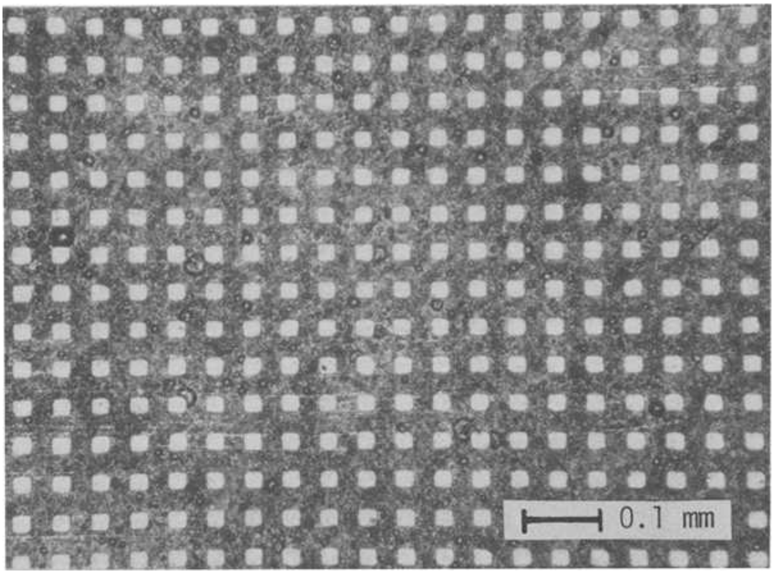

FIG. 2—*Moiré grid etched on Nitronic 40 specimen.*

imately 0.025 mm on a side; the distance between centers was approximately 0.050 mm.

The image of the specimen grid was projected through a reference grid onto a ground glass as shown in Fig. 1. Focal distances were selected such that the specimen and reference grid frequencies were slightly mismatched, thus creating an interference pattern. Since there was no angular mismatch between the reference and specimen grids, the initial image is a magnified version of the specimen grid pattern. Initial fringe spacing was approximately 25 times the 0.050-mm dot pattern spacing.

Strains were determined by observing changes in the moiré fringe spacing using the relationship

$$\epsilon = \frac{P}{F} - \epsilon_0 \tag{1}$$

where P is the grid pattern spacing, F the moiré fringe spacing, and $\epsilon_0 = P/F_0$. Thus the initial apparent strain created by mismatching the specimen and fringe spacing is subtracted from the measured strain to obtain the actual strain. The changes in the moiré fringe pattern were recorded every 0.4 s using a time-controlled 35-mm camera.

The dynamic out-of-plane displacement behavior was measured using inductance-type displacement gages. Spherical contacts were used on the displacement gages to minimize thermal losses into the transducers. Residual contours were measured using a profilometer.

Since it was impossible to make all the measurements desired during a single weld, data were obtained during several tests. Every effort was made to provide identical energy inputs and flux distribution into each of the specimens by using identical weld parameters. The current was 160 A for a 3-s arc duration. The same electrode material and electrode shape was maintained, namely a 3.2-mm-diameter thoriated tungsten electrode with a tip machined to a slender, sharp point. The electrode gap was carefully set to be the same from one experiment to the next. The argon shielding gas flow rate was 990 L/h, with a 10-s pre- and postpurge, and gas compositions were unchanged throughout the experiments.

Temperature data were recorded on an oscillograph; displacement measurements were made with a strip-chart recorder. A recording of the time of arc initiation was produced by a signal from the welding power supply.

Thermal and Deformation Modeling

Although thermal and mechanical response are coupled during welding, simultaneous calculation of the temperature and stress variation is a formidable task. Fortunately, coupling effects are not controlling, and it is possible to treat the thermal and mechanical problems separately. A general-purpose FE heat transfer program (TACO), recently developed by Mason [*8*], was used to calculate temperature variation. This is an implicit program which solves the nonlinear heat conduction with arbitrary heat input and boundary conditions. Since Lagrangian coordinates are used, only relatively small movement can be tolerated. This requires the weld pool to be modeled as stationary. Pool convection is accounted for by using a high value of the thermal conductivity. The heat of fusion is simulated with a step increase in specific heat capacity. Thermal property variations that were used are presented in Fig. 3, and are based on handbook and manufacturer's data. The radial variation in heat input was specified by (from Ref 5):

$$q(r) = \frac{3Q}{\bar{r}^2} \exp\left[-3 \left(\frac{r}{\bar{r}} \right)^2 \right] \tag{2}$$

Here, $\bar{r}$ equals the radius within which 95 percent of the energy is transferred. This was determined as the radius of the discolored area on the heated surface outside the fusion region. The total heat transferred, q, was determined by requiring the predicted depth of penetration to approximately match the value determined from a cross-sectioned specimen. The reasoning involved was to match approximately the volume of metal melted by the arc with that predicted from the assumed heat flux distribution.

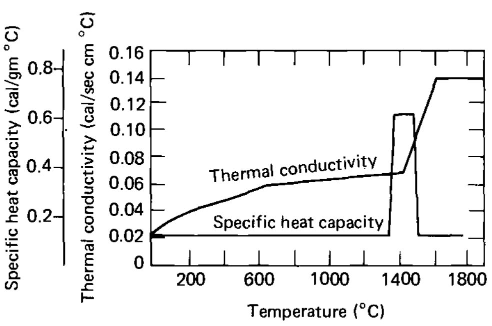

FIG. 3—*Variation of thermal properties with temperatures (based on data from Refs* 10 *and* 11*).*

The deformation behavior was calculated by using an implicit FE program (NIKE2D) developed by Hallquist [*9*]. The temperature variation calculated by TACO has been incorporated as the input to NIKE2D, which accounts for the thermal strain behavior and temperature-dependent material properties by means of a thermoplastic constitutive model. The code compares current stress levels against the following yield criterion:

$$0 \le \frac{1}{2}\left|\sigma_{ij} - \frac{\sigma_{kk}}{3}\delta_{ij}\right|\left|\sigma_{ij} - \frac{\sigma_{kk}}{3}\sigma_{ij}\right| - \frac{\bar{\sigma}^2}{3} \qquad (3)$$

where $\bar{\sigma}$ is the effective yield stress, including work-hardening effects. When plastic behavior is considered, the following differential expression describes the thermo-mechanical behavior:

$$d\sigma_{ij} = C_{ij,k\ell}(d\epsilon_{k\ell} - d\epsilon_{k\ell}{}^{P} - d\epsilon_{k\ell}{}^{T}) + \frac{dC_{ij,k\ell}}{dT}(\epsilon_{k\ell} - \epsilon_{k\ell}{}^{T})dT$$

where $C_{ij,k\ell}$ is the temperature elastic constitutive matrix, and $d\epsilon_{k\ell}$, $d\epsilon_{k\ell}{}^{P}$, and $d\epsilon_{k\ell}{}^{T}$ are the incremental total, plastic, and thermal strains, respectively. NIKE2D calculates incremental stresses and strains so that the constitutive implemented in the code is formulated accordingly.

Since the mechanical properties are a function only of temperature (as illustrated in Fig. 4 for Nitronic 40), the behavior is modeled as being a function only of the current temperature state without accounting for the effect of the temperature history. Thus, annealing, high-temperature creep, recrystallization, phase change behavior, and solidification substructure effects are not accounted for. Also, the secant modulus is used for the plastic region, based on ultimate strength, yield strength, and elongation to failure. It is recognized

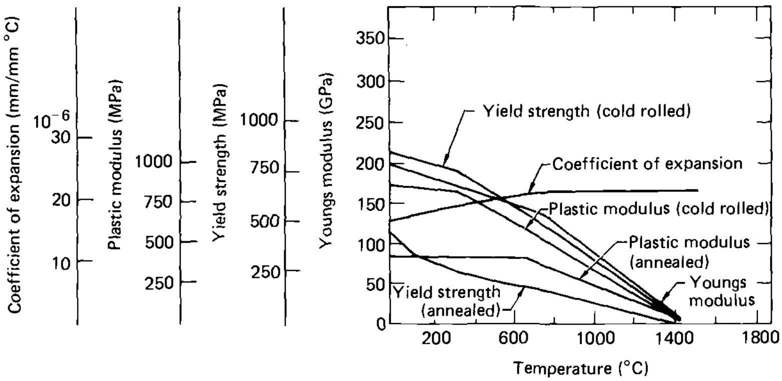

FIG. 4—*Variation of mechanical properties with temperature (based on data from Ref* 11*).*

that the tangent modulus would be more accurate, but necessary data were not available.

Illustrative calculated results for the residual effective stress and strain are shown in Fig. 5.

Discussion

Measured and predicted temperature variations at three locations are shown in Fig. 6 for an annealed Nitronic 40 specimen. The weld current of 160 A and time of 3 s were selected to produce a partial penetration weld and to cause as little damage as possible to the grid pattern on the unheated surface. The general trends of the measured and predicted curves are in good agreement. Maximum deviations on the order of 50°C are thought to be primarily due to differences between actual thermal properties and those shown in Fig. 3, and the approximate modeling of the convection in the molten fusion zone.

Lorentz-force-induced convective cells in the molten pool and the stagnation point flow of the arc plasma gas on the pool surface are primary contributors to the fusion zone shape. Fortunately, the length-squared nature of heat conduction causes the errors between predicted and observed isotherms to dampen out quickly in the HAZ. This can be seen by comparing the shape of the recrystallized region of the cold-worked specimen in Fig. 7 with the overlayed isotherm. Local errors in the temperature gradients in and near the fusion zone cause relatively small errors in the deformation predictions, since materials at near-melt temperatures have relatively little mechanical strength.

Illustrative frames of the moiré fringe pattern photographs are shown in Fig. 8. Hoop strain distributions determined from the photographic sequences for annealed and cold-rolled specimens are compared with the predicted varia-

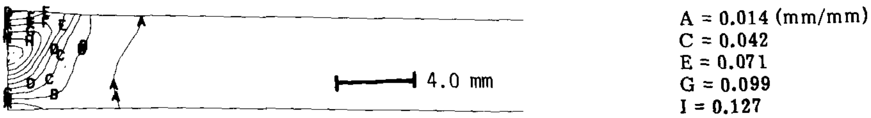

a) Effective strain for annealed specimen.

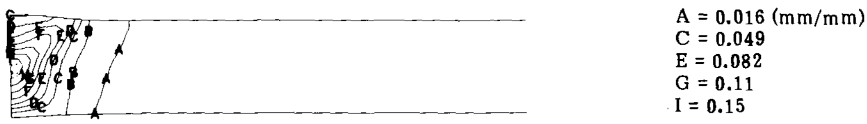

b) Effective strain for cold-rolled specimen.

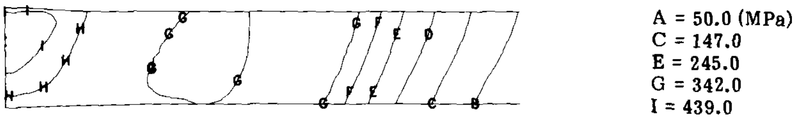

c) Effective stress for annealed specimen

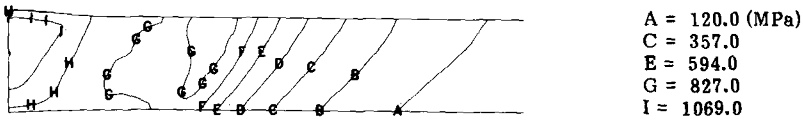

d) Effective stress for cold-rolled specimen

FIG. 5—*Contour plots of effective stress and strain for annealed and cold-rolled specimens. The plots show a portion of a cross section; the axis of the circular plate is the left edge of the plots.*

tions in Figs. 9 and 10 at 2.5 and 3.6 s after arc initiation. A similar comparison of residual hoop strain variation is presented in Fig. 11.

Referring to Figs. 9, 10, and 11, it can be seen that the moiré fringe measurements show the unheated surface to experience tensile stain initially, but that this is gradually changed to a compressive strain. In contrast, the calculated distributions for the annealed specimens remain tensile in the central region. The possibility of this being due to inappropriate mechanical properties was investigated by acceptable variations of the coefficient of expansion, the yield strength, and the plastic modulus in the computer calculations. Results still indicated a tensile strain in the central 2.50-mm region. It is

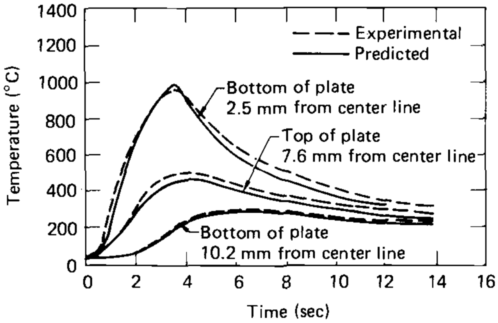

FIG. 6—*Temperature variation in Nitronic 40 stainless steel.*

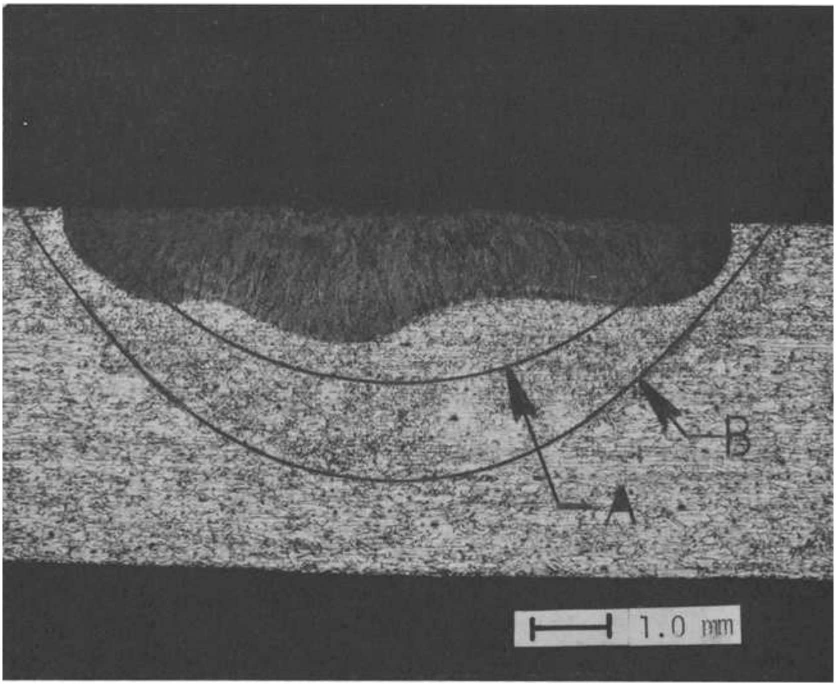

FIG. 7—*Micrograph of weld on cold-rolled specimen with overlayed isotherms representing the* (A) *predicted fusion zone and* (B) *approximate recrystallization region.*

therefore hypothesized that the reason for this is due to substantial changes of the mechanical properties of the fusion and heat-affected zones. It is also possible that a different constitutive relation or relations are needed to describe the deformation of this material when it is at temperatures near melting. The

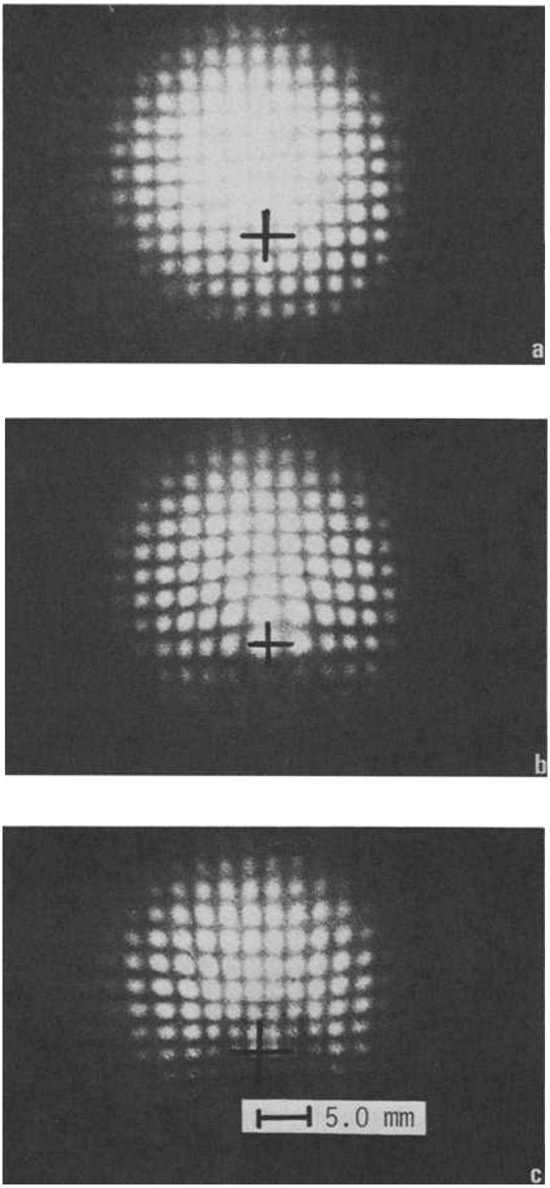

FIG. 8—*Photographs of moiré fringe patterns taken at 2.45 s, 3.6 s, and 2 min. The center of the specimen is indicated by the cross.*

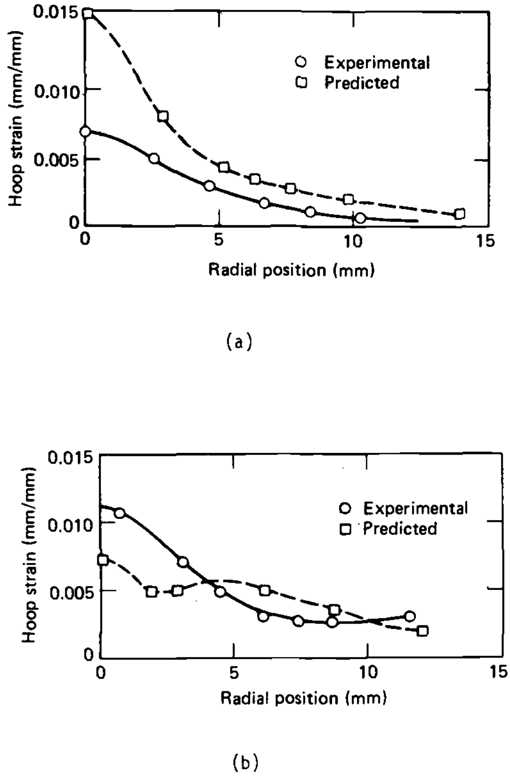

FIG. 9—*Hoop strain profiles for the unheated surface of* (a) *annealed and* (b) *cold-rolled specimens at 2.4 s.*

fact that the predictions of the residual hoop strain for the cold-rolled specimens becomes compressive in the central region is attributed to the much higher strength of this material and to the increased ease of creep in the high-temperature regions of the weld.

As a first step to improving the modeling of material behavior, the inclusion of a maximum-temperature-controlled constitutive model should be considered. After a region exceeds a temperature where a structural property change occurs (that is, recrystallization, melting, etc.), the code would switch to the material behavior description for that region to a new set of property versus temperature curves. Thus, during the heating cycle one set of property curves is used; during cooling, different material property curves are followed. The rationale for this type of model is based upon the concept that many material structure changes occur at high temperatures where the mechanical strength is low. Thus the region is nearly stress free. This type of model would

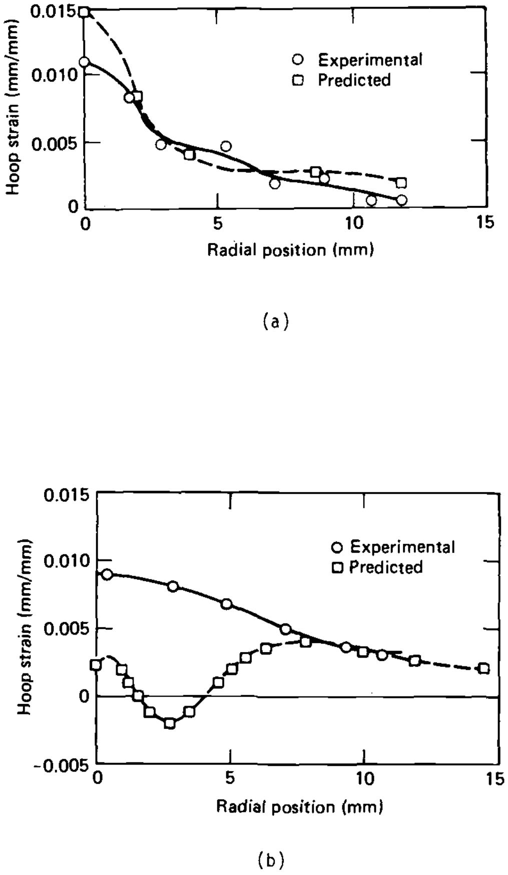

FIG. 10—*Hoop strain profiles for the unheated surface of* (a) *annealed and* (b) *cold-rolled specimens at 3.6 s.*

not be valid for low-temperature structure changes, the near melt temperature strain behavior, nor would it better model creep behavior. In the following section, note how annealing and recrystallization had virtually no effect on the deformation during the heating portion of the weld thermal cycle.

Measured and predicted vertical displacement variations with time at the specimen centerline and 18.0 mm from the center are plotted in Figs. 12 and 13. Comparisons of the final vertical distortions with radial distance are shown in Fig. 14.

The time variation of the predicted and observed vertical deformations at the center and 18.0 mm from the center can be seen in Figs. 12 and 13 to be in acceptable agreement during the time the arc is operating. However, for the
]

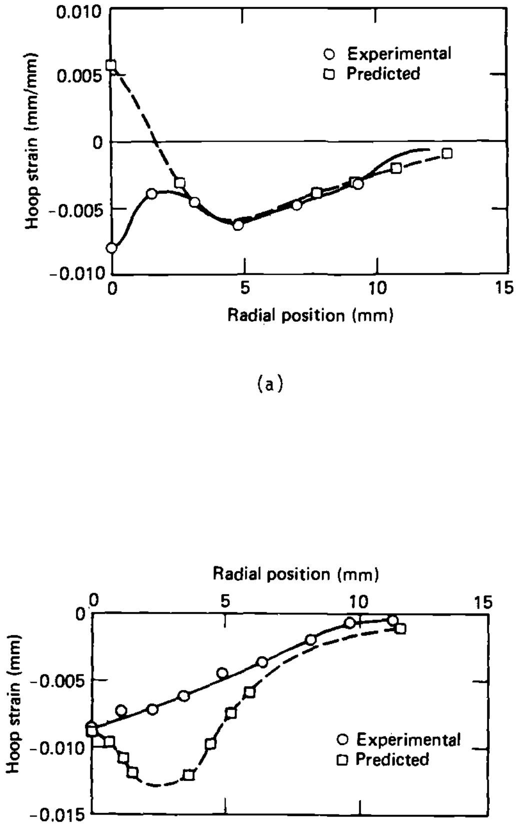

FIG. 11—*Residual hoop strain profiles for the unheated surface of* (a) *annealed and* (b) *cold-rolled specimens.*

cold-rolled specimens, shortly after the arc is extinguished and cooling begins, the predicted and measured curves start to deviate. This trend continues through the cooling period, leading to a dramatic difference between predicted and measured residual deformations (Fig. 14). This behavior, attributed to creep in the cold-rolled specimens, may occur due to the high density of dislocations present. It is interesting to note that this effect continues long after the temperature gradients in the plate thickness direction have become negligible.

In contrast, the predicted and measured vertical deformation variations of the annealed specimens are in relatively good agreement during both the welding and cooling periods. The residual deformations shown in Fig. 14 illustrate that little creep behavior occurred throughout the cooling period, as might be anticipated for an annealed microstructure.

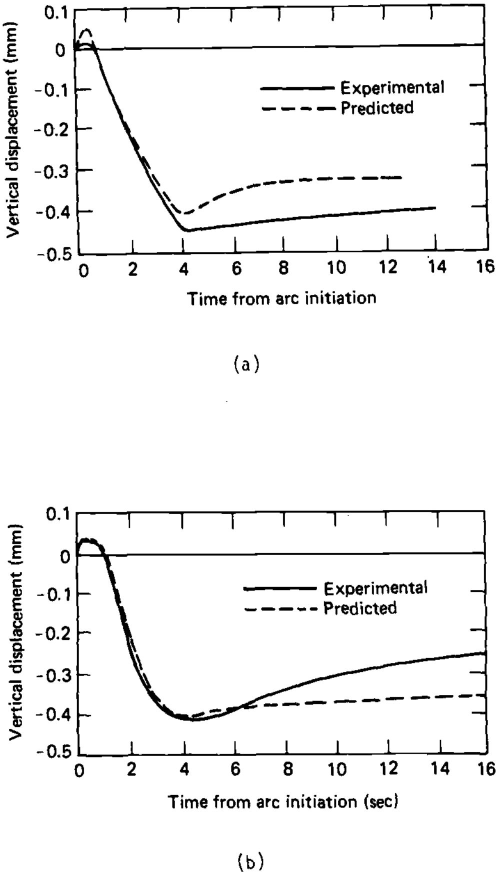

FIG. 12—*Measured and predicted vertical distortion for* (a) *annealed and* (b) *cold-rolled specimens at the centerline.*

Conclusions

Temperature variations as measured with thermocouples adjacent to the fusion zone were satisfactorily predicted by the FE thermal code used. This can be attributed to the program calculating the general shape of the fusion zone. Local differences between the shape of the actual and predicted molten regions occurred, however, which were due to incorrectly accounting for molten zone convection and inaccurate high-temperature thermal property values. Errors in temperature gradients in this region contributed to observed differences between predicted and measured hoop strains at the center of the unheated surface of the specimens. However, this had relatively little effect

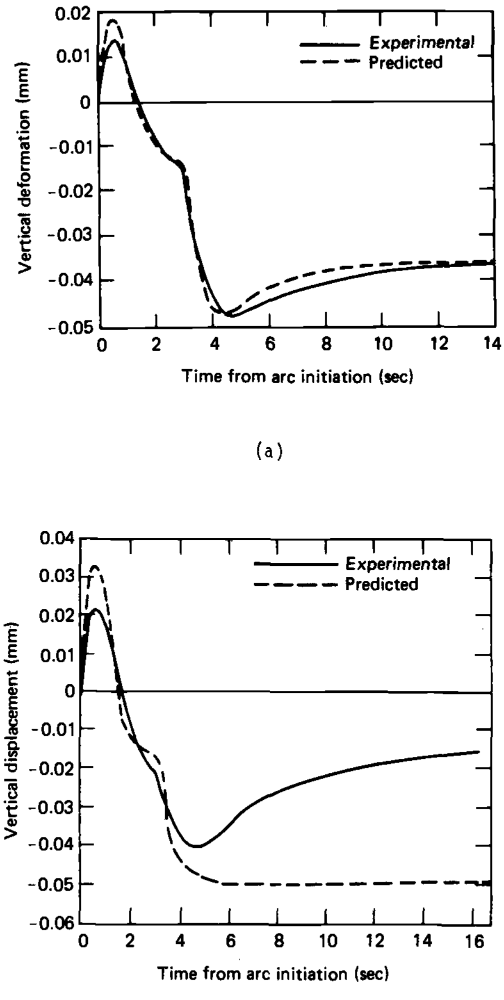

FIG. 13—*Measured and predicted vertical distortion for* (a) *annealed and* (b) *cold-rolled specimens at 18.0 mm from the centerline.*

on the accuracy of deformation predictions, as was evidenced by the experiments on annealed specimens. Failure to account for time-dependent behavior of the cold-rolled material introduced significant errors in the deformation predictions. The use of a thermoplastic constitutive model was satisfactory for the prediction of deformation behavior in welds on an annealed specimen.

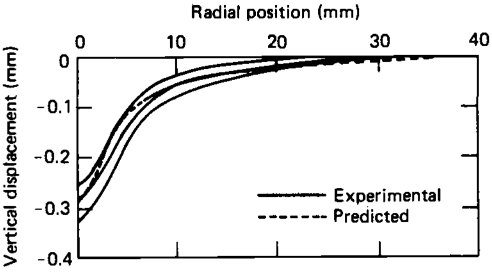

(a)

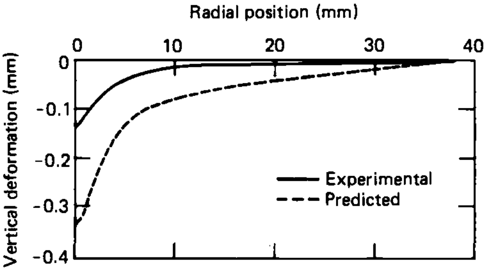

(b)

FIG. 14—*Comparison of final measured and predicted distortion profile for* (a) *annealed and* (b) *cold-rolled specimens.*

Acknowledgments

The authors wish to express sincere appreciation for the invaluable assistance of James Moore in setting up and carrying out the experimental measurements. This work was performed under the auspices of the U.S. Department of Energy by the Lawrence Livermore National Laboratory under Contract Number W-7405-Eng-48.

References

[*1*] Myers, P. S., "Fundamentals of Heat Flow in Welding," Welding Research Council Bulletin No. 123, 1967.

[*2*] Rosenthal, D., "Mathematical Theory of Heat Distribution During Welding and Cutting," *Welding Journal*, 1941, pp. 220-234.

[*3*] Masubuchi, K., *Analysis of Welded Structures*, Pergamon Press, New York, 1980.

[*4*] Hibbitt, H. D. and Marcal, P. D., *Computers and Structures*, Vol. 3, 1973, pp. 1145-1174.

[*5*] Friedman, E., *Journal of Pressure Vessel Technology, Transactions of ASME*, Vol. 97, Series J, No. 3, 1975, pp. 206-213.

[*6*] Rybicki, E. F., Schmueser, D. W., Stonesifer, R. B., Groom, J. J., and Mishler, H. W., *Journal of Pressure Vessel Technology, Transactions of ASME*, Vol. 100, 1978, pp. 258-262.

[*7*] Duncan, D. B., "Thermo-Mechanical Modeling of the Gas-Tungsten-Arc (GTA) Welding Process," Ph.D. thesis, University of California, Lawrence Livermore National Laboratory, Rept. UCRL-52891, 1980.

[*8*] Mason, W. E., Jr., "TACO - A Finite Element Heat Transfer Code," University of California, Lawrence Livermore National Laboratory, Rept. UCID-17980, Rev. 1, 1980.

[*9*] Hallquist, J. O., "NIKE2D - An Implicit, Finite-Deformation, Finite-Element Code for Analyzing the Static and Dynamic Response of Two-Dimensional Solids," University of California, Lawrence Livermore National Laboratory, Rept. UCRL-52678, 1979.

[*10*] Peckner, D., *Handbook of Stainless Steels*, McGraw-Hill, New York, 1977.

[*11*] "Armco Nitronic 40 Stainless Steel Sheet and Strip," Armco Steel Corporation, Baltimore, Md., Rept. S-26e.

A. K. Miller[1] *and A. A. Ziaai-Moayyed*[1]

Some Critical Experimental Tests of the MATMOD Constitutive Equations with Respect to Directional Hardening and Cyclic Deformation

---

REFERENCE: Miller, A. K. and Ziaai-Moayyed, A. A., "**Some Critical Experimental Tests of the MATMOD Constitutive Equations with Respect to Directional Hardening and Cyclic Deformation,**" *Mechanical Testing for Deformation Model Development, ASTM STP 765,* R. W. Rohde and J. C. Swearengen, Eds., American Society for Testing and Materials, 1982, pp. 202-222.

ABSTRACT: Cyclic torsion data on pure aluminum and Type 304 stainless steel have been generated recently that test several assumptions and predictions of the MATMOD equations (a unified, broad, phenomenological model for nonelastic deformation). Generally the new data support the model, but in at least one area they suggest a needed improvement. Firstly, the data show that when back stresses are measured by a Bauschinger effect technique (as opposed to the usual stress-drop method) the ratio of the steady-state back stress to flow stress is essentially a constant, independent of the flow stress level; this helps confirm a key assumption in the equations, but also suggests the need for an additional directionally-hardenable contribution to the strain rate. Secondly, strain softening is observed within some of the hysteresis loops, especially at large strain ranges after cyclic hardening; this is in agreement with predictions of the model. Finally, the peak back stresses observed at a given strain range are observed to increase along with the isotropic strength level; this behavior differs from that predicted by the constitutive equations.

KEY WORDS: constitutive equations, mechanical properties, cyclic deformation, aluminum, austenitic stainless steel, creep, back stresses, strain softening

In the course of bringing mechanistic studies of nonelastic deformation to bear upon the technological problems of predicting elevated-temperature deformation in engineering structures, the concept of *unified* constitutive equations is emerging as an approach that is both useful and physically satisfy-

---

[1] Associate Professor and Research Assistant, respectively, Department of Materials Science, Stanford University, Stanford, Calif. 94305.

ing. Instead of the traditional separate calculations of "time-independent plastic" and "time-dependent creep" strains, the unified approach considers these to be simply two different manifestations of the same entity, hereafter to be called "nonelastic strain" and denoted as ϵ. This approach is satisfying from a physical viewpoint because very often both "plastic" and "creep" strains result from a single common mechanism (dislocation slip); the approach is useful for engineering purposes because it gives us an inherent capability for predicting *interactions* between "plastic" and "creep" strains (for example, [*1*]),[2] and the general response to complex changes in stress, strain rate, and temperature.

In developing such unified constitutive equations, one must inevitably select the phenomena that are of greatest importance and weight these most heavily in proposing specific equations and in calculating constants for particular alloys. These judgements are necessary because of our incomplete state of knowledge about micromechanisms and their connections to the various macroscopic phenomena. As various investigators weight different subsets of phenomena differently, various unified constitutive equations arise (for example, [*1-8*]).

One of these, the MATMOD ("MATerials MODel") approach [*1, 9-13*] has emphasized cyclic deformation, monotonic deformation, creep, dynamic strain aging effects, and their mutual interactions. The emphasis on modeling the quantitative aspects of these four phenomena has led to equation forms which make several interesting predictions; these in turn provide the opportunity to test the model experimentally in order to verify and/or modify the proposed equations. In particular, three predictions arise from the manner in which the combination of monotonic deformation, cyclic deformation, and steady-state creep has been modeled. These predictions of the MATMOD equations are:

1. During steady-state flow at various stresses, the ratio of the back stress to the flow stress should be a constant, independent of the flow stress (definitions of back stress and flow stress will be given shortly).
2. Strain softening should be possible as the back stress passes through zero during cyclic deformation.
3. At a given cyclic nonelastic strain range, the peak back stress should be independent of the peak flow stress.

These three predictions have been tested recently using cyclic torsion experiments on pure aluminum and Type 304 stainless steel. The use of torsion as the testing mode permitted large strain amplitudes (up to ±20 percent) which in turn permitted steady-state back stresses to be reached within each half-cycle. This was important for testing Prediction 1 above. The use of

---

[2] The italic numbers in brackets refer to the list of references appended to this paper.

relatively thin-walled hollow cylindrical specimens ($r_i/r_o = 0.75$ where r_i and r_o are the inner and outer radii, respectively) minimized the strain gradients in the specimens; the estimated error due to strain gradients, in the back stresses inferred from the data, is on the order of 6 percent of the flow stress or less and is shown by error bars in the figures. The cyclic torsion apparatus was driven at constant angular velocity by an MTS servohydraulic machine whose function generator was specially modified. Shear stresses and strains were converted to equivalent normal stresses and strains (denoted as σ and ϵ for simplicity) using the Von Mises relations. Full experimental details are given elsewhere [*14,15*].

In the following sections, experimental results that bear on the foregoing three predictions will be summarized and their implications discussed. σ denotes the macroscopic applied stress or flow stress. The term *back stress*, σ_b, will be used in a general sense to mean a directional stress which opposes continued straining in the same direction as the deformation which created it but assists straining in the opposite direction. The ratio of σ_b to σ will be termed the back stress ratio. The term *internal stress*, σ_i, often used in connection with stress-drop experiments [*16,17*] will be used in a more specific sense to indicate the applied stress at which the nonelastic strain rate $\dot{\epsilon}$ equals 0. The term *rest stress*, *R*, often used to describe the center of the yield surface in multiaxial stress space [*18*], will also be used in a specific sense to indicate the results of Bauschinger effect measurements; R lies halfway between the applied modulus-compensated stress for "forward" deformation (σ_f/E) and that (σ_r/E) for "reversed" deformation (0.02 percent offset) with approximately the same structure and strain rate [*19*]. The fact that σ_i has the units of stress (for consistency with prior notation [*16*]) whereas R is dimensionless (also for consistency with prior work [*11-13,20*]) has no effect on the conclusions of the present paper. The subscript "ss" indicates the steady-state value reached under particular constant loading conditions (for example, constant strain rate and temperature).

In including back stress terms within constitutive equations, the general multiaxial development of Rice [*18*] can be utilized. For uniaxial loadings this reduces to a formulation in which the back stress is subtracted from the applied stress and the sign of $\dot{\epsilon}$ follows the sign of $\sigma - \sigma_b$; hence in general $\dot{\epsilon} = f(|\sigma - \sigma_b|)\cdot\text{sgn}\,(\sigma - \sigma_b)$ where sgn is the *signum* function which equals the algebraic sign of its argument. Thus if for particular conditions of temperature, strain range, etc., a value of σ_b has been determined by a Bauschinger effect experiment (as shown below in Eq 4), $\dot{\epsilon}$ ought to equal zero when σ equals σ_b. Hence an additional prediction is that with constitutive equations following the simple form given above, the back stress as measured by stress transient or strain transient techniques ought to equal the back stress as measured by Bauschinger effect technique, for the same previous history. The present paper will focus on this prediction also.

Ratio of Back Stress to Flow Stress at Steady State

As stated previously, one of the predictions of the MATMOD equations is that $\sigma_{b,ss}/\sigma_{ss}$ is a constant, independent of σ_{ss}. This result, developed in Ref *9*, arises from two considerations. Firstly, to simulate kinematic hardening (a simple shift in the yield locus with straining which, to a first approximation, correctly represents directional hardening in multiaxial stress space [*21*]), $\dot{\epsilon}$ is taken to be a signed function of the difference between σ/E and R. When isotropic hardening, assumed to be parabolic in the strain-hardening regime [*11*], is introduced and represented as F_{def} ("friction stress due to deformation") we obtain at any particular temperature T:

$$\dot{\epsilon}\,|_T = f\left(\frac{|\sigma/E - R|}{\sqrt{F_{\text{def}}}}\right) \text{sgn}(\sigma/E - R) \tag{1}$$

The second consideration is that at steady state, $\dot{\epsilon}_{ss}$ is a function solely of σ_{ss}/E; for example, utilizing the Garofalo hyperbolic-sine equation [*22*],

$$\dot{\epsilon}_{ss}\,|_T = K[\sinh(|A\sigma_{ss}/E|)]^n \,\text{sgn}(\sigma_{ss}/E) \tag{2}$$

where A is a constant and K depends on temperature.

A straightforward way in which to satisfy these two considerations is to construct the auxiliary equation governing R so that at steady state R is proportional to σ/E; that is, $R_{ss} = C_1\sigma_{ss}/E$ where C_1 is a constant. Additionally, the equation governing F_{def} is constructed so that

$$F_{\text{def},ss} = [(A/A_2)\,(\sigma_{ss}/E)]^{0.667}$$

where

$$A_2 = [A/(1 - C_1)]^3$$

and the strain rate equation is specified as

$$\dot{\epsilon} = B\theta'\left\{\sinh\left[\left(\frac{|\sigma/E - R|}{\sqrt{F_{\text{def}}}}\right)^{1.5}\right]\right\}^n \text{sgn}(\sigma/E - R) \tag{3}$$

where B is a constant and θ' is a temperature-dependent factor similar to $\exp(-Q/kT)$ [*9*]. At steady state Eq 3 reduces to Eq 2 with $K = B\theta'$.

Thus we have satisfied the two considerations concerning kinematic hardening and steady-state flow; in the process we have predicted that the ratio of R_{ss} to σ_{ss}/E should be a constant, where, as stated before, R represents the modulus-compensated back stress as measured by a Bauschinger-effect-type experiment.

Published data on the ratio of $\sigma_{b,ss}$ to σ_{ss} show, however, instances in which this ratio is clearly *not* a constant. For example, stress-drop experiments on aluminum (measuring σ_i) indicate that $\sigma_{i,ss}/\sigma_{ss}$ decreases as σ_{ss} increases [*16*]. Resolving this apparent contradiction was a major purpose of the cyclic torsion experiments. Use of cyclic torsion permitted strain amplitudes large enough to produce steady-state back stresses within each half-cycle [*14,15*]; reversal of the direction of straining then allowed determination of this steady-state value of R, using the equation

$$R = \left(\frac{\sigma_f}{E} + \frac{\sigma_r}{E}\right)\Big/2 \tag{4}$$

where σ_r, the stress for reversed plastic flow, was determined at 0.02 percent strain offset on a strip-chart recording of load against time. (It is being assumed that R does not change significantly between the points σ_f and σ_r.)

Figures 1*a* and 1*b* show the data on R_{ss} in aluminum and Type 304 stainless steel, respectively, plotted as $R_{ss}/(\sigma_{ss}/E)$ versus σ_{ss}/E.

We see that the back stress ratio, as determined by the Bauschinger effect is, in fact, approximately constant and independent of σ_{ss}/E over the regime covered. Hence to a certain extent the predictions of the MATMOD equations are vindicated.

The equations predict, however, that if the back stresses were measured by strain-transient or stress-transient techniques [*16*] then the back stress ratio should also be independent of σ_{ss} because, according to Eq 3, $\dot{\epsilon} = 0$ when $R = \sigma/E$. Accordingly, additional experiments using the stress transient technique were performed on the same experimental apparatus; these involved unloading (after any given half-cycle in which steady state was reached) to the stress ($\sigma_{i,ss}$) at which zero stress relaxation was observed. (Again, it is being assumed that the back stresses do not change significantly during the measurement.) Figure 2 shows these results for $\sigma_{i,ss}$ on pure aluminum along with the measurements of R_{ss} and the strain-transient data of Ahlquist and Nix [*16*] on $\sigma_{i,ss}$. We see that the new measurements of $\sigma_{i,ss}$ are in good agreement with the prior data and also extend the prior trend to higher values of σ/E. We also see, as a consequence, that there is a very definite difference between the two back stresses $R_{ss} \cdot E$ and σ_i. In particular, at the high-stress end of Fig. 2, $\sigma_{i,ss}$ is clearly less than $R_{ss} \cdot E$.

Figure 3 shows similar results for Type 304 stainless steel. As was the case for aluminum, the ratio of R_{ss} to σ_{ss}/E is approximately constant. Also, as in aluminum, $\sigma_{i,ss}/\sigma_{ss}$ decreases as σ_{ss} increases; the trend line which is drawn has a somewhat greater slope than the actual data points because it is believed that the leftmost (850°C) data point for $\sigma_{i,ss}$ is somewhat low, due to recovery occurring during the measurement at this high temperature [*15*]. In any event, at the low-stress end of this data, $\sigma_{i,ss}$ is greater than $R_{ss} \cdot E$.

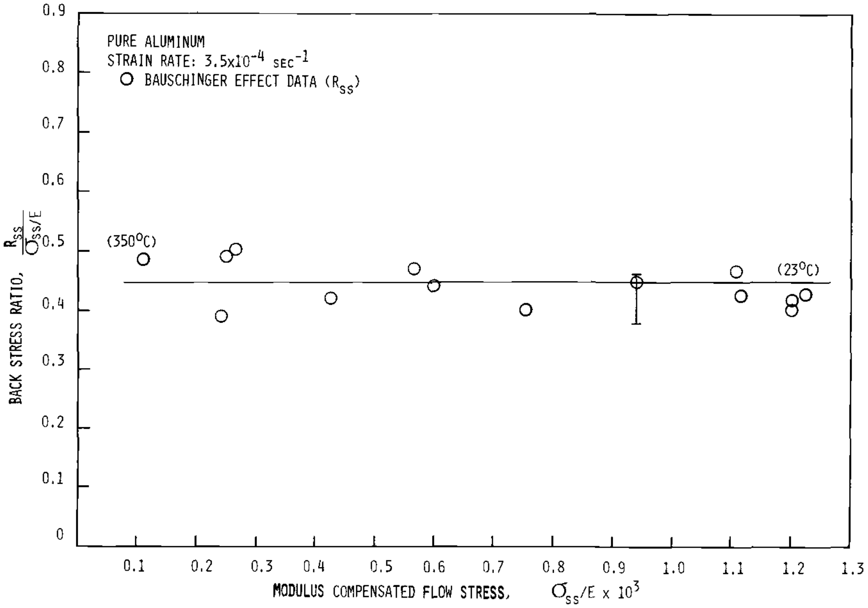

FIG. 1*a*—*Steady-state back stress ratio as a function of stress, as measured by Bauschinger-effect experiments on aluminum. Constancy of the back stress ratio is in agreement with the MATMOD equations.*

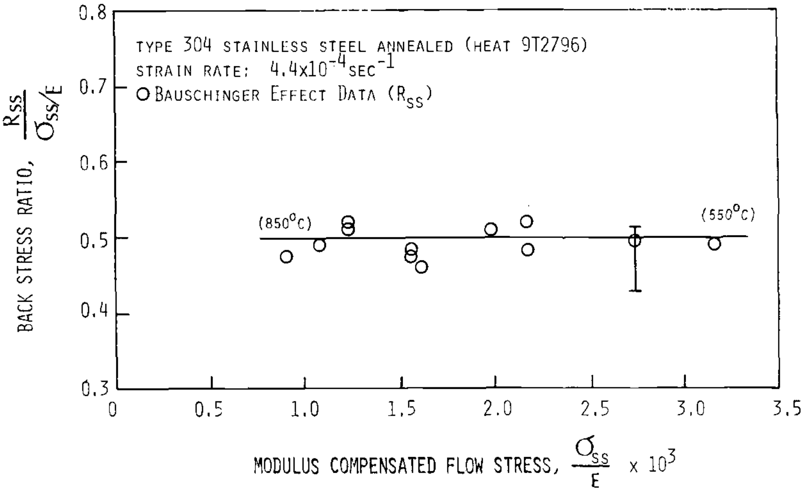

FIG. 1*b*—*Same as Fig. 1*a *but for Type 304 stainless steel.*

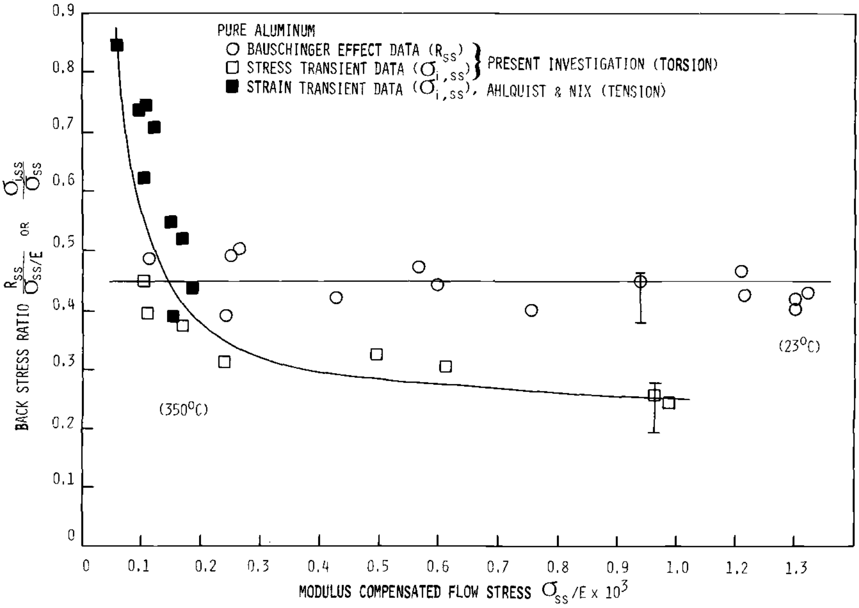

FIG. 2—*Steady-state back stress ratio as measured by Bauschinger effect* (R_{ss}) *and by strain transient* [16] *or stress transient techniques* ($\sigma_{i,ss}$)*, for aluminum.*

Figures 2 and 3, taken together, appear to indicate a similar trend in which back stresses as measured by Bauschinger effect (R) are different quantitatively from back stresses measured by stress or strain transient methods (σ_i), with $\sigma_{i,ss} < R_{ss} \cdot E$ at high stresses but $\sigma_{i,ss} > R_{ss} \cdot E$ at low stresses. This difference may be related to the different strain-rate regimes involved, and we shall return to this point in the Discussion.

Strain Softening

Another of the predictions which come out of the MATMOD equations is that strain softening may be observed during cyclic deformation [*13*]. This result originates with the need to model monotonic deformation, cyclic deformation, or mixtures of the two in a *unified* manner, the detailed reasoning being as follows. With a unified approach, at any given point in the middle of a strain cycle (that is, in between the upper and lower strain limits), the current boundary conditions (such as strain rate) do not "tell" the material whether it is part of a cyclic history or part of a monotonic history; the *internal state* of the material must supply this information. Experiments on monotonic and cyclic straining (Ref *23*, for example) show that extensive *monotonic* deformation tends to produce relatively large flow stresses at steady state, while *cyclic* defor-

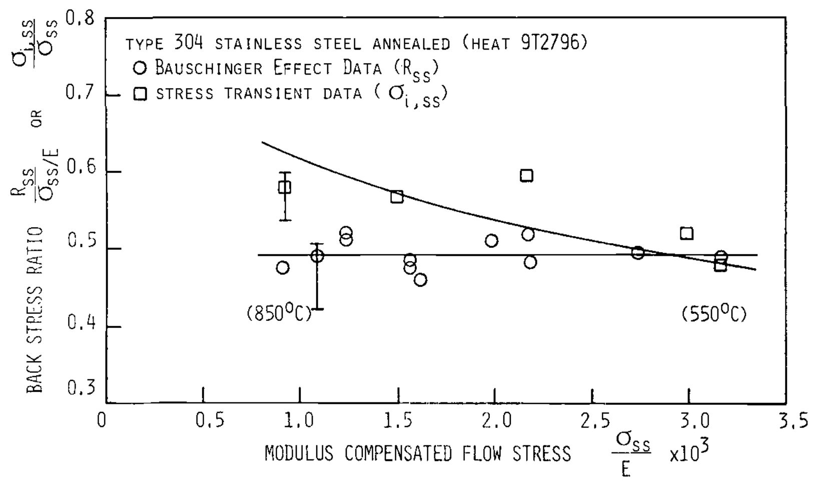

FIG. 3—*Same as Fig. 2 but for Type 304 stainless steel.*

mation (even to saturation) tends to produce lower stress amplitudes within each half-cycle, for the same temperature and strain rate. Thus with unified constitutive equations it is changes in the internal state variables that must determine whether the material will harden or soften to produce such effects as cyclic hardening, cyclic softening, and cyclic stabilization.

The most relevant internal state variable for allowing the material to distinguish between monotonic and cyclic histories is the back stress. As discussed previously [*9*] monotonic histories should produce relatively high back stresses whereas cyclic histories, because of the repeated reversals in straining direction, repeatedly unload the back stresses and should produce lower amplitudes of back stresses. Therefore we can use R (the state variable which corresponds to the back stresses) to distinguish between monotonic and cyclic loadings. Specifically we do this by having the magnitude of the back stress ($|R|$) serve as the "driving force" for changes in the isotropic strain hardening variable, F_{def}. To achieve the proper cyclically saturated stress, the rate of isotropic strain hardening ($\dot{F}_{\text{def}}$) must also decrease as F_{def} increases. Thus there is a coupling between F_{def} and R, that is, between isotropic hardening and directional hardening. The specific equations developed [*1,9*], are

$$\dot{R} = H_1\dot{\epsilon} - H_1 B\theta'[\sinh(A_1|R|)]^n \operatorname{sgn}(R) \tag{5}$$

$$\dot{F}_{\text{def}} = H_2[C_2 + |R| - (A_2/A_1)F_{\text{def}}^{1.5}]\,|\dot{\epsilon}| - H_2C_2B\theta'[\sinh(A_2F_{\text{def}}^{1.5})]^n \tag{6}$$

where A_1, A_2, C_2, H_1, and H_2 are constants.

For the usual strain cycles, Eq 5 causes R to oscillate between positive and negative limits. Figure 4, in which it is assumed that the time consumed by elastic loading and unloading is negligible, shows this schematically. Thus, according to Eq 6, near the strain limits, where $|R|$ is relatively large, $\dot{F}_{\text{def}}$ is positive; as R passes through zero, however, $\dot{F}_{\text{def}}$ can be negative, particularly when F_{def} is large. This produces the desired behavior, namely a lower value for F_{def} at cyclic saturation than at monotonic steady state. However, it also produces the prediction under discussion in this section. If $\dot{F}_{\text{def}}$ is sufficiently negative when $|R|$ is small (so that the effects of F_{def} in *decreasing* the magnitude of the stress outweigh the effects of R in increasing the stress magnitude), then strain softening is predicted. This strain softening will be

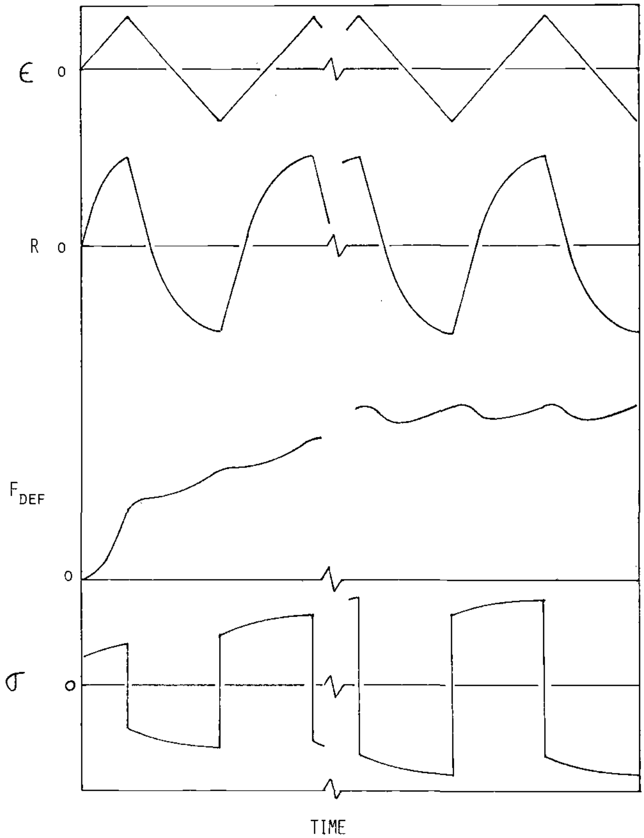

FIG. 4—*Variations with time of some of the variables in the MATMOD equations during strain cycling.* ϵ *is the nonelastic strain,* R *is the "rest stress" (directional hardening),* F_{def} *is the "friction stress for deformation" (isotropic hardening), and* σ *is the applied stress. The local decreases in* F_{def} *represent isotropic strain-softening predictions (see text).*

predicted only *locally* within the hysteresis loop; strain hardening occurs elsewhere in the cycle so that on the average the stress amplitude does not necessarily decrease. (This local strain softening is different from the more common cyclic softening which shows up as a cycle-to-cycle decrease in stress amplitude.) It should also be noted that strain softening for $R \approx 0$ is predicted only under certain circumstances, particularly large F_{def} (that is, after the material has been substantially strain hardened, cyclically or monotonically) and relatively small values of C_2.

Figure 5 shows some data that support this prediction. We see that for aluminum cycled at a strain amplitude of about ±10 percent at room temperature, strain softening *does* in fact occur within the hysteresis loops. Because of the high purity of the material, it is unlikely that the behavior is

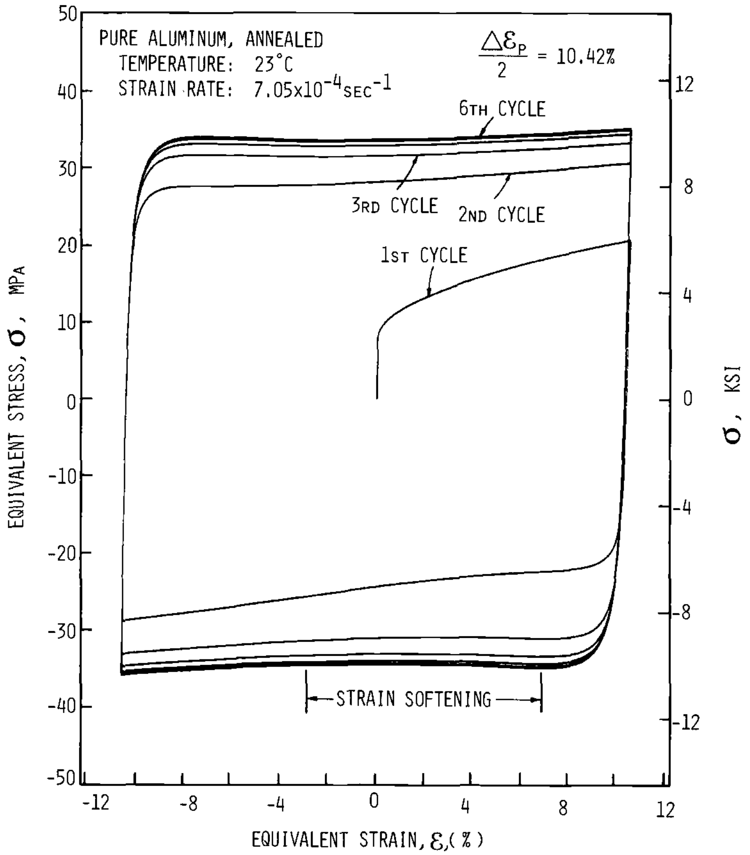

FIG. 5—*Experimentally observed hysteresis loops for aluminum at a high strain range (about ±10 percent). Strain softening is observed after cyclic hardening, in agreement with the MAT-MOD equations.*

caused by strain aging. The local strain softening is observed only after cyclic hardening, as predicted.

That the strain softening observed in the present investigation is due to isotropic softening can be inferred from similar experiments conducted by Hasegawa et al [*24*]. At various temperatures, specimens of aluminum were prestrained about 10 percent in tension. Upon subsequent straining in compression, a "region of constant flow stress" or RCFS (which upon close examination of the published results includes a region of local strain softening) was observed. Transmission electron microscopy demonstrated that the RCFS was associated with successive dissolution and re-formation of a cellular dislocation substructure. Since we expect dislocation cells to constitute an isotropic hardening mechanism, the experiments confirm the occurrence of isotropic strain softening following reversals in straining direction.

As mentioned previously, the MATMOD equations predict that strain softening *may* be observed during cyclic straining. Figure 6 shows hysteresis loops for Type 304 stainless steel (strain amplitude of ±8 percent) at 650°C, which indicate the *absence* of strain softening despite the rather large strain amplitude. Thus material differences appear to be important, and these may

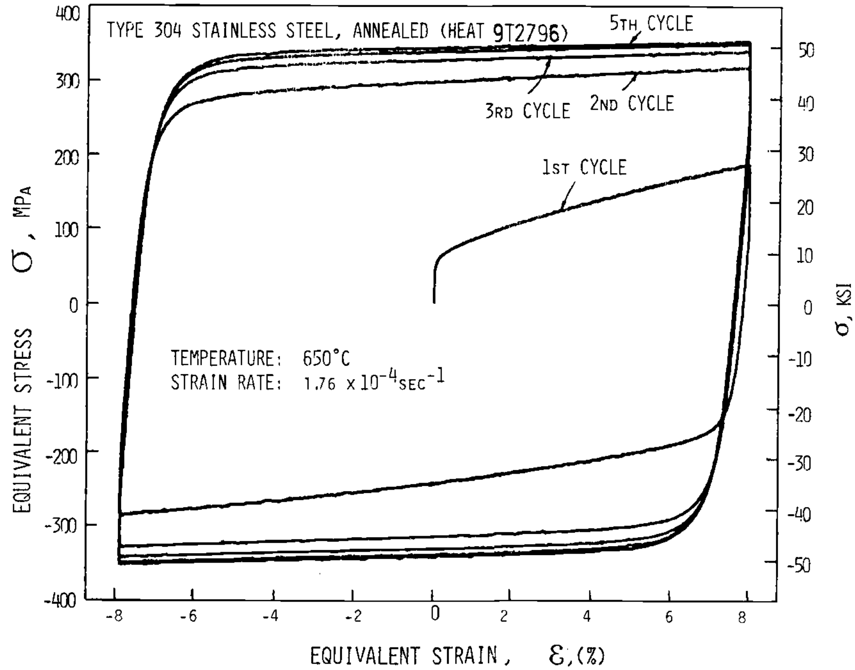

FIG. 6—*Experimentally observed hysteresis loops for Type 304 stainless steel, indicating an absence of strain softening despite the large strain amplitude (±8 percent).*

be reflected in a value of C_2 (Eq 6) which is larger for Type 304 stainless steel than for aluminum.

The discussion above indicated that strain softening, according to Eq 6, ought to be associated with high values of F_{def}. Hence it is more likely at large strain ranges than at small strain ranges. Figure 7 shows that this is, in fact, the case experimentally. For both aluminum and Type 304 stainless steel, the strain amplitude regime is divided to indicate the ranges in which a tendency toward strain softening was observed. Locally concave-outward regions in the hysteresis loops were taken as an indication of a developing strain-softening tendency. We see that for both materials, such concave-outward regions occur at high strain ranges, but not at low strain ranges. We also see that Type 304 stainless steel has an inherently smaller tendency toward strain softening, which may be related to the relative irreversibility of strain hardening in low stacking fault energy materials, as discussed by James and Sleeswyk [25].

Effect of Cyclic Hardening on Back Stresses

Figure 4, showing the predicted histories of the directional hardening variable R and the isotropic hardening variable F_{def} during strain-controlled cyclic deformation, indicates that the amplitude of R does not change as cyclic hardening proceeds at fixed strain range even though F_{def} and thus σ do

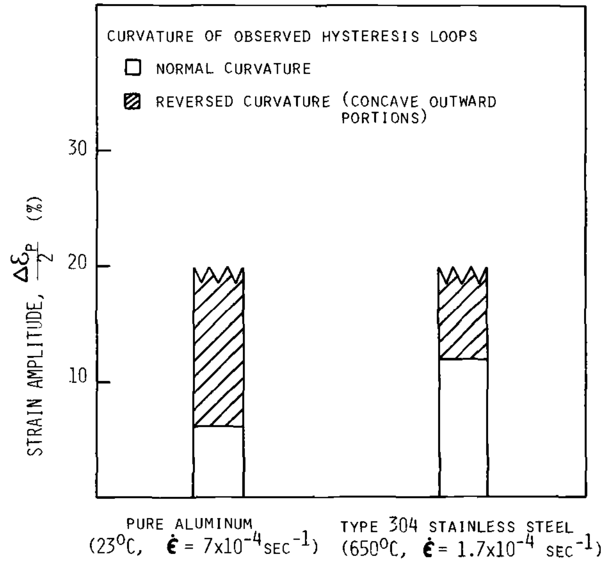

FIG. 7—*The experimentally observed strain amplitude dependence of strain softening. For both aluminum and Type 304 stainless steel, reversed curvature portions of the hysteresis loops (indicating a strain-softening tendency) occur at high strain ranges only.*

change. This result arises from the assumptions, made for simplicity, that H_1 in Eq 5 is a constant, that the recovery term in Eq 5 is a function only of R and T, and that $\dot{\epsilon}$ is a function of $\sigma/E - R$. (In an improved version of the equations [*13*] H_1 is made an exponential function of R multiplied by the algebraic sign of $\dot{\epsilon}$ in order to improve the curvature of simulated hysteresis loops, but this modification does not affect the present discussion.) Since R goes through a fixed cycle at a given strain range, the equations predict that the "peak" back stress R_p (that is, the value of the back stress when the plastic strain is at one of the strain limits, as measured by the Bauschinger effect) should not change even though the material undergoes cyclic hardening.

In a previous analysis [*26*] this prediction was shown to be approximately true; data of Lee [*27*] on hysteresis loops for Zircaloy-2 (tested at room temperature) indicated that for plastic strain ranges of 0.0194, 0.0445, and 0.0883 the peak back stress varied by less than 10 percent even though the flow stress increased by up to 24 percent because of cyclic hardening. (For a small plastic strain range, 0.0087, significant changes in the peak back stress were observed.) However, a relatively large offset ($\Delta\epsilon = 0.4$ percent) was used in defining the point of reversed yielding, and this may have obscured the more subtle changes in back stress.

In the present investigation, using much smaller offsets ($\Delta\epsilon = 0.02$ percent) the results indicate substantial increases in the peak back stress during cyclic hardening. For example, Fig. 8 plots the changes in peak back stress (R_p) and the corresponding flow stress (σ_p) for the test whose hysteresis loop was shown in Fig. 5. We see that R_p increases from 2.3×10^{-4} to 5×10^{-4} during cyclic hardening at constant strain range, as σ_p/E increases from 6.1×10^{-4} to 10.4×10^{-4}. Similar results were obtained for Type 304 stainless steel. For the test which was shown in Fig. 6 ($\Delta\epsilon_p/2 = 8.9$ percent) R_p increased from 5×10^{-4} to 12.5×10^{-4} during cyclic hardening while σ_p increased from 13×10^{-4} to 24.5×10^{-4}. It should be noted that in both cases, the increases in the values of σ_p/E with cycling are greater than the corresponding increases in the values of R_p, which indicates a definite contribution by isotropic hardening. Thus isotropic hardening appears to cause increases in the peak back stress in both materials.

Discussion

Behavior of Rest Stress (R) *in the MATMOD Equations*

As stated previously, considerations of kinematic hardening plus steady-state flow originally led to the prediction that at steady state, the back stress would be a constant fraction of the flow stress. Interestingly, if only that portion of the new data which relates to kinematic hardening (that is, the Bauschinger effect data) is considered, this prediction is borne out (Figs. 1*a*

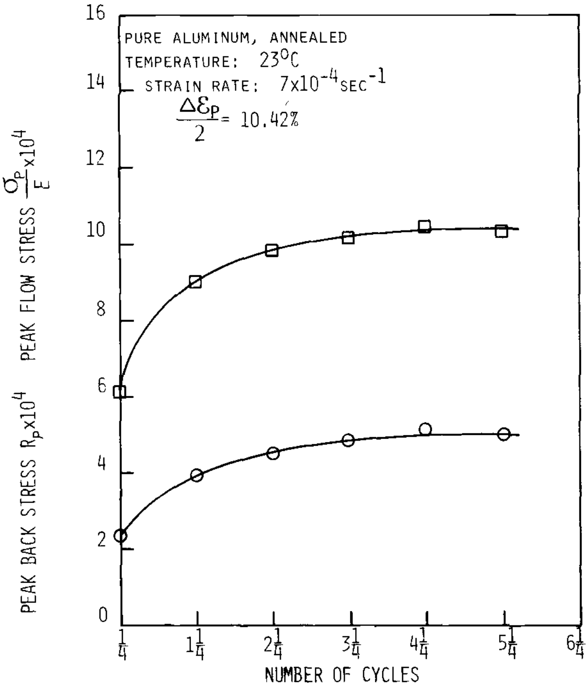

FIG. 8—*Observed changes in peak back stress at constant strain range. The peak back stress increases as the isotropic strength level increases during cyclic hardening.*

and 1*b*). As will be discussed subsequently, however, the stress transient data indicate that an additional strain rate term appears necessary for a complete description of directional hardening effects in uniaxial flow. Despite this necessary addition, the data help verify those portions of the equations responsible for the prediction that $R_{ss}/(\sigma_{ss}/E)$ is a constant, especially the recovery term in Eq 5.

Differences Between Rest Stress (R) *and Internal Stress* (σ_i)

The data reported in the section on Ratio of Back Stress to Flow Stress at Steady State indicate that the steady-state back stresses as measured by the Bauschinger effect ($R_{ss} \cdot E$) can be either greater or less than the back stresses as measured by stress or strain transient techniques ($\sigma_{i,ss}$). It appears that these differences can be explained by quantitative consideration of the strain rates involved in each measurement. Determination of R involves nonelastic strain rates on the order of the imposed total strain rate (perhaps 10^{-4} s^{-1}), whereas measurement of σ_i involves searching for a point of *zero* nonelastic strain rate, as determined from strain rate measurements on the order of 10^{-6} s^{-1} or less. The fact that two different strain rate regimes are involved suggests that two separate processes, each involving a back stress, may be operating.

If we assume two *additive* strain rates ($\dot{\epsilon} = \dot{\epsilon}_1 + \dot{\epsilon}_2$), an assumption which will be justified shortly, then this concept could explain the results. One contribution to the strain rate ($\dot{\epsilon}_1$) corresponds to Eq 3; for simplicity if $n = 5.3$ and F_{def} is constant, then $\dot{\epsilon}_1 = k_1 (|\sigma/E - R|)^8 \operatorname{sgn}(\sigma/E - R)$. The other contribution ($\dot{\epsilon}_2$) would depend on the difference between σ and σ_i, raised to a power less than 8. For reasons described subsequently, this power might be taken to be on the order of 1; thus $\dot{\epsilon}_2 = k_2(|\sigma - \sigma_i|)^{1.0} \operatorname{sgn}(\sigma - \sigma_i)$.

We see from Fig. 9 that $\dot{\epsilon}_1$ will dominate experiments involving reversed yielding, but $\dot{\epsilon}_2$ will dominate experiments where $\dot{\epsilon} \approx 0$. Thus the differences between the two types of measurements can be explained; we would say that at relatively low temperatures (as in Fig. 2 for aluminum) R/E exceeds σ_i (Fig.

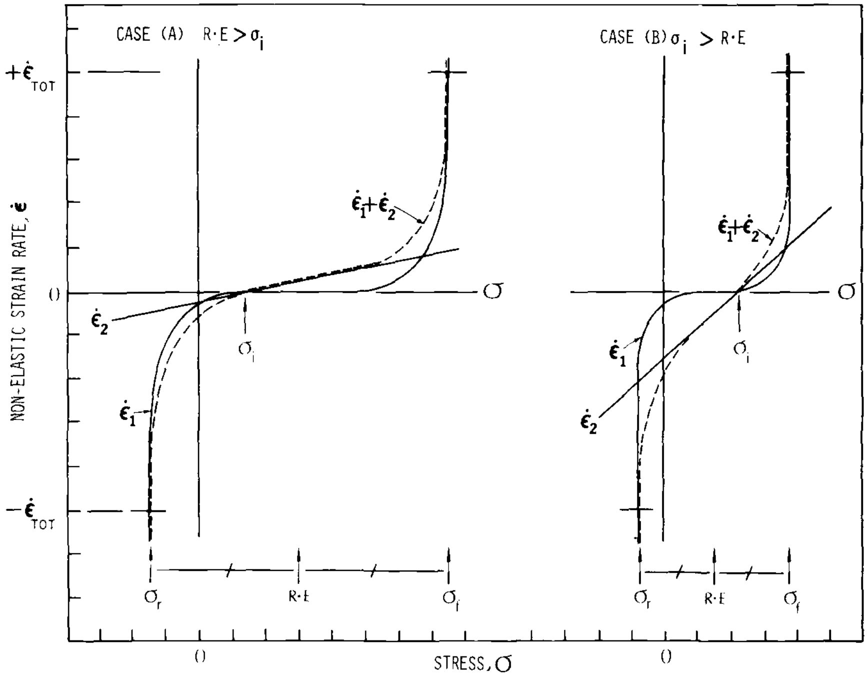

FIG. 9—*Schematic illustration of the expected behavior if the nonelastic strain rate is the sum of two contributions* $\dot{\epsilon}_1$ *and* $\dot{\epsilon}_2$, *where* $\dot{\epsilon}_1$ *is a strongly nonlinear function of* $\sigma/E - R$ *but* $\dot{\epsilon}_2$ *is a linear function of* $\sigma - \sigma_i$. *Bauschinger effect experiments will measure a back stress equal to* R·E, *stress transient or strain transient experiments will measure a back stress equal to* σ_i, *which can be less than* R·E *(left, as observed for aluminum at 23°C) or greater than* R·E *(right, as observed for Type 304 stainless steel at 650°C).*

9*a*), but that at relatively high temperatures (such as Fig. 3 for Type 304 stainless steel) R/E is less than σ_i (Fig. 9*b*).

Some evidence supporting this interpretation more directly is presented in Fig. 10, which utilizes data from stress transient tests on Type 304 stainless steel involving various degrees of stress reduction following cycling at 1 percent strain range. From the stress relaxation rates immediately following each stress reduction, a curve of $\dot{\epsilon}$ versus σ was constructed; also shown are the stresses for "forward" and "reversed" flow. We see that the overall curve of $\dot{\epsilon}$ versus σ is not inconsistent with the type of curve expected from Fig. 9*b*. This similarity helps justify the assumption of $\dot{\epsilon} = \dot{\epsilon}_1 + \dot{\epsilon}_2$.

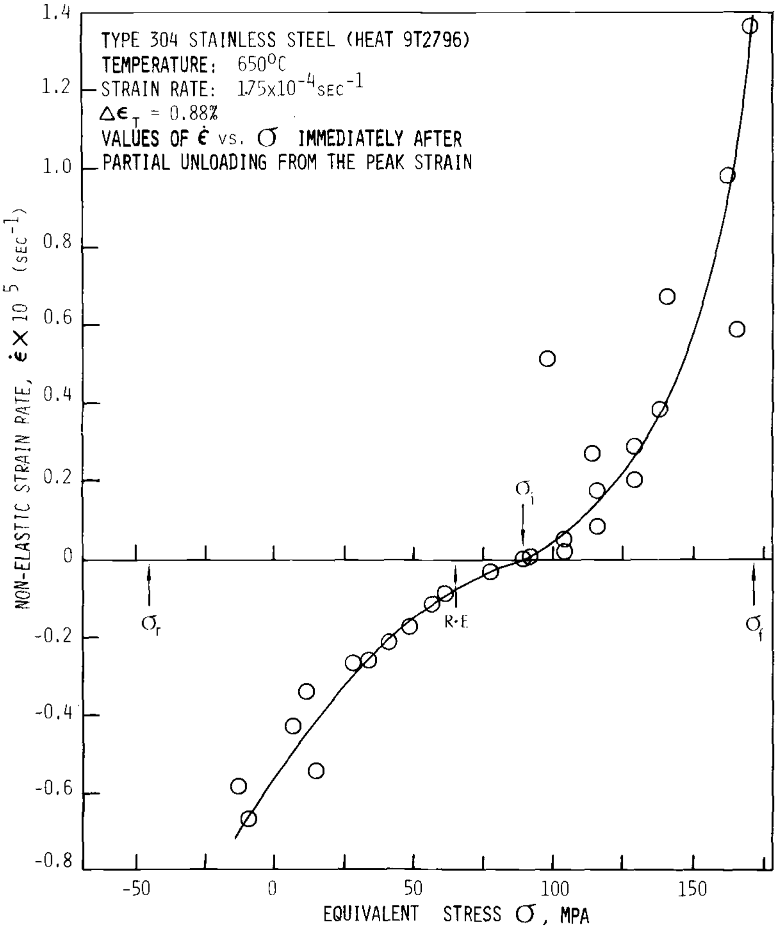

FIG. 10—*Stress transient test data on Type 304 stainless steel. The qualitative trend is similar to Fig. 9*b.

This interpretation in terms of two additive, directionally hardened processes can also be related to experimental observations of anelastic backflow following substantial stress reductions. Gibeling and Nix [28] show that curves of the anelastic strain rate ($\dot{\epsilon}_a$) versus the remaining anelastic strain (ϵ_a) (on log-log coordinates) show two regimes. At high values of $\dot{\epsilon}_a$ (corresponding to the early part of the anelastic transient) $\dot{\epsilon}_a$ depends strongly on ϵ_a; with $\dot{\epsilon}_a \propto \epsilon_a^N$, N varies between 3.3 and 20. At lower values of $\dot{\epsilon}_a$ (later in the transient) $\dot{\epsilon}_a$ depends approximately on the first power of ϵ_a. By way of comparison, Fig. 11 shows a prediction of the anelastic transient obtained from a model consisting of $\dot{\epsilon}_1 + \dot{\epsilon}_2$ as outlined above in which the two anelastic straining processes can occur in parallel. The shape of the predicted anelastic transient is similar qualitatively to the behavior observed by Gibeling and Nix, which helps to verify the interpretation that there are two additive strain rates, each affected

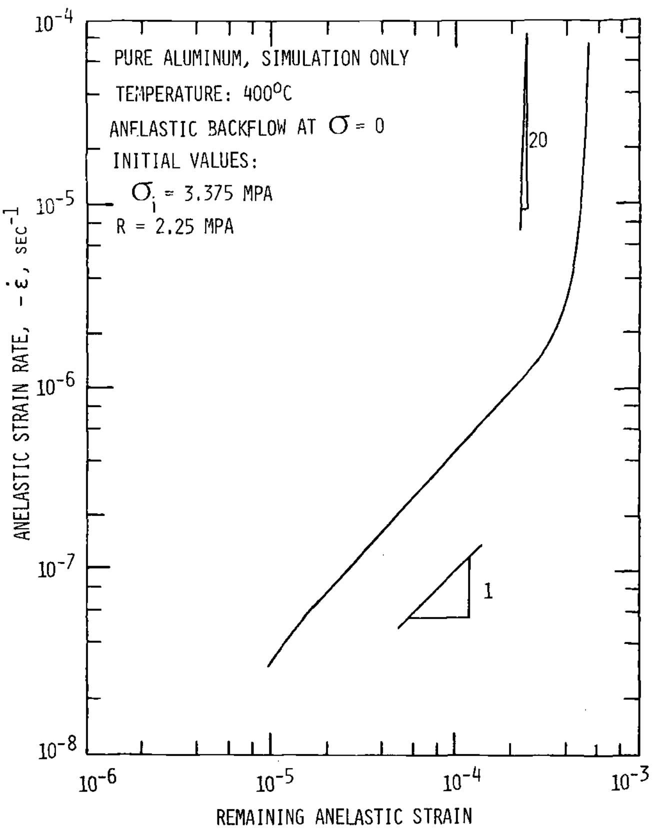

FIG. 11—*Predictions of a model consisting of* $\dot{\epsilon}_1 + \dot{\epsilon}_2$ *(see text) for the anelastic strain rate as a function of remaining anelastic strain. The predicted shape is qualitatively similar to experimental observations* [28].

by directional hardening so that at $\sigma \simeq 0$, each contributes to anelastic backflow.

To summarize this section, the present results suggest that the existing MATMOD equations (Eqs 4, 5, and 6) are a reasonably accurate form for the $\dot{\epsilon}_1$ term, but that an $\dot{\epsilon}_2$ term (in which $\dot{\epsilon}_2$ varies as $\sigma - \sigma_i$ to a relatively low power such as 1) must be added to the present equations for a more complete description of behavior at low strain rates following stress reductions.

Strain Softening

The experimental observations concerning strain softening, taken together with the similar observations and microscopy of Hasegawa et al [*24*] appear to help verify the concept of back stresses as the "driving force" for isotropic hardening ($\dot{F}_{\text{def}}$ increasing with $|R|$, Eq 6). In particular, the occurrence of strain softening in the middle of the strain cycle, followed by strain hardening towards the end of each half-cycle (Fig. 5) lends support to the present equation in which $\dot{F}_{\text{def}}$ is negative when $|R|$ is small but $\dot{F}_{\text{def}}$ is positive when $|R|$ is large. Also, the fact that the observed strain softening occurs only after hardening by prior cycling (Fig. 5) helps to verify the negative dependence of $\dot{F}_{\text{def}}$ on F_{def} for $\dot{\epsilon} \neq 0$ (first term in Eq 6).

Further work is necessary to confirm or improve the specific relation by which $\dot{F}_{\text{def}}$ depends upon R and F_{def}. For example, experiments by Washburn and Murty [*29*] involving prestraining followed by changes in the *direction* of straining (on single crystals of copper) indicate that strain softening can occur immediately after the change when, presumably, $|R|$ is still strongly nonzero. Assuming that such behavior is relevant to polycrystals as well, these data can be interpreted to say that $\dot{F}_{\text{def}}$ should, perhaps, be an increasing function of $R \cdot \dot{\epsilon}$ in Eq 6, instead of $|R|$, so that strain hardening would occur mainly when R and $\dot{\epsilon}$ are in the same direction. (In the multiaxial version of the MATMOD equations [*12*], $\dot{F}_{\text{def}}$ would, with this change, become a function of the scalar product $R_{ij}\,\dot{\epsilon}_{ij}$ instead of the present $\bar{R}$, where R_{ij} is a rest stress tensor, $\dot{\epsilon}_{ij}$ is the nonelastic strain rate tensor, and $\bar{R}$ is a scalar "effective rest stress" dependent upon R_{ij} according to a Von Mises-like equation.)

It is interesting that in the constitutive equations proposed by Hart [*2*] in which isotropic hardening is represented by the state variable σ^* and directional hardening is represented by the state variable σ_a, the isotropic hardening rate Γ is stated [*2*] (in words) to increase with σ_a but decrease with σ^*; this has some similarities to the MATMOD equation (6) and perhaps represents a point of convergence of various approaches.

Effect of Dislocation Substructure on Back Stresses

The finding that the peak back stresses increase as isotropic hardening proceeds, in strongly work-hardening materials like pure aluminum and Type 304 stainless steel, is not altogether surprising, since creation of back stresses depends upon the existence of local obstacles to dislocation motion and cyclic hardening increases the density of such obstacles. Other data are certainly not inconsistent with the same trend; specifically, in aluminum the total recoverable anelastic strains [*28*] and internal stresses [*16*] increase during transient creep, and in Cu-16Al the internal stress increases as a cellular dislocation substructure develops [*30*].

These findings suggest that a second cross-coupling between directional hardening (R) and isotropic hardening (F_{def}) should be present in the MATMOD equations; in particular, in the equation which governs R (Eq 5), as F_{def} increases, the R-values produced by a given strain cycle should increase. This could conceivably be accomplished by either of two approaches: as F_{def} increases, either (*1*) the work-hardening coefficient in Eq 5 could increase, or (*2*) the rate of recovery could decrease. Data from additional tests of the type described herein indicate that R increases with σ_p both in the larger-strain range regime (where R reaches a steady-state value within each half-cycle) and also at smaller strain ranges where R does not reach steady state because, presumably, only neglible recovery of R occurs. These data tend to indicate that the *first* of these two approaches is the more appropriate choice; further examination of this possible modification is currently underway.

Conclusions

The following conclusions with respect to the MATMOD constitutive equations are reached from the cyclic torsion data:

1. In both pure aluminum and Type 304 stainless steel, the ratio of the steady-state back stress (measured by the Bauschinger effect) to the steady-state flow stress is a constant; this helps verify the term, in the MATMOD equations, which governs recovery of directional hardening.

2. In both materials, the back stresses measured by stress transient techniques differ quantitatively from those measured by Bauschinger-effect techniques; this indicates the possible need for a second directionally hardenable strain rate to be added to the present strain rate equation.

3. Strain softening is observed in the middle portions of the hysteresis loops (especially at high strain ranges and after cyclic hardening); this helps to verify the concept and general equation form in which back stresses serve as the "driving force" for isotropic hardening.

4. At a given strain range, in both aluminum and Type 304 stainless steel, back stresses increase as the isotropic strength level increases during cyclic hardening; this indicates that the directional work-hardening coefficient should be an increasing function of the isotropic-hardening variable.

Acknowledgments

Discussions with J. C. Gibeling, M. L. Kassner, T. C. Lowe, W. D. Nix, and O. D. Sherby have been very helpful. Aluminum was kindly provided by Dr. Ron Kelsey of the Alcoa Corporation. Fabrication of the cyclic torsion apparatus and its control system was supported by the National Science Foundation (through the Stanford Center for Materials Research), the U.S. Department of Energy, and the Stanford Institute for Energy Studies. The research was supported by the Department of Energy, Office of Basic Energy Sciences, under Contract No. DE-AT03-76ER70057.

References

[*1*] Miller, A. K., *Nuclear Engineering and Design*, Vol. 51, 1978, pp. 35–43.

[*2*] Hart, E. W., *Journal of Engineering Materials and Technology*, Vol. 98, 1976, pp. 193–202.

[*3*] Krieg, R. D., Swearengen, J. C., and Rohde, R. W., "A Physically-Based Internal Variable Model for Rate-Dependent Plasticity," presented at Congress on Pressure Vessels and Piping, Montreal, 1978.

[*4*] Gittus, J. H., *Acta Metallurgica*, Vol. 26, 1978, pp. 305–317.

[*5*] Robinson, D. H., "A Unified Creep-Plasticity Model for Structural Metals at High Temperatures," ORNL/TM-5969, Oak Ridge National Laboratory, Oct. 1978.

[*6*] Bodner, W. R., Partom, I., and Partom, Y., "Uniaxial Cyclic Loading of Elastic-Viscoplastic Materials," Material Mechanics Laboratory, Report No. 61, Technion, Haifa, Israel, June, 1978.

[*7*] Ghosh, A. K., *Acta Metallurgica*, Vol. 28, 1980, pp. 1443–1465.

[*8*] Krempl, E., *Journal of Engineering Materials and Technology*, Vol. 4, 1979, pp. 380–386.

[*9*] Miller, A. K., *Journal of Engineering Materials and Technology*, Vol. 98, 1976, pp. 97–113.

[*10*] Miller, A. K. in *Zirconium in the Nuclear Industry, ASTM STP 633*, American Society for Testing and Materials, 1977, pp. 523–540.

[*11*] Miller, A. K. and Sherby, O. D., *Acta Metallurgica*, Vol. 26, 1978, pp. 289–304.

[*12*] Oldberg, S. T., Miller, A. K., and Lucas, G. E. in *Zirconium in the Nuclear Industry, ASTM STP 681*, American Society for Testing and Materials, 1979, pp. 370–389.

[*13*] Miller, A. K., *Journal of Engineering Materials and Technology*, Vol. 102, 1980, pp. 215–222.

[*14*] Ziaai-Moayyed, A. A., and Miller, A. K., "Modelling of Deformation and Fracture in High-Temperature Structural Materials," Stanford University, Department of Materials Science and Engineering, Report No. SU-DMS-80-R-2, 1980.

[*15*] Ziaai-Moayyed, A. A., "Back Stresses in Monotonic and Cyclic Deformation: Transient and Steady-State Behavior," Ph.D. dissertation, Stanford University, Department of Materials Science and Engineering, 1981.

[*16*] Ahlquist, C. N. and Nix, W. D., *Acta Metallurgica*, Vol. 19, 1971, pp. 373–385.

[*17*] Davies, P. W., Nelmes, G., Williams, K. R., and Wilshire, B., *Metal Science Journal*, Vol. 7, 1973, pp. 87.

[*18*] Rice, J. R., *Journal of Applied Mechanics*, Vol. 37-E, 1970, pp. 728–737.

[*19*] Lloyd, D. J., *Acta Metallurgica*, Vol. 25, 1977, pp. 459–466.

[*20*] Barrett, C. R., Ardell, A. J., and Sherby, O. D., *Transactions of the Metallurgical Society of AIME*, Vol. 230, 1964, pp. 200.

[*21*] Prager, W., *Journal of Applied Mechanics*, Vol. 78, 1956, pp. 493.

[*22*] Garafalo, F., Richmond, O., Domis, W. F., and Von Gemmingen, F., *Joint International Conference on Creep*, London, 1963, pp. 1-31 to 1-39.

[*23*] Abdel-Raouf, H. and Plumtree, A., *Metallurgical Transactions*, Vol. 2, 1971, pp. 1251-1254.

[24] Hasegawa, T., Yakou, T., and Karashima, S., *Materials Science and Engineering*, 1975, pp. 267-276.
[25] James, M. R. and Sleeswyk, A. W., *Acta Metallurgica*, Vol. 26, 1978, pp. 1721-1726.
[26] Miller, A. K. and Sherby, O. D., "Development of the Materials Code, MATMOD," EPRI Report NP-567, Dec. 1977.
[27] Lee, D., General Electric Company, unpublished data.
[28] Gibeling, J. C. and Nix, W. D., *Acta Metallurgica*, Vol. 29, 1981, pp. 1769-1784.
[29] Washburn, J. and Murty, G., *Canadian Journal of Physics*, Vol. 45, 1967, pp. 523-539.
[30] Hasegawa, T., Ikeuchi, Y., and Karashima, S., *Metal Science Journal*, Vol. 6, 1972, pp. 78-82.

Y. S. Garud[1]

Prediction of Stress-Strain Response under General Multiaxial Loading

---

REFERENCE: Garud, Y. S., "**Prediction of Stress-Strain Response under General Multiaxial Loading,**" *Mechanical Testing for Deformation Model Development, ASTM STP 765,* R. W. Rohde and J. C. Swearengen, Eds., American Society for Testing and Materials, 1982, pp. 223-238.

ABSTRACT: This paper deals with verification of a mathematical model capable of predicting rate-independent elastic-plastic stress-strain response of materials subjected to general multiaxial loading. The model is based on the concepts of incremental plasticity and a new hardening rule. Its application to predict steady response is illustrated for the case of combined cyclic out-of-phase (nonproportional) axial and torsional loading. The predictions are presented in the form of computer-generated hysteresis loops showing axial and torsional stress-strain response. The predicted response is shown to be in good agreement with available test results on two metals. Capabilities, limitations, and extensions of the model are briefly discussed in relation to the observed and predicted response.

KEY WORDS: constitutive relations, multiaxial cyclic loading, incremental plasticity, hardening rule, verification

Mathematical representation of the mechanical behavior of a material plays a central role in the design and analysis of many components and structures in transportation systems, power generation systems, and several other industrial applications. In particular, it is extensively used in the deformation and failure analyses. Several mathematical models, also referred to as the constitutive relations, have been developed over more than the past century covering a wide spectrum of representations. At one end of the spectrum we have the most simple form of representation, such as the linear elastic relations (that is, Hooke's law), and at the other end we have complex forms such as the integral representation [*1*] or thermodynamically based relations [*2*].[2] In practical applications, simplicity of a model often dictates its choice.

---

[1] Consulting Engineer, S. Levy, Inc., Campbell, Calif. 95008.

[2] The italic numbers in brackets refer to the list of references appended to this paper.

This choice is also influenced by the adequacy of a particular model, depending on the application. These applications often involve components and structures that are subjected to complex load variations resulting from more than one source, which lead to nonproportional multiaxial stresses. Further, the severity of loads in many cases is such that inelastic analysis is becoming increasingly necessary.

It is therefore not surprising to find that a number of recent symposia [*3, 4*] were devoted to the subject of constitutive relations. One of the specific research needs pointed out in Ref *3* was to increase the interaction between experimentation, computation, and (analytical) representation of the mechanical behavior of materials. This paper is an attempt directed generally towards fulfilling that need. In particular, only "time-independent" behavior of metals is considered. Its representation is based on the existing structure of incremental plasticity theory utilizing a new hardening rule proposed recently [*5*]. It is applicable to simple as well as complex loading situations, the latter being defined as a situation in which induced principal stresses are nonproportional or their directions change during loading. Here its application to the case of complex loading produced by combined cyclic axial and torsional straining is illustrated.

Mathematical Model

In this section basic assumptions used in the present investigation are briefly summarized. With the exception of the hardening rule, these assumptions are commonly used in incremental plasticity models. For more details on these, reference may be made to excellent review articles [*6–9*].

The following notation is used in this paper: a second-order tensor quantity is denoted by an underscore, a dot between two tensors denotes their inner product (that is, summation over both the indices of second-order tensors). $\underline{I}$ represents the unit tensor and the prefix symbol "Δ" is used to denote increment. It is common practice to refer to some of the underscored quantities as "vectors". This practice is followed where convenient.

Strain Decomposition

It is assumed that the total strain can be decomposed into an elastic and a plastic part by the following relation, expressed in increments:

$$\Delta\underline{\epsilon}^{t} = \Delta\underline{\epsilon}^{e} + \Delta\underline{\epsilon}^{p} \tag{1}$$

where $\underline{\epsilon}^{t}$, $\underline{\epsilon}^{e}$, and $\underline{\epsilon}^{p}$ are the total, elastic, and plastic strains, respectively.

Volume Constancy

The volume change due to plastic strains is assumed to be zero; that is,

$$\Delta\underline{\epsilon}^{p} \cdot \underline{I} = 0 \tag{2}$$

Elastic Strain-Stress Relations

The elastic strain is assumed to be linearly related to the stress as follows:

$$\Delta\underline{\epsilon}^{e} = \frac{1+\nu}{E}\left[\Delta\underline{\sigma} - \frac{\nu}{1+\nu}\,(\Delta\underline{\sigma}\cdot\underline{I})\,\underline{I}\right] \tag{3}$$

or, inversely,

$$\Delta\underline{\sigma} = \frac{E}{1+\nu}\left[\Delta\underline{\epsilon}^{e} + \frac{\nu}{1-2\nu}\,(\Delta\underline{\epsilon}^{e}\cdot\underline{I})\,\underline{I}\right] \tag{4}$$

where

$\underline{\sigma}$ = stress,
E = Young's modulus of elasticity, and
ν = Poisson's ratio.

Initial Yield Condition

The concept of an initial yield condition is a generalization of the idea of elastic limit. It expresses the condition, in terms of stresses, of deciding whether or not initial plastic straining will occur during an increment of loading. The two commonly used yield conditions are known as Tresca (maximum shear stress) and von Mises (distortion energy or octahedral shear stress). The latter condition is used explicitly in this investigation. Its mathematical form is covered in the next subsection. The yield condition is often represented as a surface in the stress space with stress components as coordinates. The material response is assumed to be elastic if the state of stress is within the yield surface.

The Field of Plastic Moduli

A useful generalization of the uniaxial stress-strain curve was introduced by Mroz [*10,11*]; it is known as the field of plastic moduli. Instead of using only one point such as the elastic limit, several points are selected on the uniaxial stress-strain curve. Corresponding to each point, a surface in the stress space (or a function of stress components) is defined similar to the initial yield surface (or the yield function). These surfaces are assumed to be convex and similar. In particular, these are of the von Mises type:

$$f_i\,(\underline{s}, \underline{a}_i, R_i) = (3/2)\,(\underline{s} - \underline{a}_i)\cdot(\underline{s} - \underline{a}_i) - R_i^2 \equiv 0; \qquad \text{for } i = 1, 2, \ldots, m \quad (5)$$

where

$\underline{s}$ = stress deviator,
$\underline{a}_i$ = vector denoting coordinates of the current origin of ith surface in deviatoric stress space,
R_i = size parameter of ith surface or stress value at the end of the ith linear segment (see Fig. 1),
f_i = ith surface of constant plastic modulus, and
m = number of surfaces or linear segments of constant plastic moduli.

Initially these surfaces are assumed to be concentric about the origin for an isotropic stress-free material. The surface f_1 defines the yield condition. Each surface defines a region of constant plastic modulus. In general, the plastic modulus c is defined as

$$c = (\Delta\underline{\sigma}\cdot\Delta\underline{\epsilon}^p)/(\Delta\underline{\epsilon}^p\cdot\Delta\underline{\epsilon}^p) \qquad (6)$$

Figure 1 illustrates the concept of field of plastic moduli. The aforementioned definition of plastic modulus, when applied to the uniaxial stress-strain curve, yields the following result:

$$c_i = \frac{2E}{3}\cdot\frac{R_{i+1} - R_i}{E(\epsilon_{i+1} - \epsilon_i) - (R_{i+1} - R_i)} \qquad (7)$$

where

ϵ_i = strain at the end of ith linear segment of the uniaxial stress-strain approximation (see Fig. 1), and
c_i = constant plastic modulus of $(i+1)$th linear segment, applicable to ith surface.

If the state of stress $\underline{s}$ is on the surface f_i but not on f_{i+1}, then c_i is "the plastic modulus in effect".

The Flow Rule

The plastic strain increment is related to the stress increment by means of a flow rule. The most commonly used flow rule for metals is known as the associative flow rule or the normality condition. According to this rule, com-

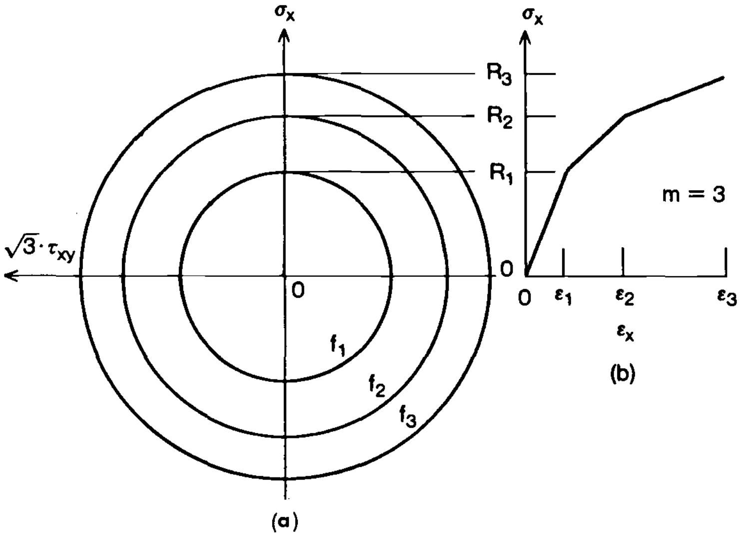

FIG. 1—*Illustration of* (a) *the field of plastic moduli using von Mises type of functions* (f_1, f_2, and f_3) *in tension (compression)-torsion stress space based on* (b) *the cyclic stress-strain curve approximated by three linear segments.*

ponents of the plastic strain increment are proportional to corresponding components of the unit normal to yield surface at the present state of stress on the surface. The constant of proportionality is dependent on the plastic modulus in effect, the stress increment, and the unit normal:

$$\Delta\underline{\epsilon}^p = (1/c_i)(\Delta\underline{s}\cdot\underline{n})\,\underline{n} \tag{8}$$

where $\underline{n}$ is the unit vector along the exterior normal to the surface f_1 at the present state of stress $\underline{s}$ when $\underline{s}$ is on f_1, ($\underline{n}\cdot\underline{n} = 1$). From Eq 5 it follows that

$$\underline{n} = (\partial f_1/\partial\underline{s})/[(\partial f_1/\partial\underline{s})\cdot(\partial f_1/\partial\underline{s})]^{1/2} \tag{9}$$

$$\underline{n} = \sqrt{3/2}\,(\underline{s} - \underline{a}_1)/R_1 \tag{10}$$

The Hardening Rule

It has been observed experimentally that as a result of plastic straining the yield condition is changed and plastic anisotropy is eminent under multiaxial loading. A hardening rule is used to specify these changes in a suitable analytical form. It is often described with reference to the yield surface in stress space. Thus the isotropic hardening rule specifies that the (initial) yield surface expands uniformly as a result of plastic straining, whereas the kinematic rule [*12,13*] specifies that the yield surface translates in a certain direction in the stress space. Several other rules based on these ideas have been proposed with modifications specifically oriented to model cyclic plasticity [*11,14,15*]. Although these rules are applicable to proportional loading (which results in radial stress path), their application to nonproportional loading (leading to nonradial stress path) may lead to certain difficulties for the following reason.

In all the rules which involve translation of the yield surface in stress space, the direction of translation is independent of the direction of stress increment. The magnitude of translation is proportional to the component of stress increment along the exterior normal to yield surface determined by the present state of stress [*11-15*]. Now consider Fig. 2, which shows a few of the infinitely many stress increments (such as $\Delta\underline{s}_1$, $\Delta\underline{s}_2$, etc.) having a fixed component along the exterior normal $\underline{n}$. The translation rules [*11-15*] suggest a unique translation for all such stress increments (although the unique translation may differ from rule to rule). With a unique translation of the yield surface the incremented state of stress may not lie on the translated

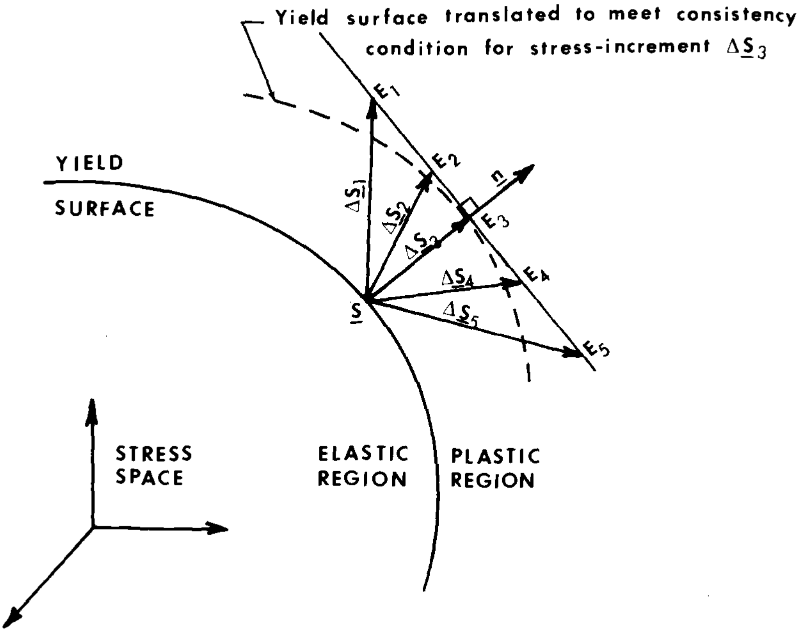

FIG. 2—*Effect of various stress increments with common components along the exterior normal* n *on satisfying consistency condition by translational rules cited in the text (schematic).*

yield surface. This is indicated by points E_1, E_2, E_4, and E_5 in Fig. 2. Therefore, in general, the consistency condition is not satisfied, no matter how small the stress increment is. (Consistency condition requires that the incremented stress should lie on the new yield surface if plastic flow has occurred during the increment.)

In order to avoid this difficulty a new hardening rule was proposed recently by the author [5]. To maintain generality, the concept of field of plastic moduli was used to generalize the uniaxial stress-strain relation. In what follows only the necessary relations pertinent to the assumptions used in this work are given. In particular, it is assumed that the size and shape of the surfaces $f_1, f_2, \ldots, f_m$ do not change (as a result of plastic flow). Thus the functional form of f_i and the parameters R_i and a_i in Eq 5 do not change.

Let f_i be the active surface (that is, the current state of stress is on f_i but not on f_{i+1}). Then, during plastic flow, the following shifts are made:

$$\Delta \underline{a}_i = p\underline{d} \tag{11}$$

$$\Delta \underline{a}_r = \underline{s}' - (R_r/R_i)(\underline{s}' - \underline{a}_i') - \underline{a}_r\,;\, r = 1, 2, \ldots, i - 1 \tag{12}$$

$$\Delta \underline{a}_r = \underline{0} \qquad ;\, r = i + 1, \ldots, m \tag{13}$$

where

$$\underline{d} = [1 - (R_i/R_{i+1})](\underline{s} - \underline{a}_{i+1} + k\,\Delta\underline{s}) + (\underline{a}_{i+1} - \underline{a}_i) \tag{14}$$

$$\underline{s}' = \underline{s} + \Delta\underline{s}$$

$$\underline{a}_i' = \underline{a}_i + \Delta\underline{a}_i$$

k is the positive root of

$$(3/2)\,(\underline{s} - \underline{a}_{i+1} + k\Delta\underline{s})\cdot(\underline{s} - \underline{a}_{i+1} + k\Delta\underline{s}) - R_{i+1}{}^2 = 0 \tag{15}$$

and p is the positive root of

$$(3/2)\,(\underline{s} + \Delta\underline{s} - \underline{a}_i - p\underline{d})\cdot(\underline{s} + \Delta\underline{s} - \underline{a}_i - p\underline{d}) - R_i^2 = 0 \tag{16}$$

The translation of the active surface f_i, given by Eq 11, is obtained by using the consistency condition. The translations, Eqs 11, 12, and 13, are such that there is no overlap or intersection of any of the surfaces f_i to f_m.

Other Assumptions

The material is assumed to be homogeneous, (initially) isotropic, and inviscid (that is, no time-rate effects). The loading is assumed to be isothermal.

Modulus of elasticity and (elastic) Poisson's ratio are assumed to be constant. The steady response under uniaxial cyclic loading, often referred to as the cyclic stress-strain curve [*16,17*], is sufficient to characterize the steady response under multiaxial loading.

Verification

Material Data

The basic material data required in the application of the aforementioned model consist of the modulus of elasticity, E, elastic Poisson's ratio, ν, and the uniaxial cyclic stress-strain data to obtain R_i (see Fig. 1) and c_i (see Eq 7). These data are summarized for two materials in Table 1. The cyclic stress-strain approximation for 1 percent Cr-Mo-V steel was obtained from experimental results of uniaxial cyclic loading [*18*]. In the case of annealed OFHC copper, the cyclic stress-strain data were obtained from the steady hysteresis loop in axial loading of previously undeformed specimen [*19*] using the scale factor of two (that is, assuming Masing hypothesis [*16*]). In both the cases six linear segments were used to fit the data and extrapolation was necessary to cover the range of loading in combined load tests; the uniaxial stress-strain data were based on specimens similar to those used in combined load tests.

Experimental Results

Two experimental investigations [*19,20*] were available in the published literature which reported the stress-strain response under combined cyclic nonproportional loading. In both the investigations, combined axial and tor-

TABLE 1—*Material data.*

	1 % Cr-Mo-V[a]		OFHC Copper[b]	
	$E = 208\ 000$ MPa $\nu = 0.29$		$E = 115\ 000$ MPa $\nu = 0.33$	
i	R_i, MPa	c_i, MPa	R_i, MPa	c_i, MPa
1	560	10000	72	87600
2	610	3000	110	24280
3	640	700	135	7540
4	680	300	145	1655
5	740	100	185	900
6	800	...	225	...

[a] Based on data from Ref *18*.
[b] Based on data from Ref *19*.

sional straining of tubular specimens was employed as shown schematically in Fig. 3. The values of experimentally controlled (fully reversed sinusoidal) strain amplitudes and phase angles for which steady stress-strain response was reported are given in Table 2. The table includes the reported stress amplitudes obtained from the respective load measurements. The steady response in the form of axial and torsional hysteresis loops for these tests is reproduced in Figs. 4 to 10 (shown by the dashed lines).

Analytical Results

A computer program was developed using the mathematical model described in the previous section to predict the stress-strain response for a given multiaxial loading. In the present study the imposed strains (Table 2) were used as the known loading. Each cycle of loading was divided into 180 increments (that is, two degree increment in the sinusoidal strains). Nearly steady response was obtained within three cycles. The predicted response for the seven different loadings is shown in Figs. 4 to 10 (shown by the solid lines). The predicted stress amplitudes are given in Table 2.

The results of analysis show a good agreement with the experimental

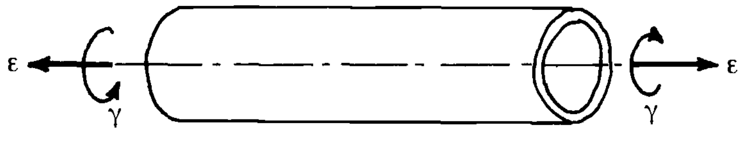

Tubular test-section (schematic)

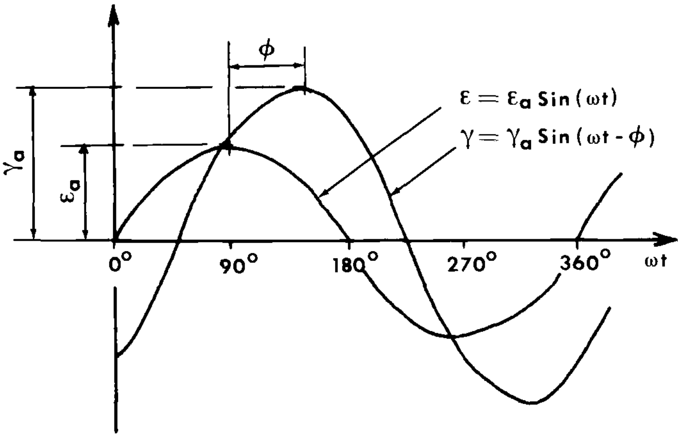

FIG. 3—*Schematic illustrating combined cyclic axial and torsional straining of a tubular specimen and the associated loading parameters.*

TABLE 2—*Observed and predicted stress-strain response.*

Test	Controlled[a]			Observed[b]		Predicted		
No.	ϵ_a, %	γ_a, %[c]	ϕ, deg	σ_a, MPa	τ_a, MPa	σ_a, MPa	τ_a, MPa	Figure No.
1	0.51	2.05	0	288	314	269	335	4
2	0.51	2.07	90	625	366	694	405	5
3	1.01	1.55	45	634	360	703	403	6
4	1.02	1.54	90	669	366	693	399	7
5	1.01	1.52	135	674	349	698	404	8
6	0.99	1.54	180	528	230	474	248	9
7	0.625	1.125	90	214	107	201	116	10

[a] See Fig. 3 for explanation of symbols.

[b] Tests 1 to 6 on 1 percent Cr-Mo-V [*18*]; Test 7 on OFHC copper [*19*].

[c] Engineering shear strain amplitude.

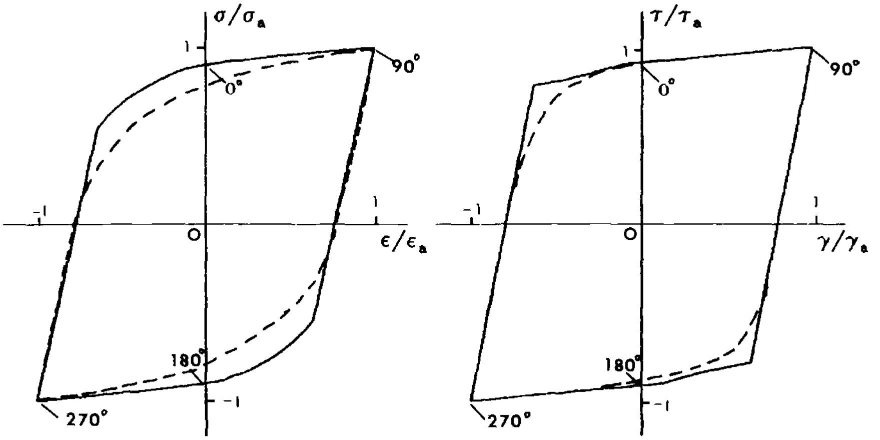

AXIAL RESPONSE TORSIONAL RESPONSE

FIG. 4—*Steady stress-strain response of 1 percent Cr-Mo-V steel under combined cyclic loading with* ϵ_a *= 0.51 percent,* γ_a *= 2.05 percent, and* ϕ *= 0 deg (solid line—predicted; dashed line—observed).*

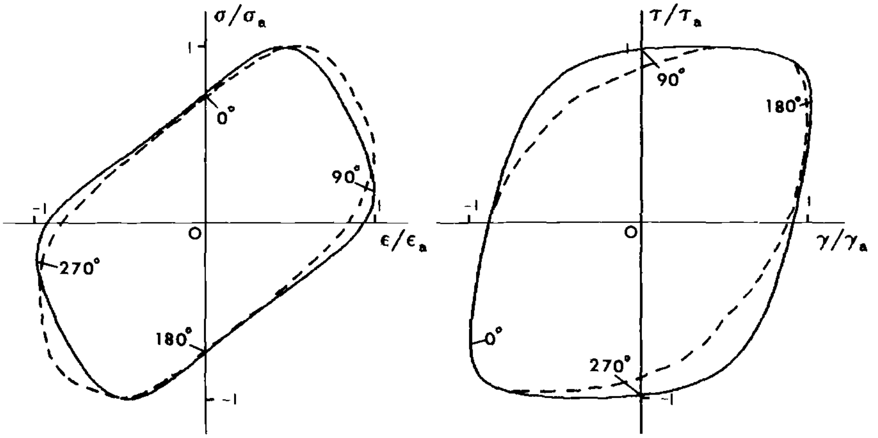

AXIAL RESPONSE TORSIONAL RESPONSE

FIG. 5—*Steady stress-strain response of 1 percent Cr-Mo-V steel under combined cyclic loading with* ϵ_a *= 0.51 percent,* γ_a *= 2.07 percent, and* ϕ *= 90 deg (solid line—predicted; dashed line—observed).*

results for both the materials. Some of the important features correctly predicted by the model are (*1*) relatively clear elastic unloading for $\phi = 0$ deg, 180 deg (Figs. 4 and 9), and nearly complete rounding of corners at strain reversals for the remaining tests; (*2*) the pronounced cross softening

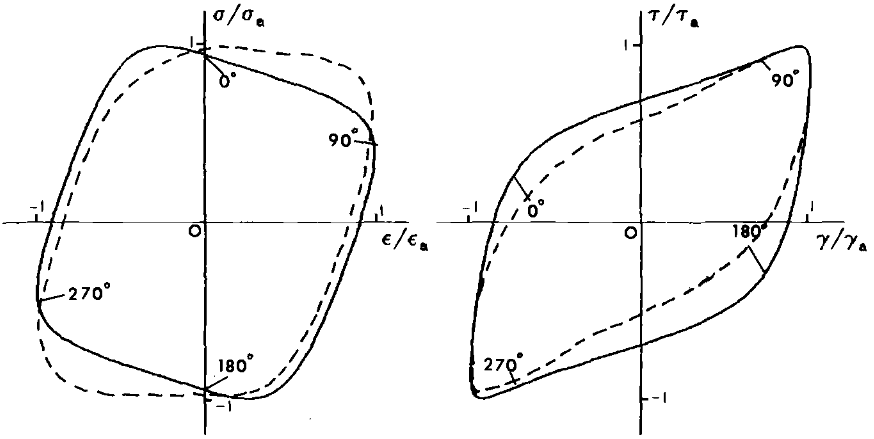

AXIAL RESPONSE

TORSIONAL RESPONSE

FIG. 6—*Steady stress-strain response of 1 percent Cr-Mo-V steel under combined cyclic loading with* ϵ_a *= 1.01 percent,* γ_a *= 1.55 percent, and* ϕ *= 45 deg (solid line—predicted; dashed line—observed).*

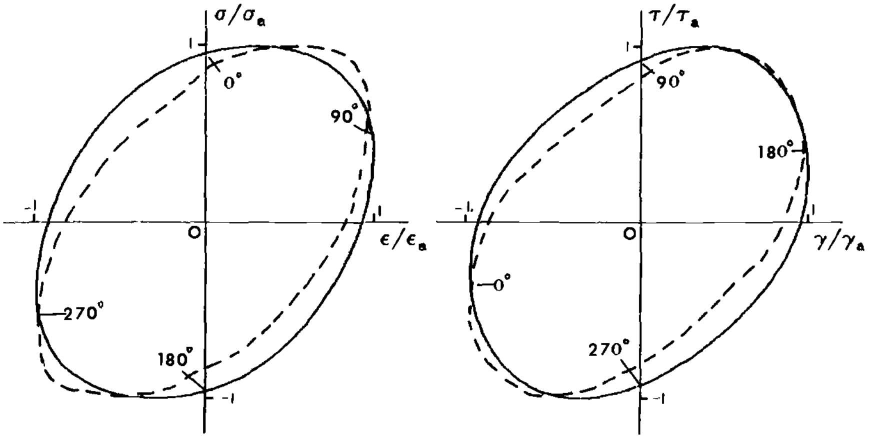

AXIAL RESPONSE

TORSIONAL RESPONSE

FIG. 7—*Steady stress-strain response of 1 percent Cr-Mo-V steel under combined cyclic loading with* ϵ_a *= 1.02 percent,* γ_a *= 1.54 percent, and* ϕ *= 90 deg (solid line—predicted; dashed line—observed).*

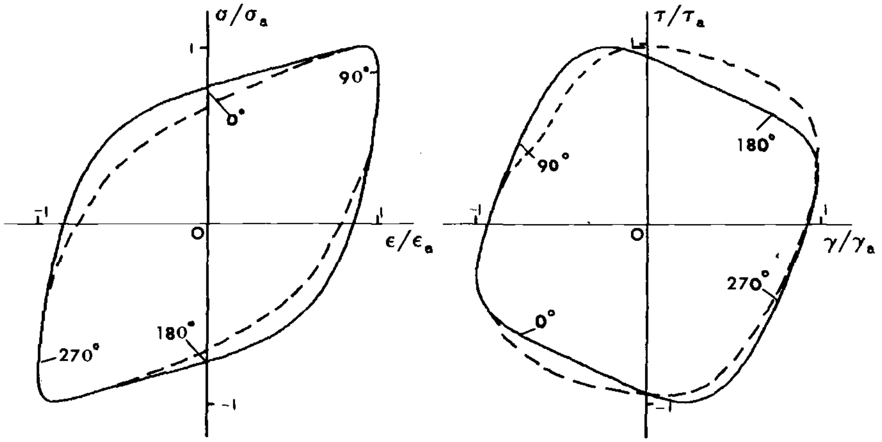

AXIAL RESPONSE

TORSIONAL RESPONSE

FIG. 8—*Steady stress-strain response of 1 percent Cr-Mo-V steel under combined cyclic loading with* $\epsilon_a = 1.01$ *percent,* $\gamma_a = 1.52$ *percent, and* $\phi = 135$ *deg (solid line—predicted; dashed line—observed).*

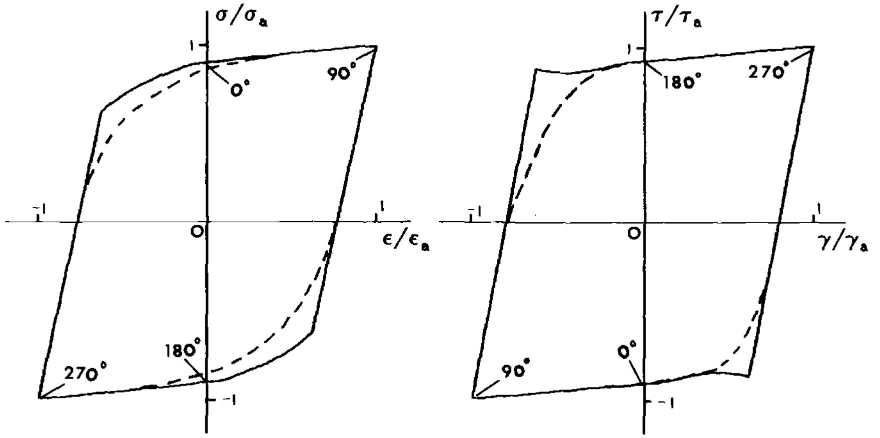

AXIAL RESPONSE

TORSIONAL RESPONSE

FIG. 9—*Steady stress-strain response of 1 percent Cr-Mo-V steel under combined cyclic loading with* $\epsilon_a = 0.99$ *percent,* $\gamma_a = 1.54$ *percent, and* $\phi = 180$ *deg (solid line—predicted; dashed line—observed).*

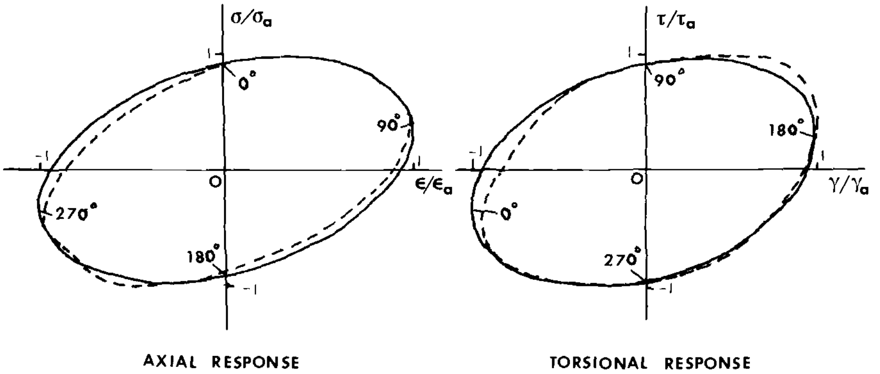

FIG. 10—*Steady stress-strain response of annealed OFHC copper under combined cyclic loading with $\epsilon_a = 0.625$ percent, $\gamma_a = 1.125$ percent, and $\phi = 90$ deg (solid line—predicted; dashed line—observed).*

[that is, decrease in (axial) stress with increasing (axial) strain] in Test 2 (Fig. 5, going from maximum axial stress to maximum axial strain conditions); (*3*) the change in hysteresis loops when only the phase angle was changed from 45 to 135 deg (Figs. 6 and 8); and (*4*) the changes in the stress amplitudes when only the phase angle was changed. In Ref *19* it was stated that nearly identical response was observed for Test 7 when performed on three different specimens: the first was initially cycled to steady state in axial straining, the second was initially cycled to steady state in torsional straining, and the third was initially undeformed. This similar response is also predicted by the model.

Discussion

Since the available experimental data were obtained under strain control, verification of the model was limited to this condition. Analytically, the model can be used under stress control condition as well. The verification was limited to steady response, which is generally observed to follow in uniaxial [*16,17*] as well as multiaxial [*18-20*] loading conditions. The transient behavior is necessarily influenced by factors such as time, cycles, rate, history of loading, or a combination of these. Such a behavior may be modeled by making the parameters c_i and R_i or the functional form of f_i dependent on the influencing factors; however, further analytical and experimental work is necessary.

Two of the assumptions which may appear to be restrictive in the development of this model are (*1*) the functions f_i s are similar to one another; and

(*2*) the steady stress-strain response under uniaxial loading (that is, the cyclic stress-strain curve) is sufficient to characterize the steady response under multiaxial loading. However, even with these and other usual assumptions of the incremental plasticity theory, analytical predictions are in fairly good agreement with the experimental results.

No attempt was made to study the effect of increasing the number of linear segments approximating the uniaxial stress-strain curve (Fig. 1) or of decreasing the size of load (strain) increments, although both these effects are expected to increase the accuracy of results.

If the hardening behavior of a metal is regarded to be represented by the isotropic and kinematic (anisotropic) parts then, in the present analysis, isotropic part is accounted for in the use of the cyclic uniaxial stress-strain relation. In multiaxial loading experiments, if measurements could be made on changes in the directional hardening moduli (that is, $\Delta\sigma_x/\Delta\epsilon_x$, etc.), then such information should prove to be valuable in further development of predictive models on better foundation.

This model was used in Ref *5* to calculate plastic work during the multiaxial loading cycle, which was shown to be a promising parameter for predicting fatigue life to crack initiation.

Conclusion

A mathematical model has been described that is capable of predicting "rate independent" elastic-plastic stress-strain response of metals. It is applicable to multiaxial loading which may involve nonproportional stresses or changing principal stress directions. The model was developed using the concepts of incremental plasticity and a new hardening rule. Its application to predict the steady response was illustrated for the case of combined in-phase and out-of-phase cyclic axial and torsional loading. The predicted response was shown to be in good agreement with available test results on 1 percent Cr-Mo-V steel and OFHC copper. The model may prove to be useful, at least as an engineering approximation, in stress-strain analysis of structures and components and in elastic-plastic fracture analysis.

Acknowledgments

The author is grateful to the Electric Power Research Institute (EPRI), Palo Alto, California, for financial support of this work under Contract No. RP1123-1 at Stanford University. The author acknowledges the support from Drs. Robin Jones and Theordore Marston of EPRI. The author is pleased to acknowledge the help and encouragement he received from Professors H. O. Fuchs, A. K. Miller, and D. V. Nelson of Stanford University.

References

[*1*] Findley, W. N., Lai, J. S., and Onaran, K., *Creep and Relaxation of Nonlinear Viscoelastic Materials,* North-Holland Publishers, Amsterdam, 1976.
[*2*] Nemat-Nasser, S., in *Mechanics Today-2,* S. Nemat-Nasser, Ed., Pergamon Press, New York, 1975, pp. 94-158, 391-405.
[*3*] *Workshop on Inelastic Constitutive Equations for Metals,* "Experimentation—Computation-Representaton," E. Krempl et al, Eds. Rensselear Polytechnic Institute, New York, April 1975.
[*4*] *Proceedings,* Symposium on Constitutive Equations in Visco-plasticity: Computational and Engineering Aspects, Applied Mechanics Division, ASME, New York, Vol. 20, J. A. Stricklin and K. J. Saczalski, Eds., Dec. 1976.
[*5*] Garud, Y. S. in *Proceedings,* Symposium on Methods for Predicting Material Life in Fatigue, ASME, New York, W. J. Ostergen and J. R. Whitehead, Eds., 1979, pp. 247-264; also in *Journal of Engineering Materials and Technology, Transactions of ASME,* Vol. 103, No. 2, April 1981, pp. 118-125.
[*6*] Michno, M. J., Jr., and Findley, W. N., *International Journal of Non-Linear Mechanics,* Vol. 11, No. 1, 1976, pp. 59-82.
[*7*] Armen, H., *Computers and Structures,* Vol. 10, Nos. 1/2, April 1979, pp. 161-174.
[*8*] Hecker, S. S. in *Proceedings,* Symposium of Constitutive Equations in Viscoplasticity: Computational and Engineering Aspects, Applied Mechanics Division, ASME, New York, Vol. 20, Dec. 1976, pp. 1-33.
[*9*] Olszak, W., Mroz, Z., and Perzyna, P., *Recent Trends in the Development of the Theory of Plasticity,* Pergamon Press, New York, 1963.
[*10*] Mroz, Z., *Journal of the Mechanics and Physics of Solids,* Vol. 15, No. 3, May 1967, pp. 163-175.
[*11*] Mroz, Z., *Acta Mechanica,* Vol. 7, No. 2-3, 1969, pp. 199-212.
[*12*] Prager, W. in *Proceedings,* Institute of Mechanical Engineers, London, Vol. 169, No. 21, 1955, pp. 41-57.
[*13*] Ziegler, H., *Quarterly of Applied Mechanics,* Vol. 17, No. 1, 1959, pp. 55-65.
[*14*] Eisenberg, M. A., *Journal of Engineering Materials and Technology, Transactions of ASME,* Paper No. 75-WA/Mat-3, Series H, Vol. 98, No. 3, July 1976, pp. 221-228.
[*15*] Lamba, H. S. and Sidebottom, O. M., *Journal of Engineering Materials and Technology, Transactions of ASME,* Paper No. 77-WA/Mat-13, Series H, Vol. 100, No. 1, Jan. 1978, pp. 104-111.
[*16*] Morrow, JoDean in *Internal Friction, Damping and Cyclic Plasticity, ASTM STP 378,* American Society for Testing and Materials, 1965, pp. 45-87.
[*17*] Sandor, B. I., *Fundamentals of Cyclic Stress and Strain,* University of Wisconsin Press, Madison, 1972.
[*18*] Kanazawa, K., Miller, K. J., and Brown, M. W., *Fatigue of Engineering Materials and Structures,* Vol. 2, No. 2, 1979, pp. 217-228.
[*19*] Lamba, H. S. and Sidebottom, O. M., *Journal of Engineering Materials and Technology, Transactions of ASME,* Paper No. 77-WA/Mat-12, Series H, Vol. 100, No. 1, Jan. 1978, pp. 96-103.
[*20*] Brown, M. W. and Miller, K. J., *Fatigue of Engineering Materials and Structures,* Vol. 1, 1979, pp. 93-106.

D. C. Stouffer[1] *and S. R. Bodner*[2]

A Relationship Between Theory and Experiment for a State Variable Constitutive Equation

---

REFERENCE: Stouffer, D. C. and Bodner, S. R., "**A Relationship Between Theory and Experiment for a State Variable Constitutive Equation,**" *Mechanical Testing for Deformation Model Development, ASTM STP 765,* R. W. Rohde and J. C. Swearengen, Eds., American Society for Testing and Materials, 1982, pp. 239-250.

ABSTRACT: A state variable constitutive equation that can be solved for the state variables can then be used to calculate the state variable histories from the stress and strain histories observed during an experiment. This was done using the Bodner-Partom flow equation for wrought René 95 at 650°C. The evolution equation was determined for a state variable that characterizes the resistance to plastic flow, and some properties of a damage state variable were established. Analysis of the tensile and creep data suggested that two different mechanisms were active during deformation. A limited number of experimental results were compared with the response calculated from the flow and evolution equations.

KEY WORDS: state variables, evolution equation, flow equation, inelastic response, mechanical properties, René 95 at 650°C

The usefulness of any constitutive equation depends on three major factors: (*1*) how well the constitutive equation can predict the mechanical response of material to a broad range of load histories; (*2*) how easily the equation can be used in computer algorithms and, in particular, its adaptability to finite-element analyses of structural components; and (*3*) how easily the parameters in the constitutive model can be determined from experimental data. Any equation that does not satisfy all these conditions is severely limited in its scope of application.

---

[1] Professor, Department of Aerospace Engineering and Applied Mechanics, University of Cincinnati, Cincinnati, Ohio 45221.

[2] Professor, Faculty of Mechanical Engineering, Technion - Israel Institute of Technology, Haifa, Israel.

This paper is concerned with procedures for the determination of evolution equations in a state variable constitutive theory, and a partial evaluation of the predictive capability of those equations with the determined constants. The equations are characterized by two internal state variables that represent the resistance of the material to plastic flow and internal damage. The particular set of equations used in this exercise are those developed by Bodner and Partom [*1,2*],[3] but other equations of the same general class could be treated by similar methods.

The method of developing the state variable evolution equations suggested in this paper permits direct evaluation of the material parameters from the experimental data and thereby minimizes subsequent trial-and-error computation. Since state variable constitutive equations predict the strain rate as a function (not functional) of the stress, temperature, and state variable histories, the constitutive function may be algebraically inverted to calculate the state variable history from stress, strain rate, and temperature histories that are determined from an experiment. A systematic analysis of the experimental data can therefore contribute to the formulation of the evolution equations for the state variables as well as define the material constants.

An interesting consequence of this technique is that it can be used to evaluate more than one state variable. This allowed for the consideration of a damage state variable [*3*]. Although a general development for the damage evolution equation is not included, a few properties of the variable were deduced from the aforementioned analysis.

The procedure is demonstrated for wrought René 95 at 650°C using data currently available in the literature [*4,5,6*]. The results are also compared with an earlier application of the Bodner-Partom equation [*7*] for the same material. Examples of the calcuated response are compared with observed tensile and creep results.

The Flow Equation

The basic equations of Bodner-Partom will be summarized for reference. These equations were motivated by the concepts and equations of "dislocation dynamics" (for example, Refs *8* and *9*), and were formulated in the context of continuum mechanics [*10*]. For small strains, the strain rates are considered to be decomposable into elastic (reversible) and inelastic (nonreversible) components:

$$\dot{\epsilon}_{ij} = \dot{\epsilon}_{ij}^{e} + \dot{\epsilon}_{ij}^{p} \tag{1}$$

where $\dot{\epsilon}_{ij}^{e}$ are given in terms of stress rates determined from the time derivative of Hooke's Law. Both components in Eq (1) are always nonzero for

---

[3] The italic numbers in brackets refer to the list of references appended to this paper.

nonzero stresses and stress rates, which implies that a yield criteria and loading/unloading conditions are not required.

The plastic strain rate is written in a form similar to the Prandtl-Reuse flow law:

$$\dot{\epsilon}_{ij}{}^{p} = \dot{e}_{ij}{}^{p} = \lambda s_{ij} \tag{2}$$

where $\dot{e}_{ij}{}^{p}$ and s_{ij} are the deviatoric strain rate and stress tensors, respectively. Equation 2 satisfies the condition of incompressibility. Squaring Eq 2 leads to

$$D_2{}^{p} = \lambda^2 J_2 \tag{3}$$

where $D_2{}^{p}$ and J_2 are the second invariants of the deviatoric plastic strain rate and stress tensors.

A basic assumption of the formulation of Bodner-Partom is that all inelastic deformations are controlled by a relationship between $D_2{}^{p}$ and J_2 which involves other state variables; that is,

$$D_2{}^{p} = f(J_2, T, Z_i) \tag{4}$$

where T is the temperature and Z_i are history-dependent internal state variables. Combining Eqs 2, 3, and 4 leads to a representation for the inelastic strain rate tensor that can be written as a function of stress, temperature, and internal state variables; that is,

$$\dot{\epsilon}_{ij}{}^{p} = \dot{e}_{ij}{}^{p} = f^{1/2}[J_2, T, Z_i]\,\frac{s_{ij}}{\sqrt{J_2}} \tag{5}$$

A particular form for Eq 4 was established from the relationship between dislocation velocity and stress [*8, 9*] by Bodner and Partom. In a constant temperature environment this representation is

$$f^{1/2} = D_o \exp[-(Z^2/3J_2)^n (n + 1)/(2n)] \tag{6}$$

In Eq 6, D_o is the limiting strain rate in shear, n is a material constant that controls strain rate sensitivity and also influences the overall level of the stress-strain curves, and Z is interpreted as an internal state variable that governs resistance to plastic flow. That is, an increase of Z would correspond to work hardening and would require an increase of stress to maintain a given plastic strain rate. Physically, Z can be interpreted as a measure of the stored energy of cold work [*11, 12*].

In the earlier references it was proposed that Z should be taken to be a scalar function of plastic work for isotropic hardening conditions. This was later extended to include both isotropic and kinematic hardening by using different values of Z for positive and negative stress in uniaxial reversed loading conditions [*12*]. The model was subsequently generalized by Stouffer and Bodner [*13*] to deformation-induced anisotropic flow. In this case Z was shown to be a second-order tensor in a six-dimensional vector space. The discussion in this paper is limited to isotropic hardening for which Z is a single valued scalar for reversed plastic flow.

Let us also briefly note some recent work [*3*] where isotropic damage was included as an additional state variable in the flow equations. Using the Kachanov definition [*14*], let ω be a history-dependent variable that represents the deterioration in the ability of a material to support a stress. In this formulation stress, σ_{ij} is replaced by a pseudo stress $\sigma_{ij}/(1 - \omega)$. Introducing this result into the flow equations ultimately reduces to replacing Z by $Z(1 - \omega)$.

Applying the preceding model to the case of a uniaxial stress σ, the one-dimensional flow equation can be written as

$$\dot{\epsilon}^p = \frac{2}{\sqrt{3}}\left(\frac{\sigma}{|\sigma|}\right) D_o \exp\left\{-\frac{1}{2}\left[\frac{Z(1-\omega)}{\sigma}\right]^{2n}\left(\frac{n+1}{n}\right)\right\} \tag{7}$$

for the uniaxial inelastic strain rate, $\dot{\epsilon}^p$. A direct method of developing the evolution equations for the state variables Z and ω is introduced in the next section. The method is general and can be applied to any state variable equation. Equation 7 will be used in this particular example.

Structure of the Evolution Equations

Let us consider the evolution equation for the state variable Z in the absence of damage. Therefore tertiary creep and the large strain range of a tensile test are excluded from this analysis. The evolution equation for the state variable Z is generally sought in the form of a differential equation:

$$\dot{Z} = f(\sigma_{ij}, Z) \tag{8}$$

A more specific representation is based on the concept that plastic work, W^p, controls the hardening process, and that W^p and $\dot{W}^p$ are functions of σ_{ij} and $\dot{\epsilon}_{ij}{}^p$ which can be determined from σ_{ij} and Z. That is, assume

$$\dot{Z} = f_1{}'(W^p)\,\dot{W}^p - f_2(Z) \tag{9}$$

where f_1 and f_2 are material functions and $f_1{}'(W^p)$ denotes differentiation with respect to plastic work. Equation 9 is a generalization of the specific representation developed by Bodner. The underlying philosophy in assuming the structure of Eq 9 is to allow for the assignment of physically useful properties to the functions f_1 and f_2. Specifically, f_2 is chosen so that the second term is negligible during short-time histories. Thus f_1 is selected so that Eqs 1 and 7 will reproduce the family of stress-strain curves run at high strain rates; the function f_2 is neglected in this situation. Conversely, both f_1 and f_2 are required to predict secondary creep. Mathematically, f_2 is a perturbation term that must be added for long-time response.

The main thrust of this work is directed towards establishing representations for f_1 and f_2, and developing the relationships between these representations and the experimental response of the material. The first step in achieving this goal is to recognize that, for any experiment, the stress and inelastic strain rate histories can be determined from the experimental data. Then, by inverting Eq 7,

$$Z(1-\omega) = \sigma(t)\left[\frac{2n}{n+1}\ln\left(\frac{2D_o}{\sqrt{3}\,\dot{\epsilon}^p(t)}\right)\right]^{1/2n} \tag{10}$$

the history of the state variable product $Z(1-\omega)$ can be calculated for each particular experiment. This provides a powerful technique to directly determine the functions f_1, f_2, and ω.

Evaluation of Tensile Response

The coefficient n in Eq 7 controls the strain rate sensitivity of the model with increases in n corresponding to a decrease in strain rate sensitivity. The properties of Eq 7 are such that for each choice of n, a family of rate-dependent stress-strain curves can be predicted from a single representation of Z. Thus the family of Z-histories calculated from Eq 10 using experimental data can be reduced to a single response curve Z with the correct value of n. The relationship $Z(W^p) = Z_0 + f_1(W^p)$ is valid for this analysis, provided that the time duration of the tension tests is short compared with the creep response and that material damage is not significant.

The response of René 95 at 650°C published in Ref 5 was used for this analysis. This work contains a family of four tensile response curves run at strain rates of 8.3×10^{-3}, 8.3×10^{-4}, 8.3×10^{-6}, and 1.6×10^{-7} s^{-1}. The observed tensile response at the highest strain rate had a 0.2 percent yield stress of about 1200 MPa and almost no strain hardening with the ultimate stress less than 1300 MPa. The other tensile response curves were similar with a lower value of yield stress. From a family of creep curves, it was observed that for the highest value of creep stress, 1200 MPa, the corresponding minimum creep rate was 2.7×10^{-5} s^{1}. Thus it was concluded that the two tensile curves run at 8.3×10^{-3} and 8.4×10^{-4} s^{-1} had a negligible amount of creep and could be used for evaluating the rate sensitivity constant n. Unfortunately, the highest rate is only a factor of ten greater than the next rate, and the resulting tensile curves crossed. Thus we used the value of $n = 3.2$ reported in Ref 7 for René 95 at 650°C.

The history of Z as a function of plastic work was established with $n = 3.2$ for the tension test run at a strain rate of $8.3 \times 10^{-4}\ \text{s}^{-1}$. The state variable history is shown in Fig. 1. The curve appears to be of an exponential form with a saturation value of $Z_1 = 2193$ MPa. The condition of a saturation value of Z agrees with the observed behavior that the stored energy of cold work increases with deformation at a decreasing rate. A further investigation showed that $\ln(Z_1 - Z)$ was very close to a linear function of the plastic work, W^p. Thus the representation

$$Z = f_1 + C_0 = Z_1 - (Z_1 - Z_0)\exp(-mW^p) \tag{11}$$

was established from the data with the constants $Z_0 = 1682$ MPa and $m = 0.37\ \text{MPa}^{-1}$ determined using a least-squares analysis. The initial hardness Z_0 was determined by extrapolating $\ln(Z_1 - Z)$ to zero plastic work. Data

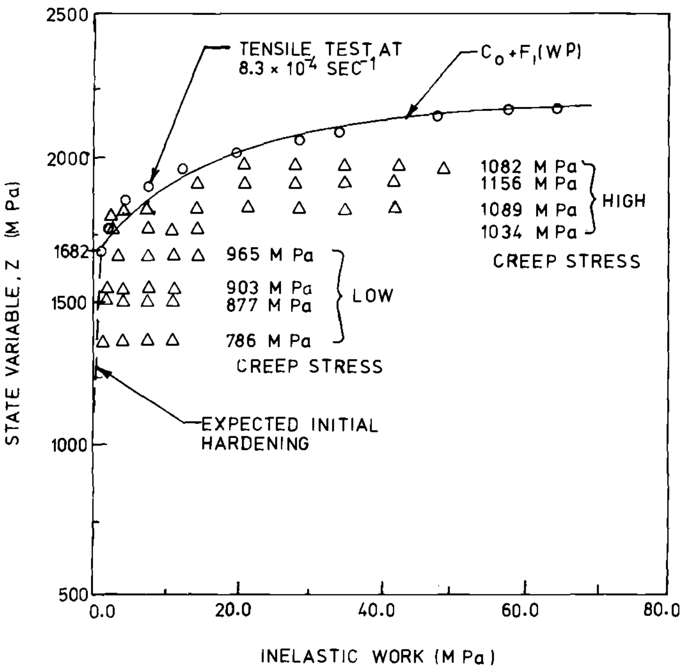

FIG. 1—*Internal state variable history for one tensile test and eight creep tests. The representation for tensile function* $f_I(W^p) + C_0$ *is compared with the experimental data.*

could not be accurately determined for small values of plastic work; however, it is expected that values of Z exist below Z_0 as indicated by the dotted line in Fig. 1.

The first term of the evolution equation, Eq 9, for tensile response can be obtained by differentiating Eq 11 to obtain

$$\dot{Z} = m(Z_1 - Z_0)\exp(-mW^p)\,\dot{W}^p = f_1{}'(W^p)\,\dot{W}^p \tag{12}$$

An alternative formulation for the tensile data was established by Bodner [7] by combining Eqs 11 and 12 to obtain

$$\dot{Z} = m(Z_1 - Z)\,\dot{W}^p = f_1{}'(Z)\,\dot{W}^p \tag{13}$$

Even though $f_1{}'(W^p)$ and $f_1{}'(Z)$ are equivalent for tensile response alone, the two representations for $f_1{}'$ give two different forms for the evolution equation with different properties. In this presentation we elect to investigate the consequences of using the second representation, Eq 13.

In closing, it should be noted that Eq 11 is different from the representation reported in Ref 5 for the same material. Both models predict essentially the same value through the range of interest; however, the asymptotic behavior of Eq 11 appears to be more consistent with the observed response of the material.

Evaluation of the Creep Response

During secondary creep (when the strain rate is approximately constant) the value of Z must be constant if Eq 7 is to be satisfied. Thus for secondary creep, Eq 9 becomes

$$\dot{Z} = 0 = f_1{}'(Z)\,\dot{W}^p - f_2(Z) \tag{14}$$

The stationary value of Z corresponds to a stable material microstructure during the secondary creep regime.

In general, $f_1{}'(Z)$ is known from the tensile data, and the stationary value of Z can be calculated from Eq 9 using the creep response data. The Z-histories from eight creep tests are also shown in Fig. 1. It is interesting to note that for the duration of each test, Z is nearly constant. This occurs because the amount of primary creep during a typical test is very small compared with the amount of secondary creep.

To start to establish a representation, let us assume the Bodner representation for f_2; that is,

$$f_2(Z) = A\,Z_1\left[\frac{Z - Z_2}{Z_1}\right]^r \tag{15}$$

where Z_2 is constant defining the minimum value of Z. If Eq 15 is valid, then $\ln[f_1'(Z)\dot{W}^p]$ must be a linear function of $\ln[(Z - Z_2)/Z_1]$ for Eq 14 to be satisfied. The experimental data were reduced and plotted as shown in Fig. 2. The value $Z_2 = 1300$ MPa was chosen (arbitrarily) so that $Z - Z_2$ is always positive.

Many of the creep properties of René 95 are summarized in Fig. 2. First notice that the data are bilinear with a sharp change in slope. The constants for each region were calculated using a least-squares analysis. It was found that the curves intersected at $Z = 1682$ MPa; a value that corresponds to a creep stress of approximately 980 MPa. Since $r = 12.0$ and $r = 1.34$ for stress above and below 980 MPa, it appears that different physical properties control deformation in the "high stress" and "low stress" domains. Further observe that the intersection point, $Z = 1682$ MPa, is the initial value of hardness, Z_0, determined in the tension tests. Thus the two response domains are segregated by the apparent initial value of hardness, Z_0.

Next recall that Z_0 was estimated by extrapolation to zero plastic work; but it was expected that values of Z below Z_0 existed at very small values of plastic work. The creep data give further evidence that Z_0 is not the initial value of Z. Equation 7 requires the initial value of Z in a creep test must be below the stationary value during secondary creep in order to predict a primary creep rate greater than the secondary creep rate. This indicates that the initial rate of hardening, Z, is very high for values of Z below $Z_0 = 1682$ MPa. This fur-

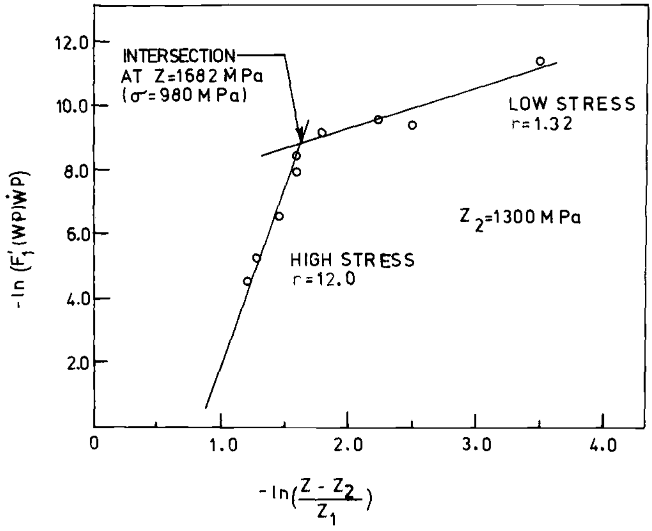

FIG. 2—*Bilinear representation for the stationary values of the internal state variable during secondary creep.*

ther confirms the existence of different deformation properties being active above and below a stress of 980 MPa.

It is difficult to accurately model the total creep and tensile response of René 95 when the response data are not available for very small values of plastic work. However, a reasonable approximation can be constructed by observing that the low stress data in Fig. 2 are nearly constant when compared with the high stress data. Let us set $Z_2 = Z_0$ and neglect changes in Z below 1682 MPa. In this case $r = 3.0$ and $A = 5.34\ \mathrm{s}^{-1}$.

If damage is assumed to be the major mechanism that produces tertiary creep, an estimate of the value of the damage, ω, at failure can be obtained from the creep data. A total evaluation of the damage variable is not included, since the creep curves were established using constant load rather than constant stress conditions. However, after adjustment for area reduction, it was found that the value of $Z(1-\omega)$ decreased about one to four percent between secondary creep and failure. It follows that the value of ω at failure can be expected to be very small in most cases. Thus the popular approach of assuming $\omega = 1$ at failure [*15,16*] is not applicable to René 95. This indicates that failure occurs due to a mechanism other than the Kachanov damage parameter. In René 95 this is probably unstable crack growth.

Comparison of the Model and Data

The hardening law for René 95 at 650°C can be written by combining Eqs 9, 12, and 14 to obtain

$$\frac{\dot{Z}}{Z_1} = m\left[1 - \frac{Z}{Z_1}\right]\dot{W}^p - A\left(\frac{Z - Z_2}{Z_1}\right)^r \tag{16}$$

with Z_0 the initial value Z. This can be used in combination with Eqs 1 and 7 to calculate the response of the material, assuming $\omega = 0$. The constants developed for René 95 are:

$D_0 = 10^4\ \mathrm{s}^{-1}$ (assumed)
$n = 3.2$
$Z_0 = 1682$ MPa
$Z_1 = 2193$ MPa
$E = 1.77 \times 10^5$ MPa

$m = 0.37\ \mathrm{MPa}^{-1}$
$Z_2 = 1682$ MPa
$A = 5.34\ \mathrm{s}^{-1}$
$r = 3.0$

where E is the elastic modulus. The final formulation for the hardening rule, Eq 16, is identical to that proposed by Bodner [*7*]. The constants Z_0, Z_1, and m that were determined from the tension test are very close to those reported by Bodner. The constants Z_2 and r developed from the creep data are different. The constant $Z_2 = Z_0$ was used as an approximation.

The foregoing equations were used to predict the tensile response of René 95 at constant stress rate. Recall the constants were developed from a tension test run at constant strain rate. The predictions are shown with two test results in Fig. 3. The agreement between theory and experiment is acceptable. Observe that the stress, $\sigma = 980$ MPa, corresponding to the intersection point in Fig. 2, is very close to the yield stress.

The creep response of René 95 was also calculated for three stress levels: 903, 1034, and 1206 MPa. These three stresses are at the high and low ends of the two curves in Fig. 2 and also the intersection. The calculated curves and experimental data are shown in Fig. 4. The minimum creep rates for the

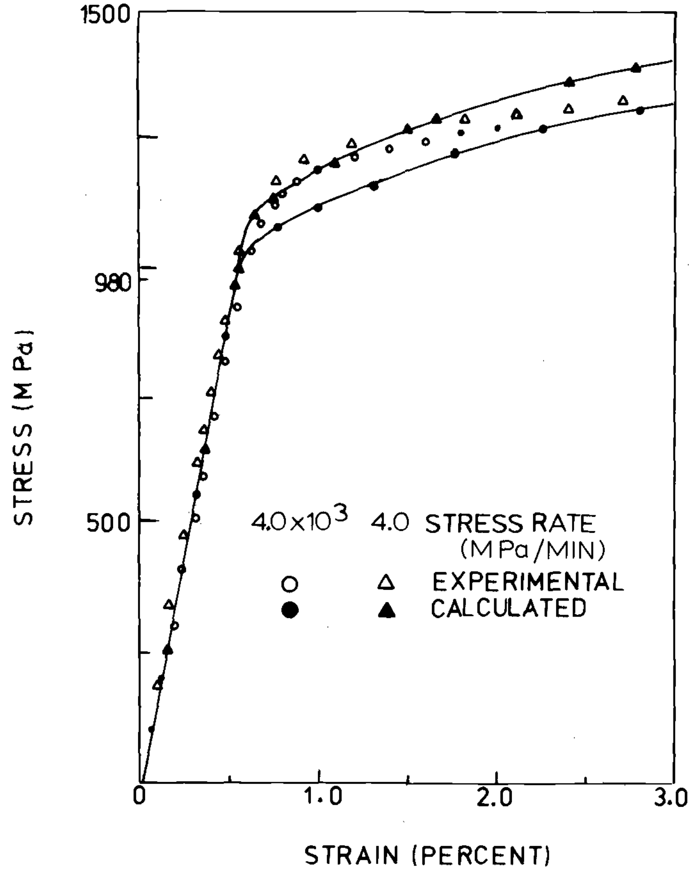

FIG. 3—*Calculated and experimental tensile response of René 95 at 650°C under constant stress rate control.*

1206 and 1034 MPa tests are very close, but the secondary creep rate for the 903 MPa was underpredicted. This resulted from the approximation that was used for Z at the low stress levels.

The results in the previous two sections suggest that two different micromechanical mechanisms are active at high and low levels of stress. This effect can also be seen in the creep response curves displayed in Fig. 4. The stress increments of 131 and 172 MPa between the three creep tests are approximately equal. However, the minimum creep rate changes by factors of 4 and 140, respectively. This difference in secondary creep rate reflects the consequences of a possible change in micromechanical mechanism.

In closing, it is important to point out that these results show how all phenomenological theories must be used with caution. That is, the value of the parameters that are determined for a material under a given range of conditions may not apply in another range of conditions. For example, if the value of 12.0 is assigned to r for the high stress region, the predicted response in the low stress region would be poor. However, this system of equations could be modified to account for the physical change in the response, and extrapolation in both the high and low stress regions may be possible. Of course, the new formulation should be experimentally verified before application.

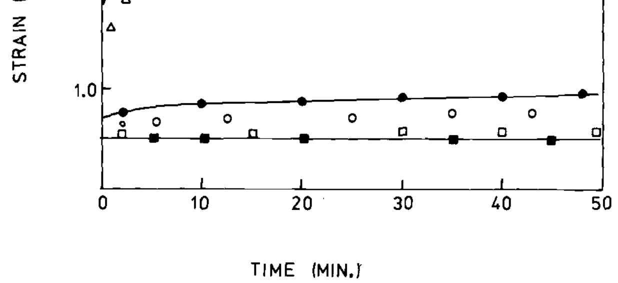

FIG. 4—*Calculated and experimental creep response of René 95 at 650°C at high, low, and intermediate values of stress.*

Acknowledgments

This research was sponsored by the U.S. Air Force Wright Aeronautical Laboratory, Air Force Systems Command, under Contract No. F33615-78-C-5199.

References

[*1*] Bodner, S. R. and Partom, Y., *Journal of Applied Mechanics*, ASME, Vol. 39, 1972, pp. 751-757.

[*2*] Bodner, S. R. and Partom, Y., *Journal of Applied Mechanics*, ASME, Vol. 42, 1975, pp. 385-386.

[*3*] Bodner, S. R., "A Procedure for Including Damage in Constitutive Equations for Elastic Viscoplastic Work Hardening Materials," to appear in *Proceedings*, IUTAM Conference, Senlis, France, May 1980.

[*4*] Stouffer, D. C., "An Evaluation of the Monotonic Response of René 95 at 1200°F," Final Technical Report, Grant AFOSR-77-3101, Feb. 1978.

[*5*] Stouffer, D. C., Papernik, L., and Bernstein, H. L., "An Experimental Evaluation of the Mechanical Response Characteristics of René 95," Technical Report AFWAL-TR-80-4136, Air Force Material Laboratory, Dayton, Ohio, 1980.

[*6*] Stouffer, D. C., Papernik, L., and Bernstein, H. L., "Prediction of the Mechanical Response of a High Temperature Super-Alloy René 95," Technical Report AFWAL-TR-80-4184, Air Force Materials Laboratory, Dayton, Ohio, 1980.

[*7*] Bodner, S. R., "Representation of Time Dependent Mechanical Behavior of René 95 by Constitutive Equations," Technical Report AFML-TR-79-4114, Air Force Materials Laboratory, Dayton, Ohio, 1979.

[*8*] Vreeland, T. J., "Dislocation Velocity Measurements," in *Techniques of Metals Research*, R. F. Bunshak, Ed., Wiley-Interscience, NewYork, 1968, Vol. 2, Part 1, p. 341.

[*9*] Gilman, J. J., *Micromechanics of Flow in Solids*, McGraw-Hill, New York, 1969.

[*10*] Bodner, S. R., *Mechanical Behavior of Materials Under Dynamic Loads*, U. S. Lindholm, Ed., Springer-Verlag, New York, 1968, p. 176.

[*11*] Narayana, A. D., "A Representation for the Deformation of a Metal Including the Effects of Strain Hardening and Recrystallization," Ph.D. thesis, Department of Engineering Science, University of Cincinnati, Cincinnati, Ohio.

[*12*] Bodner, S. R., Partom, I. and Partom, Y., *Journal of Applied Mechanics*, ASME, Vol. 46, 1979, pp. 805-810.

[*13*] Stouffer, D. C. and Bodner, S. R., *International Journal of Engineering Science*, Vol. 17, 1979, pp. 757-764.

[*14*] Kachanov, L. M. (in Russian), *Izv. Akad. Nauk. SSR, Otd. Tekhn. Nauk.*, 1958, pp. 26-31; also in *Problems of Continuum Mechanics*, Society for Industrial and Applied Mathematics, Philadelphia, 1961, pp. 306-310.

[*15*] Leckie, F. A., "Phenomenological Constitutive Equations of Damage and Physical Interpretation," in *Workshop on a Continuum Mechanics Approach to Damage and Life Prediction*, General Butler State Park Lodge, Carrollton, Ky., sponsored by NSF Solid Mechanics Program, 1980.

[*16*] Kachanov, L. M., "Influence of Damage of Crack Growth," in *Workshop on a Continuum Mechanics Approach to Damage and Life Prediction*, General Butler State Park, Carrollton, Ky., sponsored by NSF Solid Mechanics Program, 1980.

J. Klepaczko[1] *and J. Duffy*[2]

Strain Rate History Effects in Body-Centered-Cubic Metals

REFERENCE: Klepaczko, J. and Duffy, J., "**Strain Rate History Effects in Body-Centered-Cubic Metals,**" *Mechanical Testing for Deformation Model Development, ASTM STP 765,* R. W. Rohde and J. C. Swearengen, Eds., American Society for Testing and Materials, 1982, pp. 251-268.

ABSTRACT: This paper presents a discussion of the strain rate history effects that occur during the deformation of body-centered-cubic (BCC) metals. It is divided into two parts: a brief review of previous work, which also includes some new data, followed by an analysis of material behavior based on previous and new results. The review discusses early experiments on steels and other BCC metals in which interrupted tests were performed. These tests consist of loading initially at one strain rate, unloading, and reloading at a second strain rate, either higher or lower than the first. Early experiments of this type had revealed a substantial difference in response between BCC and face-centered-cubic (FCC) metals. The review also includes results of incremental strain rate tests with large jumps in strain rate, augmented by a series of experiments designed to study strain rate history effects in steel. The latter consist of incremental tests performed on specimens of an AISI 1020 hot-rolled steel over the temperature range 83 K $\leq T \leq$ 494 K. Results indicate that at temperatures near the ambient and for relatively small shear strains (up to $\gamma \approx 0.20$) strain rate history effects play a minor role compared with strain rate effects per se. However, for low temperatures and for dynamic aging temperatures, strain rate history effects are shown to be of considerable importance. The second part of the paper concentrates on an analytical discussion of adiabatic coupling during deformation and on constitutive modeling of deformation in BCC metals.

KEY WORDS: steels, dynamic plasticity, shear properties, strain rate sensitivity, constitutive equations

The strain rate behavior of body-centered-cubic (BCC) polycrystalline metals including steels has been the subject of extensive research during the past decades. Most of the early results relate to tests performed at constant strain rate and nominally at constant temperature. Even in these results, as

---

[1] Professor, Institute of Fundamental Technological Research, Warsaw, Poland; currently Visiting Professor, Division of Engineering, Brown University, Providence, R.I. 02912.

[2] Professor of Engineering, Brown University, Providence, R.I. 02912.

for example in ferritic steels tested over a wide range of constant strain rates and temperatures, an extremely complex behavior is revealed which later research was to show is further complicated by strain rate history and temperature history effects [*1-4*].[3] During the past decade, it has been shown that history effects are substantial in the case of face-centered-cubic (FCC) polycrystalline metals [*3,5,6*]. However, there have been few investigations thus far into strain rate history effects for metals of the BCC structure. The purpose of the present paper is to analyze more systematically strain rate history effects in such metals.

Polycrystalline BCC metals exhibit certain characteristic features, one of which is delayed yielding associated with the yield point phenomenon. Early experiments implied the existence of a finite delay time before macroscopic yield occurs. This delay time for the onset of gross yielding was measured systematically for mild steels by Clark and Wood [*7,8*] and by Campbell [*9*], among others. Summaries of this work can be found in Campbell [*5*] and Hall [*10*]. Very little experimental data exist concerning the influence of loading history on the phenomenon of delayed yielding, although some early results were obtained by Belsheim [*11*] and by Vigness et al [*12*].

As regards behavior beyond the yield point, many investigators have observed that the flow stress of iron or steels at constant temperature and at a given strain is not a linear function of the logarithm of strain rate, and that even at room temperature a minimum flow stress is observed at a certain value of strain rate. This minimum becomes more pronounced at higher temperatures and at larger strains, as was observed for mild steel at 473 and 673 K by Manjoine [*13*], and for iron at 293 K by Davidson et al [*14*] and by Klepaczko [*15*]. The reasons for the existence of a minimum, which indicates the beginning of a diffusion controlled process generally referred to as strain aging, have been discussed by Hahn et al [*16*] and by Tanaka and Kinoshita [*17*]. It is interesting to note that for low-carbon steel at 293 K, according to the data of Manjoine [*13*], this minimum flow stress appears at a strain rate on the order of 10^{-4} s^{-1}, but at 473 K the minimum is observed at $\dot{\epsilon} \approx 0.5$ s^{-1}, and at 693 K shifts to 1.5×10^2 s^{-1}. At strain rates lower than that at which the minimum flow stress occurs, sufficient time elapses during deformation so that strain-aging effects appear [*18*]. Indeed, dynamic strain-aging effects associated with the diffusion of impurities and alloying elements may produce the appearance of a negative strain rate sensitivity if experiments are limited to different constant strain rates. However, as will be shown later, the full complexity of strain rate history effects in BCC metals is only brought out by experiments in which the imposed strain rate is not constant, and in particular by experiments in which large enough jumps in strain rate are imposed. It may be expected then that strain rate history effects will be present, which implies a departure from a univalued function of stress, strain, strain

---

[3] The italic numbers in brackets refer to the list of references appended to this paper.

rate, and temperature [*5*]. This occurs when the strain rate is large enough so that strain aging, that is, diffusion, no longer accompanies plastic deformation.

At the same time, the stress-strain behavior of most BCC metals shows dynamic strain-aging at low strain rates when the testing temperature lies in the intermediate range; that is, between 0.3 and 0.5 T_m, where T_m is the melting temperature. In this range one may see an abnormally high work-hardening rate with a loss in ductility or one may obtain serrated yielding [*18*]. This is also the temperature range where a local maximum is seen in the curve of flow stress plotted as a function of temperature (at constant strain rate and for a given value of strain). Both manifestations of strain aging, the minimum in flow stress as a function of strain rate at constant temperature, or the maximum in flow stress observed when temperature is changed at constant strain rate, can produce strain rate history and temperature history effects.

In addition to these factors, at high strain rates where deformation times are very short the rate dependence may be affected by thermal softening caused by adiabatic heating. This adiabatic coupling becomes more pronounced in the low-temperature regions because of the low specific heat and high-temperature sensitivity of the flow stress. Since the isothermal and adiabatic stress-strain characteristics are different, adiabatic coupling may give rise to strain rate history effects. Such behavior may be of great importance for steels at low temperatures.

The main source of strain rate history effects, however, lies in the microstructural changes that take place during plastic deformation. Due to the large variety of possible deformation mechanisms, such as thermally activated, diffusion controlled, dislocation interactions, twinning, etc., the response of BCC metals and alloys to strain rate changes may differ substantially under different deformation conditions. Therefore a systematic experimental study is needed to accumulate more data on strain rate history effects for a variety of steels and for BCC metals in general. The only extensive investigation of these effects thus far is the study conducted with mild steel specimens by Eleiche and Campbell [*1*]. Some preliminary experimental data of limited extent are briefly discussed in the next section.

Experimental Evidence of Strain Rate History Effects in BCC Metals and Alloys

An understanding of strain rate history and temperature history effects on the microstructural scale is fundamental to modeling material behavior on the macroscale. One of the most useful experiments developed thus far for this purpose involves the imposition during the course of deformation of a sudden increment in strain rate or a sudden change in temperature. Many of the investigations of rate effects at low strain rates have been carried out by making small sudden changes in strain rate during the test; see, for example, Ref *19*. However, a convincing demonstration of history effects by means of a rapid change in strain rate frequently requires an increment of more than three orders of magnitude.

The first investigations of the effects of strain rate history or temperature history usually involved interrupted testing in which the specimen was completely unloaded before the new strain rate or temperature was imposed. Thus, in interrupted tests, specimens are loaded into the plastic range at one strain rate, unloaded, and then reloaded at a different strain rate. The resulting values of the flow stress are then compared with those obtained in tests conducted at a constant strain rate. Among the first interrupted experiments on steel were those of Ripling and Sachs [*20*]. In addition, Campbell and Duby [*21*] and Campbell and Maiden [*22*] demonstrated that after dynamic deformation of a medium-carbon steel at room temperature, the reloading portion of the quasi-static stress-strain curve is lower than the curve obtained entirely at the quasi-static strain rate. Metallographic examination showed that during loading at a strain rate of 5×10^2 s^{-1} deformation occurs by fine slip, but during straining at 10^{-3} s^{-1}, the slip bands are coarse. Other investigators who performed interrupted tests on steels include Smith [*23*] and Chou and Ting [*24*].

The complicated nature of strain rate history effects for high-purity iron was demonstrated by Harding [*2*], who performed interrupted tests with annealed specimens of iron loaded in tension (Fig. 1). Curve A was obtained by loading the specimen at a strain rate of $\sim 10^3$ s^{-1} after imposing a small pre-strain, ϵ_i, equal to 0.016 at the quasi-static rate of $\sim 10^{-3}$ s^{-1}. As may be seen, Curve A lies above Curve B which was obtained at a continuous strain rate of $\sim 10^3$ s^{-1}. This behavior contrasts with that of FCC metals in which a pre-strain at the lower strain rate serves to reduce rather than increase the subsequent flow stress at the higher rate [*3*].

As mentioned previously, the most useful experiment for studying history effects is probably the incremental one. The earliest incremental results with a high strain rate jump reported for steel are those of Nicholas [*25*]. Tubular specimens of an AISI 1020 steel were tested in torsion using a pneumatically driven piston acting through a lever arm to apply a dynamic torque; at the other end of the specimen a motor was used to apply a torque quasi-statically. The maximum shear strain rate attained in these experiments was about 25 s^{-1}. Nicholas's results for a strain rate of 25 s^{-1} and a static pre-strain of 0.02 are consistent with those of Harding (Fig. 1) and of Smith [*23*]. All results show that the flow stress after a strain rate increment is higher than would result from deforming only at the dynamic strain rate. On the other hand, incremental stress wave propagation experiments performed by one of the authors on deep-drawing steel revealed that at low initial strains,

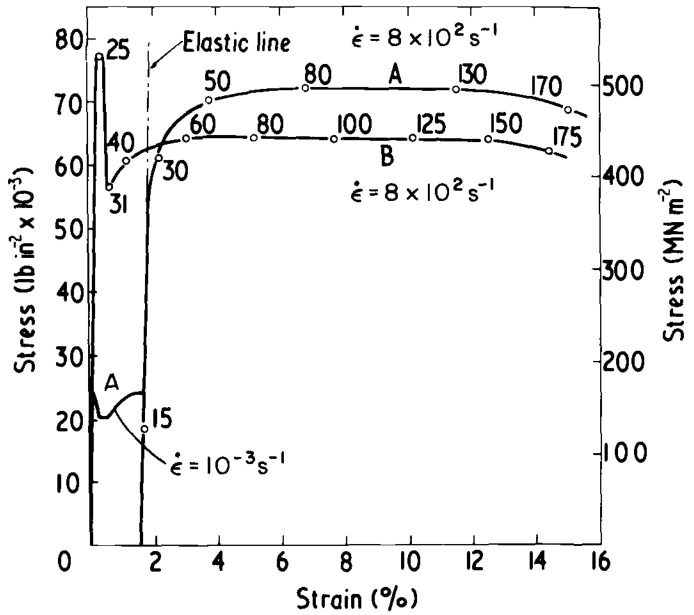

FIG. 1—*Stress-strain behavior of high-purity annealed iron. A—interrupted test; B—constant strain rate test. Numbers indicate times of deformation in microseconds. Data from Harding* [2], *courtesy of Institute of Physics.*

on the order of 0.01, the rate sensitivity is high, although the strain rate history effects at room temperature are negligible [26]. These last results may be viewed as preliminary, since the incremental portion of the stress-strain diagram was obtained by an integration of the wave equation. Tests were conducted at two initial values of strain, $\epsilon_i \approx 3.6 \times 10^{-3}$ and 7×10^{-3}, with an initial strain rate of $\dot{\epsilon}_i \approx 10^{-3}$ s^{-1}, and an average dynamic strain rate of $\dot{\epsilon}_r \approx 1.4 \times 10^2$ s^{-1}.

With reference to other BCC metals, Campbell and Briggs [27] reported results of incremental tests on annealed polycrystalline molybdenum and niobium. Testing was performed in compression in one of two machines, depending on the desired strain rates. In either case, the strain rate change was from a lower to a higher strain rate, and the change was imposed after an accumulation of a strain $\epsilon_i \approx 0.08$. A standard testing machine was used to provide strain rates ranging from 1.7×10^{-4} s^{-1} to 8.3×10^{-3} s^{-1}, and a hydraulically operated machine to attain the range of 8.5×10^{-3} s^{-1} to 10^2 s^{-1}. The results were compared with those of tests conducted at constant strain rates to show that the flow stress in both materials depends on strain rate history. Furthermore, it was found that significantly different results are obtained within each of the two strain rate ranges and for different deformation rate histories. These differences vary in a complex manner with the initial and final strain rates. For molybdenum a change in strain rate from $\dot{\epsilon}_i = 0.51\ s^{-1}$ to $\dot{\epsilon}_r = 4.25\ s^{-1}$ produces a result qualitatively similar to that shown for steel in Fig. 1. In the lower strain rate region, however, a strain rate change from $\dot{\epsilon}_i = 1.7 \times 10^{-4}\ s^{-1}$ to $\dot{\epsilon}_r = 8.3 \times 10^{-3}\ s^{-1}$ produces a result similar to that found in FCC metals: the stress in the incremental portion of the stress-strain diagram is lower than that obtained at the entirely constant strain rate of $\dot{\epsilon} = 8.3 \times 10^{-3}\ s^{-1}$.

Tanaka and Nojima [*28,29*] employed a split-Hopkinson bar together with a two-step striker bar to perform incremental tests in compression in the high strain rate region. In their experiments $\dot{\epsilon}_i \approx 10^2\ s^{-1}$ and $\dot{\epsilon}_r \approx 10^3\ s^{-1}$. Both constant strain rate and incremental strain rate tests were carried out within the temperature range of 78 to 290 K for two steels (0.02 and 0.45 percent carbon). For both steels the strain rate sensitivity, defined as $\beta = \Delta\sigma/\Delta \log \dot{\epsilon}$ and calculated at $\epsilon_i = 0.05$ on the basis of incremental test results, is greater than that obtained from the slope of σ versus $\log \dot{\epsilon}$ curves based on the constant strain rate tests. This effect is more pronounced at low strain rates, and again is in agreement with the results shown in Fig. 1.

Incremental Tests with Large Jumps in Strain Rate

During the last decade considerable improvements have been achieved in the experimental techniques for testing metals under dynamic conditions. These have led to reliable results, especially for incremental experiments in the high strain rate region. The experimental method most commonly used for this purpose is probably the split-Hopkinson bar modified for torsional loading [*30*]. This apparatus employs a thin tubular specimen loaded in torsion and subjected to a strain rate increment of six orders of magnitude at large strains and over a wide range of temperatures.

The first systematic study of mild steel using this technique was performed by Campbell and associates [*1,31*]. The increments in strain rate were imposed at shear strains, γ_i, equal successively to 0.08, 0.20, and 0.34, with an initial strain rate of $\dot{\gamma}_i = 6 \times 10^{-3}\ s^{-1}$ and a dynamic rate of $\dot{\gamma}_r = 1.2 \times 10^3\ s^{-1}$. Specimens were tested at six nominal temperatures ranging between 123 and 673 K.

The same technique was employed by Wilson et al [*4*] to perform incremental strain rate tests on two low-carbon steels: a 1020 hot-rolled and a 1018 cold-rolled steel. The purpose of the investigation was to determine the influence of strain rate and strain rate history in steels of nearly identical composition, but of quite different forming histories. Results showed strain rate history effects in both steels to be small at the ambient temperature.

Although each of the aforementioned investigations provides valuable results, it would appear that the effects of strain rate history in polycrystalline

BCC metals are still not fully understood. This situation is due in large measure to the limited number of investigations performed thus far and particularly to the need for incremental strain results covering a fairly extended temperature range. As a result, additional incremental strain rate experiments were undertaken and results compared with existing data.

The experiments were performed on tubular specimens of 1020 hot-rolled steel (HRS) with a composition of 0.25 percent carbon, 0.50 percent manganese, 0.017 percent phosphorus, and 0.029 percent sulfur. A torsional split-Hopkinson bar was employed to load the specimens at either of two strain rates in shear, $\dot{\gamma} \approx 5 \times 10^{-4}$ s^{-1} or $\dot{\gamma} \approx 10^3$ s^{-1}, or in incremental strain rate tests between these two strain rates. Testing covered the temperature range of 83 to 394 K, and the strain rate increments were imposed at initial shear strains, γ_i, ranging from 0.2 to 0.10. Representative stress-strain curves for three temperatures (83, 116, and 144 K) are shown in Figs. 2 to 4. As expected, strain rate has a significant effect on the flow stress of 1020 HRS, as made evident by the constant strain rate tests. The most interesting result, however, is obtained in the incremental strain rate experiments. At the lowest temperatures the stress-strain curves show a somewhat unexpected result: pre-straining the specimen at the quasi-static rate raises the subsequent dynamic flow stress above the value found in testing at a constant dynamic rate. This effect is substantial at 83 K, less pronounced at 116 K, and almost invisible at 144 K. The remaining incremental strain rate experiments in the series, performed at higher temperatures, showed little if any

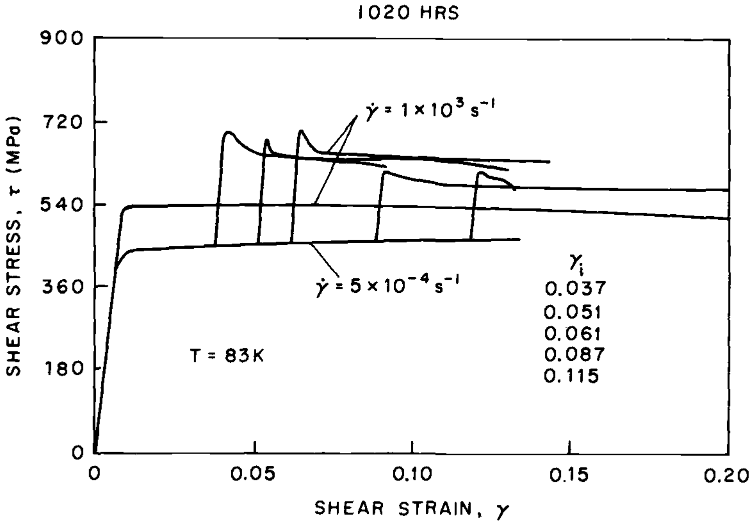

FIG. 2—*Results of constant and incremental strain rate tests on 1020 HRS at 83 K.*

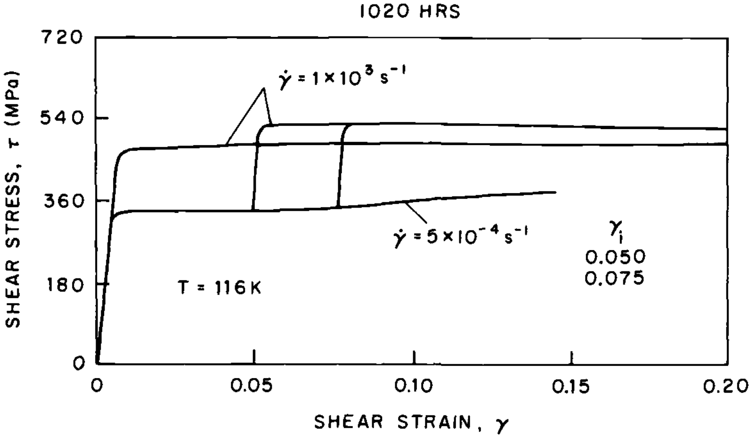

FIG. 3—*Results of constant and incremental strain rate tests on 1020 HRS at 116 K.*

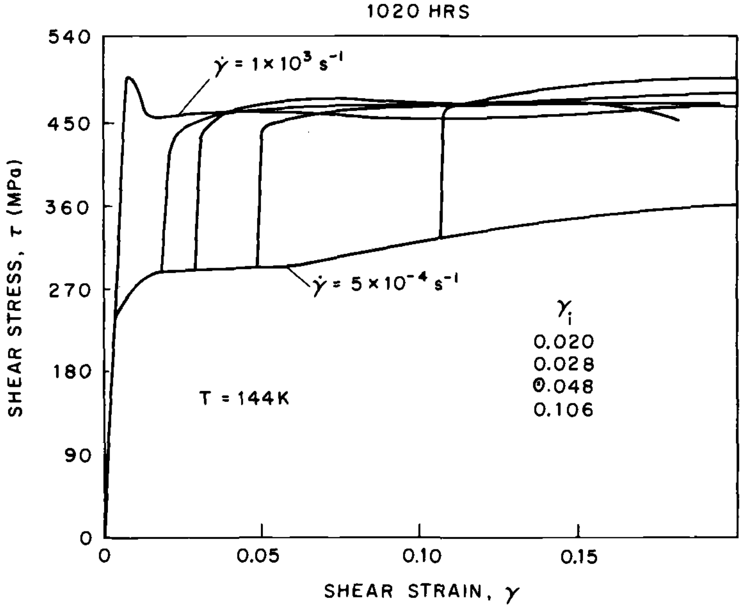

FIG. 4—*Results of constant and incremental strain rate tests on 1020 HRS at 144 K.*

strain rate history effects. However, at 394 K (Fig. 5) the incremental portion of the stress-strain curves show some transients, especially for the two highest values of pre-strain, $\gamma_i = 0.05$ and $\gamma_i = 0.10$. In addition, the quasi-static and dynamic stress-strain curves obtained at constant strain rates converge

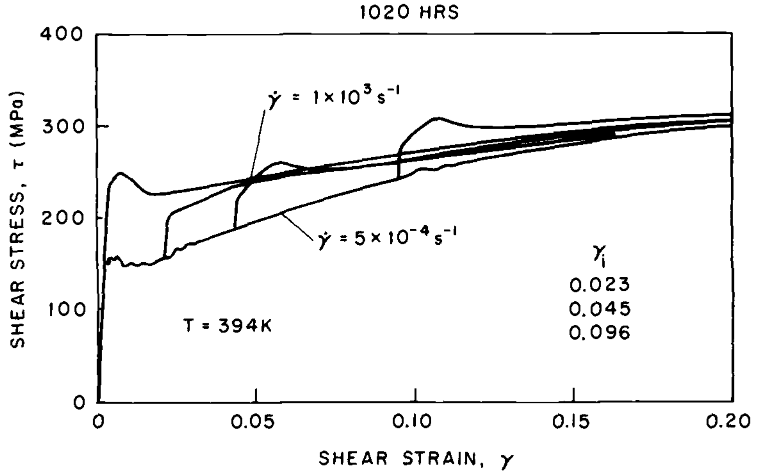

FIG. 5—*Results of constant and incremental strain rate tests on 1020 HRS at 394 K.*

at increasing strains. Some of these effects are related to dynamic strain aging, which starts to become important at about this temperature [*10*].

Strain rate history effects within the dynamic strain-aging region were observed in a mild steel (0.125 percent carbon, 1.15 percent manganese, and 0.37 percent phosphorus) by Eleiche and Campbell [*1*]. Their results at 473 and 673 K are shown in Figs. 6 and 7, respectively. Evidence of dynamic strain aging is seen at 473 K in the serrated stress-strain curve and in the relatively high work-hardening rate obtained for $\dot{\gamma} = 10^{-4}$ s^{-1}. For incremental experiments performed at relatively large values of γ_i a significant drop in stress was observed at the beginning of yielding. The work-hardening rate in the incremental portions of the stress-strain diagrams is substantially lower than that resulting from quasi-static deformation. It is expected that for mild steel in the dynamic strain-aging region the flow stress depends not only on strain rate but also on time itself. Thus strain aging should have a pronounced influence during slow deformation but little effect during dynamic loading. This would explain why constant strain rate tests show a negative strain rate sensitivity in this range of temperatures (Figs. 6 and 7), while there is no indication of a negative strain rate sensitivity for the initial portion of the incremental tests.

Thus it appears that for small values of pre-strains, that is, up to $\gamma_i \approx 0.20$, strain rate history effects for mild steel are important only in two temperature regions: for temperatures lower than ~150 K and for dynamic strain-aging temperatures of 500 K ± 100 K. At temperatures from about 150 to 350 K, strain rate history effects are of little importance. The situation is different, however, for pre-strains greater than ~0.20. As pointed out by

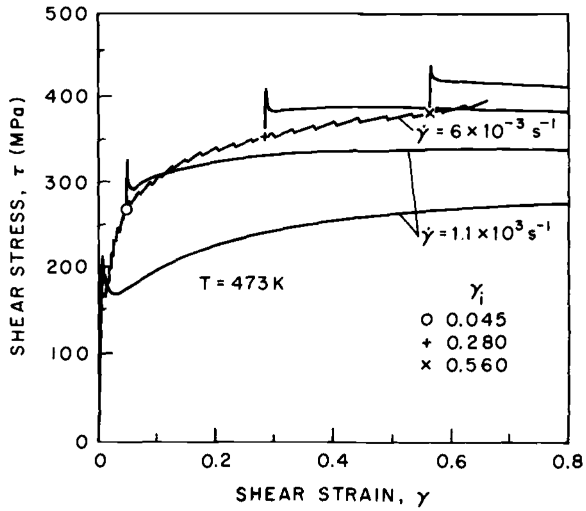

FIG. 6—*Test results for mild steel (0.125 percent carbon; 1.15 percent manganese) at 473 K, after Eleiche and Campbell* [1].

Eleiche and Campbell [*1*], strain rate history effects in this range may be substantial even at intermediate temperatures.

Constitutive Modeling

In view of the complicated nature of strain rate history effects in BCC metals, the development of more precise constitutive models is of great importance. The various approaches pursued in recent years can be separated into two categories. The first approach is based on results of macroscopic tests and on analyses based on continuum mechanics viewpoint. This approach leads to formulations directly applicable to engineering applications. Strain rate dependence is generally included in such theories; see, for example, Refs *32* to *40*. The second approach to constitutive modeling is based on physical principles; it combines solid mechanics and materials science in its development (for example, Refs *6,41,42,43,* and *44*). It is the second approach which is adopted in the present discussion of strain rate history effects.

We first examine the role of deformation-induced temperature changes under adiabatic conditions in producing history effects at low temperatures. As mentioned previously, a feature characteristic of the behavior of steel and some other BCC metals is that the flow stress following a sudden increase in strain rate may exceed that found in a test conducted entirely at the higher

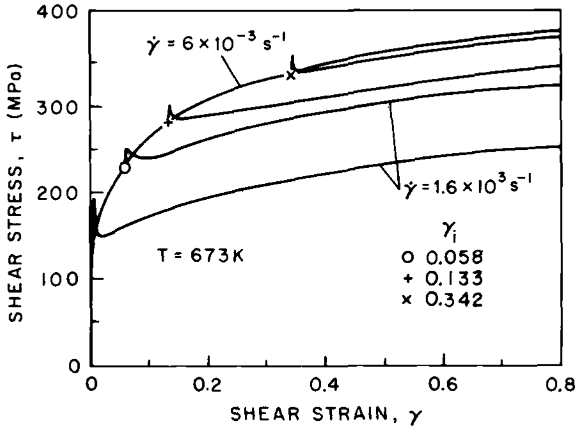

FIG. 7—*Test results for mild steel (0.125 percent carbon; 1.15 percent manganese) at 673 K, after Eleiche and Campbell* [1].

rate. Zener and Hollomon [*45*] working with steel showed the importance of adiabatic coupling at low temperatures and high strain rates. Later Campbell and Briggs [*27*], testing molybdenum and niobium, attributed strain rate history effects to the thermal softening resulting from plastic work converted into heat. At a high strain rate the instantaneous temperature of the specimen may rise appreciably from its initial value due to the conversion of the plastic work into heat, thus resulting in a gradual softening of the metal. Consequently, the rate of strain hardening is lower under adiabatic than isothermal conditions, if one ignores for the moment the dynamic-aging temperature region and the possibility that it provides an explanation for the effect seen in Fig. 1. On the microscopic scale, the temperature distribution during deformation is probably not uniform. Heat will be generated on the dislocation planes, following which the dislocations will concentrate into slip lines, and a substantial increase in temperature will occur within the immediate neighborhood. Following this the heat will be conducted to cooler microvolumes, and only after an appropriate short interval of time will the temperature become substantially uniform within the whole of the deformed volume. This two-step process must be kept in mind in discussing the adiabatic increase in temperature and in evaluating thermal softening, since the temperature increase may be far higher locally than estimated by a direct conversion of plastic work into heat, and since local heating on this scale may lead to significant changes in the microstructure [*46,47*].

It is important, when interpreting macroscopic test results, to have an estimate of the adiabatic increase in temperature, ΔT, due to plastic work.

For this purpose, the flow stress, τ, is taken as a univalued function of the shear strain, γ, the shear strain rate, $\dot{\gamma}$, and the temperature, T, so that

$$\tau = \tau(\gamma, \dot{\gamma}, T) \tag{1}$$

It follows from energy conservation that

$$\frac{dT}{d\gamma} = \frac{[1 - \xi(\gamma, T)]\tau(\gamma, \dot{\gamma}, T)}{J\rho_0(T)C_v(T)} \tag{2}$$

where $\xi(\gamma,T)$ is a coefficient representing stored energy in the lattice, J is a conversion factor of mechanical energy into heat, $\rho_0(T)$ is the density of the metal, and $C_v(T)$ is its specific heat at constant volume. The stored energy of cold work is usually a small fraction of the total plastic work [*48*]; on an average, $\xi \approx 0.05$. Equation 2 cannot be integrated in closed form unless certain simplifications are made. Since ρ_0 is only weakly dependent on temperature it can be taken as constant; at higher temperatures than ~100 K, C_v may also be assumed constant. Furthermore, T can be set equal to the initial temperature T_0. Integration now becomes possible so long as one specifies $\dot{\gamma}(\gamma)$; that is, so long as one specifies changes in strain rate during the course of deformation. Thus an explicit form, $\Delta T(\gamma_m, T_0)$, is derived for the increase in temperature per unit volume during adiabatic deformation. With these simplifications, Eq 2 can be expressed as

$$\Delta T = \frac{1 - \xi}{J\rho_0(T_0)C_v(T_0)} \int_0^{\gamma_m} \tau[\gamma, \dot{\gamma}(\gamma), T_0]\, d\gamma \tag{3}$$

Once $\Delta T(\gamma_m, T_0)$ has been evaluated, then Eq 1 provides values of $\Delta\tau(\gamma_m, T_0)$. Thus

$$\Delta\tau = \tau_T(\gamma_m, \dot{\gamma}, T_0) - \tau_A[\gamma_m, \dot{\gamma}, (T_0 + \Delta T)] \tag{4}$$

where τ_T and τ_A are respectively the flow stress under isothermal and adiabatic conditions of deformation. Equation 4 can be used to compare adiabatic and isothermal stress-strain curves, and to compare these curves with those of incremental strain rate experiments.

The simplest method of obtaining an upper bound for $\Delta\tau$ is to measure experimentally the drop in the flow stress caused by the temperature increase during deformation. In other words, one evaluates the partial derivative $(\partial\tau/\partial T_0)_{\gamma,\dot{\gamma}}$ for specified values of γ and for various strain rates $\dot{\gamma}$. Then the adiabatic decrease in flow stress is calculated from

$$\Delta\tau = \left(\frac{\partial\tau}{\partial T_0}\right)_{\gamma,\dot{\gamma}} \Delta T \tag{5}$$

in which it should be remembered that the value of $(\partial\tau/\partial T_0)$ is negative. Experimental results for steels and other BCC metals indicate that $(\partial\tau/\partial T_0)$ is approximately constant at lower temperatures [*1,27,49,50*]. The temperature sensitivity $(\partial\tau/\partial T_0)_{\gamma,\dot\gamma}$, defined above, was calculated for niobium, molybdenum, and three steels, including 1020 HRS, using experimental data from different sources (Fig. 8). It appears from the results shown that temperature sensitivity does not depend on strain rate to any great extent. Its average values for different metals are as indicated; for mild steel, including 1020 HRS, the average value is $(\partial\tau/\partial T_0)_{\gamma,\approx 0.05} \approx -2.08$ MPa K^{-1} [*51*].

To estimate the adiabatic decrease in flow stress, $\Delta\tau$, it may be assumed, as a first approximation, that the flow stress has a constant value τ_0 at $\dot\gamma \approx 10^3\ \text{s}^{-1}$ and at the initial temperature T_0. This is a relatively good assumption for mild steel. Thus the constant value of $(dT/d\gamma)_{\dot\gamma}$ resulting from this assumption and integration of Eq 3 leads to

$$\Delta T = A\tau_0\gamma_m; \qquad \dot\gamma = 10^3\,\text{s}^{-1} \tag{6}$$

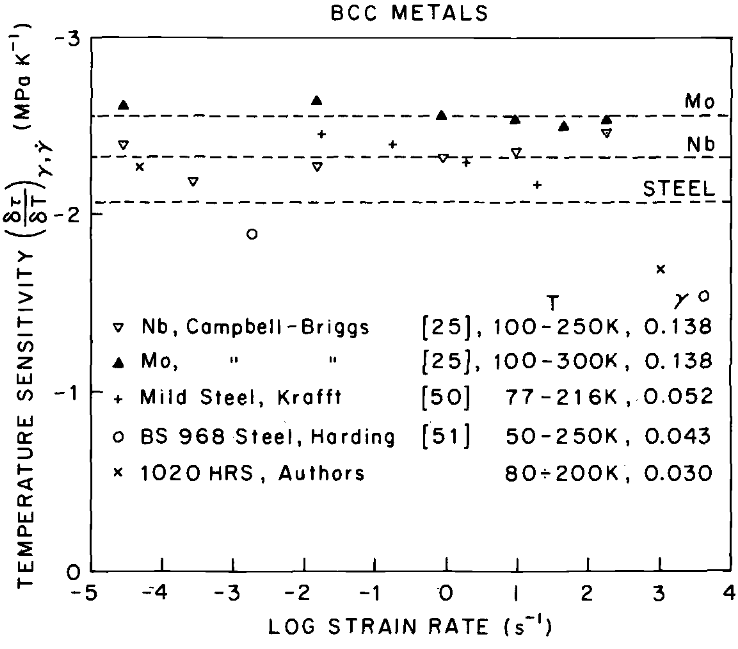

FIG. 8—*Temperature sensitivities of different BCC metals as a function of the shear strain rate* $\dot\gamma$. *For purposes of comparison, data originally presented in terms of axial components of stress and strain* (σ, ϵ) *are transformed to shear by the equations* $\tau = \sigma/\sqrt{3}$ *and* $\gamma = \sqrt{3}\,\epsilon$.

where $A\tau_0$ is a constant evaluated at T_0, and A is the coefficient of the integral of Eq 3. Introducing Eq 6 into Eq 5, one obtains

$$\frac{\Delta\tau}{\tau_0} = A\gamma_m \left(\frac{\partial\tau}{\partial T_0}\right)_{\gamma,\dot{\gamma}} \tag{7}$$

It follows from Eq 7 that $\Delta\tau/\tau_0$ is approximately a linear function of γ_m, and consequently the strain rate history effects due to adiabatic coupling will intensify with strain, leading to the incremental flow stress curves in Figs. 1 to 3. The constant A can be evaluated using tabulated data of $C_v(T_0)$, which give for the low and ambient temperature region $A \approx 0.4$ K/MPa. Using the value of $(\partial\tau/\partial T_0)$ given above yields

$$\frac{\Delta\tau}{\tau_0} = -0.83\,\gamma_m \tag{8}$$

Thus the relative adiabatic decrease in flow stress intensifies with the amount of strain. Furthermore, for a given material the actual drop in stress $\Delta\tau$ generally will be greater at lower temperatures due to the higher values of τ_0. For a test at $T_0 = 83$ K (Fig. 2), at $\gamma_i = 0.10$ and $\tau_0 = 540$ MPa we have $\Delta\tau \approx$ 45 MPa. For $T_0 = 116$ K (Fig. 3), τ_0 remains nearly constant at 470 MPa, and we have $\Delta\tau \approx 20$ MPa at $\gamma_m = 0.05$ and $\Delta\tau \approx 30$ MPa at $\gamma_m = 0.075$. These values of $\Delta\tau$ account for about half the amount by which the incremental flow stress exceeds the all-dynamic value at 116 K. While $\Delta\tau$ is greater at 83 K than at 116 K, it is somewhat less in proportion to the difference between incremental and constant strain rate values of flow stress. In the intermediate temperature region, from 144 to 350 K, adiabatic coupling is small for values of strain up to $\gamma_m \approx 0.1$, and $\Delta\tau$ is on the order of the experimental error. But even in this temperature range, Eleiche and Campbell [*1*], found that the post increment flow stress at larger strains is always greater than that in a constant-rate dynamic test.

Thus one may conclude that there are at least two possible causes for strain rate history effects in BCC metals: the adiabatic coupling which occurs at high but not at low strain rates, and the different microstructural changes which accompany plastic deformation at different strain rates and temperatures. As another example of history caused by microstructural changes, one can mention twinning. Twinning is observed under rapid deformation at low temperatures [*10*]. On the other hand, at dynamic strain-aging temperatures there is a high rate of dislocation multiplication [*18, 52*].

It is generally agreed that strain rate effects at low temperatures are due to the thermally activated motion of dislocations [*19, 44, 53*]. However, because crystalline materials exhibit a variety of different strain rate and temperature effects, there is no simple, universally applicable rate equation that will model material behavior at different strain rates and with different histories. The rate equation which is frequently used in the following form relates strain rate and temperature at constant structure [*54*]:

$$\dot{\gamma}_i = v(\tau, T) \exp\left[-\frac{\Delta G(\tau^*, T)}{kT}\right] \tag{9}$$

where $v(\tau, T)$ is the so-called pre-exponential factor, $\Delta G(\tau^*, T)$ is the activation free energy, and τ^* is the thermally activated component of stress:

$$\tau^* = \tau - \tau_\mu(\tau, \rho) \tag{10}$$

Analyses performed by different authors seem to indicate that in BCC metals at low temperatures dislocations overcome the Peierls potential by forming kink pairs through a thermally activated deformation mechanism [*55-59*]. Kocks et al [*60*] proposed an "averaged" relation for this process:

$$\Delta G_P = 2H_k(T)\left[1 - \left(\frac{\tau^*}{\tau_p(T)}\right)^p\right]^q \tag{11}$$

where $H_k(T)$ is the total activation energy of kink formation, and $\tau_p(T)$ is the Peierls stress; both these parameters are functions of temperature through changes in the elastic constants. To provide a good fit for present experimental data, the two exponents were evaluated at $p = 3/4$ and $q = 4/3$. Introducing Eqs 10 and 11 into Eq 9, one obtains

$$\tau = \tau_p(T)\left\{\frac{\tau_\mu(T, \rho)}{\tau_p(T)} + \left[1 - \left(\frac{kT}{2H_k(T)} \ln \frac{v_p(\tau, T)}{\dot{\gamma}}\right)^{1/q}\right]^{1/p}\right\} \tag{12}$$

In its most general form, Eq 12 cannot be solved explicitly for τ, since the pre-exponential factor also depends on τ. However, because the dependence of v_p on τ is weak, v_p is usually taken as stress independent. In many cases this is a quite satisfactory approximation, but Figs. 2 and 3 suggest that in steels deforming at high strain rates and low temperatures, there may be a stronger dependence of v_p on τ, due perhaps to an increase in the mobile dislocation density [*61*]. The estimated value of v_p for the kink mechanism is on the order of $\sim 10^{10}\ \mathrm{s}^{-1}$ [*60*].

The question that now arises is which is the best way to model strain rate and temperature history effects in polycrystalline BCC metals. There are two possible ways to introduce structural evolution into Eq 12. The first, which seems more pertinent to lower temperatures and higher strain rates, concentrates on the changes in the mobile dislocation density; this approach requires a structural dependence of the pre-exponential function $v_p(\tau, T)$. The second possibility, applicable to higher temperatures, involves the introduction of structural evolution into the athermal component of stress $\tau_\mu(T,\rho)$ through a variation in the total dislocation density ρ [*55, 62, 63*].

It is beyond the scope of this paper to discuss the details of structural evolution or to propose explicit forms for the evolutionary relation. These problems will be treated in extended form elsewhere [*64*]. The present analysis, however, has shown the importance of evolutionary structural changes in obtaining a more complete picture of strain rate and temperature effects as well as of strain rate history effects. The contribution of these evolutionary changes can also be investigated by making use of an independent source of information, namely, transmission electron microscopy.

It should be mentioned that the form assumed for the activation free energy, ΔG_p, in Eq 11 is better suited for the ambient and low-temperature regions. High-temperature behavior, including the rapid recovery following strain rate changes, has been studied by Barraclough and Sellars [*65*] and by Jonas and McQueen [*66*]; both these investigations include experiments with steels.

The experimental results included in this paper point to the significance of evolutionary microstructural changes at low and at dynamic-aging temperatures. However, a different approach must be employed to model the behavior in each of these temperature regions.

Conclusions

The following conclusions may be drawn on the basis of the present analysis:

1. Strain rate and temperature history effects play an important role in the deformation of BCC polycrystalline metals at low temperatures and in the dynamic strain-aging temperature range.
2. Up to approximately the ambient temperature, strain rate history effects do not dominate for shear strains less than ~0.20. But at larger strains, strain rate history effects may exist even at room temperature, and can be attributed to adiabatic coupling if the plastic deformation is fast enough.
3. Constitutive modeling of history effects is possible but requires the coupling of two relations: an expression for strain rate based on the particular thermally activated process which is currently dominant, plus a second equation describing evolutionary changes in the microstructure.

Acknowledgments

The results presented in this paper were obtained in the course of research sponsored by the National Science Foundation under Grant CME 79-23742 and the Materials Research Laboratory at Brown University. The helpful suggestions of Mr. R. H. Hawley and the competent assistance in experiments and data processing of Mr. G. LaBonte and Ms. K. A. Hartley are gratefully acknowledged.

References

[1] Eleiche, A. M. and Campbell, J. D., "The Influence of Strain-Rate History and Temperature on the Shear Strength of Copper, Titanium and Mild-Steel," Technical Report AFML-TR-76-90, Air Force Materials Laboratory, Dayton, Ohio, March 1976.

[2] Harding, J., discussion of paper by Klepaczko and Duffy, in *Proceedings*, Conference on Mechanical Properties at High Rates of Strain, Institute of Physics, Conference Series No. 21, London, 1974, p. 191.

[3] Klepaczko, J., Frantz, R. A., and Duffy, J., *Rozprawy Inzynierskie (Engineering Transactions)*, Vol. 25, 1977, p. 3.

[4] Wilson, M. L., Hawley, R. H., and Duffy, J., "Strain Rate and Strain Rate History Effects in Two Mild Steels," Technical Report NSF-18532/8, Division of Engineering, Brown University, Providence, R.I., March 1979.

[5] Campbell, J. D., *Dynamic Plasticity of Metals*, Springer, 1972 (Lectures at International Centre for Mechanical Sciences, Udine, Italy, 1970).

[6] Klepaczko, J., *Materials Science and Engineering*, Vol. 18, 1975, p. 121.

[7] Clark, D. S. and Wood, D. S. in *Proceedings*, American Society for Testing and Materials, Vol. 49, 1949, p. 717.

[8] Wood, D. S. and Clark, D. S., *Transactions*, American Society for Metals, Vol. 43, 1951, p. 571.

[9] Campbell, J. D., *Acta Metallurgica*, Vol. 1, 1953, p. 706.

[10] Hall, E. O., *Yield Point Phenomena in Metals and Alloys*, Plenum Press, New York, 1970, p. 65.

[11] Belsheim, R. O., "Delayed-Yield Time Effects in Mild Steel Under Oscillatory Axial Loads," NRL Report 4312, Naval Research Laboratory, Washington, D.C., March 1954.

[12] Vigness, I., Krafft, J. M., and Smith, R. C. in *Proceedings*, Conference on Properties of Materials at High Rates of Strain, Institution of Mechanical Engineers, London, 1957, p. 138.

[13] Manjoine, M. J., *Journal of Applied Mechanics*, Vol. 11, 1944, p. A-211.

[14] Davidson, D. L., Lindholm, U. S., and Yeakley, L. M., *Acta Metallurgica*, Vol. 14, 1966, p. 703.

[15] Klepaczko, J., *International Journal of Solids and Structures*, Vol. 5, 1969, p. 533.

[16] Hahn, G. T., Reid, C. N., and Gilbert, A., *Acta Metallurgica*, Vol. 10, 1962, p. 747.

[17] Tanaka, K. and Kinoshita, M., *Bulletin*, Society of Mechanical Engineers, Japan, Vol. 10, 1967, p. 429.

[18] Keh, A. S., Nakada, Y., and Leslie, W. C. in *Dislocation Dynamics*, A. R. Rosenfield et al, Eds., McGraw-Hill, New York, 1968, p. 381.

[19] Basinski, Z. S. and Christian, J. W., *Australian Journal of Physics*, Vol. 13, 1960, p. 299.

[20] Ripling, E. J. and Sachs, G., *Transactions*, AIME, Vol. 185, 1949, p. 78.

[21] Campbell, J. D. and Duby, J., *Properties of Materials at High Rates of Strain*, Institution for Mechanical Engineers, London, 1957, p. 214.

[22] Campbell, J. D. and Maiden, C. J., *Journal of Mechanics and Physics of Solids*, Vol. 6, 1957, p. 53.

[23] Smith, R. C., *Experimental Mechanics*, Vol. 1, 1961, p. 153.

[24] Chou, S. C. and Ting, T. C. T. in *Proceedings*, Symposium on the Mechanical Behavior of Materials, Vol. 2, 1974, p. 63.

[25] Nicholas, T., *Experimental Mechanics*, Vol. II, 1971, p. 370.

[26] Klepaczko, J. in *Foundations of Plasticity*, A. Sawczuk, Ed., Noordhoff, Leyden, 1973, p. 451.

[27] Campbell, J. D. and Briggs, T. L., *Journal of Less-Common Metals*, Vol. 40, 1975, p. 235.

[28] Tanaka, K. and Nojima, T. in *Proceedings*, International Conference on Materials Behavior, Japan Society of Materials Science, Kyoto, 1972, p. 176.

[29] Tanaka, K. and Nojima, T., *Mechanical Properties of High Rates of Strain*, J. Harding, Ed., 1979, Institute of Physics, Conference Series No. 47, London, 1979, p. 166.

[*30*] Frantz, R. A., and Duffy, J., *Journal of Applied Mechanics*, Vol. 39, Dec. 1972, pp. 939-945.

[*31*] Campbell, J. D., Eleiche, A. M., and Tsao, M. C. C., *Fundamental Aspects of Structural Alloy Design*, R. I. Jaffee and B. A. Wilcox, Eds., Plenum Press, New York, 1977, p. 545.

[*32*] Perzyna, P., *Quarterly of Applied Mathematics*, Vol. 20, 1963, p. 321.

[*33*] Perzyna, P., *International Journal of Non-linear Mechanics*, Vol. 6, 1971, p. 707.

[*34*] Valanis, K. C., *Archives of Mechanics*, Vol. 27, 1975, p. 857.

[*35*] Wu, K. C. and Yip, M. C., *International Journal of Solids and Structures*, Vol. 16, 1980, p. 515.

[*36*] Bodner, S. R. and Partom, Y., *Journal of Applied Mechanics*, Vol. 42, 1975, p. 385.

[*37*] Liu, M. C. M. and Krempl, E., *Journal of the Mechanics and Physics of Solids*, Vol. 27, 1979, p. 377.

[*38*] Cernocky, E. P. and Krempl, E., *International Journal of Non-linear Mechanics*, Vol. 14, 1979, p. 183.

[*39*] Cristescu, N., *Dynamic Plasticity*, North-Holland, Amsterdam, 1967.

[*40*] Suvorova, J. V., Izv. AN-USSR, *MTT*, Vol. 9, 1974, p. 73; *English Translation in Mechanics of Solids*, Vol. 9, No. 1, 1974.

[*41*] Alden, T. M., *Metallurgical Transactions*, Vol. 6A, 1975, p. 1597.

[*42*] Hart, E. W., *Journal of Engineering Materials and Technology*, Vol. 98, 1976, p. 97.

[*43*] Swearengen, J. C. and Rohde, R. W., *Metallurgical Transactions*, Vol. 8, 1977, p. 577.

[*44*] Klahn, D., Mukherjee, A. K., and Dorn, J. E. in *Proceedings*, Second International Conference on the Strength of Metals and Alloys, Asilomar, Calif., 1970.

[*45*] Zener, C. and Hollomon, J. H., *Journal of Applied Physics*, Vol. 15, 1944, p. 22.

[*46*] Longo, W. P. and Reed-Hill, R. E., *Metallography*, Vol. 7, 1947, p. 181.

[*47*] Luft, A., Brenner, B., and Ritschel, C., *Kristall und Technik*, Vol. 14, 1979, p. 1293.

[*48*] Bever, M. B., Holt, D. L., and Titchener, A. L., *The Stored Energy of Cold Work; Progress in Materials Science*, Vol. 17, Pergamon Press, Oxford, 1973.

[*49*] Krafft, J. M. in *Techniques of Metals Research*, R. F. Bunshah, Ed., Vol. 5, Part 2, Wiley-Interscience, New York, 1971.

[*50*] Harding, J., *Metals Technology*, Vol. 4, 1977, p. 6.

[*51*] Costin, L. S., Crisman, E. E., Hawley, R. H., and Duffy, J., *Mechanical Properties at High Rates of Strain*, J. Harding, Ed., Institute of Physics, Conference Series No. 47, London, 1979, p. 90.

[*52*] Keh, A. S. and Leslie, W. C., *Materials Science Research*, Plenum Press, New York, 1963, p. 208.

[*53*] Conrad, H., *Journal of Metals*, Vol. 16, 1964, p. 582.

[*54*] Sherby, O. D. and Miller, A. K., *Journal of Engineering Materials and Technology*, Vol. 101, 1979, p. 387.

[*55*] Seeger, A., *Philosophical Magazine*, Vol. 1, 1956, p. 651.

[*56*] Dorn, J. E. and Rajnak, S., *Transactions*, AIME, Vol. 230, 1964, p. 1052.

[*57*] Hirth, J. P. in *Inelastic Behavior of Solids*, M. F. Kanninen et al, Eds., McGraw-Hill, New York, 1970, p. 281.

[*58*] Conrad, H., *High Strength Materials*, Wiley, New York, 1965, p. 436.

[*59*] Sestak, B., *Kristall und Technik*, Vol. 14, 1979, p. 1298.

[*60*] Kocks, U. F., Argon, A. S., and Ashby, M. F., *Thermodynamics and Kinetics of Slip*, Pergamon Press, Oxford, 1975.

[*61*] Orava, R. N., *Transactions of the Metallurgical Society*, AIME, Vol. 238, 1964, p. 1619.

[*62*] Gilman, J. J., *Micromechanics of Flow in Solids*, McGraw-Hill, New York, 1969, p. 189.

[*63*] Bergstrom, Y. and Roberts, W., *Acta Metallurgica*, Vol. 21, 1973, p. 741.

[*64*] Klepaczko, J., "A Model for Yielding and Flow of Iron and BCC Metals Based on Thermal Activation," Technical Report, No. NSF CME79-23742/4. Division of Engineering, Brown University, Providence, R.I., June, 1981.

[*65*] Barraclough, D. R. and Sellars, C. M., *Mechanical Properties at High Rates of Strain*, J. Harding, Ed., Institute of Physics, Conference Series No. 21, London, 1974, p. 111.

[*66*] Jonas, J. J. and McQueen, H. J. in *Treatise on Materials Science and Technology, Vol. 6: Plastic Deformation of Materials*, R. J. Arsenault, Ed., Academic Press, New York, 1975, p. 394.

T. S. Cook[1]

Cyclic Stress-Strain Behavior of Inconel 718

REFERENCE: Cook, T. S., "**Cyclic Stress-Strain Behavior of Inconel 718,**" *Mechanical Testing for Deformation Model Development, ASTM STP 765,* R. W. Rohde and J. C. Swearengen, Eds., American Society for Testing and Materials, 1982, pp. 269–283.

ABSTRACT: An investigation of the cyclic stress-strain behavior of forged Inconel 718 is described. The study was conducted at 294, 616, and 839 K, and R_ϵ ($\epsilon_{\min}/\epsilon_{\max}$) = 0, −1. The material showed moderate amounts of cyclic strain softening, with the extent and rate of softening increasing as the temperature increased. It was expected that the cyclic stress-strain curve defined by the amplitude of the load-displacement hysteresis loops would be independent of R_ϵ; specimen-to-specimen scatter prevented such a conclusion, although the data tended to support it. A second cyclic stress-strain curve, defined by the locus of the tips of the hysteresis loops, incorporates the mean stress of the loop and was dependent on R_ϵ. The presence of the mean stress in this definition of the cyclic stress-strain curve produced a curve with a hump; after reaching a maximum value at about 0.8 percent strain range, the stress decreased as strain range increased further. This hump shape is not the result of transient behavior, but represents the stable cyclic curve. The transient behavior and the stable state reached by the material during the test is discussed.

KEY WORDS: nickel-base superalloys, Inconel 718, mechanical properties, cyclic stress-strain analysis, fatigue (metals), cycles, stress, strain, cyclic softening, tests, evaluation, low cycle fatigue

Nomenclature

τ	Generalized stress
τ_A	Alternating stress, $\Delta\tau/2$
τ_M	Mean stress
τ_T	Stress at tensile tip of hysteresis loop
$\Delta\tau$	Stress range
ϵ	Generalized strain
ϵ_A	Alternating strain, $\Delta\epsilon/2$

---

[1] Engineer, Materials Life and Methods, General Electric Company, Cincinnati, Ohio 45215.

ϵ_{max}	Maximum strain
ϵ_{min}	Minimum strain
ϵ_T	Strain at tensile tip of hysteresis loop
$\Delta\epsilon$	Strain range
N_f	Cycles to failure
R_ϵ	Strain ratio, $\epsilon_{min}/\epsilon_{max}$

In order to predict the low-cycle fatigue life of a notched component, most techniques require the determination of the stress and strain fields in the vicinity of the notch. Since the component will usually be undergoing plastic deformation at the base of the notch, significant changes can occur in the yield stress of the deformed material [*1*].[2] The nature of these changes has been documented for a number of materials [*1–4*]. The approach generally taken in these studies has been to conduct constant or varying amplitude fatigue tests and to connect the tips of the stable hysteresis loops; the curve so defined is termed the cyclic stress-strain curve (CSSC).

The cyclic material response represented by the CSSC has been useful in understanding the processes of fatigue and damage accumulation [*5–6*]. When applied to the general problem of structural life assurance, however, the effect of variables like mean stress must be included in the analysis [*7*]. These effects have received scant attention, but as the use of CSSC in life analysis increases, an understanding of their role becomes crucial. The work described in this paper is part of an ongoing program to determine the cyclic properties and the fatigue behavior of forged Inconel 718. Specifically, the original objective of this portion of the program was to determine the stable cyclic stress-strain behavior—that is, the extent of softening—as a function of temperature and R_ϵ-ratio. While the overall objective remained the same throughout the effort, a number of unanticipated problems led to some secondary objectives. It was necessary, for example, to evaluate several techniques for the determination of the CSSC. The behavior of the material as a function of cycles and the achievement of steady-state values was also examined.

Experimental Program

The material selected for study in this program was Inconel 718, a nickel-base superalloy commonly used in gas turbines because of its high-temperature fatigue and creep properties. Typical properties and nominal composition are given in Table 1. Inconel 718 shows only a small amount of strain hardening and modest levels of ductility during monotonic testing. The specimens were all removed from ring-rolled ingots after the completion of the forging sequence. The ring-rolling process heavily works the outer

---

[2] The italic numbers in brackets refer to the references appended to this paper.

TABLE 1—*Properties of forged Inconel 718.*

Temperature, K (°F)	0.2 % Yield Strength, MPa (ksi)	Ultimate Strength, MPa (ksi)	Elongation, %
294 (70)	1151 (165)	1365 (195)	20
616 (650)	965 (138)	1117 (160)	20
839 (1050)	931 (133)	1083 (155)	18

Nominal Composition

Cr	19.0	Cu	0.75 max
Cb + Ta	5.1	Si	0.45 max
Mo	3.0	Mn	0.35 max
Ti	1.0	C	0.10 max
Al	0.5	Ni	52.5
B	0.006	Fe	balance

material of the ingot, but the interior receives much less work. Away from the rolled surface, the interior of the material had a coarse grain size, averaging ASTM 5. At any given cross section, the grain size ranged from about ASTM 4.5 to 7.0; this degree of variation is typical of ring-rolled Inconel 718. All specimens were oriented tangentially with respect to the pancake forging. The elevated temperature test specimens were obtained from four forgings, while the room temperature specimens were all removed from one of these four pancakes. Tests were conducted at 294 (room temperature), 616, and 839 K; two R_ϵ-ratios, 0 and -1 were used. The cylindrical test specimens were smooth round bars, 5.1 mm in diameter, with a gage length of 19.1 mm; button heads were used for gripping purposes. The tests were conducted on closed-loop hydraulic testing machines. Axial extensometers, 12.7 mm gage length, were used to control the strain. Load was recorded on strip charts or by computerized data acquisition; load-strain hysteresis loops were obtained with *X-Y* recorders. The specimens were heated by open induction coils controlled by thermocouples welded to the specimen. Testing procedure generally followed [*8*] except that axial rather than diametral strain was controlled.

Two experimental methods were used to produce the CSSC; these are shown schematically in Fig. 1 for $R_\epsilon = 0$. The first of these, called incremental step technique (Fig. 1*a*) by Landgraf et al [*9*], was used exclusively for the elevated temperature tests. For the room temperature tests, both incremental and constant-amplitude strain technique (Fig. 1*b*) were used. While Fig. 1*a* shows only a single value of ϵ_{max}, the room temperature tests maximized specimen usage by employing four values of ϵ_{max} per test in a manner analogous to the constant-amplitude tests of Fig. 1*b*. Regardless of the experimental procedure, the usual definition of the CSSC involves plotting either the locus of the tips, (τ_T, ϵ_T), or half the range, ($\Delta\tau/2$, $\Delta\epsilon/2$), of the

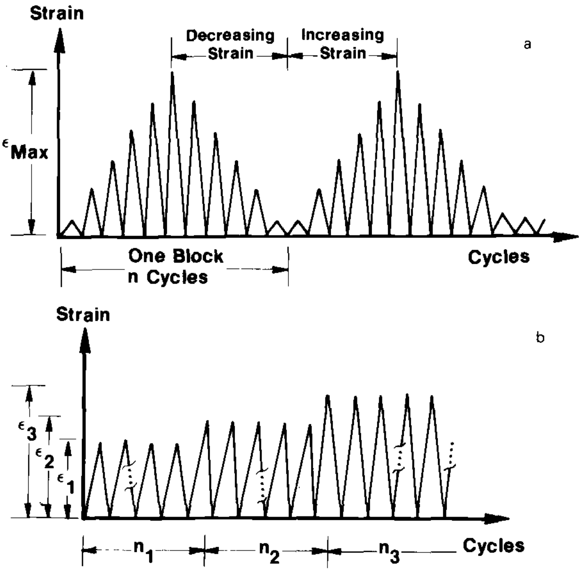

FIG. 1—*Strain-cycle waveforms used to obtain cyclic stress-strain curves.* (a) *incremental strain amplitude;* (b) *constant strain amplitude block sequence.*

stable stress-strain loops from several specimens subjected to different levels of completely reversed strain amplitudes [*9*]. For convenience, the material behavior is usually defined to be stable at half-life, $N_f/2$ [*4,6*]. However, the bulk of the alteration of the yield stress after repeated loading has been estimated to take place in approximately the first 20 percent of life, with only small changes taking place after that [*9*]. This suggests that because of the estimated rapid achievement of steady-state strain conditions, test efficiency can be improved by block loading where each specimen is cycled at several levels of applied strain (Fig. 1*b*).

It should be noted that the cyclic techniques are all based on testing experience at $R_\epsilon = -1$. In an $R_\epsilon = -1$ test, material undergoes fully reversed loading about a mean strain of zero, resulting in load-displacement records that are essentially asymmetric about the origin. (The specimens do frequently develop a small, less than 35 MPa, compressive mean stress, however. Potential mean stress effects under other conditions have been recognized by recommendations that multiple strain level tests be conducted using a high-to-low load sequence to eliminate the mean stress [*9*].) For a constant strain amplitude test, the stable hysteresis loop tip or half amplitude yields a single point, (τ, ϵ), on the cyclic curve; a number of specimens, or several strain blocks per specimen must be used to generate the entire cyclic curve. However, if the incremental step technique of Fig. 1*a* is used, then for $R_\epsilon =$

-1, the entire cyclic curve can be obtained from a single test. This is because each strain cycle in the block yields a hysteresis loop and a corresponding point on the CSSC. If the block of Fig. 1*a* contains 20 cycles, then 20 points on the CSSC are obtained. This economy of testing led to all the elevated temperature tests being conducted in the incremental step technique, not only for $R_\epsilon = -1$ but also for $R_\epsilon = 0$.

When analyzing the data for the $R_\epsilon = 0$, it became apparent that there was an inconsistency between the CSSC using the loop tip and loop range definitions. This is simply because the tip stress is given by

$$\tau_T = \Delta\tau/2 + \tau_M \qquad (1)$$

Hence when the mean stress is zero, as it is for $R_\epsilon = -1$, the two definitions—that is, loop tip and range—of the CSSC are consistent; when the mean stress is not zero—for example, when $R_\epsilon = 0$—the two definitions will yield different cyclic curves. In the following investigation, the curve defined by the range will be called the cyclic amplitude or just the cyclic curve, while the one defined by the tip values will be termed the complete cyclic curve. The difference between the two curves will be discussed in detail in a subsequent section.

For the initial elevated temperature tests, all specimens were tested in the incremental step technique to the same maximum strain level, 1.5 percent. The CSSC was obtained from the loop ranges. The resulting curve described the cyclic softening with the result shown in Fig. 2 for one specimen, $R_\epsilon = -1.0$, 616 K. This specimen was loaded initially in tension to obtain a portion of the monotonic curve and cycled to 50 percent of the estimated life. The cyclic test was halted and the specimen monotonically loaded to failure. The CSSC obtained from the last hysteresis loop was taken as the stable cyclic curve. The figure shows fairly good agreement between the monotonic and stable cyclic curves at half-life as expected [9]. The curve shows the degree of cyclic softening of Inconel 718 at this temperature was about 9 percent from the monotonic curve. Figure 3 compares the cyclic results for two different R_ϵ-values at the same temperature, 616 K. At this temperature, softening takes some time to develop. An examination of the test records showed no softening during the first three blocks of cycles. Both specimens softened about 12 percent from the initial to the stable configuration, with the stable values obtained from the loop at $N_f/2$. Comparing the two pairs of curves in Fig. 3, we see that if those of Specimen 1 are shifted upward they will essentially overlap those of Specimen 4. The initial cyclic response of the specimens is different, but the subsequent amount of softening is the same. The two specimens were removed from different locations in different forgings so property variations are expected. More work is needed to ascertain whether the difference in the stable cyclic curves results solely from material differences or includes an effect of R_ϵ.

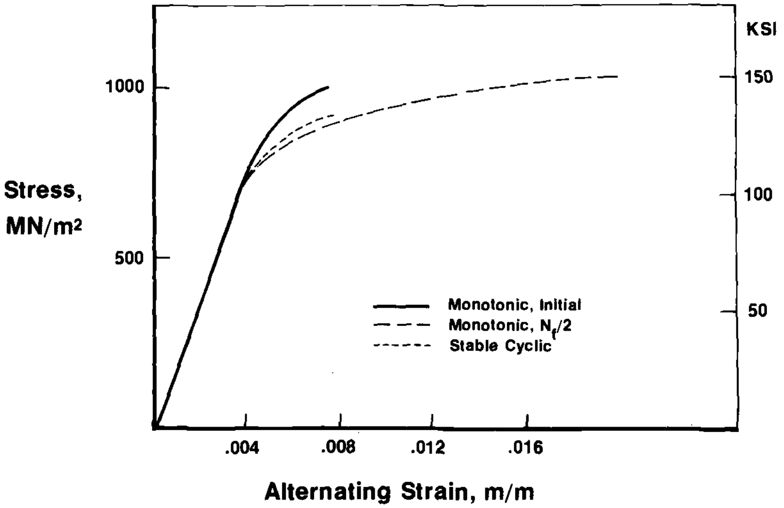

FIG. 2—*Initial monotonic, half-life monotonic, and cyclic stress-strain curves,* $R_\epsilon = -1.0$, *616 K.*

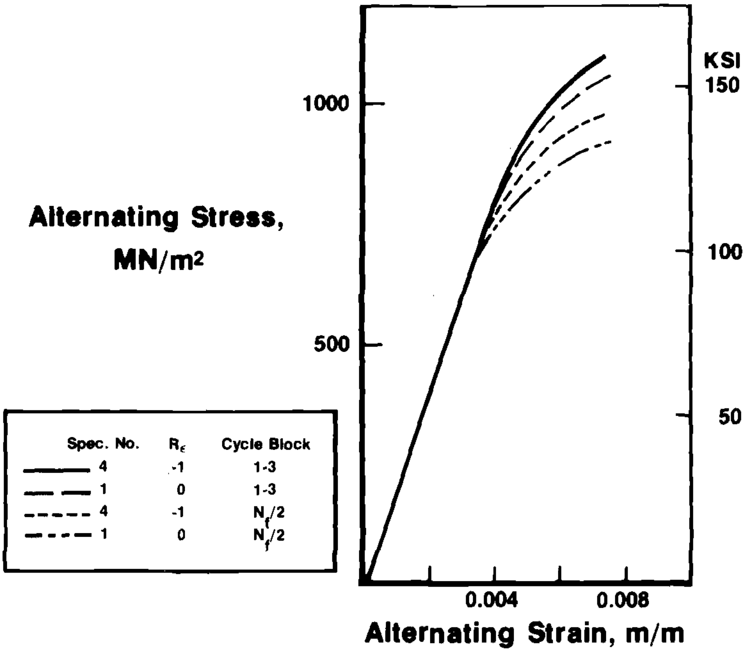

FIG. 3—*Comparison of initial and half-life cyclic stress-strain curves for* $R_\epsilon = -1.0$ *and 0, 616 K.*

A similar set of tests was performed at 839 K. At this temperature, softening began during the first strain block, but had apparently stabilized by specimen half-life; $N_f/2$ was used to define the stable CSSC. Figure 4 compares the monotonic and cyclic curves for Specimen 11, $R_\epsilon = 0$, with the cyclic curve for Specimen 3, $R_\epsilon = -1$. The cyclic test of Specimen 3 was halted at half the estimated specimen life. The specimen was then monotonically loaded to failure, with the resulting curve agreeing fairly well with the curve obtained from the loop amplitude at $N_f/2$. The cyclic test for Specimen 3 was not started in a manner that the monotonic curve could be obtained, but the cyclic curve agrees fairly well with the CSSC of Specimen 11 showing a lack of effect of R_ϵ. There is a much larger degree of softening here than at the lower temperature. While not shown, several other specimens were cycled at this temperature and CSSC obtained. There was a large variation in both monotonic and cyclic behavior of these specimens, but the amount of softening observed was generally consistent from specimen to specimen, just as at the lower temperature, 616 K. Again, the specimens were removed from different locations in all four forgings, so a considerable amount of specimen-to-specimen scatter is expected. More tests need to be conducted to be certain whether the amount of softening is, in fact, constant.

The results of the cyclic tests displayed in Figs. 2 to 4 show the extent of softening that takes place at 616 and 839 K. The results tended to indicate that the amount of softening is independent of R_ϵ, but a definitive answer

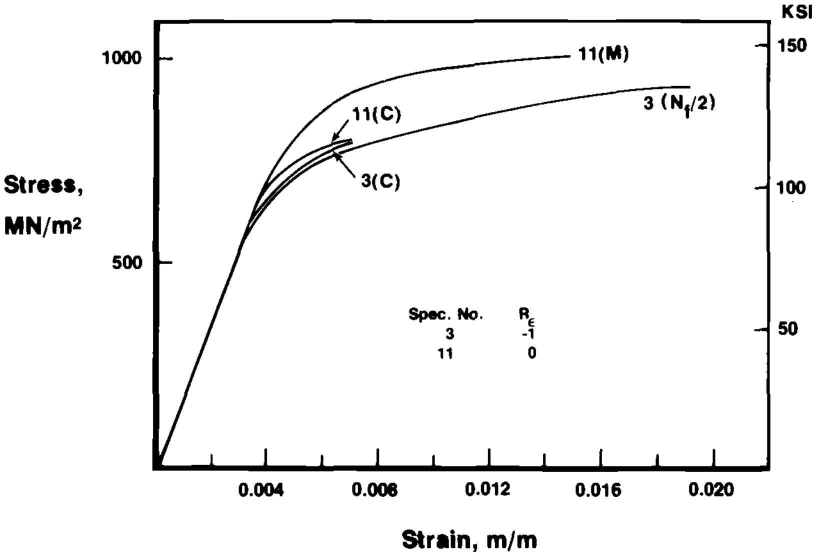

FIG. 4—*Comparison of stress-strain curves for* $R_\epsilon = -1.0$ *and 0 at 839 K.* M *indicates initial monotonic,* $N_f/2$ *indicates half-life monotonic, and* C *is the cyclic stress-strain curve.*

cannot be given. The original objective had been therefore largely accomplished, but there remained a question: What was the source of the disagreement between the CSSC defined by the loop amplitude and tips for $R_\epsilon = 0$? Moreover, is there any physical significance to the disagreement? The answer to both these questions lies in the definition of the complete CSSC (Fig. 1).

Figure 5 replots the monotonic and cyclic curves for Specimen 11. In addition, the figure shows the tip stress, τ_T, from the hysteresis loops of a number of low-cycle fatigue (LCF) specimens removed from the same Inconel 718 material, although the specimens were oriented in an axial direction. The LCF program was conducted over a fairly broad range of strain, 0.60 to 1.10 percent, constant amplitude, all at $R_\epsilon = 0$ [*10*]. Using the strip chart data for the tests, the mean stress was determined as a function of cycles throughout the specimen life. By adding the mean stress, τ_M, determined from the LCF tests to half the loop amplitude, $\Delta\tau/2$, determined by the cyclic stress-strain tests, the complete hysteresis loop as a function of strain range was obtained as in Eq 1. The tips of the resulting loops define the complete cyclic stress-strain curve (Fig. 5). Note that the curve is drawn to fit the one data point determined by the incremental cyclic test at 1.5 percent strain range.

The cyclic stress-strain curve defined in this way has the unusual feature of possessing a "hump", thereby giving a multiple valued function. The

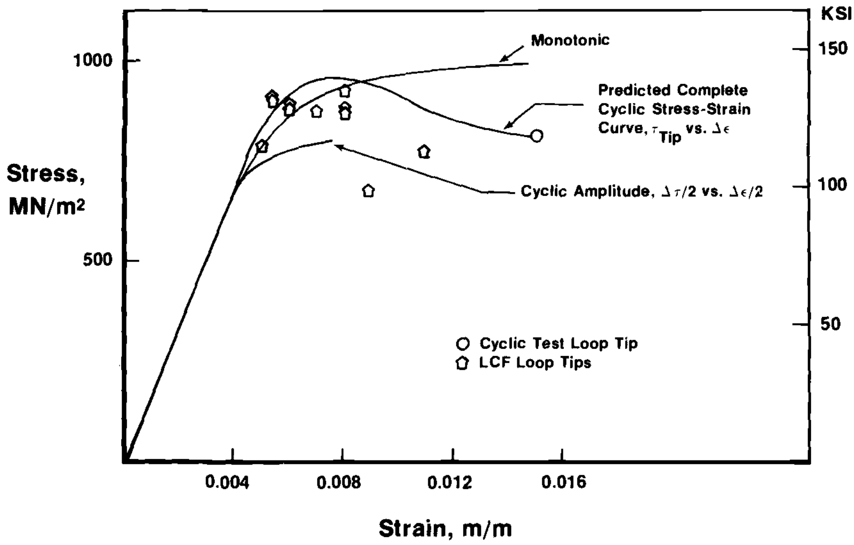

FIG. 5—*Monotonic and cyclic stress-strain curves from Fig. 4 compared with the complete cyclic stress-strain curve. The cyclic amplitude curve and the LCF data were used to obtain the predicted complete cyclic curve.*

behavior results from the buildup of high mean stresses during loading at small strain ranges. In fact, until "some" yielding has taken place, the cyclic curve and the monotonic curve are essentially identical. As the applied strain range increases however, the material cyclically softens and the mean stress decreases; the decrease in mean stress is due to the accumulation of plastic strain in the material. The importance of the complete CSSC is shown by the LCF tip stresses in Fig. 5. These are the stresses that exist in the specimens; a constitutive model that accounts only for the cyclic amplitude will yield only range values and not the actual stress values existing in the specimen. A cyclic constitutive model used in a structural analysis—for example, a finite-element analysis—must incorporate the mean stress through the complete CSSC in order to obtain a complete description of the stress and displacement fields in the body.

In order to confirm the existence and interpretation of the predicted curve of Fig. 5, a second set of cyclic tests, $R_\epsilon = 0$, was performed at room temperature. Four specimens were tested in the constant-amplitude mode of Fig. 1*b*. Two of the specimens were tested at seven strain levels, two at four levels of strain. The cyclic amplitude and complete CSSC are shown in Fig. 6. The results show relatively little scatter among the specimens except for Specimen N-7 which lies above the other data. An examination of the experimental data showed that the cycle block lengths used for this specimen were shorter than desired. Hence the mean stress decay and softening process was not complete and a stable hysteresis loop had not been achieved.

Before concluding that the complete CSSC does possess this humped shape, a check was made to determine whether the CSSC curve depends on the technique used to obtain it [*11*]. Two specimens were cycled according to the incremental method of Fig. 1*a*. Each specimen was cycled at a given maximum strain until a stable hysteresis loop was achieved; the maximum strain was then increased and another series of cycle blocks applied. In this manner, four strain levels were obtained for each specimen. The results are presented in Fig. 7 and are compared with the data of Fig. 6; for clarity, only the curves and not the data points of Fig. 6 are replotted in Fig. 7. The data obtained using the incremental step technique are in substantial agreement with both the humped complete CSSC and the cyclic-amplitude curve obtained using the constant-strain amplitude blocks. Note that Specimen M-6 at a strain range of 1.2 percent lies somewhat above both curves. Figure 8 shows the cyclic amplitude from the loops as a function of plastic strain range for the five stable tests; that is, Specimen N-7 is excluded. We see that Specimen M-6, at a given stress, had a much smaller amount of plastic strain than the other specimens. Hence Specimen M-6 with smaller amounts of plastic deformation would not begin to soften until a higher level of applied strain had been reached. This specimen-to-specimen difference again reflects the specific specimen locations within the forging and the scatter associated

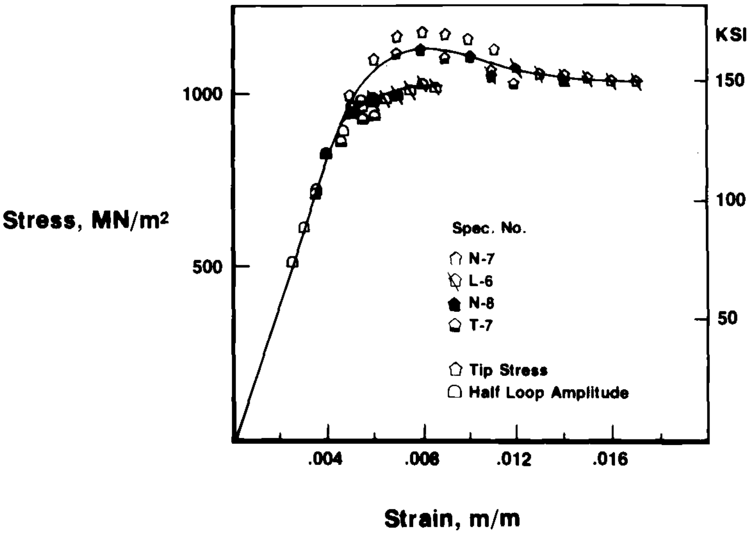

FIG. 6—*Cyclic stress-strain data after* n_i*-cycles per block of constant-amplitude cycling,* $R_\epsilon = 0$*, 294 K. The tip stress curve is the complete CSSC, while the half-loop amplitude curve is the CSSC based on hysteresis loop amplitude.*

with this process. Figure 8 shows a couple of data points taken form Landgraf [*12*]; the agreement is satisfactory.

In addition to the incremental tests, six constant-amplitude LCF tests were conducted at room temperature [*10*]. The tip and alternating values obtained from the hysteresis loops are given in Fig. 7. Again, the agreement with the humped CSSC is good and confirms this characteristic of the cyclic behavior of Inconel 718.

At the conclusion of the strain blocks depicted in Fig. 6, all four specimens were intact. Each of the four specimens was examined optically and, when necessary, with liquid penetrant. All were found to be cracked. The extent of cracking ranged from Specimen N-7 with three large (approximately half a millimetre long) cracks and numerous small indications to Specimen L-6 which was cracked almost completely around the circumference.

The discovery of the cracks led to a concern as to whether the decreases in load-displacement records were due to the cyclic material behavior or crack propagation. Moreover, the cyclic behavior presented in this paper has been stated as representing a stable or steady-state condition. Had the behavior in fact stabilized? In order to examine the changes that occur during cycling, a plot was made of the mean (τ_M), alternating (τ_A), and tensile tip (τ_T) stress as a function of cycles for several strain ranges. These plots generally showed that during the first strain block the specimen softens (τ_A decreases) considerably; during subsequent blocks the softening continues but at a reduced

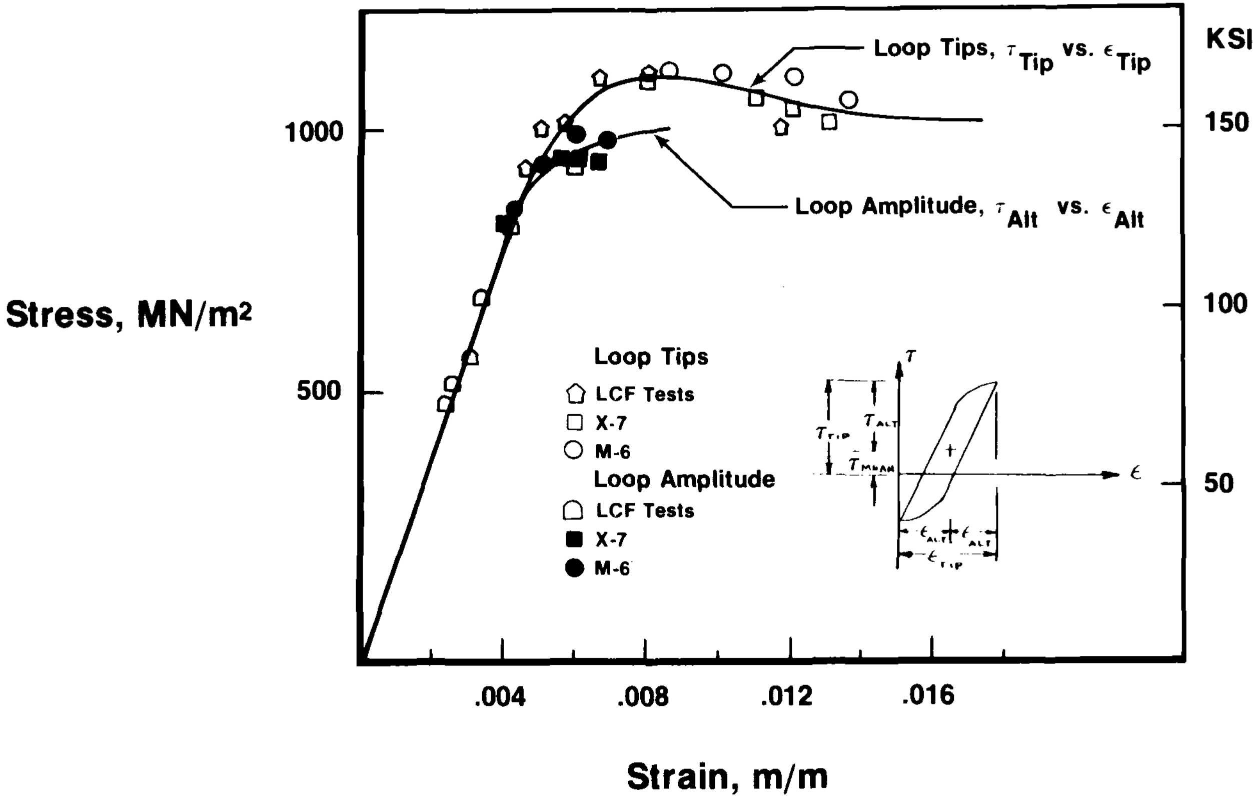

FIG. 7—*Comparison of cyclic data obtained using the incremental waveform and the constant-amplitude data of Fig. 6, as well as constant-amplitude LCF data.* $R_\epsilon = 0$, *294 K.*

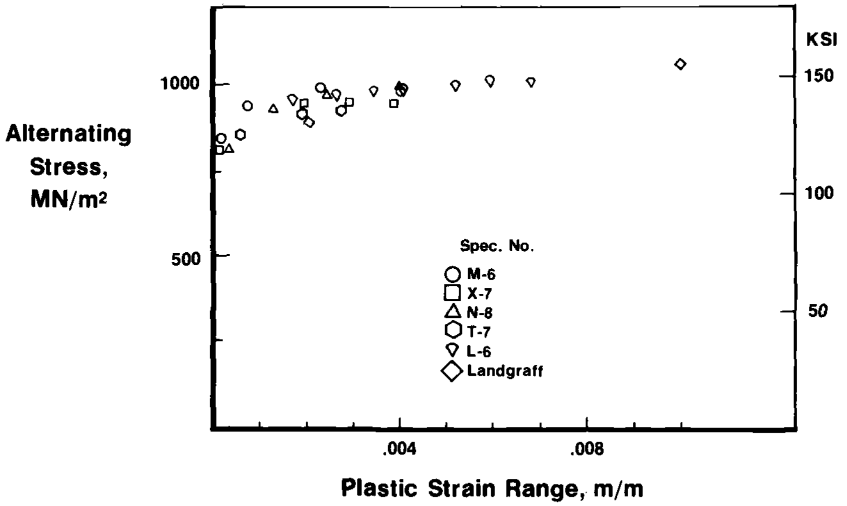

FIG. 8—*Alternating stress versus plastic strain range,* R_ϵ *= 0. 294 K.*

rate. On the other hand, the decrease in mean stress, τ_M, proceeds at a relatively uniform rate throughout the test. Figure 9 compares the behavior of three specimens at $\Delta\epsilon = 1.1$ percent; note, however, that there is a considerable difference in the previous history of each specimen. The strain block $\Delta\epsilon = 1.1$ percent is the first block for Specimen L-6, but is the last block for Specimen N-7; it is the third block for Specimen T-7. The alternating stress decreases rapidly for Specimen L-6 as it accumulates plastic strain. The slopes of the alternating stress curves for Specimens N-7 and T-7 are about the same and somewhat less than that of Specimen L-6. The rate of decrease of the mean stress is approximately the same for all three specimens. The lower level of mean stress in Specimen L-6 apparently reflects the effects of different specimen location, since it has been subjected to no prior plastic work during testing.

Discussion

The tests conducted at elevated temperature were conceived from the experience gained during cyclic stress-strain testing a *R*-ratio of minus one. This experience led to the experiments being conducted under strain control using the incremental loading of Fig. 1*a*. The test results showed that the load-displacement hysteresis loops were symmetric about (τ_M, $\Delta\epsilon/2$); that is either the tension or compression going portion of the loops could be used to obtain the cyclic curves. A study of these curves at 839 K showed that cyclic softening began on the first cycle and was quite rapid. At 616 K, the loop

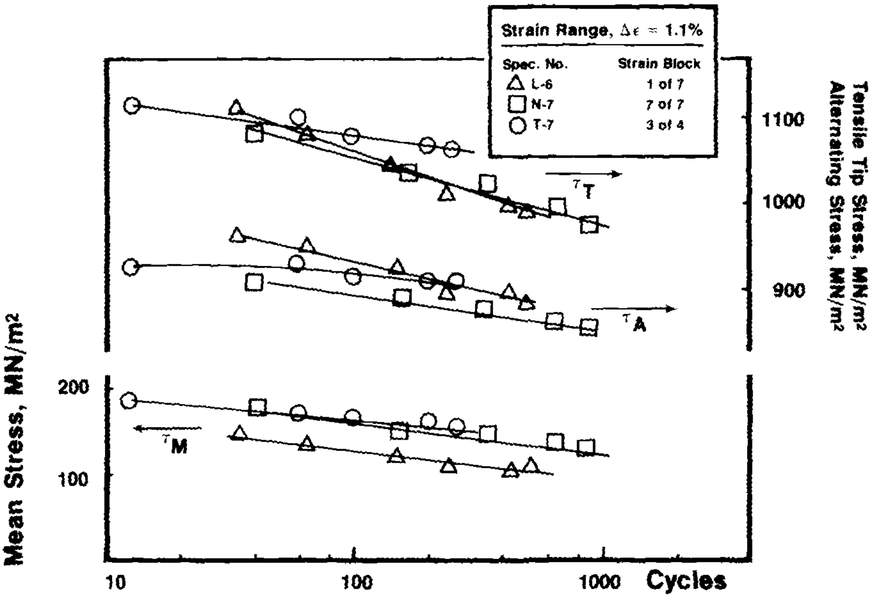

FIG. 9—*Tensile tip, alternating, and mean stress as a function of cycles for 1.1 percent strain range,* $R_\epsilon = 0$, *294 K.*

amplitudes for the first three cycles were virtually identical, indicating that cyclic softening is a more gradual procedure at the lower temperature. At both temperatures, the softening was complete at half-life; comparisons with loops from 10 cycle blocks before and after $N_f/2$ showed no difference within the resolution obtainable from strip charts. Monotonic stress-strain tests at half-life were in good agreement with the stable CSSC at both temperatures. A comparison of the two R_ϵ-ratios, zero and minus one, showed that the loop amplitudes were generally similar. At 616 K, the two stable amplitude curves differed by about 42 MPa, while at 839 K the two curves were fairly close. The extent of the variation is sufficient to preclude the conclusion that the CSSC defined from the hysteresis amplitude is independent of R_ϵ, although the data trend is in that direction.

The cyclic stress-strain curve is frequently defined by the tips of the hysteresis loops rather than the loop amplitudes, although for $R_\epsilon = -1$ the resulting CSSC is essentially the same. For the present case, the development of the tensile mean stress at $R_\epsilon = 0$ leads to a significant discrepancy between the two curves for strain ranges less than 1.4 percent. This mean stress results in the complete cyclic curve possessing a hump in the intermediate strain ranges of $0.6 < \Delta\epsilon < 1.2$ percent. This hump flattens out and the complete cyclic curve approaches the amplitude curve as the mean stress approaches zero. This decrease in mean stress is a function of the plastic strain; the rate of decay, at least at low plastic strains, will be a function of temperature.

The room temperature test program used constant and incremental amplitude tests to confirm the humped form of the complete CSSC for $R_\epsilon = 0$. The two different test techniques were used along with LCF test results to show that at this temperature and R-ratio the CSSC is independent of the method of generation. The incremental method did appear to produce a more rapid approach to a stable condition, however.

The examination of the load-displacement records as a function of cycles showed that the achievement of completely stable behavior requires the application of a considerable number of cycles. The larger the applied strain range, the larger the number of cycles required. Reference *9* suggests that 20 percent of life should be sufficient to achieve steady state. The present results show that for strain ranges greater than 1 percent, small changes in the maximum stress are still occurring, even after 25 percent of life has been expended. From a practical viewpoint, the lack of absolutely stable state may not be all that important. While the load drop continues thoughout the test, the slope is very shallow, resulting in small load reductions. In Fig. 9, for example, Specimen L-6 at a strain range of 1.1 percent shows a drop in maximum load of 28 MPa in the last 270 cycles, or 103.7 Pa per cycle. On a relative basis, this amounts to a 2.5 percent decrease in load over 53 percent of the test. Similar results have been reported in Ref. *6*, but for much larger strain ranges. It is better, therefore, to use the term stable rather than steady state to describe the cyclic properties after about 20 to 25 percent of N_f. Steady state is less appropriate as it implies no further change. The changes that occur in load are so small as to be generally negligible and the behavior may be termed stable.

The load-displacement records were also examined to see if any effects of specimen cracking were apparent. No effect was observed except for the sharp load drop very near N_f. For example, Specimen L-6 was subjected to seven blocks of constant-amplitude cycling. During the first block, the maximum load on the specimen decreased 7.5 percent, and thus meets the 5 percent load drop criteria for crack initiation. During the seventh and last block, the maximum load decreased a little more than 4 percent, with blocks two to six producing even smaller load drops. The specimen was in one piece, although cracked at the conclusion of the seventh block; if crack initiation had occurred during the first block as indicated by the load drop, the specimen should have failed well before the seventh block was reached. This indicates that any drop in maximum load due to specimen cracking has not affected the cyclic results presented here. It also points out that an arbitrary load drop definition of crack initiation is not a very reliable indication of cracking.

Conclusions

The general behavior of the forged Inconel 718 studied in this program was qualitatively similar at the three test temperatures of 294, 616, and 839 K. The forged material showed moderate amounts of cyclic strain softening and mean stress decrease. As would be expected, the extent and rate of cyclic softening and mean stess decay decreased as the temperature was lowered.

The experimental scatter and lack of duplicate conditions prevents an unambiguous evaluation of R_ϵ ratio effects on cyclic behavior. In general, the cyclic curve should be independent of R_ϵ; the specimen-to-specimen variability observed in this program was sufficient to prevent such a conclusion, although the data trend was in this direction. Of course, the complete cyclic stress-strain curve incorporates the mean stress, so these curves will depend on R_ϵ.

The CSSC was found to be independent of the method by which it was generated, although a stable condition was approached more quickly using the incremental technique. Careful examination of the load data showed small changes in load were still taking place at specimen half-life. However, these changes were very small and could be neglected in practice.

The unusual shape of the complete cyclic stress-strain curve postulated in the high-temperature program was confirmed by the series of room temperature tests. This curve points out the necessity of using appropriate constitutive relations when performing life assurance studies.

References

[*1*] Jaske, C. E., Mindlin, H., and Perrin, J. S. in *Cyclic Stress-Strain Behavior—Analysis, Experimentation, and Failure Prediction, ASTM STP 519,* American Society for Testing and Materials, 1973, pp. 13-27.

[*2*] Calabrese, C. and Laird, C., *Materials Science and Engineering,* Vol. 13, 1974, pp. 141-157.

[*3*] Borchert, B. in *High Temperature Alloys for Gas Turbines,* D. Coutsouradis et al, Eds., Applied Science Publishers, 1978, pp. 573-598.

[*4*] Cowles, B. A., Sims, D. L., and Warren, J. R., "Evaluation of the Cyclic Behavior of Aircraft Turbine Disk Alloys," NASA CR-159409, Oct. 1978.

[*5*] Calabrese, C. and Laird, C., *Metallurgical Transactions,* Vol. 5, Aug. 1974, pp. 1785-1793.

[*6*] Fournier, D. and Pineau, A., *Metallurgical Transactions A,* Vol. 8A, July 1977, pp. 1095-1105.

[*7*] Wetzel, R. M., *Journal of Materials,* Vol. 3, No. 3, Sept. 1968, pp. 646-657.

[*8*] Slot, T. and Stentz, R. H., *Experimental Mechanics,* Vol. 8, March 1968, pp. 107-114.

[*9*] Landgraf, R. W., Morrow, J. Dean, and Endo, T., *Journal of Materials,* Vol. 1, No. 4, March 1969, pp. 176-188.

[*10*] Cook, T. S., unpublished research.

[*11*] Laird, C. in *Cyclic Stress-Strain and Plastic Deformation Aspects of Fatigue Crack Growth, ASTM STP 637,* American Society for Testing and Materials, 1977, pp. 3-35.

[*12*] Landgraf, R. W. in *Work Hardening in Tension and Fatigue,* American Institute of Mechanical Engineers, 1977, pp. 240-259.

A. S. Krausz[1] *and Bernard Faucher*[2]

A Kinetics Approach to the Derivation and Measurement of the Constitutive Equations of Time-Dependent Deformation

REFERENCE: Krausz, A. S. and Faucher, Bernard, "**A Kinetics Approach to the Derivation and Measurement of the Constitutive Equations of Time-Dependent Deformation,**" *Mechanical Testing for Deformation Model Development, ASTM STP 765,* R. W. Rohde and J. C. Swearengen, Eds., American Society for Testing and Materials, 1982, pp. 284-297.

ABSTRACT: The approach is based on a model that is an intermediate between the specific micromechanics models of the structural theory of plasticity and the phenomenological continuum-mechanics models of anelasticity. It is considered that the fundamental physical processes, producing the deformation of any solid, are the breaking and mending of atomic bonds, and that plastic flow occurs by the movement of flow units that very often have to overcome a series of energy barriers. Therefore the constitutive relations are derived from the kinetics analysis of the energy barriers and the deformation rate is determined from rate theory. The constitutive equations obtained in the study are in the form of ordinary differential equations and are based on a rigorously defined physical model. Numerical solutions of the equations applied to a system of two consecutive energy barriers show excellent agreement with experimental results obtained under various testing conditions. Furthermore, calculations show that the stiffness of the testing machine can have a considerable influence on the observed behavior during stress relaxation experiments.

KEY WORDS: constitutive equations, deformation kinetics, thermal activation, yield behavior, stress relaxation, machine effects

There has been a long established search for a satisfactory functional relationship among the parameters that control the processes of time-dependent deformation. As early as 1909, Ludwig [*1*] found that the relation between the

---

[1] Professor and Chairman, Department of Mechanical Engineering, University of Ottawa, Ontario, Canada.

[2] Research Associate, Industrial Material Research Institute, Division of National Research Council of Canada, Montreal, Quebec, Canada; formerly Department of Mechanical Engineering, University of Ottawa, Ontario, Canada.

flow stress and the deformation rate is consistent with a logarithmic function.[3] Somewhat later, Becker [2] took into account the effect of temperature through an Arrhenius-type equation. The rigorous, physical foundation of the absolute rate theory, developed by Eyring in 1936 [3], produced further development when it was incorporated into dislocation theory by Orowan [4]. Zener and Holloman [5] showed that the effect of both the strain rate and the temperature may be combined into a single relationship, similar to the equation of state of a perfect gas. Other relations, many phenomenological, have also been suggested to describe plastic flow. Of these, the most commonly used is the power law. Rohde and Swearengen [6], for example, have found that the power law gives an excellent description of the experimental results as compared to other relations and, therefore, can be very valuable for engineering applications.

It is generally agreed that because the flow stress is structure sensitive and because the dislocation configurations are not in thermodynamic equilibrium, most of these relations are valid only for systems that are essentially static, or when the load increase is monotonous [7]. Improvement was achieved by Hart [8] with the introduction of a state variable called "hardness" that depends on the deformation history of the material through its internal structure. In fact, it was shown by Swearengen et al [9] that at least one variable that takes into account the internal structure of the material is necessary to describe inelastic deformation. Because the effects of the strain rate and of the deformation history are important, the time-dependent constitutive equations are employed increasingly [10,11].

Time-dependent—that is, thermally activated—plastic deformation is accomplished by the movements of structural imperfections such as dislocation movement or vacancy migration in crystalline solids, or the glide of molecular segments in polymers. Although a first approach to the derivation of the constitutive relations will be based on dislocation theory, the following discussion is valid for polymers and ceramic materials as well, and, on occasion, "flow units" and "dislocations" will be used interchangeably.

Several equations have been proposed to relate the deformation parameters [6,12-21]. Most of these constitutive equations consider a single structural variable and are of the Bailey-Orowan type [22,23]; that is, the deformation is assumed to be controlled by two competing phenomena: strain hardening due to dislocation entanglement, and recovery due to dislocation annihilation. They are based, in general, on specific dislocation models [18-21], and have the general form [24]:

$$\begin{aligned} \dot{\epsilon}_p &= f(\sigma, T, x) \\ \dot{x} &= H(\sigma, T, x)\dot{\epsilon} - r(\sigma, T, x) \\ \dot{\sigma} &= E(\dot{\epsilon} - \dot{\epsilon}_p) \end{aligned} \qquad (1)$$

---

[3] The italic numbers in brackets refer to the list of references appended to this paper.

where r is the recovery rate, x represents n-variables that describe the internal structure of the material, and the other symbols have their usual meaning.

Almost independently from the development of deformation theory based on dislocation movements, the theory of viscoelastic solids was developed on a phenomenological basis which describes the macroscopic behavior without considering the structural changes in the deforming material [*25,26*]. The fundamental postulate is that the actual state of the strain (or stress) depends on the past history of the stress (or strain) to which the material was subjected. The theory introduced the "fading memory" concept: The recent deformation history has a stronger effect on the behavior of the material than the ancient one.

It has been shown in recent works that the two theories can be correlated [*10*]. The concept of the fading memory, developed from the deformation theory that describes the behavior of polymeric materials [*27-30*], is also applicable to metals and ceramic materials [*31*]. On the other hand, the Bailey-Orowan model is increasingly used in conjunction with the continuum-mechanics models of anelasticity [*32*].

The present study is based on an intermediate approach. The required activation parameters are determined from the evaluation of the experimental results and from the testing conditions, while the structural changes are also taken into account. It has been realized [*33*] that plastic flow and chemical reactions are essentially identical processes, since both are solely the consequence of breaking and establishing of atomic bonds. Because of this fundamental and general fact, plastic deformation may be considered as a chemical reaction in which the composition remains unchanged, but the bond structure of the molecule changes. Thus the rate of activation is obtained from the rate theory of thermally activated processes [*33,34*]. Usually the material behavior is determined by summing the behavior of the individual dislocations. The proposed model considers all flow units together. It is assumed that the units move by overcoming a system of consecutive energy barriers presented by the consecutive bond breaking steps that result in the plastic deformation process. The constitutive equations are then obtained from the kinetics analysis of the dislocations overcoming the consecutive energy barriers [*35*].

The Physical Models

Numerous physical processes in materials science may be associated with consecutive energy barriers. It is well established that each step of a nucleation and growth mechanism corresponds to one of the barriers in series. The most important example for the present purpose is the plastic deformation of crystalline solids. The development of dislocation theory was based on the concept that the shear displacement of the atomic planes is initiated by the nucleation of dislocation loops which eventually move over the glide plane (growth step) to produce a unit amount of slip [*36*].

The mechanism of dislocation movement itself may also be governed by consecutive energy barriers. The glide of dislocations over the Peierls-Nabarro stress field occurs by the nucleation and subsequent sideways spreading of double kinks [*37*]. The cross-slip of extended dislocations that must recombine over a critical length before leaving the slip plane, the superposition of a periodic internal stress field over the short-range obstacles that control dislocation motion [*38*], dislocation climb, and the glide of jogged dislocations [*39*] are other examples of mechanisms that are controlled by consecutive energy barriers.

The Constitutive Equation

In the present study, the constitutive equations are derived for small uniaxial deformation that can be considered as the sum of the elastic deformation ϵ_e and the plastic (time-dependent) deformation ϵ_p. The elastic deformation is proportional to the applied stress:

$$\epsilon_e = \sigma_a / E \tag{2}$$

and the applied stress is the sum of the internal stress σ_{int} and the effective stress σ that does the work when the dislocations (or other flow units) are activated over an energy barrier. The internal stress is assumed to be proportional to the plastic strain:

$$\sigma_{int} = H\epsilon_p . \tag{3}$$

The rate of the effective stress $\dot{\sigma}$ is expressed from the time derivatives of Eqs 2 and 3 as

$$\dot{\sigma} = \dot{\sigma}_a - \dot{\sigma}_{int} = E\dot{\epsilon}_e - H\dot{\epsilon}_p = E(\dot{\epsilon} - \dot{\epsilon}_p) - H\dot{\epsilon}_p = E\dot{\epsilon} - (E + H)\dot{\epsilon}_p \tag{4}$$

The plastic strain rate $\dot{\epsilon}_p$ is determined by the rate at which the dislocations overcome the energy barriers. For the general system of n-barriers in series illustrated in Fig. 1, the contribution of each flow unit to the plastic strain rate after activation over the ith barrier is δ_i, and therefore

$$\dot{\epsilon}_p = \sum_i \delta_i F_i \tag{5}$$

where F_i, the net flux, is obtained from the kinetics theory as [*33*]:

$$F_i = \rho_i \, {}_i\mathfrak{k}^i - \rho_{i+1} \, {}^i\mathfrak{k}_{i+1} \tag{6}$$

In Eq 6, ρ_i represents the density of the flow units in front of the ith barrier, and ${}_i\mathfrak{k}^i$, ${}^i\mathfrak{k}_{i+1}$ are the rate constants of activation in the forward and backward

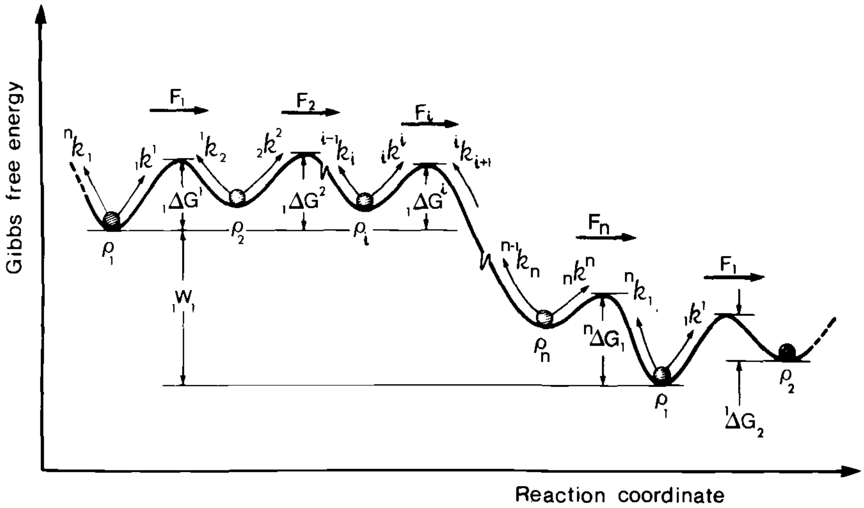

FIG. 1—*Schematic representation of a system of* n *consecutive energy barriers. The figure identifies the activation parameters and illustrates the sense of direction as conveyed by the subscripts and superscripts.*

direction over the barrier, respectively. The subscripts and superscripts are arranged to indicate the sense of direction. The rate constants are expressed also from kinetics theory, as

$${}_ik^i = \frac{kT}{h}\exp\left(-\frac{{}_i\Delta G^i}{kT}\right) = \frac{kT}{h}\exp\left[-\frac{{}_i\Delta G^{\ddagger i} - {}_iW^i(\sigma)}{kT}\right] \qquad (7)$$

and

$${}^ik_{i+1} = \frac{kT}{h}\exp\left(-\frac{{}^i\Delta G_{i+1}}{kT}\right) = \frac{kT}{h}\exp\left[-\frac{{}^i\Delta G^{\ddagger}_{i+1} + {}^iW_{i+1}(\sigma)}{kT}\right]$$

where k and h are the Boltzmann and Planck's constant, respectively, T is the absolute temperature, $\Delta G^{\ddagger}$ is the activation energy, and the work W is the function of the effective stress σ. The rate of change of the dislocation density $\dot{\rho}_i$ in the ith valley is given by the difference between the flow into and the flow out from the valley:

$$\dot{\rho}_i = F_{i-1} - F_i \qquad (8)$$

Figure 1 shows schematically a deformation mechanism in which the overcoming of the first barrier is the nucleation step, the subsequent barriers are associated with the spreading steps, and the nth barrier represents the last step. After the overcoming of the *n*th barrier, the flow units are again in front of an identical energy barrier system; that is,

$$\rho_{n+i} \equiv \rho_i$$

(It should be noted that the schematic representation of the consecutive energy barriers in Fig. 1 does not take into consideration the attractive forces between two kinks and the resulting bias for forward activation as they approach each other.) From Eqs 5 and 6, Eqs 4 and 8 become

$$\begin{aligned}
\dot\rho_1 &= \rho_n\,{}_nk^n - \rho_1\,({}_1k^1 + {}^nk_1) + \rho_2\,{}^1k_2 \\
\dot\rho_2 &= \rho_1\,{}_1k^1 - \rho_2\,({}_2k^2 + {}^1k_2) + \rho_3\,{}^2k_3 \\
&\vdots \\
\dot\rho_i &= \rho_{i-1}\,{}_{i-1}k^{i-1} - \rho_i\,({}_ik^i + {}^{i-1}k_i) + \rho_{i+1}\,{}^ik_{i+1} \\
&\vdots \\
\dot\rho_n &= \rho_{n-1}\,{}_{n-1}k^{n-1} - \rho_n({}_nk^n + {}^{n-1}k_n) + \rho_1\,{}^nk_1 \\
\dot\sigma &= E\dot\epsilon - (E + H) \sum_{i=1}^{n} \delta_i(\rho_i\,{}_ik^i - \rho_{i+1}\,{}^ik_{i+1})
\end{aligned} \tag{9}$$

where each activation rate constant k_i depends on the effective stress σ as given by Eqs 7. This system of ordinary differential equations is the constitutive relation that can predict the behavior of materials when the deformation is controlled by energy barriers in series and is of the general form as given by Eqs 1. Equations 9 are valid for the process shown in Fig. 1 where the total number of dislocations is constant, as indicated by the relation

$$\sum_{i=1}^{n} \dot\rho_i = 0$$

When the total number of the dislocations is not constant, additional terms must be introduced into the differential equations to take into account either dislocation multiplication or dislocation annihilation, or both. This can be easily accomplished. For example, the deformation process is terminated at the *n*th barrier when the two dislocation segments meet and annihilation takes place, or the flow units reach the edge of the specimen. (This corresponds to an absorbing barrier in probability theory.) Therefore, after overcoming the *n*th barrier, backward activation cannot take place, and therefore

$${}^nk_1 = 0$$

and $\dot\rho_1$ and $\dot\rho_n$ in Eqs 9 become

$$\begin{aligned}
\dot\rho_1 &= \rho_n\,{}_nk^n - \rho_1\,{}_1k^1 + \rho_2\,{}^1k_2 \\
\dot\rho_n &= \rho_{n-1}\,{}_{n-1}k^{n-1} - \rho_n({}_nk^n + {}^{n-1}k_n)
\end{aligned}$$

As a rule, one of the external conditions imposed on the system is the temperature. When the strain rate is the other imposed external condition, then the applied stress is the variable. In the present investigation, the relation between σ_a and σ is obtained from Eqs 2 and 3 as

$$\sigma_a = (\sigma + H\epsilon)/(1 + H/E)$$

A specific material is characterized by the shape of the energy barriers—that is, by the individual values of each ΔG_i and δ_i—and by the functional forms of W_i. The parameters can be determined from the analysis of the results obtained in steady-state experiments when the flux of the flow units over the barriers is uniform, and therefore

$$\dot{\rho}_i = 0; \qquad i = 1, \ldots, n$$

The consideration of the steady-state condition leads to much simpler constitutive relations than Eqs 9 [*40,41*]. Moreover, a comprehensive study showed [*40*] that the activation parameters have to satisfy very restrictive conditions when the steady-state behavior is controlled by two energy barriers. Therefore it can be expected that most thermally activated processes are controlled by a few consecutive barriers only, and consequently the number of parameters that have to be determined is limited. The parameters are precisely defined physically: k and h are universal physical constants, the temperature is accurately measurable, $\Delta G^{\ddagger}$ is related to the (chemical) bond energy, and the mechanical work is defined by the stress and the mechanism. These parameters are not "free"; they are defined precisely, or have upper and lower limits that are quite narrowly set by the physical conditions. The application of the powerful methods of chemical kinetics to plastic deformation and to the establishment of the constitutive equations removes the practice of "curve fitting" and the adjusting of the parameters associated with empirical equations and provides a rigorous physical basis for the study of thermally activated processes.

Applications

In the following, numerical solutions of the constitutive equations for two consecutive energy barriers under various testing conditions will be presented. Utilizing the notations

$$y = \rho_2/(\rho_1 + \rho_2); \qquad \eta = \delta_1/(\delta_1 + \delta_2)$$

and

$$\epsilon_0 = (\delta_1 + \delta_2)(\rho_1 + \rho_2)$$

Eqs 9 are reduced to

$$\begin{aligned} \dot{y} &= {}_1k^1 + {}^2k_1 - y\,({}_1k^1 + {}_2k^2 + {}^2k_1 + {}^1k_2) \\ \dot{\sigma} &= f(\sigma, \dot{\epsilon}, \rho_i) = E'\dot{\epsilon} - (H + E')\,\epsilon_0\,[\eta\,(1 - y)\,{}_1k^1 + (1 - \eta)\,y\,{}_2k^2 \qquad (10) \\ &\quad - \eta y\,{}^1k_1 - (1 - \eta)(1 - y)\,{}^2k_1] \end{aligned}$$

where E' is a combined elastic modulus that takes into account the elastic deformation of the testing machine. The two moduli are related as

$$\frac{1}{E'} = \frac{1}{E} + \frac{a_0}{K\,\ell_0}$$

where a_0 and ℓ_0 are the initial cross-sectional area and length of the specimen, respectively, and K is the stiffness of the testing machine.

Figure 2 shows the behavior that corresponds to constant elongation rate tests, carried out at various temperatures [*42*]. The strain rate was 1.67 × 10^{-4} s^{-1}, and the activation parameters, associated with *Ge* [*40*], were

$$\begin{gathered} {}_1\Delta G^{\ddagger 1} = {}^2\Delta G_1^{\ddagger} = 3.6 \times 10^{-19}\text{J}; \qquad {}_2\Delta G^{\ddagger 2} = {}^1\Delta G_2^{\ddagger} = 2.9 \times 10^{-19}\text{J} \\ {}_1W^1(\sigma) = {}^2W_1(\sigma) = \frac{V_1\sigma}{2}; \qquad {}_2W^2(\sigma) = {}^1W_2(\sigma) = \frac{V_2\sigma}{2} \\ V_1 = 6.5 \times 10^3\ \text{Å}^3; \qquad V_2 = 393\ \text{Å}^3; \qquad \epsilon_0 = 0.1; \qquad H = 0 \\ E' = 200\ \text{MPA} \end{gathered}$$

while η was chosen to be 0.01. The initial values $\dot{y}(t = 0) = 0$ and $\sigma(t = 0) = 0$ secured the pre-test steady-state condition. The calculated curves show a maximum yield drop in the intermediate temperature range. Figure 3 demonstrates that a soft tensile machine—that is, the effect of a small combined elastic modulus—causes the yield drop to disappear. On the other hand, a hard tensile machine produces more and larger oscillations of the stress around its steady-state value.

Figure 4 describes the behavior of LiF observed during stress relaxation and repeated stress relaxation experiments [*43*]. The curves were calculated from Eqs 10, and the activation parameters are

$$\begin{gathered} {}_1\Delta G^1/k = 13\,383 - 873\sigma; \qquad {}_2\Delta G^2/k = 17\,940 - 2013\sigma \\ {}^1\Delta G_2/k = 9600 + 218\sigma; \qquad {}^2\Delta G_1/k = 21\,723 + 2013\sigma \\ \epsilon_0 = 0.0029; \qquad \eta = 0.01 \end{gathered}$$

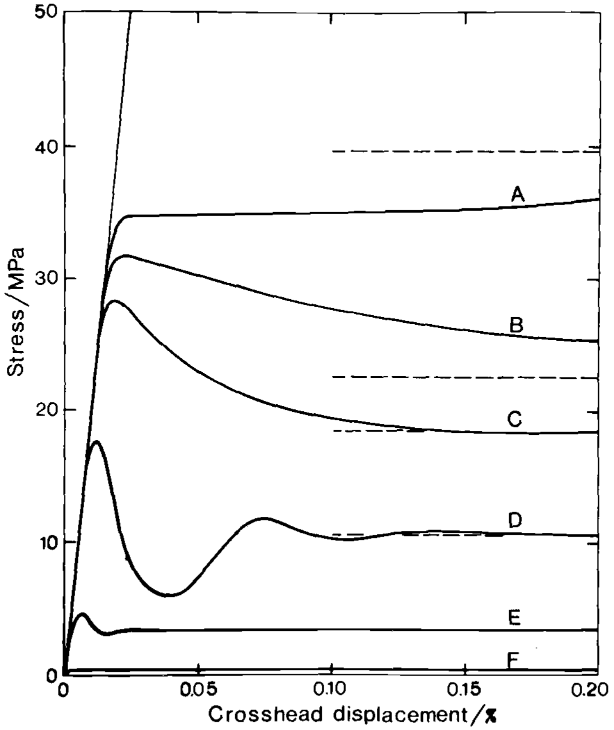

FIG. 2—*Calculated yield behavior as a function of temperature. From* A *to* F *the temperature is 560, 580, 600, 650, 700, and 750 K.*

The external conditions were $E' \simeq 5$ GPa; $H \simeq 0$; $T = 302$ K. The initial values of y and σ were equal to the steady-state values that would give a strain rate of $1.67 \times 10^{-4}\ \text{s}^{-1}$. The calculated curves show excellent agreement with the experimental results.

The effect of the stiffness of the testing machine on stress relaxation tests has been investigated theoretically for a system of two consecutive energy barriers. The parameters are

$$\frac{{}_1\Delta G^{1\ddagger}}{k} = \frac{{}^2\Delta G_1^{\ddagger}}{k} = 15\,400\ \text{K}; \qquad \frac{{}_2\Delta G^{2\ddagger}}{k} = \frac{{}^1\Delta G_2^{\ddagger}}{k} = 13\,700\ \text{K}$$

$${}_1W^1(\sigma) = {}^2W_1(\sigma) = {}_1V^1\sigma; \qquad {}_2W^2(\sigma) = {}^1W_2(\sigma) = {}_2V^2\sigma$$

$$\frac{{}_1V^1}{k} = 10\,500\ \text{K MPa}^{-1}; \qquad \frac{{}_2V^2}{k} = 6900\ \text{K MPa}^{-1}$$

$$\epsilon_0 = 3 \times 10^{-4}; \qquad \eta = 0.01 \quad \text{and} \quad H = 0$$

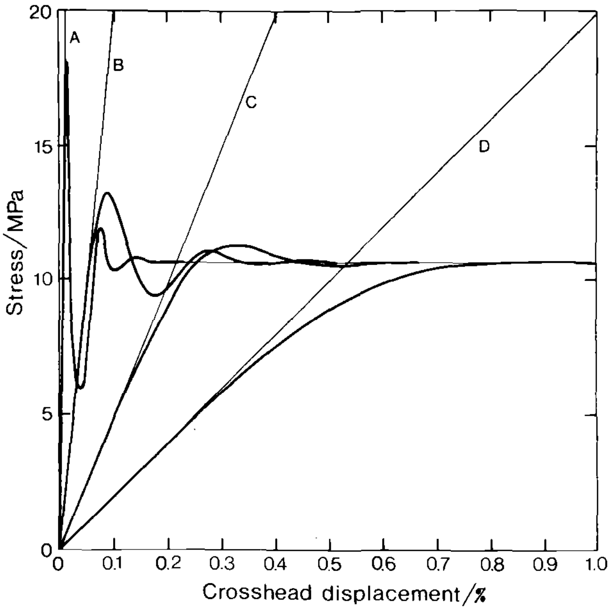

FIG. 3—*Calculated yield behavior as a function of testing machine stiffness. From* A *to* D, E′ = *200, 20, 5, and 2 GPa.*

The initial values of σ and y produced a steady-state value of the strain rate of $1 \times 10^{-4}\ \mathrm{s}^{-1}$. Solutions of Eq 10 have been obtained in the temperature range of 200 to 400 K for two values of the combined elastic modulus associated with a soft ($E' = 0.5$ GPa) and with a hard ($E' = 50$ GPa) testing machine. Typical results at 350 K are shown in Fig. 5.

An experimental activation volume was determined from the relation

$$\frac{V_{\mathrm{exp}}}{k} = T\frac{\Delta \ln \dot{\epsilon}_p}{\Delta\sigma}$$

where $\Delta\sigma$ is a strain rate difference spanning one order of magnitude in the middle range of the curves. The temperature dependence of V_{exp} is shown in Fig. 6. At low temperature the activation volumes are identical for both machines and equal to ${}_2V^2$. As the temperature increases the volume associated with the hard machine remains unchanged, while the volume associated with the soft machine increases near to ${}_1V^1$. It should be noted that at high temperature the stress level is low and therefore the backward activation becomes noticeable; that is, the strain rate becomes very small and the experimental activation volume very large. The results presented in Fig. 6 are in qualitative agreement with the reports of many investigators that the ex-

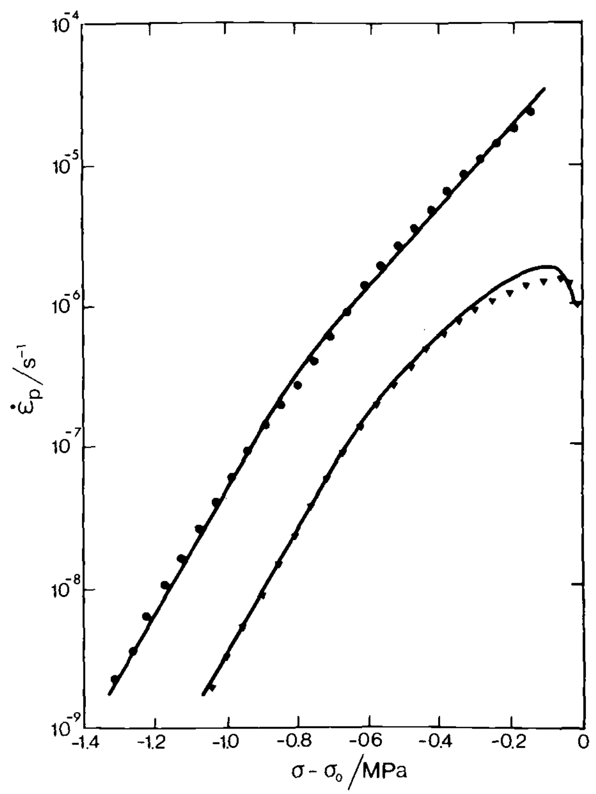

FIG. 4—*Behavior of LiF during stress relaxation* (●) *and repeated stress relaxation* (▼) *experiments* [43]. *The curves were calculated from Eqs 10.*

perimental activation volume increases with temperature. Furthermore, it has been established that in several materials the experimental activation volume is larger when it is determined with a soft machine [*44,45*]. These results clearly indicate that the behavior determined with a soft machine is close to the steady-state behavior of a system of two consecutive energy barriers [*46*], and that the behavior determined with a hard machine may be associated, erroneously, with a single energy barrier. Therefore, under the experimental conditions described previously, the use of a soft testing machine would be preferable, although the time required to obtain a specified range of results increases with the increasing softness.

Conclusions

The present derivation, based on a rigorous physical theory and on a general physical model, extends the validity of the constitutive equations to a large

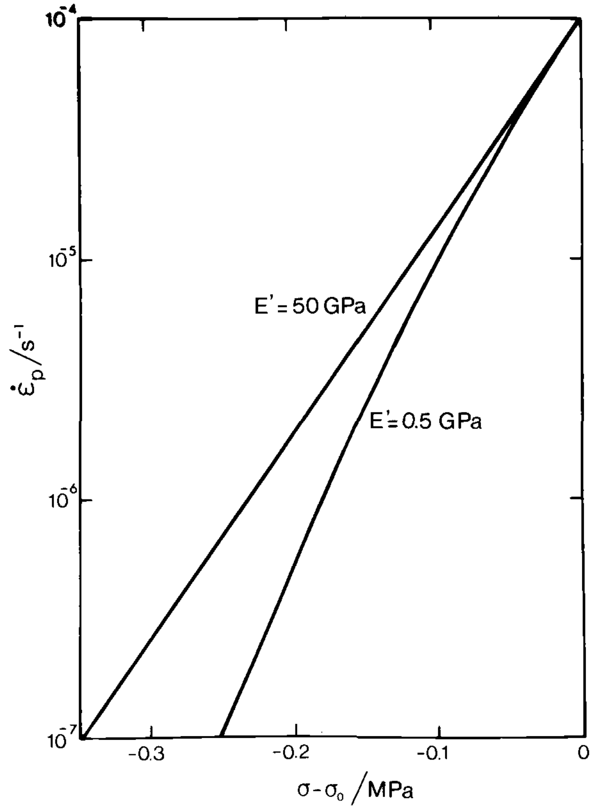

FIG. 5—*Effect of a soft and a hard testing machine on the stress dependence of the strain rate.*

number of materials tested under various conditions. It has been shown that, for deformation mechanisms controlled by consecutive energy barriers, even the reduced form, applied to two barriers in series, describes very well several unusual experimental results. Refinements, such as dislocation multiplication, work hardening, etc., may easily be introduced into the formulation. It is expected that the constitutive relations, based on deformation kinetics theory, will be capable of describing experimental results obtained under steady-state conditions, as well as during transients that occur, for example, in strain rate change experiments or in fatigue. Finally, it will contribute to our understanding of deformation mechanisms.

A study on the kinetics theory of yield conditions is submitted elsewhere [*47*].

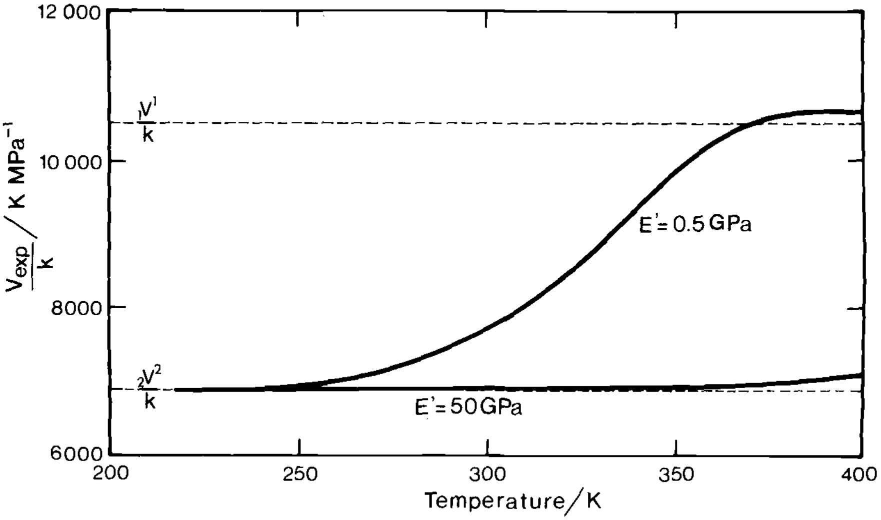

FIG. 6—*Effect of a soft and a hard testing machine on the temperature dependence of the experimental activation volume.*

Acknowledgments

The financial assistance provided by the Natural Sciences and Engineering Research Council of Canada is gratefully acknowledged.

References

[*1*] Ludwig, P., *Elemente der Technologischen Mechanik*, Julius Springer, Berlin, 1909.
[*2*] Becker, R., *Physikalische Zeitschrift*, Vol. 26, 1925, pp. 919-925.
[*3*] Eyring, H., *Journal of Chemical Physics*, Vol. 4, 1936, pp. 283-291.
[*4*] Orowan, E., *Zeitschrift für Physik*, Vol. 89, 1934, pp. 605-613.
[*5*] Zener, C. and Holloman, J. H., *Journal of Applied Physics*, Vol. 17, 1946, pp. 69-76.
[*6*] Rohde, R. W. and Swearengen, J. C., *Journal of Engineering Materials and Technology, Transactions of the ASME*, Vol. 99, Jan. 1977, pp. 59-64.
[*7*] McClintock, F. A. and Argon, A. S., *Mechanical Behavior of Materials*, Addison-Wesley, Reading, 1966.
[*8*] Hart, E. W., *Acta Metallurgica*, Vol. 18, June 1970, pp. 599-610.
[*9*] Swearengen, J. C., Rohde, R. W., and Hicks, D. L., *Acta Metallurgica*, Vol. 24, 1976, pp. 969-975.
[*10*] *Constitutive Equations in Plasticity*, A. S. Argon, Ed., M.I.T. Press, Cambridge, 1975.
[*11*] *Constitutive Equations in Viscoplasticity: Computational and Engineering Aspects - Phenomenological and Physical Aspects*, AMD-Vol. 20, J. A. Stricklin and K. J. Saczalski, Eds; Vol. 21, K. C. Valanis, Ed.; ASME, New York, 1976.
[*12*] Bodner, S. R. in *Mechanical Behavior of Materials under Dynamic Loads*, U. S. Lindholm, Ed., Springer-Verlag, New York, 1968, pp. 176-190.
[*13*] Bodner, S. R. and Partom, Y., *Journal of Applied Mechanics, Transactions of the ASME*, Vol. 42, June 1975, pp. 385-389.

[*14*] Bodner, S. R. and Merzer, A., *Journal of Engineering Materials and Technology, Transactions of the ASME*, Vol. 100, Oct. 1978, pp. 388-394.

[*15*] Ponter, A. R. S. and Leckie, F. A., *Journal of Engineering Materials and Technology, Transactions of the ASME*, Vol. 98, Jan. 1976, pp. 47-51.

[*16*] Hart, E. W., *Journal of Engineering Materials and Technology, Transactions of the ASME*, Vol. 98, July 1976, pp. 193-202.

[*17*] Krieg, R. D., Swearengen, J. C., and Rohde, R. W. in "Inelastic Behavior of Pressure Vessel and Piping Components," Series PVP-PB-028, T. Y. Chang and E. Krempl, Eds., ASME, New York, 1978, pp. 15-28.

[*18*] Ostram, P. and Lagneborg, R., *Journal of Engineering Materials and Technology, Transactions of the ASME*, Vol. 98, April 1976, pp. 114-124.

[*19*] Miller, A. K., *Journal of Engineering Materials and Technology, Transactions of the ASME*, Vol. 98, April 1976, pp. 97-105.

[*20*] Gittus, J. H., *Journal of Engineering Materials and Technology, Transactions of the ASME*, Vol. 98, Jan. 1976, pp. 52-59.

[*21*] Larsson, B. and Storåkers, B., *Journal of Engineering Materials and Technology, Transactions of the ASME*, Vol. 100, Oct. 1978, pp. 395-401.

[*22*] Bailey, R. W., *Journal of the Institute of Metals*, Vol. 35, 1926, pp. 27-40.

[*23*] Orowan, E., *Journal of West Scotland Iron Steel Institute*, Vol. 54, 1947, pp. 45-82.

[*24*] Shih, C. F., Delorenzi, H. G., and Miller, A. K. in *Transactions*, 4th International Conference on Structural Mechanics in Reactor Technology, T. A. Jaeger and B. A. Boley, Eds., L2/2, North-Holland, 1977.

[*25*] Christensen, R. M., *Theory of Viscoelasticity—An Introduction*, Academic Press, New York, 1971.

[*26*] Lockett, F. J., *Nonlinear Viscoelastic Solids*, Academic Press, New York, 1972.

[*27*] Tobolsky, A. V. and Catsiff, E., *Journal of Polymer Science*, Vol. 19, 1956, pp. 111-121.

[*28*] Ferry, J. D., *Viscoelastic Properties of Polymers*, 2nd ed., Wiley, New York, 1970.

[*29*] DeHoff, P. H., Lianis, G., and Goldberg, W., *Transactions of the Society of Rheology*, Vol. 10, No. 1, 1966, pp. 385-398.

[*30*] Findley, W. N. and Onaran, K., *Transactions of the Society of Rheology*, Vol. 12, No. 2, 1968, pp. 217-242.

[*31*] Lubliner, J., *Acta Mechanica*, Vol. 8, 1969, pp. 75-81.

[*32*] Kelly, J. M. in *Constitutive Equations in Viscoplasticity*, K. C. Valanis, Ed., ASME, New York, 1976, AMD-Vol. 21, pp. 33-49.

[*33*] Krausz, A. S. and Eyring, H., *Deformation Kinetics*, Wiley, New York, 1975.

[*34*] Glasstone, S., Laidler, K. J. and Eyring, H., *The Theory of Rate Processes*, McGraw-Hill, New York, 1941.

[*35*] Krausz, A. S. and Faucher, B., *Advances in Molecular Relaxation and Interaction Processes*, Vol. 18, 1980, pp. 11-20.

[*36*] Orowan, E., *Zeitschrift für Physik*, Vol. 89, 1934, pp. 634-641.

[*37*] Hirth, J. P. in *Inelastic Behavior of Solids*, M. F. Kanninen, W. F. Adler, A. R. Rosenfield, and R. I. Jaffee, Eds., McGraw-Hill, New York, 1970.

[*38*] Faucher, B. and Krausz, A. S., *Materials Science and Engineering*, Vol. 41, 1979, pp. 37-42.

[*39*] Hirth, J. P. and Lothe, J., *Canadian Journal of Physics*, Vol. 45, 1967, pp. 809-826.

[*40*] Faucher, B. and Krausz, A. S., *Journal of Applied Physics*, Vol. 49, July 1978, pp. 3946-3953.

[*41*] Faucher, B. and Krausz, A. S., *Zeitschrift für Naturforschung*, Vol. 35A, June 1980, pp. 1152-1161.

[*42*] Faucher, B. and Krausz, A. S., *Scripta Metallurgica*, Vol. 12, 1978, pp. 175-179.

[*43*] Faucher, B. and Krausz, A. S., *Scripta Metallurgica*, Vol. 12, 1978, pp. 913-918.

[*44*] Krausz, A. S. and Craig, G. B., *Acta Metallurgica*, Vol. 14, 1966, pp. 1807-1813.

[*45*] Rohde, R. W. and Nordstrom, T. V., *Scripta Metallurgica*, Vol. 7, 1973, pp. 317-322.

[*46*] Krausz, A. S., *Journal of Applied Physics*, Vol. 49, July 1978, pp. 3774-3778.

[*47*] Krausz, A. S. and Aggarwal, M. L., *Materials Science and Engineering*, Vol. 48, 1981, pp. 271-281.

Microstructural Evolution and Derived Models

W. D. Nix,[1] *J. C. Gibeling,*[1] *and K. P. Fuchs*[1]

The Role of Long-Range Internal Back Stresses in Creep of Metals

---

REFERENCE: Nix, W. D., Gibeling, J. C., and Fuchs, K. P., "**The Role of Long-Range Internal Back Stresses in Creep of Metals,**" *Mechanical Testing for Deformation Model Development, ASTM STP 765,* R. W. Rohde and J. C. Swearengen, Eds., American Society for Testing and Materials, 1982, pp. 301-321.

ABSTRACT: The use of back stress terms in constitutive equations implies the existence of inhomogeneous stresses within the solid. We suggest that such inhomogeneities arise naturally from dislocation processes and are associated with the development of hard and soft regions within the substructure. We point out that back stresses act in the soft parts of the substructure and that constitutive equations containing back stresses should be based on flow mechanisms in these regions. Constitutive equations based on flow in the hard parts of the substructure should contain forward internal stresses. We envision flow in the hard regions to be controlled by recovery and to dominate at high temperatures, while flow in the soft regions involves other kinds of thermally activated dislocation motion and is most important at low temperatures. Power law breakdown is explained with a composite model as a natural consequence of the transition from high temperature to low temperature deformation.

KEY WORDS: constitutive equations, creep, deformation, recovery, thermally activated glide, dislocations, anelasticity, internal stresses, back stresses, subgrains, power law breakdown, substructure

One of the principal objectives of research on deformation mechanisms is to provide guidelines for the development of constitutive equations for describing nonelastic deformation of metals. Because engineering applications invariably involve complex thermal and mechanical histories it is necessary that the constitutive equations be of such form that both steady-state and non-steady-state deformation phenomena can be described. Transient creep, anelasticity, cyclic creep, and the Bauschinger effect are all examples of important deformation phenomena that need to be described.

---

[1] Professor, Research Associate, and Graduate Research Assistant, respectively, Department of Materials Science and Engineering, Stanford University, Stanford, Calif. 94305. Mr. Fuchs is currently Senior Process Engineer, Intel Corporation, Livermore, Calif. 94550.

The idea of an internal back stress which reduces the stress acting within the solid is commonly used in constitutive equations to help explain transient creep effects. When this is done the general form of the constitutive equation may be written as

$$\dot{\gamma} = f\left(\frac{\tau - \tau_B}{\hat{\tau}}\right) \tag{1}$$

where τ is the applied shear stress, τ_B is the back stress, $\hat{\tau}$ is a strength parameter related to the microstructure, and $f(x)$ represents the form of the constitutive equation and includes other factors such as temperature.[2] The terms τ_B and $\hat{\tau}$ are often associated with directional and isotropic hardening, respectively. We consider $\hat{\tau}$ to represent the average strength of the obstacles which limit dislocation motion, and $\tau - \tau_B$ to be the shear stress which drives the dislocations past the obstacles. In the present paper we examine the conditions for which back stresses can be included in constitutive equations, and we discuss the restrictions associated with this procedure.

It is well known that the back stress results from internal stresses, $\tau_i(x)$, which vary from place to place within the solid. In the present discussion we will let Λ represent the characteristic wavelength of this internal stress variation. The actual stress acting at a particular place within the solid is then $\tau + \tau_i(x)$. In cases where internal stresses are important, we assume that the local dislocation velocity or strain rate may be expressed as $v(x) = f[\tau + \tau_i(x)]$ or $\dot{\gamma}(x) = f[\tau + \tau_i(x)]$, respectively. It should be recognized that this procedure is valid only if Λ, the wavelength of the internal stress variation, is much greater than λ, the spacing between the obstacles that limit dislocation motion. We might call this a principle of superposition. For $\Lambda \gg \lambda$ a typical volume element within the solid is subjected to a local stress $\tau + \tau_i(x)$ which drives dislocations past the obstacles in that small region. For $\Lambda \approx \lambda$ the sources of internal stress become a part of the obstacle structure and the simple method of superposition cannot be used.

Even if the internal stresses are long range ($\Lambda \gg \lambda$), it does not follow that a net back stress, τ_B, acts over the entire solid. The internal stresses must integrate to zero to satisfy mechanical equilibrium conditions. This means that the internal stresses reduce the stress in some regions and increase it in others. It is necessary to properly average over the entire internal stress field to determine if a net resistance to deformation is caused by the fluctuating internal stresses.

To illustrate these points we review the problem of dislocation motion past point defect and homogeneously distributed dislocation obstacles and conclude that internal stresses associated with the dislocations themselves lead to

---

[2] The use of the symbol τ is not meant to restrict our discussion to single crystals.

a net back stress in the first case but not in the second. The evidence for long-range internal back stresses in dislocation-hardened metals is then reviewed and interpreted in terms of the development of hard and soft regions within the substructure.

In the last part of the paper we present a mixed composite model of flow in which diffusion-controlled recovery occurs in the hard parts of the substructure and other kinds of thermally activated glide occur in the soft regions. We show that power law breakdown can be described as a natural consequence of the transition from high temperature to low temperature flow with this model.

Effect of Internal Stresses on Dislocation Motion

Point Defect Obstacles

When dislocation motion is limited by closely spaced obstacles (such as impurity atoms, point defect clusters, or even very fine precipitates), long-range internal stresses associated with the dislocations themselves may become important. The wavelength of the internal stress variation corresponds to the dislocation spacing, $\Lambda = \rho^{-1/2}$, and this is typically much greater than λ, the spacing between the point defect obstacles. In this case it is valid to write

$$v(x) = f\left(\frac{\tau + \tau_i(x)}{\hat{\tau}}\right) \tag{2}$$

or, for the special case of a power law function,

$$v(x) = B[\tau + \tau_i(x)]^m \tag{3}$$

To determine the net effect of the internal stresses it is necessary to find the average dislocation velocity by integrating over the entire path of the dislocation. Li [*1*][3] has described this kind of averaging and has shown that for sinusoidal internal stresses described by $\tau_i(x) = \tau_i^{o} \sin (2\pi x/\Lambda)$, the average dislocation velocity can be described by

$$\bar{v} = B(\tau - \tau_B)^m \tag{4}$$

where

$$\tau_B = \tau\left\{1 - \frac{1}{\xi[P_{m-1}(\xi)]^{1/m}}\right\} \tag{5}$$

---

[3] The italic numbers in brackets refer to the list of references appended to this paper.

where $P(x)$ is a Legendre function and $\xi = [1 - (\tau_i^{\circ}/\tau)^2]^{-1/2}$. In this case the fluctuating internal stresses lead to a net back stress and the presence of τ_B in a constitutive equation is justified.

Homogeneously Distributed Dislocation Obstacles

We consider now the case of hardening associated with a homogeneous distribution of dislocations. Although dislocations are commonly distributed in an inhomogeneous manner, there are many cases in which dislocations appear to be homogeneously distributed, particularly in solid solution alloys in which cells or subgrains do not form readily [*2-5*]. When the dislocations themselves are the primary obstacles to plastic flow, the obstacle spacing is about equal to the interdislocation spacing, $\lambda = \rho^{-1/2}$. But if the dislocations are homogeneously distributed, the internal stresses associated with them also fluctuate with a wavelength equal to the dislocation spacing, $\Lambda = \rho^{-1/2}$. Since in this case $\Lambda \approx \lambda$, the sources of internal stress become a part of the obstacle structure, and we are not able to separate the effects of internal stresses from the obstacles themselves.

Hardening by homogeneously distributed dislocation obstacles is illustrated in Fig. 1. The internal stresses, $\tau_i(x)$, fluctuate inside the region R with a wavelength $\Lambda = \lambda = \rho^{-1/2}$ but integrate to zero over that region: $\int_R \tau_i(x)\, dx = 0$. Thus the average stress acting on the region R is simply the applied stress. In this case there are no long-range internal back stresses.

If we regard the dislocations as point-like obstacles [*6-7*], then we may expect the constitutive equation for flow to be of the form

$$\dot{\gamma} = f'(\theta/\theta_c) \tag{6}$$

where θ is the angle shown in Fig. 1 and θ_c is the critical angle at which the obstacle is mechanically activated. Alternatively, this may be written as

$$\dot{\gamma} = f(\tau/\hat{\tau}) \tag{7}$$

where $\hat{\tau} = \mu b/\lambda \cos(\theta_c/2) \sim \mu b\sqrt{\rho}$ is the mechanical threshold stress. In this case dislocation hardening appears entirely in the obstacle strength term, $\hat{\tau}$.

This example serves to indicate that for dislocation hardening, back stresses must arise from very long-range internal stresses $\Lambda \gg \rho^{-1/2}$. Clearly additional hardening that might be caused by solutes or very fine precipitates should not be expressed as a back stress. Provided the same flow law can be used, these defects would modify the obstacle strength term $\hat{\tau}$. In the next section of the paper we turn our attention to inhomogeneous distributions of dislocations which are capable of producing very long-range internal stresses and which lead to back stresses in the case of dislocation hardening.

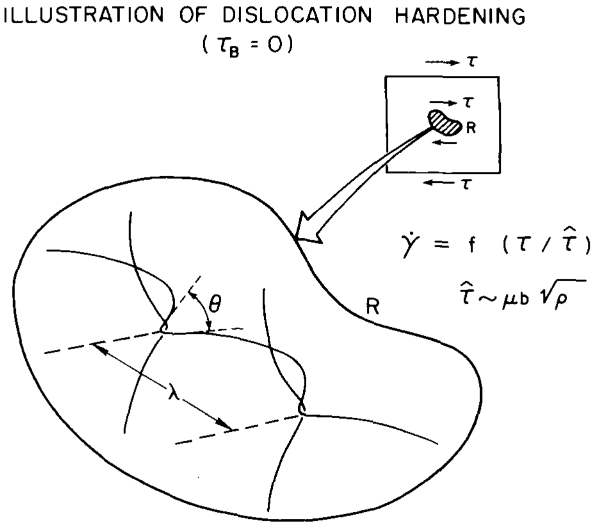

FIG. 1—*Illustration of hardening associated with a homogeneous distribution of dislocations. The internal stresses integrate to zero over the region* R *so that no long-range internal back stresses act on the dislocations.*

Review of Evidence for Long-Range Internal Stresses in Dislocation-Hardened Metals

The preceding discussion indicates that homogeneous dislocation hardening does not lead to long-range internal stresses. However, plastic deformation in relatively pure metals generally gives rise to inhomogeneous dislocation substructures, especially at elevated temperatures. There is now considerable experimental evidence, both direct and indirect, linking the formation of heterogeneous structures to the development of long-range internal stresses.

The indirect evidence is based on observations of negative strain rates following large stress reductions during creep. Following the original work of Gibbs [*8*], virtually all experimental investigations involving stress changes include reports of time dependent or anelastic back flow for sufficiently large stress decrements. In order for such anelastic back flow to occur there must be an inhomogeneous distribution of stresses within the solid which is redistributed following a reduction in the applied stress. Thus creep anelasticity is simply a manifestation of internal back stresses. In fact, numerous authors have used this concept as a method to measure average back stresses during creep [*9-11*].

Recently, Gibeling and Nix [*12*] have studied creep anelasticity separately from other transient effects. A typical result following a 90 percent stress reduction during creep of an aluminum single crystal is illustrated in Fig. 2.

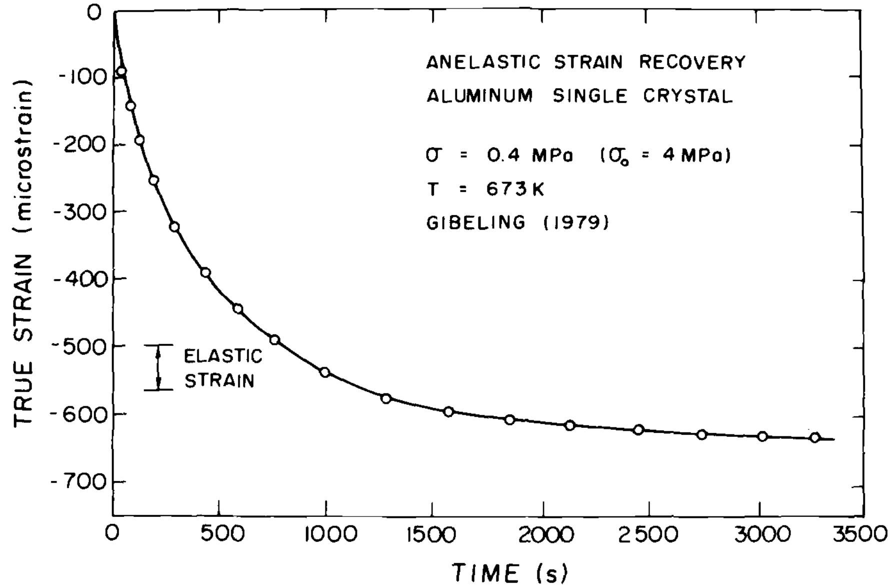

FIG. 2—*Anelastic backflow transient for an aluminum single crystal crept to a strain of 0.22 (673 K; initial stress = 4 MPa).*

Since this result was obtained for a single crystal, the back flow cannot be attributed to grain boundary sliding. In addition, the magnitude of the observed anelastic strain is large in comparison to the calculated elastic strain. This large anelastic strain cannot be described by simple models of dislocation unbowing, which invariably predict recoverable strains about equal to the elastic strain. Further, the rate of the observed back flow is considerably slower than expected for simple unbowing. On this basis, we conclude that the observed anelasticity represents the motion of dislocations driven by long-range internal stresses [*12*].

This evidence suggests that the periodicity of the internal stress fields is large in comparison to the spacing of the obstacles to dislocation motion. If we imagine that the mechanism of dislocation motion involves interaction processes such as cutting, junction unpinning, or bowing between pinning points, then it is reasonable to associate the obstacle spacing with the interdislocation spacing, $\lambda = \rho^{-1/2}$. The problem, then, is to identify the source of the long-range internal stresses such that $\Lambda \gg \lambda$. One piece of evidence can be obtained by examining the recoverable anelastic strain as a function of prior creep strain. The data shown in Fig. 3 were obtained by conducting a series of unloading experiments similar to those described above. The recoverable anelastic strain is small when the stress reduction is made during

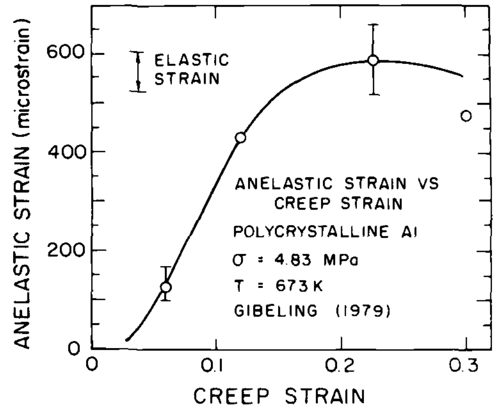

FIG. 3—*Increase in the magnitude of the anelastic backflow with creep strain in polycrystalline aluminum.*

primary creep, but increases as steady state is reached. This observation can be correlated with changes in substructure which are known to occur during primary creep. Numerous investigators have shown that dislocations are homogeneously distributed just after loading, but during primary creep they begin to collect together to form cells and subgrains. In this way the substructure becomes more heterogeneous due to clustering of dislocations. The increasing recoverable anelastic strain during primary creep suggests that the inhomogeneous substructure produces an inhomogeneous stress distribution which in turn provides the driving force for back flow.

The most direct evidence of the relation between long-range internal back stresses and inhomogeneous substructures has been obtained by Hasegawa et al, who made an extensive study of substructure and measured back stress as a function of creep strain in a Cu-16Al alloy [*13*]. As shown in Fig. 4, this material exhibits sigmoidal creep characteristics, in which the dislocation density is initially low, increases in a homogeneous manner with strain, and eventually leads to subgrain formation. The measured back stresses are low when the dislocations are homogeneously distributed, but increase dramatically as subgrain formation occurs. This result clearly illustrates that long-range internal stresses are associated with heterogeneous substructures. We conclude that long-range internal stresses in relatively pure metals depend on the formation of cells or subgrains. The characteristic wavelength of the fluctuating internal stress fields must be on the order of the subgrain size, which is many times larger than the interdislocation spacing. Thus, the internal stresses may be separated from the dislocation obstacles, $\Lambda \gg \lambda$, and it is appropriate to describe deformation in terms of internal stresses. However, it is still necessary to do the proper averaging in order to justify the use of a net back stress to describe the overall deformation.

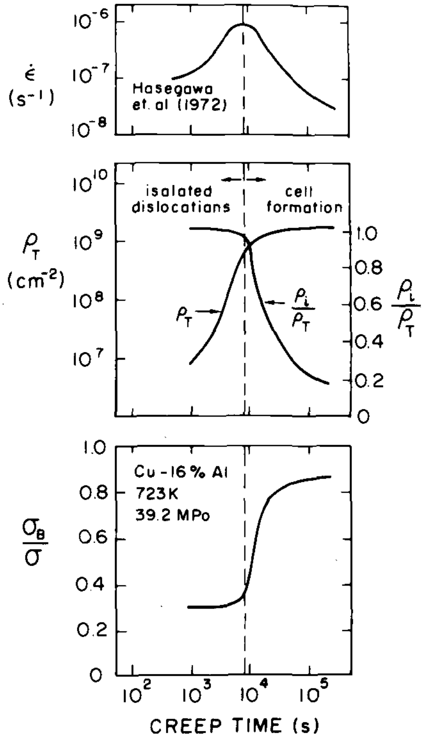

FIG. 4—*Relation between cell formation and the development of long-range internal back stresses* [13].

The suggestion that subgrain boundaries provide long-range internal stresses may be somewhat unusual. Normally, subgrain walls are thought to be composed of stable dislocation arrays which have no long-range stress fields. However, this result is only true for perfect low-angle boundaries which are infinite in extent. Based on a calculation by Vreeland [*14*], Argon has suggested that long-range internal stresses may be developed when the substructure is biased by the applied stress [*15*]. Gibeling and Nix have recently presented the results of a numerical study of stresses associated with subgrains composed of simple two-dimensional tilt boundaries [*16*]. The model is illustrated in Fig. 5. With no applied shear stress, the internal shear stresses can be obtained by summing up the contributions of the individual dislocations. As shown in Fig. 5*a*, the shear stresses at $y = 0$ are essentially zero except very near to the wall. However, under the action of an applied shear stress, the walls flex, since the dislocations are free to glide. We note that in this model the corners have been artificially constrained to stabilize

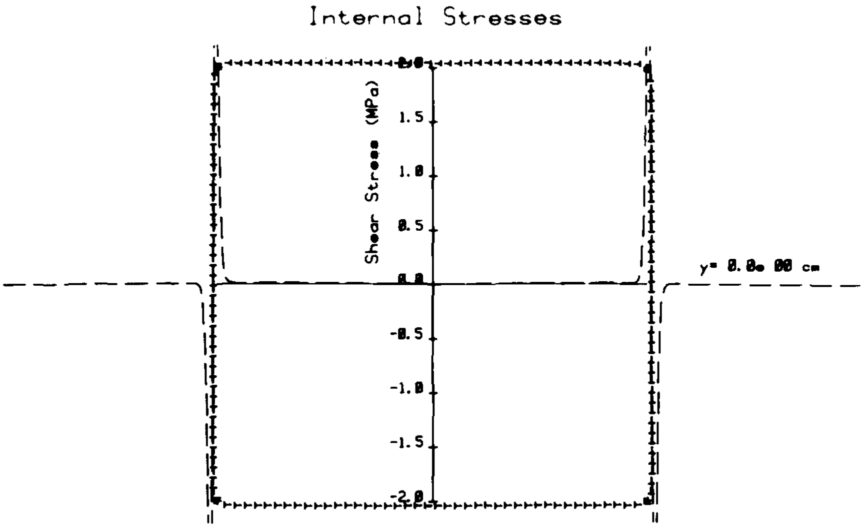

a) Applied Shear Stress = 0 MPa

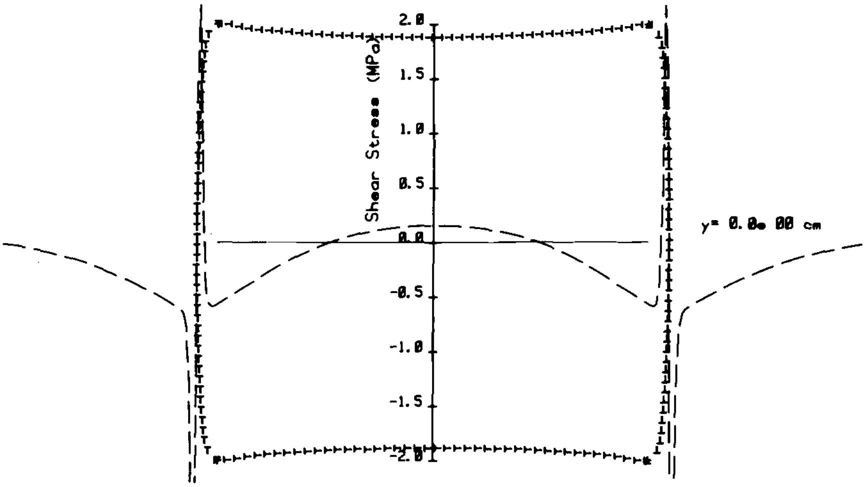

b) Applied Shear Stress = 0.7 MPa

FIG. 5—*The configuration of subgrain boundaries and the associated internal shear stresses* (τ_{xy} *calculated along* y = 0), *for the cases* (a) *of no applied shear stress and* (b) *an applied shear stress of 0.7 MPa.*

the structure with respect to glide. After allowing this glide relaxation to occur, the internal stresses can again be calculated. As shown in Fig. 5*b*, appreciable long-range internal stresses are developed in the biased condition. Further, these stress fields have a characteristic wavelength equal to the subgrain size, in agreement with the requirements cited above. From this simple model we conclude that it is possible to develop long-range internal stresses in inhomogeneous substructures which are biased by the applied stress. It should be added that long-range internal stresses with wavelengths on the order of the grain size can also be produced by nonuniform deformation from grain to grain.

Mechanistic Interpretation of Heterogeneous Substructures

The aforementioned evidence suggests that long-range internal stresses are related to the development of subgrains, or more generally, to dislocation clustering. We wish to provide a general description of the role of heterogeneous substructures as a basis for developing models which describe the flow properties of metals.

As described earlier, we know that in a creep test the dislocation distribution just after loading is relatively homogeneous. We assume that during the early stages of primary creep the dislocations move by a variety of thermally activated processes, such as dislocation cutting or cross-slip. Since the dislocation distribution is not completely uniform, there is an inherent distribution of obstacle strengths. Dislocations are able to move easily through the soft regions where the obstacle spacing is large, and tend to collect in the hard regions where the dislocation density is somewhat higher. As a consequence, the hard regions become harder and the substructure becomes more heterogeneous. This process is illustrated schematically in Fig. 6. We envision that recovery is necessary to move dislocations through the hard regions, while thermally activated motion continues to predominate in the soft regions.

The development of hard and soft regions for deformation at high temperatures and low stresses is equivalent to a picture developed by Kocks et al [*17,18*]. With initial straining, islands of hard material develop, although the soft region remains continuous. Strain hardening leads to growth of the hard regions, with the consequence that the hard phase eventually becomes continuous.

Compatibility requires that spatial variations in plastic strain must be accommodated by elastic strains. In this way the load is redistributed such that the stress in the soft region is small while the stress supported by the hard region is large. This stress distribution is illustrated schematically in Fig. 7. We now adopt a simple composite view of the creep substructure.

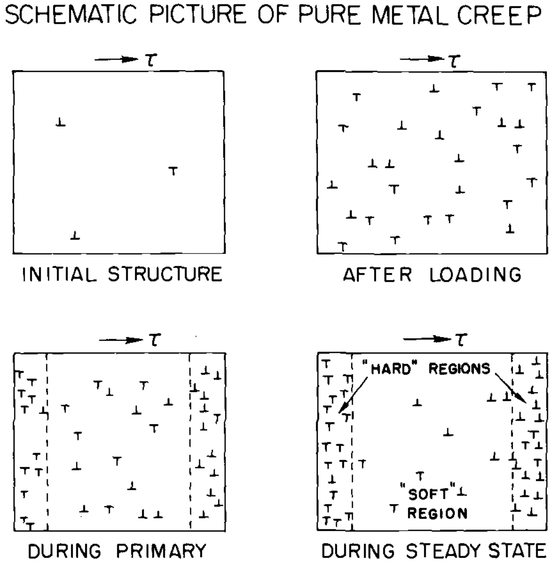

FIG. 6—*Schematic illustration of the development of hard and soft regions within a deformation substructure.*

If α_S represents the volume fraction of soft region and α_H the volume fraction of hard material, mechanical equilibrium requires that

$$\tau = \alpha_S \tau_S + \alpha_H \tau_H \tag{8}$$

where τ_S and τ_H are the stresses acting in the soft and hard regions, respectively. As shown schematically in Fig. 7, the stress acting in the soft region is less than the applied stress, and may be obtained by subtracting the long-range back stress from the applied stress:

$$\tau_S = \tau - \tau_B \tag{9}$$

Finally, from Eq 8, the stress acting in the hard region must be greater than the applied stress, and is given by

$$\tau_H = \tau + \left(\frac{1 - \alpha_H}{\alpha_H}\right)\tau_B \tag{10}$$

This picture indicates that long-range internal stresses develop as a natural consequence of the inhomogeneity of deformation. Cell boundaries, subgrain walls, or dense clusters of dislocations act as hard regions which support

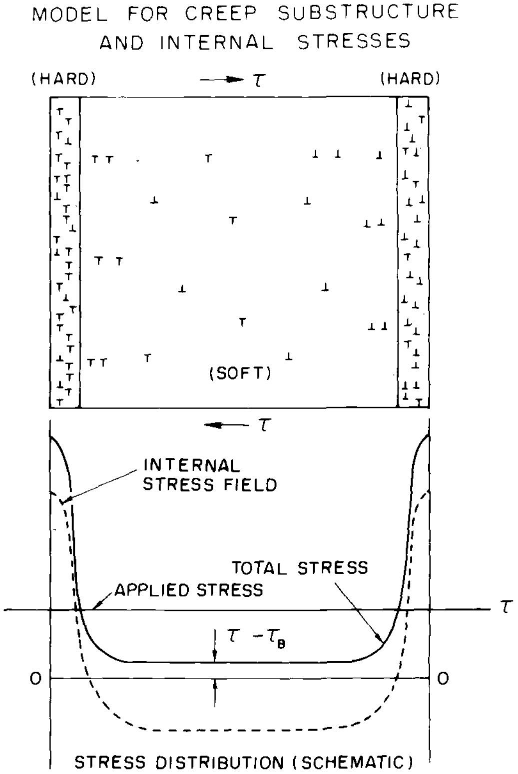

FIG. 7—*Model for creep substructure and long-range internal back stresses.*

large forward stresses. The stresses in the softer regions are thereby relieved, and are less than the applied stress (Eq 9).

Evaluation of Composite Models of Creep Flow

The preceding interpretation of inhomogeneous substructures suggests that it is appropriate to modify the applied stress by an internal stress term to provide a description of deformation in the hard and soft regions. However, in order to describe the overall strain rate in terms of a net back stress (Eq 1), it is necessary to first do the proper averaging of the behavior in the two regions, as outlined previously. In the following sections we analyze several approaches to making these averages.

Iso-Strain Rate Model

During deformation, dislocation clustering leads to the formation of hard regions in which flow can only occur by the recovery or rearrangement of obstacles. Under creep conditions at elevated temperatures, these hard regions form a continuous "phase" of subgrain boundaries. The picture shown in Fig. 7 suggests that is is natural to describe the deformation in terms of an iso-strain rate model, in which

$$\dot{\gamma} = \dot{\gamma}_S = \dot{\gamma}_H \tag{11}$$

and, from Eq 8,

$$\tau = \alpha_S \tau_S + \alpha_H \tau_H$$

where the subscripts refer to the hard and soft regions. In this interpretation, deformation occurs sequentially in the two regions. This model is particularly attractive because it leads to the notion that creep is controlled by recovery in the hard regions, which is a very old and well accepted idea. Anelastic back flow also follows as a natural consequence in that deformation in the soft phase is blocked by the hard regions.

Using Eq 9 for the stress in the soft region, we can write

$$\dot{\gamma} = \dot{\gamma}_S = f_S(\tau - \tau_B) \tag{12}$$

where the function f_S represents a law describing the physics of deformation in the soft region. In this case, it is appropriate to consider the overall deformation in terms of the applied stress minus a back stress term. It is important to note, however, the functional form which is used must describe the physical processes occurring in the soft region. As discussed earlier, it is natural to expect that dislocations can surmount the relatively weak obstacles in the soft region by thermally activated glide processes. Accordingly, f_S can be replaced by an appropriate rate law for thermally activated dislocation glide.

Alternatively, the overall deformation process can be described by considering the hard region, in which case

$$\dot{\gamma} = \dot{\gamma}_H = f_H\left[\tau + \left(\frac{1 - \alpha_H}{\alpha_H}\right)\tau_B\right] \tag{13}$$

where f_H represents the functional form of the physics of deformation in the hard region. As before, we assume that deformation in the hard region is controlled by recovery. But it is important to note that the strain rate is a function of the applied stress plus an internal stress term. Since we have presumed that the physical processes in the two regions are different, it is valid to write, as in Eq 12,

$$\dot{\gamma} = f_S(\tau - \tau_B)$$

but not correct to write

$$\dot{\gamma} = f_H(\tau - \tau_B) \tag{14}$$

More specifically, the use of a recovery law for deformation coupled with a term $(\tau - \tau_B)$ appears to be inconsistent. Rather, use of a recovery law requires that we add a forward internal stress term to the applied stress, as in Eq 13.

As noted earlier, the iso-strain rate approach leads naturally to the concept that steady-state flow is controlled by recovery events in the hard regions. This is appropriate at high temperatures (or low stresses) where diffusion-controlled recovery appears to control the steady-state strain rate and power law creep is observed. But as the temperature is lowered or the stress increased, the steady-state data exhibit a much smaller strain rate sensitivity typical of low temperature flow. This behavior is known as power law breakdown, and is illustrated in Fig. 8 for pure aluminum. As shown, the deviation from power law behavior (dashed line) is described quite well by a hyperbolic sine relationship. If we wish to retain the iso-strain rate model, the functional form of the rate law, f_H, must include low-temperature dynamic recovery or rearrangement contributions which will naturally explain power law breakdown. Such processes might involve cross-slip, for example. Although this is a promising approach and is being pursued by a number of investigators [*18-20*], it is difficult to identify a physical mechanism which allows for recovery without diffusion. Because theoretical justification of a recovery law leading to a form such as $\dot{\epsilon} \propto \sinh \sigma$ has not yet been obtained, it is reasonable to consider alternative models of deformation in heterogeneous structures.

Iso-Stress Model

One disadvantage of the iso-strain rate interpretation is that it does not include the traditional concept that flow occurs by thermally activated motion of dislocations past obstacles at low temperatures and by diffusion-controlled recovery of obstacle structures at high temperatures. One way in which to separate these two ideas of "plasticity" and "creep" is to adopt an iso-stress model, in which

$$\tau = \tau_S = \tau_H \tag{15}$$

$$\dot{\gamma} = \alpha_S \dot{\gamma}_S + \alpha_H \dot{\gamma}_H \tag{16}$$

In this description, deformation in the soft regions and hard regions occurs independently. This model permits a natural transition from high temperature to low temperature flow in accordance with observations of power law

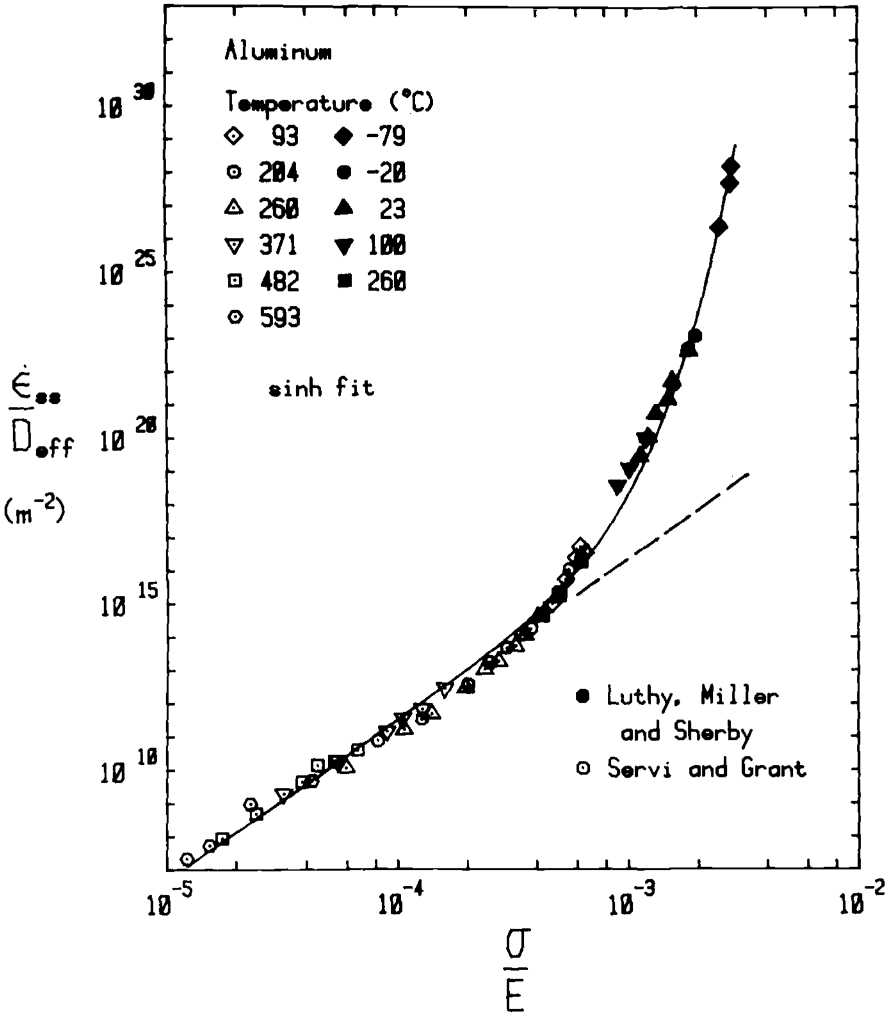

FIG. 8—*Transition from high temperature to low temperature flow for aluminum. The solid line represents the sinh fit given by Luthy et al* [27].

breakdown. However, it is unacceptable from the point of view that anelasticity and internal stresses play no role in the description of flow. Further, the structures represented by this model would be inherently unstable, as the soft region would be expected to harden until a homogeneous substructure is developed. For these reasons it appears that a simple isostress model is entirely inappropriate.

Mixed Composite Model of Dislocation Substructures

The simple iso-strain rate and iso-stress models outlined in the preceding sections do not permit us to include both anelasticity and power law breakdown in the same description. In an attempt to account for both of these effects, we adopt a mixed composite model. This model is characterized by two equations. The first,

$$\dot{\gamma} = \alpha_S \dot{\gamma}_S + \alpha_H \dot{\gamma}_H \tag{17}$$

accounts for the transition from high temperature to low temperature flow. In addition, as in Eq 8, we may write

$$\tau = \alpha_S \tau_S + \alpha_H \tau_H$$

which provides a basis for anelastic and back stress effects. Based on these two equations, it is apparent that the model is neither iso-strain rate nor iso-stress. Rather, it is a mixed composite description incorporating features from both simple models. We now show how this model can be used to describe power law breakdown. The deficiencies of the model are briefly described in the last part of this section.

In order to give an explicit description of power law breakdown as a natural transition from recovery-controlled processes at high temperatures to thermally activated glide controlled processes at low temperatures, it is necessary to write governing equations for each of these processes. The equations we use here are taken from the work of Nix and Ilschner [*21*] and presented in modified form.

Recovery in the hard parts of the structure is assumed to be controlled by edge dislocation climb. As Weertman [*22*] and others have observed, most treatments of this process lead to a third power stress law. However, all of these treatments consider the dislocation to act as a perfect source and sink for vacancies all along its length. Ilschner pointed out that an additional stress term arises if climb is assumed to take place at jogs formed by intersection processes [*23*]. This modified form of the natural law given by Nix and Ilschner can be written as

$$\dot{\epsilon}_r = 170 D_e \frac{\mu b}{kT} \frac{\sigma}{\sigma_H} \left(\frac{\sigma_H}{\mu} \right)^4 \tag{18}$$

where σ is the applied tensile stress, σ_H is the stress in the hard region given by

$$\sigma_H = \sigma + \left(\frac{1 - \alpha_H}{\alpha_H} \right) \sigma_B \tag{19}$$

and D_e is the effective diffusion coefficient (to account for diffusional transport down dislocation cores [*24-27*]). The term σ_H appears in this expression because recovery occurs in the hard parts of the substructure where the stresses are σ_H. The applied stress term appears because the jog spacing is expected to scale with the average dislocation spacing, which in turn scales with the applied stress. σ_B is the internal back stress which acts in the soft parts of the substructure.

We assume that deformation in the soft regions is controlled by thermally activated glide of dislocations past obstacles. This might involve such processes as dislocation intersection, junction unpinning, or cross-slip. Following the work of Ashby and Frost [*28*], Nix and Ilschner [*21*] used a phenomenological equation for "square" obstacles to describe this process. In a modified form this equation reads

$$\dot{\epsilon}_{th} = 5.26 \times 10^8 \frac{\sigma}{\mu} \phi \exp \frac{-\Delta F}{kT} \left\{ \exp \left(\frac{\Delta F}{kT} \frac{\sigma_S}{\hat{\sigma}} \right) - 1 \right\} \tag{20}$$

where ΔF is the Helmholtz free energy associated with moving a dislocation past an obstacle, σ_S is the stress acting in the soft region and given by $\sigma - \sigma_B$, $\hat{\sigma}$ is the average obstacle strength related to $\mu b \sqrt{\rho}$ (and set equal to 0.85 σ in the present treatment because the dislocation density scales with the applied stress), and ϕ is a function which accounts for the distribution of obstacle strengths and is equal to the fraction of obstacles that are thermally activatable. We use the treatment of Gasca-Neri and Nix [*29*] to estimate the fraction of obstacles that can be surmounted by thermal activation

$$\phi = \frac{\sigma_S}{\hat{\sigma}} \exp - \left(\frac{1 - (\sigma_S/\hat{\sigma})}{\sigma_S/\hat{\sigma}} \right) \tag{21}$$

The steady-state strain rate for the mixed composite model may be expressed as

$$\dot{\epsilon} = \alpha_H \dot{\epsilon}_r + \alpha_S \dot{\epsilon}_{th} \tag{22}$$

where $\dot{\epsilon}_r$ and $\dot{\epsilon}_{th}$ are given by Eqs 18 and 20, respectively. Power law breakdown in pure aluminum and iron can be described by this relation. To fit the data we set $\alpha_H = 0.05$ ($\alpha_S = 0.95$) and $\Delta F = 0.44\ \mu b^3$. These are not considered to be unreasonable values for these parameters. The terms σ_H and σ_S are calculated from measured values of the internal back stress, σ_B. The measured back stresses for aluminum and aluminum-magnesium alloys [*30*] can be described by $\sigma_B = \sigma - 0.11\ \sigma^{1.39}$ (stress in MPa), and we use this to estimate σ_B for pure aluminum. The measured back stresses in iron [*31*] can be described by $\sigma_B = \sigma - 0.057\ \sigma^{1.4}$ (stresses in MPa).

The predictions of the mixed composite model are compared with the steady-state flow properties of aluminum and iron in Figs. 9 and 10, respectively. At high temperatures, in the power law creep regime, the creep rate is dominated by $\dot{\epsilon}_r$, whereas at low temperatures, in the power law breakdown region, the creep rate is dominated by $\dot{\epsilon}_{th}$. These results are consistent with the predictions of the model.

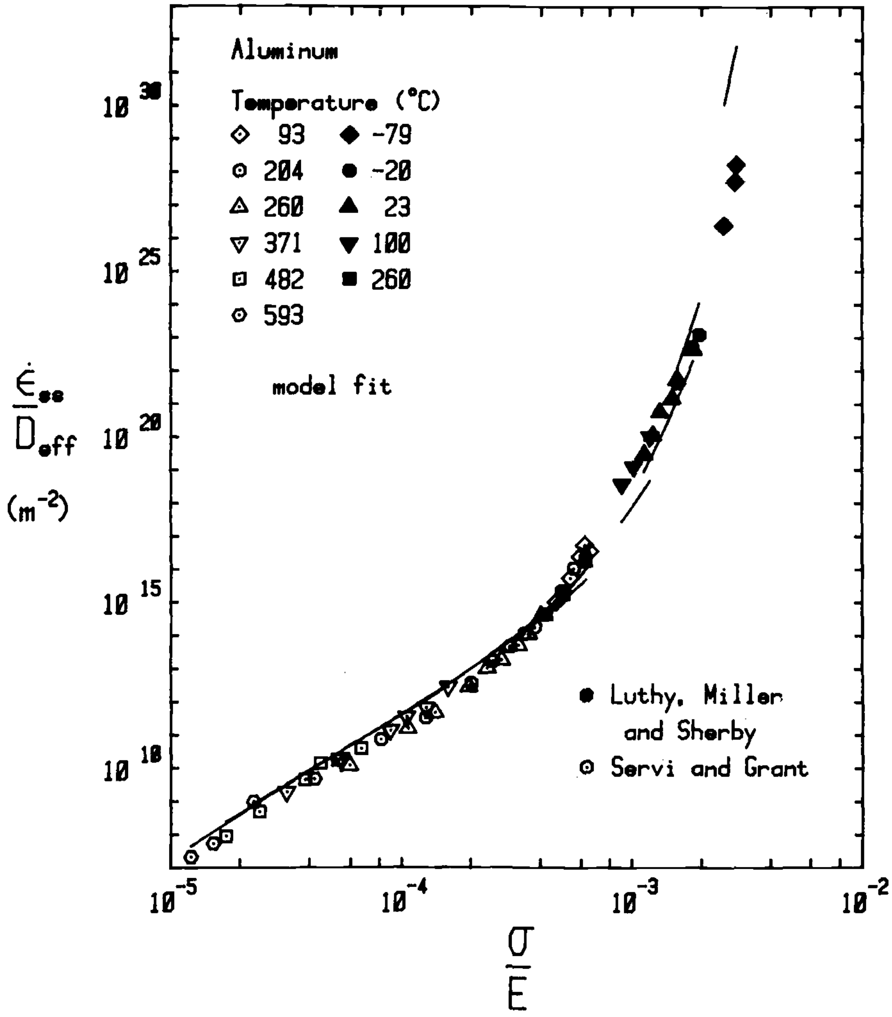

FIG. 9—*High temperature and low temperature creep data for aluminum. The solid lines represent the predictions of Eq 22. The effective diffusivity given by Luthy et al* [27] *was used both in Eq 18 and in the normalization of the data. The back stress data of Oikawa et al* [30] *were used in the analysis.*

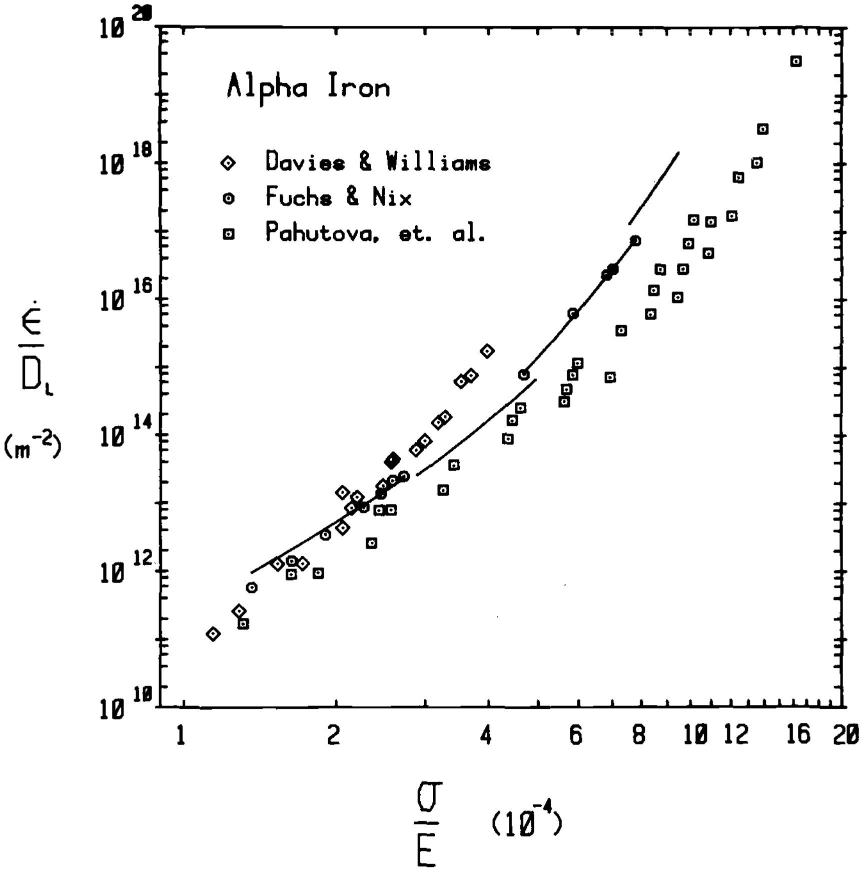

FIG. 10—*High temperature and low temperature creep data for iron. The solid lines represent the predictions of Eq 22. The lattice self-diffusion coefficient rather than the effective diffusivity was used in this analysis. The back stress data of Pahutová et al* [31] *were used in the analysis.*

Although these results are encouraging, it is difficult to give a convincing microscopic rationale for the mixed composite model. In particular, it is not easy to justify the use of Eq 17 for steady-state deformation. For steady-state conditions it is usually assumed that the cell walls or subgrain boundaries are continuous and that the interiors of the cells or subgrains are isolated from each other. Thus for closed cell structures the hard phase (cell wall) is expected to be continuous while the soft phase (cell interior) is discontinuous. For this morphology, it is not clear how deformation within the two phases can contribute independently to the strain rate, as required by Eq 17. We can only suggest that at high stresses and low temperatures, where deformation is dominated by flow in the soft regions, dislocations are able to cut through the cell walls easily. Although this seems like an unnatural assumption, some support for it can be found in the substructure observations of Blum and coworkers [32]. These investigators found that the subgrain size L and the spacing of dislocations not associated with subgrain boundaries, $\rho^{-1/2}$, both vary inversely with stress. However, the spacing of dislocations within subgrain walls, s, depends less sensitively on stress. Thus, at low temperatures and high stresses, we might expect the stresses in the walls to exceed the strength there and this in turn would allow dislocations to pass through the cell walls easily.

The problem of steady-state flow of composite cell structures is still not fully understood, although work in progress by McClintock and Argon [33] promises to resolve some of the important questions. Whether overall deformation is controlled by flow in the hard or soft regions is still not known. Chen and Argon [34] have recently studied power law creep in composite materials and have concluded that when the hard phase occupies only a small volume fraction, overall creep is governed by the soft phase at all stress levels. The opposite conclusion would be reached if the hard phase were assumed to be continuous and the isostrain rate model were used, even if the hard phase occupies only a small volume fraction. The work of Chen and Argon [34] is based on a self-consistent method in which inclusions of the hard and soft phases are assumed to be imbedded in a matrix with average (in a self-consistent sense) creep properties. The inclusion model breaks down when the hard phase is continuous, even for small volume fractions. Thus it is not clear how the creep properties of composite cell structures should be described. Although the mixed composite model we have presented here appears to be inconsistent with the observations of closed cell structures, we offer it as a possible description of power law breakdown.

Acknowledgments

The authors wish to thank their colleagues at Stanford University for their contributions to the concepts presented in this paper. This work was supported in part by the National Science Foundation through Grant No. NSF-DMR-79-23942 and by the United States Department of Energy under Contract No. DE-AS03-76SF00326.

References

[1] Li, J. C. M. in *Dislocation Dynamics*, A. R. Rosenfeld, G. T. Hahn, A. L. Bement, Jr., and R. I. Jaffee, Eds., McGraw-Hill, New York, 1968, pp. 87–116.
[2] Ajaja, O. and Ardell, A. J., *Scripta Metallurgica*, Vol. 11, No. 2, Dec. 1977, pp. 1089–1093.
[3] Horiuchi, R. and Otsuka, M., *Transactions of Japan Institute of Metals*, Vol. 13, No. 4, July 1972, pp. 284–293.

[*4*] Lagneborg, R., *International Metallurgical Reviews,* Vol. 17, June 1972, pp. 130-146.
[*5*] Stang, R. G., Nix, W. D., and Barrett, C. R., *Metallurgical Transactions A,* Vol. 6A, No. 11, Nov. 1975, pp. 2065-2071.
[*6*] Kocks, U. F., *Philosophical Magazine,* Vol. 13, No. 123, March 1966, pp. 541-566.
[*7*] Morris, J. W. and Klahn, D. H., *Journal of Applied Physics,* Vol. 45, No. 5, May 1974, pp. 2027-2083.
[*8*] Gibbs, G. B., *Philosophical Magazine,* Vol. 13, No. 122, Feb. 1966, pp. 317-329.
[*9*] Ahlquist, C. N. and Nix, W. D., *Acta Metallurgica,* Vol. 19, No. 4, April 1971, pp. 373-385.
[*10*] Blum, W., Hausselt, J., and König, G., *Acta Metallurgica,* Vol. 24, No. 4, April 1976, pp. 293-297.
[*11*] Pahutová, M., Hostinský, T., and Čadek, J., *Acta Metallurgica,* Vol. 20, No. 5, May 1972, pp. 693-702.
[*12*] Gibeling, J. C. and Nix, W. D., *Acta Metallurgica,* Vol. 29, No. 10, Oct. 1981, pp. 1769-1784.
[*13*] Hasegawa, T., Ikeuchi, Y., and Karashima, S., *Metal Science Journal,* Vol. 6, No. 5, May 1972, pp. 78-82.
[*14*] Vreeland, T., *Acta Metallurgica,* Vol. 7, No. 4, April 1959, pp. 240-245.
[*15*] Argon, A. S., MIT, private communication.
[*16*] Gibeling, J. C. and Nix, E. D., *Acta Metallurgica,* Vol. 28, 1980, pp. 1743-1752.
[*17*] Kocks, U. F. in *Constitutive Equations in Plasticity,* A. S. Argon Ed., MIT Press, Cambridge, 1975, Chapter 3, pp. 81-115.
[*18*] Kocks, U. F., Hasegawa, T., and Scattergood, R. O., *Scripta Metallurgica,* Vol. 14, No. 4, April 1980, pp. 449-454.
[*19*] Alden, T. H., University of British Columbia, private communication.
[*20*] Blum, W., University of Erlangen, private communication.
[*21*] Nix, W. D. and Ilschner, B. in *Strength of Metals and Alloys* (*Proceedings,* ICSMA 5), P. Haasen, V. Gerold, and G. Kostorz, Eds., Pergamon Press, New York, 1980, Vol. 3, pp. 1503-1530.
[*22*] Weertman, J. in *Rate Processes in Plastic Deformation of Materials,* J. C. M. Li and A. K. Mukherjee, Eds., American Society for Metals, 1975, pp. 315-336.
[*23*] Ilschner, B., *Zeitschrift für Physik,* Vol. 190, No. 2, Jan. 1966, pp. 258-266.
[*24*] Hart, E. W., *Acta Metallurgica,* Vol. 5, No. 10, Oct. 1957, p. 597.
[*25*] Evans, H. E. and Knowles, G., *Acta Metallurgica,* Vol. 25, No. 8, Aug. 1977, pp. 963-975.
[*26*] Spingarn, J. R., Barnett, D. M., and Nix, W. D., *Acta Metallurgica,* Vol. 27, No. 9, Sept. 1979, pp. 1549-1561.
[*27*] Luthy, H., Miller, A. K., and Sherby, O. D., *Acta Metallurgica,* Vol. 28, No. 2, Feb. 1980, pp. 169-178.
[*28*] Ashby, M. F. and Frost, H. J. in *Constitutive Equations in Plasticity,* A. S. Argon, Ed., MIT Press, Cambridge, 1975, Chapter 4, pp. 117-147.
[*29*] Gasca-Neri, R. and Nix, W. D., *Acta Metallurgica,* Vol. 22, No. 3, March 1974, pp. 257-264.
[*30*] Oikawa, H., Kariya, J., and Karashima, S., *Metal Science Journal,* Vol. 8, No. 4, April 1974, pp. 106-111.
[*31*] Pahutová, M., Orlová, A., Kucharová, K., and Čadek, J., *Philosophical Magazine,* Vol. 28, No. 5, Nov. 1973, pp. 1099-1110.
[*32*] Blum, W., Absenger, A., and Feilhauer, R. in *Strength of Metals and Alloys* (*Proceedings,* ICSMA 5), P. Haasen, V. Gerold, and G. Kostorz, Eds., Pergamon Press, New York, 1979, Vol. 1, pp. 265-270.
[*33*] McClintock, F. A. and Argon, A. S., MIT, private communication.
[*34*] Chen, I. W. and Argon, A. S., *Acta Metallurgica,* Vol. 27, No. 5, May 1979, pp. 785-791.

A. P. L. Turner[1] *and Tadashi Hasegawa*[2]

Deformation Microstructures and Mechanical Equations of State

---

REFERENCE: Turner, A. P. L. and Hasegawa, Tadashi, **"Deformation Microstructures and Mechanical Equations of State,"** *Mechanical Testing for Deformation Model Development, ASTM STP 765,* R. W. Rohde and J. C. Swearengen, Eds., American Society for Testing and Materials, 1982, pp. 322-341.

ABSTRACT: Results of experiments involving various monotonic and cyclic deformation paths and annealing treatments are described. The results show that a state variable theory for constitutive behavior must be based on several independent parameters. Correlations which show that different mechanical responses may depend on the same state variables are discussed. Transmission electron microscopy (TEM) characterizations of the microstructures developed during the tests are reported. Some correlations between microstructure and mechanical behavior are shown, but other cases are reported where no correlation can be found.

KEY WORDS: constitutive equations, state variables, plastic deformation, cyclic deformation, recovery, cyclic creep, mechanical testing, annealing

The use of internal state variables in constitutive equations for mechanical deformation behavior is an attractive way of accounting for the effects of the previous thermo-mechanical history of a material [*1-5*].[3] From the mechanics point of view, this is done by including in the constitutive equations some number of parameters that change as the result of deformation and annealing. There are two types of constitutive equations needed for the description of material behavior. One is the kinetic law, which relates the strain rate to the applied stress and temperature. The other type is an evolution law, which is given by differential equations describing how the state variables change with strain and time. The kinetic law and the evolution laws

---

[1] Metallurgist, Materials Science Division, Argonne National Laboratory, Argonne, Ill. 60439.

[2] Visiting Scientist, Materials Science Division, Argonne National Laboratory, Argonne, Ill. 60439; permanent address, Associate Professor, Department of Mechanical Engineering, Tokyo University of Agriculture and Technology, Koganei-shi, Tokyo, Japan.

[3] The italic numbers in brackets refer to the list of references appended to this paper.

may contain the same state variables, but there is no reason why the evolution laws for the state variables that appear in the kinetic law cannot depend on additional state variables. These additional state variables will require their own evolution laws.

If the number of state variables n required to characterize the mechanical state of the material and the structure of the constitutive equations were known, there would be a straightforward procedure for quantitatively describing material behavior. By performing a number of mechanical tests sufficient to measure n independent material responses, the present state of the material could be specified. By using a testing program in which the state is measured at intervals along a thermo-mechanical path, the evolution equations could be established. Once the state variables and evolution and kinetic equations are known, it would be possible to describe the behavior in any mechanical test from a measured beginning state by integrating the evolution laws over the prescribed test path.

Unfortunately, there is little theoretical guidance as to either the number of state variables that may be required or the structure of the constitutive laws. It is therefore difficult to establish meaningful independent tests to measure the state variables, or to ascertain that a given set of state parameters is sufficient to characterize the mechanical state of the material. State variable constitutive equations must be created by a trial-and-error procedure. Equations can first be formulated that contain enough parameters to describe behavior in simple tests. More complicated testing sequences can then be employed to see if they can also be described by the same equations. If not, new state variables must be introduced, and new equations formulated. This procedure must be repeated until the description is adequate to cover all of the test paths of interest.

From a microstructural viewpoint, it is known that the effects of thermomechanical history are to alter the dislocation microstructure of the material. The characteristics of the microstructure should then correspond to the state variables introduced into the mechanics equations. If it were possible to quantitatively relate macroscopic behavior to the microstructure, this correlation would be known and the microstructural characterization could be substituted for the measurement of the mechanical state variables. This is not now possible, because the complexity of the dislocation arrangements usually precludes such a calculation. Nevertheless, transmission electron microscopy (TEM) has been utilized extensively to examine the microstructures produced by various types of deformation history. If empirical correlations can be established between particular microstructural quantities and mechanical behavior, the extensive TEM information can be used for qualitative guidance in the construction of state variable constitutive laws.

In the remainder of this paper, the results of a number of deformation experiments will be presented. They will be analyzed to determine how many independent parameters are needed for their description. Correlations will be shown between behavior observed in different mechanical tests indicating dependence on the same state variables. Where possible, microstructural information will be presented to show correlations between specific aspects of the microstructure and the mechanical behavior.

Tensile Deformation

In order to account for work hardening, a state description of large-strain plastic behavior must include a parameter which is a measure of the flow stress. Hart [*2*] has proposed that this is the only parameter that is required to describe plastic behavior beyond about 1 percent deformation. This was based on the fact that the kinetic law measured by a stress relaxation test was found to depend on a single parameter after hardening by various prestraining methods. In addition, Turner [*6*] found that the shapes of the stress-strain curves for monotonically or cyclically hardened stainless steel were identical beyond the initial few percent strain. This result is shown in Fig. 1. Here the stress-strain curve is presented in terms of its slope $\theta \equiv d\sigma/d\epsilon$ versus the flow stress σ. On this representation, the stress-strain behavior must be a unique curve if only one state variable is required to describe it. The single state variable can only determine at what point on the curve deformation begins. For the single amplitude cyclic prehistory, the behavior does obey this rule (curve *b*). However, this is not an exhaustive test, and more complicated test histories show different behavior (for example, curve *c* in Fig. 1) for a sample prestressed to a level higher than the cyclic stress amplitude.

During cyclic deformation after cold work, the plastic strain amplitude at constant stress amplitude increases. In a constant plastic strain amplitude test, the stress amplitude decreases. Both of these effects are called cyclic softening. In a single state variable theory, this softening should correspond to a reversal of some of the previous work hardening, that is, a reduction in the flow stress. Instead, an entirely different stress-strain path is followed after cyclic softening. Curve *c* in Fig. 1, which is for a sample that was prestressed to a high level and then cycled at a lower stress amplitude shows an example of this behavior. After this prehistory, the stress-strain behavior no longer follows the original curve; that is, θ is now a different function of σ and an additional parameter will be required to describe the behavior.

Cyclic deformation at constant stress or constant plastic strain amplitude produces a considerably different microstructure from that formed by monotonic deformation that produces the same amount of hardening. This is shown by Figs. *2a* and *2b*. Monotonic deformation produces a microstructure composed of loose dislocation tangles. Cyclic deformation produces a tight cell structure. However, the large strain plastic behavior does not ap-

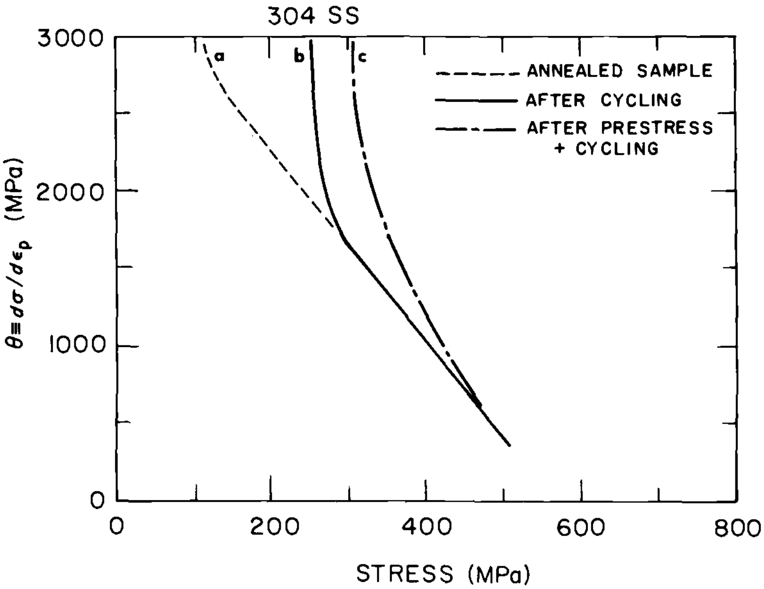

FIG. 1—*Work-hardening rate* $\theta \equiv d\sigma/d\epsilon_p$ *versus flow stress* σ *for Type 304 stainless steel at 560°C.* (a) *Annealed;* (b) *after 1000 cycles at a constant stress amplitude of 250 MPa;* (c) *after prestressing to 330 MPa followed by 5000 cycles at a stress amplitude of 250 MPa.*

pear to be influenced by this structural difference (Fig. 1). (It will be shown later that the small strain and cyclic behavior is influenced.)

On the other hand, prestressing to a higher stress followed by cyclic deformation at a lower stress does affect the large strain plastic behavior, and yet this history produces a microstructure that is not significantly different from that produced by constant amplitude cycling (Fig. 2*b*). In conclusion, there is no one-to-one correlation between the obvious features of the dislocation cell structure and tensile behavior in this material.

Cyclic Deformation

The description of the cyclic behavior of a material for strain amplitudes on the order of 1 percent requires the introduction of additional state parameters. The very existence of a hysteresis loop of nonzero width during small strain amplitude cycling requires the introduction of an additional parameter that changes its value with progress around the loop. This parameter will be called the polarity parameter p because it accounts for the fact that the stress-strain behavior depends on the direction of the previous increment of strain. The easiest way to account for this behavior is by a generaliza-

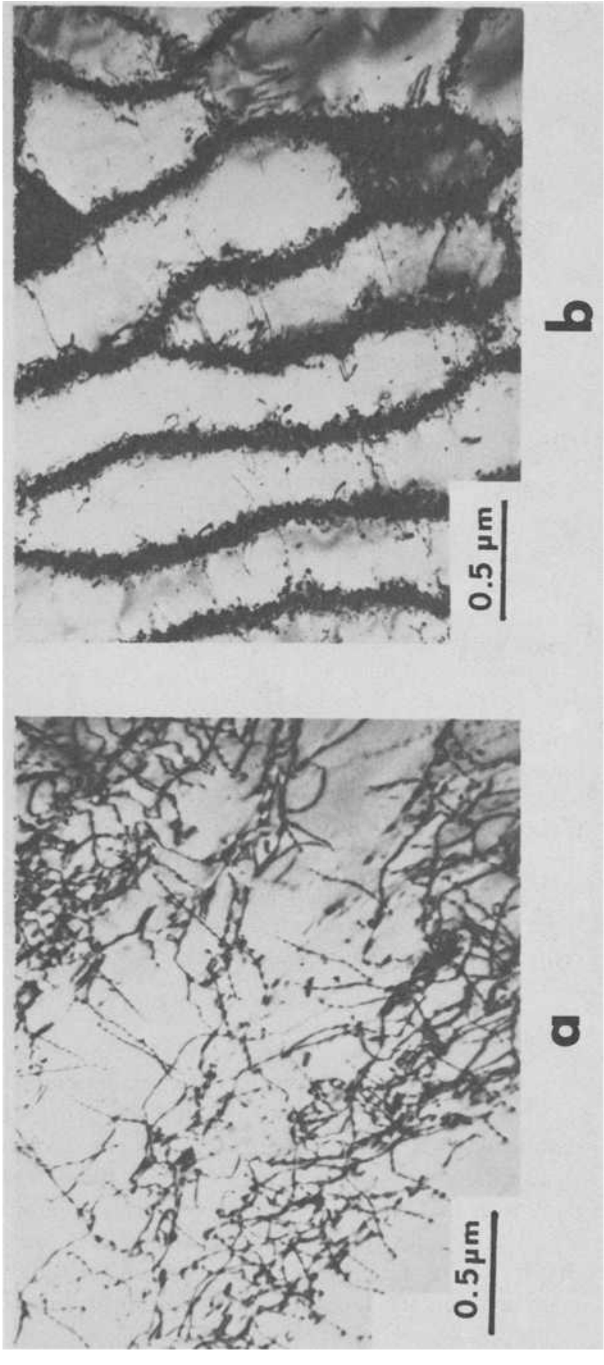
0.5 μm
b
0.5μm
a

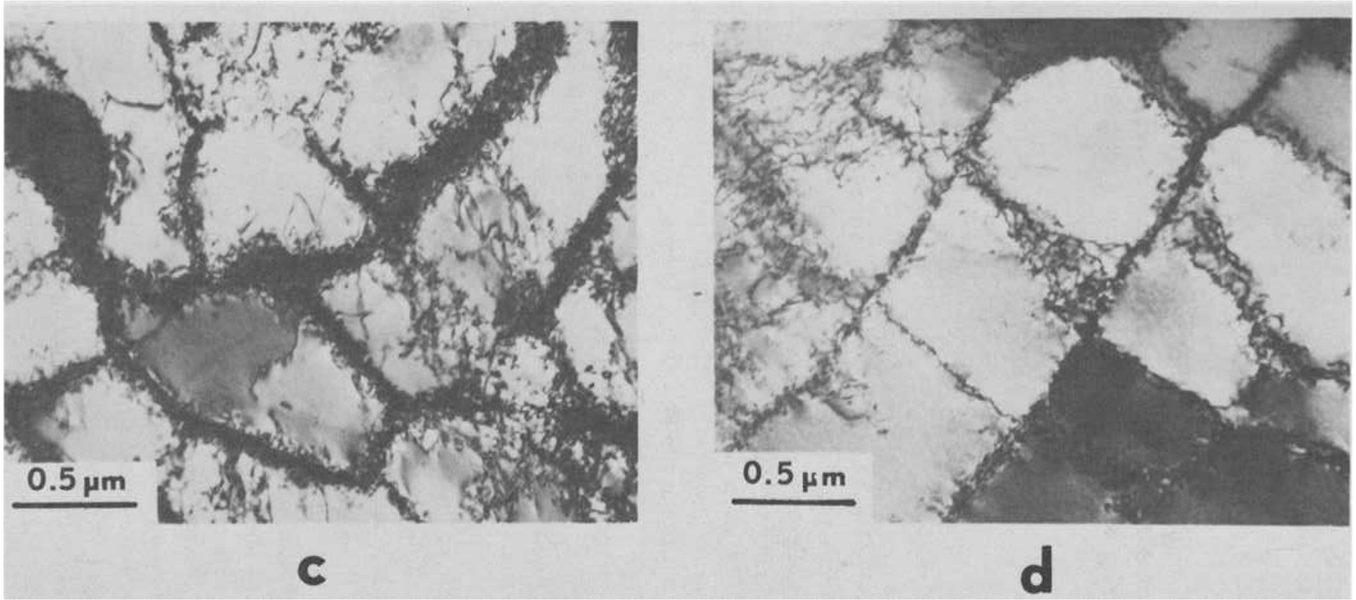

FIG. 2—*Dislocation structures in Type 304 stainless steel deformed at 300°C.* (a) *After loading to 250 MPa;* (b) *after 1000 cycles at a constant stress amplitude of 250 MPa;* (c) *after 1000 cycles at a constant stress amplitude of 250 MPa and 5 percent additional tensile strain;* (d) *after 1000 cycles of cyclic creep.*

tion of the kinematic work-hardening model [*7*]. (Similar models with more detail have been proposed by others [*2,8,9*].) The constitutive law for such a model can be written in the form

$$\dot{\epsilon}_p = \dot{\epsilon}_k(\sigma, T, \sigma_f, p) + \dot{\epsilon}_h(\sigma, T, \sigma_f) \tag{1}$$

where $\dot{\epsilon}_k$ is a kinematic strain rate and $\dot{\epsilon}_h$ is the plastic strain rate that is associated with work hardening. ϵ_h will be called the hardening strain. σ_f is the flow stress parameter, and p is the polarity parameter. The associated evolution laws are of the form

$$dp = f(\sigma, T, \sigma_f, p)\, d\epsilon_k \tag{2}$$

$$d\sigma_f = g(\sigma, T, \sigma_f)\, d\epsilon_h \tag{3}$$

The nature of the function for $\dot{\epsilon}_k$ is such that only a limited amount of strain can be produced in one direction, but the dependence on the polarity parameter p is such that increasing the strain in one direction makes straining in the other direction easier. Because the flow stress only changes with increments of strain $d\epsilon_h$, the kinematic strain can be reversed repeatedly without causing any hardening. The stress dependencies of the two strain rates are such that the kinematic strain always occurs first after a stress reversal, but is exhausted as the stress approaches the flow stress. The hardening strain rate is negligible until the stress approaches the flow stress and then increases rapidly until it accounts for nearly all of the plastic strain rate.

Cyclic hardening leading to a stable hysteresis loop can occur in this model without the need for any additional state parameters. For the initial deformation cycles of an annealed material, the maximum kinematic strain that can be produced is less than the imposed plastic strain amplitude. The stress will therefore reach the flow stress and some hardening strain will occur. This will increase the flow stress and the kinematic strain that can be produced on the next cycle. As hardening increases, the ratio of kinematic strain to hardening strain will increase until the kinematic strain amplitude equals the imposed plastic strain amplitude. Beyond this point, the hardening strain rate is zero and the hysteresis loop reaches its stable shape.

This model requires only one state parameter in addition to the flow stress parameter introduced to explain tensile behavior. The model can account for cyclic hardening leading to a stable hysteresis loop of nonzero width. These are the major features of cyclic deformation.

The model is, however, not sufficient to account for all of the characteristics of cyclic and monotonic straining when more complex histories are introduced. Figure 3 shows how the plastic strain amplitude changes as a function of the number of cycles for Type 304 stainless steel subjected to constant

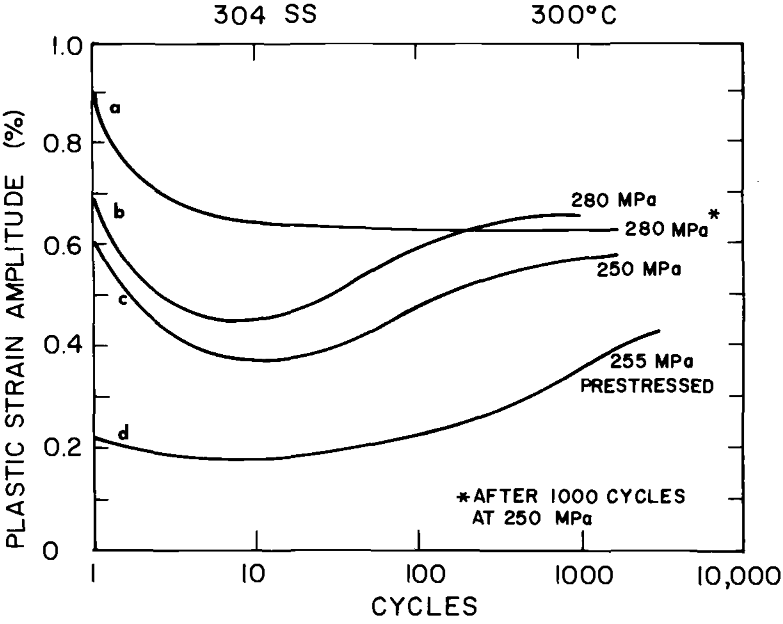

FIG. 3—*Plastic strain amplitude of Type 304 stainless steel during constant stress amplitude cycling at 300°C.* (a) *At a stress amplitude of 280 MPa after 1000 cycles at a stress amplitude of 250 MPa;* (b) *at a stress amplitude of 280 MPa from the annealed state;* (c) *at a stress amplitude of 250 MPa from the annealed state;* (d) *at a stress amplitude of 255 MPa after prestressing to 300 MPa.*

stress amplitude cycling at 300°C after different prior histories. Curves *b* and *c* show the behavior of annealed samples in constant stress amplitude tests. The decreasing amplitude portions of the curves that last for approximately 10 cycles can be ascribed to cyclic hardening that results because not all of the strain in the first few cycles is kinematic. The plastic strain amplitude is decreasing because the flow stress is increasing while the applied stress remains constant [*10*]. If only the flow stress were changing, the strain amplitude would decrease until the entire strain amplitude was kinematic, and then a stable hysteresis loop would be achieved. The rising portions of the plastic strain amplitude curves cannot be accounted for by the simple kinematic strain model. They cannot be accounted for by a reduction in the flow stress, because there is no reason why the material should first exhibit hardening and then softening. The rising portions of the plastic strain amplitude curves must be related to a change in an additional state variable.

Additional evidence that the rising portions of the curves are not associated with any changes in the flow stress parameter was obtained by doing tension tests on samples that had been cycled for 10, 100, or 1000 cycles [*6*].

It was found that the tensile behavior of these samples was identical once the stress exceeded the peak stress of the cycle. From these results, it appears that the maximum kinematic strain that can occur after a stress reversal increases with increasing numbers of cycles. A parameter that describes this strain must be included as a state variable.

Additional evidence that such a parameter is required and that it is independent of the hardening that accounts for the falling portion of the plastic strain amplitude curves is found in curve *a* in Fig. 3. This curve shows how the plastic strain amplitude changes after the cyclic stress amplitude is abruptly changed from 250 to 280 MPa after 1000 cycles. In this case the falling portion of the curve associated with hardening is observed, but the rising portion of the curve is absent. This indicates that the state change associated with the rising portion of the curve cannot be repeated after the small increase in the stress amplitude. The material "remembers" the previous cycles at the lower stress.

The behavior shown in the stepped stress amplitude cyclic test is an example of how some tests can be sensitive to certain state variables while others are not. In this case, a tension test could not be used to distinguish between a sample that had been prestressed once to 280 MPa and a sample cycled for 1000 cycles at 250 MPa and then loaded to 280 MPa. As shown by curve *b* in Fig. 1, loading a sample cycled at 250 to 280 MPa is sufficient to put the tensile behavior back into a portion of the stress strain curve for an annealed sample. The tensile behavior for that sample was then the same as that of a sample that had never been cycled. The differences in the states of the two samples can, on the other hand, be clearly distinguished from their behavior in a cyclic test at 280 MPa, because the plastic strain amplitude for one will follow curve *a* while that for the other will follow curve *b*.

Transmission electron microscopy examination of the microstructures of samples used in these experiments gives a strong indication that the state variable associated with the increasing plastic strain amplitude portions of the plastic strain amplitude versus cycles curves is related to the development of a cellular microstructure. It was shown in previous work [*6*] that between 1 and 1000 cycles, the dislocations are rearranged into increasingly well-defined cells. The extremes of the structure after 1 cycle and after 1000 cycles are shown in Figs. 2*a* and 2*b*. The previous study also showed that a tension test up to a sufficiently high stress to put the tensile behavior back on the annealed material stress-strain curve does not destroy the cells (Fig. 2*c*). This indicates that the tensile behavior is insensitive to the presence of the cells. However, if cycling is resumed at a higher stress (as in the experiment described by curve *a* Fig. 3), the original cell structure is still present, and the plastic strain amplitude change associated with the conversion of the microstructure from random tangles to cells is not observed.

Cyclic Creep

The phenomenon of cyclic creep illustrates an additional difficulty with the simple kinematic hardening model of cyclic behavior proposed in the last section. Figure 4 shows the cyclic creep behavior of Type 304 stainless steel at 300°C [*11*]. In the tests, the samples were subjected to stress cycles with a mean tensile stress. In the figure, R is the ratio of the compression peak stress to the tension peak stress, and the mean strain measures the position of the center of the hysteresis loop. As the figure shows, a rapid elongation of the sample takes place. This elongation is much more rapid than the creep that would occur if the peak tension were maintained statically, so that the cycling is clearly accelerating the net elongation process. Since the rate of net elongation is greatest for R closest to -1, which corresponds to the situation when the mean stress is minimum and the plastic strain amplitude is maximum, it can be concluded that the net elongation of the sample is being driven by the reversible or kinematic strain. The simple model proposed for cyclic deformation does not allow for the kinematic strain to accelerate the hardening strain rate, so it is clear that some additional features will have to be introduced into the model to account for cyclic creep.

If a tension test is performed on a cyclically crept sample, an additional difficulty is discovered. Figure 5 shows the stress-strain curve of a sample

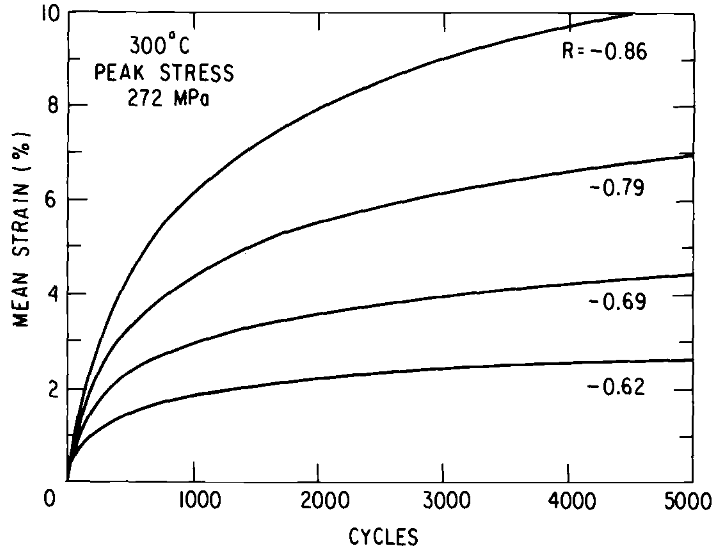

FIG. 4—*Cyclic creep of Type 304 stainless steel at 300°C.* R *is the ratio of the compression peak stress to the tension peak stress. Mean strain is net elongation.*

after 5000 cycles of cyclic creep. The stress-strain curve of an annealed sample is also given for reference. The zero of strain for the sample is kept fixed in the figure so that the post-cyclic tension test begins at the strain accumulated in the cyclic creep portion of the test. It is clear from the tension test that the net strain accumulated during cyclic creep has had a negligible hardening effect. In the model proposed in the last section, the work hardening must be at least as great as that which the net strain would produce in a tension test. The hardening will generally be greater than this because some of the reversed strain was actually hardening strain, but it cannot be less. Clearly some additional feature, such as a softening effect from the kinematic strain, must be introduced into the constitutive equations in order to account for this effect.

One final point must be made about the cyclic creep behavior. The cyclic creep rate decreases as the net strain or number of cycles increases. Since only negligible hardening is found to occur as the result of the cyclic creep strain, this decreasing creep rate is not caused by an increase in the flow stress parameter. A different state variable must be changing along this deformation path [*11*].

Effects of Annealing

Figure 6 shows a series of θ-σ curves for aluminum single crystals from the work of Hasegawa and Kocks [*12*]. If a sample is deformed to a given prestress and then subjected to elevated temperature annealing treatments for varying times, the subsequent stress-strain behavior is as shown. For short annealing times, the recovery only affects the shape of the yield transient. After these anneals, the θ-σ curves rejoin the reference curve of an annealed sample. The shape of the stress strain curve at large strain is still unique, and the behavior can still be described by a single state variable, the flow stress parameter. However, after a critical annealing time, in this case 2 h, the entire shape of the subsequent stress-strain curve is altered as shown by the 30-h anneal curve. Again the lack of uniqueness of the stress-strain curve requires that a second parameter be introduced into the state equations.

The micrographs shown in Fig. 7 again demonstrate the relative insensitivity of the tensile behavior to the details of the dislocation arrangement in the microstructure. (Although the deformation experiments of Hasegawa and Kocks [*12*] were, in fact, done in compression, the stress-strain curve obtained coincided exactly with a tensile stress-strain curve. The term "tensile" will be used here to refer to any large-strain monotonic deformation experiment.) Figure *7a* shows the microstructure after deformation and unloading. The effect of an annealing treatment for the critical period is the formation of sharp subgrain walls from the original more loosely tangled dislocations (Fig. *7b*). This structural change does not have a large effect on the tensile behavior of the material, because this sample follows the reference curve

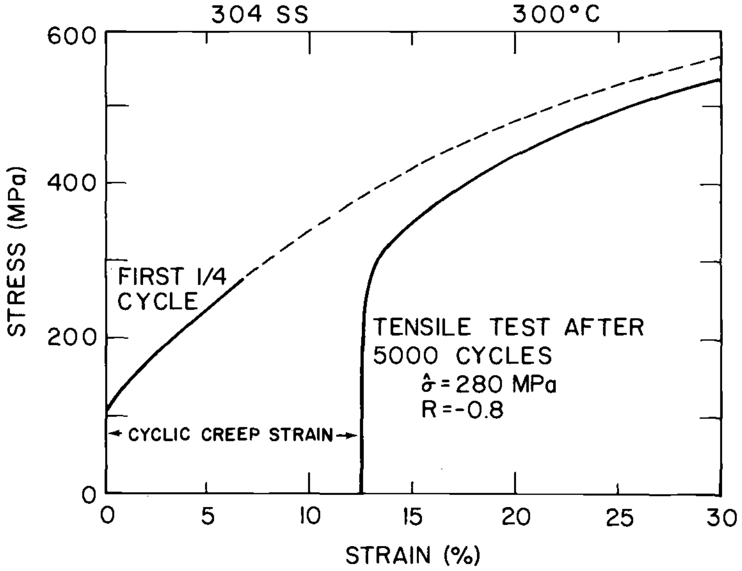

FIG. 5—*Tensile behavior of a specimen of Type 304 stainless steel after 5000 cycles of cyclic creep.*

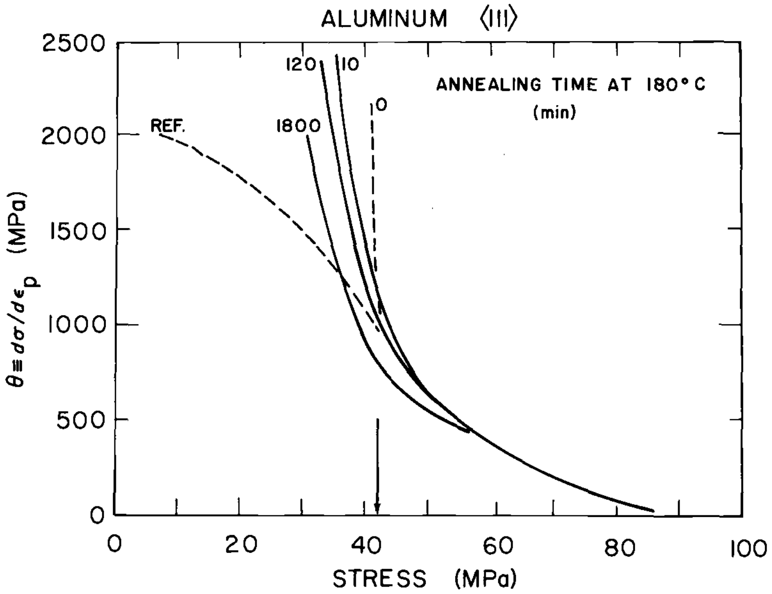

FIG. 6—*Stress-strain behavior, in compression, of aluminum single crystals at room temperature after prestressing and annealing at 180°C.*

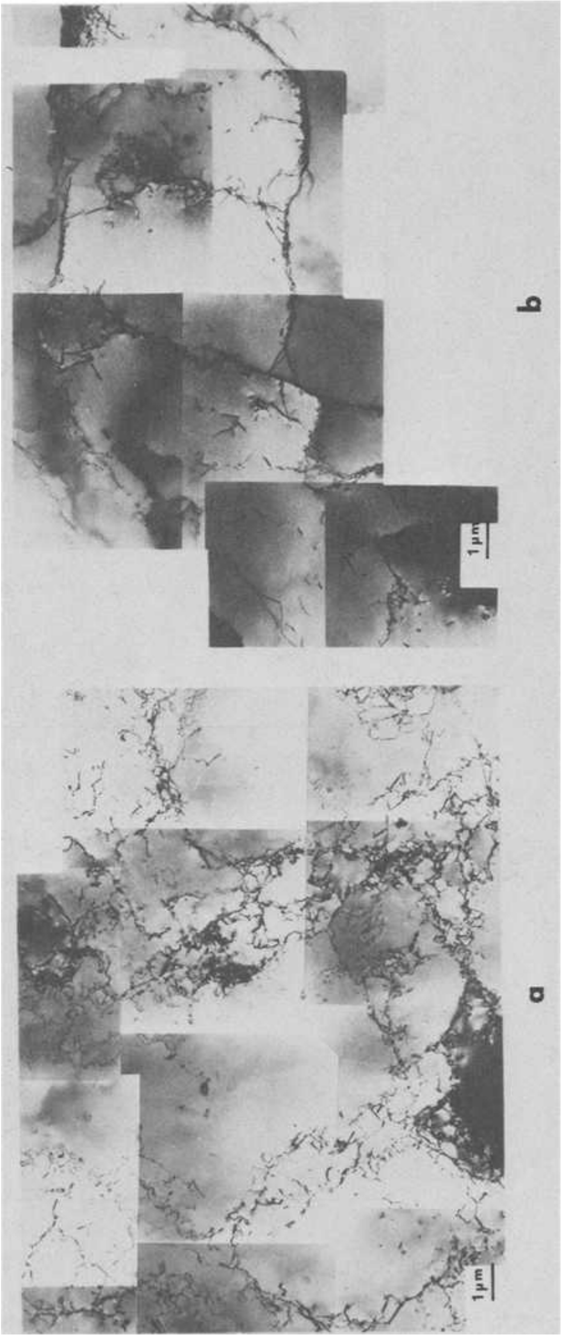
1 µm
b
1 µm
a

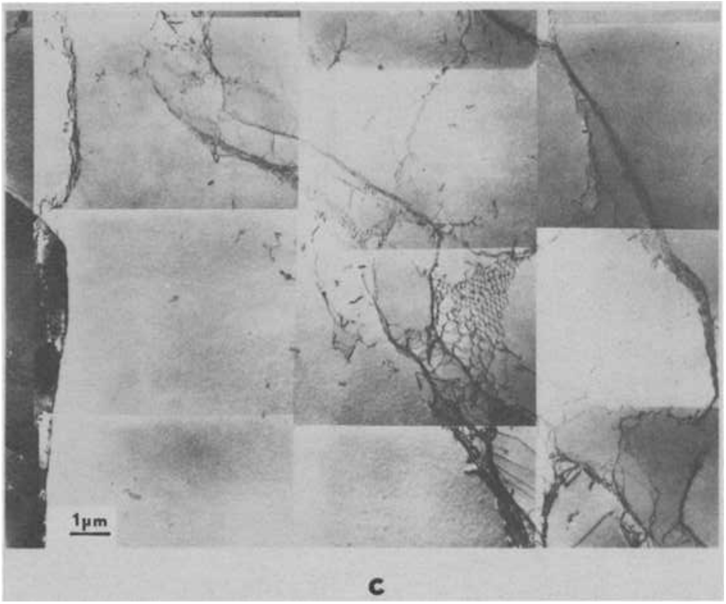

FIG. 7—*Microstructures in deformed and annealed aluminum single crystals.* (a) *After stressing to 42 MPa;* (b) *after stressing to 42 MPa and annealing at 180°C for 2 h;* (c) *after stressing to 42 MPa and annealing at 180°C for 30 h.*

after the prestress level is exceeded. Annealing for more than the critical time results in rapid growth of some subgrains (as shown in Fig. 7c for a 30-h anneal). This structural change is apparently correlated with the change in the subsequent tensile behavior.

The behavior of aluminum single crystals when subjected to multiple deformation and annealing cycles is another example that tensile behavior can be insensitive to important aspects of the mechanical state. As can be seen from the θ-σ curve for the 2-h anneal in Fig. 6, reloading to 42 MPa after the anneal is sufficient to return the stress-strain behavior to the reference curve. This means that so far as tensile behavior is concerned, the material has "lost its memory" of the intermediate anneal. If the state of the material has been returned to what it was before the anneal in every sense, it should behave in the same way as an unannealed sample in any test. Specifically, its annealing behavior should be the same as it was after the previous loading. This would mean that the sample could be repeatedly loaded to 42 MPa and then annealed for 2 h without undergoing any state change. Figure 8 shows that this is not the actual behavior observed. The curve in Fig. 8 labeled 180°C, 2 h shows the reloading behavior after a single anneal. It returns to the reference curve at 42 MPa as was shown before. The curve labeled 2 × 180°C, 2 h shows the behavior after the sample has been annealed for an additional 2 h

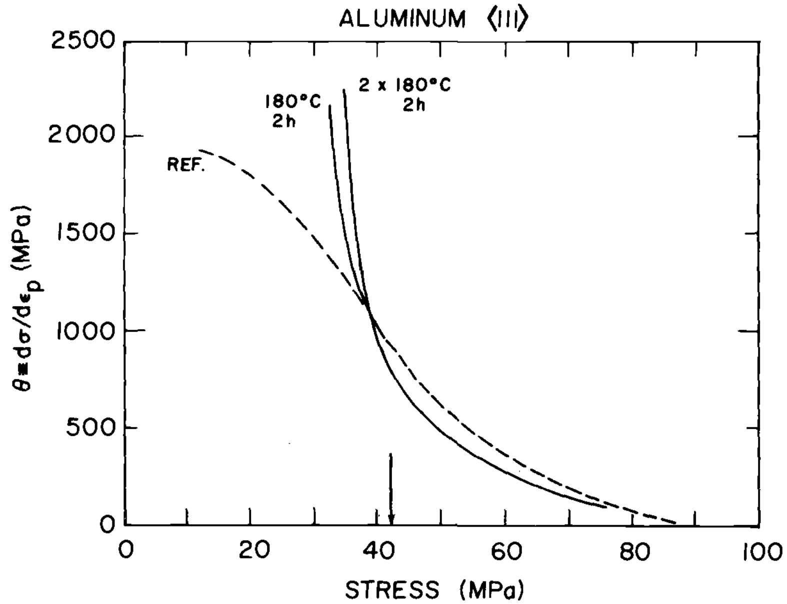

FIG. 8—*Stress-strain behavior, in compression, of aluminum single crystals.* (a) *After prestressing to 42 MPa and annealing at 180°C for 2 h;* (b) *after two cycles of stressing and annealing.*

and then reloaded. Except in the yield transient region, the behavior is clearly characteristic of annealing times longer than 2 h. The two 2-h annealing treatments have acted cumulatively. The tension test is again inadequate to distinguish all differences in state. Two samples that have identical tensile behavior may not anneal in the same way.

Microstructural examination of annealed and reloaded samples, as shown in the sequence in Fig. 9, indicates that the microstructure always retains information about prior annealing treatments even after reloading. As shown in Fig. 9*b*, annealing for 2 h after loading to 42 MPa causes the dislocation structure to become refined into subgrain boundaries. Reloading the sample after annealing does not disturb the subgrain boundaries (Fig. 9*c*). It only increases the density of dislocations that are not incorporated into the boundaries. These collect near the subgrain boundaries. This means that the boundaries are altering the manner in which the dislocations are stored during work hardening, but this does not appear to affect the shape of the stress-strain curve. Repeated annealing treatments do not cause this process to change noticeably. Figure 10 shows the microstructure in a sample after six load-anneal cycles. In Fig. 10*a* the structure is shown as it is after the final anneal; in Fig. 10*b* as it is after an additional reloading. The persistence of the subgrain boundaries once formed is evident. The fact that reloading causes only a minor change in this structure is consistent with the observation that the anneals act cumulatively. The effect of six load-anneal cycles on subsequent large-strain tensile behavior is roughly equivalent to a single loading followed by a 12-h anneal.

Summary

1. The stress-strain curve of a material was shown not to be unique. Therefore at least two state parameters are required to describe tensile behavior after an arbitrary prior history. However, the tensile behavior was shown to be relatively insensitive to differences in microstructure and differences in state that clearly change cyclic and annealing behavior.

2. Description of cyclic deformation at constant amplitude was shown to require at least two parameters in addition to the two required to describe tensile behavior. One is a rather trivial polarity factor that describes the current position on the hysteresis loop. A suitable mechanical measure of the second parameter has not been identified, but it describes the cellularity of the microstructure in the structural sense.

3. Cyclic creep is evidence that a simple limited-strain kinematic model of cyclic behavior is inadequate. A state parameter other than the flow stress and the two cyclic parameters will be needed to describe cyclic creep. It has not been shown that this additional parameter is distinct from the second parameter needed describe tensile behavior [*11*].

4. Sufficient recovery annealing was shown to alter the shape of the subse-

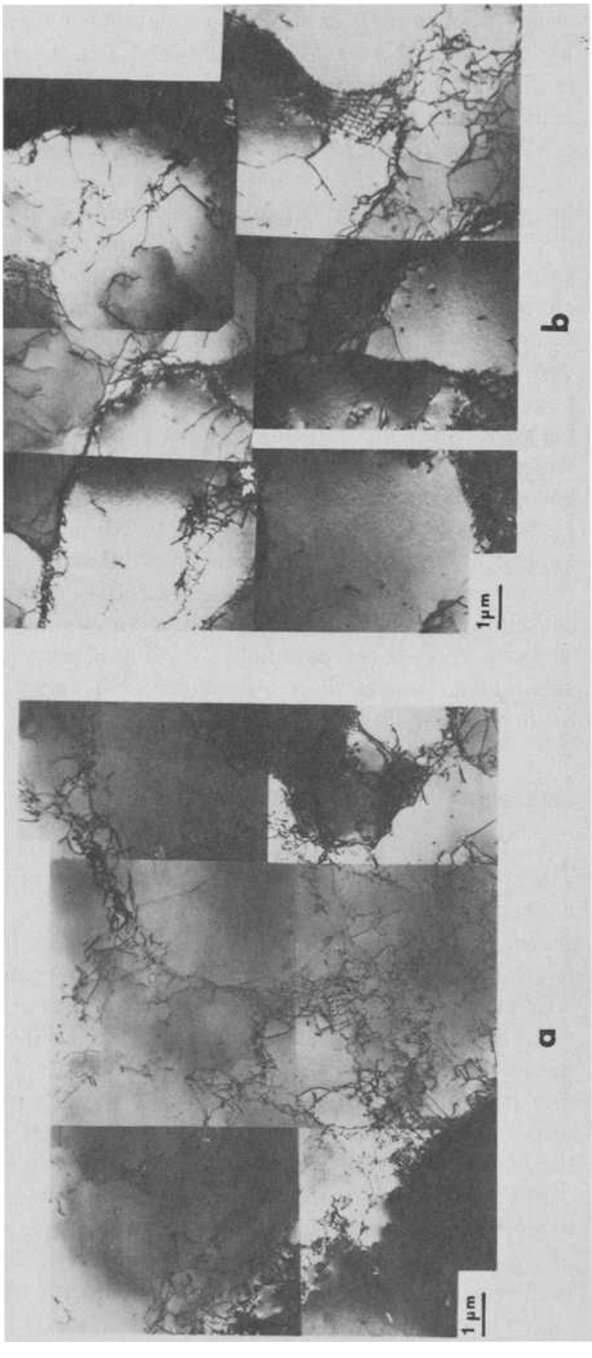
1 μm
b
1 μm
a

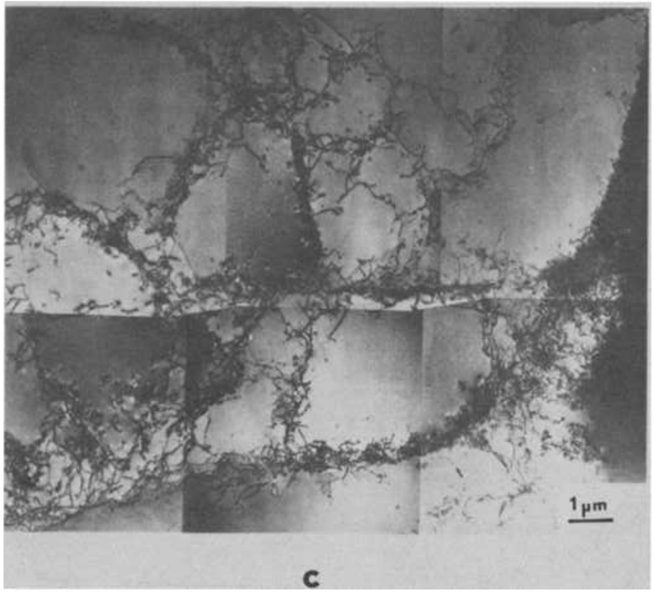

FIG. 9—*Microstructures in deformed and annealed aluminum single crystals.* (a) *After stressing to 42 MPa;* (b) *after stressing and annealing at 180°C for 2 h;* (c) *after stressing, annealing, and reloading to 42 MPa.*

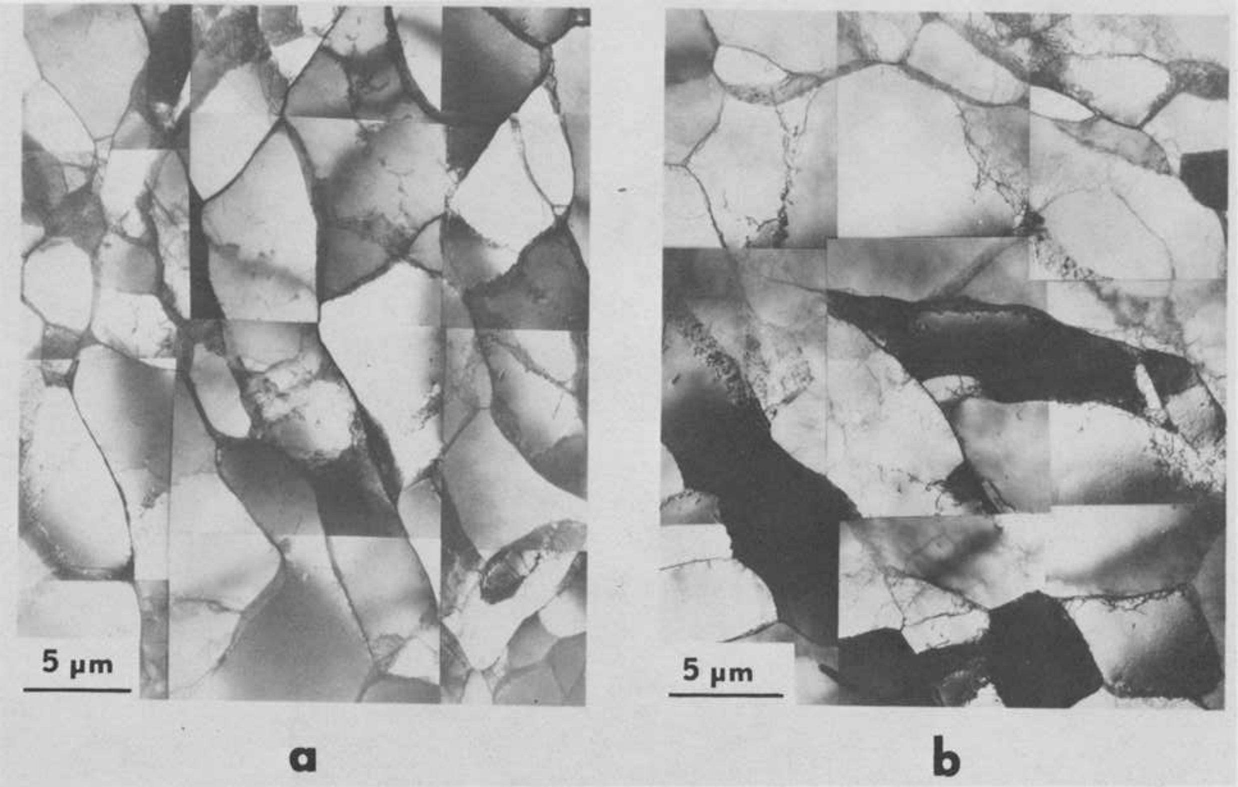

FIG. 10—*Microstructures of deformed and annealed aluminum single crystals.* (a) *After six cycles of stressing to 42 MPa and annealing for 2 h at 180°C;* (b) *after six cycles of stressing and annealing with an additional reloading.*

quent stress-strain curve. However, it was shown that the tension test is not a sensitive measure of the changes brought about by annealing.

5. The relationship between microstructure and mechanical properties has been shown to be complex and often subtle. Obvious differences in microstructure are often found to have small effects on mechanical behavior, while significantly different behavior is often observed for structures that look similar [*13,14*].

Acknowledgments

This work was supported by the U.S. Department of Energy.

References

[*1*] Hart, E. W., *Acta Metallurgica,* Vol. 18, 1970, pp. 599-610.

[*2*] Hart, E. W., *Journal of Engineering Materials and Technology,* Vol. 98, 1976, pp. 97-105.

[*3*] Kocks, U. F. in *Constitutive Equations in Plasticity,* A. S. Argon, Ed., MIT Press, Cambridge, Mass., 1975, Chapter 3, pp. 81-115.

[*4*] Miller, A., *Journal of Engineering Materials and Technology,* Vol. 98, 1976, pp. 97-105.

[*5*] Miller, A., *Journal of Engineering Materials and Technology,* Vol. 98, 1976, pp. 106-113.

[*6*] Turner, A. P. L., *Metallurgical Transactions A,* Vol. 10A, 1979, pp. 225-234.

[*7*] Prager, W. in *Proceedings* Institute of Mechanical Engineers, London, Vol. 169, 1955, p. 41.

[*8*] Kettunen, P. O. and Tiainen, T., *Physica Fennica,* Vol. 9, 1974, pp. 173-183.

[*9*] Jackson, M. S., Cho, C. W., Alexopoulos, P., and Li, C.-Y., "A Phenomenological Model for Transient Deformation Based on State Variables I: Theory," submitted to *Journal of Engineering Materials and Technology.*

[*10*] Kettunen, P. O. and Kocks, U. F., *Czechoslovak Journal of Physics,* Vol. B19, 1969, pp. 299-314.

[*11*] Turner, A. P. L. and Martin, T. J., *Metallurgical Transactions A,* Vol. 11A, 1980, pp. 475-481.

[*12*] Hasegawa, T. and Kocks, U. F., *Acta Metallurgica,* Vol. 27, 1979, pp. 1705-1716.

[*13*] Alden, T. H., *Metallurgical Transactions,* Vol. 4, 1973. pp. 1047-1057.

[*14*] Alden, T. H., *Metallurgical Transactions A,* Vol. 6A, 1975, pp. 1597-1605.

A. Arieli,[1] *H. C. Heard,*[2] *and A. K. Mukherjee*[1]

Deformation Modeling in Sodium Chloride at Intermediate and Elevated Temperatures

---

REFERENCE: Arieli, A., Heard, H. C., and Mukherjee, A. K., "**Deformation Modeling in Sodium Chloride at Intermediate and Elevated Temperatures,**" *Mechanical Testing for Deformation Model Development, ASTM STP 765,* R. W. Rohde and J. C. Swearengen, Eds., 1982, pp. 342-365.

ABSTRACT: The flow stress dependence on temperature and strain rate of annealed, isotropic polycrystalline NaCl has been determined at temperatures of 296 to 673 K (0.28 to 0.63 T_M) and strain rates of 10^{-1} to 10^{-8} s^{-1}.

At elevated temperatures ($T > \sim 0.44\ T_M$) and relatively low stress the Na^+ diffusion-controlled climb of dislocations was found to be the rate-controlling deformation mechanism, and the experimental data could be fitted by a power-law function. In the same range of temperatures, at high stresses the deformation process was controlled by dislocation climb creep due to Cl^- ion diffusion. At intermediate temperatures and low strain rates and at elevated temperatures and high strain rates the deformation was rate-controlled by the lattice resistance to the dislocation glide motion (Peierls mechanism).

The constitutive equations for each deformation mechanism as well as that for the transition from one deformation mechanism to another were developed in terms of strain rate, temperature, and stress. The implications of the transition from one deformation mechanism to another over a wide range of temperatures on the deformation modeling for this material are discussed. The application of such analysis to understand and predict the rheological behavior of halite aggregates in nature in buried salt deposits is considered.

KEY WORDS: NaCl, stress-strain rate-temperature, deformation modeling, creep mechanism, rheological prediction in salt structure, deformation mechanism diagram

Plastic deformation of crystalline solids occurs by the same basic microscopic mechanisms, regardless of other details such as crystal structure or bond type [*1*].[3] In this respect, the nonmetallic crystalline solids are in many

---

[1] Division of Materials Science and Engineering, Department of Mechanical Engineering, University of California, Davis, Calif. 95616.

[2] Lawrence Livermore Laboratory, University of California, Livermore, Calif. 94550.

[3] The italic numbers in brackets refer to the list of references appended to this paper.

ways rather similar to the metals, although important differences occur because of the greater structural and chemical complexity of nonmetals.

The need for understanding the plastic deformation behavior of nonmetallic crystalline materials stems from their increased utilization in nuclear reactors, gas turbines, and electronic components, to name only a few. Furthermore, the earth's crust and mantle is also composed of other nonmetallic crystalline materials which move slowly by plastic deformation. Hence the interest for plastic deformation of these materials from a geological point of view.

Sodium chloride can be regarded as a prototype of the simple, six-fold coordination ionic compounds. At normal conditions it occurs in the face-centered-cubic (FCC) structure. This phase has a wide temperature and pressure stability that makes it suitable for basic studies of the plastic deformation behavior in such materials. Furthermore, recent proposals to use massive salt structures for storage of hydrocarbons and radioactive waste products requires improved knowledge of their plastic deformation behavior in order to facilitate an accurate prediction of their rheological properties *in situ*. Recently, the flow behavior of impure naturally occurring bedded and domal salt from New Mexico, Louisiana, and West Germany have been investigated by several workers [*2-5*] and certain material parameters deduced.

The deformation behavior of pure NaCl over large ranges of strain rate and temperature was investigated in some detail by Verrall et al [*1*], and the elevated temperature creep properties were investigated earlier by Burke [*6*] and by Langdon and Mohamed [*7*]. The latter investigations basically observed power-law creep behavior and, in addition, Burke noted a change in the activation energy of creep with change in temperature. He attributed the higher activation energy above 530°C to that for bulk diffusion of Cl^- ions and the lower activation energy below that temperature to that for core diffusion. Verrall et al [*1*] suggested that at low-to-intermediate temperatures, the strain rate is controlled by thermally activated motion of dislocations overcoming the Peierls barrier. With increase in temperature, the rate-controlling mechanism switches to that for obstacle-limited glide. Finally, at temperatures around 0.4 of the melting point (the exact temperature depends upon the strain rate), other creep mechanisms (power law, core-diffusion controlled, diffusional-creep controlled by boundary diffusion, etc.) become dominant.

The purpose of this paper is to present an analysis of plastic deformation behavior of high-purity polycrystalline NaCl over a wide range of stresses, strain rates, and temperatures, using previously published data [*8*] as well as new data generated during this investigation.

Experimental Procedure and Test Results

All stress-strain-time-temperature data forming the basis for this study were determined using a deformation apparatus identical to that employed by Carter and Heard [*9*] and Heard [*8*] for deformation of halite single crystals and polycrystalline aggregates. Briefly, the apparatus consists of an externally heated pressure vessel fitted with an internal force transducer to measure axial loads applied to a right circular cylindrical sample. Wide range of constant strain rates at the specimen was accomplished by a synchronous motor driving a variable-speed transmission coupled to the loading piston through an efficient ball screw assembly. The CO_2 confining pressures were measured with a manganin coil and maintained at 200×10^6 Pa during all tests, the accuracies being estimated at ± 0.5 percent. Temperatures were measured with chromel-alumel thermocouples, and gradients along the 4 to 5 cm long samples were <2 K at the highest test temperature (673 K); accuracies are estimated at ~ 1 K. After calibration, the signal from the internal force gage corresponded to an accuracy of 0.1 to 0.2×10^6 Pa axial stress on the 2 to 2.5 cm diameter test samples.

The true stress-strain curves were derived by calculating the applied stress (total axial stress minus the confining pressure) from recorded values of force and computed cross-sectional areas of the sample after correcting for the force borne by the 0.25-mm lead or aluminum jacket and assuming that all deformation was homogeneous, with no volume change. The resulting values were plotted against axial strain calculated from piston displacements (corrected for apparatus distortion) and initial sample length.

The test cylinder billets were formed by warm pressing of Baker reagent grade NaCl at 1.7×10^8 Pa, 400 K for 2 h. These billets were then machined to final dimensions and annealed 14 h at 770 K and 2×10^8 Pa pressure. This treatment yielded homogeneous test cylinders having an interlocking mosaic of equant polygonal crystals with an average size of 2 to 3 mm and a range of 0.5 to 5 mm. Final densities ranged from about 99.5 to 99.7 percent of the theoretical value.

Most data analyzed here were taken from Heard [*8*]. Subsequent to that work it was found that the 573 K results taken at $\dot{\epsilon}$ of 10^{-2} to 10^{-8} s^{-1} were in error due to use of an aluminum alloy (not pure aluminum) in assessing the jacket correction for calculation of the NaCl σ-ϵ curve. The flow behavior of pure aluminum at those conditions has been measured, and the NaCl data have been corrected and are reported here in Table 1. Additional σ-ϵ tests, primarily at the lower temperatures, are also reported in Table 1.

Analysis

Stress-Strain Behavior

Typical differential stress-strain curves are shown in Fig. 1 for various test temperatures. Figure 1 indicates that there are two types of stress-strain behavior, depending upon the test temperature: (*1*) at temperatures below

TABLE 1—*Deformation tests on annealed polycrystalline halite at 200 × 10^6 Pa pressure.*

Experiment	Temperature, K	Strain Rate, s^{-1}	Differential Stress at Selected Strains, Pa × 10^6			
			4 %	6 %	8 %	10 %
1010[a]	338	1.50×10^{-3}	40.5	44.7	47.5	49.3
1012[a]	338	1.52×10^{-4}	40.9	43.5	45.7	46.5
1016[a]	338	1.48×10^{-5}	35.7	37.4	38.8	40.0
1011[a]	423	1.51×10^{-3}	25.0	27.2	28.7	29.8
1013[a]	423	1.52×10^{-4}	22.9	25.0	26.6	27.7
1017[a]	423	1.53×10^{-5}	18.0	19.7	20.9	21.7
828[b]	573	1.82×10^{-2}	11.5	13.1	14.3	15.3
783[b]	573	1.15×10^{-3}	10.2	11.4	12.2	12.7
814[b]	573	1.54×10^{-4}	7.9	8.8	9.3	9.5
779[a]	573	1.15×10^{-4}	7.1	7.7	8.1	8.3
858[b]	573	1.18×10^{-4}	6.6	7.3	7.8	8.1
782[b]	573	1.18×10^{-5}	5.2	5.7	6.1	6.2
787[b]	573	1.18×10^{-6}	3.6	3.7	3.8	3.9
806[b,c]	573	1.15×10^{-7}	2.7	(2.8)	(2.9)	(3.0)
840[b,c]	573	1.15×10^{-8}	2.4	(2.4)	(2.4)	(2.4)

[a] New data not reported in Ref *8*.

[b] Data from Ref *8*, but recalculated to include correct jacket strength.

[c] Parentheses indicate extrapolated values.

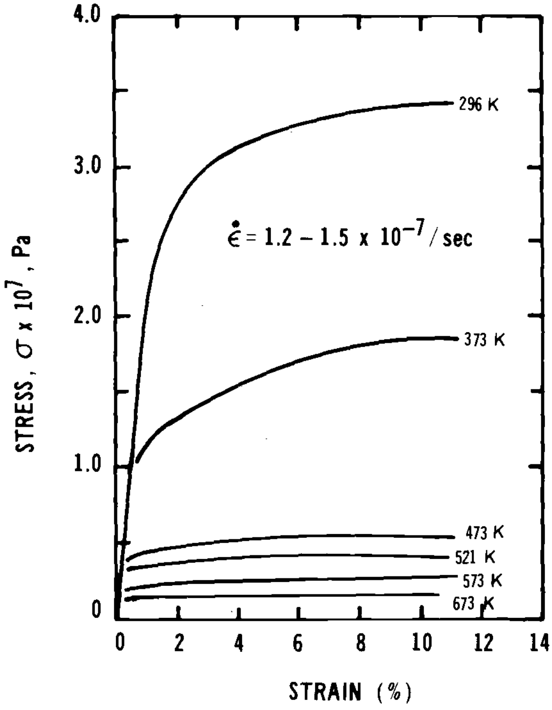

FIG. 1—*Stress-strain curves for polycrystalline NaCl at intermediate and elevated temperatures.*

473 K, once the plastic flow regime is attained there is substantial strain hardening, the steady-state plastic flow being reached at strains of about 8 to 10 percent; (*2*) at 473 K and above, no strain hardening is discernible, the steady-state plastic flow taking place almost immediately after the plastic flow regime is reached.

*Deformation at Low Temperatures (*T *< 473 K)*

At temperatures below $\sim 0.4\ T_M$ the platic deformation of crystalline materials occurs by the dislocation glide motion, and the plastic strain rate is given by

$$\dot{\epsilon} = \rho b \bar{v} \quad (1)$$

where $\dot{\epsilon}$ is true plastic strain rate, ρ is density of mobile dislocations, b is Burger's vector, and $\bar{v}$ is average velocity of dislocations. If the crystal and the motion of the dislocations past obstacles is thermally activated, then

$$\dot{\epsilon} = \dot{\epsilon}_o \exp - \left(\frac{\Delta G}{kT} \right) \tag{2}$$

where $\dot{\epsilon}_o$ is a parameter depending upon the type and nature of the obstacles, their distribution in the material, and the specific deformation mechanism; G is the Gibbs free energy of activation, and kT has the usual meaning of Boltzmann's constant times the absolute temperature. The exponential term arises from the fact that the velocity of dislocations will be limited by the probability that a dislocation will successfully overcome an obstacle under the externally applied stress when thermally activated. Equation 2 is the general expression for the low-temperature, thermally activated plastic flow of crystalline solids, and its applicability is independent of any specific deformation mechanism.

In order to evaluate the experimental results obtained in a range of strain rates and temperatures where a thermally activated deformation mechanism is suspected to be operative, the following quantities can be derived directly from the principles of dislocation dynamics [*10*]:

$$A = kT \left. \frac{\partial \ell\text{n}\, \dot{\epsilon}}{\partial \sigma} \right|_T \tag{3}$$

$$Q = -TA \left. \frac{\partial \sigma}{\partial T} \right|_{\dot{\epsilon}} \tag{4}$$

where A is activation area and Q is activation energy for deformation. The activation area has the dimensions of a volume only because we consider the externally applied stress rather than the force. This activation area and the activation energy for deformation are related to the Gibb's free energy of activation; that is,

$$\Delta G = Q - A\sigma \tag{5}$$

and by introducing Eq 5 into Eq 2 one obtains

$$\dot{\epsilon} = \dot{\epsilon}_o \exp \left[- \frac{Q + A\sigma}{kT} \right] \tag{6}$$

The variation of $\ell\text{n}\, \dot{\epsilon}$ with σ at $\epsilon = 10$ percent for temperatures between 296 and 423 K is shown in Fig. 2. The slope of the lines and, hence, the activation area increase with increasing test temperature. Figure 3 illustrates the variation of the flow stress at $\epsilon = 10$ percent with test temperatures for three strain rates. The flow stress decreases continuously with increasing test

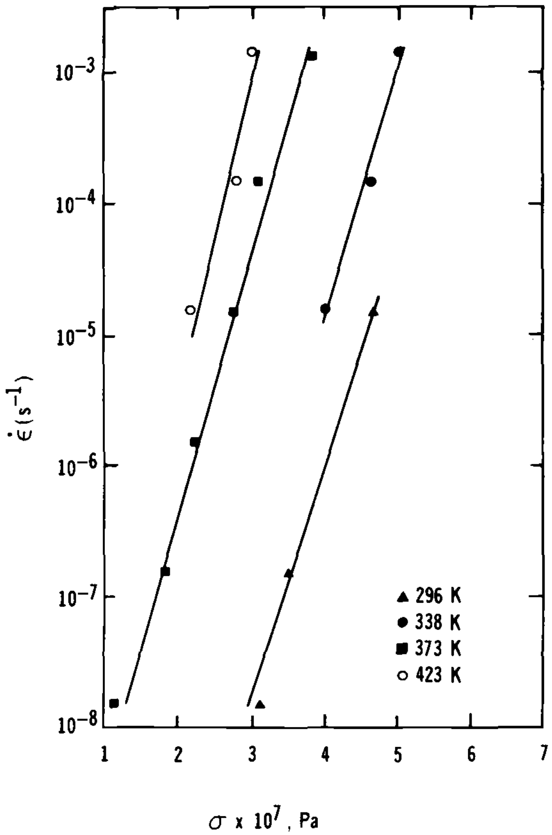

FIG. 2—*Strain rate versus flow stress (at 10 percent strain) at intermediate temperatures.*

temperature, the shape of the curves depending upon the actual temperature range. At low temperature the stress is inversely and linearly dependent on temperatures, whereas at high temperature an inverse exponential dependence is observed. The temperature where the transition from inverse linear to inverse exponential dependence occurs depends strongly on strain rate.[4]

Deformation at High Temperatures (T $\geq$ 473 K)

When crystalline solids are deformed at temperatures above ~0.4 T_M the deformation is usually diffusion controlled. When deformation is diffusion

---

[4] Since steady state has not been reached in our experiments at temperatures below 423 K (that is, σ increases with increasing ϵ), the activation energy Q will be slightly dependent on strain.

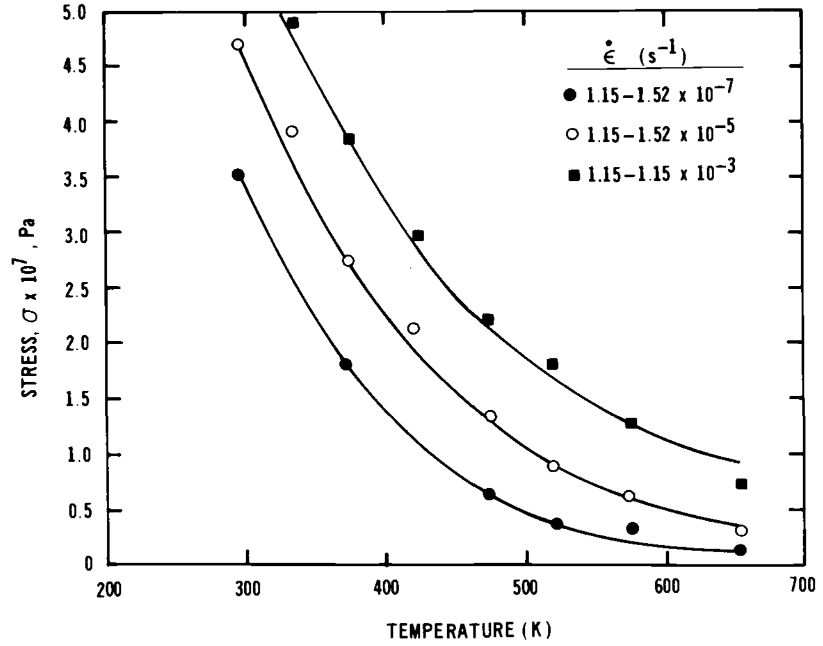

FIG. 3—*Variation of flow stress with temperature.*

controlled, the applied stress, σ, can be related to the steady-state strain-rate, $\dot{\epsilon}$, by the dimensionless expression

$$\frac{\dot{\epsilon} k T}{D G b} = B \left(\frac{\sigma}{G} \right)^n \tag{7}$$

where D = diffusivity = $D_o \exp(-Q_d/RT)$ [D_o is the diffusion parameter, Q_d is activation energy for diffusion, and R is the gas constant (equal to the product of the Boltzmann Constant k and Avogadro's number N_o)], G is temperature-compensated shear modulus, B is a dimensionless parameter that includes the effects of microstructure, and n is a stress sensitivity index. The expression given by Eq 7 has a general applicability to high-temperature deformation in a similar fashion to Eqs 2 and 6 for low-temperature deformation and is independent of any specific diffusion-controlled deformation mechanism. The quantities which can be determined from Eq 7 are

$$n = \left. \frac{\partial \ln \dot{\epsilon}}{\partial \ln \sigma} \right|_T \tag{8}$$

and

$$Q_d = -R \left. \frac{\partial \ell n \, [\sigma^{-n} (G)^{n-1} T]}{(1/T)} \right|_{\dot{\epsilon}} \qquad (9)$$

Figure 4 is a double logarithmic plot of $\dot{\epsilon}$ versus σ for temperatures between 473 and 673 K. It is evident from Fig. 4 that two stress-strain rate regions can be defined, one at low applied stresses yielding a stress sensitivity index, $n = 5.3$, and another at high applied stresses with $n = 11.3$.[5] The transition between these two regions is strongly dependent on the test temperature. The transition is shown in Fig. 4 by the broken line. The activation energy for deformation, Q, was determined for each of these regions (Figs. 5 and 6) yielding Q-values of 102.1 kJ/mol and 166.6 kJ/mol for the low stress regions and high stress regions, respectively.[6]

In an earlier work [*8*], the data shown here in Fig. 4 at low stress were fitted to an equation similar to Eq 7. Those results yielded $n = 5.6$, $Q = 98.2$ kJ/mol when calculated at 10 percent ϵ and only about a 10 percent increase in either quantity when recalculated at 4 percent ϵ. More recently, it was discovered that due to a calibration error at 573 K, $\dot{\epsilon} = 10^{-3}$ to 10^{-8} s^{-1}, a portion of the data reported in Table 1 of Ref *8* were incorrect. When the corrected 573 K stress values were used along with the remaining high-temperature data in Ref *8* at 10 percent ϵ, n becomes 5.8 and $Q = 96.1$ kJ/mol. Closely similar values are found at lower strains. In addition, it was also found [*8*] that virtually identical results (including standard deviations) could be obtained from Eq 7 as compared to a simplified form which deletes the term $T\,G^{(n-1)}$ in Eq 9. The difference between $n = 5.6$, $Q = 98.2$ kJ/mol [*8*] and $n = 5.3$, $Q = 102.1$ kJ/mol from Eqs 8 and 9 for the low-stress region here is due to the method of calculation and is not regarded as significant.

Discussion

The experimental results reported in the previous section indicate that if one constructs a deformation space having stress, strain rate, and temperature as axes, three different mechanism regions will be obtained: (*1*) at low temperatures the deformation occurs by thermally activated dislocation motion; in our investigation we did not observe a second thermally activated

---

[5] In the high-stress region a constant stress was not achieved at the highest strain investigated (~10 percent). Thus n could be expected to change with ϵ. Comparison between the calculated n at 10 percent ϵ with that at 6 percent ϵ showed only a 7 percent increase with this increment of ϵ.

[6] Efforts to correlate the data obtained at high temperatures and high stresses with an exponential expression in stress yielded a somewhat poorer fit when compared with the power law with $n = 11.3$. In addition, the exponential expression led to an unreasonably high dislocation density value.

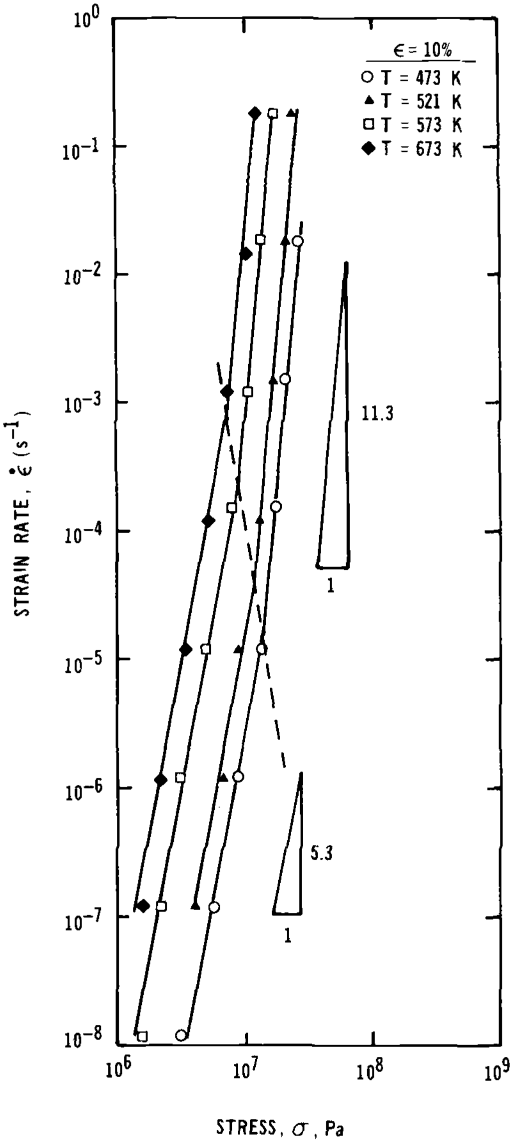

FIG. 4—*Log strain rate versus log stress at elevated temperatures.*

mechanism (for example, obstacle-limited flow postulated by Verrall et al [*1*]); (*2*) at high temperature and low stresses the deformation is diffusion controlled and characterized by $n = 5.3$ and $Q = 102.1$ kJ/mol; and (*3*) at high temperature and high stress, still another diffusion-controlled deforma-

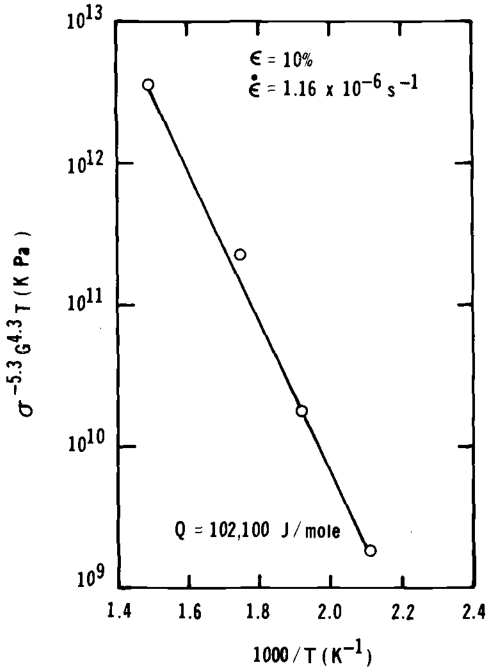

FIG. 5—*Activation energy for creep in the low-stress region.*

tion mechanism is operative, characterized by $n = 11.3$ and $Q = 166.6$ kJ/mol. Henceforth it seems appropriate to discuss each of these regions separately.

Deformation at Low Temperatures

The Rate Equation—Figure 7 shows a plot of log $\dot{\epsilon}$ versus log $[1/2.3 \exp(-Q + A\sigma/kT)]$. All the experimental data fall onto a straight line with a slope equal to 2 and an intercept, $\dot{\epsilon}_o$, equal to $9.2 \times 10^7\ s^{-1}$.

Therefore the rate equation for the deformation at low temperature can be written as

$$\dot{\epsilon} = 9.2 \times 10^7 \left[\exp\left(-\frac{Q + A\sigma}{kT}\right)\right]^2 \qquad (10)$$

The activation area is independent of strain (Fig. 8) and only depends on temperature; this observation is important when the identification of the specific deformation mechanism is attempted, as will be shown in the next section. The activation energy for deformation varies with both strain rate

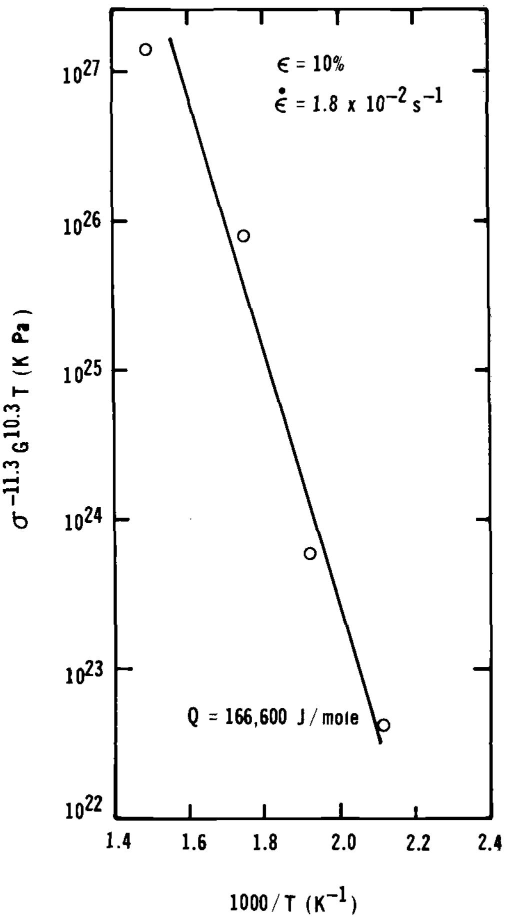

FIG. 6—*Activation energy for creep in the high-stress region.*

and temperature (Fig. 9), the dependence on temperature at constant strain rate being linear. Again, the linear dependence of the activation energy on the test temperature is important in the effort to identify the deformation mechanism.

Identification of the Deformation Mechanism—As was stated before, at low temperatures and nominal strain rates (approximately between 10^{-8} and 10^{-1} s^{-1}), plastic flow in crystalline materials occurs by one or more thermally activated deformation mechanisms. Since the probability for activation is exp $(-\Delta G/kT)$, only those mechanisms that have low activation energies (usually less than the activation energy for self-diffusion) can be activated at low temperatures. In parallel processes the activation energy for rate-

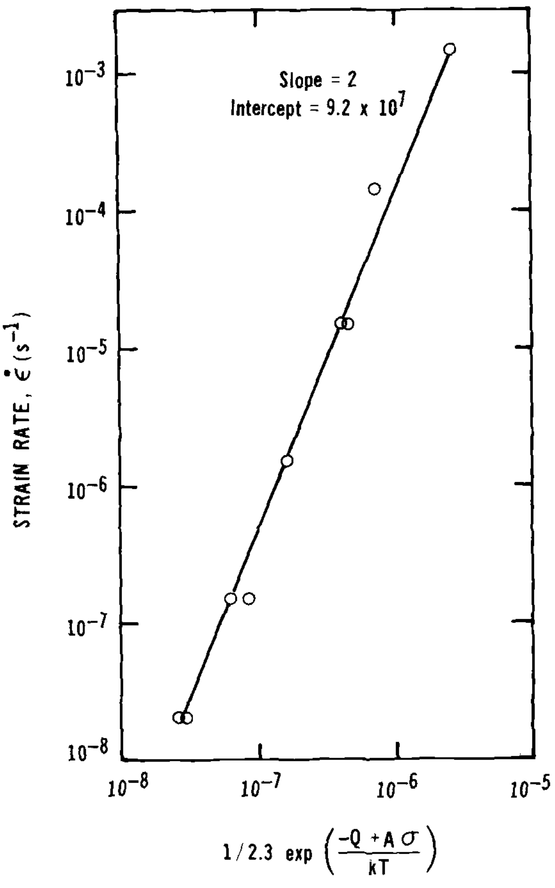

FIG. 7—*Normalized plot for stress-temperature-strain rate in the low-temperature region.*

controlling thermally activated dislocation motion is expected to increase with an increase in temperature. At constant temperature, the activation energy will decrease with an increase in strain rate (or alternatively with increase in stress); *vide* Fig. 9, low temperature region. Since the activation area was found to be independent of stress at constant temperature, it is evident (*vide* Eq 5) that the free energy of activation increases with an increase in temperature at constant stress and decreases as the stress is increased at constant temperature.

The two major types of obstacles over which dislocations can be thermally activated are linear and localized. A linear obstacle is usually the intrinsic lattice resistance to the dislocation motion, whereas localized obstacles are other dislocations, solute-atoms, Guinier-Preston zones, etc. The experimental results obtained in this investigation and earlier work [*8*] clearly indicate

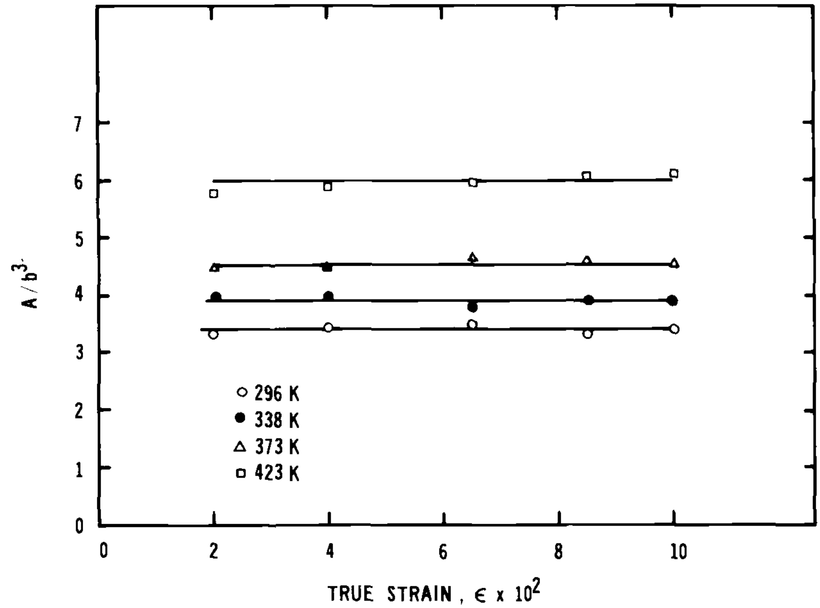

FIG. 8—*Activation area versus true strain in the low-temperature region.*

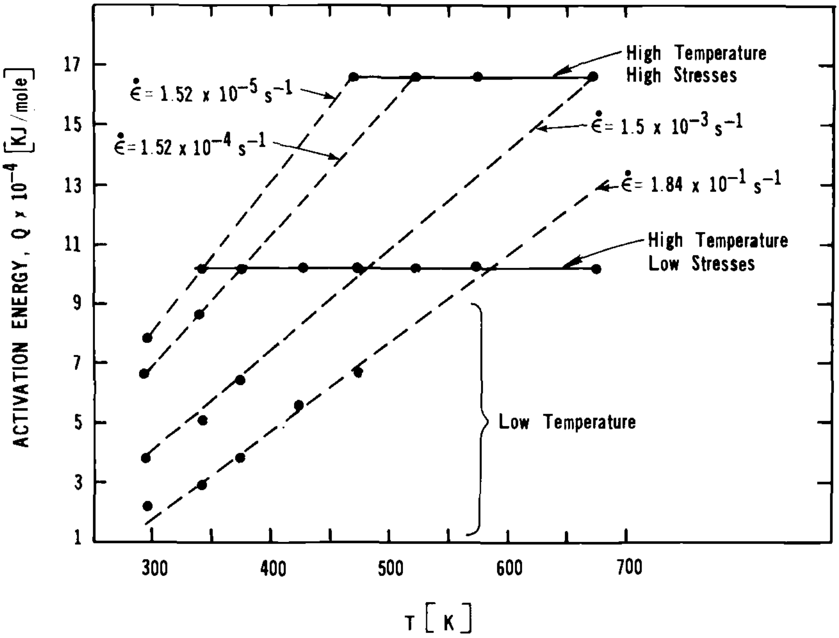

FIG. 9—*Variation of the activation energy with temperature.*

(Fig. 8) that the activation area is independent of strain, which strongly suggests that a thermally activated mechanism of dislocation motion past linear obstacles is rate controlling at low temperatures.

Although there are several subtype mechanisms for thermal activation of dislocations past linear obstacles [*11*], all are characterized by critical bowing out of short dislocation segments and spreading of the bowed-out region along the length of the dislocation. In the Peierls mechanism [*12*], which considers the intrinsic lattice resistance to dislocation motion, thermally activated nucleation of a kink-pair on the dislocation line enables the dislocation to move over to the next minimum energy configuration. Thus the dislocation line moves from one valley to the next along the slip plane in the slip direction. The free energy for nucleation of pairs of kinks is given by [*13*]:

$$U_n = RT\,\ell\mathrm{n}\left.\frac{\rho L a b^2 \nu}{2\,\omega^2\,\dot{\epsilon}}\right|_{\dot{\epsilon}} \qquad (11)$$

where ρ is the dislocation density, L is the dislocation length, a is the mean distance between "valleys', ν is the Debye frequency, ω is the width of kink separation, and $\dot{\epsilon}$ is the plastic strain rate. The interesting feature in Eq 11 is that U_n increases linearly with temperature; this should be compared with our results in Fig. 9.

Equation 11 also predicts that the slope in the plots of activation energy versus temperature will be proportional to $1/\ell\mathrm{n}$ (strain rate). The calculated slopes of the lines in Fig. 9 are listed in Table 2 together with the ratio of the slope to $\ell\mathrm{n}$ (strain rate) for four strain rates. Although there is some variation among the calculated ratios, it seems that the results in Table 2 tend to confirm that $\partial Q/\partial T\ \alpha\ (1/\ell n\ \dot{\epsilon})$ for the low-temperature deformation in NaCl.

For the Peierls mechanism, the parameter, $\dot{\epsilon}_o$, in Eq 6 is given by

$$\dot{\epsilon}_o = \frac{\rho L a b^2 \nu}{2\,\omega^2} \qquad (12)$$

where all the symbols have the same meaning as before. In order to evaluate Eq 12 some values must be assigned to the parameters a, ω, and L. Taking

TABLE 2—*Variation of activation energy with temperature and strain rate.*

Strain Rate, $\dot{\epsilon}(\mathrm{s}^{-1})$	$(\partial Q/\partial T)$	$(\partial Q/\partial T)/\ell\mathrm{n}\ \dot{\epsilon}$
1.5×10^{-5}	500	−45.1
1.3×10^{-4}	450	−51.2
1.5×10^{-3}	330	−50.8
1.8×10^{-1}	100	−57.7

[*13*] $a = 10b$, $\omega = 20b$, $L = 100b$, $b = 8 \times 10^{-8}$ cm, $\nu = 5.86 \times 10^{12}\,\text{s}^{-1}$, and $\dot{\epsilon}_o = 9.2 \times 10^7\,\text{s}^{-1}$, the average dislocation density is $2.0 \times 10^8/\text{cm}^2$. This value compares extremely well with the dislocation densities determined experimentally for NaCl [*14*].

Further confirmation of the operation of Peierls mechanism was achieved by correlating the experimental results to the theoretically predicted normalized plots for the temperature dependence of the activation energy and stress dependence of the activation area according to the Dorn-Rajnak model [*12*]. In both instances, the correlation was quite reasonable. In order to conserve space, these plots are not presented here. As mentioned earlier, in our relatively pure specimens we did not observe the operation of an obstacle-limited glide regime that was postulated by Verrall et al [*1*].

Deformation at High Temperatures

Diffusivity—It is evident from Fig. 9 that as the temperature is increased, the low activation energy Peierls mechanism takes place with increased frequency so that at a critical temperature T_c the lattice resistance ceases to be a barrier to dislocation motion. At temperatures higher than T_c the activation energy for plastic deformation is constant and independent of temperature and stress (or strain rate) and approximates that for self-diffusion. In metals [*15*], lattice self-diffusion occurs principally by a vacancy mechanism.

Regarding NaCl, the situation is more complex. Impurities have an important effect on the defect structure of alkali halides [*16*]. In the extrinsic range, divalent impurities greatly retard [*1*] the anion vacancy concentration and hence affect creep rates. Impurities also alter the electrical charge carried by dislocations and grain boundaries, and this imbalance seems to enhance diffusion at or near the core [*17*]. A comparison between the activation energies for high-temperature creep obtained in this work and those for ion self-diffusion in NaCl in the extrinsic range (below 823 K) are shown in Table 3.

Inspection of the data shown in this table clearly indicates that the activation energy for deformation under low stresses is close to that for Na^+ self-

TABLE 3—*Activation energies for deformation and self-diffusion in NaCl.*

		Q (kJ/mol)	D_o (m^2/s)	Reference
Creep	low stresses	102.1		this work
	high stresses	166.6^a		this work
Diffusion	Cl^-	155.2 to 250	3.2×10^{-6}	*15,16,19,20*
	Na^+	72.2 to 96.0	1.4×10^{-10}	*15,18,21*

[a] Slightly dependent on strain.

diffusion, whereas at high stresses the activation energy for deformation is nearly identical to that for Cl^- self-diffusion.

The Rate Equations—Figure 4 indicates two strain rate—stress behavior regimes. For deformation under low stresses, the rate equation can be written as

$$\frac{\dot{\epsilon} R T}{D_{o\,Na^+} G b} = 1.47 \times 10^{34} \left(\frac{\sigma}{G}\right)^{5.3} \exp\left(-\frac{102.1 \text{ kJ/mol}}{RT}\right) \tag{13}$$

where $D_{o\,Na^+} = 1.4 \times 10^{-10}$ m^2/s [*18*].

When deformation takes place under high stresses the rate equation is[7]

$$\frac{\dot{\epsilon} R T}{D_{o\,Cl^-} G b} = 8.55 \times 10^{53} \left(\frac{\sigma}{G}\right)^{11.3} \exp\left(-\frac{166.6 \text{ kJ/mol}}{RT}\right) \tag{14}$$

where $D_{o\,Cl^-} = 3.2 \times 10^{-6}$ m^2/s [*19*].

Both Eqs 13 and 14 represent a power-law creep behavior and differ by the values taken by the stress sensitivity coefficient, the activation energy for deformation and parameter B in Eq 7, which suggests that two different deformation mechanisms are rate controlling at low and high stresses, respectively.

Deformation Mechanisms—Since no systematic microstructural studies were carried out in this work, the rate-controlling deformation mechanisms can only be inferred by comparison with known deformation mechanisms and similar materials. The high-temperature diffusion-controlled plastic deformation of crystalline solids occurs by the same deformation mechanisms regardless of their crystalline structure and type of bonding [*1,22,23*]. Hence it seems appropriate to compare the deformation behavior of NaCl in this work with those of metals for which a wealth of information is available. Moreover, since at low temperatures the Peierls mechanism was found to be dominant and this mechanism is mainly characteristic of body-centered-cubic (BCC) metals [*13*], the comparison will be made mainly to these metals.

At low stresses, Eq 13, the values of the stress sensitivity coefficient and the parameter B compare well with those for molybdenum and tungsten [*22*]. The possible deformation mechanisms for creep in these cases is the climb of edge dislocations. The activation energy for creep for the high-temperature, low-stress region appears to be close to that for Na^+ diffusion. It is generally accepted that in ionic solids, the slower of the diffusing species should control the diffusion rate; hence one would normally expect that the Cl^- ion dif-

---

[7] Equation 14 strictly applies only at $\epsilon = 10$ percent. However, the effect of strain on n and Q in Eq 14 is quite small.

fusion (vide Table 3) should always control the diffusion rate in NaCl. However, Paladino and Coble [*24*] observed that creep of polycrystalline Al_2O_3 occurs at a faster rate than is possible through control by lattice diffusion of oxygen. (In single-crystal Al_2O_3 oxygen ion diffusion is several orders of magnitude less than aluminum ion diffusion.) They postulated that enhanced oxygen diffusion in regions adjacent to boundaries allows aluminum ion bulk diffusion to be rate controlling in their creep work.

The anion diffuses more slowly than the cation at all temperatures in NaCl single crystals. However, Laurent and Bernard [*25*] observed that anion diffusion was greater in polycrystalline sodium and potassium halides than in single crystals and increased with decreasing grain size. Autoradiographic measurements revealed preferential anion diffusion near grain boundaries but the kinetics supported bulk diffusion. This requires that enhanced diffusion occurs along grain boundaries or within dislocation cores, regions whose radius can be as much as 200 Å [*25*]. Hence, whereas for larger grain sizes kinetic phenomena require that diffusion of both ions will be limited by the more slowly diffusing species, at finer grain sizes the situation can be reversed. The influence of grain size on anion diffusion leads to the conclusion that in our rather fine-grained NaCl specimens, at low stresses, the kinetic process is controlled by bulk diffusion of the cation. It should be pointed out that these low stresses correspond to higher test temperatures (see Fig. 1) and at these temperatures, the postulated preferential transport of anions along grain boundaries will be substantial.

When deformation takes place under high stresses there is a transition in the diffusion mechanism. Under these conditions, the slower rate of Cl^- diffusion prevails and there is an increase in the values of n and B. There is not, at this time, any detailed model for a deformation mechanism which will predict $n > 6$. However, Myshlaev and Khodes [*26,27*] studied the dislocation structures in molybdenum and tungsten and observed that regular dislocation networks are in a nonequilibrium condition. Dislocations are continuously emitted from nonequilibrium segments of the network, and travel towards other segments where they are annihilated or create nonequilibrium conditions in the new segment. The observed dislocation networks can be hexagonal, tetragonal, triangular, or combinations thereof. If the deformation proceeds by a mechanism controlled by dislocation emission and motion through networks, then stress sensitivities higher than 6 might be expected [*26*]. The possibility of such mechanisms is interesting because it would agree with $n = 11.3$ obtained in this work. The transition from Na^+ diffusion to Cl^- diffusion at high stresses may possibly be explained by the fact that at these high stresses which correspond to lower test temperatures (see Fig. 1) the grain boundary transport of anions is no longer fast enough and the slower diffusion rate of Cl^- ion through the bulk will control the diffusion rate in creep.

Application

The results obtained in this work can eventually be used to understand and predict the rheological behavior of halite aggregates in nature. Figure 10 is divided in three fields, each corresponding to one of the rate-controlling deformation mechanisms identified in this work: Peierls; high temperature, high stress; and high temperature, low stress.

The boundaries between the fields on the map were constructed by pairing Eqs 10, 13, and 14, and solving for stress as a function of temperature. Using the same equations (each one in its own applicable field), constant strain rate contours (solid lines) are superimposed on Fig. 10, whereas the circles represent actual experimental datum points. The deviation of some experimental datum points from the calculated ($\dot{\epsilon} = 1.5 \times 10^{-x}$ s^{-1}, $x = 1$ to 7) constant strain rate contours is due to the fact that the strain rates used in this work varied between 1.12×10^{-x} and 1.84×10^{-x} s^{-1}. In the left-hand side of Fig. 10 the calculated strain rate contours corresponding to $\dot{\epsilon} = 10^{-11}$ s^{-1} and $\dot{\epsilon} = 10^{-15}$ s^{-1} (shown as broken lines) represent the expected "geological" strain rate range [*8*]. Also, the temperature range between 325 and 390 K is that expected in buried salt deposits [*8*]. The superposition of the strain rate range results in the hatched region in Fig. 10, representing the stress-strain rate-temperature conditions expected for buried salt structures.

Inspection of Fig. 10 indicates that plastic flow at strain rates of at least 10^{-15} s^{-1} will take place at stresses of $\sim 7.9 \times 10^5$ Pa at 325 K and 5.5×10^5 Pa at 390 K.

One might argue that extrapolation of our results to lower strain rates (stresses) is misleading, since at these low strain rates other deformation mechanisms such as Coble creep [*28*] and Nabarro-Herring creep [*29,30*] can conceivably become rate controlling. In Fig. 11 only the Coble mechanism was added to those identified in this investigation. The constitutive equations used are

$$\frac{\dot{\epsilon} R T}{D_{ob}\, G\, b} = 2.9 \times 10^{25} \left(\frac{b}{d}\right)^3 \left(\frac{\sigma}{G}\right) \exp\left(-\frac{77.5\ \text{kJ/mol}}{RT}\right) \tag{15}$$

for Coble creep, where $d = 3 \times 10^{-3}$ m, D_{ob} was taken as 1 m^2/s and the activation energy for the process was taken as one half [*16*] of that for Cl$^-$ lattice self-diffusion, since only anion grain boundary diffusion has been observed experimentally [*15*].

The hatched area in Fig. 11 representing the stress-strain rate-temperature conditions for buried salt structures was constructed using the same procedure as for Fig. 10. Nabarro-Herring creep is not shown in Fig. 11, since calculations have indicated that for $d = 3 \times 10^{-3}$ m grain diameter it can be expected only at temperatures above 678 K. At $d = 3 \times 10^{-3}$ m, the interesting feature in Fig. 11 is that now most of the hatched area falls onto the

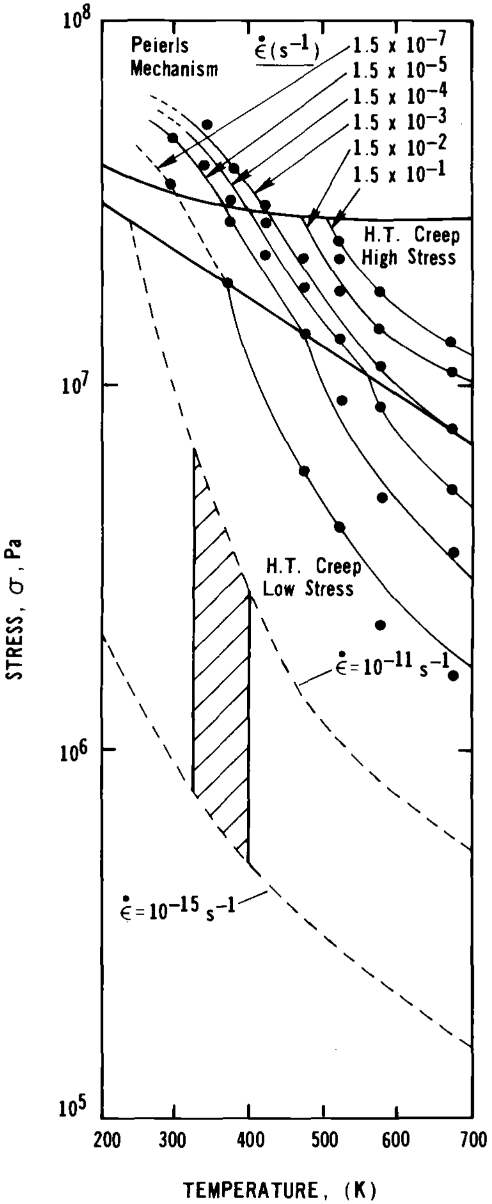

FIG. 10—*Deformation mechanism map for NaCl.*

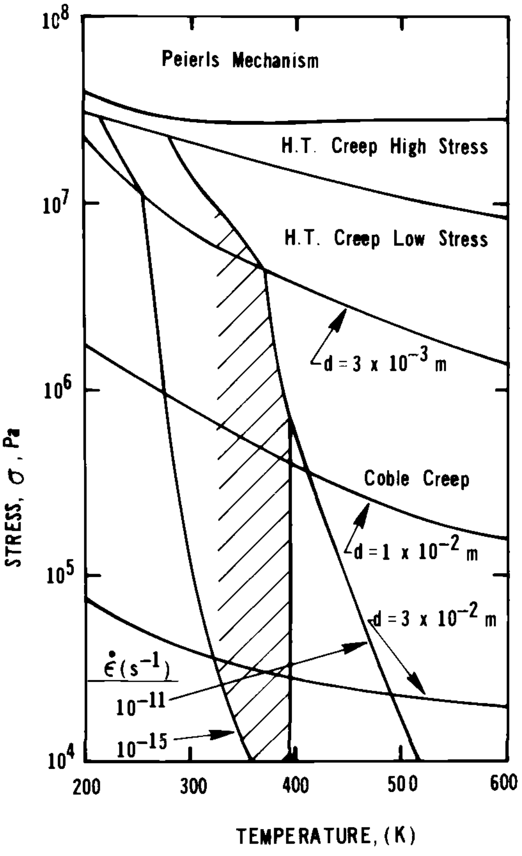

FIG. 11—*Modeling for ranges of operation of Peierls, Creep, and Coble mechanisms.*

Coble creep field. Plastic flow at a rate of at least 10^{-15} s^{-1} will occur at stresses of ~2.9 × 10^4 Pa at 325 K and 2.4 × 10^3 Pa at 390 K. As the grain size is increased the boundary between the high-temperature, high-stress region and the Coble creep region is displaced toward lower stress levels (Fig. 11). It is likely that Coble creep will not be very important in natural salt deformation, since the average grain size of Gulf Coast salt domes is ~1 to 2 cm [*31*]. It should be emphasized, however, that Coble creep was not experimentally observed [*8*] and its occurrence in NaCl is only inferred in Fig. 11. One possible way to check which mechanism is operative in the strain rate—temperature field of interest is to calculate expected viscosities and to compare them with estimates of probable viscosities (> 10^{17} to 10^{19} poises) based on limited observations in natural halite bodies [*32*]. The calculated viscosities for the high-temperature, low-stress mechanism and the Coble creep mechanism are listed in Table 4. These results seem to indicate that the viscosities associated with the high-temperature, low-stress mechanism correlate better with those observed in natural halite [32] than those for the Coble creep mechanism. More experimental work is required before a definite conclusion on this aspect can be drawn.

Summary and Conclusions

The flow stress dependence on temperature and strain rate of annealed, isotropic polycrystalline NaCl has been determined at temperatures of 296 to 673 K (0.28 to 0.63 T_M) and strain rates of 10^{-1} to 10^{-8} s^{-1}.

1. At temperatures below 0.44 of the melting point, the rate-controlling deformation mechanism relates closely to that given by the Peierls mechanism due to nucleation of kink-pairs on the dislocation line.

2. At elevated temperatures ($T \geq 0.44$ melting point) and relatively low stresses, the Na^+ ion diffusion-controlled creep by climb of edge dislocations appears to be the rate-controlling deformation mechanism.

3. At elevated temperatures and high stresses, the creep deformation is controlled by Cl^- ion diffusion which produces corresponding changes in the activation energy and stress dependence of the creep rate.

4. The constitutive equations for each deformation mechanism as well as that for the transition from one deformation mechanism to another were developed in terms of strain rate, temperature, and stress. The implications of the transition from one deformation mechanism to another over a wide range of temperatures on the deformation modeling for this material are discussed.

5. Such analysis can eventually be used to understand and to predict the rheological behavior of halite aggregates in nature in buried salt deposits. At

TABLE 4—*Calculated viscosities.*[a]

	Viscosities, poises	
Temperature, K	High Temperature, Low Stress ($\dot{\epsilon} = 10^{-13}$ s^{-1})	Coble ($d = 1$ cm)
300	2.59×10^{19}	3.53×10^{18}
325	1.46×10^{19}	3.55×10^{17}
350	8.91×10^{18}	1.40×10^{17}
375	5.82×10^{18}	9.21×10^{15}
400	4.01×10^{18}	2.09×10^{15}
425	2.89×10^{18}	5.71×10^{14}
450	2.17×10^{18}	1.80×10^{14}
475	1.67×10^{18}	6.43×10^{13}

[a] The viscosities, η, were calculated as $\eta = \sigma/3\dot{\epsilon}$ for the high-temperature, low-stress mechanism, and as $\eta = \sigma/\dot{\epsilon}$ for the Coble creep mechanism.

the stress-strain rate-temperature conditions expected in salt structures buried at depths of 1 to 2 km, the most likely rate-controlling deformation mechanism appears to be that controlled by dislocation climb creep due to Na^+ ion diffusion. The viscosities associated with this mechanism correlate better than that for Coble creep when the viscosity values are compared with those observed in natural halite. However, more experimental work is needed before a definite conclusion on this aspect can be drawn.

References

[*1*] Verrall, R. A., Fields, R. J., and Ashby, M. F., *Journal of American Ceramic Society*, Vol. 60, 1977, p. 211.

[*2*] Hansen, F. D. and Carter, N. L., "Creep of Rocksalt at Elevated Temperatures," in *Proceedings*, 21st Symposium on Rock Mechanics, Rolla Missouri, American Institute of Mechanical Engineers, 1980, in press.

[*3*] Wawersik, W. R. and Hannum, D. W., *Journal of Geophysical Research*, Vol. 84, 1980, p. 891.

[*4*] Langer, M., "Rheologisches Verhalten von Gesteinen und Fels-Generalbericht," in *Proceedings*, 4th International Congress on Rock Mechanics, Vol. 3, Montreux, 1979, in press.

[*5*] Munson, D. E. and Dawson, P. R., "Constitutive Model for Low Temperature Creep of Salt (with Application to WIPP)," SAND 79-1853, Sandia Laboratories, Albuquerque, N.M., 1979.

[*6*] Burke, P. M., "High Temperature Creep of Polycrystalline Sodium Chloride," Ph.D. Thesis, Stanford University, Stanford, Calif., 1968.

[*7*] Langdon, T. G. and Mohamed, F. A., *Journal of Materials Science*, Vol. 11, 1976, p. 317.

[*8*] Heard, H. C., in *Flow and Fracture of Rocks*, Geophysical Monograph Series, Vol. 16, H. C. Heard et al, Eds., American Geophysical Union, Washington, D.C., 1972, p. 191.

[*9*] Carter, N. L. and Heard, H. C., *American Journal of Science*, Vol. 269, 1970, p. 193.

[*10*] Li, J. C. M., *Canadian Journal of Physics*, Vol. 45, No. 2, Part 2, 1967, p. 493.

[*11*] Klahn, D., Mukherjee, A. K., and Dorn, J. E. in *Proceedings*, ICSMA 2, Vol. III, Asilomar, Calif., 1970, p. 951.

[*12*] Dorn, J. E. and Rajnak, S., *Transactions of American Institute of Mechanical Engineers*, Vol. 230, 1964, p. 1052.

[*13*] Guyot, P. and Dorn, J. E., *Canadian Journal of Physics*, Vol. 45, 1967, p. 983.

[*14*] Argon, A. S., Nigani, A. K., and Padanier, G., *Philosophy Magazine*, Vol. 25, 1972, p. 1095.

[*15*] Adda, Y. and Phibert, J., *La Diffusion Dans Les Solides*, Presses Universitaire De France, Paris, 1966.

[*16*] Shewmon, P. G., *Diffusion in Solids*, McGraw-Hill, New York, 1963.

[*17*] Kliewar, K. L. and Koehler, J. S., *Physical Review*, Vol. 140A, 1965, p. 1226.

[*18*] Mapother, D., Crooks, N. L., and Maurer, R., *Journal of Chemistry and Physics*, Vol. 18, 1950, p. 1231.

[*19*] Harrison, L. G., Morrison, J. A., and Rudhain, R., *Transactions of Faraday Society*, Vol. 54, 1958, p. 106.

[*20*] Barr, L. W., Hoodless, I. M., Morrison, J. A., and Rudham, R., *Transactions of Faraday Society*, Vol. 56, 1960, p. 697.

[*21*] Aschner, J. F., Ph.D. dissertation, University of Illinois, Urbana, Ill., 1954.

[*22*] Bird, J. E., Mukherjee, A. K., and Dorn, J. E., in *Quantitative Relation Between Properties and Microstructure*, D. G. Brandon and A. Rosen, Eds., Israel University Press, Jerusalem, 1969, p. 255.

[*23*] Sherby, O. D. and Burke, P. M., *Progress in Material Science*, Vol. 13, 1967, p. 325.

[*24*] Paladino, A. E. and Coble, R. L., *Journal of American Ceramic Society*, Vol. 46, 1963, p. 133.

[25] Laurent, J. F. and Bernard, J., *Physical and Chemical Solids*, Vol. 7, 1958, p. 218.
[26] Myshlaev, M. M. and Khodos, I. I., *Strength of Metals and Alloys*, P. Hassen Et Al, Eds., Pergamon Press, London, 1979, p. 357.
[27] Myshlaev, M. M., Khodos, I. I., Senikov, O. N., and Romanov, Y. A., *Fizika Metallov Metallovedenie*, Vol. 48, 1979, p. 148.
[28] Coble, R. L., *Journal of Applied Physics*, Vol. 34, 1963, p. 1679.
[29] Nabarro, F. R. N., *Report of a Conference on the Strength of Solids*, Physical Society, London, 1948, p. 75.
[30] Herring, C., *Journal of Applied Physics*, Vol. 21, 1950, p. 437.
[31] Kupfer, D. H., "Structure of Salt in Gulf Coast Domes," Symposium on Salt, A. C. Bersticker, Ed., Geological Society, Inc., Northern Ohio, 1963.
[32] Odé, H., "Reviewing Mechanical Properties of Salt Related to Salt Dome Genesis and Saline Deposits," Special Paper No. 88, R. B. Mattox, Ed., Geological Society of America, Boulder, Colo., 1968, pp. 543-595.

Robin Stevenson[1]

Inferring Microscopic Deformation Behavior from the Form of Constitutive Equations for Low-Carbon Steel and 5182-0 Aluminum

---

REFERENCE: Stevenson, Robin, "**Inferring Microscopic Deformation Behavior from the Form of Constitutive Equations for Low-Carbon Steel and 5182-0 Aluminum,**" *Mechanical Testing for Deformation Model Development. ASTM STP 765,* R. W. Rohde and J. C. Swearengen, Eds., American Society for Testing and Materials, 1982, pp. 366-381.

ABSTRACT: Earlier work has demonstrated that the formability of a low-carbon sheet steel can be improved by deforming at temperatures below room temperature. In this work the tensile properties of a 5182-0 aluminum alloy were determined at low temperatures, and a significant increase in work-hardening rate resulted. The forms of the constitutive equations which best fitted the deformation behaviors of low-carbon steel and 5182-0 aluminum were completely different and could be rationalized in terms of the operative microscopic deformation mode. It appears that it may be possible to infer the operative microscopic deformation mechanism from the form of the constitutive equation.

KEY WORDS: constitutive equations, 5182-0 aluminum, AK steel, recovery, saturation

Substitution of thinner gage materials in stamped parts is an obvious means of reducing vehicle mass and improving fuel economy. However, to maintain stiffness, such an approach usually requires somewhat deeper draws to increase section depth and thus compensate for the reduction in stiffness which would otherwise result from downgaging. The inherent formability of the material then constitutes a natural restriction on the degree of mass reduction attainable. Thus it is desirable to optimize material formability.

Significant improvements in the formability of low-carbon steel, achieved

---

[1] Staff Research Engineer, General Motors Research Laboratory, Warren, Mich. 48090.

by controlling the interstitial carbon content and deforming at temperatures below room temperature, were reported earlier [*1*].[2] This increase in formability was shown to result from the marked improvement in strain rate sensitivity occurring at low temperatures. Further it was demonstrated that the strain rate hardening of low-carbon steel is additive to its strain hardening [*2*].

Improvements in the formability of aluminum alloys by forming at low temperature have also been reported [*3*]. No analysis of the origin of the effect was put forward; however, by analogy with the results of others on pure aluminum [*4,5*], it might reasonably be considered to be due to dynamic recovery effects. In view of this, the low-temperature deformation behavior of 5182-0 aluminum alloy was investigated at temperatures between room temperature and 77 K. Also, the data obtained previously on low-carbon steel [*1,2*] were reanalyzed as a function of temperature (rather than strain rate). The intent was to develop an understanding of the microscopic deformation behavior in these two materials and to correlate this with the character of the constitutive equations describing this behavior.

Experimental Procedure

The chemical compositions of the low-carbon steel and 5182-0 aluminum are listed in Table 1. Both materials were tested in the as-received condition. For the low-carbon steel the interstitial carbon content, determined by internal friction, was less than 5 ppm by weight. All physical tests used an Instron universal testing machine; sheet specimens were cut to ASTM Methods of Tension Testing of Metallic Materials (E 8) specifications. Except for room temperature tests, all tests were conducted with the specimen immersed in a low-temperature bath of either refrigerated ethyl alcohol or, for tests at 77 K, liquid nitrogen. Because the sample was immersed an extensometer could not be used. Therefore crosshead displacement (inferred from load-time traces) was converted to strain by means of experimentally determined calibration curves. Further, all tests were terminated just prior to fracture, and strain was measured directly from two scribe marks on the specimen which were initially 50.8 mm apart. The total elongation measured from the scribe marks and that computed from crosshead displacement never differed by more than 2 percentage points.

Most tests were conducted at a nominal strain rate of 3.4×10^{-3} s^{-1}; however, nominal strain rates ranging from 1.7×10^{-4} s^{-1} to 6.8×10^{-2} s^{-1} were employed for one series. Strain rate sensitivity was determined from strain rate change tests [*6*] using strain rates of 1.7×10^{-3} s^{-1} and 1.7×10^{-2} s^{-1} except as noted.

Analysis of the stress-strain curves was performed using a computer pro-

---

[2] The italic numbers in brackets refer to the list of references appended to this paper.

TABLE 1—*Material chemistry.*

AK steel	0.068 % C	0.27 % Mn	0.017 % S
5182-0 aluminum	4.25 % Mg	0.26 % Mn	0.27 % Fe

gram of Wagoner [*7*]. The program fits those different constitutive equations which have been proposed for the experimental stress strain curves.[3]

Hollomon [*8*] $$\sigma = K\epsilon^n \tag{1}$$

Swift [*9*] $$\sigma = K(\epsilon + x_0)^n \tag{2}$$

Voce [*10*] $$\sigma = \sigma_s[1 - \alpha\exp(-B\epsilon)] \tag{3}$$

where σ is (true) flow stress; ϵ is (true) plastic strain, and K, n, x_0, α, σ_s, B are parameters, independent of stress and strain, but which may depend on temperature and strain rate.

For each fit the standard error of estimate in stress is computed along with the relevant parameters for each of the three equations. Thus the determination of which law provides the best fit to the data is reduced to noting which yields the lowest overall standard error of estimate. The program also yields a graphical output that permits a visual determination of goodness-of-fit. All flow curves were fitted over the strain range from 0.02 to uniform elongation, and any serrations due to dynamic strain aging in the 5182-0 were ignored. The flow curve for 5182-0 exhibiting serrations was described by a smooth curve drawn so that it bisected the serrations.

Results

AK Steel

The fitting parameters for the low-carbon steel and their associated standard errors of estimate deviations at four temperatures are shown in Table 2. By considering the standard errors of estimate it is clear that of the three, the equation which best describes the experimental data is Eq 2; this is confirmed by the graphical representation, a typical example of which is shown in Fig. 1. The data points in Fig. 2 show the flow stresses at strains of 0.1, 0.2, 0.5, and 1.0 as a function of temperature computed using Eq 2 from the

---

[3] The use of the terms "constitutive equation" or "constitutive law" should not be taken to imply any theoretical basis for these equations. In their inception [*8-10*] all these equations were clearly presented as empirical or convenient representations of the data, although in a later publication [*11*] Voce did try to rationalize Eq 3. It is obvious that there are other equations one could apply (see, for example Ref *12*), but those chosen are in common use and extension of the analysis to the more obscure relations [*12*] hardly seems justified.

TABLE 2—*Fit parameters and standard errors of estimate for AK steel.*

		$\sigma = K\epsilon^n$			$\sigma = K(\epsilon + x_0)^n$				$\sigma = \sigma_s[1 - \alpha \exp(-B\epsilon)]$			
Temperature, K	Strain Rate, s^{-1}	n	K, MPa	Standard Error of Estimate, MPa	n	K, MPa	x_0	Standard Error of Estimate, MPa	σ_s, MPa	α	B	Standard Error of Estimate, MPa
295	0.0034	0.220	535.7	1.90	0.202	520.7	−0.005	1.23	389.8	0.530	11.626	2.10
253	0.0034	0.220	576.4	1.97	0.249	601.7	+0.008	0.90	442.6	0.519	8.758	1.36
253	0.0034	0.221	571.7	1.71	0.246	593.0	+0.007	0.62	440.3	0.521	8.587	1.44
223	0.0034	0.177	575.0	3.52	0.235	623.1	+0.022	0.70	486.0	0.450	7.265	1.05
200	0.0034	0.134	574.1	4.37	0.211	634.9	+0.039	0.85	524.2	0.376	6.251	1.06

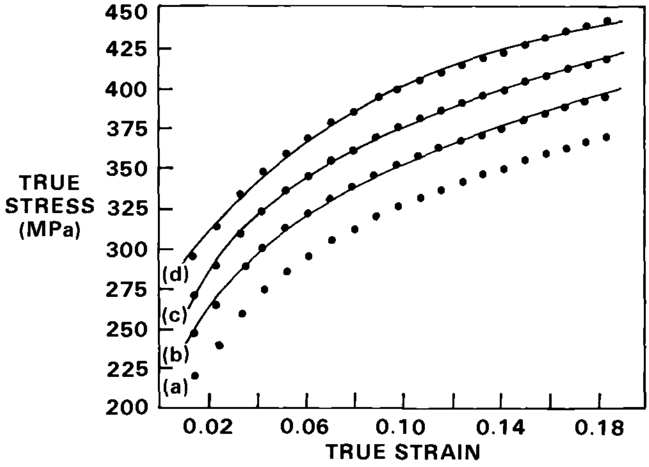

FIG. 1—*Comparison of the fits, achieved by minimizing the stress variance of three work-hardening laws (lines) to one set of tensile data for AK steel (points).* (a) *Data;* (b) $\sigma = K\epsilon^n$; (c) $\sigma = K(\epsilon + x_0)^n$; (d) $\sigma = \sigma_s[1 - \alpha\, exp(-B\epsilon)]$. *To separate the curves each set of data has been displaced by approximately 25 MPa from the preceding curve. The ordinate labels apply to data points* (a) *only.*

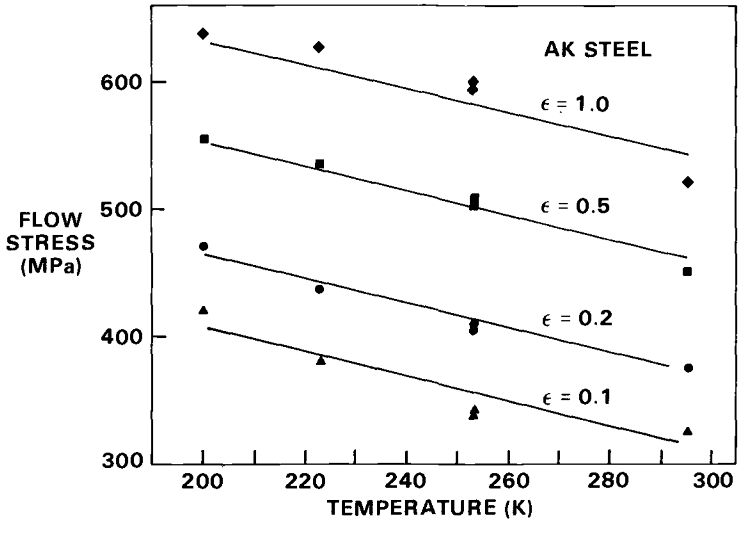

FIG. 2—*Flow stresses for AK steel as a function of temperature at strains of 0.1, 0.2, 0.5, and 1 computed from the fit parameters given for the relationship* $\sigma = K(\epsilon + x_0)^n$ *listed in Table 2. All straight lines have been drawn parallel.*

parameters given in Table 2. Note that at each strain level the flow stress varies in an approximately linear manner with temperature. Further, as shown in Fig. 2, a straight line of the same slope adequately describes the data at all strain levels. Thus for tests at constant strain rate one can write

$$\sigma = \sigma(\epsilon) + ZT \tag{4}$$

where T is temperature and Z is constant.

Earlier studies [2] indicated that at constant temperature the flow stress could be described by

$$\sigma = \sigma(\epsilon) + m' \ln \dot{\epsilon} \tag{5}$$

where m' is constant and $\dot{\epsilon}$ is strain rate. Thus the behavior of the AK steel is in accord with the classic equation of thermally activated flow [13]. This description of the variation of the flow stress with temperature and strain rate might have been anticipated on the basis of the work of Peyrade et al [14,15]. These workers consider the low-temperature deformation behavior of iron to result from the difficulty of nucleating kinks in screw dislocations, a process which is modified by the presence of interstitial atoms. Thus, this is a classical thermally activated flow problem. As an aside it may be noted that if one measures the strain rate sensitivity coefficient defined as

$$m = \frac{d\ln\sigma}{d\ln\dot{\epsilon}} \approx \frac{\Delta\ln\sigma}{\Delta\ln\dot{\epsilon}} \tag{6}$$

in this material it will be a function of strain [2].

Returning to the constitutive equations, it is clear that the only relation which can readily embody the temperature dependence of Eq 4 is Eq 2. In addition, by comparing Eqs 2 and 4, it is apparent that the parameter x_0 should vary in a quasi-linear manner with temperature. This is shown in Fig. 3.

5182-0 Aluminum

The fit and standard error of estimate data for 5182-0 at temperatures of 298, 253, 233, 173, and 77 K are shown in Table 3. Clearly over this temperature range the data are best fit by Eq 3. The only exception is one test at 173 K, but even in this case the companion specimen is best described by Eq 3.[4]

---

[4] Equation 3 is frequently referred to as either the Voce relation or as a saturation stress relation. As strain tends to infinity the flow stress tends to "saturate" or asymptotically approach the constant value σ_s (Eq 3). σ_s is thus commonly referred to as the saturation stress.

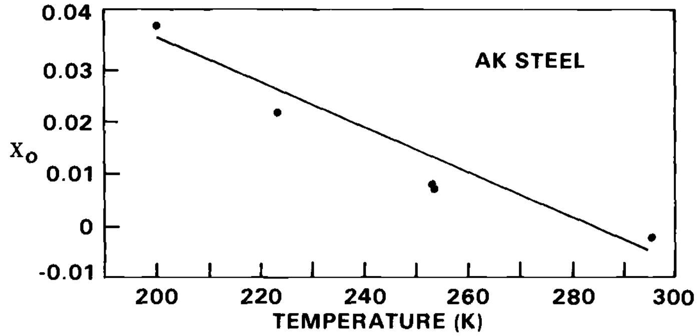

FIG. 3—*Variation of the parameter* x_0 *in the relation* $\sigma = K(\epsilon + x_0)^n$ *for AK steel as a function of temperature. Data from Table 2.*

A consideration of the microscopic mechanism which might be responsible for Voce or saturation stress (Eq 3) behavior has led several authors [*4,5*] to conclude that dynamic recovery is occurring as testing proceeds. Two views of the character of this recovery can be found in the literature. Kocks [*4*] postulates a recovery rate proportional to strain, while a view originally put forward by Bailey and Orowan (see, for example, Ref *16*) suggests that the recovery rate is proportional to elapsed time.

Following Routbort [*17*] one can test the applicability of the Bailey-Orowan approach by plotting the work-hardening rate (θ), at constant structure, against the reciprocal of strain rate ($1/\dot{\epsilon}$). A linear relation of negative slope should be observed if a Bailey-Orowan mechanism is operative, the absolute value of the slope being the recovery coefficient. Constant structure is less readily defined in this work then in Routbort's study [*14*]. However, from the fitting parameters already deduced for the continuous flow curves (Table 3), it is straightforward to compute work-hardening rates, both at constant stress and at constant strain. (From dislocation density arguments one would expect that constant stress would be more indicative of constant structure than constant strain.) The results are shown in Fig. 4 plotted against the reciprocal strain rate ($1/\dot{\epsilon}$). A simple linear fit has been made to each set of data. Disregarding the imperfect fit to a linear relationship at some stress and strain levels, the most obvious feature is that the sign of the slope of the line which fits the rate changes with both strain and flow stress. This is not in accord with the Bailey-Orowan model; however, it is clear that slight uncertainties in the data could modify the slopes considerably. Thus these data, although suggestive, are not in themselves sufficient to invalidate the Bailey-Orowan mechanism.

As a further test of the model a series of strain-rate-change experiments was conducted. Specimens were prestrained at 77 K to 3 percent elongation

TABLE 3—*Fit parameters and standard errors of estimate for 5182-0 aluminum.*

		$\sigma = K\epsilon^n$			$\sigma = K(\epsilon + x_0)^n$				$\sigma = \sigma_s[1 - \alpha \exp(-B\epsilon)]$			
Temperature, K	Strain Rate, s^{-1}	n	K, MPa	Standard Error of Estimate, MPa	n	K, MPa	x_0	Standard Error of Estimate, MPa	σ_s, MPa	α	B	Standard Error of Estimate, MPa
298	0.0034	0.303	545.8	2.01	0.295	539.0	−0.002	2.01	354.5	0.654	10.574	0.67
298	0.0034	0.304	548.5	2.26	0.290	537.5	−0.003	2.14	358.7	0.657	10.385	1.57
298	0.0034	0.301	542.2	3.27	0.281	525.5	−0.004	3.02	348.2	0.661	11.407	1.18
253	0.0034	0.316	558.2	2.37	0.305	548.0	−0.002	2.32	354.6	0.673	10.622	0.79
233	0.0034	0.308	556.6	2.02	0.307	555.6	−0.000	2.08	363.8	0.657	9.978	1.24
173	0.0034	0.320	588.1	1.54	0.318	586.6	−0.000	1.57	403.9	0.677	8.134	1.74
173	0.0034	0.319	592.1	2.00	0.316	589.6	−0.001	2.03	403.7	0.678	8.379	1.33
77	0.068	0.418	899.6	6.22	0.469	945.5	+0.012	3.21	712.0	0.789	4.030	1.73
77	0.017	0.424	903.3	5.29	0.477	953.0	+0.013	2.71	702.7	0.790	4.108	1.29
77	0.0034	0.414	884.5	5.44	0.462	929.7	+0.012	3.4	681.5	0.780	4.304	1.64
77	0.0017	0.418	870.7	4.98	0.462	911.0	+0.011	3.18	665.2	0.784	4.350	1.37
77	0.00017	0.403	849.4	4.52	0.436	879.2	+0.008	3.39	637.1	0.770	4.742	1.41

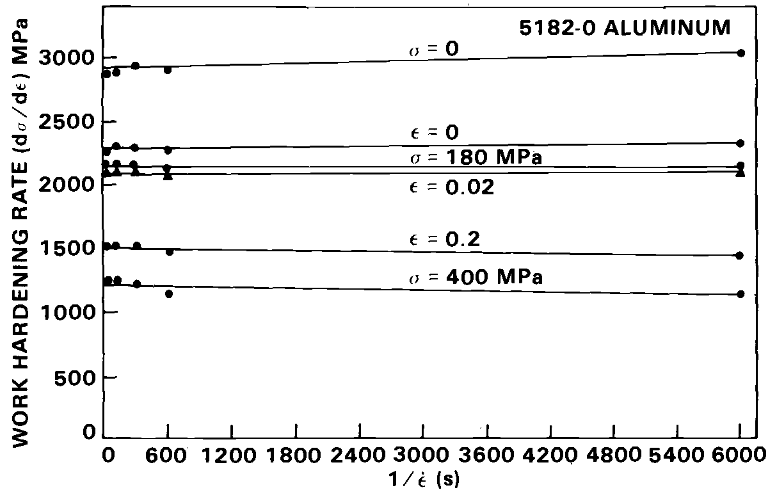

FIG. 4—*Work-hardening rate* (dσ/dϵ) *for 5182-0 aluminum as a function of reciprocal of strain rate* ($1/\dot{\epsilon}$) *computed using the fit parameters for the relation* $\sigma = \sigma_s[1 - \alpha \exp(-B\epsilon)]$ *(Table 3). The work-hardening rate is indicated at stresses of 0, 180, and 400 MPa and at strains of 0, 0.02, and 0.2. (The work-hardening rate at* $\sigma = 0$ *is equivalent to* θ_0 [4].*) A linear relationship between work-hardening rate and reciprocal strain rate has been assumed. All tests were conducted at 77 K.*

at a nominal strain rate of 1.7×10^{-3} s^{-1}, and the strain rate changed to a series of strain rates ranging from 1.7×10^{-4} s^{-1} to 6.8×10^{-2} s^{-1}. The work-hardening rates for the "old" and "new" strain rates at the time of the strain rate change (that is, at constant structure) were then determined directly from the load-time chart record with the aid of the calibration curve described earlier. These work-hardening rates, again plotted against the reciprocal of strain rate ($1/\dot{\epsilon}$), are shown in Fig. 5; for comparison, the computed work-hardening rates derived from the continuous curve rate at 3 percent elongation and 207 MPa flowstress have also been plotted.[5] Again it is clear that Bailey-Orowan behavior is not observed. In addition, it is obvious that work-hardening rates at constant stress most closely mimic those determined in a strain rate change test [*6*], which indicates that, as suggested earlier, constancy of structure is better indicated by constant stress than constant strain. The origin of the deviation between the strain rate change test results and the continous flow curve results was not pursued. Thus the question of the history dependence of the flow behavior cannot be addressed.

The Kocks analysis of dynamic recovery indicates that a linear relationship

---

[5] The experimentally determined flow stresses at 3 percent elongation and a nominal strain rate of 1.7×10^{-3} s^{-1} for the six tests conducted ranged between 202.9 and 209.6 MPa with a mean of 206.6 MPa. This compares with a flow stress of 207.5 MPa calculated from the data of Table 3.

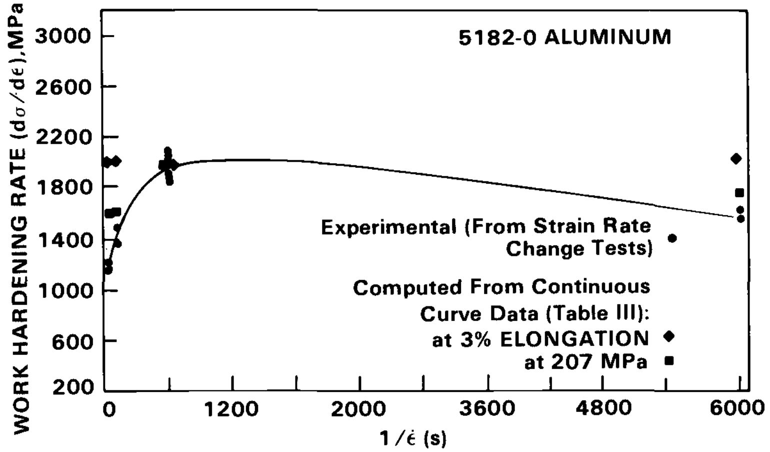

FIG. 5—*Work-hardening rate* (dσ/dϵ) *for 5182-0 aluminum as a function of reciprocal strain rate* ($1/\dot{\epsilon}$) *following a strain rate change. Initially a nominal strain rate of* $1.7 \times 10^{-3} s^{-1}$ *was employed to 3 percent elongation (flow stress = 207 MPa) and the strain rate changed. The work-hardening rates at 3 percent elongation and 207 MPa flow stress, computed from the data of Table 3 are included for comparison. All tests were conducted at 77 K.*

should exist between ($\ell n \sigma_s$) and ($\ell n \dot{\epsilon}$), and that the slope should be kT/A (see Ref *4*, Eq 8). This behavior is shown in Fig. 6. Interestingly, the slope of the line is not dissimilar to that determined for pure aluminum and yields a value of $\mu b^3/A$ of ~11 (compared with 9 for 99.99 percent pure aluminum [*4*]).

Although the variation in flow behavior with strain rate fits the Kocks analysis well, the variation with temperature is somewhat less satisfactory. According to the analysis [*4*], a plot of $\ell n \sigma_s/\mu$ versus $kT/\mu b^3$ (μ = temperature-corrected shear modulus; b-Burgers vector; k = Boltzmann's constant) should yield a straight line for tests at constant strain rate, and extrapolate to a constant stress, independent of strain rate, at absolute zero. Indeed this behavior was assumed (implicitly) in plotting the strain rate data. Figure 7 shows the appropriate semilogarithmic plot of σ_s/μ versus $kT/\mu b^3$; the curved form is evident. It should be noted that a similar, concave up, curve was shown by Kocks for copper [*4*]. Kocks suggested that is was consistent with the known decrease in the Cottrell-Stokes ratio with increasing temperature. Possibly similar behavior is being observed in this case, particularly since the lowest temperature used in this work (77 K) is slightly lower than that used by Kocks (100 K) and would thus tend to accentuate this effect. An alternative explanation might be that the higher temperature data are influenced by the dynamic strain aging which occurs at these temperatures.

It was noted earlier that, for the AK steel, the strain rate dependent contribution to the flow stress was additive to the strain hardening. Since the rate-limiting process in this material involves the motion of individual

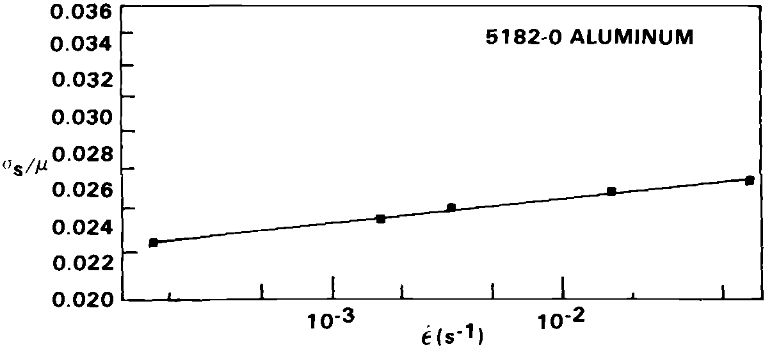

FIG. 6—*(Logarithm of) saturation stress* (σ_s) *from relation* $\sigma = \sigma_s[1 - \alpha \exp(-B\epsilon)]$ *normalized to the temperature-corrected sheet modulus* (μ) *versus (logarithm of) strain rate for 5182-0 aluminum at 77 K. Data from Table 3.*

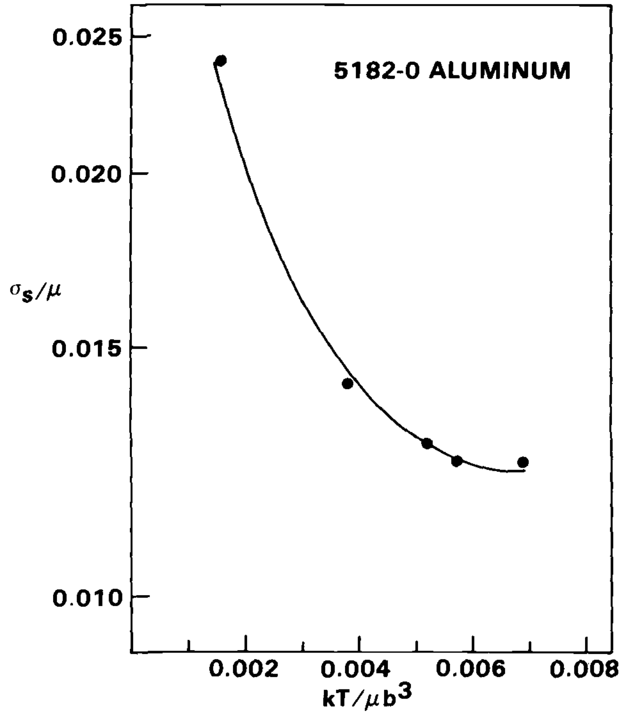

FIG. 7—*Saturation stress* (σ_s) *from relation* $\sigma = \sigma_s[1 - \alpha \exp(-B\epsilon)]$ *normalized to the temperature-corrected shear modulus* (μ) *versus* ($KT/\mu b^3$) *(see text for details) for 5182-0 aluminum.*

dislocations, the insensitivity of strain rate hardening to dislocation density is not surprising. As shown, however, in 5182-0 aluminum, dynamic recovery is occurring, and thus one might expect that the extent of strain-rate hardening would depend on strain or (equivalently) dislocation density. This behavior is embodied in a constitutive law in which the effect of strain rate enters as a multiplicative factor

$$\sigma = f(\epsilon) \cdot g(\dot{\epsilon}) \tag{7}$$

of which one example is

$$\sigma = f(\epsilon) \cdot \dot{\epsilon}^m \tag{8}$$

If this particular law holds then m, defined as before, is a constant. Table 4 illustrates that a constant m was observed for a pair of strain rate change tests conducted during this study.

Discussion

It was noted earlier that none of the constitutive equations proposed has any theoretical basis. Thus the question of which equation is appropriate for a given material reduces to which equation best fits the experimental data. Frequently, however, this procedure is not followed, a particular equation is assumed, and the data are analyzed on that basis. Because of its simplicity the Hollomon relation (Eq 1) is frequently employed, leading to the amiable eccentricity of a strain dependent n-value [*18,19*], but the Voce relation (Eq 3) has also been employed [*20*]. To the author's knowledge the only other investigations in which the applicability of various constitutive laws was compared were those of Wagoner [*7*], Hockett [*21*], and Kleemola and Ranta-Eskola [*22*]. Hockett [*21*] studied 1100-0 aluminum and followed a procedure essentially identical to that employed in this study. Tests were conducted at a vari-

TABLE 4—*Variation of* m-*value with strain in 5182-0 aluminum at 77K.*

Engineering Strain, %	Test 1	Test 2
5.3	0.0061	0.0060
9.5	0.0071	0.0060
14.0	0.0065	0.0061
18.0	0.0073	0.0061
22.6	0.0062	0.0056
27.5	0.0065	0.0063
33.0	0.0059	0.0062

ety of strain rates and temperatures, and the data were analyzed by fitting to four constitutive equations. Neglecting those relations which yielded negative coefficients, Hockett [*21*] on the basis of statistical measures of goodness-of-fit concluded that Eq 1 (this work) fitted better than Eq 3 (this work). This is, of course, at variance with the conclusions of this study but, neglecting for the moment differences between 1100-0 and 5182-0 aluminum, examination of the statistical parameters (Ref *21*, Tables I and IV) indicates that the situation is not as clear cut as in this study. In Wagoner's [*7*] evaluation of the applicability of constitutive equations for 2036-T4 aluminum, Eq 3 best fit the data. Kleemola and Ranta-Escola [*22*] (K and R-E) studied steel, copper, and brass at room temperature, and concluded that Eq 1 best fit the data for steel while copper and brass were best fitted by Eq 3. The observation that Eq 1 rather than Eq 2 best fits K and R-E's data appears to be in disagreement with the data reported here. However, although Eq 2 was considered in an earlier study [*23*], the K and R-E study [*22*] considered only Eqs 1 and 3. From Table 1 of this study Eq 1 would also be preferred over Eq 3 at room temperature.

In this study, the intent has been not only to try to determine which constitutive equation best fits the data, but also to try to relate it to the underlying deformation mechanisms. In this regard it is important to note that for both the steel and aluminum in the temperature ranges studied no change in deformation mechanism is expected; thus *one* equation (though not necessarily the same one for each material) should consistently fit the data best. In general this is observed. Further, one might anticipate that the relevant parameters should vary in a systematic manner as test conditions (for example, temperature, strain rate) are changed. The variation of x_0 with temperature was shown in Fig. 3; Fig. 8 shows the variation of σ_s and B for 5182-0 aluminum. In both cases a systematic variation in the parameters is observed. This is in contrast to the results of Hockett on 1100-0 aluminum in which σ_s varied systematically with temperature, but not strain rate, and B varied systematically with neither [*21*].

This study has shown that the constitutive equation which best fits the data is consistent with, and can be rationalized by, an understanding of the microscopic deformation behavior. Ideally, of course, one would prefer to determine which constitutive equation best fits the data and from that infer the microscopic deformation behavior. Substantially more data will have to be analyzed before one may draw those conclusions. However, the results of this study suggest that it is reasonable to associate Voce (Eq 3) behavior with recovery, and thus to infer the significance of recovery processes by consideration of constitutive equations. In this regard it is encouraging that copper, whose behavior Kocks [*4*] analyzed on the basis of recovery, also exhibits Voce (Eq 3) behavior [*22,23*].

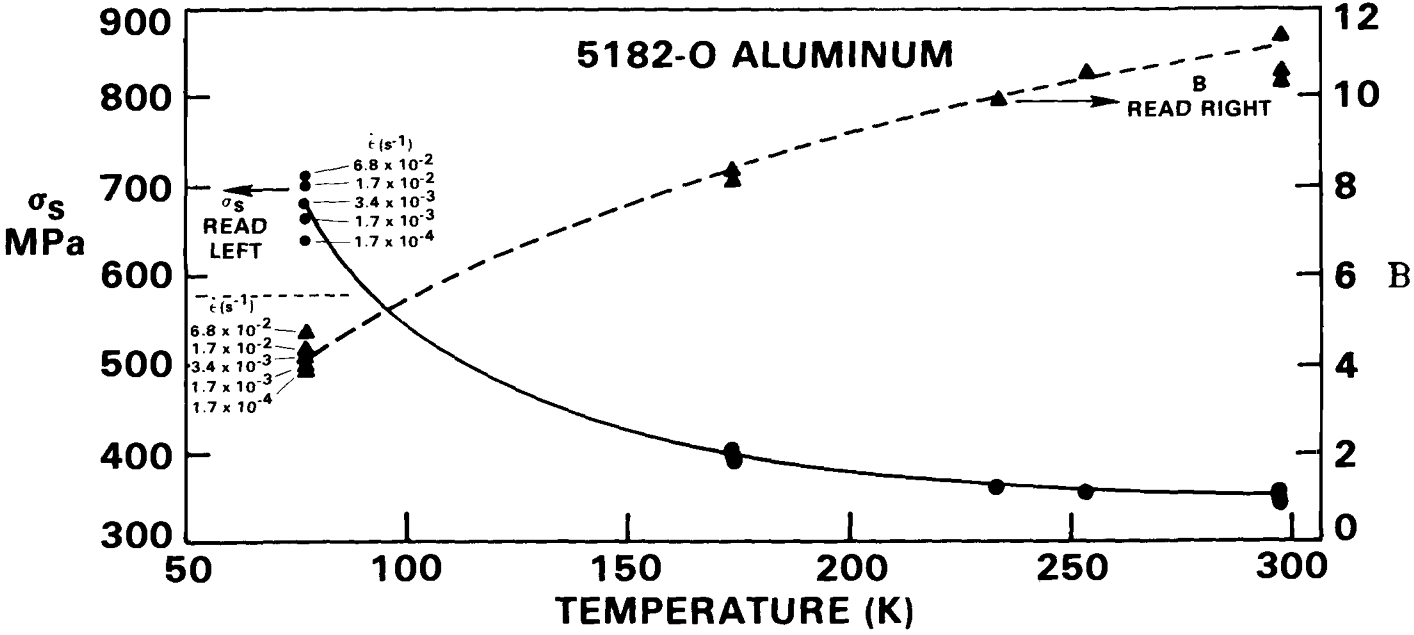

FIG. 8—*Variation of the parameters* σ_s *and* B *in the relation* $\sigma = \sigma_s[1 - \alpha \exp(-B\epsilon)]$ *with temperature and strain rate for 5182-0 aluminum.*

Conclusions

1. Over the aforementioned ranges of temperatures and strain rates, an AK steel and a 5182-0 aluminum alloy were each best fitted by two different constitutive equations:

steel	$\sigma = K(\epsilon + x_0)^n$
5182-0 aluminum	$\sigma = \sigma_s[1 - \alpha \exp(-B\epsilon)]$

2. The forms of the constitutive equations which best fitted steel and 5182-0 aluminum were in accord with their microscopic deformation behavior as determined in this study. Further, the parameters in the constitutive equations used varied systematically with temperature and strain rate.

3. It appears that it is possible to infer some features of the microscopic deformation behavior of a material from the constitutive law which best describes it. This understanding can then provide the basis for the extrapolation of experimental results to other strain rate/temperature regimes.

Acknowledgments

I would like to thank E. G. Brewer for his very capable assistance in all aspects of this work and R. H. Wagoner for making his computer program available and for many stimulating discussions.

References

[*1*] Stevenson R., *Metallurgical Transactions,* Vol. 11A, 1980, p. 1909.
[*2*] Stevenson, R., *Journal of Engineering Materials and Technology, Transaction of ASME,* Vol. 103, 1981, p. 261.
[*3*] Kobayashi, M., Kamada, A., Terabayashi, T., and Asao, H., U.S. Patent 4,083,220, 11 April 1978.
[*4*] Kocks, U. F., *Journal of Engineering Materials and Technology, Transactions of ASME,* Vol. 98, 1976, p. 76.
[*5*] Bullen, F. P. and Hutchison, M. M., *Philosophical Magazine,* Vol. 7, 1962, p. 557.
[*6*] Backofen, W. A., Turner, J. R., and Avery, D. H., *Transactions of American Society for Metals,* Vol. 57, 1964, p. 980.
[*7*] Wagoner, R. H., *Metallurgical Transactions,* Vol. 11A, 1980, p. 165.
[*8*] Hollomon, J. H., *Transactions of AIME,* Vol. 162, 1945, p. 268.
[*9*] Swift, H. W., *Journal of the Mechanics and Physics of Solids,* Vol. 1, 1952, p. 1.
[*10*] Voce, E., *Journal of the Institute of Metals,* Vol. 74, 1948, pp. 537, 760.
[*11*] Voce, E., *The Engineer,* Vol. 195, 1953, p. 23.
[*12*] Osgood, W. R., *Journal of Aeronautical Science,* Vol. 13, 1946, p. 45.
[*13*] *Progress in Materials Science,* B. Chalmers, J. W. Christian, and T. B. Massalski, Eds.—*Vol. 19; Thermodynamics and Kinetics of Slip,* U. F. Kocks, A. S. Argon, and M. F. Ashby, Eds., Pergamon Press, 1975.
[*14*] Cottu, J. P., Peyrade, J. P., Chomel, P., and Groh, P., *Acta Metallurgica,* Vol. 26, 1978, p. 1179.

[*15*] Peyrade, J. P., Groh, P., and Cottu, J. P. in *Proceedings,* 5th International Conference on the Strength of Metals and Alloys, P. Haasen, V. Gerold, and G. Kostorz, Eds., Pergamon Press, 1979.
[*16*] Kocks, U. F., *Rate Processes in Plastic Deformation of Materials,* J. C. M. Li and A. K. Mukherjee, Eds., American Society for Metals, Ohio, 1975, p. 356.
[*17*] Routbort, J. L., *Acta Metallurgica,* Vol. 27, 1979, p. 649.
[*18*] Rashid, M. S., *Formable HSLA and Dual-Phase Steels,* A. T. Davenport, Ed., Metallurgical Society of American Institute of Mining, Metallurgical, and Petroleum Engineers, 1979, p. 1.
[*19*] Laukonis, J. V. and Ghosh, A. K., *Metallurgical Transactions,* Vol. 9A, 1978, p. 1849.
[*20*] Lloyd, D. J., Sang, H., Embury, J. D., Wycliffe, P., and Leroy, G., *Materials Science and Engineering,* Vol. 36, 1978, p. 35.
[*21*] Hockett, J. E., *Transactions of AIME,* Vol. 239, 1967, p. 969.
[*22*] Kleemola, H. J. and Ranta-Eskola, J., *Metallurgical Transactions,* Vol. 7A, 1976, p. 595.
[*23*] Kleemola, H. J. and Nieminen, M. A., *Metallurgical Transactions,* Vol. 5, 1974, p. 1863.

K. L. Murty[1] *and B. L. Adams*[2]

Multiaxial Creep of Textured Zircaloy-4

REFERENCE: Murty, K. L. and Adams, B. L., "**Multiaxial Creep of Textured Zircaloy-4,**" *Mechanical Testing for Deformation Model Development, ASTM STP 765,* R. W. Rohde and J. C. Swearengen, Eds., American Society for Testing and Materials, 1982, pp. 382-396.

ABSTRACT: Extremes of anisotropic multiaxial creep behaviors were considered by analyzing the strain rate ratios versus applied stress ratio for highly cold-worked stress-relieved and partially recrystallized Zircaloy-4 tubings. Power-law creep was modeled by using the upper-bound estimate with the assumption that prism, basal, and pyramidal slip modes are possible mechanisms. Experimental strain rate ratios were compared with those calculated by statistical averaging of crystallite behavior using the crystallite orientation distribution function (CODF). The experimental data on the stress-relieved material were in excellent agreement with the model predictions based on basal slip as the dominant deformation mode. Data on partially recrystallized material were in reasonable agreement with the predictions based on a combination of basal and prism slip modes.

These results are also correlated with the Von-Mises—Hill phenomenological description with appropriate contractile strain ratios (anisotropy parameters), *R* and *P*. The parameter *R* is relatively insensitive to partial recrystallization and is related to the basal pole angle. The *P*-parameter, however, is shown to be very sensitive to fabrication procedures and is greater than unity for well-annealed material with split prism pole distributions. As the amount of cold work increased, *P*-parameter decreased to well below unity.

KEY WORDS: zirconium alloys, multiaxial deformation, creep, anisotropy, texture, annealing, slip, crystallite orientation, distribution function, strain ratios

Zirconium alloys are commonly used in light-water reactors as tubing materials to clad nuclear fuel. The mechanical properties, in particular the multiaxial deformation characteristics, of hexagonal close packed (hcp) metals such as Zircaloy are very sensitive to fabrication variables and the resulting crystallographic texture. However, attempts thus far in correlating the

---

[1] Senior Engineer, Westinghouse R&D Center, Pittsburgh, Pa. 15235; presently Associate Professor, North Carolina State University, Raleigh, N.C. 27650.

[2] Assistant Professor, University of Florida, Gainesville, Fla.

multiaxial creep behavior with texture have not been very fruitful. Recrystallized Zircaloy cladding, for example, was shown to exhibit relatively (with respect to axial) higher hoop creep resistance compared with the cold-worked stress-relieved material [*1,2*].[3] These results are not explicable from analyses based on basal pole textures alone [*3*]. A complete analysis including the basal and prism pole distributions is required to understand and explain the observed behavior.

In the present study, extremes of anisotropic multiaxial creep behaviors were considered by analyzing the strain rate ratios versus applied stress ratio for highly cold-worked stress-relieved (CW-SR) [*4*] and partially recrystallized [*3*] Zircaloy-4 tubings. Power-law creep was modeled by using the upper-bound estimate with the assumption that prism, basal, and pyramidal slip modes are possible mechanisms [*5*]. The strain rate ratios were computed from the crystallographic texture pole figures (basal, prism, and pyramidal) typical of CW-SR materials by statistical averaging of the crystallite behavior through use of the crystallite orientation distribution function (CODF) [*6,7*]. In addition, these results are correlated with the Von-Mises—Hill phenomenological description with the appropriate contractile strain ratios (anisotropy parameters), R and P [*8*].

Crystallographic Textures of Zircaloy-4

The most commonly observed texture of Zircaloy tubing is a bimodal distribution of the basal poles concentrated in the plane normal to the tube axis (r-θ plane) with intensity maxima at ±30-45 deg from the radial direction (Fig. 1). The basal [0001] pole texture angle $\hat{\phi}$ (defined as the angle between the radial direction and the $\hat{c}$-axis of the average crystal in the r-θ plane) is sensitive to the strain path or cold work prior to final annealing. The final annealing temperature has at best a minor effect on the basal pole angle and increases the population of randomly oriented crystallites (Fig. 1), which results in a shallow maximum at $\hat{\phi}$ [*2*].[4] However, the final annealing temperature significantly affects the prism [$10\bar{1}0$] pole distribution, as illustrated in Fig. 1 where the texture pole figures for CW-SR and recrystallized tubing are depicted. The major texture modification due to increased amounts of partial recrystallization involves the rotation of the basal plane about the c-axis. Thus there exists a relatively high population of prism poles along the axial direction in CW-SR, while the population at ±30 deg from the axial direction increases as the annealing temperature increases [*1,2*]; at complete recrystallization essentially no first order ($10\bar{1}0$) prism poles are observed along the tube axial direction [*3*].

---

[3] The italic numbers in brackets refer to the list of references appended to this paper.

[4] This results in a decrease, albeit small, in $\hat{\phi}$ with increasing annealing temperature.

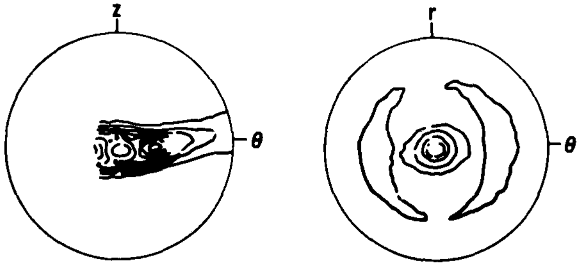

a

Stress Relieved

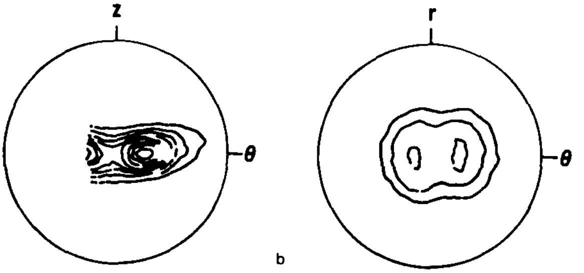

b

Recrystallized

FIG. 1—*Basal* (left) *and prism* (right) *pole distributions of* (a) *stress-relieved and* (b) *recrystallized Zircaloy-4 claddings.*

Multiaxial Creep Results

The multiaxial creep behavior of CW-SR Zircaloy-4 cladding was investigated [*4*] at stress ratios (σ_θ/σ_z) varying from 0 (uniaxial) to 2 (closed-end internal pressurization) by evaluating axial and hoop strains under steady creep conditions at ~673 K.[5] The chemical composition of the material is shown in Table 1. The tubing was tested in as-received condition; the crystallographic texture pole figures of the material are shown in Fig. 1. Within the range of stresses employed, steady-state strain rate ratios ($\dot{\epsilon}_\theta/\dot{\epsilon}_z$) were insensitive to the applied stress level. Stehle et al [*3*] made similar studies on partially recrystallized Zircaloy-4 tubings, referred to here as z1, z2, z3, and z5,[6] corresponding to increasing degrees of partial recrystallization resulting in different textures; details may be found in Ref *3*.[7] Figure 2 depicts these data

---

[5] Experimental details may be found in Ref *2*.

[6] In the figures in this paper z1 is illustrated by 1 enclosed by a circle, z2 by 2 enclosed by a circle, etc. This is the notation used in Ref *3*.

[7] Crystallographic texture pole figures of z1 and z5 are very similar to CW-SR (Fig. 1*a*) and recrystallized (Fig. 1*b*) tubings, respectively.

TABLE 1—*Chemical composition of Zircaloy-4.*

Element	Weight Percent[a]
Sn	1.51
Fe	0.21
Cr	0.12
Ni	0.003
O	0.124
Zr	balance

[a] The sum of Fe, Ni, and Cr must be between 0.28 and 0.37.

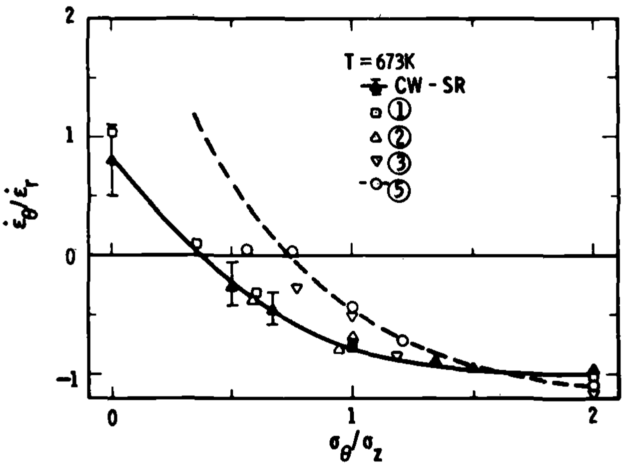

FIG. 2—*Experimental data on CW-SR* [4] *and partially recrystallized tubings z1 to z5* [3] *at 673 K.*

along with the CW-SR [*4*], plotted as $\dot{\epsilon}_\theta/\dot{\epsilon}_r$ versus σ_θ/σ_z;[8] the results for tubings z1 to z5 were evaluated from the experimental creep loci (Fig. 5 in Ref *3*). As to be noted, the results on z1 and z2 are very close to those reported by Murty [*4*] on CW-SR. These results will be used for subsequent comparison with model predictions.

Computational Scheme

Crystallite Orientation Distribution Function (CODF)

The CODF, $\omega(\theta, \psi, \phi)$, expresses the probability that a crystallite has an orientation (θ, ψ, ϕ) with respect to the specimen axes (Fig. 3*a*), and can be

---

[8] $\dot{\epsilon}_r$ is evaluated from conservation of volume, $\dot{\epsilon}_r = -\dot{\epsilon}_\theta - \dot{\epsilon}_z$.

obtained from a set of conventional pole-figure data. The pole-figure intensity data are represented as a series of spherical harmonics:

$$I_i(\chi_i, \eta_i) = \sum_{\ell=0}^{\infty} \sum_{m=-\ell}^{\ell} Q_{\ell m}{}^{i} P_\ell^m(\cos\chi_i)\exp(-im\eta_i) \qquad (1)$$

where $Q_{\ell m}{}^{i}$ are the coefficients for the ith plane-normal (pole) distribution, χ_i and η_i are the spherical polar angles of the ith plane-normal in the reciprocal lattice space (Fig. *3b*), and P_ℓ^m are spherical harmonics. The coefficients, $Q_{\ell m}{}^{i}$, are evaluated from the pole-figure intensity (I_i) data. The CODF is similarly represented by a series of generalized spherical harmonics:

$$\omega(\theta, \psi, \phi) = \sum_{\ell=0}^{\infty} \sum_{m=-\ell}^{\ell} \sum_{n=-\ell}^{\ell} W_{\ell mn} Z_{\ell mn}(\cos\theta)\exp(-im\psi)\exp(-in\phi) \qquad (2)$$

where $W_{\ell mn}$ are the appropriate series coefficients, $Z_{\ell mn}$ are the augmented Jacobic polynomials, and (θ, ψ, ϕ) are Euler angles (Fig. *3a*) connecting coordinate axes embedded in the crystallite (O-XYZ) with axes coincident with the specimen and the principal working directions of the material (o-xyz). In the analysis Z was chosen as coincident with the $\hat{c}$-axis of the crystallite, and X and Y were chosen as coincident with diagonal Type-I $[\bar{1}\bar{1}20]$ and Type-II $[10\bar{1}0]$ axes, respectively. The coefficients, $W_{\ell mn}$, are evaluated using plane-normal coefficients, $Q_{\ell m}{}^{i}$, through the Legendre theorem:

$$Q_{\ell m}{}^{i} = 2\pi\left(\frac{2}{2\ell + 1}\right)^{1/2} \sum_{n=-\ell}^{\ell} W_{\ell mn} P_\ell^n(\cos\lambda_i)\exp(in\xi_i) \qquad (3)$$

where λ_i and ξ_i are the spherical polar angles relating the ith plane-normal to the crystallite coordinate system (Fig. *3c*).

Once the CODF is developed for a set of crystallographic texture pole-figures, any orientation dependent property of a bulk polycrystal can be evaluated from single crystal data. Thus

$$\langle\rho(\theta, \psi, \phi)\rangle = \int_0^{2\pi}\int_0^{2\pi}\int_{-1}^{1} \rho(\theta, \psi, \phi)\,\omega(\theta, \psi, \phi)\,d(\cos\theta)\,d\psi\,d\phi \qquad (4)$$

where $\rho(\theta, \psi, \phi)$ is the microscopic crystal property, and $\langle\rho(\theta, \psi, \phi)\rangle$ is the corresponding property of the polycrystalline aggregate.

Upper-Bound Power-Law Creep Analysis

Hutchinson [*9*] studied creep in isotropic hexagonal polycrystals using the uniform strain rate upper-bound for crystallographic slip on prism, basal, and

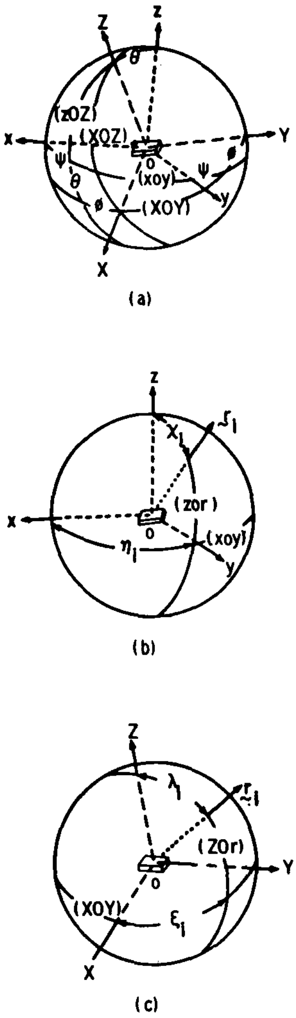

FIG. 3—*Various coordinate systems:* (a) *Crystallite coordinates* (O-XYZ) *and fabrication coordinates* (o-xyz) *connected by the Euler angles* θ, ψ, ϕ; (b) *Definition of the spherical-polar angles* χ_i, η_i *relating the fabrication coordinates* (o-xyz) *and the reciprocal lattice vector* ($\underline{r}_i$); (c) *Definition of the spherical-polar angles* λ_i, ξ_i *connecting the crystallite coordinates* (O-XYZ) *and the reciprocal lattice vector* ($\underline{r}_i$).

pyramidal planes. Slip on any discrete set of crystallographic planes is taken to be proportional to the resolved shear stress raised to a power. The strain rate perceived in the polycrystalline aggregate is imposed on each crystallite, and the stress state required to maintain this strain rate state is then computed from the power-law constitutive relationship. The stress state evaluated by averaging over the full distribution of crystallites in the material constitutes an upper-bound on the actual stress state. Thus in this uniform strain rate upper-bound method, strain compatibility between grains is automatically preserved; the stress state, however, varies from grain to grain.

We employ the method of Hutchinson [9] in applying uniform strain rate upper-bounding analysis to steady-state creep in power-law materials. Power-law creep is shown to be applicable for Zircaloy-4 at service temperatures and stresses [10]. If n is the stress exponent, the shear rate on the kth slip system can be expressed as

$$\dot{\gamma}^{(k)} = \frac{A}{\tau_0^{(k)}} \left| \frac{\tau^{(k)}}{\tau_0^{(k)}} \right|^{n-1} \tau^{(k)} \tag{5}$$

where $\tau_0^{(k)}$ is called the reference shear stress on the kth slip system and is always positive. When the resolved shear stress is equal to the reference shear stress, the strain rate is equal to the reference strain rate ($\dot{\gamma}^{(k)} = A$) independent of the stress exponent n. The total strain rate in the crystal is expressed as the sum of contributions from each of the active slip systems such that

$$\dot{\epsilon}_{ij}^{c} = \sum_{k} \mu^{(k)} \dot{\gamma}^{(k)} = M_{ijk\ell} \sigma_{k\ell} \tag{6}$$

where μ is the slip tensor and $M_{ijk\ell}$ is the tensor of creep compliances [9].

Bulk Constitutive Behavior

For a given macroscopic strain rate ($\langle \dot{\epsilon}_{\alpha\beta} \rangle$),[9] the stress states ($\sigma_{\alpha\beta}$) of crystallites are evaluated from Eqs 5 and 6; the bulk macroscopic stresses ($\langle \sigma_{\alpha\beta} \rangle$) are related to the crystallite stresses through the CODF:

$$\langle \sigma_{\alpha\beta} \rangle = \int_0^{2\pi} \int_0^{2\pi} \int_{-1}^{1} \omega(\theta, \psi, \phi)\, \sigma_{\alpha\beta}\, d(\cos\theta)\, d\psi d\phi \tag{7}$$

In evaluating the bulk stresses from this equation, proper rotations of the reference axes should be carried out prior to applying Eqs 5 and 6.

In the present analyses, the CODF for cold-worked stress-relieved Zircaloy tubing is evaluated from basal (0002), prism ($10\bar{1}0$), and pyramidal ($10\bar{1}2$) pole figures. Basal ($\{0001\}\langle 11\bar{2}0\rangle$), prismatic ($\{10\bar{1}0\}\langle 11\bar{2}0\rangle$), and pyramidal ($\{11\bar{2}2\}\langle \bar{1}\bar{1}23\rangle$) slip modes are considered, and the respective reference stresses are denoted by τ_B, τ_A, and τ_C. Values for the reference stresses are chosen to emphasize the contribution of individual or particular combinations of slip modes to the polycrystalline behavior.[10] A stress exponent of 6 for n is

---

[9] In the actual analysis the bulk stress state is specified and the principal strain rate is taken as unity.

[10] To evaluate the contribution of prismatic slip, for example, the reference stresses τ_B and τ_C are taken as 10 times τ_A.

used in these analyses, and 486 texture orientations are considered to numerically evaluate Eq 7. The isotropic texture with a random distribution of crystallites is also considered for comparison. Details on the computational scheme and computer algorithms may be found in Ref *4*.

Figure 4 compares the results of computations for basal, prismatic, and pyramidal slip modes for CW-SR texture with the isotropic case.[11] In order to fulfill the requirement for five independent slip systems, the pyramidal slip is required in any case [*9*], and Fig. 4*b* depicts the model predictions for the two cases: easy slip on basal with moderate pyramidal activity ($\tau_A > 4\tau_C = 10\tau_B$) and easy slip on prism with moderate pyramidal activity ($\tau_B > 4\tau_C = 10\tau_A$). The experimental data on CW-SR and z5 are plotted for comparison, and good correlation is noted between the CW-SR data and model predictions based on easy slip on basal and pyramidal planes. As seen in Fig. 4*a*, these experimental results also agreed very closely with computations based on basal slip alone. These results are in qualitative agreement with slip trace studies [*12,13*] which indicate increased basal and pyramidal slip activity at elevated temperatures (>700 K). However, these slip trace analyses suggest that prism slip dominates deformation of zirconium up to ~800 K [*12,13*]. The current analyses clearly indicate that preferred prism slip or combinations of prism slip with others show the greatest *deviation* from measured creep performance. Experimental results on partially recrystallized tubings z3 and z5 fall between the

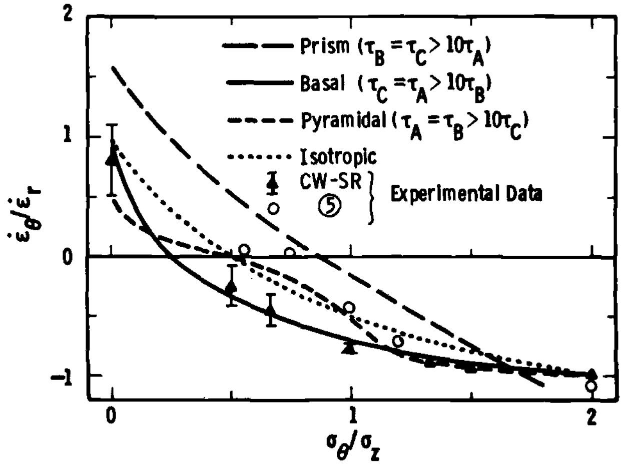

FIG. 4*a*—*Power-law predictions for the bimodal tube texture for easy slip on prism* ($\tau_B = \tau_C > 10\tau_A$), *basal* ($\tau_C = \tau_A > 10\tau_B$), *and pyramidal* ($\tau_A = \tau_B > 10\tau_C$) *planes. Isotropic texture results are included for comparison. Experimental results on CW-SR and partially recrystallized (z5) are shown.*

---

[11] Essentially identical results were obtained for different slip modes for isotropic material.

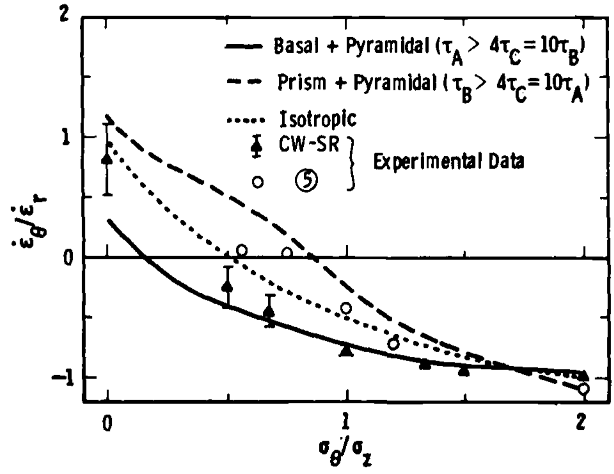

FIG. 4b—*Comparison of experimental results with predictions based on easy slip on basal + pyramidal ($\tau_A > 4\tau_C = 10\tau_B$), prism + pyramidal ($\tau_B > 4\tau_C = 10\tau_A$), and isotropic case.*

basal and prism slip computations, and are in closer agreement with analyses based on a combination of prism and basal slip modes (Fig. 5).

Phenomenological Description of Anisotropic Multiaxial Creep

Von-Mises—Hill Formulation

Hill [*14*] proposed a modified Von-Mises yield criterion for an anisotropic material with the applied stress axes coincident with the axes of anisotropy. Following the later modifications by Backofen [*15*] and Duncombe et al [*16*], a generalized stress, σ_g, is defined as the uniaxial yield stress along the axial direction so that the yield criterion reads as follows:

$$\sigma_g{}^2 = \frac{R(\sigma_r - \sigma_\theta)^2 + RP(\sigma_\theta - \sigma_z)^2 + P(\sigma_z - \sigma_r)^2}{P(R + 1)} \tag{8}$$

where σ_r, σ_θ, and σ_z are the stresses along the radial, hoop, and axial directions of the tube, and R and P are the coefficients of anisotropy [*2*]. Using the Prandtl-Reuss [*17*] energy balance and Eq 8, the strain increments or rates along the radial, hoop, and axial directions are related to the respective stresses according to the following [*8, 17*]:

$$\begin{bmatrix} \dot{\epsilon}_r \\ \dot{\epsilon}_\theta \\ \dot{\epsilon}_z \end{bmatrix} = \frac{\dot{\epsilon}_g}{P(R + 1)\sigma_g} \begin{bmatrix} (R + P) & -R & -P \\ -R & R(P + 1) & -RP \\ -P & -RP & P(R + 1) \end{bmatrix} \begin{bmatrix} \sigma_r \\ \sigma_\theta \\ \sigma_z \end{bmatrix} \tag{9}$$

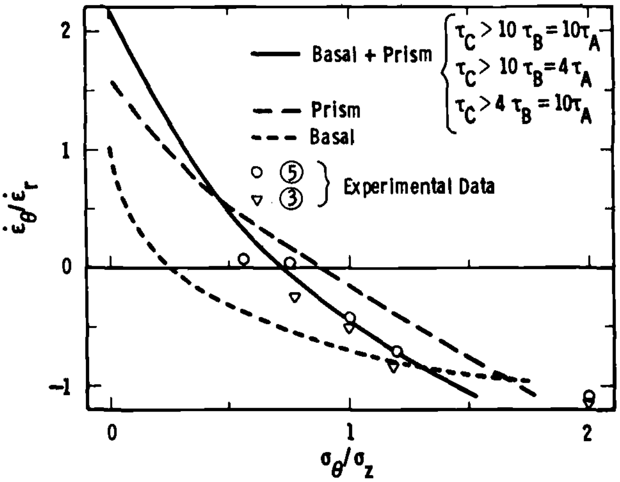

FIG. 5—*Comparison of experimental data on partially recrystallized Zircaloy-4 claddings (z3 and z5) with model predictions based on easy slip on prism, basal, and basal + prism planes.*

where $\dot{\epsilon}_g$ is the generalized strain rate equivalent to the uniaxial creep rate determined in a cylindrical specimen loaded axially to a stress σ_g. The matrix equation (9) implies that the anisotropy parameters, R and P, are given by the transverse contractile strain (rate) ratios in the uniaxial axial (z) and hoop (θ) tests, respectively:

$$R = \frac{\dot{\epsilon}_\theta}{\dot{\epsilon}_r} = \left.\frac{\Delta\epsilon_\theta}{\Delta\epsilon_r}\right)_{\epsilon_z}; \qquad \sigma_\theta = \sigma_r = 0 \qquad (9a)$$

and

$$P = \frac{\dot{\epsilon}_z}{\dot{\epsilon}_r} = \left.\frac{\Delta\epsilon_z}{\Delta\epsilon_r}\right)_{\epsilon_\theta}; \qquad \sigma_z = \sigma_r = 0 \qquad (9b)$$

For thin-walled tubing with $\sigma_r \approx 0$, the equations reduce to

$$\frac{\dot{\epsilon}_\theta}{\dot{\epsilon}_z} = \frac{[(P+1)\alpha - P]R}{[(1-\alpha)R + 1]P} \qquad (10)$$

where $\alpha = \sigma_\theta/\sigma_z$. Using constancy of volume during plastic flow, it can be shown that

$$\frac{\dot{\epsilon}_\theta}{\dot{\epsilon}_r} = \frac{P - (P+1)\alpha}{\alpha + P/R} \qquad (11)$$

The significance of Eq 11 lies in the fact that when $\alpha = 0$ the strain rate ratio is equal to R, and the strain rate ratio is zero at $\alpha = P/(P + 1)$. Thus, in principle, R and P can be inferred directly from a plot of $\dot{\epsilon}_\theta/\dot{\epsilon}_r$ versus α by noting these two conditions. In practice, however, the experimental scatter and uncertainty precludes an accurate evaluation of these parameters, in particular, R corresponding to the intercept on the strain rate axis at $\alpha = 0$ (Fig. 2).

Correlation with Experimental Results

Before describing the correlations between the predictions of Hill's formulation and the experimental creep results, it should be pointed out that R has been determined directly from contractile strain measurements for Zircaloy-4 tubing as a function of the annealing temperature (partial recrystallization) as well as the test temperature for CW-SR [*2,11*]. The contractile strain ratio, R, was shown to be essentially independent of the test temperature up to ~700 K and to be relatively insensitive to the annealing temperatures to ~843 K. Thus it can be inferred that R is a function of the fabrication parameters such as the amount of cold-work and Q-ratio,[12] which have an effect on the basal pole texture. Recent calculations [*18*] indicate that R is related to the basal pole angle, $\hat{\phi}$:

$$R = \cot^2 \hat{\phi} \tag{12}$$

and, as pointed out earlier, the final annealing temperature results in a small decrease in the basal pole angle [*2*].

In correlating the experimental results on CW-SR and partially recrystallized tubings, the R-parameters are evaluated using Eq 12. The other anisotropy parameter, P, is evaluated from the value of α at $\dot{\epsilon}_\theta/\dot{\epsilon}_r = 0$:

$$P = \left(\frac{\alpha}{1 - \alpha}\right)_{\dot{\epsilon}_\theta/\dot{\epsilon}_r = 0} \tag{13}$$

Thus evaluated, R and P parameters are shown in Table 2, where the relevant results from the experimental data are included. The ratio of the anisotropy parameters (R/P) thus evaluated can be compared with that calculated from equi-biaxial ($\sigma_\theta = \sigma_z$) test data:

$$\left.\frac{\dot{\epsilon}_\theta}{\dot{\epsilon}_z}\right)_{\sigma_\theta/\sigma_z = 1} = \frac{R}{P} \tag{14}$$

---

[12] Q is the ratio of wall thinning to diametral decrease.

and a good correlation is noted (Table 2). Figure 6 depicts the model predictions along with the experimental data.

It is interesting to note that the strain rate ratio versus stress ratio results obtained from computations based on basal and prism slip modes (Fig. 4*a*) can also be predicted by Eq 11 with appropriate R and P parameters. As illustrated in Fig. 7, the analysis based on $R = 1.0$ and $P = 0.45$ yielded results very close to the basal slip computations, while that based on $R = 1.5$ and $P = 8.5$ explains the prism slip calculations. Thus Hill's phenomenological equations are regarded as good approximations of the multiaxial creep behavior of textured Zircaloy-4 in the stress ratio regime from $\alpha = 0$ to 2.

Discussion

Prior experimental observations of slip in the zirconium lattice have suggested that prism slip plays a dominant role in deformation up to temperatures on the order of 800 K [*12,13*]. Application of the power-law upper-bounding scheme to CW-SR tubing at 673 K strongly suggests, however, that prism slip plays a secondary role in the observed deformation. Preferred activity on the basal or basal plus pyramidal slip systems most closely fits the experimental data; preferred prism slip or combinations of prism slip with basal and pyramidal activity show the *greatest deviation* from measured creep performance at this temperature. Thus the model indicates that basal and pyramidal dislocations are dominant in slip processes during creep at 673 K and presumably multiply during transient creep. The prism dislocations already present as a consequence of prior cold work during forming do not have a major role in slip, although they are important sinks for interstitials produced in irradiation [*19*]. The reason for the lack of dominance of the prism system is not clear, but it may simply indicate that the system has been hardened by the prior deformation sufficiently that the other systems become preferred during high temperature slip. Alternatively, the slip systems may be such that basal

TABLE 2—*Multiaxial creep results of Zircaloy-4.*

Material	R^a	P^b	R/P^c	$\left(\frac{\dot{\epsilon}_\theta}{\dot{\epsilon}_z}\right)_{1:1}$
CW-SR	1.50	0.40	3.75	3.65
z1	1.49	0.45	3.33	3.17
z2	1.54	0.67	2.24	2.64
z3	1.39	1.22	1.23	1.00
z5	1.51	1.94	0.77	0.87

[a] $R = \cot^2 \hat{\phi}$; $\langle R \rangle = 1.5$
[b] $P = \alpha'/1 - \alpha'$; α' is stress ratio at $\dot{\epsilon}_\theta = 0$.
[c] With $R = 1.5$.

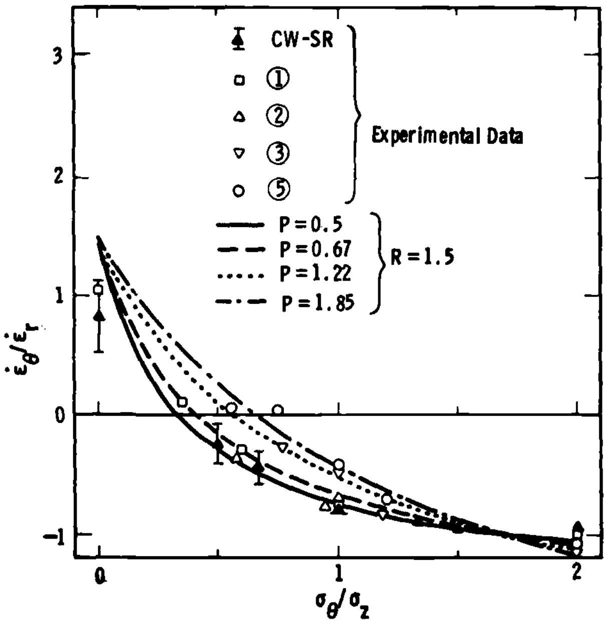

FIG. 6—*Comparison of experimental data on CW-SR and partially recrystallized Zircaloy-4 tubings with predictions based on Von-Mises—Hill formulation with* R = *1.5 and various* P-*values.*

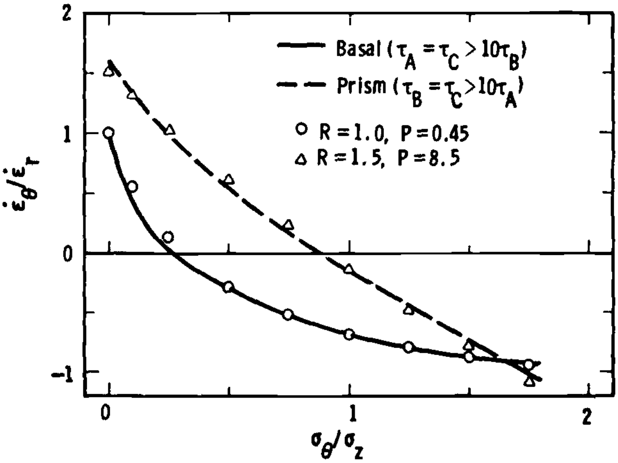

FIG. 7—*Comparison of power-law model results based on easy slip on basal and prism planes, with predictions of Von-Mises—Hill formulation with appropriate* R *and* P *parameters.*

slip is favored at elevated temperatures and low strain rates. Further work is needed to resolve this issue.

In evaluating the effect of partial recrystallization, the CODF generated for CW-SR texture is used in the computations. Preliminary calculations indicate that the minor modifications due to increasing annealing temperature affect higher order ($\ell \gtrsim 6$) terms in CODF and thus will have second-order effects on the results. It is interesting to note that increasing partial recrystallization (that is, higher annealing temperature) exhibited creep results in close agreement with the calculations based on prism and/or prism + basal slip modes. This indicates that part of the hardening of prism systems occurred during fabrication is relaxed due to higher final annealing temperatures. It is thus predicted that full recrystallization would yield creep results in agreement with preferred prism slip calculations.

As demonstrated in the previous section, the Von-Mises—Hill phenomenological formulation of anisotropic deformation yields a reasonable description of the creep behavior of the CW-SR and partially recrystallized Zircaloy tubing with appropriate anisotropy parameters, R and P. In addition, the computations based on basal and prism slip operations can be approximated by Hill's equations with appropriate R and P parameters. These analyses show that the P-parameter is less than unity for highly CW-SR material and increases with increasing partial recrystallization to relatively large values compared with unity. Thus the CW-SR tubing is predicted to exhibit relatively (compared with axial) higher uniaxial hoop creep-rate ($P < 1$) compared with the recrystallized material with $P > 1$, as experimentally observed [*1*]. These findings are also in agreement with contractile strain measurements which revealed that the room temperature P-value for recrystallized tubing is approximately three times that for CW-SR [*2*].

Summary and Conclusions

The anisotropic nature of creep of Zircaloy-4 is strongly linked to the preferred orientation of crystallites in the bulk polycrystal. Textures arise in these materials during forming operations because of the restricted number of independent slip systems. Plots of the strain rate ratio ($\dot{\epsilon}_\theta/\dot{\epsilon}_r$) versus stress ratio ($\sigma_\theta/\sigma_z$) indicate significant differences between CW-SR and partially recrystallized material. These materials have essentially identical basal pole textures, and exhibit important differences in prism pole distributions.

Multiaxial creep behaviors of these materials are examined by first determining the crystallite orientation distribution function from CW-SR texture (basal, prism, and pyramidal) pole figures. Power-law creep was modeled by use of the upper-bound estimate with the assumption that prism, basal, and pyramidal slip modes and combinations thereof are possible mechanisms. As compared with the CW-SR creep data, the model approximates the experimental results when prism slip is substantially hardened, and either easy slip on basal plane or basal slip with moderate pyramidal activity is found to be the operative mechanism. As the degree of partial recrystallization increases, the dominant slip mode is found to shift from basal slip alone to basal + prism slips, and complete recrystallization is predicted to exhibit prism slip.

These results, in addition, are correlated with Hill's phenomenological formulation of multiaxial deformation of anisotropic materials, and an excellent agreement is noted with appropriate anisotropy (R and P) parameters. The R-parameter was relatively insensitive to the annealing temperature, while P increased as the degree of partial recrystallization increased. These findings are consistent with the fact that the recrystallized cladding exhibits relatively higher hoop creep resistance with respect to the axial.

Acknowledgments

The authors would like to thank Prof. J. P. Hirth for valuable discussions and Dr. G. P. Sabol for a critical review of the manuscript.

References

[*1*] Kallstrom, K., Andersson, T., and Hofvenstem, A. in *Zirconium in Nuclear Applications, ASTM STP 551*, American Society for Testing and Materials, 1974, p. 160.

[*2*] Beauregard, R. J., Clevinger, G. S., and Murty, K. L. in *Proceedings*, 4th International Conference on SMIRT, San Francisco, August 1977, Paper C3/5.

[*3*] Stehle, H., Steinberg, E., and Tenckhoff, E. in *Zirconium in the Nuclear Industry, ASTM STP 633*, American Society for Testing and Materials, 1977, p. 486.

[*4*] Adams, B. L., "An Upper-Bound Analysis of Inelastic Deformation in Textured Hexagonal Polycrystals (ZIRCALOY)," Ph.D. thesis, Ohio State University, 1979.

[*5*] Hutchinson, J. W., *Metallurgical Transactions*, Vol. 8A, 1977, p. 1465.

[*6*] Roe, R. J., *Journal of Applied Physics*, Vol. 36, 1965, p. 2024.

[*7*] Bunge, H. J., *Zeitschrift für Metallkunde*, Vol. 56, 1965, p. 872.

[*8*] Clevinger, G. S., Adams, B. L., and Murty, K. L. in *Zirconium in the Nuclear Industry, ASTM STP 681*, American Society for Testing and Materials, 1979, p. 189.

[*9*] Hutchinson, J. W., *Proceedings of Royal Society*, London, Vol. 348A, 1976, p. 101.

[*10*] Murty, K. L. and McDonald, S. G. in *Proceedings*, 6th International Conference on SMIRT, Paris, Aug. 1981, Paper C2/3.

[*11*] Lucas, G. E., "Effects of Anisotropy and Irradiation on the Creep Behavior of Zircaloy-2," Ph.D. thesis, Massachusetts Institute of Technology, 1978.

[*12*] Martin, J. L. and Reed-Hill, R. E., *Transactions*, American Institute of Mining and Metallurgical Engineers, Vol. 230, 1964, p. 780.

[*13*] Tenckhoff, E., *Zeitschrift für Metallkunde*, Vol. 63, 1972, p. 192.

[*14*] Hill, R., *Proceedings of Royal Society*, London, Vol. 193A, 1948, p. 281.

[*15*] Backofen, W. A., *Deformation Processing*, Addison-Wesley, 1972.

[*16*] Duncombe, E., Friedrich, C. M., and Guilinger, W. H., *Nuclear Technology*, Vol. 12, 1971, p. 194.

[*17*] Lucas, G. E. and Bement, A. L., *Journal of Nuclear Materials*, Vol. 55, 1975, p. 246.

[*18*] VanSwam, L. F. P., Knorr, D. B., Pelloux, R. M., and Shewbridge, J. F., *Metallurgical Transactions*, Vol. 10A, 1979, p. 483.

[*19*] Adams, B. L., Clevinger, G. S., and Hirth, J. P. in *Proceedings*, International Conference on Fundamental Mechanisms of Radiation-Induced Creep and Growth, 1979; *Journal of Nuclear Materials*, Vol. 90, 1980, p. 75.

Alan Wolfenden[1]

Comparison of Predictions of Work-Hardening Theories for Two-Phase Alloys in Terms of Stored Energy: Eutectic Alloys Al-Al_3Fe and Al-Al_6Fe

---

REFERENCE: Wolfenden, Alan, "**Comparison of Predictions of Work-Hardening Theories for Two-Phase Alloys in Terms of Stored Energy: Eutectic Alloys Al-Al_3Fe and Al-Al_6Fe,**" *Mechanical Testing for Deformation Model Development, ASTM STP 765,* R. W. Rohde and J. C. Swearengen, Eds., American Society for Testing and Materials, 1982, 397-414.

ABSTRACT: Two theories [Brown and Clarke (B-C) and Tanaka and Mori (T-M)] that treat work hardening in two-phase alloys take into account the effects of precipitate shape, elastic inhomogeneity, and deformation mode. Both theories calculate the initial work hardening rate (θ), but in addition the T-M theory estimates the strain dependence of the stored energy, and the ratio of stored to expended energy. The experimental data of Adam and Wolfenden, which include values of stress, strain (ϵ), stored energy (E_s), and expended energy (E_w) for unidirectionally solidified eutectic alloys Al-Al_3Fe and Al-Al_6Fe, are used for comparing the abilities of the two theories to fit the data. The comparison shows that the parameters in both theories may be adjusted to give good values for θ, and that T-M theory yields excellent agreement for E_s/E_w for both alloys and for E_s/ϵ^2 for the Al-Al_6Fe alloy.

KEY WORDS: work hardening, two-phase alloys, composites, stored energy, eutectics, aluminum-iron alloys, calorimetry, stress, strain, expended energy

In two-phase alloys with a homogeneous dispersion of a second phase in the matrix, the dislocation-precipitate interactions govern the work-hardening behavior to a large extent. One set of theoretical analyses of the work-hardening characteristics of these systems deals with analyzing the problem in terms of continuum mechanics on the basis of energy considerations. Thus the free energy of the specimen is calculated for a matrix which flows plastically while the precipitates deform elastically. Boundary conditions must be

---

[1] Associate Professor, Mechanical Engineering Department, Texas A&M University, College Station, Tex. 77843; formerly Senior Engineer, Westinghouse R&D Center, Pittsburgh, Pa. 15235.

satisfied for precipitates of different shapes, and hence the effects of precipitate shape and volume fraction can be studied.

Recently Adam and Wolfenden [*1*][2] investigated the energy relations involved in the plastic deformation of several aluminum alloys, including two aluminum-iron fibrous eutectic alloys, Al-Al_3Fe and Al-Al_6Fe. The authors found that the stored energy data for the eutectic alloys were in good agreement with the predictions of the work-hardening theories for two-phase alloys of Brown and Clarke [*2*] (B-C) and Tanaka and Mori [*3*] (T-M). In both treatments of work hardening due to internal stresses in two-phase materials, expressions for the initial work-hardening rate (θ) during plastic deformation were derived, taking into account the effects of precipitate shape, elastic inhomogeneity, and deformation mode. The pertinent equations, which will be presented later, involve such terms as [*2,3*] the accommodation factor (γ), the modulus correction factor to account for elastic inhomogeneity (D), the shear modulus of the matrix (μ), the volume fraction of the precipitates (f), Young's modulus of the matrix (E), and Poisson's ratio of the matrix (ν), together with corresponding terms for the precipitates. The asterisked parameters in this paper refer to the precipitates. In their analysis Adam and Wolfenden [*1*] made the simplifying assumptions that $D = 1$, $\nu = \nu^* = 0.33$, and $E = E^*$. Here such assumptions will not be imposed. A reevaluation of the predictions from the B-C and T-M theories will be made and the results compared with the calorimetric data.

Predictions and Discussion

B-C Theory

In this theory the expression for the tensile stress (σ) which is twice the shear stress, is

$$\sigma = 4\gamma D\mu f\epsilon \tag{1}$$

where ϵ is the plastic strain. Hence the initial work-hardening rate is given by

$$\theta = 4\gamma D\mu f \tag{2}$$

The precise meanings of the terms γ and D, the accommodation factor and the modulus correction factor, respectively, are complicated and involve a yield criterion. Briefly, the values for γ and D are dependent on the shape of the precipitates and their orientation with respect to the tensile axis, and on the slip conditions for the dislocations in the matrix (for example, single slip or

---

[2] The italic numbers in brackets refer to the list of references appended to this paper.

multiple slip). For the choice of values of γ and D in this investigation we have accepted those listed in the B-C and T-M papers [*2,3*]. The precipitates have dimensions a, b, and c, measured along orthogonal axes, where the c-axis and the tensile axis (TA) of the specimen are parallel. We shall consider three cases which may be applicable to the eutectics alloys:

1. Fibers parallel to the TA, $a = b$, $c \rightarrow \infty$.

For this case the accommodation factor for multiple slip (MS), which is the likely form of slip for these alloys, is given by [*2*]:

$$\gamma_{MS} = (1.25 - \nu)/2(1 - \nu). \tag{3}$$

With ν for the aluminum matrix taken as 0.33, $\gamma_{MS} = 0.687$. The value of D for fibers is [*2*] $0.94\ \mu^*/\mu$. The shear and Young's moduli are related by

$$E = 2\mu(1 + \nu) \tag{4}$$

and

$$E^* = 2\mu^*(1 + \nu^*) \tag{5}$$

2. Ribbons parallel to the TA, $a = 3b$, $c \rightarrow \infty$.

To study the case of ribbons, we have set $a = 3b$ as typifying many of the observed ribbon-like precipitates in $Al-Al_3Fe$. The accommodation factor for ribbons is [*2*]:

$$\gamma_{MS} = [3a(1 - \nu) + b(2 - \nu)]/[4(1 - \nu)(a + b)] \tag{6}$$

Taking $a = 3b$ and $\nu = 0.33$, γ_{MS} is 0.718. Again the value of D is 0.94 μ^*/μ.

3. Discs parallel to the TA, $b = c > a$.

For this particular case γ_{MS} is 0.75 and D is μ^*/μ.

We are almost in a position to begin the computations of θ with Eq. 2. Firstly we must assign values to E^* and ν^*, the Young's modulus and Poisson's ratio of the precipitates. These values are not known, since they have never been measured for such small (~300 nm) diameter fibers or disks. We estimate the values by setting $E^* = Ex$ and $\nu^* = \nu y$, where $x = 1.0$, 1.1, or 1.2, and $y = 0.8$, 0.9, 1.0, 1.1, or 1.2. For the matrix (Al) $E = 69$ GPa and $\nu = 0.33$.

Now Eq 2 is used to compute θ for all combinations of E^* and ν^* with the measured fractions (f) for precipitates (0.045 or 0.05 for $Al-Al_3Fe$ [*1*] and 0.1 for $Al-Al_6Fe$ [*1*]) for the three cases outlined. Out of the many values thus generated for θ we search out those which agree well with the experimental values [*1*] of initial work-hardening of θ (3.8 GPa for $Al-Al_3Fe$ and 5.9 GPa for $Al-Al_6Fe$). The results of the calculations are shown in Table 1. To keep

TABLE 1—*Calculated work-hardening rates according to the theory of Brown and Clarke.*

NOTE—E^* is Young's modulus of the precipitate.
ν^* is Poisson's ratio of the precipitate.
f is the volume fraction of the precipitate.
D is the modulus correction factor to account for elastic inhomogeneity.
γ is the accommodation factor.
MS denotes multiple slip.
TA is the tensile axis.
a, b, and c are the dimensions of the precipitate with c//TA.

Experimentally Observed Work-Hardening Rate, θ/GPa	Al-Al_3Fe					Al-Al_6Fe				
	3.8					5.9				
Theoretical Values, θ/GPa	E^*/GPa	ν^*	f	D	θ^a	E^*/GPa	ν^*	f	D	θ^b
$\gamma = 0.687$	69	0.264	0.05	1.05	3.74	69	0.264	0.1	0.99	7.03
MS							0.297	0.1	0.96	6.89
Fibers//TA							0.330	0.1	0.94	6.69
$a = b; c \rightarrow \infty$							0.363	0.1	0.92	6.52
							0.396	0.1	0.90	6.37
	76	0.264	0.045	1.16	3.70	76	0.264	0.1	1.09	7.74
		0.264	0.05	1.09	3.87		0.297	0.1	1.06	7.54
		0.297	0.05	1.06	3.77		0.330	0.1	1.03	7.35
		0.363	0.05	1.07	3.82		0.363	0.1	1.01	7.18
		0.396	0.05	1.05	3.73		0.396	0.1	0.99	7.01
	83	0.264	0.045	1.19	3.80	83	0.264	0.1	1.19	8.44
		0.297	0.045	1.16	3.70		0.297	0.1	1.16	8.23

		0.330	0.045	1.20	3.84		0.330	0.1	1.13	8.02
		0.363	0.045	1.17	3.75		0.363	0.1	1.10	7.83
		0.396	0.05	1.07	3.82		0.396	0.1	1.07	7.64
$\gamma = 0.718$	69	0.297	0.05	1.03	3.82	69	0.297	0.1	0.96	7.17
MS		0.330	0.05	1.00	3.72		0.330	0.1	0.94	6.99
Ribbons//TA	76	0.264	0.045	1.16	3.88	76	0.264	0.1	1.09	8.10
$a = 3b;\ c \to \infty$		0.297	0.045	1.13	3.78		0.297	0.1	1.06	7.89
		0.330	0.05	1.03	3.85		0.330	0.1	1.03	7.69
		0.363	0.05	1.01	3.75		0.363	0.1	1.01	7.51
		0.396	0.05	1.05	3.90		0.396	0.1	0.99	7.33
	83	0.297	0.045	1.16	3.87	83	0.297	0.1	1.16	8.61
		0.330	0.045	1.13	3.78		0.330	0.1	1.13	8.39
		0.396	0.045	1.14	3.83		0.396	0.1	1.07	8.00
$\gamma = 0.750$	69	0.264	0.05	0.99	3.84	69	0.264	0.1	1.05	8.18
MS		0.297	0.05	0.96	3.74		0.297	0.1	1.03	7.97
Disks//TA		0.330	0.05	1.00	3.88		0.330	0.1	1.00	7.77
$b = c > a$		0.363	0.05	0.98	3.79		0.363	0.1	0.98	7.58
		0.396	0.05	0.95	3.70		0.396	0.1	0.95	7.40
	76	0.264	0.045	1.09	3.80	76	0.264	0.1	1.16	8.99
		0.297	0.045	1.06	3.71		0.297	0.1	1.13	8.76
		0.330	0.045	1.10	3.85		0.330	0.1	1.10	8.55
		0.363	0.045	1.07	3.75		0.363	0.1	1.07	8.34
		0.396	0.05	0.99	3.83		0.396	0.1	1.05	8.14
	83	0.363	0.045	1.10	3.85	83	0.363	0.1	1.17	9.10
		0.396	0.045	1.07	3.76		0.396	0.1	1.14	8.88

[a] Agreement between experiment and theory to within ±2.6 percent.

[b] Agreement between experiment and theory for fibers to within +(8 to 54) percent.

the number of results down to a reasonable level we show only the theoretical values of θ that agree to within ±2.6 percent (Al-Al_3Fe) or to within +(8 to 54) percent (for fibers in Al-Al_6Fe) of the measured values.

It is obvious from Table 1 that a wide variety of combinations of E^* and ν^* will give agreement between the theoretical and experimental values of θ. We shall discuss those conditions which would correspond to the known microstructures of the alloys. For the Al-Al_3Fe alloy the branched platelet microstructure can be approximated to a series of curved disks or long ribbons. Thus we examine the results of calculations for disks and ribbons. Excellent agreement (to within 2.6 percent) for the θ-values is obtained for disks with E^*/E in the range 1.0 to 1.2 and ν^*/ν values ranging from 0.8 to 1.2 (for $E^*/E = 1.0$ or 1.1) or from 1.1 to 1.2 (with $E^*/E = 1.2$). The modulus correction factor D remains within 10 percent of unity. For ribbons similar agreement is found for ν^*/ν values in the range 0.9 to 1.0 with $E^*/E = 1.0$, 0.8 to 1.2 with $E^*/E = 1.1$, and 0.9 to 1.2 with $E^*/E = 1.2$. Here D remains within 16 percent of unity. The exact value of the volume fraction is not critical for f in the range of 0.045 to 0.05. The range of E^*-values for agreement is acceptable, since one expects a fiber-reinforced composite to have $E^* > E$. Other measurements [*4*] of Young's modulus for this system using a high-precision mechanical method gave a value of E^* that is about 10 percent higher than E, that is, around 75 GPa. This investigation shows that the B-C theory predicts values of the work-hardening rate for Al-Al_3Fe that are in excellent agreement with the experimentally measured ones.

The Al-Al_6Fe composite has a microstructure that consists of very evenly spaced cylindrical Al_6Fe fibers parallel to the tensile axis (fiber diameter about 300 nm, fiber spacing around 1 μm). The volume fraction of the precipitates can be estimated quickly by considering that each fiber of diameter 300 nm occupies an area that can be approximated to a square of side 1 μm. Then $f \approx (\pi/4)\,(300\ \text{nm})^2/(1\ \mu\text{m})^2 = 0.07$. For this alloy of $f = 0.1$ we examine the calculated values of θ for fibers parallel to the TA (Table 1). The dependence of $\theta_{\text{theo}}/\theta_{\text{exp}}$ (ratio of theoretical to experimental values of θ) on the choice of E^*/E and ν^*/ν is also shown graphically for this alloy in Fig. 1. Here we see that for agreement with the experimental value of 5.9 GPa to within +(8 to 54) percent there are several acceptable conditions, namely combinations with $\nu^*/\nu = 0.8$ to 1.2 and $E^*/E = 1.0$ to 1.2 while D remains with 19 percent of unity. The best agreement is obtained with $\nu^*/\nu = 1.2$ and E^* slightly greater than E. Hence this investigation suggests that Young's modulus for the fiber may be up to about 10 percent larger than that for the matrix (in agreement with other measurements [*4*]) and its Poisson's ratio may be near 0.4. For the second alloy the B-C theory predicts θ-values that are in good agreement with experiment. The results of the calculations of θ for ribbons and disks for Al-Al_6Fe are included in Table 1 only for completeness. Such microstructures were not observed in the Al-Al_6Fe alloy,

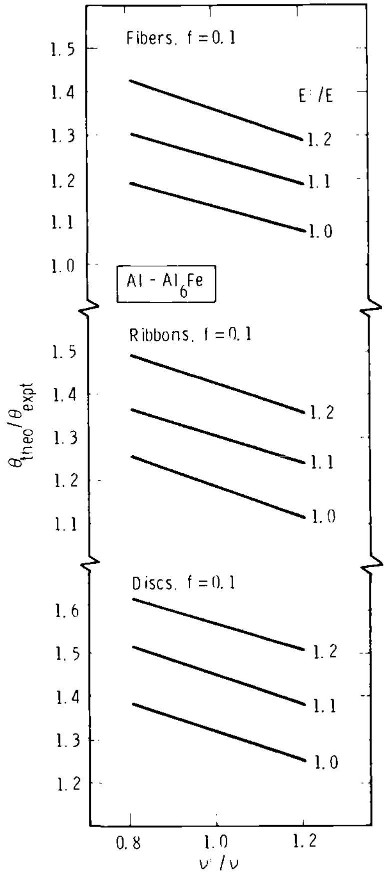

FIG. 1—*Dependence of the ratio of theoretical to experimental initial work-hardening rate for Al-Al$_6$Fe on the ratio of Poisson's ratios for the precipitate and the matrix for various shapes of precipitates and ratios of Young's moduli. Volume fraction* f = *0.1 (B-C theory).*

and in any case these calculated θ-values generally overestimate the experimentally observed work-hardening rate.

T-M Theory

This theory is comprehensive in that, besides providing relations for the initial work-hardening rate (θ) of two-phase alloys, an equation for the strain dependence of the stored energy is available. Also, by simple manipulations, an expression for the ratio of stored to expended energy can be obtained from this theory. These three functions will be presented in turn and the predictions assessed in terms of the experimental results for the two eutectic alloys.

It should be noted that the T-M theory was developed for systems which exhibit linear work hardening, independent of strain. Although the Al-Al_3Fe fits into this category quite well, the Al-Al_6Fe shows some departure from linear work hardening for strains above about 0.03, and the extension of the theory to higher strains for Al-Al_6Fe may not be justified on a theoretical basis.

Work-Hardening Rate (θ)—The theoretical work-hardening rate is given by

$$\theta = AE/(1 - B) \qquad (7)$$

where A and B are specific functions of E, E^*, ν, ν^*, and f whose values depend on the microstructure of the two-phase system. We shall consider two cases appropriate to this investigation.

1. Fibers parallel to the TA.

In this situation, which is expected to hold for the Al-Al_6Fe alloy, the terms A and B are given by Tanaka and Mori [*3*] as

$$A = [3(1 - 2\nu^*)E + 2(1 + \nu)E^*]E^*f/XE \qquad (8)$$

where

$$X = 2[(1 + \nu^*)(1 - 2\nu^*)E + (1 + \nu)E^*] \qquad (9)$$

$$B = (1 + \nu)[(1 - 2\nu^*)E + E^*]E^*f/YE \qquad (10$$

where

$$Y = (1 + \nu^*)(1 - 2\nu^*)E + (1 + \nu)E^* \qquad (11)$$

2. Disks parallel to the TA.

Here the equations for A and B are

$$A = (5 - 4\nu^*)E^*f/4E(1 - \nu^{*2}) \qquad (12)$$

$$B = [(2 - \nu^*) + \nu(1 - 2\nu^*)]E^*f/2E(1 - \nu^{*2}) \qquad (13)$$

The microstructure of the Al-Al_3Fe eutectic alloy may be approximated to this situation.

Computations with Eqs 7 to 13 were done with $E^* = Ex$, $\nu^* = \nu y$ (where $x = 1.0$, 1.1, or 1.2, and $y = 0.8$, 0.9, 1.0, 1.1, or 1.2), and values of E and ν for the matrix of 69 GPa and 0.33, respectively, for the Al-Al_3Fe ($f = 0.045$ or 0.05) and the Al-Al_6Fe ($f = 0.1$) alloys to calculate their work-hardening rates (θ). Table 2 lists the results which come close to the measured work-hardening rates of 3.8 and 5.9 GPa for Al-Al_3Fe and Al-Al_6Fe, respectively. The basis of selection this time is agreement to within ±5.3 percent for the Al-Al_3Fe data and to within +(31 to 68) percent for fibers in the Al-Al_6Fe eutectic. Graphical presentations of $\theta_{theo}/\theta_{exp}$ as a function of ν^*/ν are given in Figs. 2 and 3 for Al-Al_3Fe and Al-Al_6Fe, respectively.

In discussing the results presented in Table 2 and Figs. 2 and 3 we start with the Al-Al_3Fe alloy. As stated earlier, the microstructure of this system resembles curved disks, but has features in places that are fiber-like [*1*], though not of "infinite" length. We examine therefore the predictions of the T-M theory for both fibers or disks parallel to the TA, and find that the calculated values of θ are in excellent agreement with the measured value of 3.8 GPa. The agreement for combinations of E^* and ν^* values is to within ±5.3 percent. For example, such agreement holds for fibers or disks with ν^*/ν = 0.8 to 1.2 for E^*/E = 1.0 or 1.1 and with ν^*/ν = 1.2 for E^*/E = 1.2 Further, the agreement is excellent for disks with E^*/E = 1.1 and ν^*/ν = 0.8, which is in accord with the report [*4*] that Young's modulus for the precipitate is about 10 percent higher than that for the matrix. The difference in the volume fractions (0.045 versus 0.05) considered here has no significant impact on the calculations of θ. The terms A and B for the Al-Al_3Fe remain within 10 percent of 0.05, which indicates that these terms are not very sensitive to the particular combinations of E, E^*, ν, ν^*, and f used in the computations with Eqs 8 to 13.

The microstructure of the Al-Al_6Fe alloy consists of fibers parallel to the TA, and hence only the results of calculations for fibers given in Table 2 and Fig. 3 will be considered for the second alloy. Clearly the predicted values of θ exceed the measured value by 31 to 68 percent for the combinations of E^*/E and ν^*/ν in the ranges of 1.0 to 1.2 and 0.8 to 1.2, respectively. Closest agreement comes with E^*/E around unity and with ν^*/ν = 1.2, in accord with the trends noted earlier and elsewhere [*4*]. However, the level of agreement for Al-Al_6Fe is not as good as that found for the other alloy. Again the terms A and B remain fairly constant for $E^* \leq 76$ GPa, that is, within 16 percent of 0.100. Essentially A and B are equal to the volume fraction f when E^*/E and ν^*/ν are not far from unity. The predicted values for θ for disks in Al-Al_6Fe are given in Table 2 for completeness, but are not pertinent to the present discussion. In summary, the predicted values of θ for fibers or disks with the T-M theory fall within about 5 percent of the measured value for Al-Al_3Fe, whereas the predicted values for Al-Al_6Fe fall within 30 to 70 percent of the measured value. Some of this poorer agreement may result from our extending the application of the theory into a region beyond that of linear work-hardening.

Strain Dependence of Stored Energy (E_s/ϵ^2)—The strain energy of the matrix/precipitate system has been derived by Tanaka and Mori [*3*] for disk-

TABLE 2—*Calculated work-hardening rates according to the theory of Tanaka and Mori.*

NOTE—A and B are the terms in the equation $\theta = AE/(1 - B)$, where E is the Young's modulus of the matrix (69 GPa).

Experimentally Observed Work-Hardening Rate, θ/GPa	Al-Al_3Fe						Al-Al_6Fe					
	3.8						5.9					
Theoretical Values, θ/GPa	E^*/GPa	ν^*	f	A	B	θ^a	E^*/GPa	ν^*	f	A	B	θ^b
Fibers//TA	69	0.264	0.05	0.053	0.051	3.84	69	0.264	0.1	0.106	0.102	8.11
		0.297	0.05	0.053	0.050	3.79		0.297	0.1	0.104	0.101	8.00
		0.330	0.05	0.052	0.050	3.74		0.330	0.1	0.103	0.100	7.90
		0.363	0.05	0.051	0.050	3.70		0.363	0.1	0.102	0.099	7.82
		0.396	0.05	0.051	0.050	3.67		0.396	0.1	0.101	0.099	7.75
	76	0.264	0.045	0.052	0.050	3.78	76	0.264	0.1	0.116	0.112	8.99
		0.297	0.045	0.052	0.050	3.74		0.297	0.1	0.115	0.111	8.87
		0.330	0.045	0.051	0.050	3.70		0.330	0.1	0.113	0.110	8.77
		0.363	0.045	0.051	0.050	3.66		0.363	0.1	0.112	0.109	8.68
		0.396	0.045	0.050	0.050	3.63		0.396	0.1	0.111	0.109	8.61
	83	0.396	0.045	0.055	0.054	3.98	83	0.264	0.1	0.126	0.122	9.89
								0.297	0.1	0.125	0.121	9.77
								0.330	0.1	0.123	0.120	9.66
								0.363	0.1	0.122	0.119	9.57
								0.396	0.1	0.121	0.119	9.49

Disks//TA	69	0.264	0.05	0.053	0.051	3.85	69	0.264	0.1	0.106	0.102	8.13
		0.297	0.05	0.053	0.050	3.79		0.297	0.1	0.105	0.101	8.01
		0.330	0.05	0.052	0.050	3.74		0.330	0.1	0.103	0.100	7.90
		0.363	0.05	0.051	0.050	3.70		0.363	0.1	0.102	0.099	7.82
		0.396	0.05	0.051	0.050	3.67		0.396	0.1	0.101	0.099	7.75
	76	0.264	0.045	0.052	0.050	3.81	76	0.264	0.1	0.117	0.112	9.04
		0.297	0.045	0.052	0.050	3.75		0.297	0.1	0.115	0.111	8.91
		0.330	0.045	0.051	0.050	3.70		0.330	0.1	0.114	0.110	8.79
		0.363	0.045	0.051	0.050	3.66		0.363	0.1	0.112	0.109	8.69
		0.396	0.045	0.050	0.050	3.63		0.396	0.1	0.111	0.109	8.62
	83	0.396	0.045	0.055	0.054	3.98	83	0.264	0.1	0.127	0.122	9.98
								0.297	0.1	0.125	0.121	9.83
								0.330	0.1	0.124	0.120	9.70
								0.363	0.1	0.123	0.119	9.59
								0.396	0.1	0.122	0.119	9.50

---

[a] Agreement between experiment and theory to within ±5.3 percent.

[b] Agreement between experiment and theory for fibers to within +(31 to 68) percent.

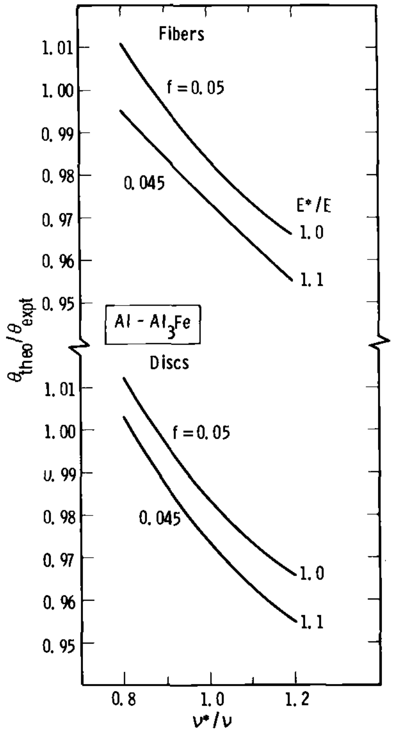

FIG. 2—*Dependence of ratio of theoretical to measured initial work-hardening rate for Al-Al_3Fe on the ratio of Poisson's ratios for the precipitate and the matrix for fibers and disks and ratios of Young's moduli 1.0 to 1.1. Volume fractions* f *are 0.045 and 0.05 (T-M theory).*

shaped and fiber-like precipitates and brings in a strain dependence. The equations for disks and fibers, respectively, are

$$E_s = (5 - 4\nu^*)E^*\epsilon^2 f/8(1 - \nu^{*2}) \tag{14}$$

and

$$E_s = [3(1 - 2\nu^*)E + 2(1 + \nu)E^*]E^*\epsilon^2 f/Z \tag{15}$$

where

$$Z = 4[(1 + \nu^*)(1 - 2\nu^*)E + (1 + \nu)E^*] \tag{16}$$

To analyze the predictions of the T-M theory the term E_s/ϵ^2, which originates in Eqs 14 and 15, has been computed for combinations of E^*/E in the range 1.0 to 1.2, ν^*/ν in the range of 0.9 to 1.1, and f values of 0.045, 0.05, and 0.1. Of the many results calculated in this way the ones which come

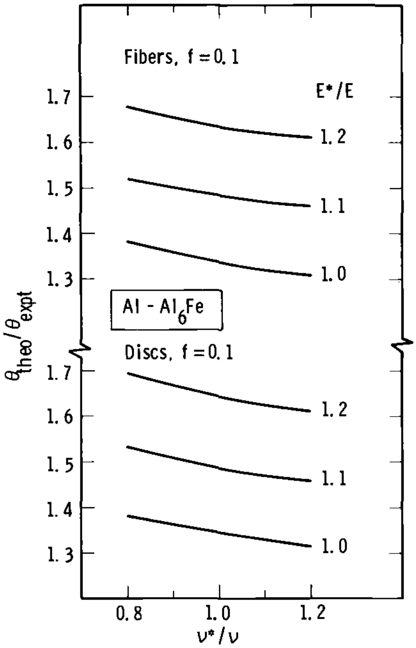

FIG. 3—*Ratio of theoretical to experimental initial work-hardening rate for Al-Al$_6$Fe as a function of the ratio of Poisson's ratios for the precipitate and matrix for fibers and disks, with volume fraction* f $= 0.1$ *and the ratios of Young's moduli 1.0, 1.1, and 1.2 (T-M theory).*

close to the experimentally measured values of E_s/ϵ^2 of 8.8 and 41.8 kJ/mol (for Al-Al$_3$Fe and Al-Al$_6$Fe, respectively) are presented in Table 3. The calculated values of E_s/ϵ^2 for disks and fibers are identical.

For the Al-Al$_3$Fe alloy the theory overestimates the measured value of E_s/ϵ^2 by at least 80 percent. Closest agreement comes with $E^* = E$ and a value of ν^* of 0.363. Undoubtedly, higher values of ν^* would improve the agreement slightly, but values of Poisson's ratio normally lie between 0.25 and 0.5. The variation in the measured values of volume fraction for the precipitate in Al-Al$_3$Fe (0.045 to 0.05) results in a difference of 11 percent in the calculated E_s/ϵ^2 values. Thus the T-M theory leads to a dependence of stored energy on plastic strain that overestimates the measured dependence. The reason for this overestimate may be ascribed to the approximation that the microstructure of the precipitates in Al-Al$_3$Fe resembles disks or fibers.

Table 3 indicates that for the Al-Al$_6$Fe alloy the calculated values of E_s/ϵ^2 are in very good agreement with the measured value, the agreement being to within +3 to −16 percent for the range of values used for E^* and ν^*. Excellent agreement is obtained with $E^* = 83$ GPa and $\nu^* = 0.396$, such a value of Young's modulus for the fiber agreeing with previous measurements

TABLE 3—*Calculated values of* E_s/ϵ^2 *from the theory of Tanaka and Mori.*

NOTE—E_s is stored energy; ϵ is plastic strain.

Experimentally Observed Value of E_s/ϵ^2(kJ/mol)	Al-Al_3Fe				Al-Al_6Fe			
	8.8				41.8			
Theoretical Values of E_s/ϵ^2(kJ/mol)	E^*/GPa	ν^*	f	E_s/ϵ^2 Disks or Fibers	E^*/GPa	ν^*	f	E_s/ϵ^2 Disks or Fibers[a]
	69	0.297	0.045	16.2	69	0.297	0.1	36.0
		0.330	0.045	16.0		0.330	0.1	35.6
		0.363	0.045	15.8		0.363	0.1	35.2
		0.297	0.05	18.0				
		0.330	0.05	17.8				
		0.363	0.05	17.6				
	76	0.297	0.045	17.8	76	0.297	0.1	39.6
		0.330	0.045	17.6		0.330	0.1	39.1
		0.363	0.045	17.4		0.363	0.1	38.7
		0.297	0.05	19.7				
		0.330	0.05	19.5				
		0.363	0.05	19.3				
					83	0.297	0.1	43.1
						0.396	0.1	41.8

[a] Agreement between experiment and theory to within +3 to −16 percent.

[4]. Hence for this alloy with a well-defined microstructure of fibers the T-M theory gives an excellent prediction of the strain dependence of stored energy.

Ratio of Stored to Expended Energy (E_s/E_w)—From Eq 7, by integration we have

$$\sigma = \sigma_0 + [AE/(1 - B)]\epsilon \tag{17}$$

where σ is the flow stress and σ_0 is the yield stress (≈ 29.0 MPa in the case of the eutectic alloys). The plastic work (E_w) is then given by

$$E_w = \int \sigma d\epsilon \tag{18}$$

$$E_w = \int [\sigma_0 + [AE/(1 - B)]\epsilon]d\epsilon \tag{19}$$

or

$$E_w = \sigma_0\epsilon + [AE/(1 - B)]\epsilon^2/2 \tag{20}$$

To obtain expressions for the ratio of stored to expended energy we combine Eq 14 with Eq 20 for disks, and Eqs 15 and 16 with Eq 20 for fibers. The required formulae for E_s/E_w are

$$E_s/E_w = [(5 - 4\nu^*)E^*\epsilon^2 f/8(1 - \nu^{*2})]/\{\sigma_0\epsilon + [AE/(1 - B)]\epsilon^2/2\} \tag{21}$$

for disks, where A and B are given by Eqs 12 and 13, and

$$E_s/E_w = \{[3(1 - 2\nu^*)E + 2(1 + \nu)E^*]E^*\epsilon^2 f/Z\}/ \{\sigma_0\epsilon + [AE/(1 - B)]\epsilon^2/2\} \tag{22}$$

for fibers, where Z is found from Eq 16 and A and B from Eqs 8 and 10. For the analysis of the T-M theory in terms of stored energy data we use Eqs 21 and 22 to generate the predicted values of E_s/E_w. For these computations we use E^*/E values of 1.0 and 1.1, ν^*/ν values in the range of 0.9 to 1.1, f values of 0.045 and 0.05 (for Al-Al$_3$Fe) and 0.1 (for Al-Al$_6$Fe), and ϵ values [1] of 0.01 (for Al-Al$_3$Fe) and 0.01, 0.02, and 0.05 (for Al-Al$_6$Fe). The calculated values of E_s/E_w for disks and fibers are identical and are presented in Table 4.

The agreement between the calculated and measured values of E_s/E_w is to within 11 percent for a range of combinations of E^* and ν^*. The predicted values of E_s/E_w (0.79 and 0.78) are not very dependent on the values of E^*/E (1.0 and 1.1) at the highest strain examined (0.05), whereas the predicted E_s/E_w values (for example, 0.52 and 0.54) are more dependent on the E^*/E values at $\epsilon = 0.01$. The dependence of the energy ratio on ν^*/ν is small (for example, 0.40 and 0.39 for $\nu^*/\nu = 0.9$ and 1.1). Agreement is to within +11

TABLE 4—*Values of the ratio of stored to expended energy calculated from the theory of Tanaka and Mori.*

NOTE—E_s/E_w is the ratio of stored to expended energy.

Al-Al_3Fe						Al-Al_6Fe					
E^*/GPa	ν^*	f	ϵ	E_s/E_w[a]		E^*/GPa	ν^*	f	ϵ	E_s/E_w[b]	
				Theory	Experiment					Theory	Experiment
69	0.297	0.045	0.01	0.35	0.36	69	0.297	0.1	0.01	0.52	0.50
	0.330	0.045	0.01	0.35			0.330	0.1	0.01	0.52	
	0.363	0.045	0.01	0.35			0.363	0.1	0.01	0.52	
	0.297	0.05	0.01	0.38	0.36		0.297	0.1	0.02	0.66	0.66
	0.330	0.05	0.01	0.37			0.330	0.1	0.02	0.66	
	0.363	0.05	0.01	0.37			0.363	0.1	0.02	0.66	
							0.297	0.1	0.05	0.79	0.75
							0.330	0.1	0.05	0.79	
							0.363	0.1	0.05	0.78	
76	0.297	0.045	0.01	0.37	0.36	76	0.297	0.1	0.01	0.54	0.50
	0.330	0.045	0.01	0.37			0.330	0.1	0.01	0.54	
	0.363	0.045	0.01	0.37			0.363	0.1	0.01	0.54	
	0.297	0.05	0.01	0.40	0.36		0.297	0.1	0.02	0.67	0.66
	0.330	0.05	0.01	0.39			0.330	0.1	0.02	0.67	
	0.363	0.05	0.01	0.39			0.363	0.1	0.02	0.67	
							0.297	0.1	0.05	0.79	0.75
							0.330	0.1	0.05	0.79	
							0.363	0.1	0.05	0.79	

[a] Agreement between experiment and theory to within +11 to −3 percent.
[b] Agreement between experiment and theory to within 8 percent.

to -3 percent for the Al-Al_3Fe alloy and to within 8 percent for the Al-Al_6Fe eutectic. The values of E^*/E used to obtain agreement to within $+11$ to -3 percent for the theoretical and experimental values of E_s/E_w are in the range expected from previous measurements [*4*], and confirm that Young's modulus for the precipitate is about 10 percent higher than that of the matrix. For these alloys the stored energy is predicted to be a substantial fraction of the expended energy, whereas for pure metals and single-phase alloys the fraction would be much lower [*5*]. Thus, the T-M theory predicts accurately the ratio of stored to expended energy for the two eutectic alloys considered.

Concluding Remarks

This investigation has compared two work-hardening theories for nondeforming precipitates in a plastic matrix. The various parameters in the theories were adjusted within acceptable ranges to obtain calculated values for the initial work-hardening rate, E_s/ϵ^2, and the ratio of stored to expended energy. While this work is not a critical test of the two theories, it does show that by appropriate adjustment of the parameters agreement between theory and experiment can be obtained. The results of this comparison in terms of the measured work-hardening and stored energy relations for the eutectic alloys Al-Al_3Fe and Al-Al_6Fe give the following conclusions:

1. The B-C theory may be manipulated to predict values of the initial work-hardening rate (θ) that are in excellent agreement with the measured rate for Al-Al_3Fe and in good agreement with that for Al-Al_6Fe.
2. The T-M theory may be manipulated to predict initial θ-values that are in excellent agreement with that measured experimentally for Al-Al_3Fe and in fair agreement with that for Al-Al_6Fe.
3. The T-M theory leads to a strain dependence of stored energy that overestimates the measured dependence for Al-Al_3Fe, but is in excellent agreement with that measured for Al-Al_6Fe.
4. The T-M theory gives an excellent prediction of the ratio of stored to expended energy for both alloys.
5. The investigation suggests that the value of Young's modulus for the precipitates in Al-Al_3Fe and Al-Al_6Fe is about 10 percent higher than that of the matrix.

Acknowledgments

The author thanks Dr. Colin Adam of Pratt and Whitney Aircraft Group, West Palm Beach, Florida, for the opportunity of doing cooperative research on intriguing alloys and for continued discussions about the relations among stored energy, mechanical properties, and microstructure.

References

[1] Adam, C. M. and Wolfenden, A., *Acta Metallurgica.* Vol. 26, 1978, p. 1307.
[2] Brown, L. M. and Clarke, D. R., *Acta Metallurgica.* Vol. 23, 1975, p. 821.
[3] Tanaka, K. and Mori, T., *Acta Metallurgica.* Vol. 18, 1970, p. 931.
[4] Keong, P. G., B. E. (Hons.) thesis, University of Auckland, New Zealand, 1976.
[5] Bever, M. B., Holt, D. L., and Titchener, A. L., *Progess in Materials Science.* Vol. 17, 1973.

A. K. Ghosh[1] *and R. Raj*[2]

A Deformation Model for Elevated Temperature Including Grain Size Distribution Effects

---

REFERENCE: Ghosh, A. K. and Raj, R., "**A Deformation Model for Elevated Temperature Including Grain Size Distribution Effects,**" *Mechanical Testing for Deformation Model Development, ASTM STP 765,* R. W. Rohde and J. C. Swearengen, Eds., American Society for Testing and Materials, 1982, pp. 415-434.

ABSTRACT: It is widely believed that grain boundary sliding, accommodated by diffusion, which leads to a Newtonian viscous behavior ($\sigma \propto \dot{\epsilon}$) and grain matrix deformation exhibiting a power law creep behavior ($\alpha \propto \dot{\epsilon}^m$), are the two concurrent deformation phenomena occurring at elevated temperatures in metals, particularly during superplastic flow. A deformation model for this combined behavior has been developed in which the grain size and its distribution are taken into account. Strain compatibility relations have been utilized to predict material flow behavior under loading, load relaxation, and steady-state conditions. Comparison with experimental results shows that the sigmoidal σ-$\dot{\epsilon}$ relationship for superplastic metals is explained well by the model. The model also simulates other experimental aspects as well as internal stress development during elevated temperature flow.

KEY WORDS: superplasticity, creep, high temperature flow, grain boundary sliding, strain rate sensitivity, grain size distribution

While grain boundary sliding is a common occurrence during creep and superplastic deformation process, the grain boundary accommodation processes are generally believed to be the rate-controlling ones [*1,2*].[3] The accommodation processes may be either diffusional flow or dislocation motion in the vicinity of grain boundaries, or creep deformation spreading within the grain interior. When the temperature is sufficiently high and strain rates are

---

[1] Manager, Metals Processing, Rockwell International Science Center, Thousand Oaks, Calif. 91360.

[2] Currently at Rockwell International Science Center, Thousand Oaks, Calif. 91360; on leave from Cornell University, Ithaca, N.Y.

[3] The italic numbers in brackets refer to the list of references appended to this paper.

sufficiently low, as in the case of superplastic deformation, diffusion along short grain boundary paths provide the most likely means of accommodation.

It has been demonstrated metallographically that grain neighbor switching occurs during superplastic deformation primarily by a process of sliding [*3,4*]. Grains have been shown to rotate and jack apart neighboring grains, leading to specimen elongation without substantial grain elongation. The neighbor-switching process was envisioned by Lee [*5*] to be composed of an initial stage of grain elongation (Fig. 1) followed by grain boundary migration to return the grains to their original shape. A similar scheme was used by Ashby and Verrall (hereafter referred to as A-V)[*6*] (Fig. 2); however, in their model the grain elongation in the first step was reduced. This is because diffusion paths shorter than that of Nabarro-Herring's creep model [*7,8*] were found, and much faster creep rates were predicted.

Ashby and Verrall's diffusion-accommodated creep model gives

$$\dot{\epsilon}_s = \frac{A\Omega\sigma}{kTd^2} D_L \left\{ 1 + \frac{3.3\delta}{d} \frac{D_B}{D_L} \right\} \tag{1}$$

where $\dot{\epsilon}_s$ = strain rate from grain boundary sliding, σ = stress, A = constant (~ 100), Ω = atomic volume, k = Boltzmann's constant, T = absolute temperature, d = grain size, D_L = lattice diffusion coefficient, D_B = grain boundary diffusion coefficient, and δ = grain boundary width ($\simeq 2 \times$ Burger's vector). The threshold stress in Ashby-Verrall's original equation, consisting of the surface energy term, is small and has been neglected in Eq 1. This equation differs from the classical diffusion creep (that is, combination of Nabarro-Herring and Coble) equations in that A is almost an order of magnitude larger.

Also, it has been pointed out that Nabarro-Herring and Coble creep models [*7-9*] are strictly valid for small strains, while the diamond or square

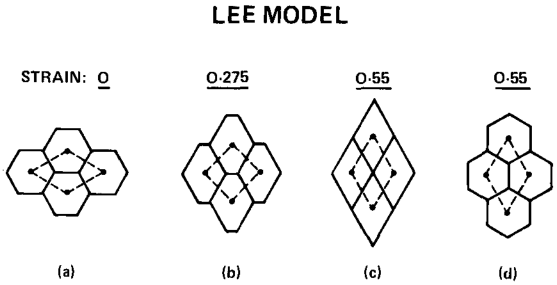

FIG. 1—*Details of grain switching according to Lee model. Grains elongate substantially before migration restores their shape.*

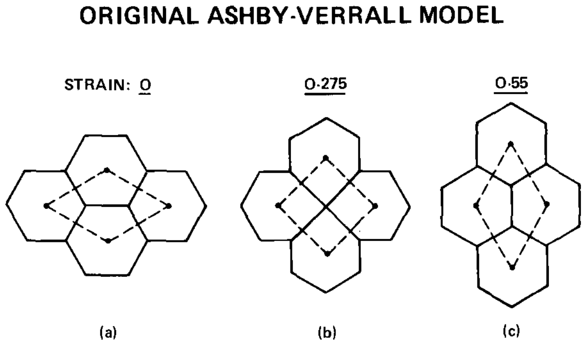

FIG. 2—*Details of grain switching according to Ashby-Verrall model. Diffusion paths are shorter and boundary migration also leads to strain.*

grain models as illustrated in Figs. 1 and 2 should be more closely applicable for large strains. It is recognized, however, that the grain-switching process in irregular polycrystalline materials is nonuniform, which might lead to strain rates lower than that expected from Ashby-Verrall model.

Spingarn and Nix [*10*] have recently pointed out that diffusional transport in the A-V model must occur from the center of grain boundaries toward the corners, if normal traction continuity across the boundary is to be maintained. This would not be true, however, if grains experienced a net torque,[4] which can cause a loss of matter from grain corners to fill in the center of grain boundaries. Whatever the actual details of the diffusion-accommodated sliding process, the models do suggest a Newtonian viscous ($\sigma \sim \dot{\epsilon}$) behavior.

In the grain boundary sliding models that consider dislocation-accommodation near the boundary regions [*11*], stress, σ, is found to be proportional to the square root of strain rate, $\dot{\epsilon}$. In many materials, however, the strain rate exponent, m ($= d\ell n\sigma/d\ell n\dot{\epsilon}$), is found to be much larger than 0.5 at a certain rate, decaying progressively toward 0.2 or 0.3 at higher strain rates. The decrease in the strain rate exponent at the higher strain rates is a direct consequence of grain creep, which leads to an approximate power law relationship. In some cases a decrease in m is also observed toward the lower strain rates, which results in a sigmoidal σ-$\dot{\epsilon}$ curve. Thus $\sigma \propto \sqrt{\dot{\epsilon}}$ does not adequately describe these behaviors. The A-V model of diffusion-accommodated sliding, on the other hand, does permit m-values to approach unity at low strain rates and also explains a sigmoidal σ versus $\dot{\epsilon}$ curve. However, the threshold stresses predicted by this model are extremely low, and if a realistic

---

[4] Unfavorable orientation for slip or climb can bring about such torques. This is often reflected in observations of grain rotation and orange-peel effect.

threshold stress is used, the strain rate range over which m is high becomes very narrow.

In models where grain boundary sliding is accommodated by nonuniform creep within the grains, the strain rate range over which transition from power law occurs is also found to be extremely narrow. Furthermore, at the lower strain rates, grain elongation, which is inherent in such models, is not observed experimentally. Thus, for high-temperature creep and superplasticity, the Ashby-Verrall equation (Eq 1) appears to be quite reasonable for representing the low strain rate behavior. This must, however, be combined with power law creep occurring at higher strain rates to obtain the complete creep equation as:

$$\dot{\epsilon} = \frac{A\Omega\sigma}{kTd^2} D_{\text{eff}} + K\,\sigma^n \qquad (2)$$

where $\dot{\epsilon}$ = overall strain rate, $D_{\text{eff}} = D_{\text{L}}\,\{\,1 + (3.3\delta/d)\,(D_{\text{B}}/D_{\text{L}})\,\}$, K = constant, and n = stress exponent for power law ($\sim$ 4 or 5).

The micromechanical models developed so far have considered a fixed grain size. It is believed that a fixed grain size can give rise to narrow transition strain rate ranges exhibited by the aforementioned models. In fact, real materials exhibit a distribution in grain size, depending on the processing history, and when this is incorporated in the constitutive model the transition in stress/strain rate curve distributed over a wide strain rate range is observed. This model has been developed in some detail and does explain the development of internal stresses, depending on the distribution of grain sizes [*12*]. A summary review of this model and its influence on steady state and transient mechanical behaviors will now be discussed.

Microstructural Model

The importance of grain size distribution is realized from an examination of Eq 2. Finer grains creep at a faster rate than coarse grains. During steady-state deformation, however, the macroscopic strain rate over a representative volume element comprising grains of different sizes is the same as the applied strain rate. Thus the fine grains in this element are constrained to strain at the same rate as the coarsest grains, which deform more slowly. While this constraint may not be applied over each individual grain, groups of grains of the same diameter within each volume element may be subjected to it. According to Eq 2, this would also lead to a nonuniformity in stress distribution, since finer grains will support lower stresses than coarser grains at the same strain rate.

The overall stress for steady state is given by

$$\sigma = \sum_i f_i\,\sigma_i \qquad (3)$$

where subscript i refers to grain groups, f_i = volume fraction of grains having diameter d_i, and σ_i = stress supported by grains of size d_i. The relationship between σ_i and $\dot{\epsilon}$ is given by

$$\dot{\epsilon} = \frac{K_d{}'\, D_{\text{eff}}\, \sigma_i}{d_i^2} + K\,\sigma_i^n \tag{4}$$

where $K_d{}' = A\Omega/kT$. Equation 4 can be numerically solved for known values of $\dot{\epsilon}$ to obtain σ_i, which when substituted in Eq 3 for each f_i (and d_i) gives the overall stress. The volume fraction, f_i, can be developed from grain size distribution in the following manner:

$$f_i = \frac{p_i d_i^3}{\sum\limits_{\text{i}} p_i d_i^3} \tag{5}$$

where p_i denotes the density of grains of size d_i, and grains are assumed to be nearly spherical.

Transient Behavior

During initial loading, the strain rate constraint among different groups of grains is not established immediately. When strain rate is not large, the very fine grains are able to relax slight loads rapidly by diffusional flow, and therefore loading up is a slow process. During loading as well as relaxation, the stress rate for each grain size group is given by

$$\dot{\sigma}_i = E(\dot{\epsilon}_t - \dot{\epsilon}_i) \tag{6}$$

where E = elastic modulus, and $\dot{\epsilon}_t$ = applied strain rate, which is zero for load relaxation. Equation 6, and not iso-strain-rate, is the appropriate constraint for transient situations. Strain rate is allowed to vary for the different grain sizes, and is calculated from the new stress (= σ_i (old) + $\dot{\sigma}_i \Delta t$) using Eq 4. Overall stress is still determined via Eq 3 and inelastic strain rate by

$$\dot{\epsilon}_{\text{inel}} = \dot{\epsilon}_t - \frac{\sigma(\text{new}) - \sigma(\text{old})}{E\,\Delta t} \tag{7}$$

If loading is started from near zero stress, finer grains will have a greater $\dot{\epsilon}_i$ than coarser grains; that is, elastic loading rate of coarse grains would be larger since $(\dot{\epsilon}_t - \dot{\epsilon}_i)$ in Eq 6 is larger. Thus coarse grains will support greater stress and continue to strain slower. This leads to a time-hardening behavior until the coarse grains attain steady state.[5] If the coarsest grain has a volume fraction of f^*, the total anelastic strain accumulated will be

$$\Delta\epsilon_{\text{anel}} = \frac{\sigma_s^*}{E}\left(\frac{1}{f^*} - 1\right) \tag{8}$$

where $\sigma_s^* =$ steady-state stress for the coarsest grain.

Results and Discussion

Before examining the effect of a continuous distribution in grain size, a preliminary evaluation of the model can be made by considering a mixture of two discrete grain sizes, d_1 and d_2 ($d_1 < d_2$). As shown in Fig. 3, at a volume fraction f_1, of the fine grains, the composite curve[6] approaches a power law behavior given by $(1 - f_1)\,(\dot\epsilon/K)^{1/n}$ on the stress scale, bounded between diffusional regimes of $\sigma = (d_1^3/K_d)\,\dot\epsilon$ and $\sigma = (1 - f_1)\,(d_2^3/K_d)\,\dot\epsilon$. The transition regions are curved, due to the interaction of two mechanisms, and show a change in slope, $m = d \log \sigma / d\ell n\dot\epsilon$, as a function of strain rate. At strain rates above A, σ versus $\dot\epsilon$ curve is sigmoidal and rate sensitivity index, m, exhibits a maximum—a behavior generally associated with superplastic deformation. Furthermore, these peaks are much broader in strain rate range than those found for a single grain size. At very low strain rates—that is, below the rates normally investigated in studies on superplasticity—m rises toward unity again. (Measurements at such low rates might, however, be obscured by concurrent grain growth effects.) As the fine grain fraction is increased to f_2 (shown in Fig. 3), a decrease in flow stress and an increase in m-value peak are found to occur. As discussed later in the paper, a finer overall grain size (that is, smaller d_1 and d_2, or just smaller d_1) causes further decrease in the flow stress, and increases in the values of peak m, as well as the strain rate at which it occurs. Finally, the transition to total diffusional creep (at the low rates) also moves to a higher strain rate.

A more detailed grain size distribution is now considered. Measured two-dimensional grain intercept length distribution does not uniquely determine the nature of grain size distribution [*13*]. However, a strong possibility exists for the grain size distribution to be made up of several narrow distributions (or discrete grain sizes). Figure 4 shows the influence of trimodal grain size distributions at median values of 2.5, 7, and 14 μm, respectively. Each median value is shown to have a triangular spread about it. The power law parameters and diffusion coefficient values selected for these plots are

---

[5] Concurrent grain growth during high temperature creep and superplastic deformation leads to a substantial degree of hardening, which acts in addition to this.

[6] Most of the calculations shown here are based on a Coble-type equation with stress following a cubic dependence on grain size. In these situations, a constant, K_d, is used in place of K_d', where $K_d = 3.3\,A\,\Omega\delta D_B/kT$. It is explicitly pointed out when this is not the case.

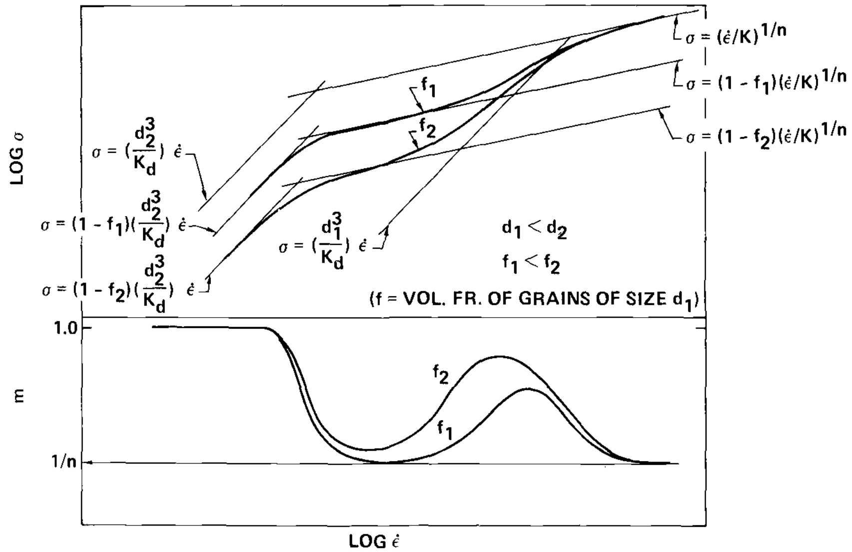

FIG. 3—*σ versus $\dot{\epsilon}$ curves for different trimodal distributions (triangular spreads) are contrasted against curves for discrete and individual grain sizes.*

similar to those for Ti-6Al-4V alloy at 927°C. The individual σ-$\dot{\epsilon}$ curves for steady state are shown by thin solid lines for each median grain size. These curves are characterized by power law regions ($m = 1/n = 0.2$) at the higher strain rates, Newtonian viscous region ($m = 1$) at the lower rates, and a transition region spread over a decade and a half in strain rates within which $0.2 < m < 1.0$. The heavy lines incorporating various mixtures of these grain sizes exhibit a much larger spread in the σ-$\dot{\epsilon}$ curves. The transition region between $m = 1$ and $m = 0.2$ can now lie over three decades in strain rates, as commonly observed in superplastic metals and not explained by single grain size behavior.

While the finest (2.5 μm) grains are largest in number, changes in the ratio of other grains can cause significant changes in the shape of the σ-$\dot{\epsilon}$ curves. For example, with a ratio of numbers 2500:50:1 of the 2.5, 7, and 14 μm grains—that is, volume fractions of 74.3, 20.5, and 5.2 percent, respectively—a nearly constant m of 0.55 is exhibited for $6 \times 10^{-5} < \dot{\epsilon} < 2 \times 10^{-3}$ s^{-1} and a gradual increase toward $m = 1.0$ for lower strain rates. As the grain number ratio is changed to 2500:15:1, or volume fractions to 81.7, 6.8, and 11.5 percent, respectively, a peak in m of 0.63 at $\dot{\epsilon} \sim 2 \times 10^{-4}$ s^{-1}, and a reduced flow stress due to a larger fraction of small grains are obtained. A decrease in m at lower strain rates is a direct result of replacement of the intermediate grain sizes by more of the larger grains. When data are collected for $\dot{\epsilon} > 5 \times 10^{-5}$ s^{-1} only, this gives the impression of a threshold

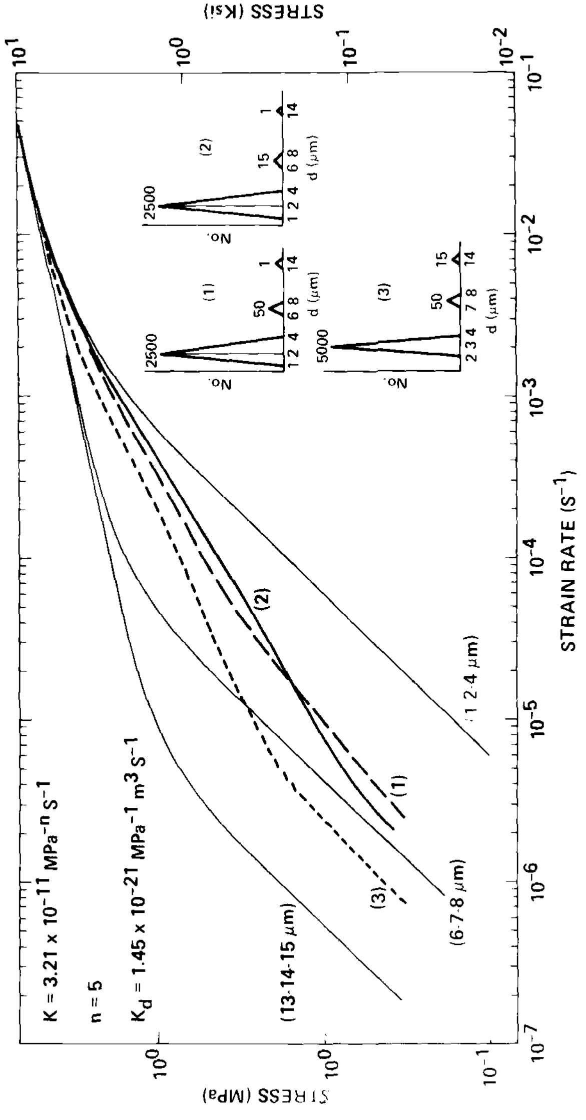

FIG. 4—*Possible variations in composite σ-ε̇ curves for changes in the mix of grain sizes, using Coble model for diffusional creep.*

stress might exist; this is often the case for data on superplastic metals found in much of the literature. Finally, for $\dot{\epsilon} < 5 \times 10^{-6}\ \text{s}^{-1}$, m begins to increase again toward unity; this has also been observed in many instances [*14*].

The Coble creep equation, by virtue of its cubic dependence on grain size, exhibits a broader distribution in stress/strain rate behavior than the Nabarro-Herring equation with square dependence on grain size. Since the A-V equation contains both of these inputs—that is, diffusion through the grain interior as well as the grain boundary—it is of interest to compare the predictions of the steady-state behavior from this model with that from the Coble model. Figure 5 shows such plots for discrete grain sizes (dashed) as well as composite grain size distributions (solid curves). The Coble model plot here refers to the A-V equation without the term containing d^2, yet maintaining the reduced diffusion path of the grain switching model. The A-V model predicts a significantly higher strain rate than the Coble model for both discrete as well as composite grain size distributions. The strain rate ratio is given by

$$\frac{\dot{\epsilon}_{\text{A-V}}}{\dot{\epsilon}_{\text{Coble}}} = 1 + \frac{d}{3.3\delta}\left(\frac{D_{\text{L}}}{D_{\text{B}}}\right) \qquad (9)$$

which suggests that the rate difference is more pronounced for the larger grain sizes than for the finer ones. This is seen in Fig. 5 by comparing the curves for composite distribution with that for discrete distribution. Furthermore, although the solid curves show a region of $m \sim 0.55$ for both models,

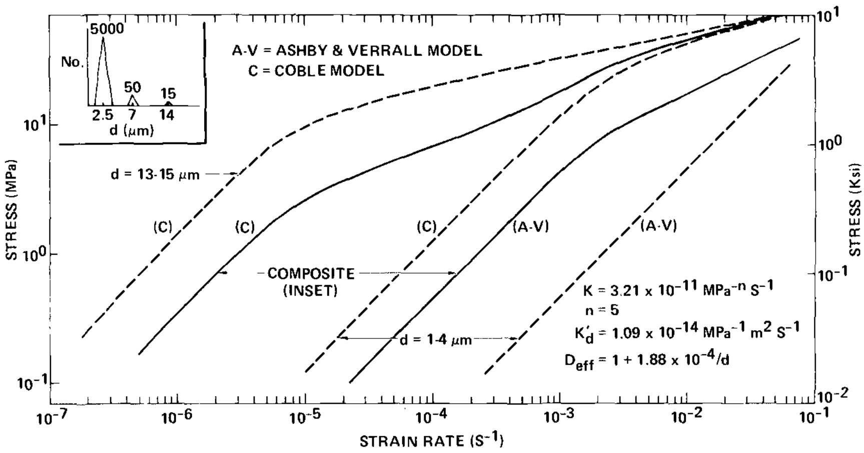

FIG. 5—*Comparison of σ-ε̇ curves between Coble and Ashby-Verrall models for discrete and distributed grain sizes.*

that for the Coble model is much broader. The slight sigmoidal shape of the Coble model does not show up in the A-V model.

Comparison with Experimental Results

Simulations were carried out for a fine-grain, superplastic aluminum alloy (7475 alloy) and a Ti-6Al-4V alloy which exhibits superplasticity in the $\alpha + \beta$ phase field. The diffusivity of titanium in α and β phases is quite different ($D_\beta \sim 100\ D_\alpha$); however, this large difference in diffusivities may not be too important in determining grain boundary diffusivity as required in the present model. When averaged over different grain sizes, and like and unlike phase boundaries, the grain boundary diffusivity would tend to be uniform and free of any grain type bias. For the case of a single-phase aluminum alloy, this problem does not exist. It does, however, contain an elongated grain structure, which is ignored in the present analysis.

Typical photomicrographs of the aluminum and titanium alloys and their grain intercept plots are shown in Fig. 6. Grain intercept plots were developed from three such micrographs of each material. While it is difficult to describe exactly the nature of grain size distribution that produce the observed two-dimensional distributions, several possible distributions used in the present calculation are listed in Table 1. The long tails present in such distributions do indicate the presence of few large grains [*15*]. Three-dimensional distributions would be expected to show a few grains even larger than these. The most important problem regarding grain boundary diffusivities is the lack of data; this is particularly complicated by the fact that diffusivities are significantly altered by deformation. Several fold increases in diffusion coefficients are possible under conditions of concurrent deformation [*16,17*]. Because of the uncertainty over its value, D_B has been used as an adjustable parameter to obtain a match between the theory and experiment. Table 2 lists the values of D_B at the superplastic temperature from the literature, along with those used in the calculations here. It may be noted that the values of D_B used for dynamic conditions are not measurable in view of the results in Ref *17*. All other parameters are also listed in Table 2.

Calculations of steady state σ versus $\dot{\epsilon}$ curves based on grain size distributions of Table 1 are compared with experimental results in Figs. 7 and 8. The experimental σ versus $\dot{\epsilon}$ data for titanium alloy are from Ref *20* and that for aluminum alloy (similar to Ref *20*) has recently been developed in our laboratory. Good agreement in stress level and slope between the model and experimental data is observed in both cases. While the Coble creep model appears to fit the data well, it cannot be concluded whether the complete form of A-V model would be just as reasonable, since (*1*) grains larger than that suggested from grain intercept distribution might be present, and (*2*) the grain-switching process is likely to be highly nonuniform.

Transient Behavior

Simulations were carried out for loading a superplastic material at a slow strain rate ($\dot{\epsilon}_t = 10^{-5}$ s^{-1}) according to the scheme discussed earlier. Figure 9 shows calculated stress and strain rate distribution among the various grain sizes during the course of loading up toward steady state. The fine grains are found to attain the applied strain rate rather rapidly, while the strain rate in coarse grains increases slowly, thereby leading to a slow time hardening transient behavior of the average σ versus t curve (Fig. 9*a*). That the coarse grains continue to deform by power law may be partly responsible for the observed "strain hardening" in aluminum alloys [*21*]. It is noteworthy that a decrease in elastic modulus or an increase in the size and volume fraction of larger grains can significantly increase strain to reach saturation stress. It is obvious that, when imposed strain rate is larger, the transient portion is reduced because of a more rapid loading of the coarse grains. However, a larger fraction of coarse grains can lead to a long transient region.

The presence of such a long transient has interesting implications on instantaneous rate sensitivity indices obtained from strain rate perturbations carried out at various strain levels [*21*]. Since fine grains can readily attain imposed strain rate, their influence ($m \sim 1$) on instantaneous rate sensitivity index is greater when coarse grains are supporting less stress—that is, at short times. At longer times, the stress supported by fine grains becomes a smaller fraction of the overall stress, and instantaneous rate sensitivity may approach that for power law creep ($m \sim 1/n$). This kind of drop in instantaneous m as a function of strain has been recorded for aluminum alloys [*21*]. Supporting observations have also been reported in which dislocation structure develops in certain grains, while other grains remain relatively dislocation free [*22*].

A large number of superplastic materials, including titanium, lead, aluminum alloys, etc., exhibit significant grain growth during deformation. Concurrent grain growth leads to additional hardening during deformation, which might last over much larger strain levels than that indicated in Fig. 9. In the case of Ti-6Al-4V alloy [*23*], this is beleived to be the dominant hardening mechanism. Grain growth also leads to a decrease in the instantaneous rate sensitivity index, because the coarser grains produce power law behavior.

The results of simulation of a load relaxation test and experiment are described in Fig. 10. The experimental data given in Fig. 10*a* have been recently developed in our laboratory. Analytical results are shown in Fig. 10*b*. The behavior is the reverse of the loading behavior. In this case, the higher stresses supported by coarser grains begin to diminish more rapidly than finer grains can shed their stresses (or strain rates). This causes a steep drop in stress for only a slight decrease in strain rate. Subsequently, as the strain rate in coarse grains decreases significantly, and that in fine grains also be-

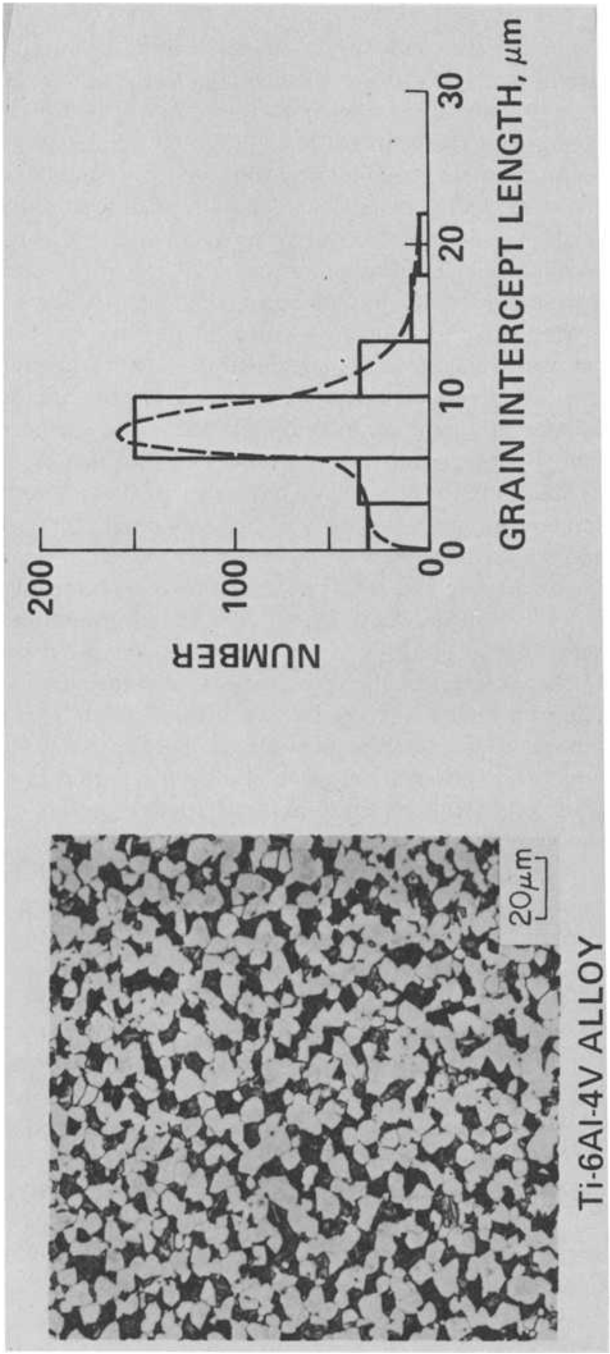
NUMBER
200
100
0
0
10
20
30
GRAIN INTERCEPT LENGTH, μm
20μm
Ti-6Al-4V ALLOY

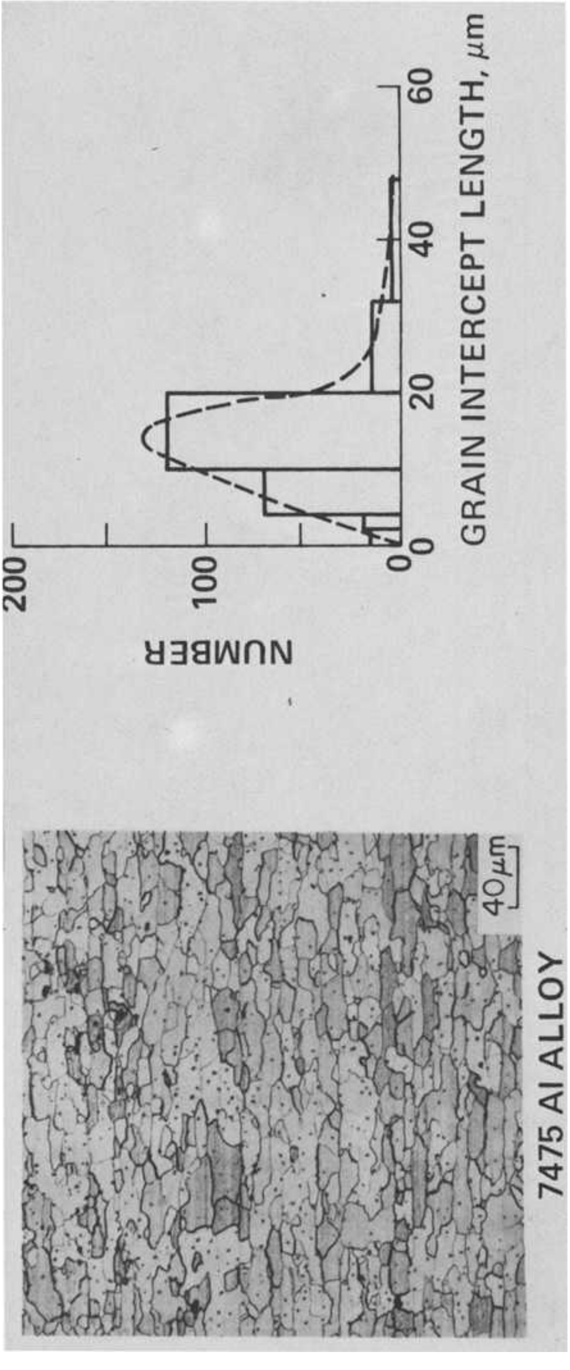

FIG. 6—*Photomicrographs of titanium and aluminum alloys and corresponding distributions of grain intercept lengths.*

TABLE 1—*Combinations of triangular grain size distributions for simulation.*

Material	Combination No.	Range of Base (μm)	Peak Value (at d μm)	Range of Base (μm)	Peak Value (at d μm)	Range of Base (μm)	Peak Value (at d μm)
7475 Al	1	6 to 10	10(8)	18 to 20	1(19)		
	2	8 to 12	100(10)	28 to 30	1(29)		
Ti-6Al-4V	1	2 to 8	100(5)	12 to 15	5(14)	28 to 30	1(29)
	2	2 to 8	500(5)	13 to 15	5(14)	33 to 35	1(34

TABLE 2—*Material data used in Eq 4.*

Material	Temperature, K	Ω, cm^3	$\delta \sim 2b$, cm	Available Diffusion Coefficient, cm^2/s	Assumed D_B, cm^2/s[a]	K, s^{-1} (MPa)$^{-n}$	n
Aluminum	790	1.62×10^{-23}	6×10^{-8}	$D_B = 2.45 \times 10^{-6}$[b]	5×10^{-6}	3.015	5.883
Ti-6Al-4V	1200	1.7×10^{-23}	6×10^{-8}	$D_\alpha = 10^{-9}$; $D_\beta = 10^{-7}$[c]	3.6×10^{-8}	5.92×10^{-3}	5.0

[a] Based on enhancement of diffusivity due to grain boundary migration effects (Refs *15* and *16*).

[b] Grain boundary diffusion coefficient from Ref *17*.

[c] Bulk diffusion coefficients for α and β phases (Refs *18* and *19*).

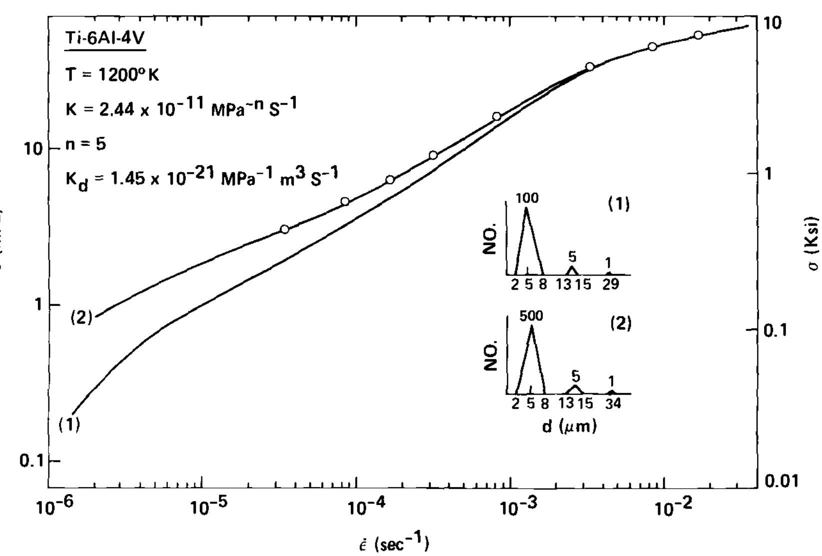

FIG. 7—*σ versus $\dot{\epsilon}$ curves calculated for Ti-6Al-4V (solid lines) compared with experimental data (open circle).*

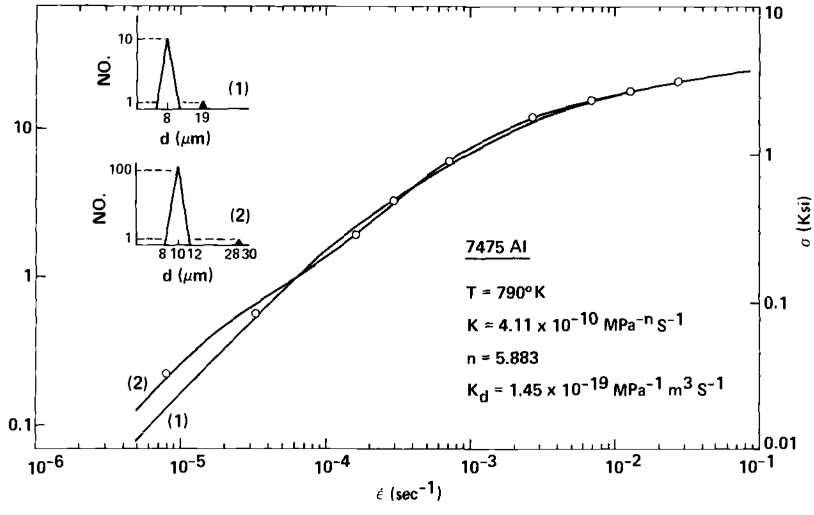

FIG. 8—*σ versus $\dot{\epsilon}$ curves calculated for 7475 Al alloy (solid lines) compared with experimental data (open circles).*

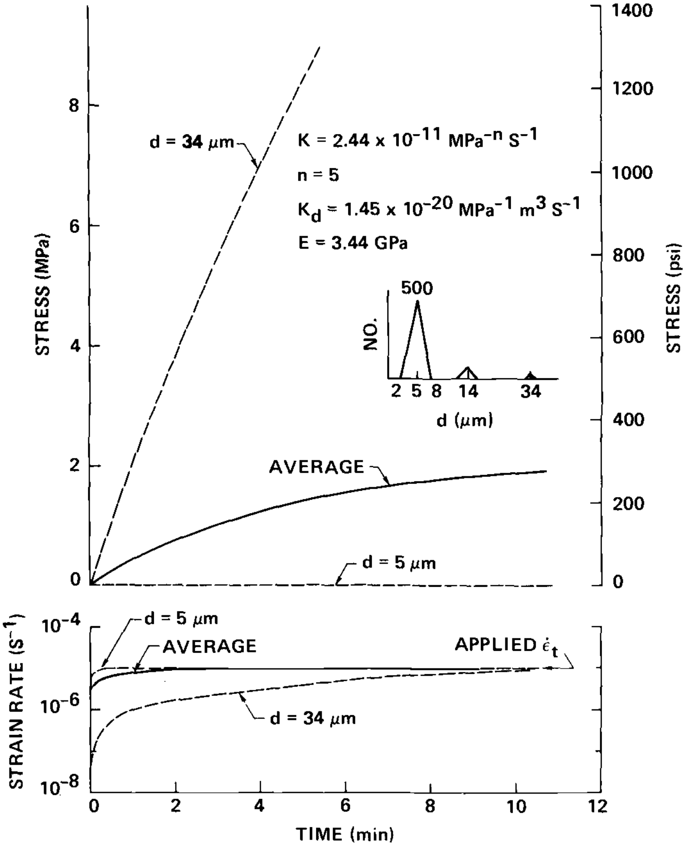

FIG. 9—*Gradual rise in stress and inelastic strain rate in coarse and fine grains as well as on the average, during loading up at a constant* $\dot{\epsilon}_t$.

gins to decrease, the overall strain rate drops at an increased rate in comparison to the stress drop. The slope of the σ versus $\dot{\epsilon}$ curve becomes less than that for steady state, and continues in this manner to lower strain rates. Thus the σ versus $\dot{\epsilon}$ curves obtained from loading and relaxation transients have different characteristics from the steady-state behavior because of different stress and strain rate distributions associated with each case. The low m-values over a large strain rate range observed in relaxation tests are reminiscent of similar observations by Woodford [*24*], Hart, [*25*], Li [*26*], and others for high-temperature deformation. This suggests that the grain size distribution effect may have a broader applicability in creep as well as superplasticity, and that more attention should be placed on its role on mechanical response.

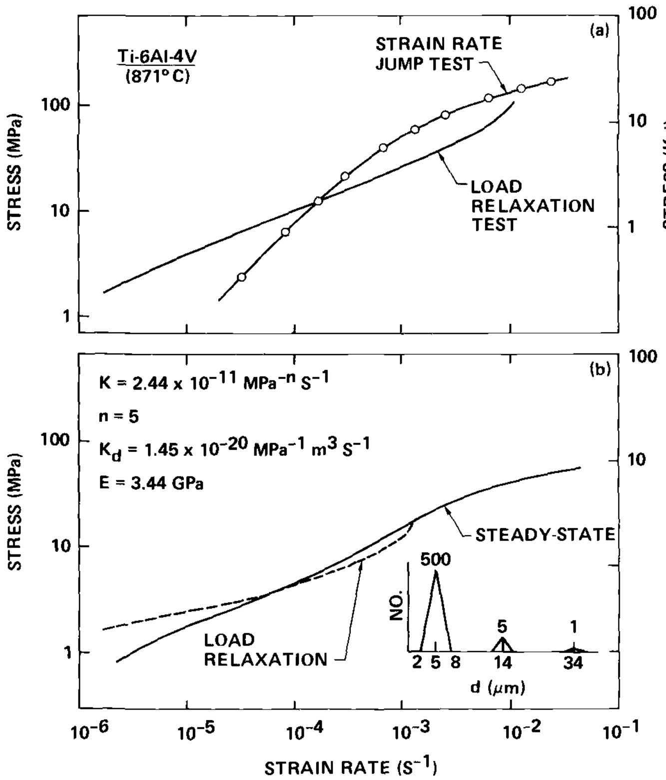

FIG. 10—(a) *Experimental σ versus $\dot{\epsilon}$ curves from strain rate jump and load relaxation tests;* (b) *simulations of the same through present model.*

Summary

Models of grain boundary sliding accommodated by diffusional processes do explain the topological features of superplastic deformation including the lack of grain elongation. It has always been argued, however, that the transition from power law behavior to diffusion creep is extremely sharp in this kind of a model. While no new mechanism for superplasticity has been suggested here, it is shown that when realistic grain size distribution of materials is accounted for in the theory, an iso-strain-rate constraint leads to a broad transition region (in log σ versus log $\dot{\epsilon}$ curves), generally found experimentally. This analysis also reveals a nonuniform internal stress distribution during high-temperature flow.

Based on the present approach, it is observed that while finer grains can deform (or slide along boundaries) by diffusional processes and support low stresses, coarse grains simultaneously deforming by power law creep, under iso-strain-rate constraints, can support larger stresses. This increases the strain rate range over which rate sensitivity index (m) changes between the power law value ($1/m$) and the Newtonian viscous value (1) by several decades. The mix of grain sizes can also produce an apparent approach toward a threshold stress at low strain rates, thereby yielding a peak in m. Using realistic grain size distributions, the experimental σ versus $\dot{\epsilon}$ results on aluminum and titanium alloys have been simulated extremely well between strain rate ranges of 10^{-6} to 10^{-2} s^{-1}.

During transients (for example, loading up and load relaxation tests), the iso-strain-rate constraint is not imposed instantaneously and the internal stress distribution develops gradually. The length of time required by the coarse grains to reach steady state causes a "time hardening" behavior during loading up, and the time required by them to shed stresses produces a lower slope of the σ versus $\dot{\epsilon}$ curve during load relaxation in comparison to steady-state results. This suggests that load relaxation tests may not be uniquely suitable for developing data for a variety of applications.

Acknowledgments

This work was supported by the Independent Research and Development Program of Rockwell International.

References

[*1*] Edington, J. W., Melton, K. N., and Cutler, C. P., *Progress in Materials Science*, Vol. 21, 1976, p. 61.
[*2*] Gifkins, R. C., *Metallurgical Transactions A*, Vol. 7A, 1976, p. 1225.
[*3*] Dingley, D. J. in *Proceedings*, 3rd Annual Scanning Electron Microscope Symposium, 1970, p. 329.
[*4*] Naziri, H., Pearce, R., Henderson Brown, M., and Hale, K. F., *Journal of Microscopy*, Vol. 97, 1973, p. 229.
[*5*] Lee, D., *Acta Metallurgica*, Vol. 1, 1969, p. 309.
[*6*] Ashby, M. F. and Verrall, R. A., *Acta Metallurgica*, Vol. 21, 1973, p. 149.
[*7*] Nabarro, F. R. N., *Bristol Conference on Strength of Soils*, Institute of Physics, 1948, p. 75.
[*8*] Herring, C., *Journal of Applied Physics*, Vol. 21, 1950, p. 437.
[*9*] Coble, R. L., *Journal of Applied Physics*, Vol. 34, 1963, p. 1679.
[*10*] Spingarn, J. R. and Nix, W. D., *Acta Metallurgica*, Vol. 26, 1978, p. 1389.
[*11*] Gifkins, R. C., *Metallurgical Transactions A*, Vol. 7A, 1976, p. 1225.
[*12*] Raj, R. and Ghosh, A. K., *Acta Metallurgica*, in press.
[*13*] Ghosh, A. K. and Raj, R., *Acta Metallurgica*, in press.
[*14*] Mukherjee, A. K., *Annual Reviews of Materials Science*, Vol. 8, 1979.
[*15*] Feltham, P., *Acta Metallurgica*, Vol. 5, 1957, p. 97.
[*16*] Cahn, J. W. and Balluffi, R. W., *Scripta Metallurgica*, Vol. 13, 1979, p. 499.
[*17*] Cahn, J. W., Pan, J. D., Balluffi, R. W., *Scripta Metallurgica*, Vol. 13, 1979, p. 503.
[*18*] Jenkins, W. D. and Digges, I. G., *Journal of Research of the National Bureau of Standards*, Vol. 47, 1951, p. 272.
[*19*] Murdock, J. F. and McHargue, C. J., *Acta Metallurgica*, Vol. 16, 1968, p. 493.
[*20*] Ghosh, A. K. and Hamilton, C. H., *Metallurgical Transactions A*, Vol. 10A, 1979, p. 699.

[*21*] Ghosh, A. K. and Hamilton, C. H. in *Proceedings,* International Conference on Strength of Metal Alloys, Aug. 1979, Aachen, Germany.

[*22*] Samuelson, L. C. A., Melton, K. N., and Edington, J. W., *Acta Metallurgica,* Vol. 24, 1976, p. 1017.

[*23*] Murdock, J. F., Lundy, T. S., and Stansbury, E. E., *Acta Metallurgica,* Vol. 12, No. 9, 1964, p. 1033.

[*24*] Woodford, D. A., *Metallurgical Transactions A,* Vol. 6A, 1975, p. 1963.

[*25*] Hart, E. W., *Journal of Engineering Materials Technology, Transactions of ASME,* Vol. 98, 1976, p. 193.

[*26*] Huang, F. H., Ellis, F. V., and Li, C. Y., *Metallurgical Transactions A,* Vol. 8A, 1977, p. 699.

T. G. Langdon[1] *and R. B. Vastava*[2]

An Evaluation of Deformation Models for Grain Boundary Sliding

---

REFERENCE: Langdon, T. G. and Vastava, R. B., **"An Evaluation of Deformation Models for Grain Boundary Sliding,"** *Mechanical Testing for Deformation Model Development, ASTM STP 765,* R. W. Rohde and J. C. Swearengen, Eds., American Society for Testing and Materials, 1982, pp. 435–451.

ABSTRACT: Grain boundary sliding is an important deformation process during high-temperature creep. Sliding often makes a significant contribution to the total creep strain of the specimen and, in addition, the sliding process is important in the nucleation, growth, and subsequent linkage of intergranular cavities.

The various theoretical deformation models for grain boundary sliding are reviewed, and it is shown that they fall into two groups depending on whether they relate to intrinsic sliding or to sliding with an associated accommodation process. Published experimental data on grain boundary sliding are tabulated for a number of different metals for comparison with the theoretical models, and the data are supplemented with recent results obtained on aluminum. It is demonstrated that all the available models lead to predictions which are inconsistent with one or more of the trends observed experimentally.

KEY WORDS: grain boundary sliding, creep

Under conditions of constant stress and at temperatures above about 0.4 T_m, where T_m is the melting point in degrees Kelvin, materials tend to exhibit a three-stage creep curve of strain, ϵ, versus time, t. Initially, there is a period in which the creep rate continuously decreases, until a situation is reached where the creep rate remains essentially constant with time. Ultimately, often after long periods of time, the material enters a region of continuously increasing creep rate, and this acceleration continues up to the point of fracture. These three regions are termed the primary, secondary (or steady-state), and tertiary stages of creep.

---

[1] Professor, Departments of Materials Science and Mechanical Engineering, University of Southern California, Los Angeles, Calif. 90007.

[2] Manufacturing Technology Specialist, Aircraft Group-Manufacturing Technology, Northrop Corporation, Hawthorne, Calif. 90250; formerly at Department of Materials Science, University of Southern California, Los Angeles, Calif. 90007.

Considerable attention has been devoted to determining and evaluating the rate-controlling mechanisms during steady-state flow. From experimental investigations, combined with theoretical considerations, it has been established that the steady-state creep rate, $\dot{\epsilon}$, may be generally represented by an equation of the form

$$\dot{\epsilon} = \frac{ADGb}{kT}\left(\frac{b}{d}\right)^p\left(\frac{\sigma}{G}\right)^n \tag{1}$$

where D is the diffusion coefficient [equal to $D_o \exp(-Q/RT)$, where D_o is a frequency factor, Q is the activation energy for the diffusion process, R is the gas constant, and T is the absolute temperature], G is the shear modulus, b is the Burgers vector, k is Boltzmann's constant, d is the grain size, σ is the applied stress, A is a dimensionless constant, and p and n are constants which represent the exponents of the inverse grain size and the stress, respectively.

The various deformation mechanisms occurring in steady-state creep may be conveniently divided into two groups, based on whether the individual processes are independent of, or dependent on, the presence of grain boundaries [*1*].[3] The first type, termed *lattice mechanisms*, are equally possible in both polycrystalline materials and single crystals, whereas the second type, termed *boundary mechanisms*, occur only in polycrystals or in special experimental configurations such as bicrystals or tricrystals.

For the former type, grain boundaries are not relevant to the deformation process and, accordingly, the grain size is not important so that $p = 0$ in Eq 1. For the latter type, the process occurs because of the presence of grain boundaries and $p \neq 0$.

Grain boundary mechanisms divide readily into two types of flow. Firstly, there is the possibility of diffusion creep, in which grain elongation occurs in the direction of the tensile stress by vacancy flow either through the lattice (Nabarro-Herring creep [*2,3*]) or along the grain boundaries (Coble creep [*4*]). Secondly, there is the possibility of grain boundary sliding without grain elongation, in which the individual grains slide over each other at, or in a zone immediately adjacent to, their common boundary. The former process has been termed *grain boundary sliding with diffusional accommodation* [*5*] or *Lifshitz sliding* [*6*], and the latter process has been termed *Rachinger sliding* [*6*].

The occurrence of grain boundary sliding is important in high-temperature creep because it may lead to the nucleation, growth, and subsequent linkage of intergranular cavities. The precise nature of the sliding deformation process, however, is not well understood at the present time. The purposes of this paper are therefore three-fold. Firstly, to briefly review the

---

[3] The italic numbers in brackets refer to the list of references appended to this paper.

theoretical models for grain boundary sliding. Secondly, to summarize the published experimental data on sliding. Thirdly, to supplement these results with recent data obtained on high-purity aluminum, and to compare these results with the theoretical predictions.

Theories of Grain Boundary Sliding

The theories of Lifshitz and Rachinger sliding divide into two distinct types. The first type is designed to predict the intrinsic rate of sliding on a grain boundary in which there is no hindrance from triple points and neighboring grains. In principle, this type of theory is applicable only to smooth, planar boundaries in bicrystal specimens. The second type considers also the accommodation of the sliding process, and thus it applies to polycrystalline materials. These two types, termed *intrinsic* and *extrinsic* sliding models, are considered separately.

Intrinsic Sliding Models

The first detailed attempts to derive relationships for the intrinsic velocity of grain boundary sliding, v_s, were performed by Ashby and co-workers [*5, 7, 8*]. By assuming that the boundary slides in a Newtonian viscous manner and that the ledges or other irregularities on the surface of the boundary are no more than atomic height, it was shown that v_s may be expressed as [*8*]:

$$v_s = \frac{8\delta D_{\mathrm{gb}} Gb}{kT}\left(\frac{\tau}{G}\right)^{1.0} \tag{2}$$

where δ is the width of the grain boundary, D_{gb} is the coefficient of grain boundary diffusion, and τ is the shear stress acting in the plane of the boundary. However, if there are ledges in the boundary plane of height h, Eq 2 is replaced by [*5*]:

$$v_s = \frac{8\delta D_{\mathrm{gb}} Gb}{kT}\left(\frac{b}{h}\right)^{2.0}\left(\frac{\tau}{G}\right)^{1.0} \tag{3}$$

Equation 3 assumes that matter is transported between the ledges by boundary diffusion, and thus it refers to Lifshitz sliding. However, this type of flow is adequately modeled for polycrystalline materials by the theories of Nabarro-Herring [*2,3*] and Coble [*4*] for diffusion creep, and it does not, in general, lead to cavity formation. In practice, it is more important to obtain a relationship for Rachinger sliding since this may lead to intergranular failure. It is anticipated that models for Rachinger sliding will be based on dislocation movement rather than vacancy flow, and two models for intrinsic sliding are now available.

Gates [9] developed a mechanism in which sliding arose from the movement of structural or intrinsic grain boundary dislocations, and it was assumed that sliding was due to a combination of glide and climb processes. For the situation where the steps in the boundary are effective obstacles to dislocation motion, it was shown that

$$v_s = \frac{\beta \delta D G b}{kT} \left(\frac{\tau}{G}\right)^{1.0} \tag{4}$$

where D is the appropriate diffusion coefficient and β is defined as

$$\beta = \pm\left(\frac{\psi \Omega^{2/3}}{x}\right) \frac{(1 + \tan\alpha \cot\gamma)}{\tan\alpha \cot\gamma} \tag{5}$$

where ψ is the inverse of the spacing of the moving dislocations in the network, Ω is the atomic volume ($\simeq b^3$), x is the length of the diffusion path (set equal to 10 b_{gb}, where b_{gb} is the Burgers vector of a boundary dislocation), and α and γ are angles relating the grain boundary to the rotation axis. Although the diffusion coefficient was not defined explicitly in this model, it would probably be equivalent to the value for grain boundary diffusion.

In a later model, Pond et al [10] considered that sliding arose from the movement of grain boundary dislocations in the boundary plane by a climb process, and the shear strain rate in the plane of the boundary due to sliding, $\dot{\gamma}_{\mathrm{gbs}}$, is then given by

$$\dot{\gamma}_{\mathrm{gbs}} = \left(\frac{2 b_{\mathrm{gb}}^3 c_j \rho_{\mathrm{gb}}}{\psi \zeta}\right)\left(\frac{D_{\mathrm{gb}} G b_{\mathrm{gb}}}{kT}\right)\left(\frac{\tau}{G}\right)^{1.0} \tag{6}$$

where c_j is the jog concentration, ρ_{gb} is the density of moving grain boundary dislocations, ψ is a factor relating b_{gb} to the distance a grain boundary dislocation climbs for each atom added ($1 \leq \psi \leq 10$), and ζ is a constant relating the orientation of b_{gb} to the grain boundary plane (typically, $\zeta \simeq 0.5$).

The important result contained in these models is that the sliding process is intrinsically Newtonian viscous in character, so that $n = 1.0$, both for the mechanism based on vacancy flow (Eqs 2 and 3) and for the two mechanisms based on dislocation climb (Eqs 4 and 6). In practice, however, experiments on polycrystals generally show $n > 1$; Pond et al [10] suggested that this may be due to a stress dependence of c_j or ρ_{gb} in Eq 6.

Extrinsic Sliding Models

The preceding models are appropriate for planar boundaries in bicrystals, but they are not directly applicable to polycrystalline materials where it is necessary to consider also the role of accommodation at the triple points.

If sliding occurs by the climb and glide of dislocations in a zone adjacent to the grain boundary, the rate of sliding is governed by the rate of climb since this is the slower process. Furthermore, if the sliding is accommodated not by an intragranular flow mechanism but by the opening of grain boundary cracks and cavities, Langdon [*11*] showed that the strain rate due to sliding in a polycrystalline material, $\dot{\epsilon}_{\mathrm{gbs}}$, is given by

$$\dot{\epsilon}_{\mathrm{gbs}} = \frac{A_1 D_\ell G b}{kT}\left(\frac{b}{d}\right)^{1.0}\left(\frac{\sigma}{G}\right)^{2.0} \tag{7}$$

where D_ℓ is the coefficient of lattice self-diffusion, and A_1 is a constant close to unity. This model therefore predicts a stress exponent of 2.0, an activation energy equal to that of lattice self-diffusion, and an inverse linear dependence on grain size.

In polycrystalline materials deforming with extensive grain boundary sliding, an important experimental observation is the formation of intragranular folds at the triple points. An example of this type of folding is shown in Fig. 1 for high-purity aluminum, where the fold A was formed by intergranular sliding on the boundary labeled B. Triple point folds are a common feature in high-temperature creep, and Gifkins [*12*] developed a model in which the formation of folds accommodated the sliding process. This model leads to a rate of sliding which is given by

$$\dot{\epsilon}_{\mathrm{gbs}} = \left(\frac{2Fy\lambda A_2}{b^2}\right)\left(\frac{D_\ell G b}{kT}\right)\left(\frac{b}{d}\right)^{2.0}\left(\frac{\sigma}{G}\right)^{4.5} \tag{8}$$

where F is a stress concentration factor due to the action of sliding at the triple point, y is the width of the triple point fold, λ is the subgrain size, and A_2 is the value of the constant in the standard rate equation for lattice creep by dislocation climb. In the early theory of climb at the head of dislocation pile-ups [*13*], A_2 is given by $3^{0.5}\pi^2/8b^{1.5}M^{0.5}$, where M is the number of active dislocation sources per unit volume; in the later theory based on climb at multipoles [*14*], A_2 is equal to $1/\beta'\pi^{0.5}b^{1.5}M^{0.5}$, where $\beta' \simeq 6$.

In practice, the subgrain size is inversely related to stress through the expression

$$\frac{\lambda}{b} = \Lambda\left(\frac{\sigma}{G}\right)^{-1} \tag{9}$$

where Λ is a constant. Thus Eq 8 is equivalent to

$$\dot{\epsilon}_{\mathrm{gbs}} = \left(\frac{2\Lambda F y A_2}{b}\right)\left(\frac{D_\ell G b}{kT}\right)\left(\frac{b}{d}\right)^{2.0}\left(\frac{\sigma}{G}\right)^{3.5} \tag{10}$$

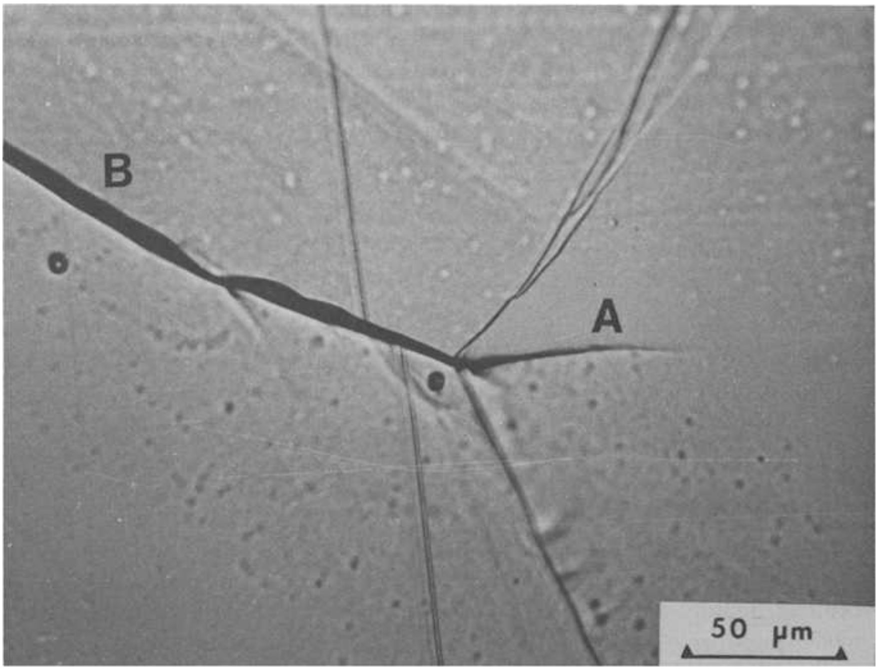

FIG. 1—*An example of a triple point fold* (A) *formed in high-purity aluminum due to intergranular sliding on boundary* B. *Specimen deformed to 7.8 percent at 573 K under a stress of 3.5 MPa; grain size = 535 µm. The stress axis is vertical.*

This model therefore gives a stress exponent of 3.5, an activation energy equal to the value for lattice self-diffusion, and an inverse grain size exponent of 2.0.

Crossman and Ashby [*15*] extended the relationship for intrinsic grain boundary sliding (Eq 3) to a polycrystalline matrix in which sliding is accommodated by plastic flow within the grains. The resultant sliding rate is

$$\dot{\epsilon}_{\text{gbs}} = \left(\frac{8\delta}{3b}\right)\left(\frac{D_{\text{gb}}Gb}{kT}\right)\left(\frac{b}{h}\right)^{2.0}\left(\frac{b}{d}\right)^{1.0}\left(\frac{\sigma}{G}\right)^{1.0} \tag{11}$$

Thus, this model predicts a stress exponent of 1.0, an activation energy equal to the value for grain boundary diffusion, and an inverse grain size exponent of 1.0.

An alternative analysis by Speight [*16*] is also available in which it is assumed that coherency is preserved at the grain boundaries. Gifkins [*17*] has pointed out that there are difficulties in applying this model to experimental data, and it also appears that the analysis represents a special limiting case [*18*]. Accordingly, the model will not be included in the present discussion.

Finally, it should be noted that several theories are available for grain boundary sliding under superplastic conditions where the grain sizes are extremely small [*19-21*]. These theories are not generally applicable to normal polycrystalline material under high-temperature creep conditions, and they are therefore excluded from this report.

Comparison with Experimental Results

The three models currently available for a calculation of $\dot{\epsilon}_{gbs}$ are summarized in Eqs 7, 10, and 11. A comparison of these equations indicates that they predict different dependences on stress, and there is also a difference between D_ℓ in Eqs 7 and 10 and D_{gb} in Eq 11 and between the term $1/d$ in Eqs 7 and 11 and the term $1/d^2$ in Eq 10. It is therefore important to compare these predictions with the available experimental evidence.

This section reviews published data with respect to the dependence on stress, temperature, and grain size. A later section describes new results which provide additional information on the basic characteristics of the sliding process.

Dependence on Stress

Many experimental measurements have been undertaken to determine the magnitude of grain boundary sliding in different materials and under various conditions of stress, temperature, and grain size. Generally, these experiments are designed to determine the strain due to sliding, ϵ_{gbs}, through a measurement of one of the three basic components of sliding, either u, v, or w. In this terminology, the process of sliding produces an offset at the boundary, and this may be resolved into a component u along the stress axis, a component v perpendicular to both the stress axis and the specimen surface, and a component w perpendicular to the stress axis in the plane of the surface. Having measured an average value of one of these three components, equations are available to calculate ϵ_{gbs} [*22*], and the value of ϵ_{gbs} is usually divided by the total macroscopic strain occurring in the sample, ϵ, to give the relative contribution of sliding to the total strain, ξ ($= \epsilon_{gbs}/\epsilon$).

In general, the experimental trends indicate that, under conditions of constant temperature and grain size, the value of ξ decreases as the stress level is increased. This trend is a consistent observation from several experiments; for example, on aluminum [*23-25*], Cu-30Zn [*26*], α-Fe [*27*], Mg-0.8Al [*28*], Pb-2Tl [*29*], and stainless steel [*30*].

The implication from these results is that the stress dependence of sliding is less than the stress dependence of the overall creep process. Thus, if the macroscopic creep rate, $\dot{\epsilon}$, is proportional to σ^n, and the grain boundary sliding rate, $\dot{\epsilon}_{gbs}$, is proportional to $\sigma^{n_{gbs}}$, where n_{gbs} is the stress exponent for sliding, then the results suggest that $n_{gbs} < n$.

Several attempts have been made to analyze the experimental data to determine directly a value for n_{gbs}. The results available to date are summarized in Table 1, divided into the three specimen categories of bicrystals, bamboo-structure wires, and polycrystals; the bamboo-structure refers to thin wires having one grain per cross section, so that in principle this procedure measures the intrinsic sliding rate without any associated accommodation process.

A review of the data in Table 1 shows large variations between the different sets of experiments. For the two experiments on bamboo-structure wires, the values of n_{gbs} are 2.0 [*36*] and 1.3 [*37*], respectively. Much higher values of n_{gbs} have been reported for bicrystals and polycrystals, although in all cases the results consistently show $n_{gbs} < n$. There is no support from the polycrystalline experiments for $n_{gbs} \simeq 1$, thereby tending to exclude the model represented by Eq 11 in which Newtonian viscous sliding is accommodated by intragranular plastic flow. Furthermore, the results indicate $n_{gbs} > 2$, thus casting some doubt on the climb-glide model given in Eq 7.

Dependence on Temperature

It is possible to obtain an indirect indication of the activation energy for grain boundary sliding by considering the change in the values of ξ as the temperature is increased under conditions of constant stress at temperatures above $\sim 0.5\ T_m$. Two sets of experiments on aluminum indicate that ξ is independent of temperature under these conditions [*25,42*], thereby implying

TABLE 1—*A comparison of the stress exponents for creep,* n, *and grain boundary sliding,* n_{gbs}.

Material	n	n_{gbs}	Reference
Bicrystals			
Al	7.9 to 8.9	2.2 to 4.6	Horton [*31*]
Al	7.2	2.6 to 4.3	Horton [*32*]
Al-0.3Cu	7.8 to 9.4	3.5 to 6.1	Horton [*31*]
Al-0.05Fe	6.0 to 8.8	2.4 to 5.8	Horton [*32*]
Pb	3.9	2.8	Strutt et al [*33*]
Sn	...	2.8 ± 0.3	Tuck [*34*]
Zn	...	4.5 ± 1.8	Horton et al [*35*]
Bamboo-structure wires			
W	...	2.0	Moon and Stickler [*36*]
Zircaloy-2	...	1.3	Burton [*37*]
Polycrystals			
Al-0.5Mg-0.5Si	($n - n_{gbs}$	$\simeq 3.9$)	Sklenička et al [*38*]
Cu-30Zn	5.1	3.3	Saxl et al [*26*]
Mg-0.8Al	5.2	2.4	Langdon [*39*]
Ni	3.8	2.3	Rozenberg [*40*]
Low-carbon steel	5.6	4.7	Horton [*41*]
316 stainless steel	6.0 ± 0.2	3.8 ± 0.2	Horton [*41*], Gates [*30*]

that $Q_{gbs} \simeq Q_\ell$, where Q_{gbs} and Q_ℓ are the activation energies for grain boundary sliding and lattice self-diffusion, respectively.

Many experiments have been conducted to determine the activation energy for sliding, and the results are summarized in Table 2. For each material, the temperature range of testing is indicated as a fraction of T_m, and the result is given as the approximate value of the ratio Q_{gbs}/Q_ℓ. This ratio is important because a value of $Q_{gbs}/Q_\ell \simeq 1$ indicates that sliding is controlled by lattice diffusion, whereas a value of $Q_{gbs}/Q_\ell \simeq 0.6$ tends to support control by grain boundary diffusion since, for most metals, $Q_{gb} \simeq 0.6\ Q_\ell$ where Q_{gb} is the activation energy for boundary diffusion. Thus an average value of Q_{gbs}/Q_ℓ close to 1 supports the inclusion of D_ℓ in the expression for $\dot{\epsilon}_{gbs}$ (Eqs 7 and 10), whereas an average value close to 0.6 supports the inclusion of D_{gb} in the sliding relationship (Eq 11).

In practice, an examination of the data in Table 2 shows a very wide scatter in the experimental results, although most, but not all, of the values of Q_{gbs}/Q_ℓ lie in the range from 0.6 to 1.0. For bicrystals, the situation is not clear from the tabulated data, and to some extent this may reflect a variation of Q_{gbs} with the angle of misorientation at the lower angles.[4] There is also an additional experimental difficulty in bicrystal tests, since some investigators concentrate on the initial sliding rates whereas others endeavor to measure a steady-state behavior. This difference is important in view of the marked slide-hardening which has been documented in some systems [*56*]. The situation is equally unresolved for polycrystalline material, with reported values of Q_{gbs}/Q_ℓ ranging from ~0.5 [*57*] to ~1.0 [*40,60*]. In the experiments on the low-carbon steel, it was observed that there was a decrease in Q_{gbs} with increasing temperature [*41*].

Dependence on Grain Size

Since grain boundary sliding depends on the presence of boundaries, the value of p is non-zero in Eq 1. However, it is difficult to determine the value of p experimentally, because it is not sufficient simply to make a direct comparison of sliding measurements taken at the same total strain, ϵ, for a series of different specimens of different grain sizes tested under the same conditions of stress and temperature. The reason is because a material having a smaller grain size will contain a larger number of boundaries and thus, *at a fixed total strain*, there are more boundaries each contributing a smaller offset.[5] This problem was not appreciated in some of the reports of a grain size dependence [*29,64*].

An analytical procedure is now available which avoids this problem

---

[4] Results obtained specifically on low-angle boundaries are excluded from Table 2.

[5] Strictly, the comparison between different grain sizes should be made *at a fixed interval of testing time.*

TABLE 2—*A comparison of the activation energies for grain boundary sliding,* Q_{gbs}, *and lattice self-diffusion,* Q_{ℓ}.

Material	Temperature Range/T_m	$\sim Q_{\text{gbs}}/Q_{\ell}$	Reference
Bicrystals			
Al	0.7 to 0.9	0.6 to 1.0	Tung and Maddin [*43*]
	0.5 to 0.6	0.3	Mima and Oka [*44*]
	0.7 to 0.8	3.0	Biscondi and Goux [*45*]
	0.8 to 1.0	1.0	
	0.6 to 0.7	0.8	Mima and Oka [*46*]
	0.5 to 0.7	0.3 to 0.7	Mima et al [*47*]
	0.6 to 0.7	0.3	Kato [*48*]
	0.6 to 0.7	1.0 to 1.2	Horton [*31*]
	0.5 to 0.7	0.3 to 0.8	Kato and Sogabe [*49*]
	0.7 to 0.8	0.2	Halliday and Beevers [*50*]
	0.8 to 0.9	1.0	
Al-0.2Ag	0.6 to 0.7	0.7	Kato [*51*]
Al-(0.1-0.3%)Cu	0.8 to 0.9	1.0	Halliday and Beevers [*50*]
Al-0.2Cu	0.6 to 0.7	0.6	Kato [*51*]
Al-0.4Cu	0.7	1.0	Horton [*31*]
Al-0.2Mg	0.6 to 0.7	0.8	Kato [*51*]
Al-0.2Zn	0.6 to 0.7	0.7	
Cu	0.7 to 0.8	0.8	Intrater and Machlin [*52*]
	0.4 to 0.5	1.0	Lagarde and Biscondi [*53*]
	0.5 to 1.0	0.2	
Fe-Cr-Ni	0.8 to 0.9	0.7 to 1.0	Michaut et al [*54*]
Pb	0.5 to 0.6	0.7	Strutt et al [*33*]
Sn	0.9	0.8	Puttick and King [*55*]
	0.9	1.8	Tuck [*34*]
Zn	0.9	0.8[a]	Horton et al [*35*]
	0.4 to 0.7	0.2	Bell et al [*56*]
	0.7 to 0.8	1.1	
Bamboo-structure wires			
W	0.7 to 0.9	0.5	Moon and Stickler [*36*]
Zircaloy-2	0.6 to 0.8	0.9	Burton [*37*]
Polycrystals			
Al	0.6 to 0.7	0.5	Rozenberg and Epshtein [*57*]
Cu-10Zn	0.6 to 0.7	0.6	Saxl et al [*58*]
Cu-30Zn	0.6 to 0.7	0.6	Sklenička et al [*59*]
Ni	0.5 to 0.6	1.0	Rozenberg [*40*]
	0.6 to 0.7	1.0	Cíha et al [*60*]
Low-carbon steel	0.5 to 0.6	0.8 to 1.0[b]	Horton [*41*]
316 stainless steel	0.6 to 0.7	0.7[c]	Gates [*61*]

[a] The experimental value of Q_{gbs} was 130 ± 21 kJ mol^{-1}, which is higher than the value of ~ 91 kJ mol^{-1} for lattice self-diffusion in zinc [*62*]. However, there is evidence of an activation energy for creep, Q_c, of ~ 160 kJ mol^{-1} in this same temperature range [*63*]. The ratio of 0.8 refers to Q_{gbs}/Q_c.

[b] This ratio represents the experimental value of Q_{gbs}/Q_c ($Q_{\text{gbs}} = 260 - 340$ kJ mol^{-1}; $Q_c =$ 340 kJ mol^{-1}).

[c] This ratio represents the experimental value of Q_{gbs}/Q_c ($Q_{\text{gbs}} = 355 \pm 38$ kJ mol^{-1}; $Q_c =$ 485 ± 17 kJ mol^{-1}).

[*39,65*], and this has been applied to a Mg-0.8Al alloy [*39,65*] and MgO [*66*]. The results from these two materials give values for the inverse grain size exponent for sliding, p_{gbs}, of 1.0 and 1.4, respectively. Thus these values of p_{gbs} tend to support the dependence on grain size shown in Eqs 7 and 11.

Grain Boundary Sliding in Aluminum

Experimental Results on Aluminum

As part of an investigation of the high-temperature creep properties of aluminum and an Al-5Mg alloy, a detailed series of measurements was taken to determine the role of grain boundary sliding in these materials. Full details of the experiments will be reported elsewhere. In this section, a brief description is given of the results obtained on pure aluminum, and a comparison of these data with the theoretical models is presented in the following section.

Experiments were conducted on tensile specimens cut from rods of high-purity (99.995 percent) aluminum. The tests were performed at various stress levels using a range of grain sizes from 200 to 4500 μm and testing temperatures from 573 to 773 K. All experiments were carried out under constant stress conditions, using a creep machine equipped with a special lever arm to maintain a constant stress in tension. Some of the basic creep results have been published elsewhere [*67*].

The extent of grain boundary sliding was determined in these experiments using two-beam interferometry to measure the v-offsets perpendicular to the specimen surface [*68*]. An example of this procedure is shown in Fig. 2 for the Al-5Mg alloy. The sliding offset, v, was recorded by measuring the displacement of the interference fringes when they were oriented approximately perpendicular to the grain boundary; the separation between adjacent fringes is 0.27 μm. In practice, it is observed that the sliding offset varies from point to point along a grain boundary; this is illustrated for aluminum by the montage of interference micrographs shown at a single boundary in Fig. 3. To obtain a statistically meaningful value of the mean offset, $\bar{v}$, it was necessary to take readings at a total of 300 randomly selected boundaries, and in each case a point on the boundary was randomly selected as the place of measurement. This procedure leads to a mean offset with an associated error bar which is, typically, ± 10 percent at the 95 percent confidence level.

Figure 4 shows a typical result obtained using this procedure; the upper curve shows the total strain, ϵ, versus the testing time, t, for a specimen of aluminum held at 573 K under a constant stress of 2.6 MPa, and the lower curve shows the corresponding plot of $\bar{v}$ versus t. It is important to note that both curves depict a similar variation with time, and that the lower curve may be used, with the appropriate equations [*22*], to calculate a rate of sliding, $\dot{\epsilon}_{gbs}$.

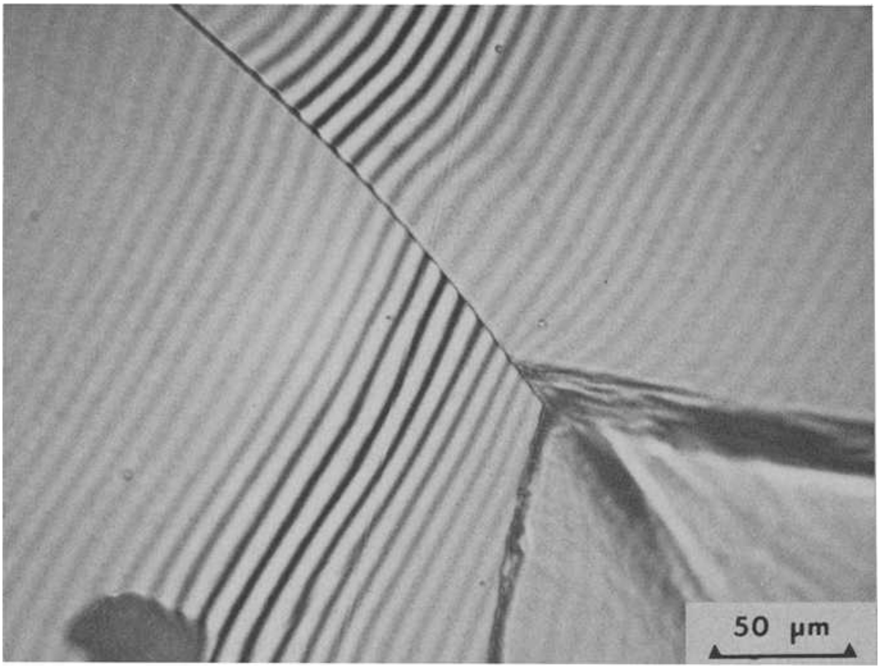

FIG. 2—*Method of measuring the v-component of sliding using two-beam interferometry. Specimen of Al-5Mg deformed to 2.5 percent at 573 K under a stress of 12.1 MPa: grain size = 575 μm.*

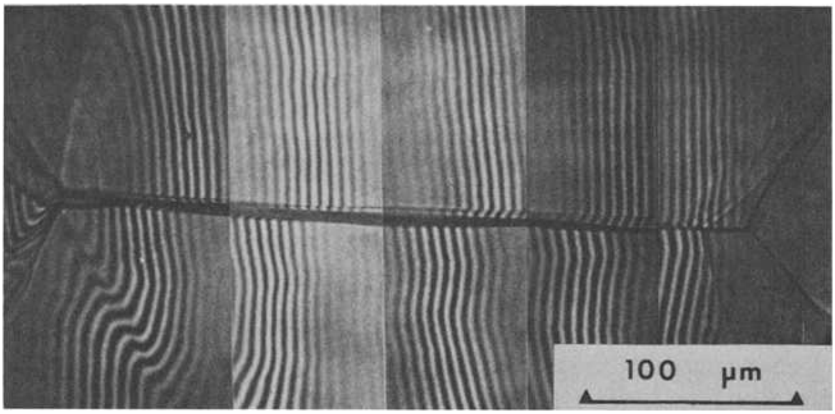

FIG. 3—*Montage of interference fringes on a single grain boundary in high-purity aluminum, showing the variation in the v-offset along the boundary. Specimen deformed to 4.3 percent at 573 K under a stress of 3.5 MPa: grain size = 300 μm.*

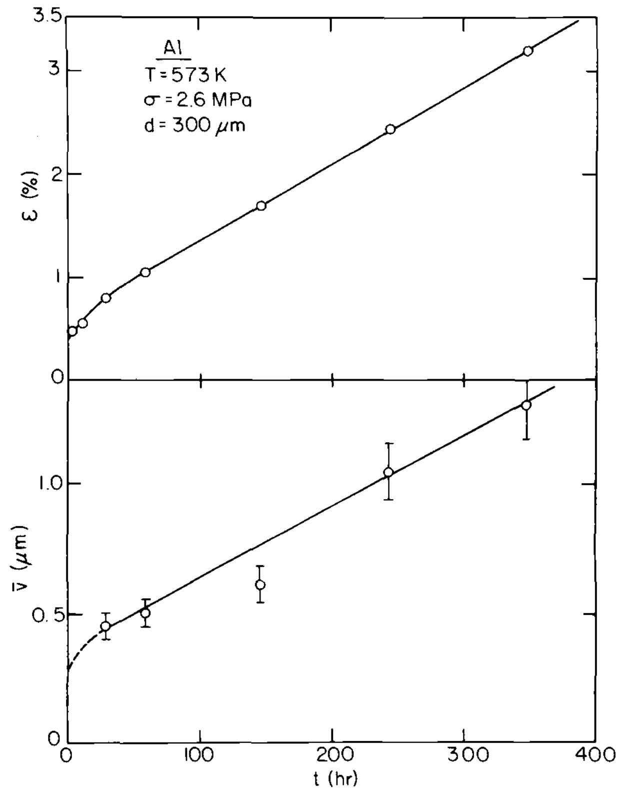

FIG. 4—*Results obtained on an aluminum specimen tested at 573 K and 2.6 MPa: total strain, ε, (upper) and mean offset, v̄, (lower) versus testing time, t.*

Two methods were used to determine the dependence of sliding on temperature. In the first method, the testing temperature was increased by about 50 to 100 K at a selected strain during the test, and the values of $\bar{v}$ were compared before and after the change. In the second method, several specimens were tested at the same stress level but at different constant temperatures. An example of the latter procedure is shown in Fig. 5 for a stress of 1.7 MPa, showing the experimental values of $\bar{v}$ as a function of ϵ for four different conditions of grain size and temperature. As indicated in Fig. 5, the experimental datum points show no obvious dependence on temperature, and the conclusion from these tests was that both the grain boundary sliding mechanism and the macroscopic creep process exhibited a similar dependence on temperature.

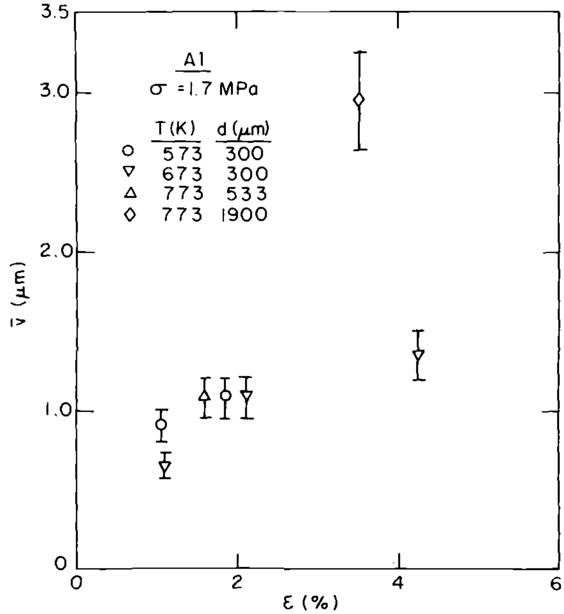

FIG. 5—*Mean offset,* v̄, *versus strain,* ε, *for specimens of aluminum tested at a stress of 1.7 MPa, with different temperatures and grain sizes.*

Comparison of Results on Aluminum with Theoretical Models

As discussed in the section on Comparison with Experimental Results, and documented in Tables 1 and 2, the published data for grain boundary sliding show no clear trend in the values of either n_{gbs} or Q_{gbs}. In fact, the only consistent feature of the published results is $1.0 < n_{\text{gbs}} < n$.

In the present experiments on polycrystalline aluminum, it was found that $n_{\text{gbs}} = 3.3 \pm 0.2$, $Q_{\text{gbs}} = 145 \pm 14$ kJ mol^{-1}, and $p_{\text{gbs}} = 0.9 \pm 0.1$. By contrast, the overall creep behavior gave $n = 4.5 \pm 0.2$ [*67*] and $Q = 145 \pm 10$ kJ mol^{-1}, and the latter value is equivalent to the activation energy for lattice self-diffusion, Q_ℓ. Thus the sliding results again show $n_{\text{gbs}} < n$, but, in addition, they yield $Q_{\text{gbs}} = Q = Q_\ell$.

Table 3 shows a comparison of the experimental values of n_{gbs}, Q_{gbs}, and p_{gbs} with the three theoretical models represented by Eqs 7, 10, and 11. From this comparison, it is apparent that none of the models is entirely consistent with the experimental results. On the one hand, the climb-glide model of Eq 7 predicts the correct activation energy and dependence on grain size but gives a stress exponent which appears to be too low; on the other hand, the accommodation of sliding by triple point folds, as given in Eq 10, predicts a

TABLE 3—*A comparison of the experimental results on aluminum with the theoretical models for grain boundary sliding.*

	n_{gbs}	Q_{gbs}	p_{gbs}
Experimental results	3.3 ± 0.2	Q_ℓ	0.9 ± 0.1
Eq 7	2.0	Q_ℓ	1.0
Eq 10	3.5	Q_ℓ	2.0
Eq 11	1.0	Q_{gb}	1.0

reasonable stress exponent and the correct activation energy, but it leads to a stronger dependence on grain size than is observed experimentally.

It is clear from this analysis that more experiments are needed to determine whether similar trends apply also in other materials, and it is apparent that new or improved theoretical models are required to more accurately describe the sliding process.

Summary and Conclusions

1. The theories of grain boundary sliding divide into intrinsic models which describe the sliding process without reference to accommodation and extrinsic models which incorporate the accommodation of sliding in a polycrystalline material. These models are reviewed, and it is demonstrated that three relationships are available to describe the rate of sliding in a polycrystal.

2. Published experimental results on grain boundary sliding are tabulated, and it is shown that there are wide variations in the apparent dependence of sliding on stress and temperature. A consistent feature of these data is that $n_{gbs} < n$, where n_{gbs} and n are the stress exponents for grain boundary sliding and the overall creep process, respectively.

3. New results on polycrystalline aluminum are described, and the experimental trends are compared with the three theoretical relationships for grain boundary sliding. It is concluded that none of the models is entirely consistent with the experimental data.

Acknowledgments

This work was supported by the United States Department of Energy under Contract DE-AM03-76SF00113 PA-DE-AT03-76ER10408.

References

[*1*] Langdon, T. G. in *Deformation of Ceramic Materials*, R. C. Bradt and R. E. Tressler, Eds., Plenum, New York, 1975, pp. 101-126.

[2] Nabarro, F. R. N. in *Report of a Conference on Strength of Solids.* The Physical Society, London, 1948, pp. 75-90.

[3] Herring, C., *Journal of Applied Physics.* Vol. 21, 1950, pp. 437-445.

[4] Coble, R. L., *Journal of Applied Physics.* Vol. 34, 1963, pp. 1679-1682.

[5] Raj, R. and Ashby, M. F., *Metallurgical Transactions,* Vol. 2, 1971, pp. 1113-1127.

[6] Cannon, W. R., *Philosophical Magazine,* Vol. 25, 1972, pp. 1489-1497.

[7] Ashby, M. F., Raj, R., and Gifkins, R. C., *Scripta Metallurgica,* Vol. 4, 1970, pp. 737-741.

[8] Ashby, M. F., *Surface Science.* Vol. 31, 1972, pp. 498-537.

[9] Gates, R. S., *Acta Metallurgica,* Vol. 21, 1973, pp. 855-864.

[10] Pond, R. C., Smith, D. A., and Southerden, P. W. J. in *Proceedings,* 4th International Conference on the Strength of Metals and Alloys, Laboratoire de Physique du Solide, E.N.S.M.I.M., Nancy, France, 1976, Vol. 1, pp. 378-382.

[11] Langdon, T. G., *Philosophical Magazine,* Vol. 22, 1970, pp. 689-700.

[12] Gifkins, R. C., *Journal of the Australian Institute of Metals,* Vol. 18, 1973, pp. 137-145.

[13] Weertman, J., *Journal of Applied Physics,* Vol. 28, 1957, pp. 362-364.

[14] Weertman, J., *Transactions of the American Society for Metals.* Vol. 61, 1968, pp. 681-694.

[15] Crossman, F. W. and Ashby, M. F., *Acta Metallurgica,* Vol. 23, 1975, pp. 425-440.

[16] Speight, M. V., *Acta Metallurgica,* Vol. 24, 1976, pp. 725-729.

[17] Gifkins, R. C., *Metallurgical Transactions A.* Vol. 8A, 1977, pp. 1507-1516.

[18] Chen, I. W. and Argon, A. S., *Acta Metallurgica,* Vol. 27, 1979, pp. 749-754.

[19] Ball, A. and Hutchison, M. M., *Metal Science Journal.* Vol. 3, 1969, pp. 1-7.

[20] Gifkins, R. C., *Metallurgical Transactions A.* Vol. 7A, 1976, pp. 1225-1232.

[21] Ronay, M. and Aliotta, C. F., *Philosophical Magazine A,* Vol. 42, 1980, pp. 161-184.

[22] Langdon, T. G., *Metallurgical Transactions.* Vol. 3, 1972, pp. 797-801.

[23] McLean, D., *Journal of the Institute of Metals.* Vol. 81, 1952-53, pp. 293-300.

[24] McLean, D. and Farmer, M. H., *Journal of the Institute of Metals.* Vol. 83, 1954-55, pp. 1-10.

[25] Davies, P. W., Stevens, R. N., and Wilshire, B., *Journal of the Institute of Metals,* Vol. 94, 1966, pp. 49-55.

[26] Saxl, I., Sklenička, V., and Čadek, J., *Philosophical Magazine,* Vol. 31, 1975, pp. 233-236.

[27] Westwood, H. J. and Taplin, D. M. R., *Journal of the Australian Institute of Metals.* Vol. 20, 1975, pp. 141-149.

[28] Bell, R. L. and Langdon, T. G., *Journal of Materials Science,* Vol. 2, 1967, pp. 313-323.

[29] Gifkins, R. C., *Journal of the Australian Institute of Metals;* Vol. 8, 1963, pp. 148-157.

[30] Gates, R. S., *Materials Science and Engineering,* Vol. 27, 1977, pp. 115-125.

[31] Horton, C. A. P., *Scripta Metallurgica,* Vol. 3, 1969, pp. 253-257.

[32] Horton, C. A. P., *Acta Metallurgica.* Vol. 20, 1972, pp. 477-484.

[33] Strutt, P. R., Lewis, A.-M., and Gifkins, R. C., *Journal of the Institute of Metals,* Vol. 93, 1964-65, pp. 71-77.

[34] Tuck, B., *Physica Status Solidi,* Vol. 8, 1965, pp. 153-159.

[35] Horton, C. A. P., Thompson, N. B. W., and Beevers, C. J., *Metal Science Journal.* Vol. 2, 1968, pp. 19-24.

[36] Moon, D. M. and Stickler, R., *Philosophical Magazine,* Vol. 24, 1971, pp. 1087-1094.

[37] Burton, B., *Acta Metallurgica,* Vol. 26, 1978, pp. 1237-1241.

[38] Sklenička, V., Pahutová, M., and Čadek, J. in *The Microstructure and Design of Alloys: Proceedings of the Third International Conference on the Strength of Metals and Alloys,* The Institute of Metals and The Iron and Steel Institute, London, 1973, Vol. 1, pp. 207-212.

[39] Langdon, T. G. in *The Microstructure and Design of Alloys: Proceedings of the Third International Conference on the Strength of Metals and Alloys,* The Institute of Metals and The Iron and Steel Institute, London, 1973, Vol. 1, pp. 222-226.

[40] Rozenberg, V. M., *Fizika Metallov i Metallovedenie,* Vol. 15, 1963, pp. 397-404.

[41] Horton, C. A. P. in *Grain Boundaries,* The Institution of Metallurgists, London, 1976, pp. E1-E6.

[*42*] Fazan, B., Sherby, O. D., and Dorn, J. E., *Transactions of the Metallurgical Society of AIME*, Vol. 200, 1954, pp. 919-922.
[*43*] Tung, S. K. and Maddin, R., *Transactions of the Metallurgical Society of AIME*, Vol. 209, 1957, pp. 905-910.
[*44*] Mima, G. and Oka, T., *Transactions of the Japan Institute of Metals*. Vol. 8, 1967, pp. 32-39.
[*45*] Biscondi, M. and Goux, C., *Mémoires Scientifiques de la Revue de Métallurgie*, Vol. 65, 1968, pp. 167-179.
[*46*] Mima, G. and Oka, T., *Journal of the Japan Institute of Metals*, Vol. 32, 1968, pp. 228-233.
[*47*] Mima, G., Oka, T., and Baba, K., *Journal of the Japan Institute of Metals*, Vol. 32, 1968, pp. 943-949.
[*48*] Kato, M., *Transactions of the Japan Institute of Metals*. Vol. 10, 1969, pp. 215-222.
[*49*] Kato, M. and Sogabe, T., *Transactions of the Japan Institute of Metals*, Vol. 12, 1971, pp. 107-112.
[*50*] Halliday, M. D. and Beevers, C. J., *Journal of Materials Science*, Vol. 6, 1971, pp. 1254-1260.
[*51*] Kato, M., *Journal of the Japan Institute of Metals*, Vol. 31, 1967, pp. 1180-1185.
[*52*] Intrater, J. and Machlin, E. S., *Journal of the Institute of Metals*. Vol. 88, 1959-60, pp. 305-310.
[*53*] Lagarde, P. and Biscondi, M., *Mémoires Scientifiques de la Revue de Métallurgie*, Vol. 71, 1974, pp. 121-131.
[*54*] Michaut, B., Silvent, A., and Sainfort, G., *Mémoires Scientifiques de la Revue de Métallurgie*, Vol. 71, 1974, pp. 527-538.
[*55*] Puttick, K. E. and King, R., *Journal of the Institute of Metals*, Vol. 80, 1951-52, pp. 537-544.
[*56*] Bell, R. L., Thompson, N. B. W., and Turner, P. A., *Journal of Materials Science*, Vol. 3, 1968, pp. 524-533.
[*57*] Rozenberg, V. M. and Epshtein, I. A., *Fizika Metallov i Metallovedenie*, Vol. 9, 1960, pp. 124-132.
[*58*] Saxl, I., Sklenička, V., and Čadek, J., *Materials Science and Engineering*, Vol. 21, 1975, pp. 49-56.
[*59*] Sklenička, V., Saxl, I., Popule, J., and Čadek, J., *Physica Status Solidi (a)*, Vol. 29, 1975, pp. 315-321.
[*60*] Cíha, K., Milička, K., and Čadek, J., *Kovové Materiály*, Vol. 6, 1968, pp. 313-331.
[*61*] Gates, R. S., *Materials Science and Engineering*, Vol. 27, 1977, pp. 127-132.
[*62*] Shirn, G. A., Wajda, E. S., and Huntington, H. B., *Acta Metallurgica*, Vol. 1, 1953, pp. 513-518.
[*63*] Tegart, W. J. M. and Sherby, O. D., *Philosophical Magazine*, Vol. 3, 1958, pp. 1287-1296.
[*64*] Gates, R. S. and Horton, C. A. P., *Materials Science and Engineering*, Vol. 27, 1977, pp. 105-114.
[*65*] Langdon, T. G. in *Rate Processes in Plastic Deformation of Materials*, J. C. M. Li and A. K. Mukherjee, Eds., American Society for Metals, Metals Park, Ohio, 1975, pp. 410-433.
[*66*] Langdon, T. G., *Journal of the American Ceramic Society*, Vol. 58, 1975, pp. 92-93.
[*67*] Vastava, R. B. and Langdon, T. G. in *Advances in Materials Technology in the Americas-1980*. I. Le May, Ed., American Society of Mechanical Engineers, New York,1980, Vol. 2, pp. 61-66.
[*68*] Langdon, T. G., *Canadian Metallurgical Quarterly*, Vol. 13, 1974, pp. 223-228.

J-Y. Guinemer[1] *and A. Plumtree*[2]

An Elevated Temperature Fatigue Crack Model for Stainless Steels

---

REFERENCE: Guinemer, J-Y. and Plumtree, A., "**An Elevated Temperature Fatigue Crack Model for Stainless Steels,**" *Mechanical Testing for Deformation Model Development, ASTM STP 765,* R. W. Rohde and J. C. Swearengen, Eds., American Society for Testing and Materials, 1982, pp. 452–466.

ABSTRACT: A model has been developed for the prediction of cyclic crack growth rates at different frequencies and has been verified for an austenitic stainless steel at elevated temperature. The model is based on the damage concept, and accounts for the viscoplastic behavior of stainless steels at elevated temperature. The inclusion of a creep component in such a model results in good correlation between the predicted and observed data.

KEY WORDS: prediction of cyclic crack growth, creep-fatigue interaction, damage concepts, high temperature fatigue, austenitic stainless steel

Nomenclature

K, ΔK	Stress intensity factor, MPa $\sqrt{m}$
F	Functional relationship
A_0	Original cross sectional area
D	Damage
dD_f	Incremental fatigue damage
dD_c	Incremental creep damage
σ	Stress
ϵ	Strain
T	Temperature
α	Hardening parameter

---

[1] Post Doctoral Fellow, Department of Mechanical Engineering, University of Waterloo, Waterloo, Ontario, Canada N2L 3G1; currently Research Engineer, Engineering System International, 94150 Rungis, France.

[2] Professor and Associate Chairman, Department of Mechanical Engineering, University of Waterloo, Waterloo, Ontario, Canada N2L 3G1.

N	Number of cycles
t	Time
ϵ_p	Plastic strain
s	Exponent-Norton law
A	Constant-Norton Law
σ_∞	Stress at infinite distance
$\Delta\sigma$	Stress range
$\Delta\epsilon$	Strain range
$\Delta\epsilon_p$	Plastic strain range
E	Young's modulus
K_σ	Stress concentration coefficient
K_ϵ	Strain concentration coefficient
f	Frequency
γ	Exponent of Manson-Coffin relation
C	Constant of Manson-Coffin relation
δa	Increment of crack length
$\delta a/\delta N$	Crack growth rate, mm/cycle
C_f	Constant of Paris law
η	Exponent of Paris law
C_c	Constant of creep crack growth law
ν	Exponent

Austenitic stainless steels, used over a wide temperature range, are often employed in nuclear reactor components which are loaded under severe conditions (strain cycling, hold time at a maximum load, and thermal cycling). Microcracks can occur where stress concentrations exist at notches, welds, etc. Growth and linkage of these microcracks through the material results in the formation of a creep or fatigue crack whose propagation is influenced by the frequency of loading and the R-ratio. Low frequencies or long hold times are associated with high fatigue crack propagation rates [*1*].[3]

Fatigue and creep crack growth may be described by several parameters. For fatigue crack propagation the reader is directed to the work of Bui [*2*]; Refs *3* to *5* should be consulted for a recent review of creep crack propagation work. A common parameter used to express the crack growth rates for both these processes is the stress intensity factor; this will be used in the present work.

Among the many applications of damage concepts to the area of fracture is the interaction between creep and fatigue at elevated temperature. This concept has been used successfully to predict failure of components [*6-8*]. Kachanov [*9*] originally proposed a theory of rupture based on a concept of continuity or damage which defined the capacity of the material to carry load

---

[3] The italic numbers in brackets refer to the list of references appended to this paper.

after a given time t. In this case, the new load bearing cross-sectional area would be $A_t = A_0(1 - D)$ where A_0 is the original cross-sectional area and D is the damage [*10*]. The boundary conditions are $D = 0$ for the virgin material $(A_t = A_0)$ and $D = 1$ at failure $(A_t = 0)$.

This concept may be used to describe creep-fatigue interaction. For a one-dimensional problem, we require differential equations with respect to time or cycles. The fatigue process may be expressed as:

$$dD_f = F_f(\sigma \text{ or } \epsilon, T, \alpha, D_f, D_c, \ldots)dN \tag{1}$$

and the creep process as:

$$dD_c = F_c(\sigma, T, \alpha, D_c, D_f, \ldots)dt \tag{2}$$

The fatigue damage increment (dD_f) and the creep damage increment (dD_c) are assumed to be additive during creep-fatigue interaction; hence

$$dD = F_c(\sigma, T, \alpha, D, \ldots)\,dt + F_f(\sigma \text{ or } \epsilon, T, \alpha, D, \ldots)dN \tag{3}$$

Definition of the Model

Austenitic stainless steels at elevated temperature display some elasto-viscoplastic behavior. Under steady-state creep this may be expressed by the Norton equation:

$$d\epsilon_p = \left(\frac{\sigma}{A}\right)^s dt \tag{4}$$

Integration of Eq 4 for a triangular stress function from zero to $\Delta\sigma$ gives:

$$\Delta\epsilon_p = \frac{1}{f}\left(\frac{\Delta\sigma}{B}\right)^s \tag{5}$$

where

$$B = 2A\,[2(s + 1)]^{1/s}.$$

This equation will apply for each stress cycle during fatigue. Neuber's rule [*11*] may be used under these cyclic conditions [*12*] to give:

$$\Delta\sigma\Delta\epsilon_p = K_t^2 \frac{\Delta\sigma_\infty^2}{E} \tag{6}$$

assuming that the elastic strain at the crack tip may be neglected.

In Eq 6, K_t^2 is equal to the product of $K_\sigma K_\epsilon$.

Combining Eqs 5 and 6 and eliminating $\Delta\sigma$ gives:

$$\Delta\epsilon_p = \frac{1}{B^{\frac{s}{s+1}}} \frac{1}{f^{\frac{1}{s+1}}} \left(K_t^2 \frac{\Delta\sigma_\infty{}^2}{E}\right)^{\frac{s}{s+1}} \tag{7}$$

This equation is now in a form to accept the damage concept, assuming that the latter is strain controlled. The Manson-Coffin relation modified for damage may be expressed [*7-8*] as

$$\frac{dD}{dN} = C(\Delta\epsilon_p)^\gamma \tag{8}$$

where γ is about 2 and D is the damage in the material. The damage in the vicinity of the crack tip may be expressed by substituting Eq 7 into Equation 8; this gives

$$\frac{dD}{dN} = \frac{C}{B^{\frac{\gamma s}{s+1}} f^{\frac{\gamma}{s+1}}} \left(K_t^2 \frac{\Delta\sigma_\infty{}^2}{E}\right)^{\frac{\gamma s}{s+1}} \tag{9}$$

If the crack is represented by a notch with a finite radius at the tip, then at a distance x ahead of the notch, the value of K_t is K_{t_x}. This value of K_{t_x} depends on the approximate shape of the crack tip under consideration.

The number of cycles needed to satisfy the condition where damage is unity (failure) at a point (A) ahead of the notch may be determined from Eq 9. Thus $D_A = 1$ accounts for the failure at a distance x ahead of the crack, and results in

$$\frac{\delta a}{\delta N} = \frac{C}{B^{\frac{\gamma s}{s+1}} f^{\frac{\gamma}{s+1}}} \left(K_{t_x}{}^2 \frac{\Delta\sigma_\infty{}^2}{E}\right)^{\frac{\gamma s}{s+1}} \tag{10}$$

where

$\delta a = x$, and

$\delta N =$ number of cycles needed to obtain $D_A = 1$.

The fatigue crack growth rate of a viscoplastic material such as stainless steel at elevated temperature is frequency dependent [*3,13,14*]. However, cobalt base alloy HS 188 did not show such an effect under the test conditions investigated [*15*]. This discrepancy may be attributed to the differences in viscoplastic behavior. The frequency dependence for crack growth is expressed by a power law, and the exponent of $\gamma/(s+1)$ in Eq 10 is estimated to be $\beta = \gamma/(s+1) \simeq 0.16$ (where $s \simeq 11$ and $\gamma \simeq 2$) for austenitic stainless steel at elevated temperature. This value is quite close to that experimentally determined by Carden [*13*].

The damage concept is used to describe the initiation of cracks. This description may be termed Damage Mechanics. When macrocracks link to form a single crack another set of parameters are introduced in order to describe propagation; that is, Fracture Mechanics are applied. However, the cause of crack growth is a continuous damage mechanism occurring at the crack tip, especially in the plastic zone. In this instance the damage concept should describe either the initiation or the propagation stage [*16*]. The propagation phase involves the initiation of microcracks ahead of the crack tip followed by their linkage.

Since the damage mechanisms occurring during crack initiation and propagation are similar, it is possible to apply the same rationale as that used by Chaboche et al [*7*] and Lemaitre and Plumtree [*8*] for creep-fatigue damage interaction to give the following form of the crack growth model:

$$\delta a = F_1(K,\ldots)\,\delta N + F_2(K,\ldots)\,\delta t \tag{11}$$

where

δa = increment of crack length,
δN = increment of cycles,
δt = increment of time,

and F_1 is characteristic of the fatigue process which, for instance, may be Paris's law, and F_2 is characteristic of the creep process. This model has been successfully applied to IN 100 at 1000°C [*17*] and to an aluminum alloy [*17*].

Regarding the modified damage equation (10), terms which include some aspect of frequency (or time) must be introduced for a complete description of viscoplastic behavior; that is,

$$F_1(K,\ldots) = C_f K^{\eta} f^{-\beta} \tag{12}$$

where C_f, η, β are constants, and

$$F_2(K,\ldots) = C_c K^{\nu} \tag{13}$$

where C_c and ν are constants.

Consequently, the model takes its final form after integration over one cycle and is

$$\delta a = [C_f K^{\eta} f^{-\beta} + \frac{C_c}{\nu + 1} K^{\nu} f^{-1}]\,\delta N \tag{14}$$

Hence, provided all the assumptions are correct, Eq 14 may now be used to predict crack growth at different frequencies. Obviously, if the model is to be of any use, the constants must be determined. It is possible to identify them from the results of one specialized set of tests. Then independent tests may be used to verify the proposed model.

Identification and Verification for AISI Type 304 Stainless Steel

Identification

The coefficients C_f and η, which represent the fatigue process, may be obtained from the plots of log *da/dN* versus log ΔK published by James [*14*] at 538°C for a frequency of 66.67 Hz (Fig. 1). The coefficient C_f was calculated to be 3.23×10^{-8}, and η, the slope 2.95.

On the other hand, the coefficients C_c and ν were obtained from the work of Kawasaki and Horiguchi [*18*] (Fig. 2) who performed creep tests between 700 and 600°C. Extrapolation of the *da/dt* versus K data to 538°C gave a value of 7×10^{-20} for C_c and 10 for ν. Good agreement of these results with the recent analysis of Lloyd [*19*] on AISI Type 316 stainless steel should be noticed (where $C_c = 2.71 \times 10^{-21}$, $\nu = 10$).

Also, these coefficients C_f, η, C_c, and ν are on the same order of magnitude as those obtained by Ellison and Walton [*20*].

Verification

The model may now be verified using different frequencies. It is possible to compare observed and predicted crack growth rates by two means. Firstly, the log-log plot of crack growth rate versus the reciprocal of frequency may be used, which is the same approach as that used by Carden [*13*] and Döner [*15*] to emphasize the influence of the frequency. With this in mind, the results are presented in Fig. 3. Good agreement between the predicted and experimental crack growth rates is seen for low ΔK-values at all frequencies and for higher ΔK-values at high frequencies. Secondly, it is possible to compare the experimental and predicted data in the form of a log crack growth rate versus log ΔK diagram (Fig. 4). Good agreement is again seen at low ΔK-values, whereas at higher values the model predicts higher crack growth rates than those obtained from an extrapolation of the Paris law.

Experimental Procedure

The present experiments were conducted at 500°C on AISI Type 304L stainless steel compact tension specimens (width of 40 mm and thickness of 15 mm) using a servocontrolled electro-hydraulic test machine. The

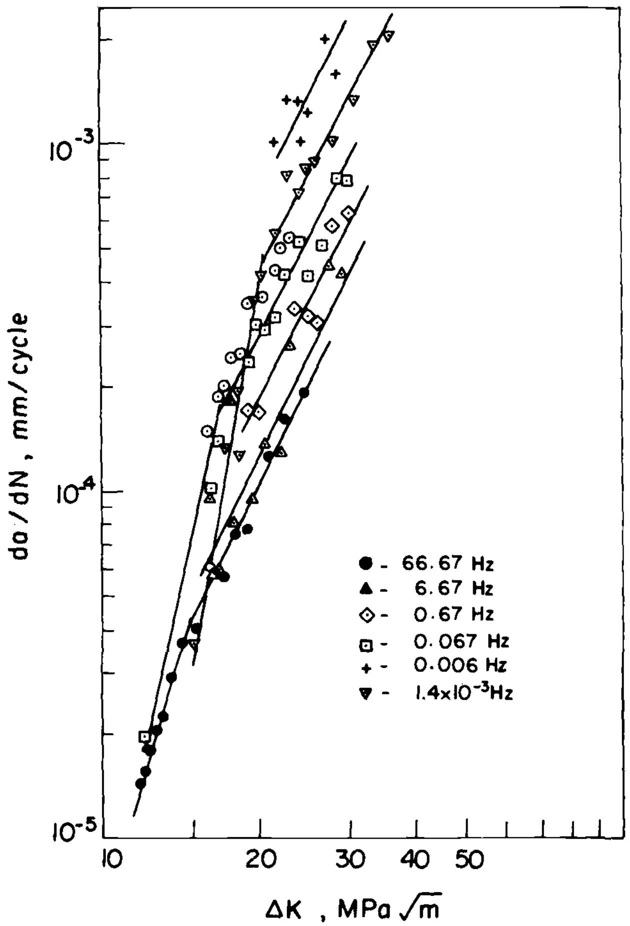

FIG. 1—*Fatigue crack growth rate versus stress intensity factor range for AISI Type 304 stainless steel at 538°C. After James* [14].

temperature was measured by a thermocouple located on the specimen, and a second thermocouple was used to control the high-frequency generator. The induction heating coil was constructed with two loops wound in counter direction on either side of the specimen. Each loop consisted of two turns. The tests were carried out under load control, and a chevron-type notch was employed with an initial crack length of 16 mm. No measurements were taken until a planar crack front had been developed. Crack growth measurements were obtained using the electrical potential technique [*21*]. The current was applied through contacts attached adjacent to the holding

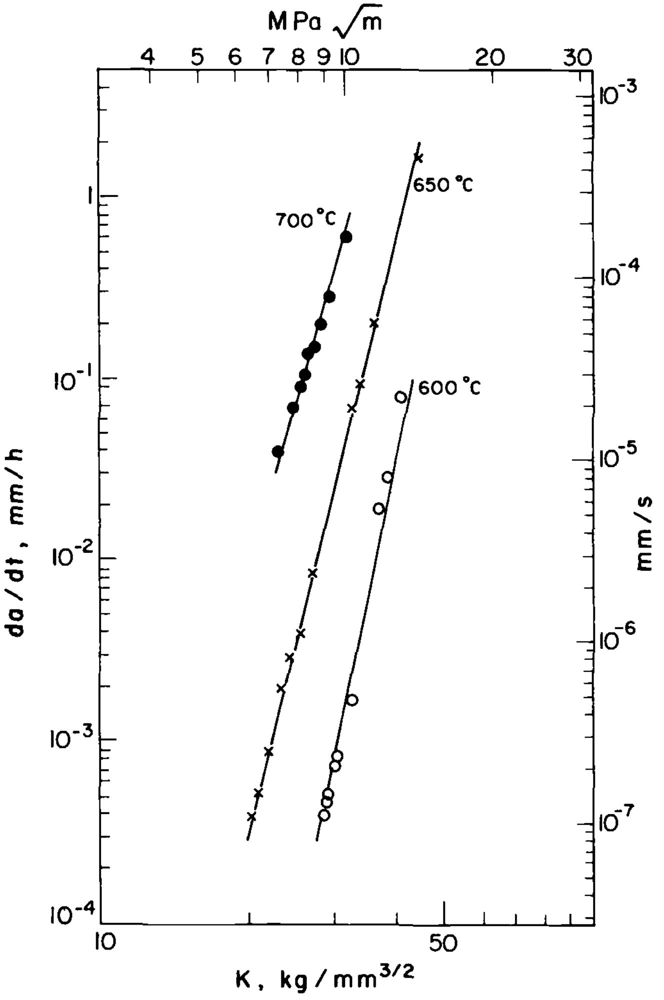

FIG. 2—*Creep crack growth rates versus stress intensity factor for AISI Type 304 stainless steel at various temperatures. After Kawasaki and Horiguchi* [18].

pins in the thickness direction. The voltage was measured with the aid of sensors placed above and below the crack on the same side of the specimen.

Two types of tests were performed. The first was a pure fatigue test at f = 5 Hz using a triangular wave, whereas the second test involved the same ramp up and down but with a dwell period of 0.8 s. The crack growth rate results are plotted in Fig. 5.

Examination of the fracture surfaces revealed that in all cases the failure

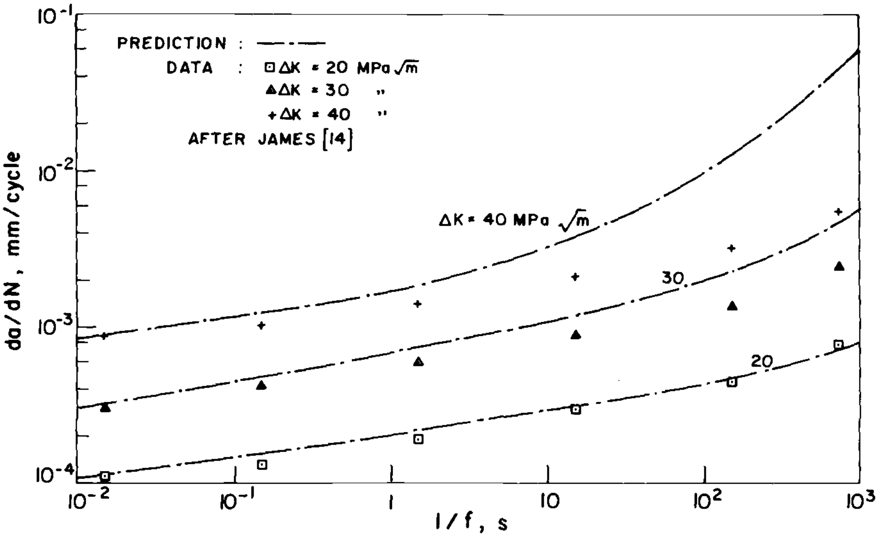

FIG. 3—*Comparison of predicted and observed crack growth rates versus reciprocal of frequency for AISI Type 304 stainless steel at 538°C.*

was transgranular. At the very low stress intensity values with a corresponding low crack growth rate close to the threshold, a faceted fracture surface was observed. At higher stress intensity values, many intergranular side cracks were seen, although the main crack was predominantly transgranular.

Identification and Verification for AISI Type 304L Stainless Steel

To determine the four coefficients (C_f, η, C_c, and ν) for AISI Type 304L stainless steel, it is possible to use the results of the fatigue test carried out at 5 Hz shown in Fig. 5. The first stage of this curve at low ΔK-values fits the fatigue part (C_f and η), and the second stage of the curve at high ΔK-values fits the creep contribution (C_c and ν).

The fatigue part gives a value of 6.49×10^{-9} for C_f and 3.54 for η. Extrapolation of C_c, as described previously, gives a value of 10^{-21} at 500°C. The exponent, ν, has been obtained from the 5 Hz fatigue test and is equal to 12.5. This evolution of ν agrees with the results of Kawasaki and Horiguchi [*18*], since ν increases with decrease in temperature.

The coefficients C_c, C_f, η, and ν may now be used for crack growth prediction in Eq 14. A comparison of the observed and predicted results is shown in Fig. 6. Good agreement between the predicted and the actual growth rates for the sequence with short dwell periods is particularly encouraging.

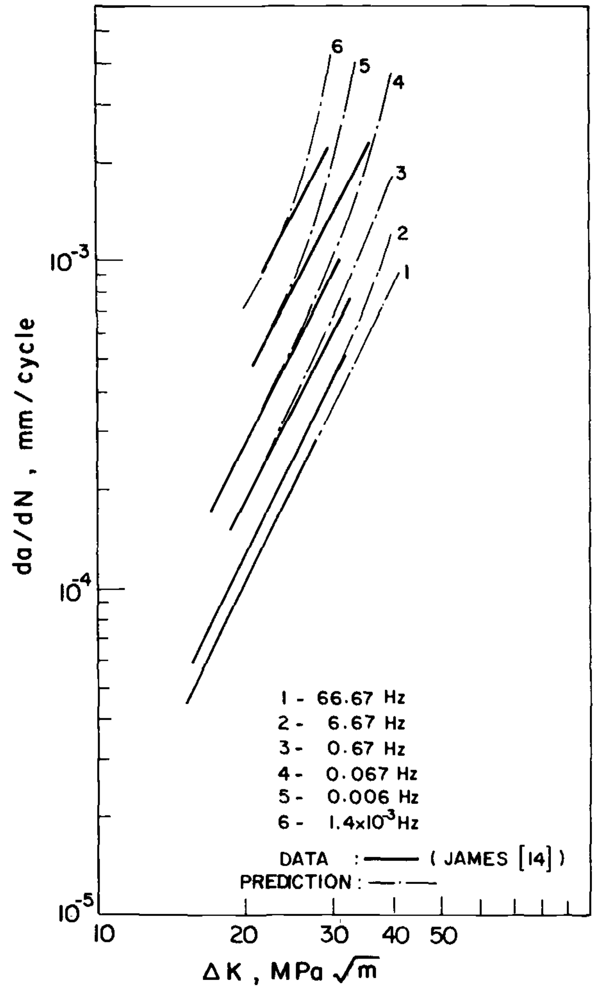

FIG. 4—*Comparison of predicted and observed crack growth rates versus stress intensity factor range for AISI Type 304 stainless steel at 538°C.*

Discussion

The proposed model, which has been presented under different forms (Carden [*13*], Döner [*15*], Policella and Poirier [*17*], Ellison and Walton [*20*]), has mechanical and mathematical support through the damage concept. This approach is based on the continuity of the phenomenon, which includes both crack initiation and propagation. The model predicts crack

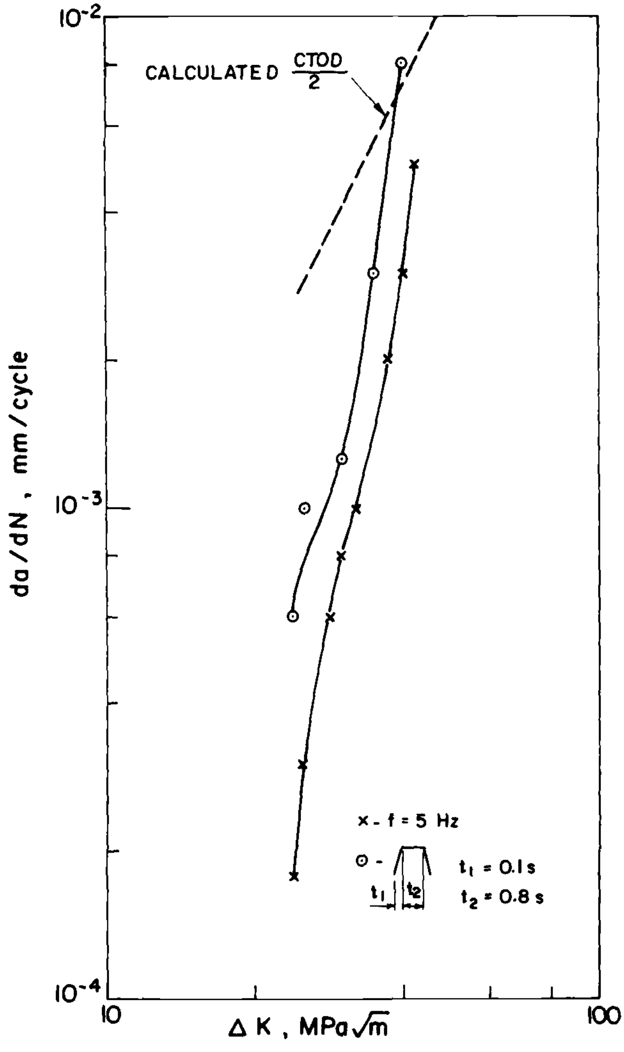

FIG. 5—*Crack propagation rate versus stress intensity factor range for AISI Type 304L stainless steel at 500°C. The calculated crack growth rate of one half the crack-tip opening displacement is also included.*

growth rates similar to those observed experimentally and is particularly suitable for application to viscoplastic materials such as austenitic stainless steel at elevated temperature. The domain for the use of the Paris law has been extended by inclusion of a creep component (Fig. 5) which allows the model to be used for the prediction of crack growth at different frequencies.

Examination of the fracture surfaces revealed a macroscopically flat sur-

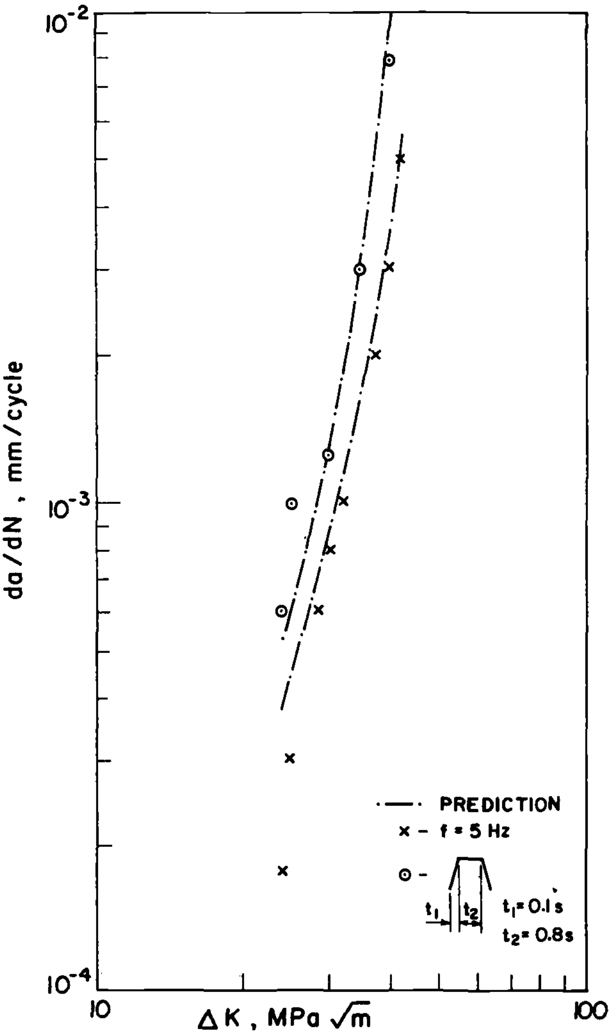

FIG. 6—*Comparison of predicted and observed crack growth rates versus stress intensity factor range for AISI Type 304L stainless steel at 500°C.*

face, particularly at low ΔK-values. Closer microscopic examination showed that faceted growth was the main mechanism. This agrees with the work of Hertzberg and Mills [22] who concluded that such growth in the low crack growth regime is common for close-packed structures. At higher crack growth rates ($da/dN \approx 10^{-3}$ mm/cycle) striations were present, although some intergranular side cracks were observed. The ΔK dependence on da/dN gave a Paris exponent of 3.54, emphasizing the dominance of a fatigue-controlled fracture process. Lloyd [*19*] indicated that for high-temperature fatigue crack growth of austenitic stainless steel, the crack-tip opening displacement (CTOD) may be used as an upper bound (that is, $da/dN = 1/2$ CTOD $= 0.225\ \Delta K^2/2E\sigma_y$ where σ_y is the yield stress). The simple relation $da/dN = 1/2$ CTOD is included in Fig. 5 for comparison with the present work. It will be noticed immediately that practically all the observed and predicted crack growth data lie below this relationship.

Introduction of a short dwell period, approximated by a decrease in frequency, increased the crack growth rate, yet the Paris slope and the predominantly transgranular fracture path remained unchanged. With an increase in dwell time, internal damage is facilitated at grain boundaries, particularly within the plastic zone at the tip of the crack [*23*]. The dominant transgranular fatigue crack will be able to move faster by linking these regions of intergranular damage ahead of the crack; this will result in an increased propagation rate. The conditions for void linkage by a moving fatigue crack have been analyzed by Anderson [*24*] and Tomkins [*25*].

The influence of changing the external load has not been taken into account for the present work. If it were, the cumulative effects of creep, fatigue, and work hardening would have to be considered. Ductile materials have a good memory effect, since the first loading sequence is important. It is suggested that the work-hardening effect may be introduced through the threshold stress intensity factor, which deals with the plastic zone size and shape as well as the work-hardening parameters. Also, other work [*26*] has shown that thermal aging influences the threshold stress intensity factor of a plain carbon steel.

Conclusions

The introduction of short dwell periods during each cycle of load controlled tests conducted on austenitic stainless steel at 500°C resulted in an increase in the crack propagation rate measured by the potential drop technique. This behavior may be predicted by applying a model developed for the crack growth rate of viscoplastic materials based on the damage concept. The inclusion of frequency terms in this model accounted for the viscoplastic behavior of austenitic stainless steel at elevated temperatures. Good correlation between the calculated and observed crack propagation rates was observed.

Acknowledgments

The authors extend their sincere thanks to Professor Jean Lemaitre, University of Paris (VI), and Dr. Jean-Louis Chaboche, ONERA, Châtillon, France, for helpful discussions regarding the damage concept. Part of this work has been supported by the Natural Sciences and Engineering Research Council of Canada through Grant A-2770.

References

[*1*] Hertzberg, R. W., *Deformation and Fracture Mechanics of Engineering Materials*, Wiley, New York, 1976.

[*2*] Bui, H. D., *Mécanique de la Rupture Fragile*, Masson Editeur, Paris, 1978.

[*3*] Fu, L. S., *Engineering Fracture Mechanics*, Vol. 13, 1980, pp. 307-330.

[*4*] Van Leeuwen, H. P., *Engineering Fracture Mechanics*, Vol. 9, 1977, pp. 951-974.

[*5*] Guinemer, J-Y., "Etude Phénomènologique de la Progression des Fissures de Fatigue dans les Métaux à Chaud," Diplome de Docteur-Ingenieur, Université P. M. Curie, Paris, June 1980.

[*6*] Lamaitre, J. and Chaboche, J-L., "A Non-Linear Model of Creep-Fatigue Damage Accumulation and Interaction," in *Proceedings*, Symposium on Mechanics of Viscoelastic Media and Bodies, International Union of Theoretical and Applied Mechanics, Gothenburg, 1974.

[*7*] Chaboche, J-L., Policella, H., and Savalle, S., "Application of the Continuous Damage Approach to the Prediction of High Temperature Low-Cycle Fatigue," Conference sur les Alliages à Haute Température pour Turbines à Gaz Cost 50 Program Liège, 25-27 Sept. 1978.

[*8*] Lemaitre, J. and Plumtree, A., *Journal of Engineering Materials and Technology, Transactions of ASME*, Vol. 101, 1979, pp. 284-292.

[*9*] Kachanov, L. M., "Time of Rupture Process under Creep Conditions," *Izv. Akad. Nauk.*, SSR Otd. Tekh. Nauk., Nr 8, 1958.

[*10*] Plumtree, A. in *Mechanical Behaviour of Materials*, Vol. 2, K. J. Miller and R. F. Smith, Eds., Pergamon, Oxford and New York, 1979, pp. 79-89.

[*11*] Neuber, H., *Journal of Applied Mechanics, Transactions of ASME*, Vol. 28, 1961, pp. 544-550.

[*12*] Topper, T. H., Wetzel, R. M., and Morrow, J. D., *Journal of Materials*, Vol. 4, No. 1, 1969, pp. 200-209.

[*13*] Carden, A. E., "Parametric Analysis of Fatigue Crack Growth," Paper C324/73, International Conference on Creep and Fatigue in Elevated Temperature Applications, Philadelphia, Sept. 1973, Sheffield, U.K., April 1974.

[*14*] James, L. A., "Frequency Effects in the Elevated Temperature Crack Growth Behaviour of Austenitic Stainless Steel—A Design Approach," ASME, Publication 78-PVP-97, Pressure Vessels and Piping Conference, Montreal, June 1978.

[*15*] Döner, M., *Journal of Engineering for Power, Transactions of ASME*, Vol. 98, 1976, pp. 473-479.

[*16*] Plumtree, A. and Douglas, M. J. in *Advances in Fracture Research*, Vol. 5, D. Francois et al, Eds., Pergamon Press, Oxford and New York, 1981, pp. 2423-2439.

[*17*] Policella, H. and Poirier, D., "Progression des Fissures de Fatigue et de Fluage dans les Milieux Viscoplastiques à Haute Temperature," Communication aux Journées d'Automne de la Métallurgie, Oct. 1979, à paraître.

[*18*] Kawasaki, T. and Horiguchi, M., *Engineering Fracture Mechanics*, Vol. 9, 1977, pp. 879-889.

[*19*] Lloyd, G. J., "The Relationship between Creep Crack Growth Rates and Creep-Fatigue Crack Growth Rates in Austenitic Type 316 Steel," Paper C213/80, International Conference on Engineering Aspects of Creep, Sheffield, U.K., Sept. 1980, pp. 239-247.

[*20*] Ellison, E. G. and Walton, D., "Fatigue, Creep and Cyclic Creep Crack Propagation in 1Cr-Mo-V Steel," Paper C173/73, International Conference on Creep and Fatigue in Elevated Temperature Applications, Philadelphia, Sept. 1973, Sheffield, U.K., April 1974.

[*21*] Baudin, G. and Policella, H. in *Advances in Fracture Research*, Vol. 4, D. Francois et al, Eds., Pergamon Press, Oxford and New York, 1981, pp. 1957-1964.

[22] Hertzberg, R. W. and Mills, W. J. in *Fractography-Microscopic Cracking Processes, ASTM STP 600,* American Society for Testing and Materials, 1976, pp. 220-234.

[23] Plumtree, A. in *Proceedings,* International Symposium on Low Cycle Fatigue Strength and Elasto-Plastic Behaviour of Materials, K. T. Rie and E. Haibach, Eds., D. V. M. Stuttgart, Oct. 1979, pp. 83-92.

[24] Anderson, H., *Journal of the Mechanics and Physics of Solids,* Vol. 25, 1977, p. 217.

[25] Tomkins, B. in *Elevated Temperature Fracture Mechanics in Fracture Mechanics: Current Status, Future Prospects,* R. A. Smith, Ed., Pergamon Press, Oxford and New York, 1979.

[26] Bailon, J. P., Masounave, J., and Dickson, J. I. in *Le Seuil de Propagation; Fatigue des Materiaux et Structures,* C. Bathias and J. P. Bailon, Eds., Maloine S. A. Editeur, Paris, 1980.

Summary

Summary

The purpose of the Symposium on Mechanical Testing for Deformation Model Development was to bring together active participants in deformation modeling from the communities of materials science and analytic mechanics with representation in each field of theory and experiment. The continuum thermodynamics community, unfortunately, was not strongly represented.

It is evident that each technical discipline involved in the development of deformation models requires, and therefore emphasizes, certain characteristics of a proposed material law, which may be summarized as follows.

Experimental

- readily measurable constants and variables, in one-dimensional stress if possible.
- formulations which provide for measurement of constants with an experimental matrix of manageable and economic size.
- recognition of development of anisotropy during large deformations, and the impositions of appropriate strain limits on model applicability.

Computational

- minimum number of constants and variables.
- material response to deformation increment must be predictable from the present state.
- evolutionary equations which can be evaluated with precision and hence do not involve small differences between large numbers.
- general flow formulations applicable to reversed, intermittent, and transient processes.
- multiaxial formulations.

Materials Science

- functions based on valid microstructural processes for reliable extrapolation.
- recognition and proper accounting of the history-dependent evolution of microstructure.

In general, deformation models are required anywhere material flow plays a role in the response. Within this broad scope, applications potentially include:

Metal Forming and Process Modeling

- analyze, optimize, and design metal-forming processes to control microstructure and properties in finished shape.
- computation of the solid-state flow associated with welding.
- powder metallurgy (for example, flow and consolidation during hot isostatic pressing).

Prediction of Deformation In Service

- distortion in components of high-temperature energy systems (for example, gas turbines, solar receivers, and nuclear reactors).
- creep of geological structures which may be used for storage of hydrocarbons and nuclear waste.

Micromechanics of Flow in Heterogeneous Media

- modeling of plastic or process zone ahead of a notch or growing crack.
- behavior of the matrix surrounding growing cavities, either tensile or creep fracture.
- behavior of the flowing matrix in composites.
- surface flow and ductile fracture in erosion and wear studies.

A few of the papers in this volume deal with the application of new deformation models to problems of current interest. The examples presented include weld modeling and creep of both geologic salt beds and nuclear fuel cladding. A need is to predict long-term behavior such as creep, fatigue, and slow crack growth, with readily and economically measurable variables such as short-term tensile strength and stress relaxation. Three papers deal with fracture prediction: the first by incorporating a "damage" measure based upon an internal state variable into the deformation model; the second by predicting crack growth rates by modeling flow and microvoid formation in the crack-tip plastic zone; and the third by predicting fatigue life from the calculated stable hysteresis loop and a phenomenological "damage" concept.

The following three sections summarize the papers from each of the groups.

Implications of Experimental Techniques

Krempl describes a model that interrelates responses under constant strain rate, constant stress, and relaxation conditions for Type 304 stainless steel.

His experimental observations indicate behavior that is independent of previous strain-rate history (perhaps because the experiments involved room-temperature deformation and strains of less than 15 percent). The model is built on an "overstress" concept in which there is a "basic" σ versus ϵ response at $\dot{\epsilon} = 0$, with the flow stress increasing as $\dot{\epsilon}$ increases above zero. The model is valid so long as the overstress does not change sign (as it would in cyclic deformation). The major theme of the paper by *Alden* is the use of tests involving jumps in loading rate to distinguish between time-dependent and time-independent deformation. The controversial nature of the paper derives from the phenomenological model presented, and a possible role of data acquisition equipment in limiting short-time observations. *Christodoulou et al* report experiments obtained with servocontrolled testing using diametral strain measurements up to and beyond necking. Data analysis shows that the work-hardening and strain-rate sensitivity coefficients are not constant but may vary appreciably during deformation.

A creeping aluminum thin rod was repeatedly twisted and untwisted by *Gacougnolle et al.* Accurate axial and rotary displacement measurement showed no influence of small twists on axial creep and an elastic torsional deformation. The authors conclude that the friction stress increases during primary creep. In a paper dealing with general considerations in model development, *Holbrook et al* present a comprehensive, detailed analysis of machine-specimen interactions. Elastic response of the testing machine can affect interpretations of mechanical test data, making experiments performed on servocontrolled machines (effectively of infinite stiffness) the most unambiguous. Finally, *Jones et al* show that interpretation of the strain transient dip test for measuring back stress depends upon the patience of the experimenter and the sensitivity of the recording instruments.

Phenomenological Modeling and Applications

Kocks reviews the various mathematical expressions used to describe tension-test behavior. Kocks favors the "Voce" law, which assumes that a saturation stress exists for each set of deformation conditions. He concludes that for variable histories a differential constitutive equation with one internal state variable is preferable. The resulting relation is probably restricted to unidirectional flow. Kocks proposes a specific investigation to delineate domains of deformation where one-internal state variable formulations are applicable. *Krieg* presents a multiaxial unified creep-plasticity model incorporating a back stress to describe the triaxial creep of geologic salt. The work presents an interesting contrast to the micromechanical model by *Arieli et al* for the same material. Krieg concludes that a single deformation mechanism operates over the stress and temperature range of interest, and that the model successfully describes primary and secondary creep and reversed loading behavior.

Alexopoulos et al present a model extending the state variable model of Hart. Two additional strain elements have been added to Hart's model. The first, denoted as "microplastic," helps simulate cyclic strain situations (small strain ranges only). The second addition is an explicit mathematical representation for grain boundary sliding. *Miller et al* present further evaluation of the MATMOD constitutive model. They measure the back stress from both stress drop tests and Bauschinger effect measurements in cyclic torsion tests. These authors find that the two tests produce different results, and that satisfactory prediction of observed behavior requires further modification of the model. *Duncan and Giedt* calculate the residual stresses and weld zone evolution in a GTA weld. They show that a time-dependent constitutive model is required to account for softening in the heat-affected zone of cold-worked material. *Garud* describes a model for multiaxial nonproportional deformation, which is an extension of and improvement on the approach of Mroz involving "nested" yield surfaces. The model (ultimately used in multiaxial fatigue failure predictions) concentrates exclusively on the cyclically saturated response, but within this domain shows good agreement against two independent investigations involving out-of-phase multiaxial test loadings. *Stouffer and Bodner* develop an evolution equation for the internal variable in the Bodner-Partoum state variable model. They describe a "damage" variable for tensile fracture related to the stored energy of inelastic work.

Klepaczko and Duffy measure the effect of strain-rate history in torsion over a wide range of strain rates, observing that FCC and BCC metals respond differently. They present a descriptive model incorporating a back stress which they relate to the Peierls stress. *Cook* points out an interesting problem encountered in developing constitutive equations for Inconel 718. In characterizing its cyclic stress-strain behavior, tests with $R = 0$ are generally used (R is the ratio of the maximum to minimum strain). The mean strain produces a mean stress. At high strain amplitudes the mean stress relaxes before cyclic saturation, but at low strain amplitudes it does not. This results in a peak tensile stress that decreases with increasing strain range, which complicates the modeling problem. *Krausz and Faucher* apply reaction rate theory to produce a constitutive model for rate-dependent deformation, and discuss its ability to describe experimentally observed trends.

Microstructural Evolution and Derived Models

Nix et al develop a composite model to describe steady-state creep and power law breakdown in dislocation-strengthened metals. They assume that hard and soft regions develop in the substructure and that each region contributes separately to elevated temperature flow. The model describes power law breakdown well, but may be difficult to justify physically since the required breakdown of cell walls at high stresses has not been observed. *Turner and Hasegawa* then present a discussion of the difficulties facing practitioners attempting to develop constitutive models based upon mechanical equation of state concepts. The authors show that to describe cyclic creep in Type 304 stainless steel, a successful model must incorporate two internal variables and an interaction between kinematic and isotropic hardening. *Arieli et al* present a micromechanical study of flow in polycrystalline NaCl. They develop constitutive equations based upon rate-controlling processes identified for separate domains of stress and temperature. The work presents an interesting alternative to the phenomenological model proposed by Krieg for the same material. *Stevenson* fits an empirical stress-strain relation to the flow behavior of a steel and an aluminum alloy, accounting for strain and strain-rate hardening in the process. He concludes that it may be possible to infer the significance of recovery processes by noting which type of empirical relation best describes the flow behavior. *Murty and Adams* successfully model anisotropic multiaxial creep in Zircaloy-4 tubing by statistically averaging crystallite behavior as functions of its orientation in the aggregate. *Wolfenden* evaluates the capabilities of two work-hardening theories for two-phase alloys to describe the behavior of unidirectionally solidified eutectics. Both models use stored energy as a measure of work hardening and are limited to small-strain monotonic flow.

Ghosh and Raj introduce grain size as a parameter in modeling superplastic flow. Actual grain size distributions were measured and used in the constitutive equation. In agreement with *Langdon and Vastava,* elevated temperature deformation in metals is grouped into intrinsic grain boundary sliding and grain matrix accommodated flow. However, *Langdon and Vastava* demonstrate that presently available theories of intrinsic sliding or matrix accommodated sliding are not in agreement with measurements. Finally, *Guinemer and Plumtree* develop a crack growth rate model for cyclic deformation at elevated temperature. The kinetics derive from a "damage" process consisting of microvoid formation in the crack-tip plastic zone. Their paper provides an example of application of a continuum flow law to micromechanical modeling.

Concluding Remarks

A number of different modeling concepts were addressed at this symposium. The editors were impressed, however, with the pervasive importance of two. Firstly, a variety of state variables were proposed and discussed, including stress rate (Alden), work-hardening rate (Kocks), and stored energy of plastic work (Stouffer and Bodner, and Wolfenden). It would be useful to identify those state variables that are general and those that are limited in applicability, or in fact not valid. For example, time and strain are two often-used, but operationally ill-defined, variables. The development of consensus models could then proceed with greater unity. Secondly, the origin and measurement of the "back-stress" presents an area of controversy. It is not clear that various authors mean the same thing by their use of the term; in fact, different authors employ the terms "threshold stress," "rest stress," "friction stress," or "internal stress," for what is apparently the same observable. The experiments by Miller et al and Jones et al suggest that the elusive variable is experiment-dependent, and Nix et al tackle the unresolved question of the microstructural origins of the internal stress.

The ever-increasing complexity required of models in order to predict ever wider variants of observed inelastic flow behavior seems to the editors to have reached a point of diminishing returns. If in seeking to simplify experiments by developing internal variable models the burden is merely shifted to the computational community, there is no net gain. A continuing dialogue among the contributing communities, such as was attempted in this symposium, would be of great value here. ASTM can play a vital role in this area through its sponsorship of interdisciplinary symposia. The editors would appeal to Pareto's Law for guiding the formulation of constitutive models. In this application the law would read "describe eighty percent of the behavior with twenty percent of the effort." Thus the additional complexity required of models in attempts to extend their application to microplasticity, anelastic transients, impurity effects, and the like, may not bring sufficient improvement in predictability or computational capability to merit the development effort required. A goodly amount of judgment and enlightened selectivity is required here as to which variables are important and which are secondary. The answer may ultimately depend upon the application. In this area as well, progress will be greatly facilitated by interdisciplinary symposia.

R. W. Rohde

Sandia National Laboratories, Albuquerque, New Mexico; symposium co-chairman and co-editor

J. C. Swearengen

Sandia National Laboratories, Livermore, California; symposium co-chairman and co-editor

Index